



HAL
open science

Contribution to the variable gain observer synthesis for nonlinear systems : application on the estimation of tyre rolling resistance

Anshul Kumar Sharma

► To cite this version:

Anshul Kumar Sharma. Contribution to the variable gain observer synthesis for nonlinear systems : application on the estimation of tyre rolling resistance. Mechanical engineering [physics.class-ph]. École centrale de Nantes, 2020. English. NNT : 2020ECDN0049 . tel-03237827

HAL Id: tel-03237827

<https://theses.hal.science/tel-03237827v1>

Submitted on 26 May 2021

HAL is a multi-disciplinary open access archive for the deposit and dissemination of scientific research documents, whether they are published or not. The documents may come from teaching and research institutions in France or abroad, or from public or private research centers.

L'archive ouverte pluridisciplinaire **HAL**, est destinée au dépôt et à la diffusion de documents scientifiques de niveau recherche, publiés ou non, émanant des établissements d'enseignement et de recherche français ou étrangers, des laboratoires publics ou privés.

THESE DE DOCTORAT DE

L'ÉCOLE CENTRALE DE NANTES

ÉCOLE DOCTORALE N° 602

Sciences pour l'Ingénieur

Spécialité : Génie mécanique

Par

Anshul Kumar SHARMA

Contribution à la synthèse d'observateur à gain variable pour les systèmes non linéaires : application à l'estimation de la résistance au roulement

Thèse présentée et soutenue à Nantes, le 17/12/2020

Unité de recherche : Aménagement, Mobilité, Environnement (AME), Université Gustave Eiffel

Rapporteurs avant soutenance :

Krishna BUSAWON Professeur, Northumbria University (Royaume-Uni)
Didier REMOND Professeur des universités, INSA Lyon, Villeurbanne

Composition du Jury :

Président :	Franck PLESTAN	Professeur des universités, École Centrale de Nantes
Examineurs :	Minh-Tan DO	Ingénieur des DTPE HDR, Université Gustave Eiffel, Bouguenais
	Rabia SEHAB	Enseignante chercheuse, ESTACA, Laval
	Mohamed DJEMAI	Professeur des universités, Université Polytechnique Hauts de France, Valenciennes

Dir. de thèse : Véronique CEREZO
Co-encadrant : Mohamed BOUTELDJA

Ingénieure IPEF HDR, Université Gustave Eiffel, Bouguenais
Chargé de recherche HDR, CEREMA, Bron

Acknowledgement

Firstly, I would like to express my sincere gratitude to my supervisors Véronique Cerezo and Mohamed Bouteldja for the continuous support of my thesis, for their patience, motivation, and immense knowledge. Their guidance helped me in all the time of research and writing of this thesis. I could not have imagined having a better advisor and mentor for my thesis.

Besides my advisor, I would like to thank the rest of my thesis committee: Prof. Mohamed Djemai, Prof. Rochdi Merzouki, Gilles Gauthier and Minh-Tan Do, for their insightful comments, proposals and criticisms, always constructive, that they were able to formulate on this work.

I would like to offer my special thanks to Angélique, Samuel and Sebastien for the various experiments on test tracks they were able to carry out for my thesis.

I also thank Prof. Krishna Busawon and Prof. Didier Remond, who agreed to be referees for this thesis, Min-Tan Do, Rabia Sehab, Prof. Mohamed Djemai and Prof. Franck Plestan, who do me the honour to participate in my thesis jury.

I also wish to thank all the people of the EASE and SACIM laboratory for their warm and friendly welcome. Thank you to Manuela, Tan, Malal, Christophe, Pierre, Nicolas, Mathias, Marie-Odile, Cedric, Jean-Giono, Agnés, Djemila and Cyrille for their sympathy during the thesis.

I could not have completed this thesis without the support of my friends Jesbeer, Ebrahim and Wiyao who provided stimulating discussions as well as happy distractions to rest my mind outside of my research.

Of course, this acknowledgement would not be complete without thanking my parents, grandparents, especially my nanaji J. P. Gaur, my brother Tarun, sister Ujjawal and family who supported me throughout my entire study. I am forever indebted to my parents for giving me the opportunities and experiences that have made me who I am. They selflessly encouraged me to explore new directions in life and seek my own destiny. This journey would not have been possible if not for them, and I dedicate this milestone to them.

Finally, but not the least I would like to thank my spouse Bhawna for her infinite patience and her unfailing support during the thesis.

Table of contents

Acknowledgement	1
General Introduction	7
Motivations.....	8
Methodology	13
Thesis contributions	15
Organisation of report	15
Chapter 1 State of art	17
1.1. Energy losses on a vehicle.....	18
1.2. Rolling resistance overview	19
1.2.1. Definition and mechanism.....	20
1.2.2. Influencing parameters of rolling resistance	21
1.2.2.1. Tyre inflation pressure variation.....	22
1.2.2.2. Load variation.....	23
1.2.2.3. Speed variation	23
1.2.2.4. Road characteristics variation.....	24
1.2.2.5. Ambient temperature variation.....	28
1.2.2.6. Tyre dimensions variation	29
1.2.3. Rolling resistance coefficient model	30
1.2.3.1. Empirical models.....	30
1.2.3.2. Physical model	32
1.2.3.3. Other models	33
1.2.4. Rolling resistance measurement methods	34
1.2.4.1. Experimental methods	34
1.2.4.2. Numerical methods.....	38
1.2.4.3. Virtual/software sensor methods	38
1.2.5. Conclusion.....	39
1.3. Virtual sensor background.....	40
1.3.1. Observability of nonlinear systems	41
1.3.2. Stability of dynamic systems.....	43
1.3.3. Canonical forms of nonlinear system	45
1.3.3.1. Canonical form	45
1.3.3.2. Particular class of the canonical form.....	45

1.3.4.	Different nonlinear observers	48
1.3.5.	Conclusion.....	50
1.4.	Different adaptive observer techniques comparison	51
1.4.1.	Quarter car	51
1.4.2.	Observer design.....	52
1.4.2.1.	State space model	52
1.4.2.2.	Observability analysis	53
1.4.2.3.	Adaptive high gain observer.....	53
1.4.2.4.	Adaptive gain second order sliding mode observer.....	54
1.4.2.5.	Simulation results and discussion.....	55
1.4.3.	Conclusion.....	59
Chapter 2	<i>Tyre modelling</i>	60
2.1.	Different tyre models comparison	61
2.2.	Development of Multi physical tyre (MPT) model	66
2.2.1.	Mechanical model	66
2.2.2.	Thermal model	69
2.2.2.1.	Heat generation.....	69
2.2.2.2.	Heat exchange	70
2.2.2.3.	Cooling by convection force	71
2.2.2.4.	Loss of heat by the viscoelastic effect	71
2.2.3.	Integration of thermal model	72
2.2.4.	Sensitivity study and simulation results	73
2.3.	Influence of road surface texture on the MPT model	78
2.4.	Conclusion.....	79
Chapter 3	<i>Vehicle modelling</i>	81
3.1.	Different vehicle model comparison	82
3.2.	Development of 3-D vehicle model	83
3.2.1.	Different hypothesis for vehicle model	84
3.2.2.	Coordinate system and transformations	85
3.2.3.	Vehicle model.....	85
3.2.3.1.	Equation of motion	86
3.2.3.2.	Model of the independent suspension system	87
3.2.3.3.	Tyre ground interaction	88

3.2.4.	Validation and simulation results	90
3.3.	Conclusion.....	97
Chapter 4	<i>Synthesis of adaptive nonlinear observers</i>	99
4.1.	System description and problem formulation.....	100
4.2.	Development of adaptive observers for nonlinear systems	102
4.2.1.	Unknown input adaptive high gain observer for regular systems	102
4.2.1.1.	State space model	102
4.2.1.2.	Observer synthesis.....	103
4.2.2.	Adaptive high gain observer for singularly perturbed systems	105
4.2.2.1.	The slow reduced systems	106
4.2.2.2.	The fast reduced system	107
4.2.2.3.	Observer synthesis.....	107
4.3.	Application on the full vehicle for estimation of tyre rolling resistance	109
4.3.1.	Estimation of tyre rolling resistance for regular systems	109
4.3.1.1.	State space model	109
4.3.1.2.	Observer synthesis.....	110
4.3.1.3.	Numerical validation	113
4.3.2.	Estimation of tyre rolling resistance for the singular perturbed system	116
4.3.2.1.	State space model	116
4.3.2.2.	Observer synthesis.....	118
4.3.2.3.	Numerical validation	119
4.4.	Conclusion.....	123
Chapter 5	<i>Instrumentation, Experimentation and Validation</i>	124
5.1.	Instrumentation.....	125
5.1.1.	Experimental site description	125
5.1.2.	Test vehicle and sensors	127
5.1.2.1.	Focus on tyre instrumentation	131
5.2.	Design of experiments.....	133
5.2.1.	Post-processing and analysis of experimental data	135
5.3.	Reference tyre rolling resistance	137
5.3.1.	Reference rolling resistance method	137
5.3.2.	Loaded radius calculation.....	138
5.3.3.	Rolling resistance influencing factors	140

5.3.3.1.	Influence of ambient temperature on Crr	140
5.3.3.2.	Influence of tyre inflation pressure on Crr	143
5.3.3.3.	Influence of vehicle load on Crr	144
5.3.3.4.	Influence of vehicle speed on Crr.....	145
5.3.3.5.	Influence of road surface roughness on Crr.....	147
5.3.4.	Validation of reference rolling resistance.....	152
5.3.5.	Conclusion.....	153
5.4.	Experimental investigation of the variation of tyre surface temperature	154
5.4.1.	Tyre surface temperature variation in different conditions	154
5.4.1.1.	Variation at a constant speed.....	155
5.4.1.2.	Variation at different ambient temperature	158
5.4.1.3.	Variation on different test surfaces.....	159
5.4.1.4.	Variation at different vehicle manoeuvres.....	163
5.4.2.	Lateral Tyre surface temperature variation	167
5.4.2.1.	Variation for various test track with different roughness	167
5.4.2.2.	Variation at a constant speed.....	170
5.4.2.3.	Variation at different vehicle manoeuvres.....	171
5.4.3.	The relation between tyre surface temperature and speed.....	175
5.4.4.	Conclusion.....	177
5.5.	Experimental validation	179
5.5.1.	Model validation.....	179
5.5.1.1.	Validation of the MPT model.....	180
5.5.1.2.	Validation of the full vehicle model	183
5.5.2.	Experimental validation of rolling resistance estimation	186
5.5.2.1.	Estimation of tyre rolling resistance for regular systems	189
5.5.2.2.	Estimation of tyre rolling resistance for the singular perturbed system	195
5.6.	Conclusion.....	205
Chapter 6	Conclusion and perspectives	206
6.1.	Conclusion.....	207
6.2.	Perspectives.....	209
6.2.1.	Modelling	209
6.2.2.	Experimentation	209
6.2.3.	Estimation technique	210
6.2.4.	Real-time estimation.....	210

<i>References</i>	211
<i>List of figures</i>	223
<i>List of tables</i>	231
<i>Appendix</i>	232

General Introduction

Motivations

The continuous rise in temperature of the planet is a major concern for humanity for a few decades. The root cause of this is global warming. Global warming begins when sunlight reaches the Earth. The clouds, atmospheric particles, reflective ground surfaces and surface of oceans then sends back about 30% of sunlight back into space, whilst the remaining is absorbed by oceans, air and land. This consequently heats the surface of the planet and atmosphere, making life feasible. As the Earth warms up, this solar energy is radiated by thermal radiation and infrared rays, propagating directly out to space thereby cooling the Earth. However, some of the outgoing radiation is re-absorbed by carbon dioxide, water vapours, ozone, methane and other gases in the atmosphere and is radiated back to the surface of Earth [1]. These gases are commonly known as greenhouse gases due to their heat-trapping capacity. It must be noted that this re-absorption process is good as the Earth's average surface temperature would be very cold if there was no existence of greenhouse gases. The dilemma began when the concentration of greenhouse gases in the atmosphere was artificially increased by humankind at an alarming rate since the past two centuries 2016 is the hottest year ever recorded [2]. The most extensive source of analysis on the potential impacts of climatic change can be found in the 5th Intergovernmental Panel on Climate Change (IPCC).

An increase of 2°C compared to the temperature in pre-industrial times is seen by scientists as the threshold. The increase beyond this is dangerous and possibly can initiate catastrophic changes in the global environment. For this reason, the international community has recognised the need to keep warming below 2°C [2].

At the global scale, the key greenhouse gases emitted by human activities are given in Figure 1, where CO₂ accounts for about 76% of total greenhouse gas emissions. Among all these gases, carbon dioxide (CO₂) is the most important, both for its role in the greenhouse effect and for its role in the human economy.

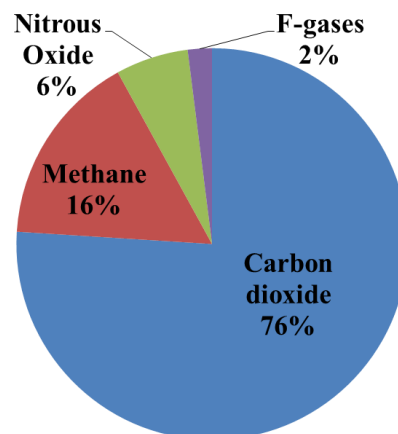


Figure 1 Distribution of emission of greenhouse gases

Its concentration in the atmosphere is currently 40% higher than the beginning of industrialisation began. Since 1751 the world has emitted over 1.5 trillion tonnes of CO₂ [3]. Fossil fuel use is the primary source of CO₂. Globally, economic and population growth continues to be the most important drivers of increases in CO₂ emissions from fossil fuel combustion.

The distribution of CO₂ emission for 2016 is presented in Figure 2. The primary sources of greenhouse gas emissions sector wise are electricity and heat (46%), transportation (22%), manufacturing (18%), Residential building (8%) and rest by others. It shows that the transportation and power generation sectors are major contributors to carbon dioxide (CO₂) emissions.

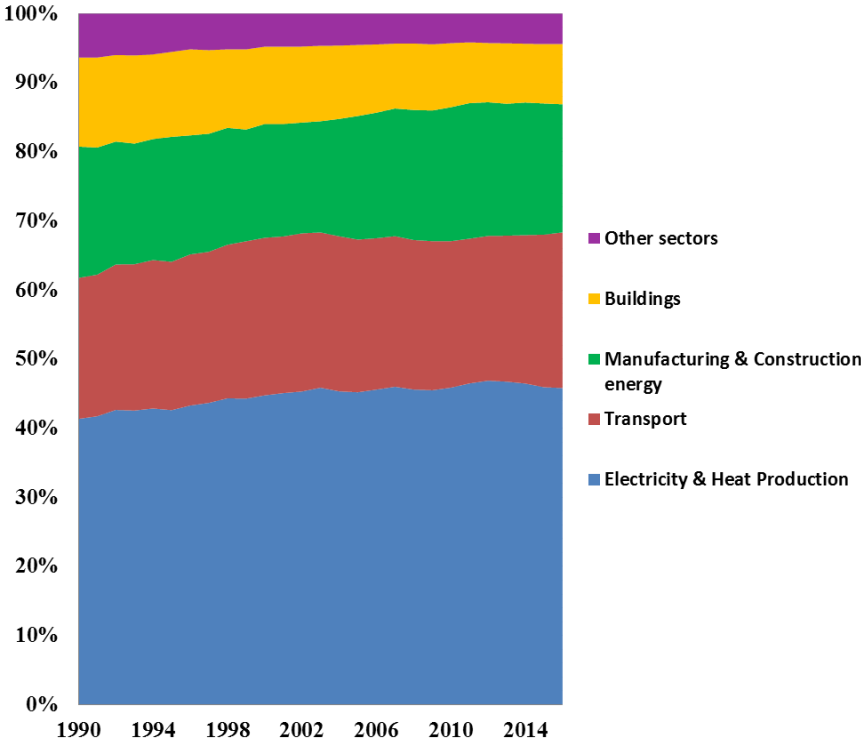


Figure 2 Global distribution of CO₂ emission sector-wise [4]

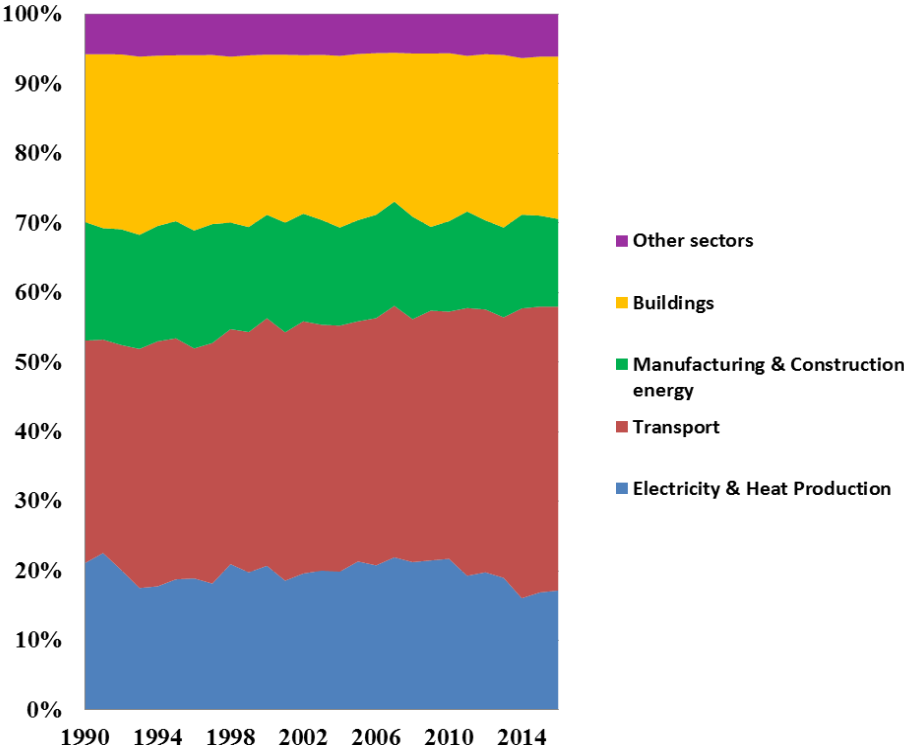


Figure 3 Distribution of CO₂ emission sector wise for France [4]

Nevertheless, France emits relatively little CO₂ for power generation (Figure 3) thanks to nuclear power. The share of transport, which relies almost entirely on the combustion of oil, is therefore logically higher than at world level, at 41%. This share is constantly increasing, while the other sectors have made notable efforts.

Transport remains very dependent on oil: oil-derived fuels account for 85% of energy consumption in transport. Since 2018, oil consumption from transport has been on an upward trend at an average rate of 2.2% each year. In Figure 4 we depict the absolute contribution of CO₂ emissions by source, differentiated between gas, liquid (i.e. oil), solid (coal and biomass), flaring, and cement production.

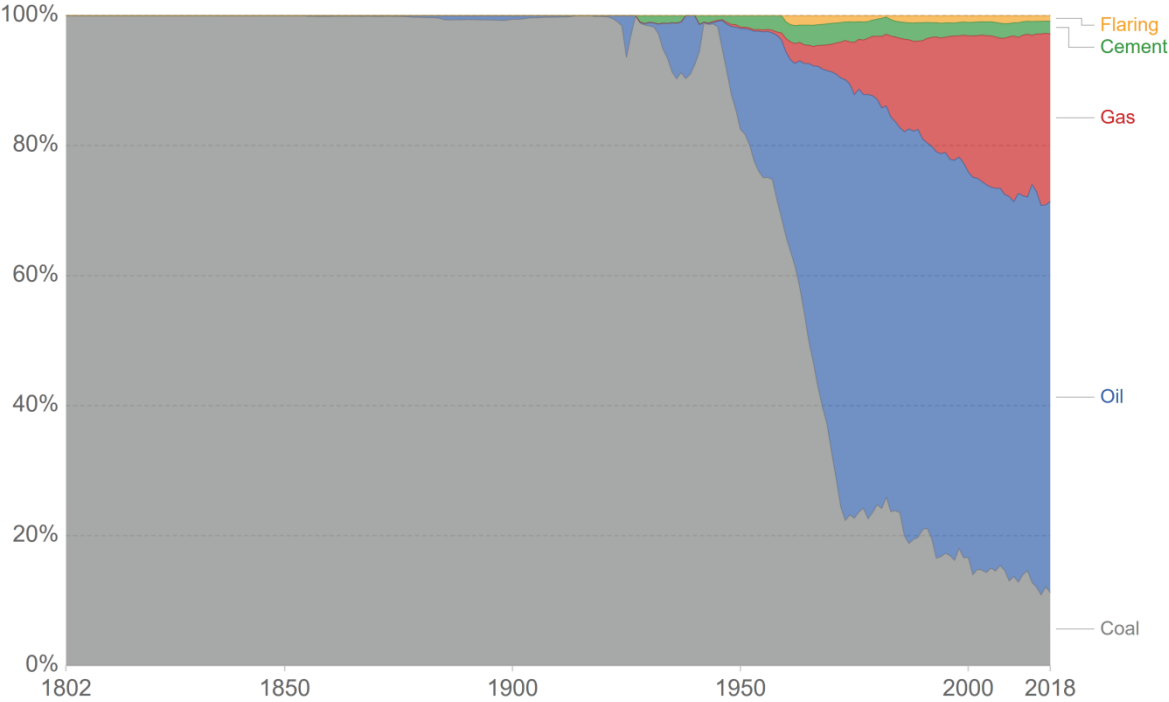


Figure 4 Distribution of CO₂ emission by fuel type for France[4]

Transport has been traditionally looked upon as a challenge in terms of reducing greenhouse gas emissions, and a lot of effort has been rightly directed to solve this issue. Transport is a ‘system of systems’ and resilience of each transport mode to the impact of future weather patterns along the entire network of global supply chains warrants consideration so that impacts, risks and vulnerabilities across transport modes are identified and addressed. There is, therefore, a major stake in reducing CO₂ emissions, which can result in the reduction of fuel consumption of vehicles.

In 2015, road transport was responsible for almost 73 % of the total greenhouse gas emissions from transport. Of these emissions, 62% were from passenger cars and two wheels, 11% from light commercial vehicles and 25% came from heavy-duty vehicles in EU as shown in Figure 5 [5]. In a world where oil tends to become scarce and expensive and where policies to reduce greenhouse gas emissions tend to be implemented in many countries, the reduction of fuel consumption by motor vehicles takes on an important dimension. Automobile manufacturers and tyre manufacturers have long been interested in this issue.

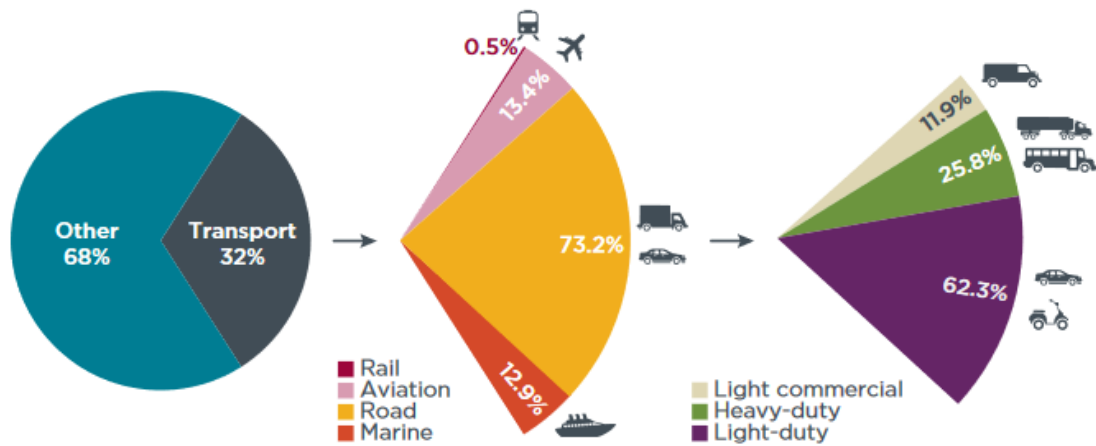


Figure 5 Distribution of CO₂ in the EU in the transport sector [5]

Fuel consumption, and hence CO₂ emission in road transport, depends on several factors that relate to the vehicles, the quality of the road, and their interaction. Fuel consumption is influenced by the energy losses experienced at different levels in the vehicle (aerodynamic effects, tyre/road contact, suspensions, etc.). According to [6], out of the energy output of fuel in a car engine, 33% is spent in the exhaust, 29% in cooling and 38% in mechanical energy, of which friction losses account for 33% and air resistance for 5% at 60km/h. By comparison, an electric car has only half the friction loss of that of a car with a conventional internal combustion engine.

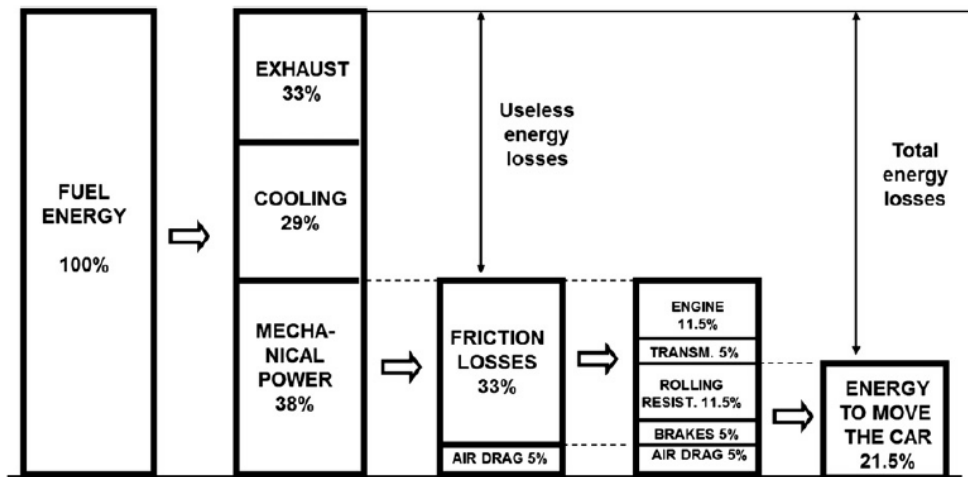


Figure 6 Breakdown of passenger car energy consumption, as approximated for a speed of 60km/h [6]

These energy losses experienced at different levels in the vehicle (aerodynamic effects, tyre/road contact, suspensions, etc.). There are five resistive forces, which oppose the advancement of the car; they are overcome by the fuel energy as shown in Figure 6.

Among all these resistive forces in a modern passenger car, depending on the driving conditions and tyre specifications, about 20–30% (in Figure 7) of total fuel consumption is related to rolling resistance [7]–[9]. Every day 2 million tonnes of fuel burns up to overcoming to rolling resistance according to [7], hence contributing to CO₂ emissions. However, recent studies have shown that even moderate decrease in rolling resistance allows for gains in fuel consumption. For instance, rolling resistance related to the road surface is responsible for about 20% of the CO₂ emitted by a passenger

car driving at 100 km/h [9]–[11]. In another study carried out in the United States [12], it is claimed that a 10% reduction in the average rolling resistance promised 1 to 2% increase in the fuel economy.

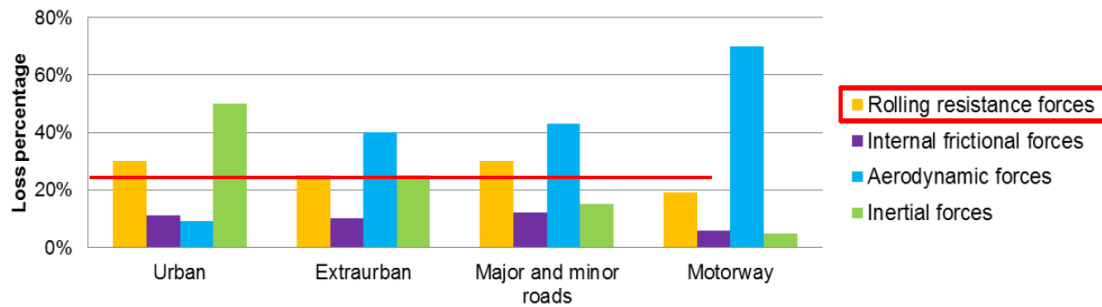


Figure 7 Percentage loss of vehicle energy with respect to different usage [1]

Tyres, which act as one of the most significant components in ground vehicles, account for 17-21% of the total energy consumption [7], [12]. Therefore, there is growing interest and demand for customers, tyre manufacturers, and governments to reduce the energy losses through tyres. According to the experimental results in [13], the hysteretic losses of tyre compounds dissipate 90-95% of tyre losses. Additionally, 2-10% of the losses are due to the tyre-road friction and 1.5-3.5% of the losses are due to the aerodynamic resistance. This dissipation of energy in tyres is called rolling resistance.

Lowering or optimizing rolling resistance in pneumatic tyres can therefore greatly contribute to the reduction of greenhouse gas emissions. Rolling resistance of pneumatic tyres has been the subject of extensive study in the past. The rolling resistance of the vehicle is still rather unknown and research should be conducted to be able to estimate it reliably and accurately. This accuracy is particularly necessary at the scale of a single vehicle, considering that the rolling resistance coefficient is a dimensionless quantity with an order of magnitude of 1 to 2% [14].

Physically, rolling resistance is unmeasurable. It highly depends on tyre parameters such as inflation pressure, temperature, road surface type, and vehicle speed [7]–[9]. Correlations with various parameters are found such as inflation pressure, tyre material properties and tyre temperature [15]–[19]. Most of these studies use either experimental data, analytical derivations on equivalent structures or finite element method (FEM) analyses to predict rolling resistance.

However, various measurement methods to measure the rolling resistance indirectly are described in [9] and [20], such as trailers, drums etc. Indeed, at present, these methods are inaccessible and very uncertain due to the quality of results, reproducibility of the measurements, limited to certain tyres and the high cost of physical sensors attached to vehicle tyres. These measurements are done in standard condition and controlled environment.

The last few decades have seen an increase in research on the development of driver assistance systems. These systems can alert the driver upstream of danger, their fuel consumptions and, for some, go as far as correcting the trajectory of the vehicle when it reaches, for example, critical situations for the dynamics. An important challenge for the development of current vehicles and autonomous vehicles is to ensure better energy management. The rolling resistance is one of the most important parameters affecting the fuel consumption and the performance of a vehicle. So there is a need to develop a system which can be installed on the vehicle itself to measure rolling resistance in real-time. Thus, the lack of complete physical phenomenon of tyre-contact dynamics to estimate it accurately is the main drawbacks.

In order to solve this difficulty, dedicated works are done in [21] with the aim to estimate the rolling resistance force by using virtual sensor based on the observer approach (sliding mode [22] and EKF). Indeed, these applications have been far from conclusive, as it served only under simplified conditions: on straight-line track at a constant speed and simplified tyre-road contact model. Therefore, no work has been done to estimate the rolling resistance in real driving conditions with experimentation validation.

Also, the influencing parameters such as the impact of road roughness and temperature are not included as far as to our knowledge. Moreover, these studies did not account for the source of uncertainty, convergence and real-time estimation. Research in this area is still quite recent and much work remains to be committed.

To address this problem, the adaptive gain nonlinear observer is explored for estimation of rolling resistance under real driving conditions that take account of all the parameters. This is motivated by the fact that the adaptive solution is the most suitable for the rolling resistance estimation because of variable dynamics and continuous change in a situation during the real driving situation. Their robustness to modelling error, parameter uncertainty and input noise used to detect the variation in the input. Their advantages and disadvantages have allowed choosing the most effective solution concerning accuracy, robustness and computing complexity.

The main objective of this thesis is to develop a system for the estimation of the tyre rolling resistance of a vehicle in real driving conditions. An indirect approach using software sensors and variable gain observers will be used. These observers will be based on the mathematical model of complete vehicle model which will be coupled with the multi-physical tyre model. It will simultaneously consider the various factors such as road roughness, tyre temperature etc. affecting rolling resistance and thus ensure accurate and robust estimation in time. This approach should reduce the sensitivity to measurement noise and ensure convergence in finite time of the numerical model. Particular attention will be paid to the inclusion of infrastructure characteristics (geometry, surface properties) and thermal properties in the model.

Methodology

The below-defined approach will make it possible to achieve the objective of the thesis in four steps Figure 8:

- State of art highlights the influencing parameters of rolling resistance and helps us to identify the most suitable approach with the help of a comparison study of different observation technique for the thesis.
- Development of multi-physical tyre model based on the influencing parameters identified in state of art. This model is coupled with a developed full vehicle model. The complete vehicle model is validated numerically with the help of simulation software SCANeR Studio (prosper).
- The synthesis of unknown input adaptive high gain observer for the estimation of rolling resistance for regular systems and the singular perturbed system is done and validated numerically. The methodology of the estimation is presented in Figure 9. From the mathematical model of a full vehicle, the dynamic states of a vehicle are then reconstructed and the tyre rolling resistance is estimated with the help of adaptive high gain observer.

- The design of experiments is proposed for the offline experimental validation for developed full vehicle model and the unknown input adaptive high gain observer for the estimation of rolling resistance tyre force.

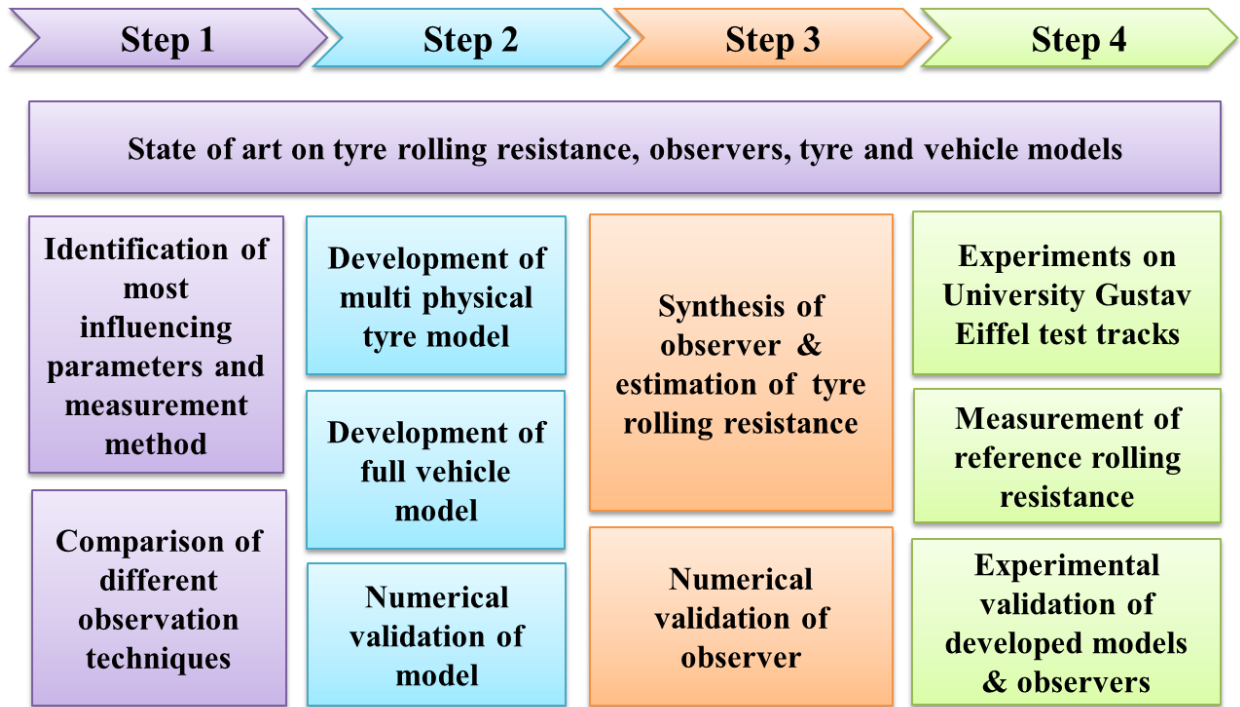


Figure 8 Thesis follow-up steps

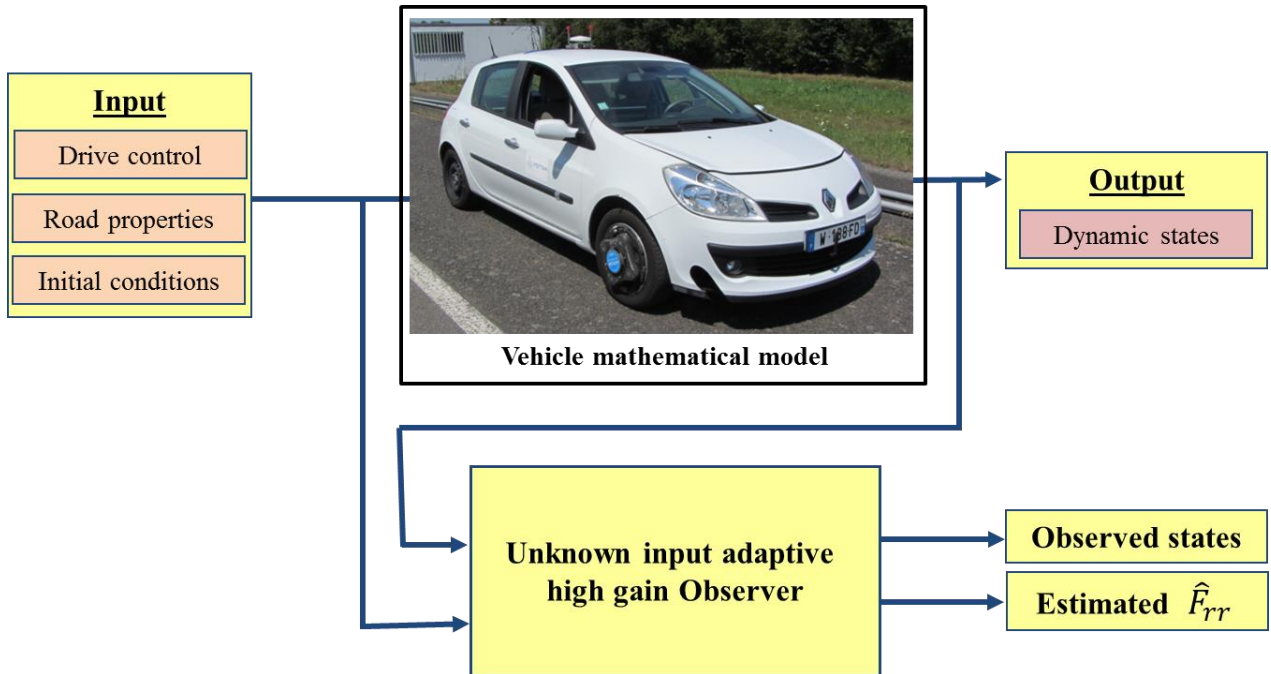


Figure 9 Methodology of tyre rolling resistance force (F_{rr}) estimation

Thesis contributions

The contributions of this thesis are as follows:

- Develop the multi-physical tyre (MPT) model with longitudinal, lateral and vertical dynamics. It integrates the mechanical, pneumatic and thermal physical phenomenon.
- Develop and validate a full vehicle dynamic model coupled with the multi-physical model.
- Develop in-situ experiments for the validation of the model and the approach of estimation of the rolling resistance on an instrumented vehicle
- Demonstrate the most influential parameters of tyre rolling resistance force and validation of a method to calculate the reference rolling resistance.
- Demonstrate the circumferential and lateral variation of tyre surface temperature.
- Develop and validate an adaptive, robust and reliable unknown input adaptive high gain observer for the estimation of rolling resistance.
- Develop and validate an unknown input adaptive high gain observer for singularly perturbed systems.
- Demonstrate the applicability of the estimator under real driving conditions.
- Develop parameter estimation methods for vehicle dynamic models using the estimated vehicle states, and contrast the performance of these methods in several scenarios.

Organisation of report

This report is organised as follows:

Chapter 1 of the thesis presents a state of the art on tyre rolling resistance force and virtual sensors. The first part addresses the tyre rolling resistance force by explaining fundamental concepts of resistive forces applied on vehicle. It discusses the mechanism and influencing parameters of tyre rolling resistance, which gives an overview of tyre rolling resistance force. Later it brings together the existing models and different measurement methods of rolling resistance with its limitations and advantages. The extensive comparison is presented for different measurement methods, which allow us to position this thesis with respect to the work done in the literature. Concerning the thesis, the virtual /software sensor or observer method is identified for estimating the tyre rolling resistance. This state of the art on rolling resistance gathers the different models, measurement method and influencing parameters from various literature studies. This will act as the base for further studies on rolling resistance. The state of art on observer starts with the background and reviews the theory of non-linear observers. It introduces the observability and stability of nonlinear systems. The synthesis of different nonlinear state observer methods existing in the literature is presented, such as Kalman filter, high gain, sliding and adaptive etc. We present an extensive discussion on different observer methods to allow identifying the approach suitable for this thesis. In the third part, particular attention is given to adaptive gain observer and the comparison study for the different adaptive gain observer on a quarter car is presented. The chapter ends with a conclusion to support the suitable observation approach for the thesis for rolling resistance estimation.

Chapter 2 is dedicated to tyre modelling. It starts with a synthesis of existing tyre contact models in the literature. It provides us with a good overview of the advantages and drawbacks of existing models. In addition to the definition of the forces and moment for each model, the steady-state characteristics of these forces and moment are computed using Matlab/Simulink. Moreover,

numerical comparison of the models is presented in this chapter. This chapter attempts to provide a critical review of the major findings. Also, an extensive reference is made to work carried out in the area of tyre thermal models and pavement interaction, since it is an important factor in the tyre-force generating procedure. The development of a novel brush-based multi-physical model is presented in this chapter with numerical validation. The study of the impact of road surface texture taken into account by the developed model is discussed at the end of the chapter.

Chapter 3 presents the vehicle modelling. It also introduces a brief synthesis of existing different vehicle models. We discuss the development of the 3-D vehicle for the thesis. It starts with the general hypothesis and coordinates transformation system. Given the complexity of the system, we resort to the use of symbolic calculation software (Maple) to establish the dynamic equations. The coupling with the developed multi-physical model is presented. These equations are developed in Matlab/Simulink. To assess the degree of representativeness of the model, the model is compared to the simulator SCANeRTM Studio (Prosper). Based on this, the numerical comparison between the developed model and simulator is analysed.

Chapter 4 revolves around the synthesis of unknown input adaptive high gain observer. The synthesis of this observer is motivated by the need to design an observer robust to noisy measurements, rapid dynamics and modelling errors. After having recalled the conditions necessary for the synthesis of nonlinear observers, we exhibit the observer synthesis from an observable form of nonlinear systems. We also discuss the synthesis of the observer for singularly perturbed systems. We present an application of developed observer on the full vehicle model to estimate tyre rolling resistance. We discuss the very first results of tyre rolling resistance for regular as well as singular perturbed system. The numerical validation of the estimation approach is also presented.

The objective of **Chapter 5** is to validate the developed vehicle model and estimation approach of rolling resistance. It is divided into two parts, first part addresses the practical part of our work; it is dedicated to the experimentation and instrumentation. It presents the description of the experimental site at University Gustave Eiffel and instrumented Clio 2 with various sensors. It also validates the influencing parameters of rolling resistance which was discussed in **Chapter 1**. This chapter also presents the method to measure reference rolling resistance. This is used while validating the estimation approach in the next chapter. The relationship between tyre surface temperature and speed is also discussed to conclude on singularly perturbed nature of the system. The second part presents the experimental validation results of this thesis. It validates the vehicle model developed in **Chapter 3** with a dedicated experimental campaign. The model is set up based on the real data provided by the University Gustave Eiffel, Nantes acquired during test campaigns carried out on known tracks with an instrumented vehicle (Clio 2). To assess the degree of representativeness of the model compared to the real system, a validation process is presented. Based on this, comparisons between simulation results and actual measurements are presented and analysed. In order to validate observers developed in **Chapter 4**, we have proposed in this chapter an offline validation campaign. Therefore this chapter also deals with the estimation of rolling resistance forces. This chapter shows that it is possible to reconstruct the dynamic states of the vehicle and estimation of parameters using the adaptive gain approach as well as singularly perturbed systems. The experiment results are presented with the major ambition of validating the idea of this new concept of estimation of rolling resistance.

In the end, we conclude the thesis by summarizing the main results and suggesting possible directions for future work.

Chapter 1

State of art

This chapter is divided into two parts first part provides an overview of rolling resistance. In section 1.1, we first identify five principle forces that contribute to CO₂ emissions and fuel consumption of a vehicle. Section 1.2 is devoted to rolling resistance definition and rolling resistance mechanism and influencing. An overview of the present rolling resistance coefficient model parameters and measurement methods is also presented in section 1.2.4. The conclusion of this part is presented in section 1.2.5. In the second part, the state of art on virtual sensors is presented. The observability on nonlinear systems is presented in section 1.3.1 and stability is discussed in section 1.3.2. The canonical form of the nonlinear system is presented in section 1.3.3. In section 1.3.4 literature review of different nonlinear observers is done. The comparison study between different adaptive observer techniques is presented in section 1.4.

1.1. Energy losses on a vehicle

As discussed above, energy losses experienced at different levels in the vehicle (aerodynamic effects, tyre/road contact, suspensions, etc.). When a vehicle is moving forward there are several resistive/frictional forces applied in the opposite direction of the motion as shown in Figure 10.

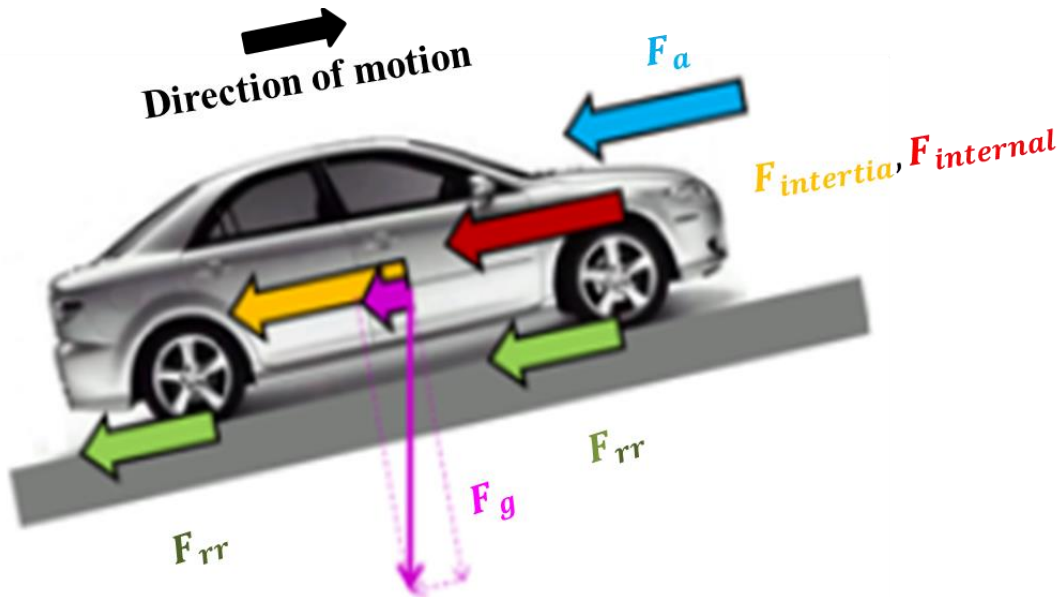


Figure 10 Resistive forces acting on a vehicle [1]

The five principle forces are identified and described below [7].

- i. Aerodynamic force (F_a): It results from a vehicle's movement through the air. It depends on the size and shape of the vehicle. It is directly proportional to the air density (ρ), Frontal area of the vehicle (A), aerodynamic drag coefficient (C_D) and square of speed (V). The aerodynamic drag coefficient is the object's resistance to movement through the air for a given frontal area.

$$F_a = \frac{1}{2} \rho \cdot A \cdot C_D \cdot V^2 \quad (1)$$

- ii. Internal frictional forces ($F_{internal}$): It corresponds to the friction of the drive train, i.e. in the differential and wheel bearing together with the brake pad.

- iii. Gravitational forces (F_g): It is only applied when the road is inclined. The greater the gradient and vehicle mass, the greater the gravitational forces.

$$F_g = M \cdot g \cdot \sin\alpha \quad (2)$$

where M is the mass of the vehicle, g is gravity, α is the angle of the gradient.

- iv. Inertial forces ($F_{inertia}$): Inertial forces are the forces, which resist the acceleration or deceleration of a vehicle. The greater the acceleration (or deceleration) we want to apply to the vehicle, the greater the inertial forces acting on the vehicle. At a constant speed, inertial forces are zero. It is also directly proportional to the vehicle's mass, which is roughly the vehicle's mass plus an extra 4% due to rotational inertia. Inertial forces are given by:

$$F_{inertia} = M_{eq} \cdot \dot{V} \quad (3)$$

where \dot{V} is the acceleration or deceleration, M_{eq} is the equivalent mass.

- v. Rolling resistance force (F_{rr}): It is defined as the energy consumed by a tyre per unit distance. It is detailed in the next section.

These above-mentioned forces must be overcome to move forward the vehicle; this effort is provided in the form of energy. This resistive force (F_{RM}) is the sum of five principle forces is given by:

$$F_{RM} = F_{rr} + F_a + F_g + F_{internal} + F_{inertia} \quad (4)$$

A large amount of energy is dissipated in the process of power generation and its transfer to advance the vehicle. Rest of the energy is dissipated to overcome all these resistive forces. Vehicle generates this power to move the vehicle by consuming fuel. Fuel consumption leads to the emission of CO₂. So the easiest way to reduce CO₂ emissions in a vehicle is to reduce its fuel consumptions. Hence rolling resistance can play an important role to reduce fuel consumption by optimizing driving or by adjusting its influencing parameters. So this work will be focussed on rolling resistance and in the next section, a brief state-of-the-art dealing with the rolling resistance of the tyre is presented.

1.2. Rolling resistance overview

When rolling, a tyre is deformed by the load exerted on it, flattening out in contact patch. This repeated deformation causes energy loss known as rolling resistance.

The part of the tyre which makes contact with the road is called the contact patch. The force distribution within the contact patch as the tyre is rolling is not uniform [7]. The resultant force is located in the front of the contact patch. This resultant force acts as a torque that opposes the wheel rotation. This torque can also be represented by the rolling resistance force (F_{rr}) which has to be overcome to maintain constant speed. The graphical representation of the mechanical manifestation of rolling resistance is shown in Figure 11.

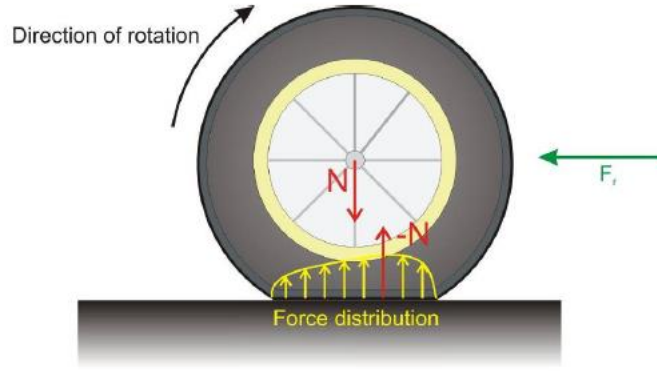


Figure 11 Graphical representation of rolling resistance force [19]

Rolling resistance forces linearly depend on the applied axle load in the practical range of axle loads [7]. Consequently, a dimensionless rolling resistance coefficient C_{rr} can be defined in which F_z represents the axle load and F_{rr} represents the rolling resistance force [7]:

$$C_{rr} = \frac{F_{rr}}{F_z} \quad (5)$$

In parallel to this definition, we also find other definitions of the coefficient of rolling resistance, such as *“The coefficient of rolling resistance is a convenient concept since it allows one to compare various tyres for use on the same vehicle. The load carried by a tyre will be the same on a given vehicle in a given tyre position, so a comparison of the rolling resistance coefficients will show which tyre is the most efficient for a given application. On the other hand, tests of tyre rolling resistance are usually carried out at the tyre rated load or at some relatively large fraction of it, such as 80% of tyre rated load. Direct presentation of the rolling resistance under these conditions is dependent on the load carried by the tyre, which, of course, varies for different tyre sizes. Hence, the concept of the coefficient is a generalizing and extremely useful one for both the presentation and interpretation of data.”* according to [23].

Various researchers such as [7], [18], [24] showed that the rubber elements deform in the contact patch and thereby consume energy as a result of their viscoelastic properties. This energy is not fully recovered when the elements return to the original state. The consumed hysteresis energy is converted to heat. The amount of energy loss due to rubber element deformation depends on the tyre geometry, tyre material properties, tyre temperature, tyre inflation pressure and road surface properties [19]. This is explained in the next section.

1.2.1. Definition and mechanism

Rolling resistance is simply the manifestation of all of the energy losses associated with the rolling of a tyre under load. Since most of the energy is dissipated through hysteretic losses as the materials of the tyre are deformed, it is important to understand the various deformations that take place during rolling. There are three important phenomena, which contribute to the rolling resistance. These phenomena are mentioned by various researchers in [7], [8], [15]. The three physical causes of rolling resistance given in these references are:

- The **deformations of the tyre at contact patch** which alone accounts for the **80 to 95%** of rolling resistance.

- **Aerodynamic drag** of the rotating tyre, which accounts for between **0 to 15%** of rolling resistance.
- **Slip between tread and road surface** or between the tyre and when a tyre is rotating, which lead to dissipation of energy and contributes to the rolling resistance. For a car running in a straight line without acceleration or braking, it accounts for less than **5%** of total rolling resistance.



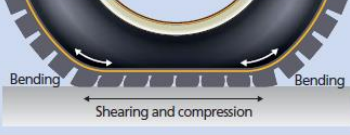
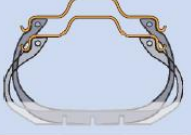
What	Tyre surface and air	Tread			Sidewall and bead area	
How	Aerodynamic drag of the rotating tyre 	Slippage on road surface 	Repeated deformation leading to energy dissipation Bending Compression Shearing 			Bending Shearing 
Contribution to rolling resistance	< 15 %	60 - 70 %			20 - 30 %	

Figure 12 Mechanism of rolling resistance force [1]

Tyre deformation constitutes a major part of rolling resistance and this is mainly due to the bending of the **tyre crown** at the leading and trailing edge of the contact patch and bending or bulging out of the side-wall because of the load on tyre structure, **compression of the tread** throughout the contact patch area and finally **shearing of tread and sidewall elements**. These phenomena cause a deformation-induced viscoelastic energy loss in the tyre [7], [15].

The carcass of the tyre is made of a belt with rubber beneath and above the belt while **bending at the leading edge or trailing edges** of the contact patch it would mean rubber layer inside gets compressed and the rubber layer outside this belt expands. Now this change in radius at the edges and rubbing of layers will manifest itself in hysteresis loss and hence contributing to rolling resistance as explained in [8], [9].

In the case of braking or acceleration, the **slip factor** contribution to rolling resistance becomes significant. There is a portion of the tyre where material shall stick to the road and the rest part of the contact patch shall slip against the road surface. The rotational aerodynamic drag depends on the tread design since the tyre has to overcome this to be able to keep rotating at a constant velocity. The contribution of rotational aerodynamic drag becomes important at high wheel velocities [8], [9].

1.2.2. Influencing parameters of rolling resistance

Various factors affect rolling resistance like temperature, tyre dimensions, inflation pressure, normal load, road profile and its characteristics and velocity. Over the years, many tests were performed in laboratories and on test tracks to obtain data for comparison of rolling losses and effect on fuel consumption. Many proposed models are polynomial expressions and include parameters like velocity, normal load and inflation pressure [11], [25]. These expressions have coefficients that are determined through curve-fitting to experimental values. This approach is specific for each type of tyre and although it predicts an accurate representation, it does not provide a physical understanding of tyre rolling resistance phenomena.

In [8], the author investigates about mathematical models based on physical understanding and literature review of tyre rolling resistance phenomenon. They have developed tyre model that explains the influence of tyre inflation pressure, tyre size and normal load on rolling resistance coefficient with certain assumptions, such as inflation pressure don't change with deflection, tyre material and tread pattern are kept constant, contact patch as a perfect rectangle, road type is fixed to a hard dry and flat surface, Temperature is assumed to be constant, steady-state parameters and only free rolling cases.

In [16], the author presents the influence of load, inflation pressure, temperature, road wetness and direction of tyre rotation on rolling resistance. Tests were performed with different test tyres and road pavements to obtain representative results. In this section, the influence of different parameters on rolling resistance is discussed.

1.2.2.1. Tyre inflation pressure variation

Rolling resistance coefficient **increases** rapidly as tyre pressure **decreases** [16]. While a lower tyre pressure reduces the compression of tread blocks in the contact patch, it also exacerbates tread bending and shearing which result is an increase in rolling resistance mentioned in [7].

A similar trend has been seen in [8], it points out an interesting fact about tyre inflation pressure and its dependency with kind of road surface as shown in Figure 13. Tyre rolling resistance decreases with an increase in pressure on the hard road surface as other parameters are kept constant. As the pressure increases, tyre holds its shape more firmly and vertical deflection decreases. Thus, the deformation of rubber is lesser compared to that in a tyre with lower pressure. Hence the hysteresis losses reduce thereby decreasing the rolling resistance in case of the level road surface.

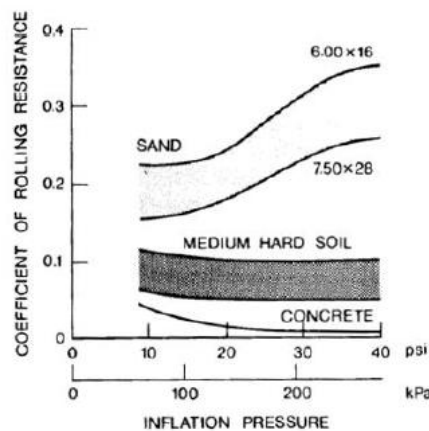


Figure 13 Effect of tyre pressure on the different road surface on the rolling resistance coefficient [13]

Authors in [16] illustrate that an increase in inflation pressure leads to a decrease in rolling resistance coefficient. It pointed out one important observation that tyre with low rolling resistance (electric vehicle) is rather insensitive to inflation pressure changes, while tyres having high rolling resistance are very sensitive.

In Figure 14 similar trends are shown [16]. The change in C_{rr} with respect to tyre inflation pressure is shown for different set of tyres and for different speed on a pavement DAC16r20 (replica of dense asphalt concrete with 16 mm aggregate) on a drum.

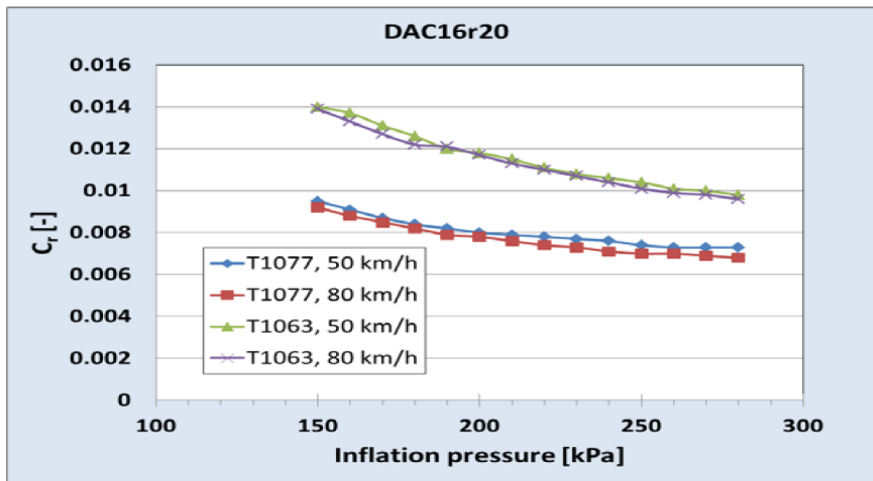


Figure 14 Inflation pressure influence on rolling resistance for speed 50 and 80 km/h Load 400 kg [16]

1.2.2.2. Load variation

According to [7], [8], tyre rolling resistance coefficient **decreases** slightly as load increases because of visco-elasticity decreases as temperature increases. However, the rolling resistance force (the result of load multiplied by the rolling resistance coefficient) increases with load. This is because a heavier load causes more bending and shearing.

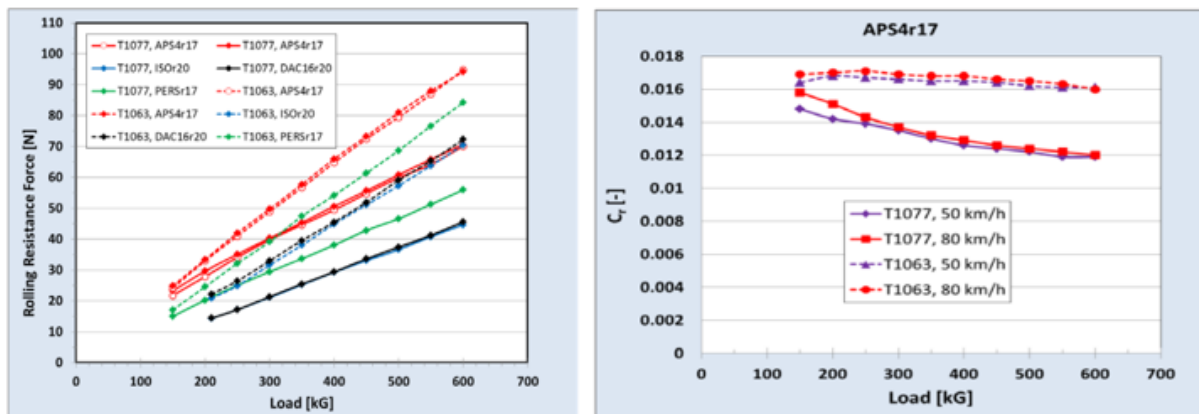


Figure 15 Load influence on rolling resistance for speed 50 and 80 Km/h, inflation pressure 2.1 bar

The coefficient of rolling resistance varies with load changes with constant inflation pressure. In Figure 15 the variation of coefficient of rolling resistance is presented for different tyres on pavement APS4r17 (replica of surface dressing 8/10 mm aggregate) which is a replica of surface dressing 8/10 mm aggregate. It has given very interesting results that increase of load is influencing rolling resistance coefficient of one tyre and it does not influence another tyre on the same surface with constant inflation pressure.

Test results from [16] show tyre inflation and tyre load are not independent variables. Higher load requires higher inflation pressure in order to ascertain proper interface between tyre and road surface, good fuel economy as well as optimal resistance to wear and damage.

1.2.2.3. Speed variation

The rolling resistance of a passenger car tyre varies little with speed up to 80 km/h and then increases significantly. This increase is due to the increase in aerodynamic drag of the rotating tyre (this force

increases in proportion to the square of the speed) and the development of strong vibrations at high speeds. The tyre becomes severely deformed, leading to greater energy dissipation [7].

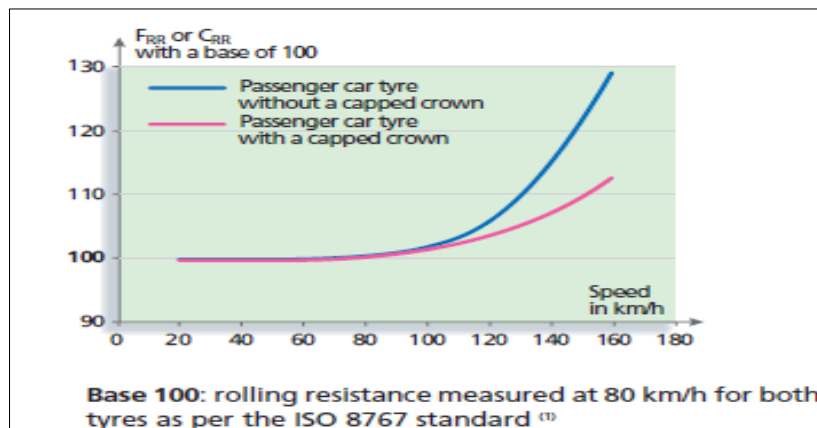


Figure 16 Effect of speed on the rolling resistance coefficient [1]

Tyre rolling resistance can hardly be explained purely with velocity. Change in velocity is accompanied by a change in temperature. A model was developed to include changes in temperature with the slow and fast change in velocity by [26]. But it is limited to the tyre shoulder temperature and inside air temperature with a very simplified thermodynamic equation. The transfer of heat from the tyre surface and carcass isn't considered by the author. Therefore a model is needed which can predict both tyre surface as well as tyre carcass temperature.

1.2.2.4. Road characteristics variation

There are different road characteristics, which have an impact on tyre rolling resistance. Here, before discussing the impact the different road characteristics on rolling resistance, some road characteristics definitions are given according to [27], [28].

a. Crossfall

The camber of a road has two uses. First, it allows the evacuation of rainwater when the slope of the road is zero, so the minimum slope is set at 2.5% to fulfil this role in all circumstances. Then, it makes it possible to reduce the tyre stresses on the side by taking up part of the lateral acceleration. The maximum camber allowed on roads is 7%. It has an impact on the load transfer of the vehicle which has a direct impact on the tyre rolling resistance.

b. Slope

The slope of the road is a factor on which it is much more difficult to state constraints. Indeed, this slope is mainly due to the topology of the land on which the road is built and the work to be undertaken to modify it or to avoid a structure.

The maximum slope is set from the vehicle dynamics for the different types of roads. Beyond the slope itself, variations in this slope are subject to minima depending on the comfort of the driver and the visibility distance. So the vertical acceleration is limited to $g/40$. This road characteristic mainly influences gravitational forces and transfer of load at the back of the vehicle which leads in the increase of the tyre rolling resistance force.

The slope influences the vehicle dynamics in terms of load distribution, vertical dynamics and its relationship to other modes. The latter are poorly represented in most models and are therefore not taken into account.

c. Road profile

This variable represents variations in the height of the surface. These variations directly influence the vertical dynamics of the vehicle. However, it will cause variations in the normal force at the level of the tyre. It can vary the normal force by almost 5% at 20m/s speed. On roads more degraded, the profile can locally vary the normal force very strongly, by more than 50%, thereby reducing the forces that can be mobilized laterally or longitudinally [27].

d. Road roughness

Road surface texture and rolling resistance relationship have been studied by several researchers [11], [16], [29]–[31]. Road roughness can be separated into different scales, unevenness, mega macro and micro-texture. The illustration of the various scale of roughness is given in Figure 17.

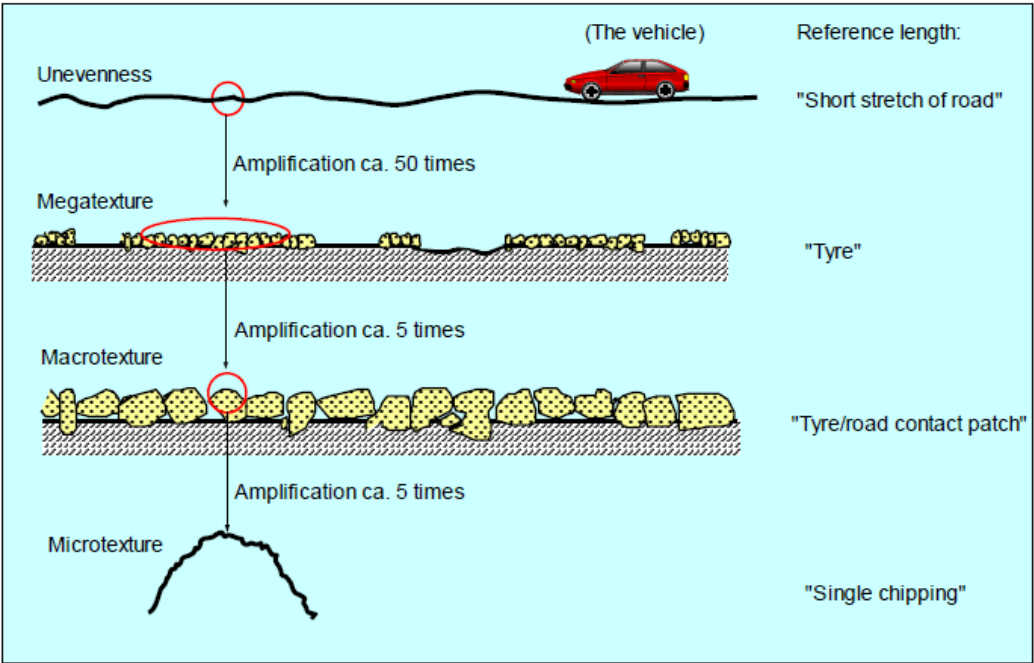


Figure 17 Illustration of the various scale of road roughness[29]

The macro-texture is defined as surface asperities that range from 0.1mm to 20mm in height and from 0.5mm to 50mm in width whereas the micro-texture is defined as the surface asperities that range from 0.001mm to 0.5mm in height and less than 0.5mm in width (Figure 18). Unevenness is the corresponding deviations with the characteristic dimensions along the surface of 0.5 m to 50 m [29].

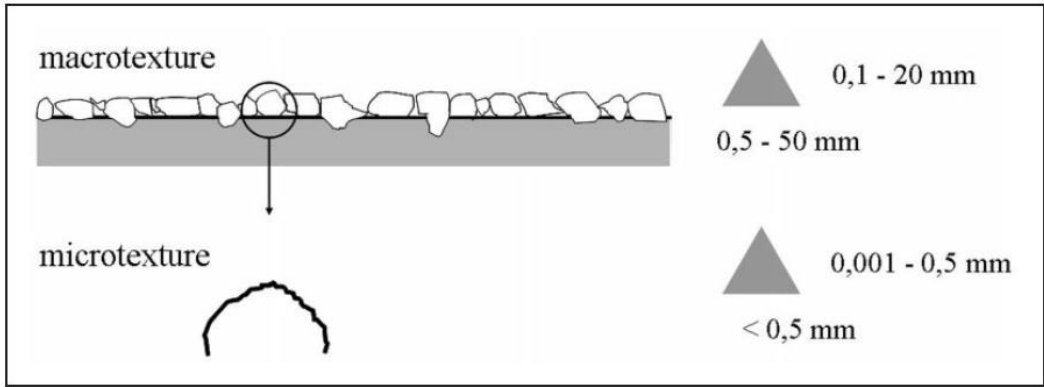


Figure 18 Road surface texture surface [32]

Road macro-texture is assessed through a parameter called mean profile depth (MPD) defined in standard ISO EN 13473-1 (Figure 19).

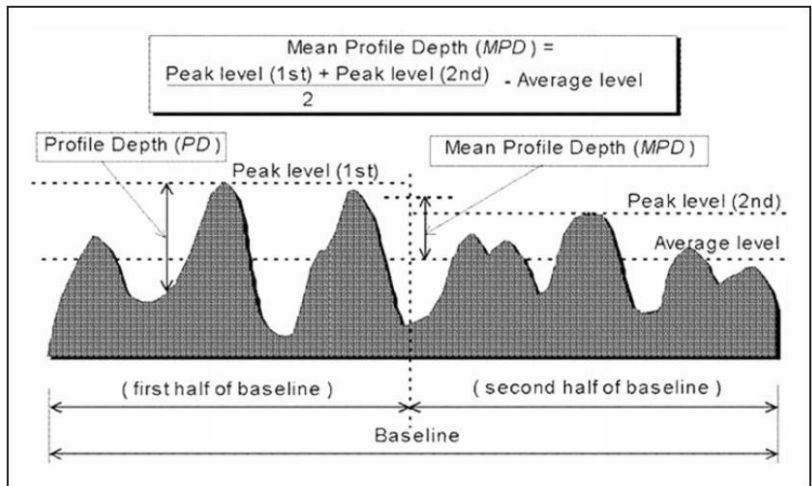


Figure 19 Definition of road surface mean profile depth [33]

Rolling resistance is often considered to be affected by the rough end of the macrotexture, the mega texture and the low end of unevenness as depicted in Figure 20 [29].

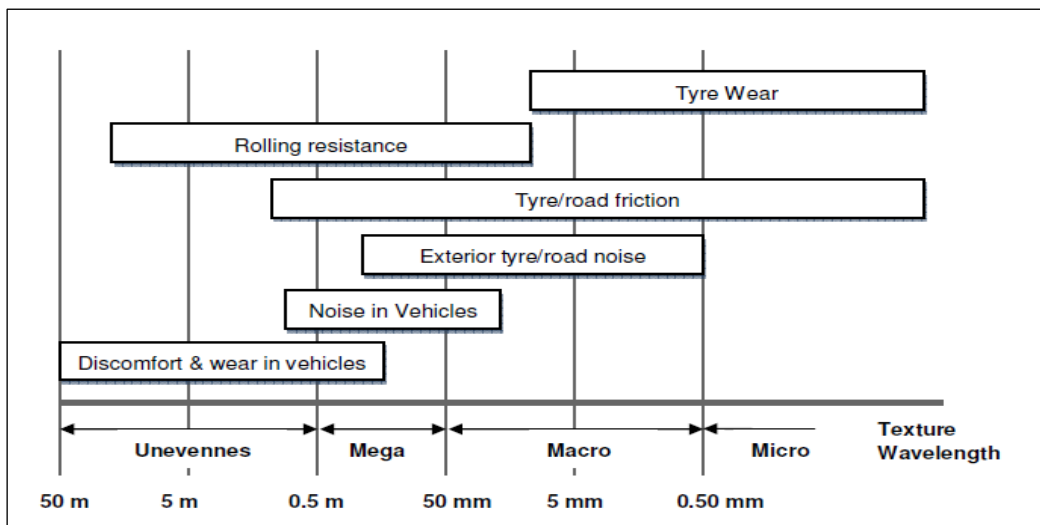


Figure 20 Effect of texture on numerous phenomena as a function of wavelength range [19]

Authors in [34], [35] stated that rolling resistance arises from hysteretic losses in the sidewalls and tread band material, which experiences a deformation cycle every revolution of the tyre. There is an additional small loss (approximately 10%) due to micro-slip in the contact patch between the tyre and the test surface. Three major mechanisms exist by which the road roughness can produce additional losses

- Excitation of the vehicle by road roughness, leading to energy dissipation in the suspension dampers and frictional losses due to vibration.
- Hysteretic losses in the contact patch due to dynamic vertical deflection of the tyres, and additional frictional losses in the contact patch due to micro-slip.
- Hysteretic losses in the tyre material due to the envelopment of the road roughness by the tyre, which also causes further frictional losses in the contact patch due to micro-slip.

Measurements in [16], [36] show that rolling resistance increases in proportion to the macro roughness of the road surface. This is because the macro rough asperities deform the tread block surface (indentation), causing local energy dissipation. The macro roughness of a road surface plays a role in the tyre grip by helping water to drain off during rainfall. However, the tyre grip on wet roads is more dependent on the micro-roughness of the road surface.

In [37] the impact of pavement properties on the vehicle rolling resistance is discussed. It has presented an analysis of the comparison of current rolling resistance models from [14] and [15]. They have assessed the vehicle fuel consumption due to rolling resistance.

It has also discussed the impact of pavement properties on rolling resistance as well as on fuel consumption. Macro- texture, pavement stiffness, roughness, rutting and transversal slope of pavement are identified as factors, which can influence rolling resistance.

Road surface wetness increases the rolling resistance coefficient with an increase in the thickness of water film on the road. It is mainly due to the change in the temperature of the tyre during wet conditions. It mentions that it decreases the tyre temperature up to 10°C in comparison to tyre temperature during rolling on the dry surface according to [16]. Rolling resistance caused by International roughness index (IRI) is dependent on speed. At a speed of 90 km/h, when IRI increased but one unit the rolling resistance of car increased by 4.6% and if MPD increase by one unit the rolling resistance for a car will increase by 15.6% [17].

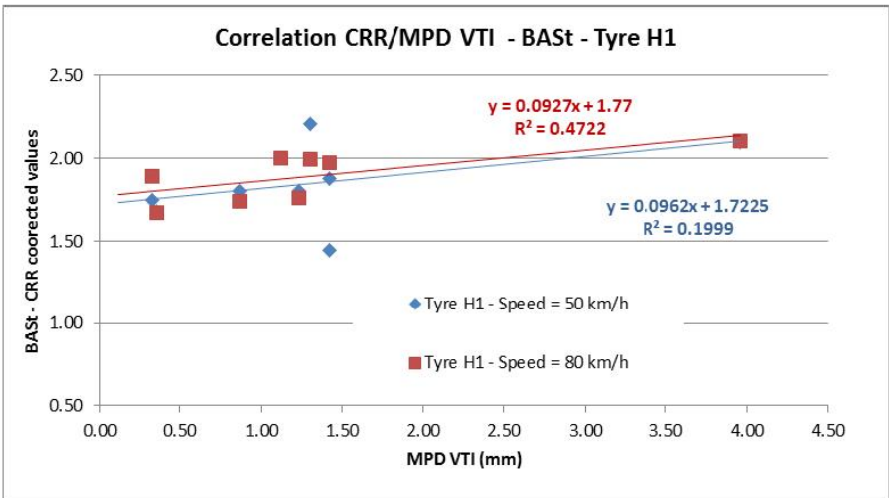


Figure 21 Rolling resistance coefficient as a function of MPD [29], [39]

1.2.2.5. Ambient temperature variation

The internal temperature of a tyre fitted to a standard European passenger car in normal use usually lies between 20 and 60°C when travelling, depending on the type of tyre, the way the car is driven and ambient temperature. Naturally, the higher the ambient temperature, the nearer to the upper limit the tyre internal temperature is likely to be. Within the tyre operating range, the amount of energy dissipated by elastomers when subjected to repeated deformation decreases as temperature increases. Rolling resistance is, therefore, lower when the ambient temperature is high. The variation in rolling resistance as a function of temperature is not linear. However, between 10 and 40°C, a variation of 1°C corresponds to a variation in rolling resistance of 0.6 % [7].

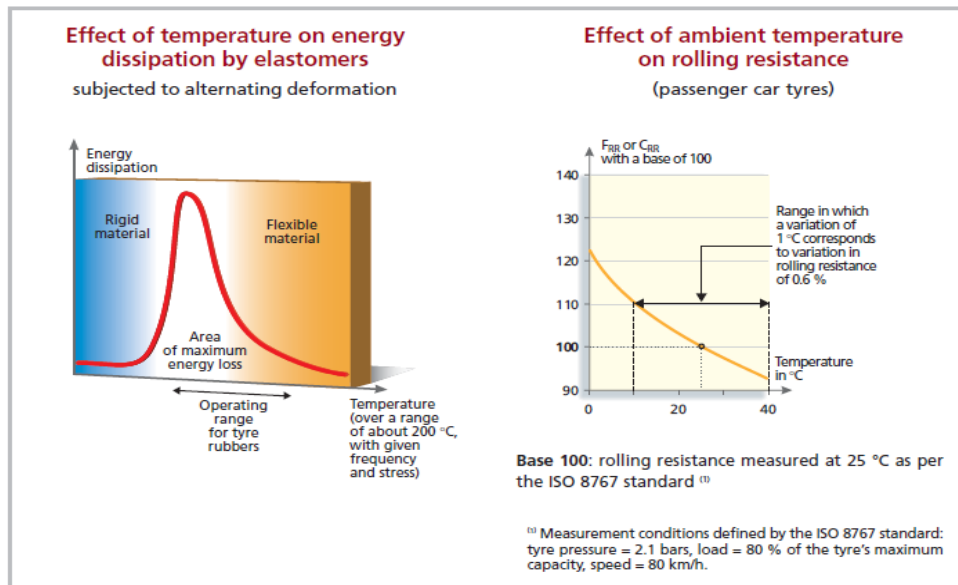


Figure 22 Effect of ambient temperature on rolling resistance [1]

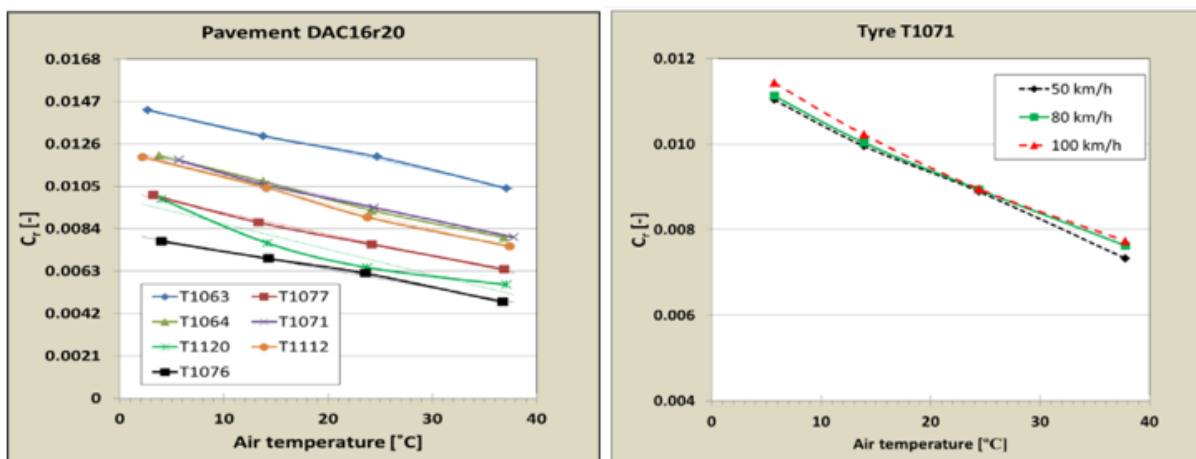


Figure 23 Influence of air temperature on rolling resistance for different tyres and different speeds [5]

According to the test report [16], tyre rolling resistance is influenced by tyre temperature and also by pavement temperature. Rolling resistance coefficient decreases with increase in the temperature as an increase in temperature increase inflation pressure of tyre in Figure 23 for different tyres and on pavement DAC16r20 (replica of dense asphalt concrete with 16 mm aggregate).

1.2.2.6. Tyre dimensions variation

The rolling resistance coefficient of a tyre decreases as its outer diameter increases. This is because the bending of the tyre on entering and leaving the contact patch is less severe with a bigger diameter. In [13], Wong has also shown from the experimental data that on a hard surface like concrete, the effect is very less, however, at the medium to hard ground the reduction of the rolling resistance coefficient with an increase in tyre diameter, with deformation surfaces, the effect is magnified [2] as shown in Figure 24.

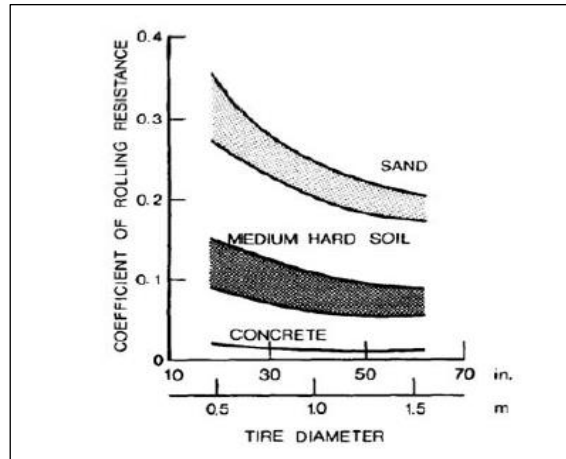


Figure 24 Effect of tyre diameter on different road surface [13]

Increasing the tyre diameter by 1 cm reduces rolling resistance by about 1 % in Figure 25. Tyre sizing is a critical operation involving not only rolling resistance but vehicle performance as a whole. It is, therefore, necessary for tyre and car manufacturers to work closely together throughout the vehicle design phase to choose the best possible options [1]. While varying the tyre size keeping other parameters constant, for example, inflation pressure, longitudinal velocity, loading capacity and tyre width, increasing tyre diameter decreases vertical deformation for the same contact patch length. Decreasing vertical deformation means the low transition of the radius on the leading and trailing edges of the contact patch and hence bending of tyre tread region is lower for the bigger diameter, which results in lower hysteresis losses.

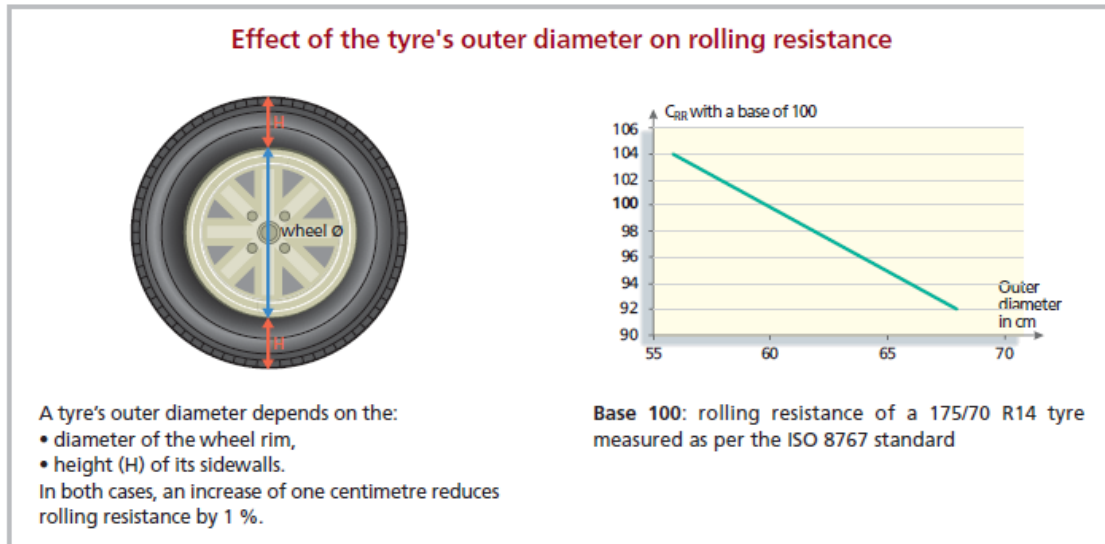


Figure 25 Effect of tyre diameter on rolling resistance[7]

In the above section, the impact of the influencing parameters of rolling resistance is discussed. The vehicle load and inflation pressure have shown direct influence on rolling resistance. Speed has shown its significant effect on rolling resistance after 100 km/h. The ambient temperature also influences the rolling resistance. There is a lot of work done in literature [16], [29] to identify these parameters as most influencing for rolling resistance.

The influencing parameters such as ambient temperature, load, speed, inflation pressure and road roughness will be taken into account while modelling the tyre road contact model for the estimation of rolling resistance in this work. This will help to evaluate the influence of these parameters on a large extent in real driving conditions. In the next section, different models of rolling resistance obtained from different studies are discussed.

1.2.3. Rolling resistance coefficient model

There have been several attempts to develop the rolling resistance coefficient model in the literature. Three methods used to define the coefficient of rolling resistance. There are empirical, physical and finite element models proposed in the literature. In this section, an effort is done to gather these different models.

1.2.3.1. Empirical models

[17], [40] propose empirical models for rolling resistance based on different influencing parameters. Experiments approaches were used to obtain these relationships. The author in [13] presents the rolling resistance coefficient with squared speed term dependence, given as

$$C_{rr} = 0.006 + 0.23 \cdot 10^{-6} v^2 \quad (6)$$

This is the simplest form to present the C_{rr} which depends only on squared speed, which is incomplete. The tyre manufacturer Michelin proposes a model of C_{rr} that includes both linear and squared speed dependence, given in [7]

$$C_{rr} = C_{r,iso} + a(v^2 - v_{iso}^2) + b(v - v_{iso}) \quad (7)$$

where $C_{r,iso}$, a and b are tyre dependent constants and $v_{iso} = 80$ [km/h].

The equation (7) is dependent only on speed but researches showed that temperature also has an influencing action, therefore, another model in [41] is derived that includes both a velocity dependence as well as a temperature dependence. But this model lacks the tyre surface temperature as it considers inside air temperature of the tyre.

$$C_{rr} = C_{rr}(v, T) = C_{r0}(T) + C_{r01}(v^2 - v_{sc}^2) \quad (8)$$

The temperature dependence of the rolling resistance is also discussed in [13]. It is shown that C_{rr} decreases with an increasing tyre temperature. It is stated that $C_{rr} = 0.020$ when the tyre temperature is 0°C , and approaches $C_{rr} = 0.007$ as the temperature increases towards 80°C . However, the actual value of C_{rr} also depends on the type of tyre, the tyre thread and how worn the tyre is, as well as on the road surface. In addition to two influencing factors another model of C_{rr} dependent on inflation pressure is also presented in [41].

$$C_{rr} = \left(\frac{P}{P_{nom}} \right)^\alpha (C_{rrstatic} + b_T(T - 25) + c_v v^2) \quad (9)$$

where P_{nom} is the nominal value of inflation pressure specified by tyre manufacturers, b_T and c_v empirical coefficients $C_{rrstatic}$ is the static part of rolling resistance, which supposed to not change during vehicle motion. This value depends on vertical load, road pavement, wheel alignment and tyre material at 25°C . The dynamical part includes a first-order function of tyre temperature and vehicle velocity second order with the assumption that P is driven by T through ideal gas law. The above model also requires the coefficients, which can be communicated by tyre manufacturers only.

Some models have been proposed in the past on the empirical formula of C_{rr} as a function of pressure and speed only but requires the experimentations to identify the constants. In [42] the variation of pressure and rolling resistance coefficient is given.

$$C_{rr} = 0.005 + (.01 + .0095 * \left(v_x * \frac{3.6}{100} \right)^2) / p \quad (10)$$

where v_x is the longitudinal velocity (m/s) and p (bars) is inflation pressure.

The above models lack in considering the influence of road characteristics on rolling resistance, which are also identified as the main influencing factor. The empirical model of the rolling resistance coefficient proposed by [20] is assumed as a linear relationship between the rolling resistance coefficient, C_{rr} MPD and IRI:

$$C_{rr}(MPD, IRI, v) = C_0 + C_{MPD} * MPD + C_{IRI} * IRI + C_v * v \quad (11)$$

where C_0 , C_{MPD} , C_{IRI} and C_v are constants and v denotes the velocity. C_0 is the basic rolling resistance coefficient, i.e. the rolling resistance on a perfectly smooth and even road surface.

MPD and IRI parameters are suitable for use in a prediction scheme for rolling resistance since they would allow, in principle, a nationwide estimation of rolling resistance properties. In MIRIAM [10] the equation for rolling resistance coefficient proposed is

$$C_{rr} = 0.00912 + 0.00210.MPD + X.IRI \quad (12)$$

where MPD is Mean profile depth in mm, and X is constant yet to be determined and IRI is road unevenness/roughness index. The equation is based on light vehicle data. This model is useful over a speed range of at least 50-110 km/h for the rolling resistance part of driving resistance.

The value of X is calculated by [17] using the controlled experiments, so the above model becomes

$$C_{rr} = (0.00912 + 0.0000210 * IRI * v + 0.00172 * MPD) \quad (13)$$

The above model does not take into account pressure and temperature influence on the rolling resistance. The main drawback of above mentioned different empirical model that it has constants which require either experiments or tyre manufacturer to communicate them. Also, there does not exist an empirical model which take into account all the influencing factors. It is required to have a model which does not have constants to define and include all the influencing parameters.

1.2.3.2. Physical model

Several tyre models are presented in the literature [43]–[46]. Common for most models, however, is that the force from the rolling resistance of the tyres is modelled as the normal force on the tyres from the ground multiplied with the rolling resistance coefficient C_{rr} . The equation is given in [47] as

$$C_{rr} = F_{rr}/mg \cos \alpha \approx F_{rr}/mg \quad (14)$$

where C_{rr} is the rolling resistance coefficient, m is the vehicle mass, g is the gravity and α is the road grade in percentage. Expressing α in percentage is common, not only in scientific publications but also on road signs [48].

The major contributors to the creation of resistance to rolling of tyre on a straight and flat road surface are energy dissipated in the process of rolling and aerodynamic drag. The energy absorbed in the heat is a manifestation of hysteresis forces because of radial deformation of the tyre.

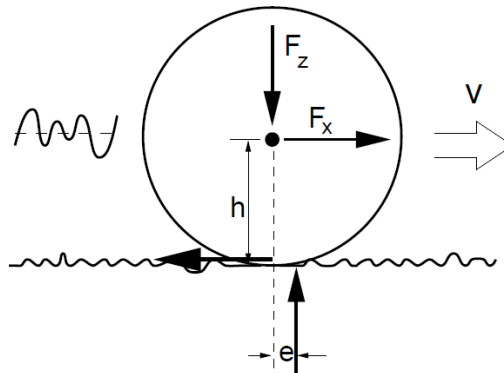


Figure 26 Rolling resistance phenomenon [34]

This energy dissipation results in normal pressure distribution, higher in the forward portion of the contact patch, where the tread elements are forced radially inwards; and lower in the rearward portion of the contact patch, where the tread elements are forced radially outwards [49]. This leads to a forward shift of the centroid of the normal pressure distribution, at a distance e in Figure 26, where the horizontal and vertical forces applied at the wheel hub are reacted. A moment balance yields the following relationship:

$$F_x h - F_z e = 0 \quad (15)$$

$$\frac{F_x}{F_z} = \frac{e}{h} = C_{rr} \quad (16)$$

where h is the loaded radius of the tyre. It is not possible to calculate the parameter e physically. This is the main reason the approximate value of C_{rr} is used by the researcher. Since it is not possible to calculate the parameter e physically this model cannot be used directly. The approximative values will not give accurate results for the variation of different influencing parameters so the physical model cannot be used in our work.

1.2.3.3. Other models

Above mention, the approach is based on the force calculation. In literature, there are other approaches such as finite element approach and bond graph approach.

Famous finite element model is MFT tyre which is industrialised and based on the finite meshing as shown in Figure 27. In FEM (finite element method) rolling resistance can be defined as the power dissipation P_{dis} at a certain axle load N_{axle} . The power dissipation depends on the resistant force F_{rr} acting on the wheel axle and the vehicle velocity v . In this study, the rolling resistance coefficient, C_{rr} , is used to quantify rolling resistance [19]:

$$C_{rr} = \frac{F_{rr}}{N_{axle}} = \frac{P_{dis}}{N_{axle}} \cdot \frac{1}{v} \quad (17)$$

To assess the influence of road texture on rolling resistance, the vibrations in the tyre and the inherent energy dissipation should be taken into account. FEM is used to take that in account in steady-state conditions. It is impossible to implement on vehicle and it is very complex so we are not going to consider FEM models for our thesis.

Another approach is called Bond graph form; it is a unified multi-energy domain modelling approach. The bond graph as a modelling and simulation tool provides many possibilities; it allows both causality and behavioural system analysis. From the behavioural point of view, a bond graph model allows dealing with a lot of equations describing the dynamic behaviour of the tyre-road system by using only one representation independent of the improved physical phenomena [50].

The bond graph is highly complex and required intensive computation. It is also a lumped parameter model and cannot model non-energetic interactions and still need to develop. This approach is also difficult to implement on the vehicle. Therefore, it is necessary to propose an innovative method for rolling resistance studies of tyres that can be used for different purposes and under different conditions.

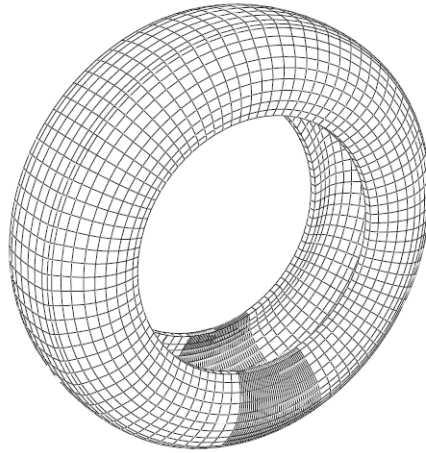


Figure 27 FEM Tyre model [19]

1.2.4. Rolling resistance measurement methods

Measurements of rolling resistance of tyres date back several decades but since a few years, a systematic treatment has been attempted to establish standards for the measurement of rolling resistance. Within recent decades, rolling resistance has been extensively and intensively studied in both the tyre design and pavement design fields. Although several approaches have been proposed, these could generally be summarised as experimental methods, numerical methods and virtual sensor method.

1.2.4.1. Experimental methods

For experimental methods, comparison studies are mainly carried out based on various measurement methodologies and results. Procedures for measuring the rolling resistance of pneumatic tyres are specified by international standards. All standards are based on laboratory drum measurement (explained below). The existing test standard includes two set by the Society of Automotive Engineers (SAE), SAE J1269 [51] and SAE J2452 [52] and two set by the International Organisation for Standardization (ISO), ISO 18164:2005 [53] and ISO 28580:2018 [54] and ECE R117[55] regulation from the United Nations Economic Commission for Europe (UNECE). All three organizations suggest similar test equipment and methods. These standards are used extensively in the tyre and automotive industries for rolling resistance measurement. The test standards for rolling resistance include four measurement techniques to measure the rolling resistance force of a tyre, as classified by [9] (although not all of them are in each standard). The comparison of the different standard can be found in [9]. These measurement techniques are:

- a. *Force* - The force at the spindle is measured when the drum is rotated in a constant velocity.
- b. *Power* - The electric power needed to maintain the drum rotation at a constant speed is measured.
- c. *Torque* - The input torque needed to maintain the drum rotation at a constant speed.
- d. *Deceleration* - The drum is firstly rotated up to a certain speed, the driving motor is then detached from the drum, and the decay in the angular velocity is measured

In each of these approaches, the raw measurement is converted into rolling resistance and the parasitic loss is subtracted. Parasitic loss is the energy consumed by the system per unit distance, excluding internal losses in the tyre. It includes sources of energy loss such as aerodynamic drag and bearing friction.

The various methods use these techniques for measurements of rolling resistance. The methods are mainly grouped into five categories in [10]:

1. **Laboratory drum (DR) method:** Laboratory measurements made with test tyres rotating on drums. The drums may be equipped with sandpaper or replica road surfaces, apart from the steel surface of the drum. The tyre is held against the drum, which is run by a motor coupled to it. The tyre's rolling resistance applies a braking effect to the drum's rotation, and this effect is translated into measurements of forces, torques, decelerations, etc. Rolling resistance is then calculated from these measurements. Figure 28 shows the configuration of this procedure.

In addition to the above-mentioned measurement techniques, the number of testing points can also differ, depending on the test conditions. A single-point test includes only one setting for tyre pressure and tyre load, while a multi-point test includes a series of settings of tyre pressure and tyre load. Rolling resistance is then calculated from the regression of the multi-point measurements.

Different testing standards ([51]–[54]) prescribe different numbers of testing points. Limitation of this method is the inclusion of aerodynamic drag which is unrepresentative of the real situation also mentioned by [10]. Several aspects of the drum testing procedure have been investigated, such as inter-laboratory correlation in [15], [24] etc.

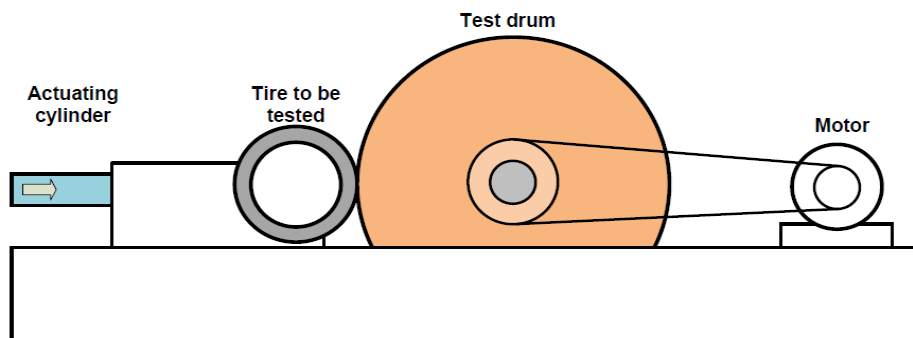


Figure 28 Drum test to measure rolling resistance [8]

2. **Trailer (TR) method:** In trailer method rolling resistance measurements are made with test tyre(s) in a special towed trailer while rolling at a constant speed. The trailer may be designed either for passenger car tyres or heavy truck tyres. The measurement may be made either of the torque on the test tyre, the towing force between towing vehicle and trailer, or the angle by which the tyre vertical support is displaced when a rolling resistance force is acting in the tyre/road interface. Several trailer equipment is available with different testing laboratories, such as BAST, BRRC, Technical University of Gdansk (TUG) FKFS and IPW automotive trailers etc. as shown in Figure 29.

The development of trailer method has been going on for three decades. [9] and [10] have documented all the existing trailers in detailed. The measurement of rolling resistance of tyres on the actual road as compared to laboratory drum method is the main advantage of trailer method although it is limited to certain conditions. It has also reduced or eliminated many disturbing factors such as transmission losses and air resistance in contrast with coast-down methods. The above-mentioned trailers focus on the personal car, but recently BAST and

Forschungsvereinigung Automobiltechnik (FAT) have developed a rolling resistance trailer using truck and truck tyres [9].

Two European projects MIRIAM [29], [38] and ROSANNE [20] have made an extensive comparative study between the BRRC, BAST, and TUG trailers on a test track in Nantes, France, and showed overall good correlations with both macro-texture and mega-texture with good short term repeatability. The comparison of the simulation model and TUG trailer measurement is done in [30], [56] and a good correlation is found. It is also concluded by [36] that the trailer measurements are a key component in creating a linear model for the rolling resistance's dependence on the road surface.

A problem with the trailer method is that it is unclear as to what extent road unevenness influences the measurements in a representative way; essentially the part which causes energy losses in the suspension. The wheel suspension may not be typical and it may even be blocked during measurements. These issues are also mentioned by [36]. As [38] suggests, this should be subject to further study. More generally, this also shows that further research and perhaps trailer standardization are needed.

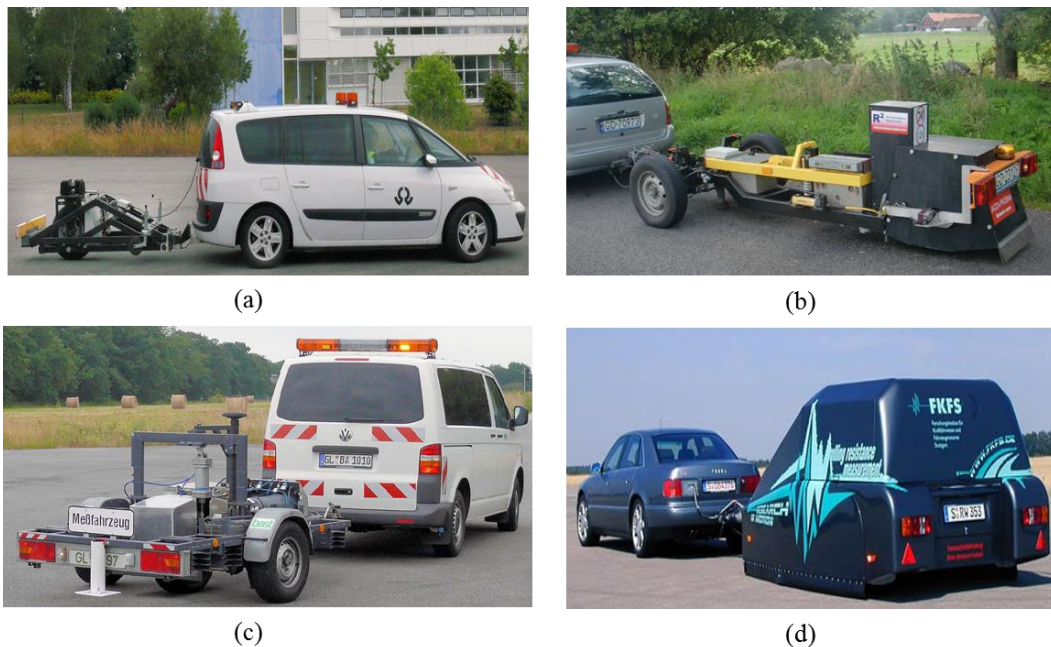


Figure 29 Rolling resistance measuring trailers from different laboratories (a) BRRC (b) TUG (c) BAST (d) FKFS

3. **Coastdown (CD) method:** A coastdown measurement on a road section is performed by letting a selected test vehicle, equipped with selected test tyres, roll freely (clutch down, gear in neutral position) between defined start and endpoints as defined in [10], [57]. The speed is measured continuously along the road section. The acceleration is either measured directly or is derived from the speed curves. A possible alternative is to measure the speed only at the start and endpoints. The various resistive forces acting on the vehicle will make it slow down. The rolling resistance is one of these forces. Air resistance is another major force. The larger the rolling resistance the larger the retardation becomes. Normally, measurements are made in both directions on the road, in an attempt to "average out" influences such as gradient and wind and to get highly varying conditions. Nevertheless, ambient winds may not be too high. This method does not yield any direct results on rolling resistance but must be fitted to a

mathematical model by, e.g., estimating parameters with least-squares regression. The formulation and complexity of the model may vary depending on the experimental setting, sources of data, and so on. More details on modelling can be found in [11], [25]

By performing several coastdown measurements, under various conditions, it is possible to distinguish and separate the contributions of the different resistances acting on the vehicle. Thus, most of the air resistance can be separated from rolling resistance and by clever measurement and analysis design, one can separate some other energy losses as well such as in transmission and wheel suspension. The coastdown method is equally sensitive to various influences as the trailer method since the rolling resistance is such a small component of the total momentary forces. It requires very careful measurement and analysis design, as well as experience and extensive competence. Its advantages are that it may equally well be performed with heavy vehicles as with light vehicles (albeit less practical and more expensive) and that also wheel suspension losses are measured.

The finding long tests site with stable characteristics such as the same slope, pavement surfaces etc. is one of the major drawbacks of coastdown test as the results are based on mean values. A serious disadvantage with the coastdown method, at least when applied to road surface effects, is that it can be implemented in many different ways and that results may differ for different implementations. The difficulty to trace any instability in results (regression coefficients) to their sources (measurement errors) is further weakness of the method. Extreme care must be taken in order to obtain reliable and stable results. Also, some other difficulties concerning the design of measurements and analyses are discussed in [9].

4. **Fuel consumption (FC) method:** The tyre rolling resistance obviously affects the fuel consumption [8], [19] but because many factors influence the energy loss experienced by a car, it is difficult to pinpoint the rolling resistance loss in the fuel consumption method. Fuel consumption method uses an especially instrumented test vehicle equipped with precision fuel flow meters, from which rolling resistance may be calculated using fuel consumption/rolling resistance model. Also, vehicle speed must be measured with high precision and ambient air, fuel and engine temperatures should also be measured. Wind speed and direction affect results and should be measured as well. In some cases, the airspeed at some points near the vehicle may be measured. FC measurements are made between two defined points on the road, in both directions, assuming a road is used with no or small gradients and bends with very high curve radius. This method is sensitive to the condition of all parts of the power unit, apart from all ambient and road parameters; especially wind conditions. The driver's skills to keep a constant speed or the efficiency of a cruise controller are also potential error sources. In [17], [31], [37] studies are done on the influence of road surface on fuel consumption. A variant of this would be when using a vehicle not powered by fuel, such as an electric vehicle. Then the method should be called Energy Consumption (EC) method instead.
5. **The steady-state wheel torque (WT) method:** This method was mainly developed in New Zealand in the 1980s by [58]. The author in [10] explained that it essentially involves a test vehicle (both a car and a truck have been used) being driven at steady speeds between 20 and 75 km/h. At each speed, the driving torque of one (driven) tyre, together with the relative wind speed and direction are continuously measured. The latter are parts of an on-board anemometry system by which air resistance is controlled. The driving torque is divided by the dynamic tyre radius and corrected for the ambient wind to obtain the driving force required to overcome all resistive forces except for driveline losses. It should be noted that this method

measures rolling resistance including the contribution by suspension losses. The latter is one of the advantages with the method; another advantage is that it may be used also with a heavy vehicle. It shares the problems of the other methods, but in this case, the elimination of the air resistance effect from the rolling resistance effect of the pavement is the major problem. For this reason, high speeds are not useful.

These methods are generally used to evaluate the rolling resistance. Indeed, at present, these methods are hardly accessible and exhibit some uncertainty due to the quality of results, reproducibility of the measurements, limited to certain tyres and the high cost of physical sensors attached to vehicle tyres. This is an experimental approach to calculate the rolling resistance coefficient in standard and controlled conditions. Even though most of them are well established it has several limitations, such as the feasibility for tyre or pavement studies. Also, it cannot provide insight into the rolling resistance mechanism.

1.2.4.2. Numerical methods

Numerical methods such as finite element (FE) analysis provide powerful tools for modelling and predicting the rolling resistance. In [19], a non-linear steady-state rolling analysis of a FEM tyre model is presented that is based on the Modal Arbitrary Lagrangian-Eulerian (M-ALE) approach. Moreover, two principal components, the smooth road rolling resistance and the road texture-induced rolling resistance, are studied. In another study [30], a waveguide finite element model is adopted to predict the tyre energy loss resulting from the rolling resistance. In order to assess the influence of road texture on rolling resistance, the vibrations in the tyre and the inherent energy dissipation should be taken into account. FEM is used to take that in account in steady-state conditions.

For numerical methods, the simplifications of the material properties in the FE simulation are not factual in real situations. The lack of proper instruments also causes difficulties in the validation of FE models. It is impossible to implement on vehicle and it is very complex in nature and cost simulation time. Therefore, it is necessary to propose an innovative method for rolling resistance studies of tyres that can be used for different purposes and under different conditions.

1.2.4.3. Virtual/software sensor methods

In modern-day automotive control [47], [59], the real-time estimates of the vehicle dynamic states and tyre-road contact parameters are invaluable for enhancing the performance of vehicle control systems, such as anti-lock brake system (ABS) [60]–[64] and electronic stability program (ESP). Today’s production vehicles are equipped with on-board sensors (e.g. a 3-axis accelerometer, 3-axis gyroscope, steering wheel angle sensor, and wheel speed sensors), which when used in conjunction with certain model-based or kinematics-based observers can be used to identify relevant tyre and vehicle states for optimal control of comfort, stability and handling. Vehicle state estimation is becoming ever more relevant with the increased sophistication of chassis control systems.

Table 1 Comparison of rolling resistance measurement methods

<i>Methods</i>	<i>Conditions</i>	<i>Tyre design investigation</i>	<i>Pavement Design investigation</i>	<i>On-vehicle testing</i>	<i>Hand on experience</i>	<i>Cost</i>	<i>Remarks</i>
Laboratory Drum method	In Laboratory	x					Different from the tyre-flat road case
Trailer	On-Road	x	x				Difficult for

method							the calibration procedure
Coast-down method	In Laboratory/ On-Road	x	x	x	x		Difficult to consider various influencing factor effect
Energy consumption method	On-Road			x			Not accurate
Numerical method	On PC/On-Road	x	x				Need more validation
Virtual sensor method	On-Road	x	x	x	x	x	Under development

Several authors have proposed online estimation schemes of rolling resistance, in addition to parameters such as longitudinal stiffness, effective radius, tyre-road friction, and wheel slip using nonlinear observation methods [42], [64], [65]. Observations techniques such as high gain [66], sliding mode [21], [67], [68] and extended Kalman filter (EKF) [69] are also widely used to estimate vehicle states and parameters. The characteristics of classical observers lie in the easiness of its implementation, robust to modelling uncertainty and external disturbances. Whereas the main drawbacks of these classical observation techniques are sensitive to measurement noise, lack of stability around real values and take longer to converge to real values. This aggravates the situation, which has rapid dynamics in real-time conditions. Therefore, it is necessary to propose an adaptive method for accurate estimation rolling resistance studies of tyres that can be used for different purposes and under different conditions.

The syntheses of different methods are presented in Table 1. The green colour means it satisfies our need for the thesis. Since the motivation of this work is on vehicle real-time testing, the virtual sensor method seems to be the best suited for the requirement (all green). In the virtual sensor method, it is possible to take into account tyre-related as well as pavement design-related influencing factor while estimating the rolling resistance. It has a low cost of implementation as well as easy hand on experience. So the development of this method will be considered in this work.

1.2.5. Conclusion

In this section, the bibliographic study is presented on the tyre rolling resistance force. An important challenge for the development of current vehicles and autonomous vehicles is to ensure better energy management. It is concluded that the rolling resistance is one of the most important parameters affecting the fuel consumption and the performances of a vehicle. The definition and mechanism of rolling resistance were presented with the different influencing parameters. The main influencing parameters are speed, load, tyre inflation pressure, and temperature and road roughness. If there is a change in any above, mention parameters have a direct influence on rolling resistance. There is also the interconnection of parameters such as load and inflation pressure. Speed has shown its significant effect on rolling resistance above 100 km/h due to wheel aerodynamic effect. The influence of ambient temperature on the tyre internal temperature and pavement temperature which influences rolling resistance is also discussed.

The existing empirical rolling resistance coefficient models are presented which are mainly obtained with correlation methods for controlled conditions. This is specific to a few tracks with limitations. So

there is a lot to be done to account this in physical tyre model. The comparison of different rolling resistance measurement method is done. Experimental methods are inaccessible and very uncertain due to the quality of results, reproducibility of the measurements, limited to the specific and the high cost of physical sensors attached to vehicle tyres. Numerical methods are also not suitable for on-vehicle testing due to its complexity and simulation time. There is a little advancement in the real-time estimation of rolling resistance. Indeed, these applications have been far from conclusive, as it served only under simplified conditions: on straight-line track at a constant speed and simplified tyre-road contact model. Therefore, no work has been done to estimate the rolling resistance in real driving conditions with experimentation validation. Also, the impact of road roughness and temperature are not included as far as to our knowledge. Moreover, these studies did not account for the source of uncertainty, convergence and real-time estimation. Research in this area is still quite recent and much work remains to be committed.

To address this problem, the virtual sensors, type observer is explored in the next section for the estimation of rolling resistance under real driving conditions that take account of all the parameters.

1.3. Virtual sensor background

Virtual sensors or observers are widely used to determine the state of a dynamical system when not all components of the state are directly measured. Real-world dynamical systems and processes must often be modelled by nonlinear differential equations, and the design of a specific nonlinear observer is not a trivial task. Nonlinear observers have attracted great attention from the automatic control community in recent years [47], [59], [66], [70]–[73]. This is due to the fact that in many real models, some variables are very expensive to measure, and in certain cases, some variables are unmeasurable because they lost their physical sense through mathematical transformations. Therefore, designing state observers is a necessary step for diagnosis, control tracking, monitoring, and other control design problems. For instance, in the field of autonomous vehicles in a platoon, measurement of some variables, such as longitudinal distances, velocities and accelerations of other nearby vehicles, requires significant expense. Some of the sensors, such as slip angle and roll angle, can be extremely expensive to measure, requiring sensors that cost thousands of dollars [21], [74], [75]. Also, several important tasks cannot be performed due to the unavailability of sensors at any cost. Because of the lack of a general design method for nonlinear systems like in the linear case, several methods have been developed in the literature, where each method corresponds to a specific class of nonlinear systems.

The construction of observers for nonlinear systems is very interesting and several methods are available. The problem of state observation for nonlinear systems is of main importance in automatic control. In recent years many contributions have been presented in the literature that solves the design problem for classes of nonlinear systems. The field of state estimation of non-linear systems is still largely open.

As discussed above several authors have proposed online estimation schemes of rolling resistance, a few dedicated works are done in [21] with the aim to estimate the rolling resistance force by using virtual sensor based on the observer approach (sliding mode [22] and EKF). Indeed, these applications have been far from conclusive, as it served only under simplified conditions. Therefore, Estimate the rolling resistance in real driving conditions using a suitable observer technique is the main goal of this thesis. The comparison of different observer technique will allow us to identify the suitable observation technique for this thesis. Before comparing different technique some preliminary definitions and theorem are presented.

1.3.1. Observability of nonlinear systems

Intuitively, observability is concerned with whether, from observing sensor measurements for a finite period of time, the state can be reconstructed for previous times. Observability or detectability of the system to be estimated is an important property to ensure correct estimations from the observer. The observability criterion states that if a system is observable, the dynamic states of the system can be reconstructed from real measurements [76]. In the same place, several methods to determine observability are presented. The Lie derivative to evaluate the observability of the nonlinear systems is defined as:

Definition 1.1 Let $f : \mathbb{R}^n \rightarrow \mathbb{R}^n$ be a vector field in \mathbb{R}^n and let $h : \mathbb{R}^n \rightarrow \mathbb{R}$ be smooth scalar function. Then, the lie derivative of h with respect of f is

$$L_f h = \nabla h f = \frac{\partial h}{\partial x} f = \sum_{i=1}^n \frac{\partial h}{\partial x_i} f_i \quad (18)$$

Remark 1.1(Dimensions) Let us consider the dimensions of the Lie derivative: f has components

$$f = \begin{bmatrix} f_1(x) \\ \vdots \\ f_n(x) \end{bmatrix} \quad (19)$$

and h associates a scalar to each point in \mathbb{R}^n . The Lie derivative is given by

$$L_f h = \begin{bmatrix} \frac{\partial h}{\partial x_1} & \dots & \frac{\partial h}{\partial x_n} \end{bmatrix} \begin{bmatrix} f_1(x) \\ \vdots \\ f_n(x) \end{bmatrix} \quad (20)$$

that is, the Lie derivative is a scalar.

Remark 1.2(Lie Derivatives of higher order) Note that, by convention, we let

$$h = L_f^0 h \quad (21)$$

be the Lie derivative of 0^{th} order. We can define higher order Lie derivatives, for examples

$$L_f^2 h = \frac{\partial}{\partial x} [L_f^1 h] f \quad (22)$$

and so on. Note that if $\dot{x} = f(x)$, then

$$\begin{aligned} \dot{h} &= \frac{\partial h}{\partial x} \frac{\partial x}{\partial t} = \frac{\partial h}{\partial x} f = L_f^1 h, \\ \ddot{h} &= \frac{\partial}{\partial x} [L_f^1 h] f = L_f^2 h \\ &\vdots \\ h^{(k)} &= L_f^k h \end{aligned} \quad (23)$$

Definition 1.2 Consider the system described by the state equation

$$\dot{x} = f(x, u) \quad (24)$$

and the measurement equation

$$y = h(x) = \begin{bmatrix} h_1(x) \\ \vdots \\ h_p(x) \end{bmatrix} \quad (25)$$

two states x_0 and x_1 are called distinguishable if there exists an input function u^* such that

$$x_0 \neq x_1 \Rightarrow y(x_0) \neq y(x_1) \quad (26)$$

That is, if the sensor readings are different, the states are also different. The system is called locally observable at point x_0 if exists a neighbourhood of x_0 such that every x in that neighbourhood other than x_0 is distinguishable from x_0 .

Theorem 1.1 Consider the system described by the state equation

$$\dot{x} = f(x, u) \quad (27)$$

and the measurement equation

$$y = h(x) = \begin{bmatrix} h_1(x) \\ \vdots \\ h_p(x) \end{bmatrix} \quad (28)$$

Let G denote the set of all finite linear combinations of the Lie derivatives of $h_1(x), \dots, h_p(x)$ with respect to f for various values of $u = u^*$ constant. Let dG denote the set of all their gradients, evaluated at x_0 . If we can find n linearly independent vectors within dG , then the system is locally observable.

Let consider the single measurement case for illustration. We have

$$\begin{aligned} \dot{x} &= f(x, u) \\ y &= h(x) \end{aligned} \quad (29)$$

Taking successive derivatives of y yields

$$\begin{aligned} y &= h = L_f^0 h \\ \dot{y} &= \dot{h} = L_f^1 h \\ &\vdots \\ y^{(n-1)} &= L_f^{n-1} h. \end{aligned} \quad (30)$$

Let

$$l(x) = \begin{bmatrix} L_f^0 h \\ \vdots \\ L_f^{n-1} h \end{bmatrix} \quad (31)$$

Expanding in the first-order Taylor series about x_0 for $u = u_0$ yields

$$l(x, u_0) \approx l(x_0, u_0) + \left. \frac{\partial l(x, u_0)}{\partial x} \right|_{x=x_0} (x - x_0) \quad (32)$$

Then set

$$dG = 0 = \left. \frac{\partial l(x, u_0)}{\partial x} \right|_{x=x_0} \quad (33)$$

for local observability, the matrix O must have rank n .

1.3.2. Stability of dynamic systems

The stability of nonlinear dynamic systems is well defined in the literature [76], [77]. We consider the case unforced, autonomous systems, described by

$$\dot{x} = f(x) \quad (34)$$

Let do not consider disturbances. In the first time, we restrict the analysis to systems that do not have explicit time dependence. We consider equilibrium points of the system, obtained as described by solving

$$f(x_e) = 0 \quad (35)$$

As previously, we then consider perturbations about the equilibrium points:

$$\begin{aligned} x &= x_e + \delta x, \\ \delta \dot{x} &\approx \left. \frac{\partial f}{\partial x} \right|_e \delta x, \\ \mathfrak{J} &= \left. \frac{\partial f}{\partial x} \right|_e \end{aligned} \quad (36)$$

If no eigenvalues of J have zero real parts, local stability can be determined from the eigenvalues of J . If at least one eigenvalue has zero real part, the centre manifold theorem can be used to determine local stability. In this chapter, we examine the issue of global stability that will converge system to the origin as local stability doesn't ensure the stability of the entire system.

Definition 1.3 (Stability in the sense of Lyapunov [99]) *For simplicity, assume that we consider an equilibrium point at the origin, $x_e = 0$. (If this is not the case, the equilibrium point can be moved to the origin through appropriate coordinate transformation). The equilibrium $x_e = 0$ is stable if and only if*

$$\forall \epsilon > 0, \forall t_0 \geq 0, \exists \delta(\epsilon, t_0) > 0: \|x(t_0)\|_2 < \delta \implies \|x(t)\|_2 < \epsilon \forall t \geq t_0 \quad (37)$$

Furthermore, the equilibrium $x_e = 0$ is asymptotically stable if and only if

1. $x_e = 0$ is a stable equilibrium
2. $\forall t_0 \geq 0, \exists \delta(t_0) : \|x(t_0)\|_2 < \delta \Rightarrow \lim_{t \rightarrow +\infty} \|x(t)\| = 0$

Finally, the equilibrium $x_e = 0$ is uniformly stable if and only if

1. $x_e = 0$ is a stable equilibrium
2. $\delta(\epsilon, t_0) = \delta(\epsilon)$

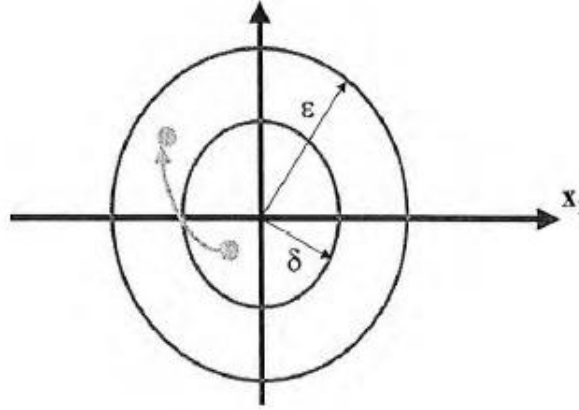


Figure 30 Stability in the sense of Lyapunov [99]

Definition 1.4 A scalar function is said to be positive definite if and only if $V(0) = 0$ and $V(x) > 0 \forall x \neq 0$.

Theorem 1.2 (Lyapunov second method) Consider the system described by

$$\dot{x} = f(x, t), \quad (38)$$

With $f(0, t) = 0 \forall t$. If a scalar function is defined such that:

1. $V(0, t) = 0$,
2. $V(x, t)$ is positive definite, that is, there exists a continuous, non-decreasing scalar function $\alpha(x)$ such that $\alpha(0) = 0$ and $\forall x \neq 0, 0 < \alpha(\|x\|) < V(x, t)$,
3. $\dot{V}(x, t)$ is negative definite, that is, $\dot{V}(x, t) \leq -\gamma(\|x\|) < 0$, where γ is a continuous non-decreasing scalar function such that $\gamma(0) = 0$,
4. $V \leq \beta(\|x\|)$, where β is a continuous non-decreasing function and $\beta(0) = 0$, that is, V is decrescent, and the Lyapunov function is upper bounded.
5. V is radially unbounded, that is, $\alpha(\|x\|) \rightarrow \infty$ as $\|x\| \rightarrow \infty$,

Then, the equilibrium point $x_e = 0$ is uniformly asymptotically stable in the large, and $V(x, t)$ is called a Lyapunov function.

Remark 1.3 It is very important to note that Theorem 1.1 provides a sufficient condition, not a necessary condition.

Remark 1.4 (Relaxed Conditions)

1. Asymptotic stability requires \dot{V} negative definite; stability requires \dot{V} negative semi-definite.

2. The condition that V be decrescent yields uniformity for time-varying systems.
3. Global stability is given by the radially unbounded condition.

Remark 1.5 The most difficult condition to obtain is that \dot{V} be negative definite. In many practical cases, \dot{V} is negative semi-definite, that is, the equilibrium point is stable but not asymptotically stable.

1.3.3. Canonical forms of nonlinear system

1.3.3.1. Canonical form

Consider the following class of nonlinear system

$$\begin{aligned}\dot{x} &= f(x) + \varphi(x, u) \\ y &= C(x)\end{aligned}\tag{39}$$

where $x = [x_1, x_2, \dots, x_n] \in \mathbb{R}^n$, the input $u \in U$ where U is a compact subset of \mathbb{R}^m , the output $y \in \mathbb{R}$, C is defined as:

$$C = [1 \ 0 \ \dots \ 0]\tag{40}$$

The function $\varphi(x, u)$ is assumed to be triangular with respect to x i.e.

$$\varphi(x, u) = \begin{pmatrix} \varphi(u, x_1) \\ \varphi(u, x_1, x_2) \\ \vdots \\ \varphi_{n-1}(u, x_1, \dots, x_{n-1}) \\ \varphi_n(u, x_1, \dots, x_n) \end{pmatrix} \in \mathbb{R}^n\tag{41}$$

There are a few hypotheses that need to be adopted before the synthesis of observer:

(H1) The function $\varphi(x, u)$ is Lipschitz with respect to x uniformly in u where $(u, x) \in U \times X$.

(H2) The state $x(t)$ and the control $u(t)$ are bounded, i.e. $x(t) \in X$ and $u(t) \in U$ for $t \geq 0$ where $X \subset \mathbb{R}^n$ and $U \subset \mathbb{R}^s$ are compact sets.

1.3.3.2. Particular class of the canonical form

We address in this section a particular class of nonlinear systems which can be put in the previous canonical form using an appropriate transformation. This class of systems has been studied in particular by [78], [79] for the characterization of a class of uniformly observable systems.

$$\begin{aligned}\dot{x} &= l(x, u) \\ y &= h(x) = l^0(x_1, u)\end{aligned}\tag{42}$$

where $x = [x_1, x_2, \dots, x_n] \in \mathbb{R}^n$, and the output is $y \in \mathbb{R}^m$, $x_k \in \mathbb{R}^{n_k}$, $k = 1, \dots, q$. $n = \sum_{k=1}^q n_k$ and $p = m_1 \geq m_2 \geq \dots \geq m_p$.

The input $u \in U$ where U is a compact subset of \mathbb{R}^u is a set of absolutely continuous functions with bounded derivatives of \mathbb{R}^+ .

We assume that the function $l(x, u)$ has the following structure:

$$l(x, u) = \begin{pmatrix} l^1(x_1, x_2, u) \\ l^2(x_1, x_2, x_3, u) \\ \vdots \\ l^{q-1}(x, u) \\ l^q(x, u) \end{pmatrix} \in \mathbb{R}^n \quad (43)$$

The following hypothesis **(H3)** is adopted for the synthesis of the nonlinear observer. It allows us to say that the system is detectable [80], that is to say, that the non-observable poles are stable.

(H3) For $0 \leq k \leq q - 1$: the function $x_{k+1} \rightarrow l^k(x_1, x_2, \dots, x_k, x_{k+1}, u)$ of $\mathbb{R}^{n_{k+1}}$ in \mathbb{R}^{n_k} is injective. Furthermore, we suppose that there exists $\alpha, \beta > 0$ such that for all $k \in 0, \dots, q - 1$,

$$\forall x \in \mathbb{R}^n, u \in U \quad (44)$$

$$0 < \alpha^2 I_{n_{k+1}} \leq \left(\frac{\partial l^k}{\partial x_{k+1}}(x, u) \right)^T \left(\frac{\partial l^k}{\partial x_{k+1}}(x, u) \right) \leq \beta^2 I_{n_{k+1}} \quad (45)$$

One introduces a change of coordinates which brings back the system (42) under the first canonical form (39). Formally, the observer's equations in the original coordinates are given by considering the pseudo-inverse of the matrix of the coordinate change function. Consider the following change of coordinates:

$$\Phi : \mathbb{R}^n \rightarrow \mathbb{R}^{mp}$$

$$x = \begin{pmatrix} x_1 \\ x_2 \\ \vdots \\ x_q \end{pmatrix} \rightarrow z = \Phi(x, u) = \begin{pmatrix} z_1 \\ z_2 \\ \vdots \\ z_q \end{pmatrix}$$

With

$$\begin{cases} z_1 = l^0(x_1, u) \\ z_2 = \frac{\partial l^0}{\partial x_1}(x_1, u) l^1(x_1, x_2, u) \\ \vdots \\ z_q = \left(\prod_{k=0}^{q-2} \frac{\partial l^k}{\partial x_{k+1}}(x, u) \right) l^{q-1}(x, u) \end{cases} \quad (46)$$

where $z_k \in \mathbb{R}^m$ for $k = 1, \dots, q$.

After hypotheses **(H3)** with an application of Φ is injective.

We put $\Lambda(x, u)$ as the following diagonal matrix

$$\Lambda(x, u) = \text{diag} \left(\frac{\partial l^0}{\partial x_1}(x, u), \frac{\partial l^0}{\partial x_1}(x, u) \frac{\partial l^0}{\partial x_2}(x, u), \dots, \prod_{k=0}^{q-2} \frac{\partial l^k}{\partial x_{k+1}}(x, u) \right) \quad (47)$$

This matrix makes it possible to carry out the change of coordinates and to obtain the following relation:

$$\Lambda(x, u)l(x, u) = Az + G(x, u) \quad (48)$$

A defined as follows is a block offset matrix:

$$A = \begin{pmatrix} 0_m & I_m & \cdots & 0_m \\ \vdots & 0_m & \ddots & \vdots \\ 0_m & \cdots & 0_m & I_m \\ 0_m & \cdots & 0_m & 0_m \end{pmatrix} \in \mathbb{R}^{mp \times mp} \quad (49)$$

and G is a matrix given by the following equation:

$$G = \begin{pmatrix} 0 \\ \vdots \\ 0 \\ \left(\prod_{k=0}^{q-1} \frac{\partial l^k}{\partial x_{k+1}}(x, u) \right) l^q(x, u) \end{pmatrix} \quad (50)$$

Hypothesis **(H3)** implies that the matrix $\Lambda(x, u)$ is invertible on the left, its inverse is noted $\Lambda^+(x, u)$. We, therefore, deduce that

$$l(x, u) = \Lambda^+(x, u)Az + \Lambda^+(x, u)G(x, u) \quad (51)$$

The dynamics of z is given by

$$\dot{z} = \frac{\partial \Phi}{\partial x}(x, u)\dot{x} + \frac{\partial \Phi}{\partial u}(x, u)\dot{u} \quad (52)$$

After solving

$$\dot{z} = Az + G(x, u) + \left(\frac{\partial \Phi}{\partial x}(x, u) - \Lambda(x, u) \right) \Lambda^+(x, u)Az + \frac{\partial \Phi}{\partial u}(x, u)\dot{u}$$

by replacing

$$\varphi(z, u) = G(x, u) + \left(\frac{\partial \Phi}{\partial x}(x, u) - \Lambda(x, u) \right) \Lambda^+(x, u)Az + \frac{\partial \Phi}{\partial u}(x, u)\dot{u}$$

Using the adopted notations, the system (42) can be written in the new z coordinates in the following form:

$$\begin{aligned} \dot{z} &= Az + \varphi(z, u) \\ y &= C(z) \end{aligned} \quad (53)$$

where $C = (I_m \ 0_m \ \dots \ 0_m) \in \mathbb{R}^{m \times mq}$.

The system (53) is in canonical form (42). Therefore, the observer (54) can be synthesized for this system. Using hypotheses **H1**, the equations of this observer are written in the new coordinates as follows:

$$\dot{\hat{z}} = A\hat{z} + \varphi(\hat{z}, u) + \kappa(y, \hat{z}) \quad (54)$$

Where $\hat{z} = [z_1, z_2, \dots, z_q]^T$ and the function κ is the correction term, which ensures us the convergence of estimated state to the real state despite the initial error. From

$$z = \Phi(x, u)$$

one gets

$$\dot{\hat{z}} = \frac{\partial \Phi}{\partial x} \dot{\hat{x}} \rightarrow \dot{\hat{x}} = \left[\frac{\partial \Phi}{\partial x} \right]^{-1} \dot{\hat{z}} = \left[\frac{\partial \Phi}{\partial x} \right]^{-1} (\varphi(\hat{z}, u) + \kappa(y, \hat{z})) \quad (55)$$

So the observer for the system (42) can be written as

$$\dot{\hat{x}} = l(\hat{x}, u) + \left[\frac{\partial \Phi}{\partial x} \right]^{-1} \kappa(y, \hat{x}) \quad (56)$$

1.3.4. Different nonlinear observers

In most applications, the process must be controlled or monitored in real-time and this requires being able to access the variations as a function of time of the state variables. This access is not always possible either due to the lack of suitable sensors or the high cost of some of these sensors. To overcome this problem, a state observer (an estimator) is generally used to reconstruct unmeasured state variables. The field of state and parameter estimation of non-linear systems is still largely open. We will see that there is no universal method for the synthesis of such observers, various observation techniques are discussed in the literature. The synthesis of possible approaches is given in Table 2, the detailed explanation can be found in appendix A.

Table 2 Synthesis of different observation techniques

Observers	Observer properties	Limitations	References
Kalman filter	<ul style="list-style-type: none"> - A set of mathematical equations that provides an efficient computational means to estimate the state of a process - Supports estimations of past, present, and even future states - Widely used in the industry - Implementation simplicity independently of the system complexity 	<ul style="list-style-type: none"> - The major drawback of this method is the lack of guaranteed stability 	[81]–[83]
Nonlinear transformation methods	<ul style="list-style-type: none"> - Technique is based on a change of coordinates which makes possible to transform a nonlinear system into a linear system. - The state of the original system is achieved using the reverse coordinate change. 	<ul style="list-style-type: none"> - Finding a non-linear transformation that linearizes the system is not always evident, and this constitutes the main drawback of this method. 	[84]–[86]
Extended nonlinear observers	<ul style="list-style-type: none"> - Extended Kalman filter and extended Luenberger observer are examples of these kinds of observers. - The design of this type of observer also consists of adding a second gain to the Luenberger observer inside the non-linear part of the system. 	<ul style="list-style-type: none"> - Initialization of the observer is also crucial - The necessary condition cannot always be satisfied, for instance with systems having high Lipchitz constant in this kind of observer. - The estimation accuracy of 	[87]–[91]

		the observers largely depends on how well the linearized model represents the nonlinear dynamics.	
High gain observers	<ul style="list-style-type: none"> - This observer is based on the observable canonical form. - High-gain observers are relatively simple to design less complex differential equations. - Stability guarantees for any arbitrarily chosen initial conditions. - It is relatively fast and robust to model uncertainty and external disturbances. - These observers guarantee that the observer error is globally asymptotically convergent to zero. - The effectiveness of such an observer has been highlighted through many successful industrial applications. 	<ul style="list-style-type: none"> - Design parameter is generally carried out through a try and error procedure to get a satisfactory compromise between the accuracy of the observer. - Sensitive to measurement noise. - They suffer from the 'peaking' phenomenon, where, due to the high-gain, there is an initial sharp spike in the response of the state estimates. This phenomenon can cause instability for some types of systems. 	[66], [72], [78], [92], [93]
Sliding mode observers	<ul style="list-style-type: none"> - Sliding mode observers have unique properties, in that the ability to generate a sliding motion on the error between the measured output and the output of the observer ensures that a sliding mode observer produces a set of state estimates that are precisely commensurate with the actual output of the plant. - The ability to generate a sliding motion on the error between the measured plant output and the output of the observer ensures that a sliding mode observer produces a set of state estimates that are precisely commensurate with the actual output. - The main advantages are conservation benefits of the sliding mode observer, its robustness and convergence in finite time, reduction of the effects of chattering and the improvement of the performance of the observer. 	<ul style="list-style-type: none"> - The analysis of the average value of the applied observer injection signal, the so-called equivalent injection signal, contains useful information about the mismatch between the model used to define the observer and the actual plant. - The discontinuous injection signals which were perceived as problematic for many control applications. - Lack of stability around real values and longer time to converge to real values. This aggravates the situation, which has rapid dynamics in real-time conditions. 	[67], [68], [94]–[97]
Adaptive observers	<ul style="list-style-type: none"> - Adaptive gain observers help to estimate simultaneously the system states and the unknown parameters. - The adaptive solution is the most suitable variable dynamics and continuous change in a situation during the real situation. - Their robustness to modelling error, parameter uncertainty and input noise used to detect the variation in the input. - The convergence of the proposed observer is guaranteed under a well-defined persistent excitation condition. - The structure of the proposed observer is simple 	<ul style="list-style-type: none"> - The observer needs to generate estimates of the vector of unknown parameters and unmeasured state components under noisy environments - Not many application in automotive industry 	[66], [93], [98]–[107]

	- A design function in the observer gain which is calibrated through the choice of a single design parameter.		
Observers for singularly perturbed systems	<ul style="list-style-type: none"> - The above approaches presuppose the availability of a dynamic process model that does not exhibit time-scale multiplicity - Singular perturbation technique is a means of taking into account neglected high frequency and parasitic phenomenon into modelling systems by decoupling the representation into slow and fast time scales. - It should be emphasized, that the design of nonlinear observers based on the reduced-order model 	<ul style="list-style-type: none"> - The state estimation problem becomes not only theoretically challenging due to the multiple timescales but practically an intriguing one. - Stiff dynamics, may lead to ill-conditioned observer gains and potentially undermine the convergence properties of an observer designed for the full-order singularly perturbed system 	[108]–[119]

1.3.5. Conclusion

The observability and stability criterion for the nonlinear observers presented at the beginning of this section allows us to ensure correct and stable estimations from the observer. Once the criteria are satisfied, it ensures that the states of the system can be reconstructed from the real measurements. The synthesis of different observation techniques outlined the advantages and disadvantages of existing observer techniques. For example, the Kalman is most used due to its implementation simplification but its main drawback lies in the lack of guaranteed stability. Similarly, the linearization technique is also attracting but it is difficult to find the non-linear transformation that linearizes the systems. The effectiveness of high gain observers has been highlighted through many successful industrial applications. However, the main drawback of this observer is the design parameter that is generally carried out through a try and error procedure to get a satisfactory compromise between the accuracy of the observer and its sensitivity to noise measurements.

The main advantages are conservation benefits of the sliding mode observer, its robustness and convergence in finite time, reduction of the effects of chattering and the improvement of the performance of the observer. Whereas the main drawbacks of these classical observation techniques are sensitivity to measurement noise, lack of stability around real values and longer time to converge to real values. This aggravates the situation, which has rapid dynamics in real-time conditions. To overcome this, an adequate strategy for using adaptive gain observers and identify the parameters of the model in real-time is proposed. This is motivated by the fact that the adaptive solution is the most suitable variable dynamics and continuous change in a situation during the real situation. Their robustness to modelling error, parameter uncertainty and input noise used to detect the variation in the input. This is achieved through the specification of a design function in the observer gain which is calibrated through the choice of a single design parameter. This is also shown in the dedicated work done in [120]. In this study, the comparison of two different adaptive gain observers is presented. This study shows the high practical interest of adaptive high gain observer due to its robustness and finite-time convergence modelling error, parameter uncertainty and input noise used to detect the variation in the input. Its advantages and disadvantages have allowed choosing the most effective solution with respect to accuracy, robustness and computing complexity.

As discussed previously, the objective of this thesis is to estimate the rolling resistance for a full vehicle. To address this problem, the adaptive gain nonlinear observer is explored for estimation of

rolling resistance under real driving conditions that take account of all the parameters. In the next section, adaptive high gain [103] and adaptive second order sliding mode observers [121] are developed for the application of estimation of rolling resistance on the quarter car.

This is motivated by the fact that the adaptive solution is the most suitable for the rolling resistance estimation because of variable dynamics and continuous change in a situation during the real driving situation. Their robustness to modelling error, parameter uncertainty and input noise used to detect the variation in the input. Their advantages and disadvantages have allowed choosing the most effective solution with respect to accuracy, robustness and computing complexity. The choice of a quarter car is made to represent the standard trailer test of rolling resistance. The work is done in [120] mainly to choose observer technique, which is most suitable to estimate the rolling resistance force in real driving conditions.

1.4. Different adaptive observer techniques comparison

This section deals with the identification of suitable observation technique for estimation of the rolling resistance of a tyre. Two nonlinear observers are developed for a quarter car model in order to get a robust and accurate estimation of rolling resistance force [120]. In this section, the adaptive high gain and the adaptive second order sliding mode techniques are compared. Their advantages and disadvantages have allowed choosing the most effective solution with respect to accuracy, robustness and computing complexity. Finally, simulation validation is carried out with software MATLAB/Simulink and SCANer Studio (vehicle dynamic software). This section presents the first results of an original estimation of rolling resistance using adaptive gain observers.

1.4.1. Quarter car

In literature, a lot of quarter car models are available [21- 23] which are easy and simple to implement in Simulink. In this section, we present the longitudinal dynamics of the quarter car model. The model presented in [7] is a model for this application in Simulink.

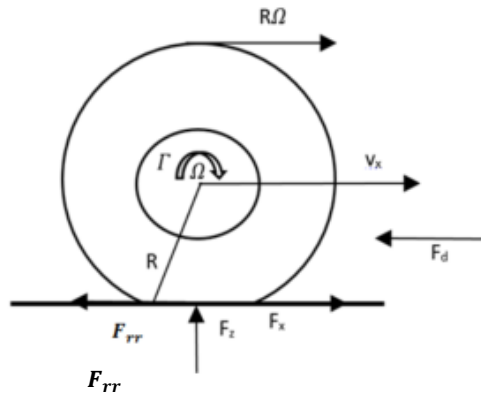


Figure 31 Longitudinal dynamics of a wheel [7]

According to Newton's 2nd law, the longitudinal and rotational dynamics of the quarter car system in Figure 31 can be represented by the following equation [21]:

$$\begin{cases} J\dot{\Omega} = \Gamma - RF_x - C_f\omega \\ M\dot{v}_x = F_x - F_d - F_{rr} \end{cases} \quad (57)$$

with v_x as longitudinal speed, ω angular speed of the wheel, Γ torque applied at the tyre, F_x is traction force, F_d is aerodynamic force, F_{rr} is rolling resistance force, J is the inertia of the wheel, M mass of the quarter car and C_f is the friction coefficient of the wheel bearing.

In this model, the author considered single point contact between tyre and ground with constant effective tyre radius and tyre pressure. The vertical displacement is also neglected. The numerical validation of this model can be found in [120].

The quarter car can be written as state variables $x = [x_1 \ x_2]^T = [\Omega \ v_x]^T$

$$\dot{x} = \begin{bmatrix} \frac{1}{J}(\Gamma - RF_x(x) - C_f x_1) \\ \frac{1}{M}(F_x(x) - F_d(x) - F_r) \end{bmatrix} \quad (58)$$

1.4.2. Observer design

In this section, the adaptive high gain observer and adaptive second order sliding mode observer are designed for a quarter car model described above, which allow the estimation of rolling resistance. The main idea is to understand the behaviour of different adaptive observer technique and compare their performances. Firstly, the model is written under state space form and observability of the system is analysed thanks to numerical evaluation technique.

1.4.2.1. State space model

In this section, the state space representation of the model is given. To write the model here in the dynamic equation of longitudinal and rotational, the dynamic of F_{rr} is supposed to have a variation and can be seen as unknown so we can write the dynamics as:

$$\dot{F}_{rr} = \eta(t) \quad (59)$$

where η as bounded function.

The model can be written directly from equation (58) the state vector as $x = [x_1 \ x_2 \ x_3]^T = [\Omega \ v_x \ F_{rr}]^T$ and $u = \Gamma$ the torque, we obtain system as

$$\dot{x} = \begin{bmatrix} \frac{1}{J}(-RF_x(x) - C_f x_1) \\ \frac{1}{M}(F_x(x) - F_d(x) - x_3) \\ \eta \end{bmatrix} + \begin{bmatrix} \frac{1}{J} \\ 0 \\ 0 \end{bmatrix} u \quad (60)$$

The output is $y = \Omega = x_1$ we can write the x_1 as measured and u is known we can write the term depends only on known variable

$$\frac{1}{J}(u - C_f x_1) \quad (61)$$

So the system (60) can be written as

$$\dot{x} = f(x) + \Delta f + g(y, u) \quad (62)$$

with

$$f(x) = \begin{bmatrix} -\frac{1}{J}RF_x(x) \\ \frac{1}{M}(F_x(x) - F_d(x) - x_3) \\ 0 \end{bmatrix}, \Delta f = \begin{bmatrix} 0 \\ 0 \\ \eta \end{bmatrix}, g(y, u) = \begin{bmatrix} -\frac{C_f}{J}x_1 + \frac{1}{J}u \\ 0 \\ 0 \end{bmatrix} \quad (63)$$

Observability will be analysed on the system without incertitude and after input-output injection $g(y, u)$

1.4.2.2. Observability analysis

The observability condition of the system is verified as explained in section 1.3.1, which is based on Lie derivatives of the outputs of the system.

$$\begin{cases} \dot{x} = f(x, u) \\ y = h(x) \end{cases} \quad (64)$$

where $x \in \mathbb{R}_n$ represent the state of the system, $u \in \mathbb{R}_m$ input and $y \in \mathbb{R}_p$ the output of the system. For each input u , a Jacobian matrix (Ψ) of output and its derivatives at state can be defined using Theorem 1.1:

$$\Psi(x, u) = \begin{bmatrix} h_i \\ L_f h \\ \vdots \\ L_f^{n-1} h \end{bmatrix} = \begin{bmatrix} y \\ \dot{y} \\ \ddot{y} \end{bmatrix} = \begin{bmatrix} x_1 \\ -\frac{1}{J}RF_x(x) \\ d[-\frac{1}{J}RF_x(x)] \end{bmatrix} \quad (65)$$

The system (62) satisfies local observability rank conditions at x_0 if:

$$\text{Rank} \left[\frac{\partial \Psi(x_0, u)}{\partial x} \right] = n \text{ or } \det \left[\frac{\partial \Psi}{\partial x} \right] \neq 0 \quad (66)$$

The state transformation proposed in [21] is applied on (64), the two adaptive gain observers are proposed next.

1.4.2.3. Adaptive high gain observer

An adaptive high gain based observer is proposed in [103] and [122] for the class of uniformly observable systems which are observable for any inputs. The structure of observer for estimation of rolling resistance, with the known longitudinal, angular velocity and torque with observation model based on the adaptive gain higher order sliding mode can be written as from [122]:

$$\begin{cases} \hat{\dot{x}} = f(\hat{x}) + g(u, \hat{x}) - \left[\frac{\partial \Psi(\hat{x})}{\partial \hat{x}} \right]^{-1} \Lambda^{-1}(\theta_1) K C^T \tilde{x}(t) \\ \dot{\theta}_1 = -\frac{\mu}{2} \theta_1(t) (a(\theta_1(t) - 1) - g(t) \gamma(\|\tilde{y}(t)\|)); \quad \theta_1(0) \geq 1 \\ g(t) = \frac{M}{1 + \min(\rho, \frac{1}{L} \int_{\max(0, t-L)}^t \|\tilde{y}(\tau)\|^2 d\tau)} \end{cases} \quad (67)$$

Where $\hat{x} = [\hat{x}_1, \hat{x}_2, \dots, \hat{x}_n] \in \mathbb{R}^n$ with $\tilde{x} = \hat{x} - x$ where x and u is the state and input of the system; Matrix K such that $A - KC$ is Hurwitz; with $C = [1 \ 0 \ 0]$ and A is deduced from $f(x)$.

$\mu = \frac{\lambda_{\min}(Q)}{\lambda_{\max}(S)}$ and $\gamma: \mathbb{R} \rightarrow \mathbb{R}^+$, $\tilde{y} = \gamma(\tilde{y})$ is a real-valued function satisfying the following properties:

- $\gamma(0) = 0$
- $\exists \gamma > 0; \forall \tilde{y} > 0, 0 < \gamma(\tilde{y}) \leq \gamma_{max}$

Matrices S and Λ^{-1} are defined as follows:

Let $\theta_1: \mathbb{R} \rightarrow \mathbb{R}, t \rightarrow \theta_1(t)$ be a real-valued function and let $\Lambda(\theta_1)$ be the following diagonal matrix:

$$\Lambda(\theta_1) = \text{diag}\left(\frac{1}{\theta_1}, \frac{1}{\theta_1^2}, \dots, \frac{1}{\theta_1^n}\right) \quad (68)$$

$$D = \text{diag}(1, 2, \dots, n) \quad (69)$$

Consider the following algebraic Lyapunov equation

$$S + A^T S + SA = C^T C \quad (70)$$

It was shown in [66] that the (70) admits a unique solution S , which is symmetric and positive definite and whose terms can be expressed as follows:

$$S(i, j) = (-1)^{(i+j)} C_{i+j-2}^{j-1} \text{ for } 1 \leq i, j \leq n, \text{ where } C_n^p = \frac{n!}{(n-p)! p!} \quad (71)$$

The main feature of this observer consists of an appropriate calibration of the observation gain through a single parameter governed by some scalar Riccati equation. It is time-varying with a dynamic which allows it to be maintained at low values while the observer continues to provide accurate estimates.

1.4.2.4. Adaptive gain second order sliding mode observer

A novel adaptive law for the gains of the second order sliding mode (SOSM) algorithm with only one tuning parameter is designed via a so-called “time scaling” approach [91]. The structure of observer for system (62) estimation of rolling resistance, with the known longitudinal, angular velocity and torque with observation model based on the adaptive gain second order sliding mode can be written as from [123]:

$$\dot{\hat{x}} = f(\hat{x}, y) + \left[\frac{\partial \Psi}{\partial x}\right]^{-1} \mu(e) \quad (72)$$

Where $\mu(\cdot)$ is the SOSM algorithm given in [124],

$$\mu(e) = \lambda(t)|e|^{\frac{1}{2}} \text{sign}(e) + \alpha(t) \int_0^t \text{sign}(e) d\tau + k_\lambda(t)e + k_\alpha(t) \int_0^t e d\tau \quad (73)$$

With $e = (y - \hat{x})$ and the adaptive gains $\lambda(t)$, $\alpha(t)$, $k_\lambda(t)$ and $k_\alpha(t)$ are formulated as:

$$\begin{cases} \lambda(t) = \lambda_0 \sqrt{l(t)} \\ \alpha(t) = \alpha_0 l(t) \\ k_\lambda(t) = k_{\lambda_0} l(t) \\ k_\alpha(t) = k_{\alpha_0} l^2(t) \end{cases} \quad (74)$$

where λ_0 , α_0 , k_{λ_0} , and k_{α_0} are positive constants to be defined and $l(t)$ is a positive, time-varying, scalar function. The adaptive law of the time-varying function $l(t)$ is given by:

$$\dot{l}(t) = \begin{cases} k, & \text{if } |e| \neq 0 \\ 0, & \text{else} \end{cases} \quad (75)$$

where k and $l(0)$ are positive constants.

1.4.2.5. Simulation results and discussion

Simulation scenarios are divided into two parts. The first part consists of a comparison of estimation of F_{rr} for two observers with SCANer™ Studio (Prosper) for validation. SCANer™ Studio (Prosper) [125] is a simulation software tool which analyses the dynamic behaviour of vehicles, developed by the company OKTAL. It is explained in detail in section 3.2.4. In order to further evaluate the quality of observer estimation, comparison of observer estimation of F_{rr} for different parametric variations is done in second part. To carry out the simulations the proposed observers are initialized by

$$\hat{x}(0) = \begin{bmatrix} 50 \\ 16.66 \\ 40 \end{bmatrix}, \theta_1 = 4 \quad (76)$$

Different conditions are simulated on a passenger car in SCANer™ prosper environment in order to get input torque and measured velocities for observers.

The precision of the observer is evaluated by calculating the relative mean estimation errors:

$$\bar{e}_{F_{rr}} = \frac{1}{N} \sum_{i=1}^N \left| \frac{F_{rr}(t_i) - \hat{F}_{rr}(t_i)}{F_{rr}(t_i)} \right| \quad (77)$$

with t_i is counted from the instant when estimated values start converging to real ones (approx. 5sec) to 40 sec and N number of samples in this period. Different simulation scenarios are given in Table 3.

The first step is to verify the observability. The jacobian matrix is evaluated and the results are shown in Figure 32. The determinant of jacobian matrix never equals 0 on the operating trajectories, it yields that the transformation $\Psi(x)$ is invertible. It satisfies the above condition of (66) which defines that the system (62) with measured variables is observable in operating conditions.

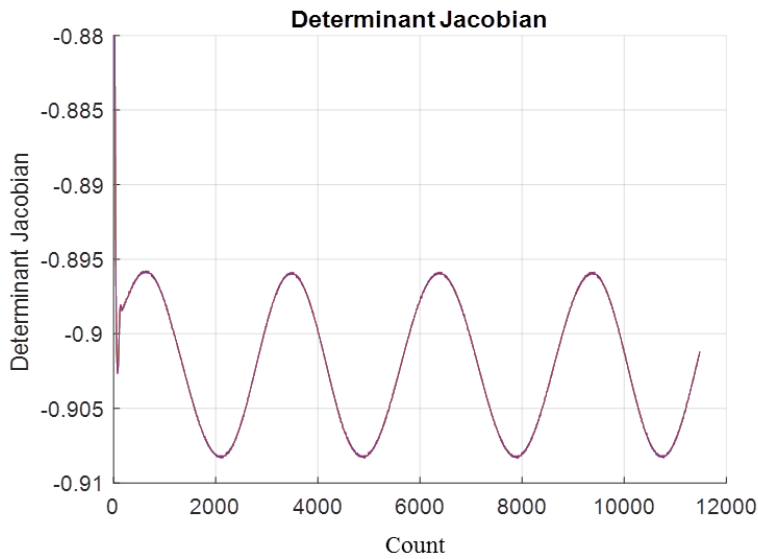


Figure 32 Determinant of Jacobian matrix

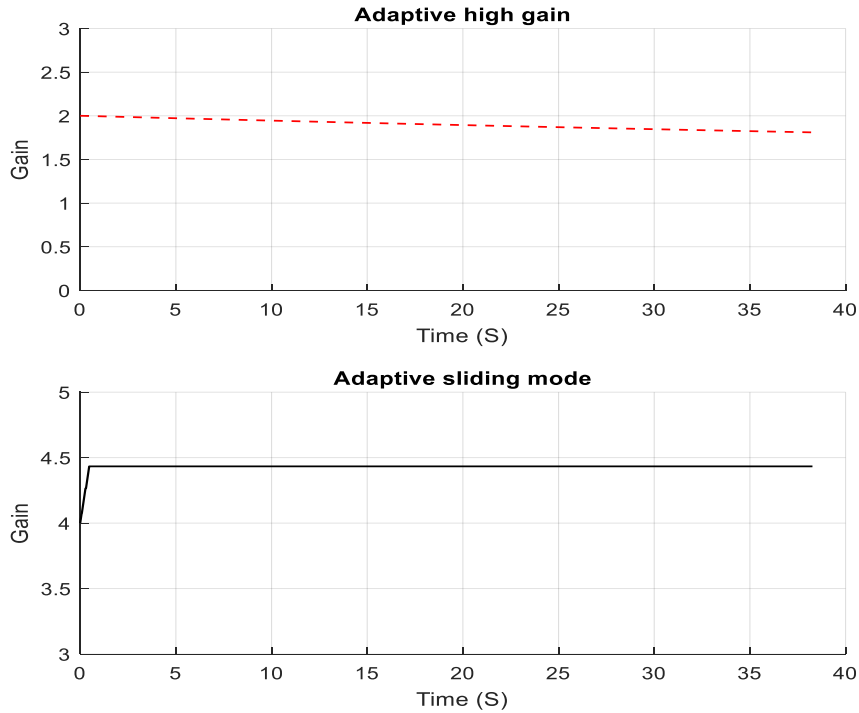


Figure 33 Gain for adaptive high gain and SOSM observer

The adaptive gain from the adaptive high gain observer is varied from its initial value to a constant value since there is no perturbation during the simulation in Figure 33.

For our simulations, we have used a full car model to simulate different conditions (see Table 3) and measurements for a single drive wheel are considered for comparison. Hypotheses considered during simulations are:

- Straight line track is considered.
- Constant speed, pressure, development radius and tyre temperature is considered.
- Road profile is considered as smooth.

The output from these 4 cases is directly injected into our observers with parameters. The results of case 3 are discussed here. The comparison of adaptive high gain and adaptive SOSM is presented and the results for case 4 we can find in the appendix G.

Table 3 Simulation test plan

Case	Speed (Km/h)	Road roughness (mm)
1	50	Smooth surface
2	80	Smooth surface
3	60 km/h with variance 0.1 km/h	Smooth surface
4	50 km/h and accelerates in 10 sec to 80 km/h.	Smooth surface

1. Different cases simulation results

The simulation is done for all the cases (defined in Table 3) and relative mean errors are calculated (see Table 4 Simulated errors of estimated values for two observers (Table 4)). Only, the simulation results from case 3 are presented here. In order to simulate sensor noise, a zero mean additive noise with variance 0.1km/h is added to speed.

In Figure 34 real values and estimated values from adaptive high gain (in red) and adaptive SOSM (in black) are presented with real values coming from SCANeR™ (in blue). In Figure 35 the relative mean error is given, for time 5 sec to 35 maximum errors is 6% only, which is acceptable. Estimated values of rolling resistance are converging towards real values in 2 sec for adaptive high gain and 4 sec for adaptive SOSM. It means that adaptive sliding mode is taking long to converge to the real values whereas adaptive high gain converges rapidly which is one of our criteria of comparison. Estimation of adaptive sliding mode shows chattering and estimation from adaptive high gain is smooth as seen in closer look in Figure 34 and Figure 35. Current gain values are a good compromise between chattering and convergence for adaptive SOSM.

Fr estimation different techniques

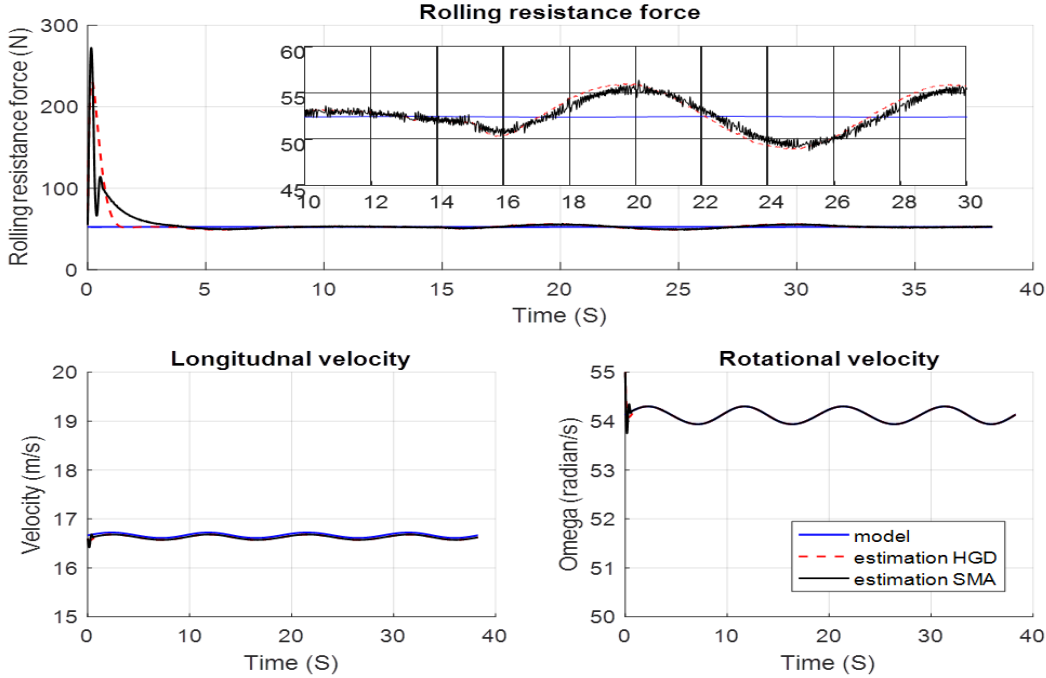


Figure 34 Estimation results of rolling resistance for case 3

Other cases are simulated and results are shared in Table 4. In constant speed, both observers estimate close to real values.

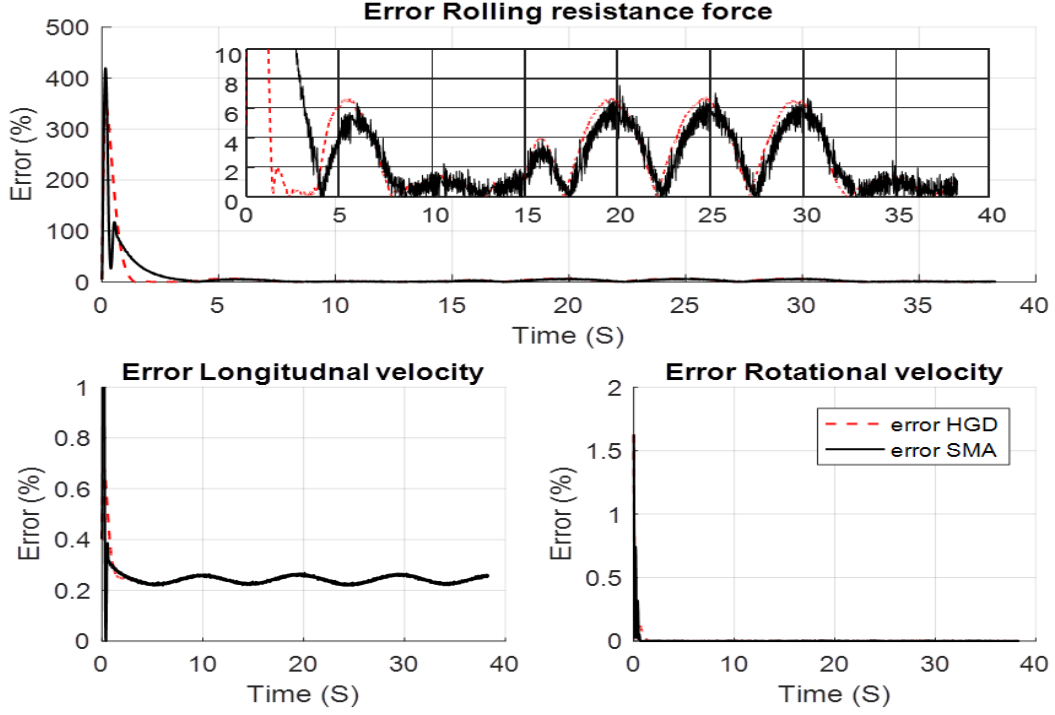


Figure 35 Estimation errors for case 3

In a variation of speed lack of complete dynamics can be seen in the results. The gain parameter for observers is changing with the variation but the estimated values of the observer are underpredicting which can be due to lack of complete vehicle dynamics. The proposed model does not account for full vehicle dynamics, it is obvious that we are going to see some differences in estimated and real values, which become wider in variation case. This also justified that for robust and accurate estimation of rolling resistance, a model must consider the complete physical phenomenon of tyre-road contact.

Table 4 Simulated errors of estimated values for two observers

Case	$\bar{\epsilon}_{F_{rr}}\text{HGD}(\%)$	$\bar{\epsilon}_{F_{rr}}\text{SMA}(\%)$
1	1.79	1.42
2	1.81	1.03
3	2.71	3.71
4	1.41	1.73

2. Parametric study

Both observers have no information of dynamics of F_{rr} which induces uncertainty to the system. In order to justify the quality of estimation, simulations with parametric variations are performed. Supposing that initial parameters are standard cases, two types of parametric variation are proposed below:

- Parametric variation 1: $\mu_0 = 0.8$ and $\lambda_0 = 0.1$.
- Parametric variation 2 : mass = 380 kg

Table 5 displays the values of the relative mean error of these two cases.

Table 5 Simulated errors of estimated values for two observers

Case	$\bar{e}_{F_{rr}}\text{HGD}(\%)$	$\bar{e}_{F_{rr}}\text{SMA}(\%)$
PV 1	1.48	1.69
PV 2	1.90	1.11

Results from Table 4 and Table 5 conclude that both observers are estimating very close to real values of F_{rr} with a relative mean error ($\bar{e}_{F_{rr}}\text{HGD}(\%)$, $\bar{e}_{F_{rr}}\text{SMA}(\%)$) less than 5%. In robustness, both the observers are showing same error results and it is difficult to choose one observer. In term of convergence adaptive high gain observer is converging faster as compare to adaptive SOSM by 2 sec. The adaptive high gain takes around 2 seconds to converge where adaptive SOSM takes 4 seconds. This difference can be important while computation in real driving conditions where dynamics are fast.

1.4.3. Conclusion

Two nonlinear adaptive high gain and adaptive SOSM are applied and compared in order to get a robust and accurate estimation of rolling resistance force. The main goal is to identify suitable observation technique for estimation of rolling resistance. This section presented the very first results of the original estimation of rolling resistance using adaptive gain observers. This is a very promising solution to use in real driving conditions. There is no significant difference in relative mean error except convergence in these two observers and both can be used for the estimations. For all the cases a quarter car used in this study, the two observers give similar results in terms of robustness and precision with less than 5% relative error on the rolling resistance value. The adaptive high gain method is better on cases 3 and 4 and not on cases 1 and 2. Cases 1 and 2 are carried out with a constant speed and without measurement noise. Case 3 present noises (variance 0.1Km / h) and case 4 present a speed variation. In the simulation, the adaptive high gain method gives better results on cases presenting noise or variations than the adaptive sliding mode method. It favours the strategy of the adaptive gain solution, which has several advantages as discussed earlier. The comparison study allowed us to consider the adaptive high gain observer that shows high practical interest due to its robustness and finite time convergence modelling error and parameter uncertainty.

It remains to validate this observation/hypothesis on a complete vehicle. The estimation results should be compared with experimental results before taking a final decision about the observers. Future research will be conducted on completing the tyre-road contact model by adding phenomenon such as road surface, temperature etc. The accurate estimation of rolling resistance also depends on considering its influencing parameters into the model, so in the next chapter, the integration of influencing parameters in the tyre model is presented.

Chapter 2

Tyre modelling

The objective of this chapter is to develop the multi-physical tyre model for this thesis. In order to achieve this objective, different tyre-models categories are briefly analysed in section 2.1 and a comparative study of the most significant models of each category is conducted. It provides us with a good overview of the advantages and drawbacks of existing models. In section 2.2, the development of a tailor-made multi-physical tyre model is proposed to fit the needs of this research work.

2.1. Different tyre models comparison

The tyre represents the only link between the vehicle and the ground, thus it is of extreme importance to have good knowledge about its behaviour under different operating conditions. Great efforts have been done by the automotive industry in the field of tyre modelling, thus an extensive bibliography is available. Semi-empirical tyre models, such as Magic Formula, that fit to tyre test data were developed to represent tyres in-vehicle dynamic simulations. With the improvement of computational power, complex tyre models were studied in order to predict the force and moment characteristics of the tyre based on its physical features and construction. While the later is widely used for ride, comfort and durability purposes, the semi-empirical models are more common for dynamic handling simulations, since the computational efforts are smaller.

Several tyre models have been developed in recent years, and they can be divided into empirical models and physical approaches [43]. Each category has a different degree of complexity and accuracy, hence they have distinct purposes. Figure 36 illustrates the main aspects that characterize the different tyre-model categories.

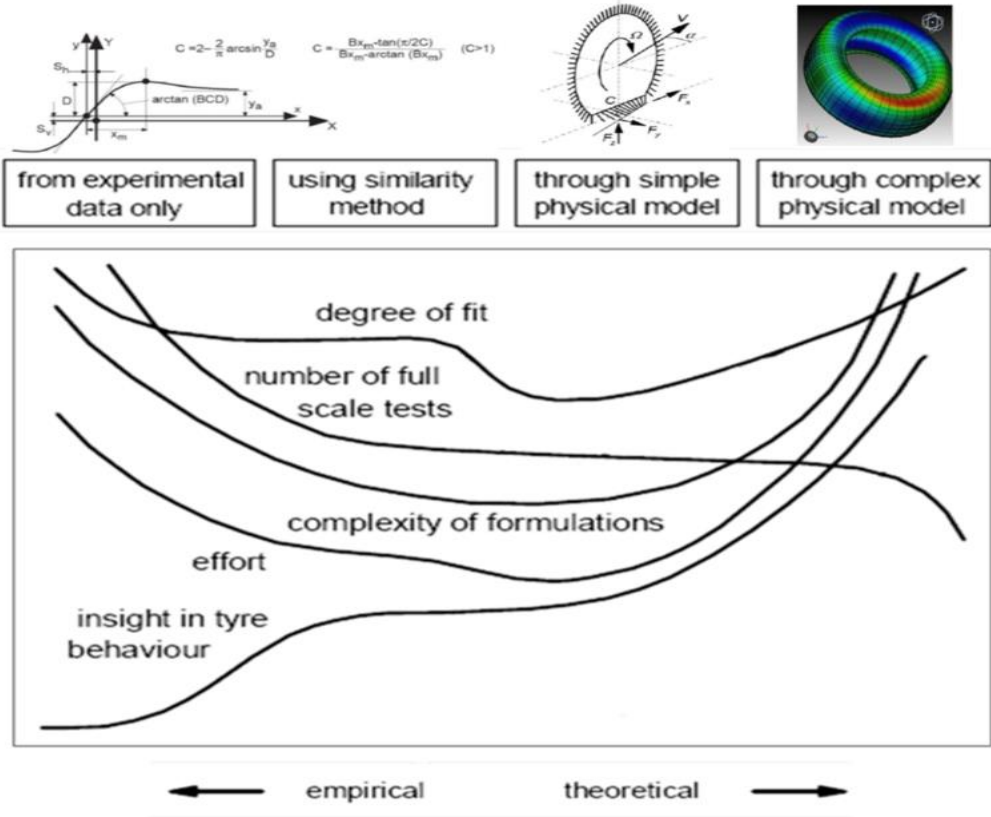


Figure 36 Tyre-model categories main characteristics[43]

From the right to the left, models are based more on full-scale tyre experiments and less on the behaviour of the structure of the tyre. On the right, the theoretical models, which are also known as

physical models, are more complex, because the tyre is described in details. The physical models are appropriate for studying tyre construction and simulate the tyre’s behaviour.

There are two categories of physical models. The first is complex finite element models that are geared towards the more detailed analysis of the tyre. These models are able to represent carcass deflection and to determine the total forces and moment through the tread elements motion and the integration of frictional forces. The models solve the deflection of the tread elements when they run through the contact patch using an iteration process. In addition, these models are capable of handling non-steady-state conditions. This type of tyre models has been used in [30].

The second category is that of the relatively simple physical models. These kinds of models help to gain a better understanding of tyre behaviour since their simple equations provide accuracy. The best-known model in this category is the “brush model” developed in [43], [45]. The four fundamental factors that it represents are parabolic pressure distribution, frictional properties between tyre and road, carcass flexibility, and compliance of the tread rubber. The LuGre Tyre model is a modification of the brush model proposed by Canudas-de-Wit in [126]. Nowadays, studies [12], [13] based on the bond graph approach are also using physical tyre model.

The empirical models are on the left-hand side of Figure 36. The first category uses the similarity method. This means that these models can describe tyre behaviour through distortion and rescaling and by combining basic tyre characteristics from measured data. They are also appropriate for real-time computations, despite being simple models and not accurate. They are also called semi-empirical models because they have some formulation based on physical models and yet they use measured data. The main disadvantage these kinds of models presents is that they only describe steady-state Tyre behaviour. The second category of empirical models contains Tyre models that describe the tyre’s behaviour using only mathematical formulae that fit real test data. The best-known model is Pacejka’s Magic Formula, a purely empirical model based on functions to describe the tyre forces and moment at combined slip on the steady-state.

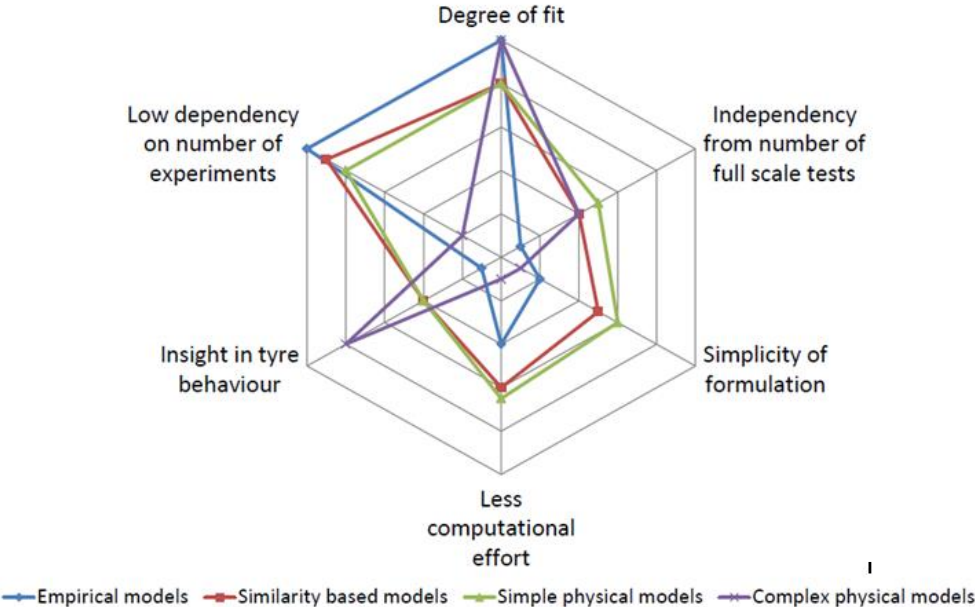


Figure 37 Spider chart for different Tyre-model categories

Table 6 Synthesis of different tyre models

Category	Tyre model	Comments	Model equation
Semi empirical	Magic Formula [43]	<ul style="list-style-type: none"> - Magic formula model is a very accurate representation of actual tyre dynamics. - But this comes at a cost since the model depends on a lot of parameters which is obtained through experiments. 	$F_x = D_x \sin[C_x \arctan\{B_x \kappa_x - E_x(B_x \kappa_x - \arctan(B_x \kappa_x))\}] + S_{vx}$ $F_y = D_y \sin[C_y \arctan\{B_y \kappa_y - E_y(B_y \kappa_y - \arctan(B_y \kappa_y))\}] + S_{vy}$
	LuGre Model [126]	<ul style="list-style-type: none"> - It describes both steady-state and dynamic tyre behaviour. - This dynamic friction model predicts the transient behaviour of the tyre-road forces under varying velocity circumstances. - Its ability to reflect the surface conditions, the effects of tyre vertical force and the effects of the vehicle speed on the friction force is main advantage. - Its weakness is that many improvements are needed in order to extend its application range. 	$\dot{z} = v_{sx} - \frac{\sigma_0 v_{sx} }{g(v_{sx})} z$ $F_x = (\sigma_0 z + \sigma_1 \dot{z} + \sigma_2 v_{sx}) F_z$ $g(v_{sx}) = \mu_c + (\mu_s - \mu_c) e^{-\sqrt{ v_{sx} /v_{st}}}$
	Dugoff model [128]	<ul style="list-style-type: none"> - The advantage of this model is that it does not require a large number of parameters since it is an analytical model - The drawback of this method is that the gradient cannot be computed directly, since there are different equations for sliding and pre-sliding. - The model is a very simplified representation. Therefore, the shape of the tyre curve is limited, such that a peak in the tyre curve cannot be modelled 	$F_x = K_x \frac{\kappa}{1 - \kappa} \tau$ $F_y = K_y \frac{\kappa}{1 - \kappa} \tau$
Physical	Brush model[43], [129]–[131]	<ul style="list-style-type: none"> - It depends on the physical parameters of the tyre and the tyre is described as a series of elastic elements, which can deflect in contact with the road. - The friction coefficient is assumed to be equal for both lateral and longitudinal direction - Moreover, using just one line of bristles, it doesn't allow having a 3D picture of all the forces acting in the contact patch, and this is a big drawback. - It explains the nature of the forces in the contact patch with a strong physical background. - It requires a smaller number of model parameters for describing the steady-state characteristic. - This model is very comparable to the Dugoff model presented earlier and has the same advantages and disadvantages. - Nevertheless, this representation is more realistic, because of the more advanced vertical pressure distribution 	$F_x = \begin{cases} \mu F_z (1 - \lambda_x^3) \text{sgn} \sigma_x & \text{if } \sigma_x \leq \frac{1}{\theta_x} \\ \mu F_z \text{sgn} \sigma_x & \text{if } \sigma_x > \frac{1}{\theta_x} \end{cases}$ $F_y = \begin{cases} \mu F_z (1 - \lambda_y^3) \text{sgn} \alpha & \text{if } \tan \alpha \leq \frac{1}{\theta_y} \\ \mu F_z \text{sgn} \alpha & \text{if } \tan \alpha > \frac{1}{\theta_y} \end{cases}$
Finite element	MFT-tyre [30]	<ul style="list-style-type: none"> - These models are based on the finite element approach. They can predict the accurate tyre temperature, but they require significant computational power, in addition to a large amount of information related to the internal structure of the tyre. 	Complex equations

In Figure 37, spider chart is shown for different tyre model categories defined above. This shows that each category has its own advantages and disadvantages. In this chapter, several tyre models from the literature have been studied and compared to choose a suitable model for our work, the synthesis of comparison is presented in Table 6. The detailed explanation on different models is given in the annex B. A comparison of different existing tyre models has been realized and results are provided in the following sections.

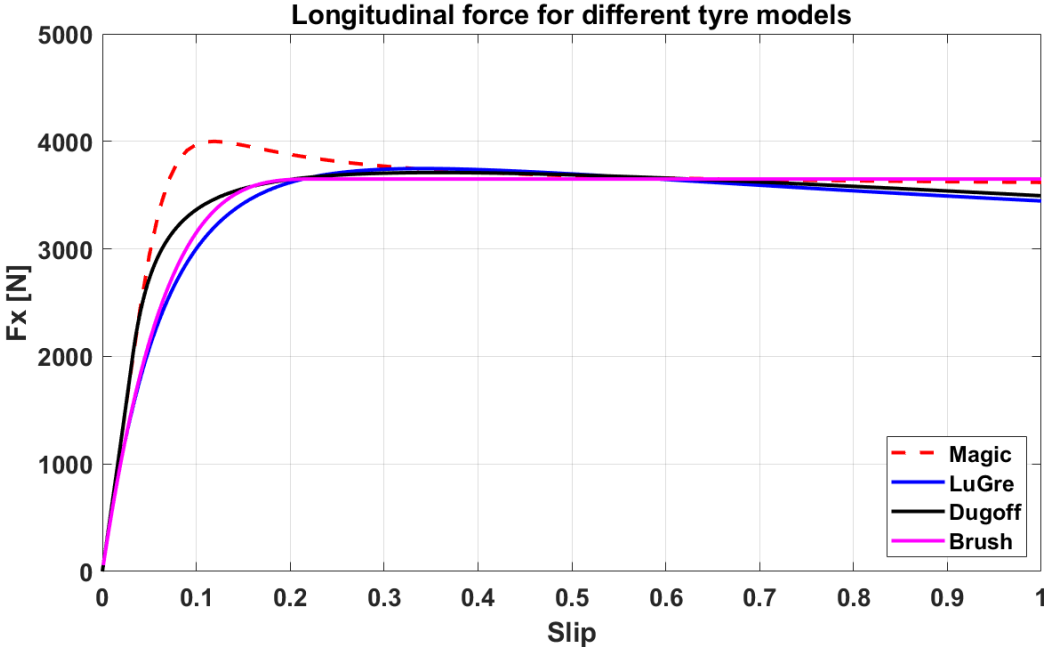


Figure 38 Comparison of different tyre models (longitudinal forces)

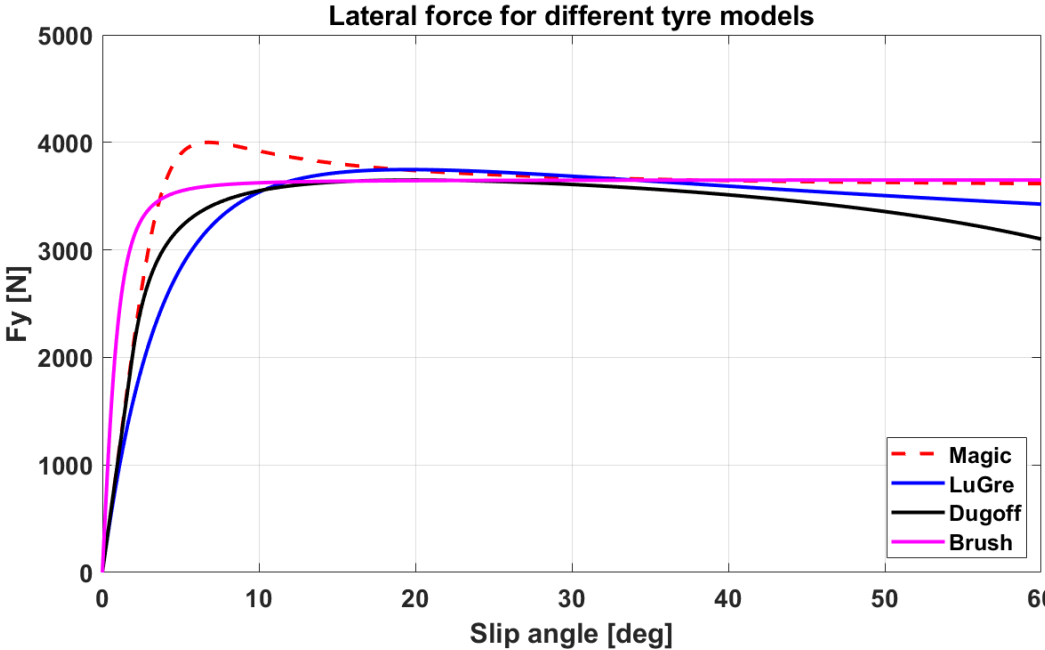


Figure 39 Comparison of different tyre models (lateral forces)

For all the models studied above in Table 6, the formulation for longitudinal and lateral forces has been presented. Then, using MATLAB, the formulation has been computed and the force versus slip plots depicted. A comparison of the characteristics force of Pacejka, LuGre, Dugoff and Brush models has been conducted. Pacejka model is considered as a reference here and other models are compared with it. When other models are compared to the Pacejka's magic formula the curve is not having an exact similar shape. As compared models are physical models it is difficult to exactly fit the curve. In Figure 38 and Figure 39 the curves of the brush model for the longitudinal and lateral forces have a very similar shape.

The main conclusions that can be drawn from this comparison are summarized below in terms of the strengths and weaknesses of the different models. The strength of Pacejka's Magic Formula is that the model best describes steady-state tyre behaviour. There is a lot of information about this model, and many extensions have been done. On the other hand, the weakness of this model is that it does not describe dynamic tyre behaviour. The model parameters do not have a physical meaning, since it describes only the curve shape also need to perform a lot of experimental tests to calibrate the model.

The LuGre tyre model strength is that it describes both steady-state and dynamic tyre behaviour. Finally, its weakness is that many improvements are needed in order to extend its application range.

In fact, Brush model is very comparable with results of magic formula. Nevertheless, this representation is more realistic, because of the more advanced vertical pressure distribution [132]. So this model is most suitable for our work. But the requirement for this work is to include the impact of infrastructure and thermal effect make us search model which can account this impact.

When a tyre is rolling on a surface, rubber compounds are deformed principally by the load exerted on it, flattening out in contact patch. This deformation is due to rubber viscoelastic properties and results in energy dissipation in the form of heat [133]. This energy dissipation and heat generated due to contact forces directly influence the tyre rubber temperature. The temperature dependence of the viscoelastic properties of tyre rubber has a significant influence on its hysteretic friction. Many researchers have shown that the coefficient of friction of viscoelastic tyres skidding/rolling against a pavement macro-texture varies with temperature [134], [135]. It is common knowledge that tyre performance is heavily affected by the tyre temperature, which is a function of the rolling speed, sideslip, ambient temperature and longitudinal slip [136], [137]. [134] Presented a review on parameters influencing measurements and tyre-pavement friction model and underlined the influence of temperature on friction. Currently, analytical tyre models used for the vehicle dynamics simulation do not take into account the variation of the model parameters as functions of the tyre temperature [138]–[143].

Sophisticated thermo-mechanical models have been developed to predict the accurate tyre temperature [133], [144]–[147]. These models are based on the finite element approach [133], [147]–[149]. They can predict the accurate tyre temperature, but they require significant computational power, in addition to a large amount of information related to the internal structure of the tyre. The other finite elements models for specific study such as to understand the impact of rain intensity or hot climatic conditions on friction while taking pavement properties into account has been developed by [146], [147]. In this work, only dry road condition has been considered.

In literature, a few single bristle brush-based thermal models have been already developed in [150]–[155]. However, there are still some modifications that can be done on these models to improve their accuracy or better explain involved physical mechanisms. So a choice of an analytic model based on brush model is done, according to the following criteria:

- The representative of the tyre- road contact model of reality,
- The multi-physical model with longitudinal, lateral and vertical dynamics.
- A model integrating all the physical phenomena (mechanical, pneumatic, thermal).

In the next section, a multi-physical tyre model is developed, which requires a negligible increase of the computational power effort within a vehicle dynamics model. It will consider the effects of temperature and surface texture on the tyre. The aim is to contribute to a better understanding and modelling of the tyre–road pavement interaction. This tyre-road interaction model can be used for friction estimation as well as rolling resistance estimation. The objective is to use it for rolling resistance estimation. However, for full vehicle dynamics simulation, tyre modelling simplifications are necessary in order to keep the model as simple and as fast as possible.

2.2. Development of Multi physical tyre (MPT) model

In this section, the development of multi-physical tyre model is explained. It is called multi-physical because it includes the mechanical and thermal physical phenomenon. This model is made out of two blocks i.e. mechanical block and thermal block which are interacting with each other via temperature-dependent parameters to give tyre forces, moments and tyre temperatures as output as shown through the flow chart (Figure 40).

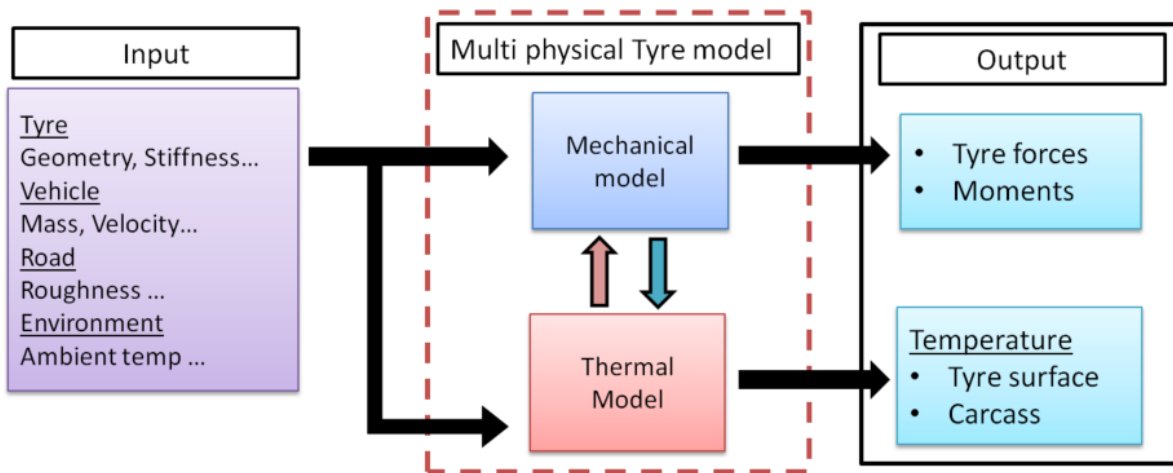


Figure 40 Multi physical tyre model

2.2.1. Mechanical model

As discussed in [43] the brush tyre model is a well-known physical model. It provides a good platform for tyre model development as there is the possibility of dealing with the force generation mechanisms of the tyre using mathematical representations to obtain solutions either analytically and numerically through simulation.

This mechanical block is based on the basic theories of the brush tyre model as well as earlier efforts in developing related tyre models [44], [46], [138]. These models are the extension of the basic brush model represented in Figure 41, which mainly consist of two zones: adhesion and sliding. The topology of the model is defined by the tyre radius, rim width, aspect ratio and side-wall inclination. In order to enable a realistic model of the tyre-road contact, the rubber properties have been implemented in all three directions, i.e., longitudinal(x), lateral (y) and vertical (z) directions. Also, the rubber treads are assumed in the form of individual bristles using a finite number of bristles that touch the

road plane as explained in Figure 42. This approach is motivated by the work done in [156]–[158]. However, as shown, unlike the basic brush tyre model where the tyre width is disregarded. The multi bristle model considers a finite number of lines parallel to each other in order to resemble the tyre width and the bristles are spread over these lines along with the contact patch. So the tyre is modelled as a rigid ring with bristles.

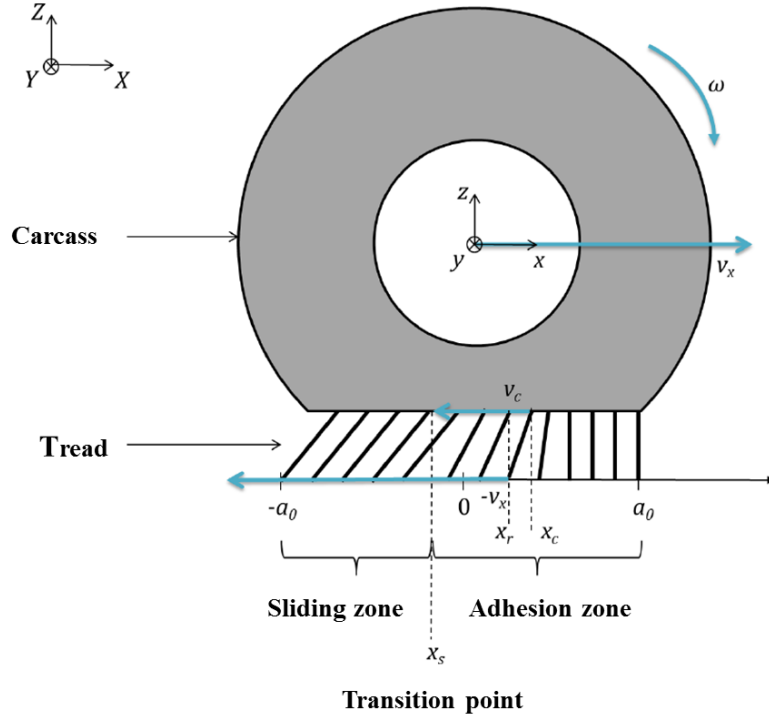


Figure 41 The brush tyre model[159]

The carcass and belt construction of the tyre are assumed to have no damping and the belt is assumed as a rigid ring to which the bristles are connected. Flexible carcass in the lateral direction based on the model suggested in [138] is also included in calculating the force distribution over the contact patch. It is considered mainly to take into account the contribution of dynamic manoeuvres and wheel alignment settings on the tyre deformation. The anisotropic nature of tyre treads is taken into account by the incorporation of individual damping c and stiffness k for bristles in x , y and z directions and their values are taken from literature mainly from [158].

In order to resemble the hysteresis characteristic of rubber material of the tyre, bristles were modelled as “3 parameters Maxwell model” (Figure 42), which is used in the tyre model. Studies such as [158] show that this is the best representation of a tyre tread which can also work for high-frequency solicitations/excitation. Therefore, the resultant force of each bristle is derived as

$$F_M^t = F_M^{ve} \quad (M = x, y, z) \quad (78)$$

where F^{ve} is the viscoelastic force and F^t are tyre forces which are calculated using equation (79)

$$\dot{F}_{ve}(\delta, t) = -\frac{k}{c}F_{ve}(t) + \frac{k \cdot k}{c}\delta(t) + (2k)\dot{\delta} \quad (79)$$

The friction between road and tread is not easy to model; it is a function of the rubber compound, the pattern of the tread as well as the road, the relative velocity of the surfaces. In original brush model the

friction is modelled with just two parameters; the static friction and dynamic friction. When the resultant force is greater than the product between the vertical force and static friction acting on the bristle, the resultant force is limited by the dynamic friction. In this work, dynamic friction is used. It is a function of the sliding velocity between the tread and the road (tip of bristle).

$$\mu(v_{s(x,y)}) = \mu_{c(x,y)} + \frac{\mu_{s(x,y)} - \mu_{c(x,y)}}{1 + |v_{s(x,y)}/v_{str(x,y)}|^{2.5}} \quad (80)$$

where $v_{s(x,y)}$ is sliding velocity of the surface in contact in longitudinal and lateral directions, $\mu_{s(x,y)}$ is static friction, $\mu_{c(x,y)}$ is friction at the asymptote and $v_{str(x,y)}$ is the Stribeck velocity. The sliding forces are calculated using the slip projection approach (SPM) given in [132]. The above given dynamic friction example is shown in Figure 43.

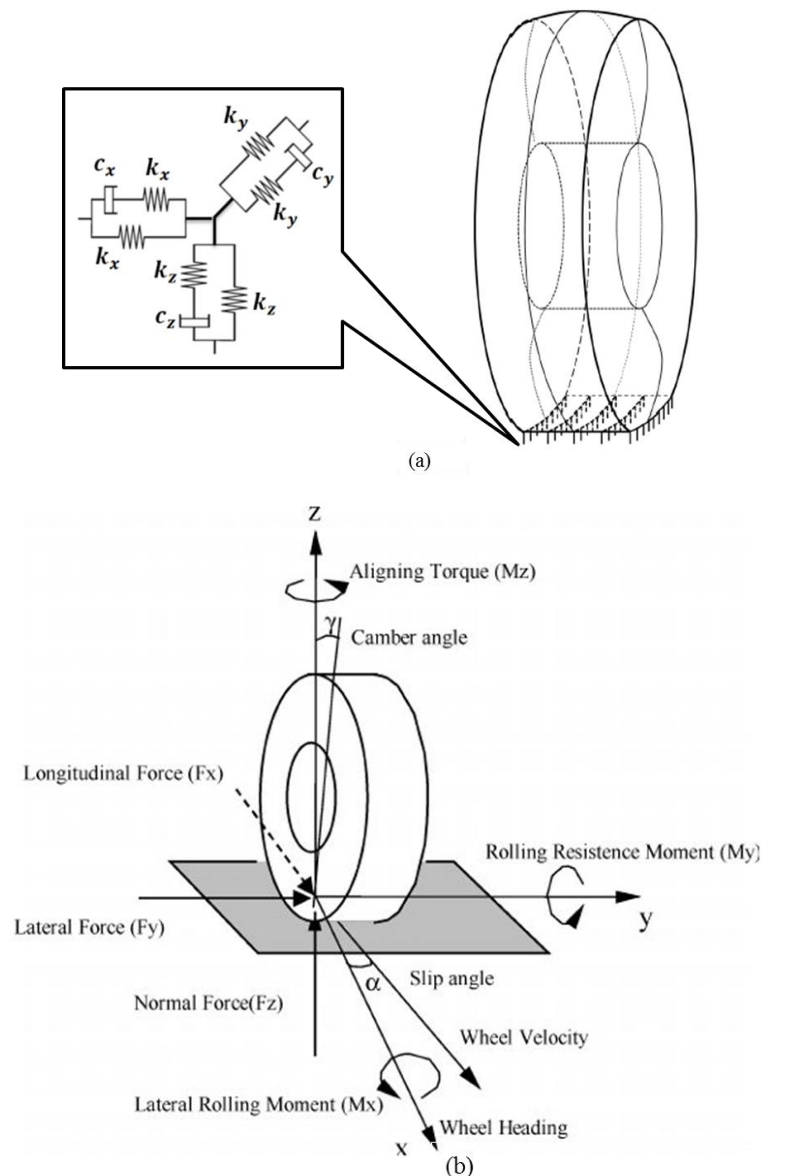


Figure 42 Schematic of (a) Multi-bristles brush model with 3 parameters Maxwell model [160] (b) Wheel reference coordinate system

The input parameters of the model are the tyre geometry including rim and tyre width, side-wall length, and tyre radius. It also consists of the tyre characteristics including stiffness, damping, and load sensitivity factors, which can be modified based on empirical data. Also, external tyre parameters are defined by the side-slip angle, the longitudinal slip and the camber angle. The model is parameterized with m number of lines where each line contains n number of bristles, which are assumed here to be massless. The state of each bristle is numerically calculated and updated during the process of rolling. The mechanical block model, in turn, gives the global forces and moments (longitudinal and lateral forces, overturning and aligning moments).

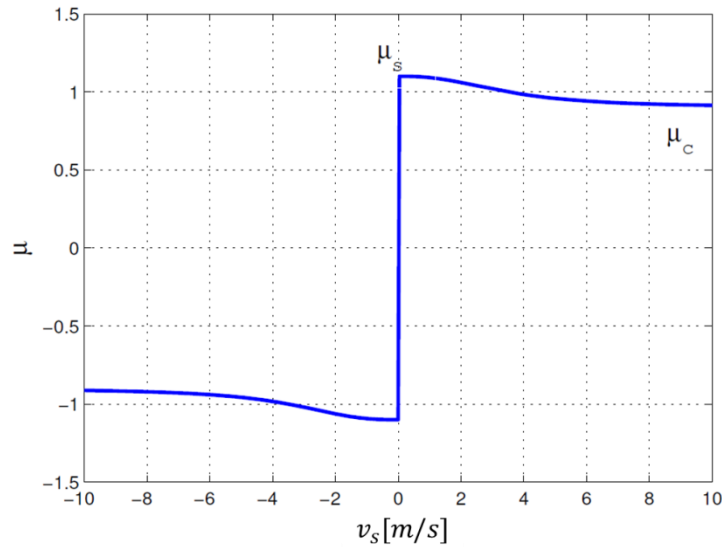


Figure 43 Dynamic friction model example values taken from [160]

The above multi bristle model can describe well the different dynamics and it gives a better understanding of tyre mechanics. However, it is based on some simplifications, which can be improved to get more accurate results and integrate more parameters which can influence friction. As discussed above friction is widely influenced by parameters such as road roughness and temperature. The model mentioned above is operated at a constant temperature. Next section is devoted to the development of a thermal model to consider the temperature effect.

2.2.2. Thermal model

In this section, the thermal model for a tyre is developed. It is a function of tyre forces so that variation of temperature is taken into account for any vehicle manoeuvres (rolling, braking and accelerating). We assume heat exchanges in a tyre as represented in Figure 44. The thickness of tyre is divided into two layers: the outer one simulates tyre treads and inner one simulates area near the carcass. The tyre during the rolling phase is subjected to three main phenomena: heat production, heat exchanges and cooling.

2.2.2.1. Heat generation

The production of heat in the contact zone is mainly caused by the frictional forces in the sliding zone [150], [151].

$$Q_{Friction\ forces} = Q_{Fx,tire} + Q_{Fy,tire} \quad (81)$$

The generation of longitudinal force and lateral force provokes the dissipation of energy in the contact area.

$$\begin{aligned} Q_{F_x,tire} &= \lambda |F_x v_{sx}| \\ Q_{F_y,tire} &= \lambda |F_y v_{sy}| \end{aligned} \quad (82)$$

Where F_x is the tyre longitudinal force, v_{sx} is the tyre longitudinal slip velocity, F_y is the tyre lateral force, v_{sy} is the tyre lateral slip velocity, and h is the thermal exchange coefficient between the tyre and the air ambient. The λ coefficient is an effective ratio of heat taking into account the proportion actually received by the tyre during contact (part being transferred to the surrounding air). In his research [151] ideally places this value between 0.5 and 0.8. In our case, a value of 0.55 is chosen based on the tuning of simulations using the trial and error method with experimental results.

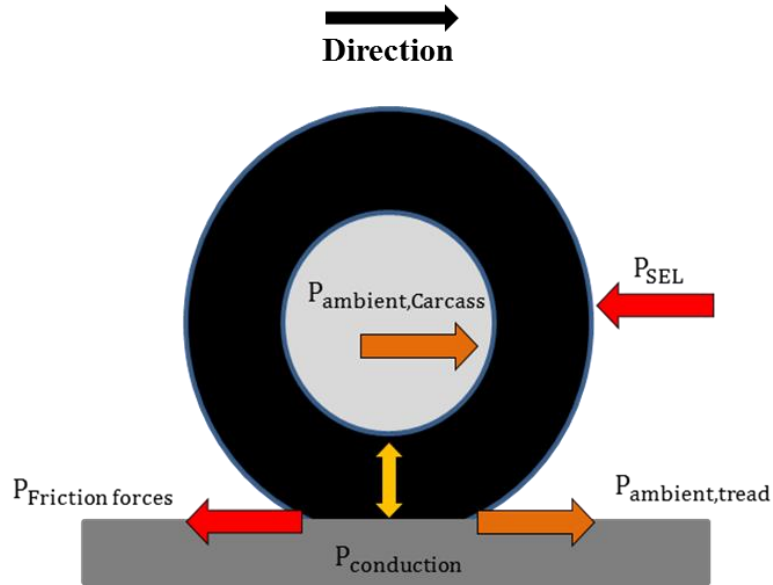


Figure 44 Heat exchange model between tyre and road

2.2.2.2. Heat exchange

In this model, heat exchange is considered between road, tread and carcass. This is mainly due to the temperature gradient in the respective surface. It is described as $Q_{conduction}$ in the model. The conduction of road is not considered previously in studies such as [150], it is added in this model to complete the conduction.

In practice, the heat exchange is happening in the adhesion region in the contact area. Since adhesion comes before the sliding zone where the absence of sliding makes temperature unchanged. This area is characterized by a heat exchange coefficient widely discussed in [21] and [22]. We define hereafter:

$$Q_{conduction} = h_c(T_{track} - T_{tread}) * S_{cont} - k_c(T_{tread} - T_{carcass}) * S_t \quad (83)$$

where h_c track-tyre exchange coefficient in W/m^2K , k_c is thermal conductivity in W/mK , T_{track} is road temperature, T_{tread} is tyre tread temperature, S_{cont} is the surface area of contact, $T_{carcass}$ is temperature near tyre belt and S_t the total surface area of the tyre.

2.2.2.3. Cooling by convection force

The forced convection $Q_{ambient,tread}$ and $Q_{ambient,carcass}$ are due to the relative movement of the air relative to the wheel given its rotational movement during the rolling phase. According to the studies of [151] and [161], it is possible to bring out a thermal resistance for this purpose:

$$\begin{aligned} Q_{ambient,carcass} &= h_{carcass}(T_{ambient} - T_{carcass}) * S_{conv} \\ Q_{ambient,tread} &= h_{tread}(T_{ambient} - T_{tread}) * S_{conv} \end{aligned} \quad (84)$$

$$h = \frac{k_{air}}{L} \left[0.318 \left(\frac{V \cdot L}{\nu} \right)^{0.571} \right] \quad (85)$$

where k_{air} is the thermal conductivity of the air, L is the characteristic length, V speed in m/s and ν kinematic viscosity of the air, $h_{carcass}$ belt-ambient exchange coefficient in W/m²K, h_{tread} ambient-tyre exchange coefficient in W/m²K, S_{conv} is the surface area of in contact of the tyre and ambient air.

2.2.2.4. Loss of heat by the viscoelastic effect

Another source of loss of heat is a heat flux (Q_{SEL}) related to the dissipations due to cyclic deformation during rolling also called strain energy loss. This contribution is related to the tyre rolling resistance coefficient.

Based on the literature, it is very difficult to evaluate this loss of energy. We have assumed a simple and common material which constitutes the tyres namely SBR vulcanized. The law of WLF on viscoelastic materials offers us the possibility of obtaining an average temperature of the materials corresponding to the current thermal stress and its frequency of use. More generally in the case of a tyre, Alfredo Corrolaro [161] proposes an approach to estimate the SEL.

This contribution of dissipation of energy entirely heats the tyre. Q_{SEL} is calculated as a function of tyre angular speed and Moment M_y .

$$Q_{SEL} = M_y \omega \quad (86)$$

M_y is calculated as a function of longitudinal force (F_x), ω is rotational velocity and loaded radius (R_L) to simplify P_{SEL} calculation.

$$M_y = F_x R_L \quad (87)$$

After considering the above-mentioned phenomenon we can apply the first principle of thermodynamics to the system. The thermal model is represented by equation (88) and (89).

$$m_c c_v \frac{dT_{carcass}}{dt} = Q_{SEL,c} + k_c(T_{tread} - T_{carcass}) * S_t + Q_{ambient,carcass} \quad (88)$$

$$m_t c_t \frac{dT_{tread}}{dt} = Q_{SEL,t} + Q_{Friction\ forces} + Q_{conduction} + Q_{ambient,tread} \quad (89)$$

2.2.3. Integration of thermal model

The multi-bristles-brush-model has been modified so that it can take into account the effect related to the variation of the temperature of the components. The coupling of the mechanical block and thermal block of Multi physical tyre model (Figure 40) is done through the parameters which are influenced by temperature. In particular, two parameters can be subjected to variations as functions of temperature:

- The friction coefficient $\mu_{x,y}$ (different in longitudinal and lateral directions) between the tread and the road pavement.
- The stiffness c_{px}, c_{py} (different in longitudinal and lateral directions) of the bristles.

The adhesion part is described with the bristle stiffness and the sliding part of the contact patch is described by the equation of the dynamic friction coefficient. This equation is introduced by [162]. It can be seen that equation takes into account the relation between the effect of velocity and the effect of temperature on the viscoelastic properties of rubber.

$$\mu_d = \mu_{base} + (\mu_{peak} - \mu_{base}) e^{-\left(K_{shape}(\log_{10}(v_s) - K_{shift}(T_{tread} - T_{REF}))\right)^2} \quad (90)$$

μ_{base} Static coefficient of friction, μ_{peak} maximal coefficient of friction for v_s , T_{tread} tyre surface temperature, v_s sliding speed and T_{REF} is the initial tyre temperature,

Dynamic friction model is already used in the multi-physical model which is a function of sliding velocity. This equation requires significant numbers of parameters which are difficult to measure. For the simplification, equations (91) & (92) are implemented into the model. The variation of the friction coefficient can be considered as a function of the estimated temperature of the tread (so it is subjected to high dynamics), whereas the variation of the stiffness of the brushes can be considered as a function of the temperature of the carcass. In the case of the multi-bristles-brush model:

$$c_{px,py} = c_{px_ref,py_ref} + k_{cp}(T_{carcass} - T_0) \quad (91)$$

$$\mu_{x,y} = \mu_{x_ref,y_ref} + k_{\mu}(T_{tread} - T_0) \quad (92)$$

T_{tread} and $T_{carcass}$ are the actual tyre surface temperature, T_0 is a reference value for the temperature, μ_{x_ref,y_ref} and c_{px_ref,py_ref} are reference values for the friction coefficient and the stiffness of the brushes defined for a reference temperature T_0 , k_{cp} and k_{μ} are the coefficients which express the amount of variation of brush properties (friction and stiffness) as functions of temperature. The tuning of equations (91) and (92) is done with the experiment in a straight line and at a constant velocity. It is necessary because these constants depend on the tyre considered for the experimental results.

The above multi-physical tyre model is then integrated with a quarter car model; the wheel is connected to the suspended mass via suspension. The suspension is modelled as spring and damper. The vertical force from the wheel model represents the input for the quarter car model (Figure 45) and it gives as output the position of sprung mass:

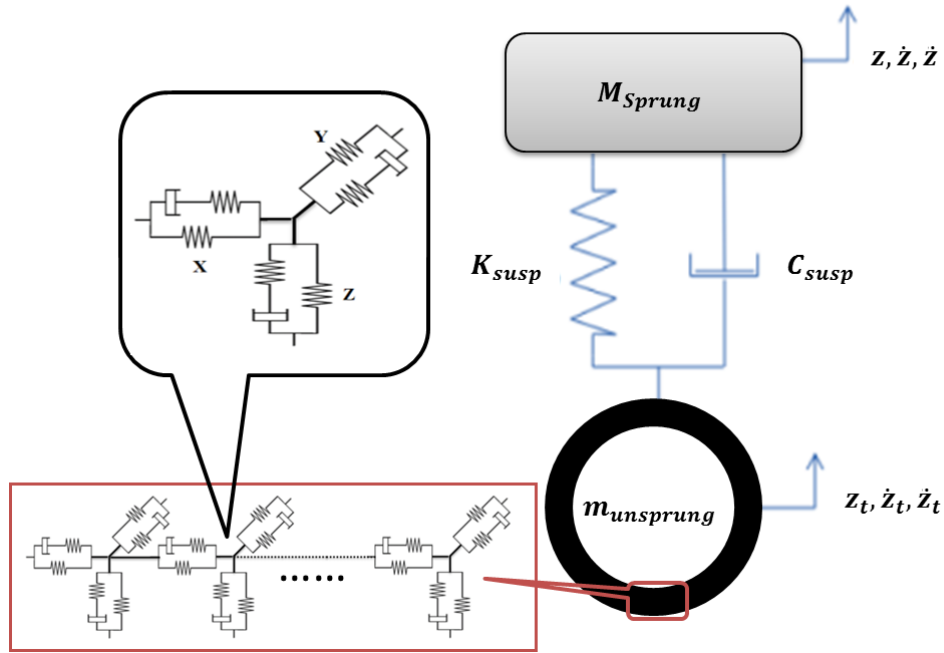


Figure 45 Quarter car model with integrated Multi-physical tyre model

The equations for a quarter car are written as:

$$\begin{aligned}
 F_{Sprung} &= K_{susp}(z_t - z) + C_{susp}(\dot{z}_t - \dot{z}) \\
 M_{Sprung}\ddot{z} &= F_{Sprung} - M_{Sprung}g \\
 m_{unsprung}\ddot{z}_t &= (F_z - F_{Sprung}) - m_{unsprung}g
 \end{aligned} \tag{93}$$

with F_{Sprung} suspended vertical force, M_{Sprung} suspended mass, $m_{unsprung}$ unsuspended mass, F_z normal force, z_t wheel vertical position, z suspended mass vertical position, K_{susp} stiffness of suspended mass and C_{susp} damping of suspended mass.

2.2.4. Sensitivity study and simulation results

In this section, a sensitivity study is done for above presented quarter car model including developed multi-physical model. The variations of different parameters are taken according to the literature representing real conditions. These variations are done separately for different blocks of quarter car and multi-physical tyre model. In Figure 46 parameters are varied for the mechanical block of the model where longitudinal, lateral and vertical rigidities of bristles have been varied up to 30%, which is how tyre rigidity varies with usage in different conditions. From Figure 46 it is concluded that the behaviour of our model respects the change in these parameters. Suspension parameters and load have been also varied for a quarter car model. The model is still responding to these variations.

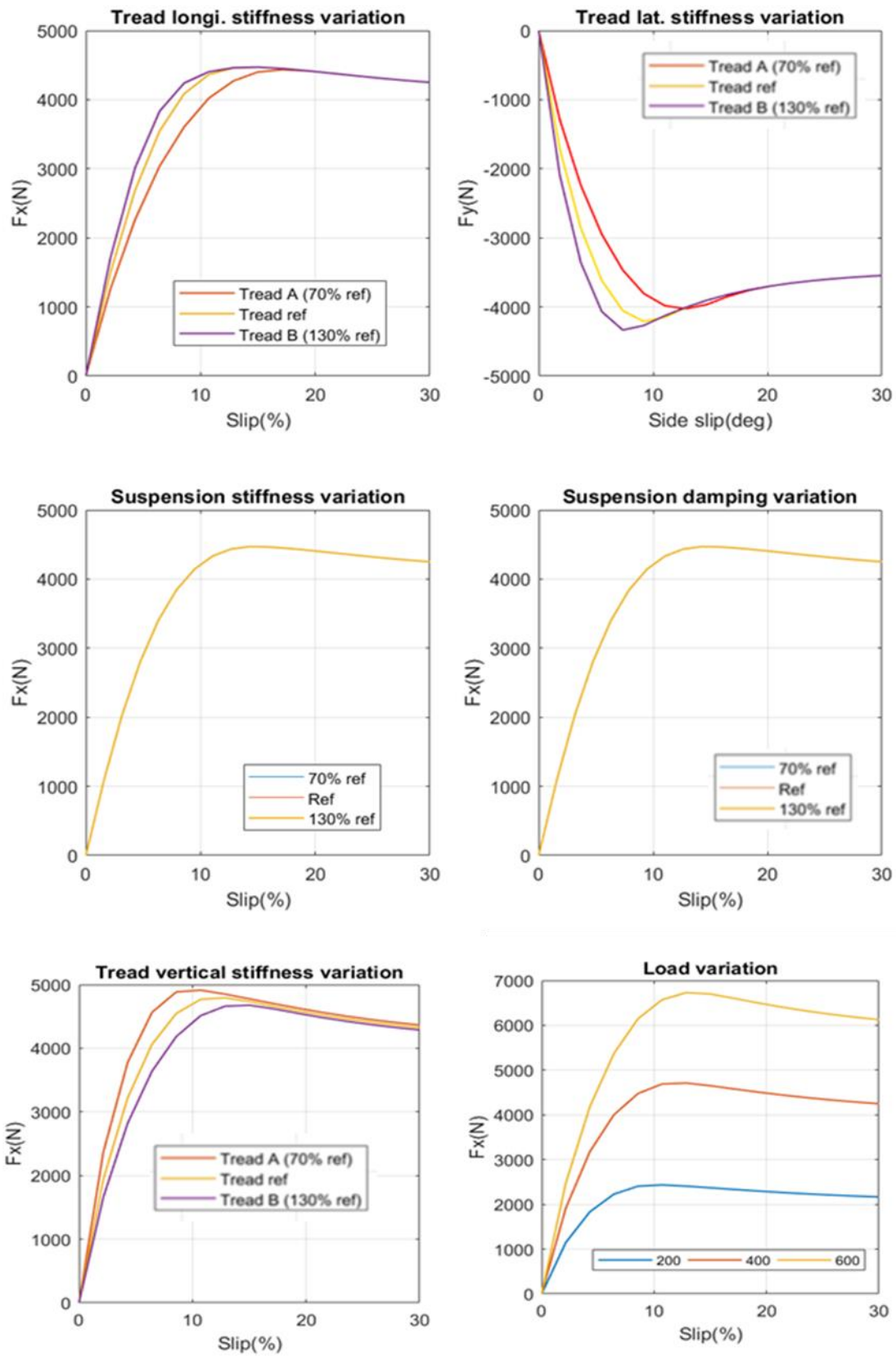


Figure 46 Sensitivity study for the mechanical block of the multi-physical tyre model

Another sensitivity study was done for the thermal block where longitudinal slip load are varied respectively. It reproduces the change in tyre surface with respect to the change in the longitudinal slip or tyre load. Results are shown in Figure 47 and Figure 48.

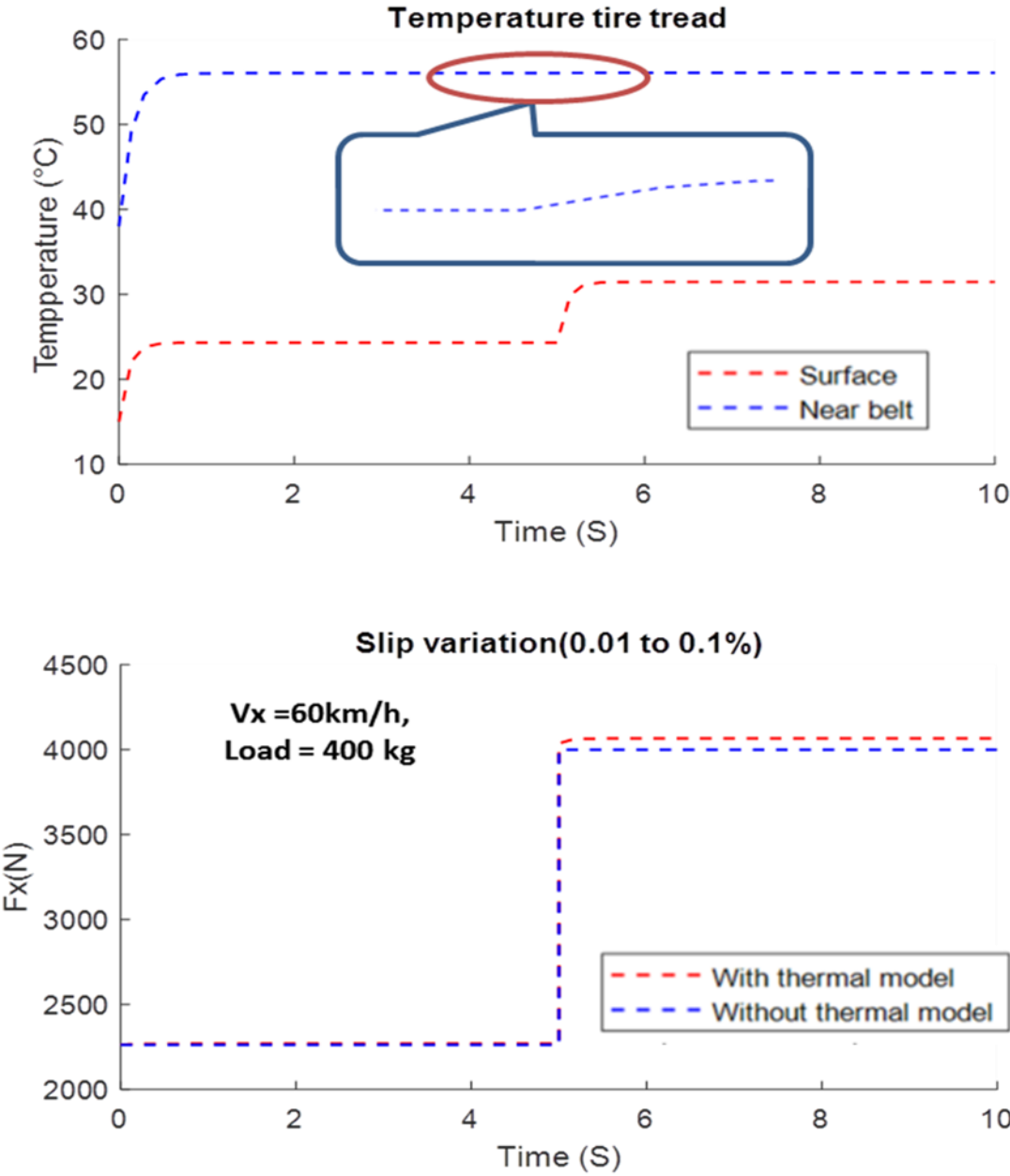


Figure 47 Sensitivity study on slip variation for the thermal block of the multi-physical tyre model

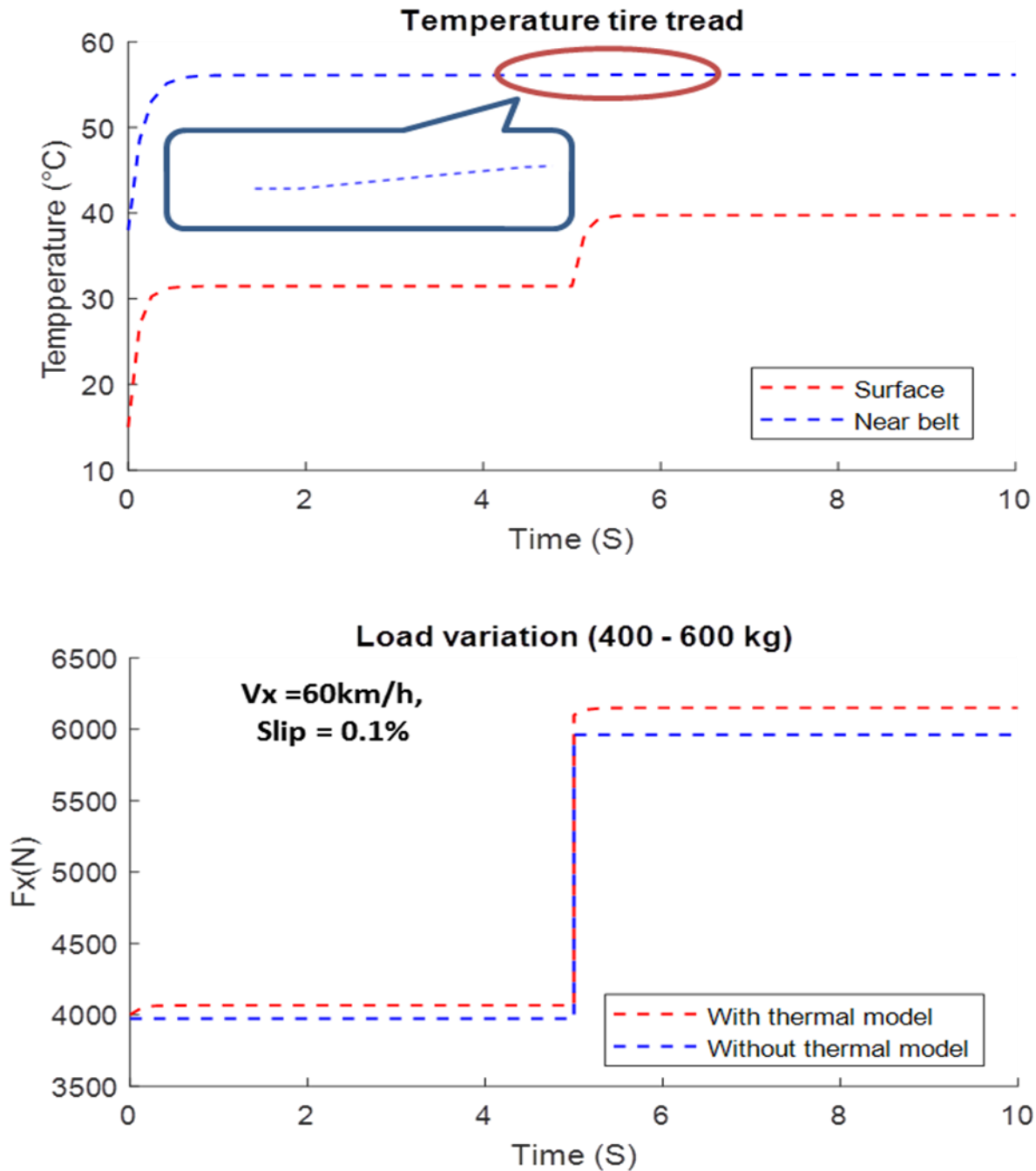


Figure 48 Sensitivity study on load variation for the thermal block of the multi-physical tyre model

Another sensitivity study was done to evaluate the evolution of temperature with speed. Two phenomena of thermal effect (heat generation and cooling) have been studied on the thermal model. Speed is varied to understand the variation of temperature with respect to speed. In Figure 49 the temperature variation for two different speeds (60km/h and 80km/h) is given. It also confirms that the model is able to reproduce the temperature variations due to heat generation induced by the speed changes. This is due to the heat generation due to the change in speed.

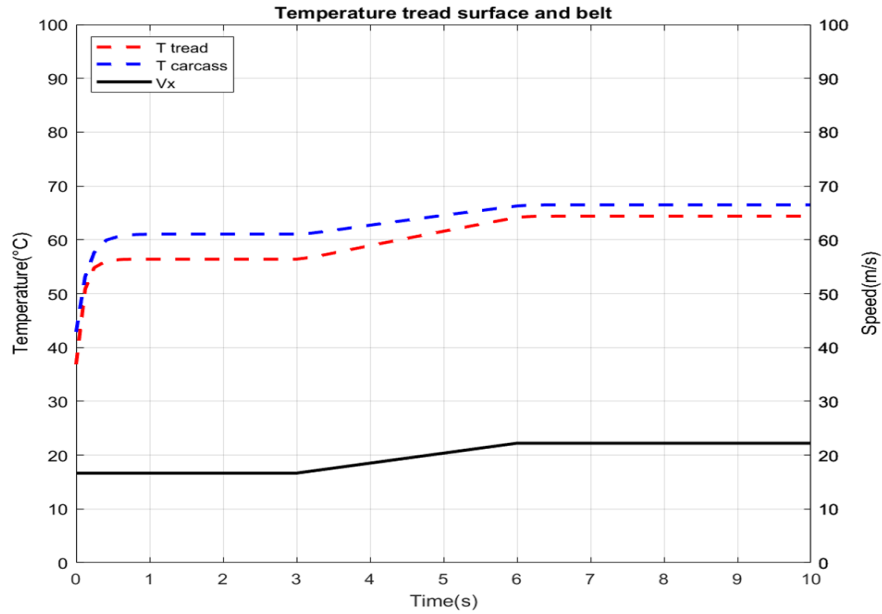


Figure 49 Tyre tread surface and Carcass temperature for variation of speed from 60 to 80 Km/h

The second simulation for a free-rolling tyre with variable speed and at constant normal load for our thermal model is done. This simulation represents the cooling phenomenon. For time less than 20 seconds speed is kept constant to 25 m/s whereas it is varied from 25 to 1 m/s in the next 60 sec. We obtained the same trends in the results shown in Figure 50 than in the literature [161]. In literature, the difference between tread and surface temperature is around 5°C whereas our model exhibits differences lying between 4°C to 10°C from Figure 49 and Figure 50. The temperature difference can come from some approximation done for the parameters used, as not all the parameters such as (v, h_c) were available for simulations.

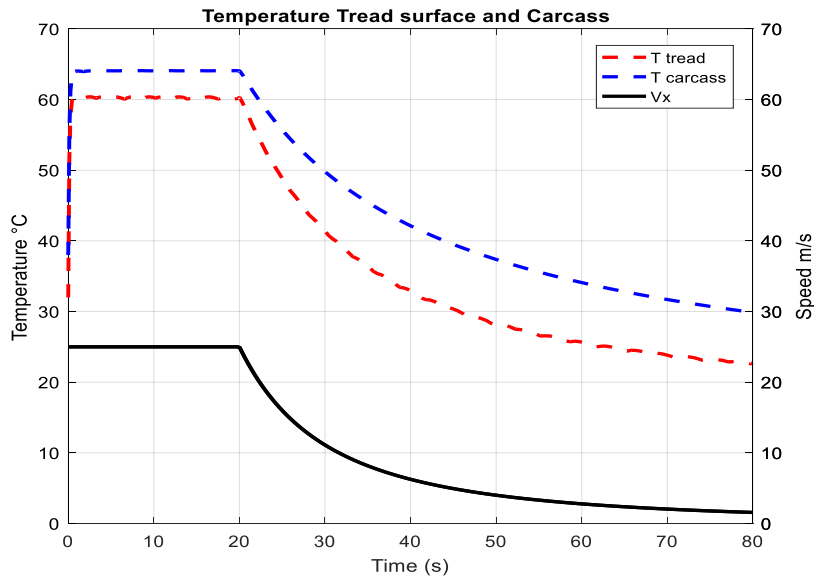


Figure 50 Thermal model simulation results for variable speed

2.3. Influence of road surface texture on the MPT model

In this section, the influence of various road surface textures on the MPT model is discussed. The deformation of bristles in contact area for different road roughness is compared. The influence of speed on the contact area for different road roughness is also discussed.

These simulations are done to understand the impact of road roughness on the deformation of bristle and loss in contact area as roughness increases which has a direct impact on friction and rolling resistance. It is difficult to get the 3D scan of real test surface for simulation; therefore a 3D randomly rough isotropic artificial road surface is modelled with MATLAB at the different macro-texture. It simulates the surface topography/roughness using fractals. It uses the Fourier concept (specifically the power spectral density) for surface generation. The artificial road surfaces with a standard deviation of 0mm, 1mm and 1.5mm for MPD, Hurst exponent of 0.5, 40 cm is the length of the final image are generated mainly to represent real test surface. This was given as input for the multi-physical tyre model to get tyre footprint under static and dynamic conditions. Simulations done in static condition presents “percentage (%) contact area” of three different surfaces obtained with the model (Figure 51). It can conclude from Figure 51 that there is a loss of 2% of bristles in contact patch for higher roughness (i.e. 1.5mm). This is not significant in dry conditions but it can have an important impact in wet conditions.

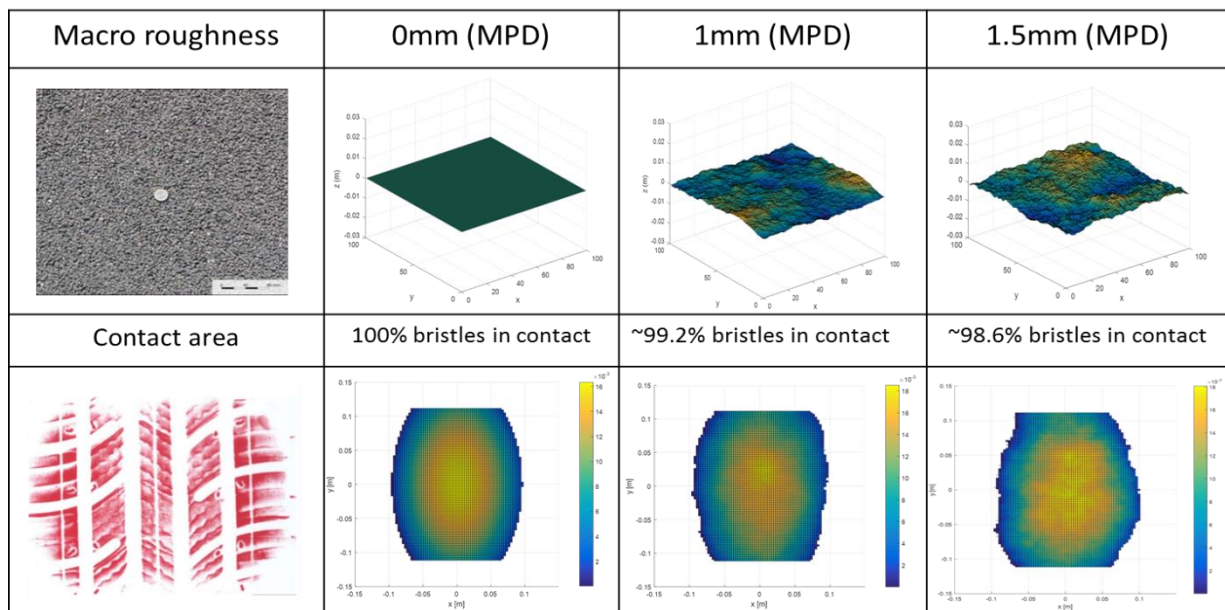


Figure 51 Contact patch deflection at different road roughness

The result of the dynamic simulation is given in Figure 52, where the evolution of contact area with speed is calculated. In literature, the evolution of the contact area with respect to speed was presented experimentally by [163], which concluded that there is no change in the contact area in dry condition. Similar results were obtained with the multi-physical tyre model.

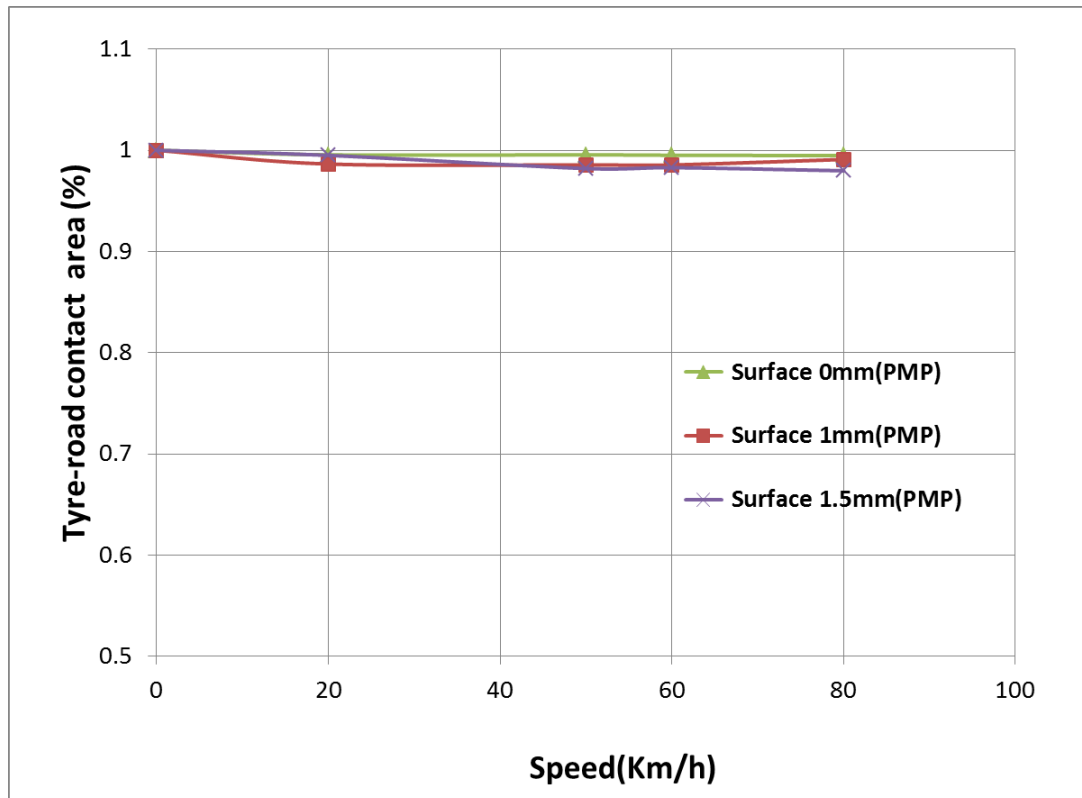


Figure 52 Evolution of contact area with speed, Contact area at road surface roughness 0mm considered as reference and 1 means all (100%) the bristle in contact.

2.4. Conclusion

The synthesis of different tyre models concludes that even though the strength of semi empirical model such as Pacejka's Magic Formula is that the model best describes steady-state tyre behaviour, but its empirical nature is the main drawback as it requires many experiments to calibrate it each time and for each tyre. The physical model such as brush model is very comparable with results of magic formula. Nevertheless, this representation is more realistic, because of the more advanced vertical pressure distribution. It fits our requirement for estimating rolling resistance. But it lacks to include the thermal effect. The finite element based sophisticated thermo-mechanical models developed in literature predict accurate tyre temperature, but they require significant computational power, in addition to a large amount of information related to the internal structure of the tyre.

The multi-physical tyre model presented in this chapter is an indispensable tool to have accurate results since the tyre tread's and carcass's temperature have a great influence on tyre road interaction. The contact forces reach their maximum values only in certain ranges and decrease significantly at high temperature. The ability to predict the tyre tread surface temperature affects both the force-producing capabilities of the tyre and the life of the tyre. The physical nature of the model allows us to minimize the number of input parameters required to feed the model as compared to finite element model. The model needs preliminary adjustments before it can be used in normal driving conditions. The impact of the road surface is also very well taken into account by the model. It can be concluded from Figure 51 that there is a loss of 2% of bristles in the contact patch for high roughness (i.e. MDP = 1.5mm). This value is not significant in dry conditions but can have an important impact in wet conditions. Also, the simulation results of the evolution of the contact area with respect to speed given by the developed model are coherent with the literature. The experimental validation of the model will

be presented in chapter 5. It confirms that the model is also able to take into account the effect of different road textures. So this chapter concludes that this is a physical model which takes into account the influencing parameters of rolling resistance. In the next chapter, this tyre model will be coupled with the vehicle model. So the next chapter will focus on the development of a full vehicle model, to be used for estimating the tyre rolling resistance based on the estimation technique developed in chapter 1.

Chapter 3

Vehicle modelling

This chapter gives an overview of different vehicle models that exist in literature and discusses the vehicle models required for estimation. As discussed in the literature, no single approach is likely to cover a wide range of vehicle manoeuvres. Accordingly in this chapter, we focus exclusively on the modelling of full vehicle dynamics. The model is obtained by stating the two fundamental principles of dynamics and by writing the forces and moments acting on the vehicle in the correct frame of reference. To complete the developments, the MPT tyre modelled in chapter 2 is coupled with the vehicle model. In this chapter, a brief synthesis dealing with vehicle models is presented in section 3.1. Then, a tailor-made full vehicle model is developed in section 3.2. Our MPT model is also coupled in this section. In the end, the numerical validation of the developed model is presented in section 3.2.4.

3.1. Different vehicle model comparison

In literature, vehicle dynamics has been the subject of numerous research studies [43], [70], [164]–[170]. These studies were performed to model a vehicle in order to develop observers, on-board estimators, driver assistance or suspension control. The vehicle is a very complex nonlinear mechanical system and the representation of the road tyre contact is not simple. The models used are either very complex or too simplified. In the first case, it is relatively difficult to identify all the parameters involved in the model considered. While in the second, we neglect several phenomena whose actions can be important and call into question the validity of the approximation made. This requires the definition of a nominal dynamic model useful for the simulation of the behaviour, the observation and the control of the vehicle [64], [74], [171]. The use of a nominal model is justified by assumptions related to the structure of the vehicle and its environment. These assumptions make it possible to reduce the complexity of the model while remaining faithful to reality. Indeed, the possibility of treating the different aspects separately and the reduction in the number of state variables to be used give a nominal model for the vehicle.

Dealing with vehicle dynamic problems, there are several models to choose from the simplest quarter vehicle model to the more complicated three-dimensional vehicle model. Each of them has its scope of application and degree of precision. Simplified models like two-dimensional (2-D) dynamic models and bicycle models are often used for these purposes. However, it is not possible to analyse rolling and pitch motions of the vehicle body or to examine the effect on safety and ride quality with respect to the variation of the wheel load if a 2-D dynamic model is used. Various approaches for 3-D vehicle models have been presented by [172]–[175]. In those models, the variation of gravity depending on the vehicle posture, change of tyre force to wheel load, the nonlinear relationship between tyre slip angle and tyre force, and the interaction of lateral and longitudinal motions may be neglected to simplify the model. There are a few commercial software packages available for 3-D dynamics analysis, for example [125], [176], [177]. These models are useful for analysing dynamic behaviours of the vehicle but are too complex to use for control system design. The quarter vehicle model is the simplest one among models suitable for studying only the vertical dynamics of the vehicle. The half vehicle model adds pitch characteristics compared to the quarter vehicle model, and the full vehicle (or four wheels) model adds the roll motion compared to the half vehicle model. The calculation amount will increase with the complexity of the model. Even the full vehicle model is still a kind of very simplified model of a vehicle. However, as the complexity increases, so do the computation time and the complexity to analyse the results. The synthesis of different vehicle model is presented in Table 7, more details are given in the appendix B.

Table 7 Synthesis of different vehicle model in the literature

Vehicle models	Associated motions and Degree of Freedoms(DoFs)	Comments
Quarter Car [178], [179]	<ul style="list-style-type: none"> - 2 DoFs model <ul style="list-style-type: none"> • One for the body motion and the other for the tyre. 	<ul style="list-style-type: none"> - Simplest model to simulate the response of the vehicle to road disturbance - All wheels can be moved independently - Only vertical dynamics considered
Bicycle model/Half car model [180], [181].	<ul style="list-style-type: none"> - 2 DoFs model <ul style="list-style-type: none"> • Include yaw rate and lateral motion • The vehicle has a constant speed. - 3-DoFs model, <ul style="list-style-type: none"> • The lateral motion, yaw rate and roll motion are considered as the DoFs of the handling system - 4 DoFs model <ul style="list-style-type: none"> • Include bounce and pitch of the body and wheels, 	<ul style="list-style-type: none"> - The vehicle is cut along the main axes of symmetry (longitudinal and lateral). - Suspensions can be study side by side or axle by axle. - In the first case, the rolling motion is neglected and in the second case, the effect of the pitch. - Do not consider roll dynamics - Do not represent the full vehicle dynamics
Full car model [182]	<ul style="list-style-type: none"> - 7 DoFs model <ul style="list-style-type: none"> • Bounce, roll and pitch and the motions of the four wheels • Ride dynamics considered - 8 DoFs <ul style="list-style-type: none"> • Lateral, longitudinal, roll and yaw motions, and four DoFs for wheel motions • Handling dynamics considered 	<ul style="list-style-type: none"> - 7 DoFs model is the best precision to simulate the dynamics of the suspension system if the vehicle has a constant speed with no steering angle. - However, these assumptions are not valid in most cases of vehicle manoeuvring. - The effect of the coupling between the ride and handling systems is neglected.

In this work, a full model is required which can be able to simulate all vehicle manoeuvres and consider the effect of pavement. In this model, all possible Degrees of Freedom (DoFs) of the dynamic model of the vehicle, the coupling between the DoFs and kinematic constraints effect among all wheels are considered. In the next section, a full 3-D vehicle model is developed with the help of model presented in the literature. It is mainly inspired by two models [183], [184]. In order to reconstruct the essential dynamics in cornering manoeuvres, to estimate the tyre forces and to identify parameters by use of the techniques of observers, the model is developed with a configuration of a vehicle representing a passenger car with 15 DoF.

3.2. Development of 3-D vehicle model

In this section, a comprehensive 15 DoF vehicle model including three-dimensional dynamic behaviours of the sprung mass, suspension, forces and moments on the tyres is developed. The dynamic model equations are basically derived using Euler's and Newton's rules. Three coordinates and rotation matrices are first defined. Motion equations of the body are represented and then the multi-physical tyre model is combined with them. The full vehicle dynamic model developed here is implemented in SIMULINK. The block diagram of the model is shown in Figure 53. The hypotheses for developing vehicle model and transformation matrix are presented first.

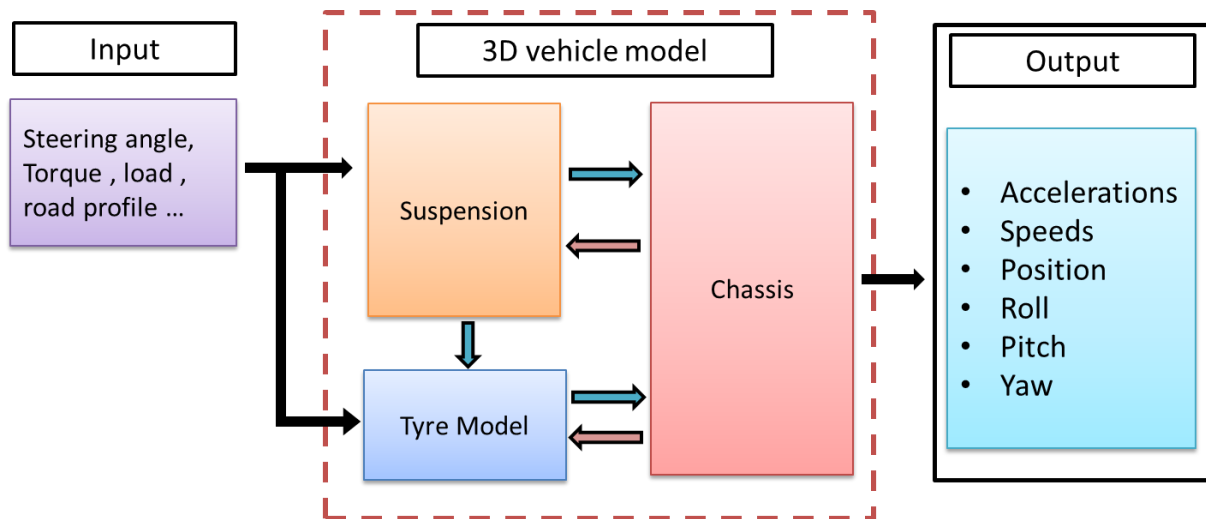


Figure 53 Block diagram of the 3D vehicle model

3.2.1. Different hypothesis for vehicle model

The vehicle is a very complex mechanical structure made up of many elements. For simple modelling, we consider the vehicle to be composed of five different sub-systems: chassis translation, chassis rotation, suspensions, steering angles and wheel rotations. To arrive at a nominal model of the vehicle's dynamic behaviour, simplifications related to the geometry, kinematics and dynamics of the links are necessary. Thus, we admit a certain number of hypotheses in order to minimize the complexity of the work. Thus, the assumptions proposed below help to reduce the complexity of the system while ensuring a certain degree of realism and modelling accuracy. These assumptions are as follows:

Hypothesis 4.1. The body is seen as a rigid body in a 3D representation;

Hypothesis 4.2. Each wheel is a rigid body in rotation with respect to its axis;

Hypothesis 4.3. The kinematics of the wheel/chassis linkage is summarized by the degrees of freedom that appear as a result of the following actions: the steering wheel, the suspension travel and the dynamic rotation of the four wheels around their axis;

Hypothesis 4.4. The road is considered to be flat.

Hypothesis 4.5. The wheel/ground contact is assumed to be punctual and located in the plane of symmetry of the wheel.

Hypothesis 4.6. The wheels always remain in contact with the road.

3.2.2. Coordinate system and transformations

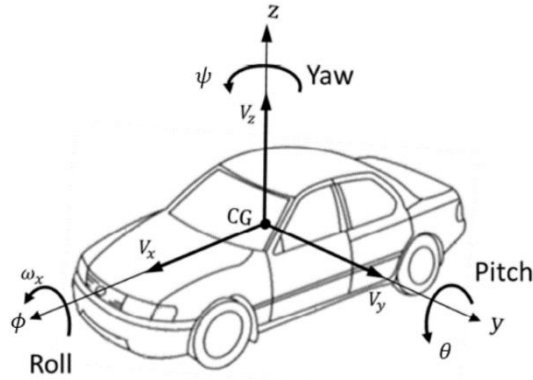


Figure 54 Vehicle Axis System ISO 8855-2011

Three moving coordinate systems are given in Figure 54. The equations are derived in the vehicle-fixed frame V , which is rotated with an angle ψ , the yaw, about the z -axis of the inertial frame, earth-fixed frame I , yielding the rotation matrix

$$R_V^I(\psi) = \begin{bmatrix} \cos(\psi) & -\sin(\psi) & 0 \\ \sin(\psi) & \cos(\psi) & 0 \\ 0 & 0 & 1 \end{bmatrix} \quad (94)$$

Moreover, the pitch θ is defined as a rotation about the y -axis of V , giving the chassis system C , with the rotation matrix

$$R_C^V(\theta) = \begin{bmatrix} \cos(\theta) & 0 & \sin(\theta) \\ 0 & 1 & 0 \\ -\sin(\theta) & 0 & \cos(\theta) \end{bmatrix} \quad (95)$$

Finally, the body system B is defined by a rotation of an angle ϕ , the roll, about the x -axis of C :

$$R_B^C(\phi) = \begin{bmatrix} 1 & 0 & 0 \\ 0 & \cos(\phi) & -\sin(\phi) \\ 0 & \sin(\phi) & \cos(\phi) \end{bmatrix} \quad (96)$$

3.2.3. Vehicle model

As, it is assumed in the previous section that the vehicle is composed of five rigid bodies; a sprung mass and four unsprung masses, and the vehicle body is connected to four wheels by springs and dampers at each corner. We consider that the vehicle body (sprung mass) has five DoF, by which longitudinal, lateral displacements and roll, pitch, and yaw motions at the centre of gravity (CoG) are described. Each suspension is assumed to be modelled by one DoF. It is also assumed that the dynamic motions of four wheels can be described by two DoF for each front wheel and by one DoF for each rear wheel Figure 55.

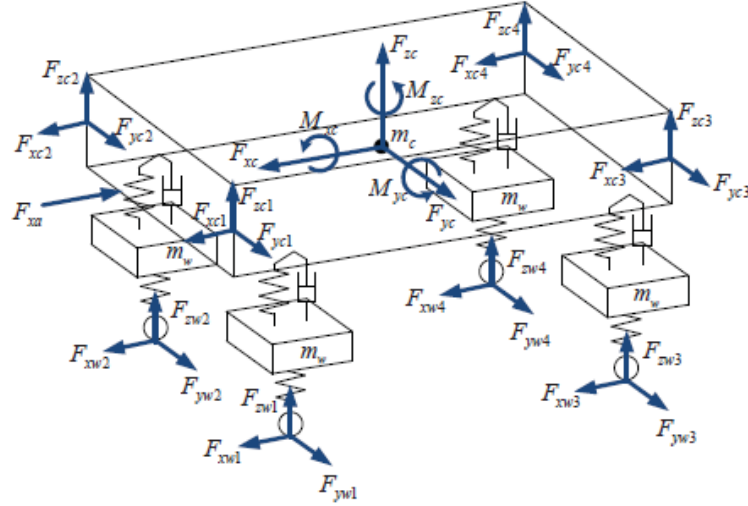


Figure 55 A three-dimensional dynamic model of full vehicle

3.2.3.1. Equation of motion

The dynamic model of the vehicle body is developed in this subsection.

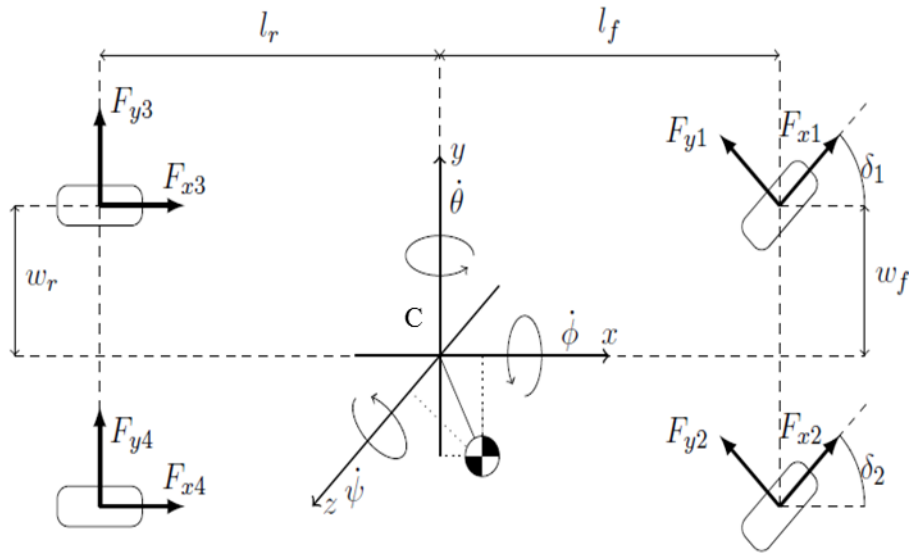


Figure 56 A dynamic model of the full vehicle. The wheels are numbered from the front left wheel to the rear right wheel [184]

Since the vehicle body is assumed to be rigid, the equation of motion can be described by using Newton's rule, which requires being aware of the total amount of forces and moments acting on the COG. The translational motion acting at the COG (C) is given by Newton's equation [172] as follows

$$\begin{aligned} \dot{v}_x = & v_y \dot{\psi} + h(\sin(\theta)(\dot{\psi}^2 + \dot{\phi}^2 + \dot{\theta}^2) - \sin(\phi)\ddot{\psi} - 2\cos(\phi)\dot{\phi}\dot{\psi} \\ & - \cos(\theta)\cos(\phi)\ddot{\theta} + 2\cos(\theta)\sin(\phi)\dot{\theta}\dot{\phi} + \sin(\theta)\sin(\phi)\ddot{\phi}) \\ & + \frac{(F_X - F_a)}{m} \end{aligned} \quad (97)$$

$$\begin{aligned} \dot{v}_y = & -v_x \dot{\psi} + h(-\sin(\theta) \cos(\phi) \ddot{\psi} - \sin(\phi) \dot{\psi}^2 - 2 \cos(\theta) \cos(\phi) \dot{\theta} \dot{\psi} \\ & + \sin(\theta) \sin(\phi) \dot{\phi} \dot{\psi} - \sin(\phi) \dot{\phi}^2 + \cos(\theta) \ddot{\phi}) + \frac{(F_Y - F_a)}{m} \end{aligned} \quad (98)$$

Where h is the height of COG, F_X , F_Y are longitudinal and lateral tyre forces, F_a is aerodynamic force and m is the mass of vehicle.

Now, we can write the dynamic equations of the vehicle body [172]. The rotational motion of the body is given by Euler's equation [172] as follows:

$$\begin{aligned} \ddot{\psi} = & (M_Z - h(F_X \sin(\phi) + F_Y \sin(\theta) \cos(\phi))) \\ & / (I_{yy} \sin(\theta)^2 + \cos(\theta)^2 (I_{yy} \sin(\phi)^2 + I_{zz} \cos(\phi)^2)) \end{aligned} \quad (99)$$

$$\begin{aligned} \ddot{\theta} = & (-K_\theta \theta - D_\theta \dot{\theta} + h(mg \sin(\theta) \cos(\phi) - F_X \cos(\theta) \cos(\phi)) \\ & + \dot{\psi}(\dot{\psi} \sin(\theta) \cos(\theta) (I_{xy} + \cos(\phi)^2 I_{yz}) - \dot{\phi} \cos(\theta)^2 I_{xx} \\ & + \sin(\phi)^2 \sin(\theta)^2 I_{yy} + \sin(\theta)^2 \cos(\phi)^2 I_{zz}) \\ & - \dot{\theta}(\sin(\theta) \sin(\phi) \cos(\phi) I_{yz}))/ (I_{yy} \sin(\phi)^2 + I_{zz} \cos(\phi)^2) \end{aligned} \quad (100)$$

$$\begin{aligned} \ddot{\phi} = & (-K_\phi \phi - D_\phi \dot{\phi} + h(F_Y \cos(\theta) \cos(\phi) + mg \sin(\phi)) \\ & + \dot{\psi} I_{yz} (\dot{\psi} \sin(\phi) \cos(\phi) \cos(\theta) + \dot{\phi} \sin(\theta) \sin(\phi) \cos(\phi)) \\ & + \dot{\psi} \dot{\theta} (\cos(\phi)^2 I_{yy} + \sin(\phi)^2 I_{zz})) \\ & / (I_{xx} \cos(\theta)^2 + I_{yy} \sin(\theta)^2 \sin(\phi)^2 + I_{zz} \sin(\theta)^2 \cos(\phi)^2) \end{aligned} \quad (101)$$

Where the moment of inertia matrix in the body frame is given by

$$\begin{bmatrix} I_{xx} & 0 & 0 \\ 0 & I_{yy} & 0 \\ 0 & 0 & I_{zz} \end{bmatrix} \quad (102)$$

3.2.3.2. Model of the independent suspension system

We consider that the suspension system of the vehicle is composed of four sets of spring-dampers connected at each corner, and the vehicle body is supported by them independently. The vertical motion of a tyre is assumed to be an ideal spring. The unsprung masses are regarded as separately lumped bodies between an individual suspension device and a tyre, as shown in Figure 57.

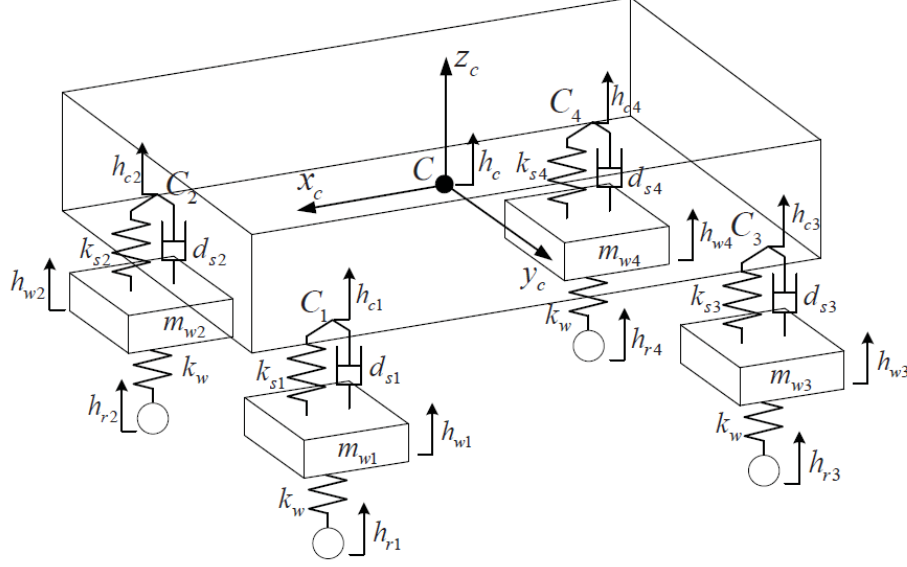


Figure 57 Independent suspensions

In Figure 57, the displacements h_c represents the vertical displacement of the COG (C) and h_{ci} are those variables at four points of action. h_{ri} indicates the vertical variations of the road surface, which are measured at the centre of tyre contact. Also, the vertical displacements of the equivalent unsprung mass (m_{wi}) are defined by h_{wi} . The spring constant k_w represents the tyre compressibility. A suspension device is represented in the schematic diagram by a dashpot symbol with friction constant d_{si} and spring with constant k_{si} .

The vertical forces acting on the points C_i of the vehicle body via each suspension device are given by

$$F_{zci} = -k_{si}(h_{ci} - h_{wi}) - d_{si}(\dot{h}_{ci} - \dot{h}_{wi}), i = 1,2,3,4 \quad (103)$$

The force F_{zci} obtained by (103) is used for computing the forces and moments of the vehicle body. The vertical forces in the z -axis are caused by the gravity of equivalent unsprung mass (m_{wi}) are given by

$$F_{zri} = -k_w(h_{wi} - h_{ri}), \quad i = 1,2,3,4 \quad (104)$$

This wheel load will be used for computing the tyre forces later (using Multi physical tyre model). Applying Newton's second law of motion to each unsprung mass yields the following suspension model: for $i = 1, 2, 3, 4$,

$$m_w \ddot{h}_{wi} = -k_w(h_{wi} - h_{ri}) + k_{si}(h_{ci} - h_{wi}) + d_{si}(\dot{h}_{ci} - \dot{h}_{wi}) + F_{zgw_i}, \quad i = 1,2,3,4 \quad (105)$$

where F_{zgw_i} is gravitation force.

3.2.3.3. Tyre ground interaction

The wheels are modelled as rotating masses with drive/brake torques and road contact tyre forces. When initiating the brake or drive pedal torque is induced over the wheels, here referred to as T_{ywi} , which makes the wheels decelerate or accelerate due to the longitudinal component of the tyre force, F_{xwi} , and the moment by the rolling resistance force F_{rri} . Therefore, applying Newton's equation results in.

$$I_w \dot{\omega}_i = T_{ywi} - (F_{xwi} - F_{rri})R_l, \quad i = 1,2,3,4. \quad (106)$$

Where the rolling resistance force is mainly due to viscoelastic properties of the rubber compounds, used to make tyres. When they are deformed, they tend to dissipate energy in the form of heat. When rolling, a tyre is deformed by the load exerted on it, flattening out in the contact patch. This repeated deformation causes energy loss known as rolling resistance. Similar to traction force, rolling resistance force is also a product of normal force F_{zwi} and rolling resistance coefficient C_{rri} .

$$F_{rri} = C_{rri}F_{zwi} \quad (107)$$

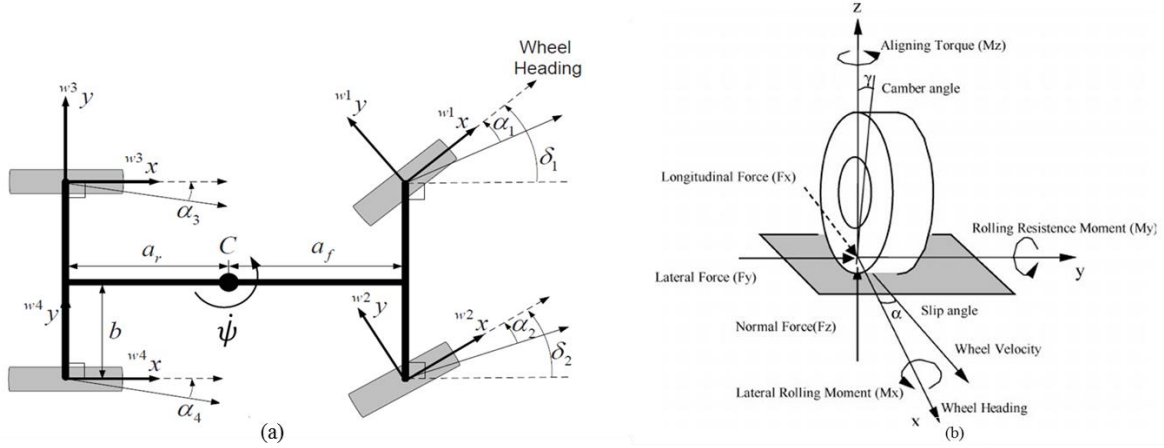


Figure 58 (a) Tyre slip and steer angles on the wheel-fixed frame[183] (b) Wheel reference coordinate system

We first define several variables and parameters used for the tyre model. As shown in Figure 58, the velocity vector of the centre of tyre contact of the i^{th} tyre is denoted by (v_y, v_x) , for $i = 1,2,3,4$. The slip angle (108) α_i represents the angle from the wheel heading to the travel direction of the centre of tyre contact. The steering angle δ_k is the angle between the projection of a longitudinal axis of the vehicle and the wheel heading. The longitudinal slip (109) of the tyre is denoted by κ .

$$\alpha_i = -\tan^{-1}(v_y, v_x) \quad (108)$$

$$\kappa_i = \frac{v_x - R_w \omega}{v_x} \quad (109)$$

where R_w is an effective tyre radius which is also defined as a function of F_{zwi}

$$R_w = R_0 \pm f(F_{zwi}) \quad (110)$$

where R_0 is static tyre radius.

Among various forces acting on the vehicle, the tyre force is the most dominant. Thus, the more accurate the tyre model, the better a model will result in the vehicle dynamics. The tyre force is a nonlinear function of slip angle, side-slip angle, physical properties of the tyre, running conditions, and so on. It can be classified into the lateral tyre force and longitudinal tyre force. The Multi physical model [185] presented in the previous chapter is reduced to single bristle to gain in simulation time and constant temperature for calculating longitudinal and lateral forces from the tyre.

$$F_M^t = F_M^{ve} \quad (M = x, y, z) \quad (111)$$

where F^{ve} is the viscoelastic force and F^t are tyre forces which are calculated using equation (112) using Crank and Nelson method.

$$\dot{F}^{ve}(\delta, t) = -\frac{k}{c} F^{ve}(t) + \frac{k \cdot k}{c} \delta(t) + (2k)\dot{\delta} \quad (112)$$

Where damping c and stiffness k for bristles in x, y and z directions and their values are taken from literature mainly from [158].

The total forces acting on the vehicle are found from force equilibrium in the x and y-directions, see Figure 56:

$$F_X = F_{x1} \cos(\delta_1) - F_{y1} \sin(\delta_1) + F_{x2} \cos(\delta_2) - F_{y2} \sin(\delta_2) + F_{x3} + F_{x4} \quad (113)$$

$$F_Y = F_{x1} \sin(\delta_1) - F_{y1} \cos(\delta_1) + F_{x2} \sin(\delta_2) - F_{y2} \cos(\delta_2) + F_{y3} + F_{y4} \quad (114)$$

By performing torque equilibrium around the vehicle z-axis we find that

$$\begin{aligned} M_Z = l_f (F_{x1} \sin(\delta_1) + F_{x2} \sin(\delta_2) + F_{y1} \cos(\delta_1) + F_{y2} \cos(\delta_2)) \\ + w_f (-F_{x1} \cos(\delta_1) + F_{x2} \cos(\delta_2) + F_{y1} \sin(\delta_1) - F_{y2} \sin(\delta_2)) \\ - l_r (F_{y3} + F_{y4}) - w_r (F_{x3} + F_{x4}) \end{aligned} \quad (115)$$

F_x , F_y , and F_z in Figure 56 are the individual axis components of gravity in the ground frame, Then the resultant moments acting on the vehicle body are M_x , M_y , and M_z .

3.2.4. Validation and simulation results

In this section, the validation of the full vehicle model is presented with reference simulator SCANeR™ Studio (Prosper). SCANeR™ Studio (prosper) [125] is a simulation software tool which analyses the dynamic behaviour of vehicles, developed by the company OKTAL. It is based on accurate, detailed and efficient methods and an ergonomic interface (see Figure 59). Prosper database includes several mathematical models for car, trucks and trailers and a convenient tool for analysing vehicle dynamics, developing passive and active safety systems (controller), performance characteristics evaluation, etc. For virtual model development, it provides an efficient set of tools for engineers to quickly evaluate complete vehicles, its sub-components (suspension, tyre, braking), and active controllers (ACC, ESP, ABS...) in complex driving environments.

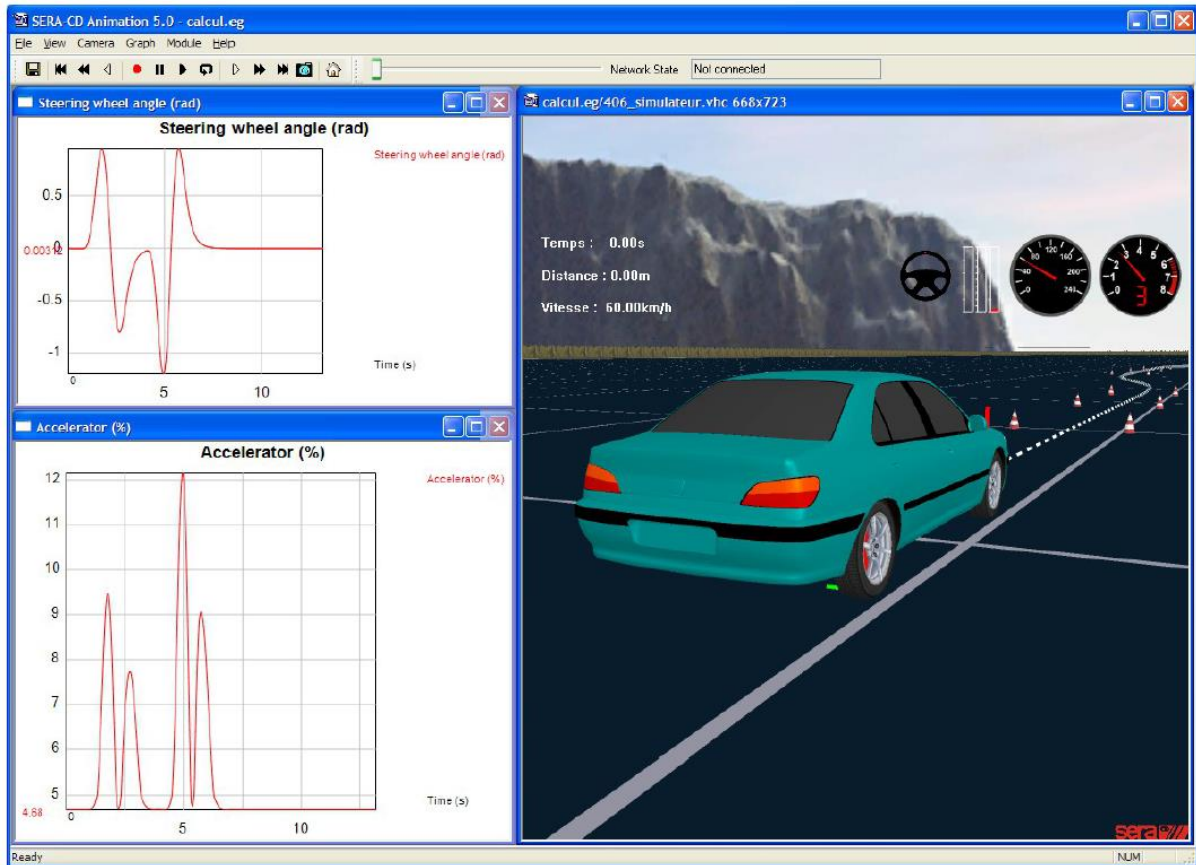


Figure 59 Interface of SCANeR™ Studio (Prosper)

Seven different test scenarios are constructed to validate our model. These scenarios cover different speed and manoeuvres. The test scenarios are given in (Table 8).

Table 8 Test conditions

Test no.	Trajectory	Speed (Km/h)	Comments
1	Straight line	50	Constant speed
2	Straight line	80	Constant speed
3	Curve at 220m	40	Constant speed
4	Curve at 220m	60	Constant speed
5	Curve at 220m	80	Constant speed
6	Curve at 320m	40	Constant speed
7	Curve at 320m	60	Constant speed
8	Curve at 320m	80	Constant speed
9	Chicane	60	Constant speed
10	Straight line	Acceleration & Braking	Variable speed

The above scenarios were simulated in SCANeR Studio (prosper) simulator and compared with the developed model. The classical approach has been used for comparison as shown in Figure 60. Steer angle and torque was given as input to the model with the same input parameters and initial conditions as used for simulation as Prosper (SCANeR Studio). The validation is demonstrated by comparing the roll, pitch and yaw rate and trajectory of the model with Simulation results of Simulator Prosper.

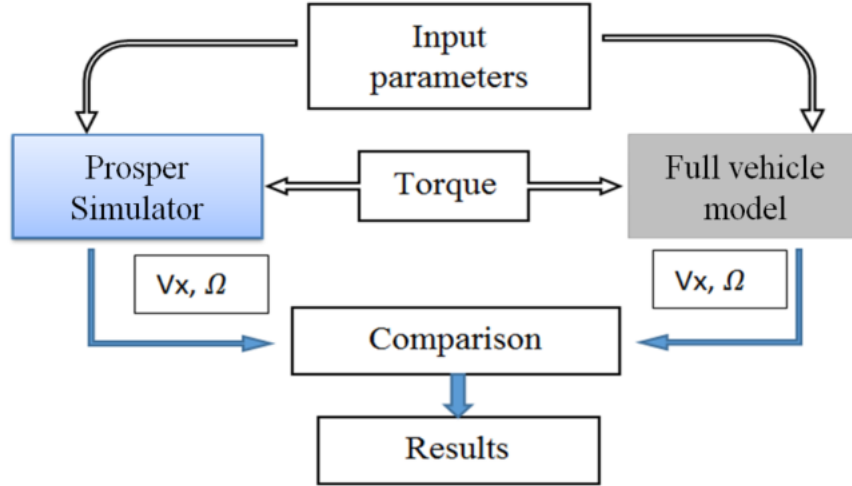


Figure 60 Methodology of model validation

In this section, the comparison results of the above defined test scenarios are presented. The model's results are compared with simulator values. The validation of the model is evaluated by calculating the relative mean errors of speed and position vectors:

$$ME = \frac{1}{N} \sum_{i=1}^N \left| \frac{ref(t_i) - model(t_i)}{ref(t_i)} \right| \leq 10\% \quad (116)$$

With t_i is counted from the instant when model start converging to real ones (approx. 2sec) to end of simulation and N number of samples in this period.

Here the simulation results for test scenarios 1, 7 and 10 are presented. The rest can be found in the appendix D. However a summary of all the test scenarios is presented.

- Car moving at 50 km/h in a straight line

In this simulation, the car is moving in a straight line and with constant velocity. It is concluded from Figure 61 and Figure 62 that for a straight line our vehicle model is following the curves coming from the simulator Prosper. The roll, pitch and yaw are very small as the vehicle is moving on a straight line. The comparison shows good trends with a relative mean error of less than 2% for parameters. This little variation in magnitude of the developed model can be explained by the fact that it is more simplified by comparison with simulator Prosper. It can be concluded from above Figure 62 that our vehicle model is showing good behaviour and validated for straight-line simulations.

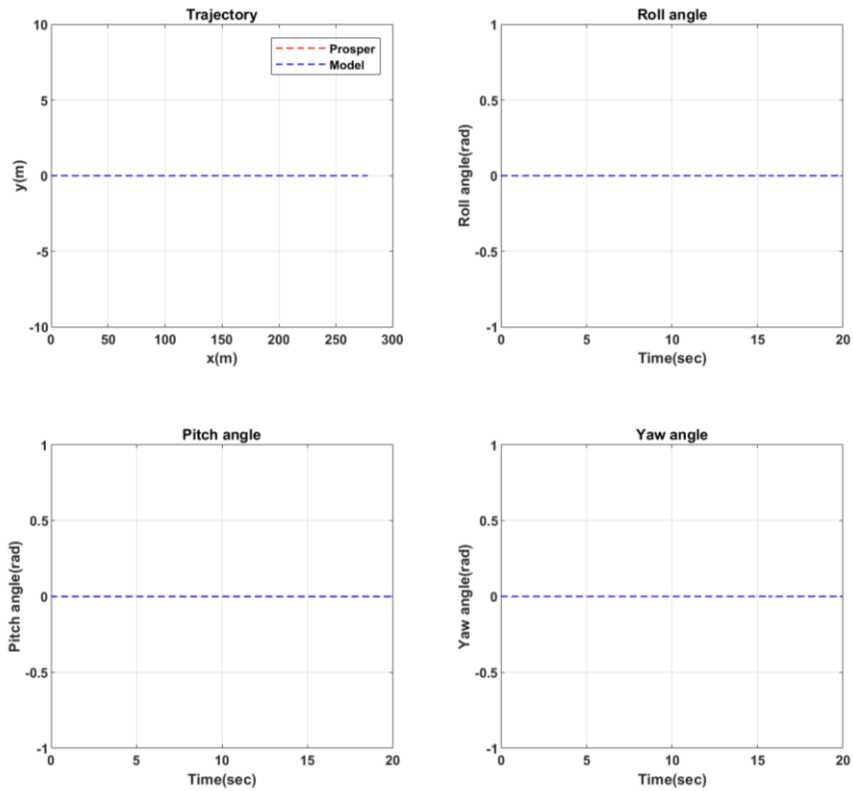


Figure 61 Comparison of position variables between Prosper and model for vehicle moving in a straight line at 50 km/h

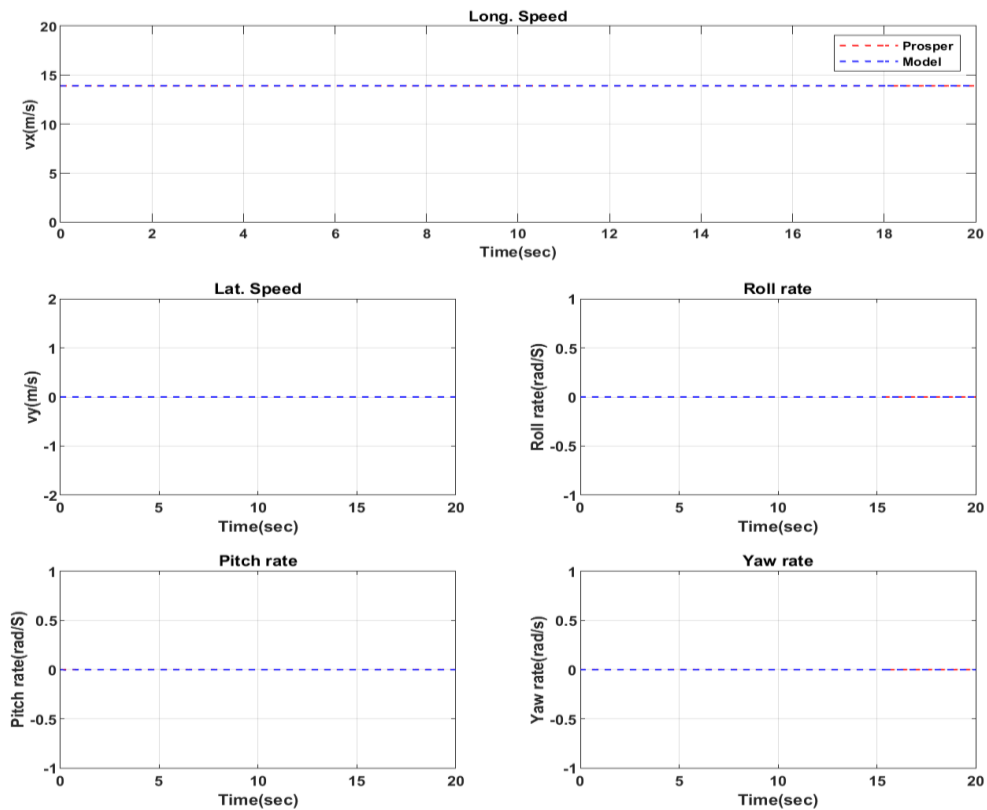


Figure 62 Comparison of speed variables between Prosper and model for vehicle moving in a straight line at 50 km/h

- Vehicle moving on a curve with constant Radius of 320m at 60 km/h

In this test, the car is moving in a curve with a constant radius of 320m and a constant speed. The results are presented in Figure 63 and Figure 64. It is observed from Figure 63 that model trajectory is following the simulator results. The comparison shows good trends with a relative mean error of less than 8% for all the parameters. This variation in magnitude remains correct as the developed model is simplified when compared to the simulator Prosper. It can be concluded from above Figure 64 that our vehicle model is exhibiting good behaviour and validated for curve manoeuvres.

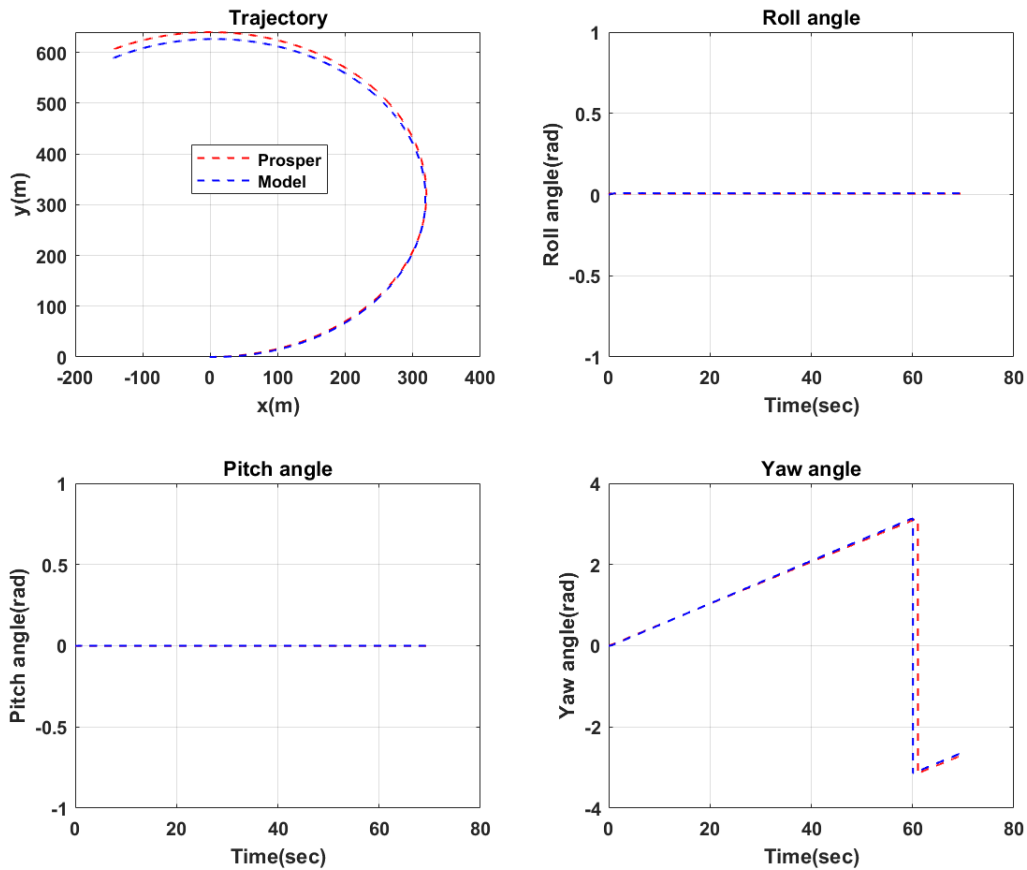


Figure 63 Comparison of position variables between Prosper and model for vehicle moving in a curve of 320m at 60 km/h

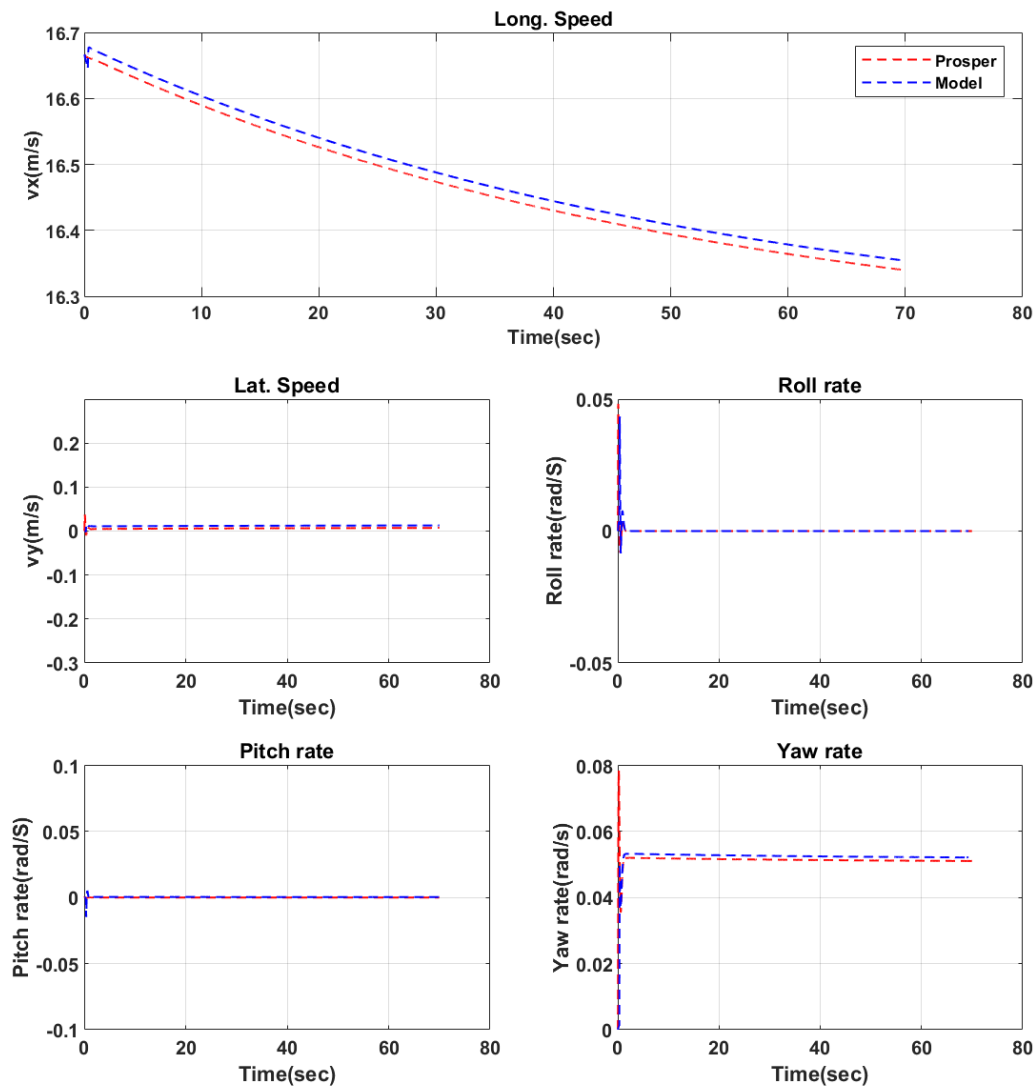


Figure 64 Comparison of speed variables between Prosper and model for vehicle moving in a curve of 320m at 60 km/h

- Vehicle accelerating and braking in a straight line

The comparison results of this test scenario are presented in Figure 65 and Figure 66. The trajectory of the vehicle is followed. The errors are less than 5% except for the acceleration manoeuvres where the error in the velocity is going up to 6.5%. The difference is due the complexity of simulator as compared to developed model. It can be concluded from above Figure 65 that our vehicle model is showing good behaviour in manoeuvres and validated.

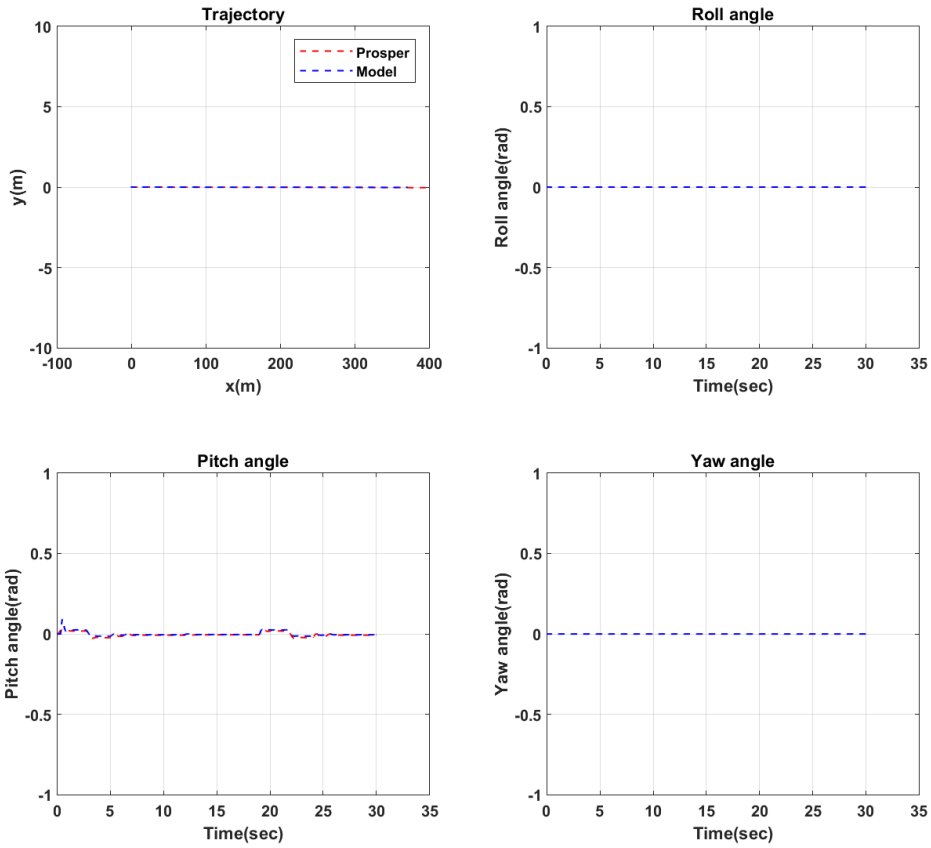


Figure 65 Comparison of position variables between Prosper and model for the vehicle is accelerating and braking

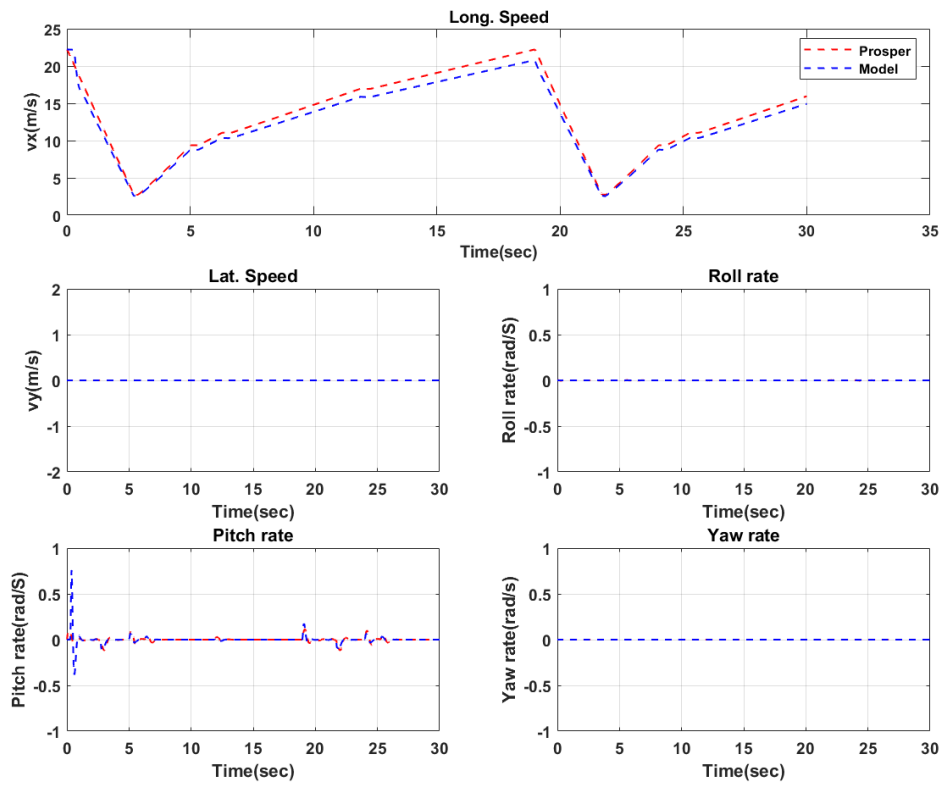


Figure 66 Comparison of speed variables between Prosper and model for the vehicle is accelerating and braking

The relative mean errors are presented in Table 9 for all the scenarios of simulation.

Table 9 Summary of results in a relative mean error (RME) for test scenarios

Test no.	Trajectory	Speed (Km/h)	Overall RME (%)	Comments
1	Straight line	50	< 2	Good results and good dynamics
2	Straight line	80	< 2	Good results and good dynamics
3	Curve at 220m	40	< 5	The model shows good results and dynamics except for the RME for Yaw and lateral speed is < 8%.
4	Curve at 220m	60	< 6	The model shows good results and dynamics except for the RME for Yaw and lateral speed is < 8%.
5	Curve at 220m	80	< 8	The model shows good behaviour and dynamics except for the RME for Yaw and lateral speed is < 12%.
6	Curve at 320m	40	< 5	Good dynamics behaviour, More error is seen on yaw rate and lateral speed but < 5%.
7	Curve at 320m	60	< 8	Good dynamics, More error is seen on yaw rate and lateral speed but < 7%.
8	Curve at 320m	80	< 8	The model shows good behaviour and dynamics except for the RME for Yaw and lateral speed is < 11%.
9	Chicane	60	< 6	Good dynamics behaviour, More error is seen on pitch rate and lateral speed but < 10%.
10	Straight line	Acceleration & Braking	< 5	The model shows good dynamics except for the RME for Yaw and lateral speed is < 7%.

3.3. Conclusion

The overview of already existing vehicle model in literature tells that these models are specific to some application. For example; the simplest models are the quarter vehicle models which are suitable for studying vertical dynamics of the vehicle. The bicycle model is to include pitch characteristics and the full vehicle (or four wheels) model adds the roll dynamics compared to the half vehicle model. Even the full vehicle model is still a kind of very simplified model of a vehicle. But the calculation amount will increase with the complexity of the model.

In this chapter a full model is developed which is able to simulate all vehicle manoeuvres. The tyre model developed in chapter 2 is also coupled with this model. This model is developed in order to develop observers and estimators for estimating rolling resistance. The numerical validation of FVM (full vehicle model) is done with the help of Prosper (SCANeR Studio). The overall relative mean errors of all the scenarios are less than 8% as shown in Table 7. This is in the acceptable range as the magnitude is very small for the absolute values. The difference is mainly due to the simplified nature

of the developed model as compared with the complex simulator model. So we can conclude that the comparison results are following the simulator results with good dynamic behaviour. The experimental validation of this model will be presented in chapter 5. This developed model will be considered as a system for the development of unknown input adaptive high gain observer to estimate tyre rolling resistance. This will be presented in the next chapter.

Chapter 4
Synthesis of adaptive nonlinear
observers

The comparison done in chapter 1 allowed us to consider the adaptive high gain observer that shows high practical interest due to its robustness and finite time convergence modelling error and parameter uncertainty. Its advantages and disadvantages have allowed choosing the most effective solution with respect to accuracy, robustness and computing complexity. This motivates us to develop the unknown input adaptive high gain observer for estimating tyre rolling resistance force. Therefore the unknown input adaptive high gain observer is designed in this chapter for regular systems as well as singular perturbed systems. The interest in the singular perturbed systems arises with the fact that it is possible to consider the parameters with slow and fast dynamics in the system. The adaptive gain approach is a novel approach for the unknown input observers in the automotive domain.

In this chapter, the development of the unknown input adaptive high gain observer for full vehicle model is presented. The chapter starts with the formulation of the main objective as the estimation of the rolling resistance force in section 4.1. Section 4.2 is dedicated to the synthesis of the observer for regular systems and singularly perturbed systems. The application on the full vehicle model is presented in section 4.3. Simulation results are discussed in relation to the observer efficiency and robustness.

4.1. System description and problem formulation

In chapter 2 and chapter 3 the modelling of the full vehicle is done. This full vehicle model is considered as the system for the development of the observer. The block diagram of the system is given in Figure 67; the mathematical model of full vehicle is defined as the system for the observer design. This model is validated numerically in chapter 3.

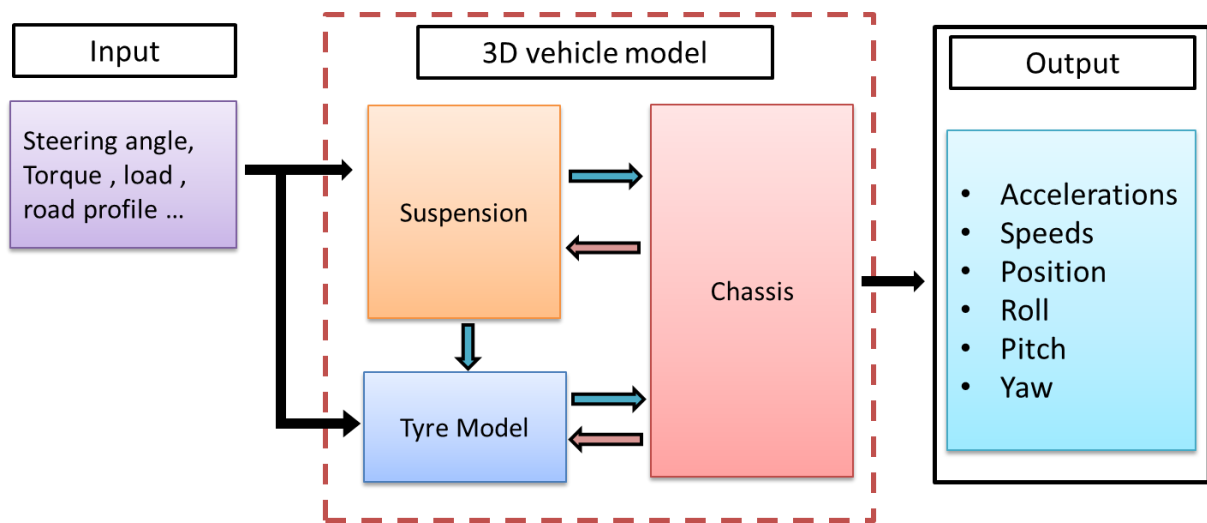


Figure 67 Block diagram of the complete vehicle model

The full vehicle model which is defined in chapter 3 can be written in the below form:

$$\dot{x} = f(x, u) \quad (117)$$

Where x is the state vector and u is the input vector. f is the function of are the matrices dependent of state vector i.e. (x) and input vector (u). The state vector is defined as

$$x = [T_{tread}, T_{carcass}, w_1, w_2, w_3, w_4, v_x, v_y, \psi, \dot{\phi}, \dot{\theta}]^T \quad (118)$$

With the variables $T_{tread}, T_{carcass}$ are tyre surface and carcass temperature respectively, w_1, w_2, w_3, w_4 as angular speed, v_x, v_y are longitudinal and lateral speeds, $\dot{\psi}, \dot{\phi}, \dot{\theta}, \psi, \phi, \theta$ represents yaw pitch and roll rate and angle respectively. The parameters are defined previously in chapter 3.

$$\begin{aligned}
f(x, u) = & [(Q_{SEL,t} + Q_{Friction\ forces} + Q_{conduction} + Q_{ambient,tread})/m_t c_t \\
& (Q_{SEL,c} + k_c(T_{tread} - T_{carcass}) * S_t + Q_{ambient,carcass})/m_c c_v \\
& (T_{yw1} - (F_{xw1} - C_{rr1}F_{zw1})R_{l1})/I_w \\
& (T_{yw2} - (F_{xw2} - C_{rr2}F_{zw2})R_{l2})/I_w \\
& (T_{yw3} - (F_{xw3} - C_{rr3}F_{zw3})R_{l3})/I_w \\
& (T_{yw4} - (F_{xw4} - C_{rr4}F_{zw4})R_{l4})/I_w \\
& v_y \dot{\psi} + h(\sin(\theta)(\dot{\psi}^2 + \dot{\phi}^2 + \dot{\theta}^2) - \sin(\phi)\ddot{\psi} - 2\cos(\phi)\dot{\phi}\dot{\psi} \\
& \quad - \cos(\theta)\cos(\phi)\ddot{\theta} + 2\cos(\theta)\sin(\phi)\dot{\theta}\dot{\phi} + \sin(\theta)\sin(\phi)\ddot{\phi}) + (F_x - F_a)/m \\
& -v_x \dot{\psi} + h(-\sin(\theta)\cos(\phi)\ddot{\psi} - \sin(\phi)\dot{\psi}^2 - 2\cos(\theta)\cos(\phi)\dot{\theta}\dot{\psi} + \sin(\theta)\sin(\phi)\dot{\phi}\dot{\psi} - \sin(\phi)\dot{\phi}^2 \\
& \quad + \cos(\theta)\ddot{\phi}) + (F_y - F_a)/m \\
& (M_z - h(F_x \sin(\phi) + F_y \sin(\theta)\cos(\phi)))/(I_{yy}\sin(\theta)^2 + \cos(\theta)^2(I_{yy}\sin(\phi)^2 + I_{zz}\cos(\phi)^2)) \\
& (-K_\theta\theta - D_\theta\dot{\theta} + h(mg\sin(\theta)\cos(\phi) - F_x\cos(\theta)\cos(\phi)) \\
& \quad + \dot{\psi}(\dot{\psi}\sin(\theta)\cos(\theta)(I_{xy} + \cos(\phi)^2 I_{yz}) - \dot{\phi}\cos(\theta)^2 I_{xx} + \sin(\phi)^2 \sin(\theta)^2 I_{yy} \\
& \quad + \sin(\theta)^2 \cos(\phi)^2 I_{zz}) \\
& \quad - \dot{\theta}(\sin(\theta)\sin(\phi)\cos(\phi) I_{yz}))/ (I_{yy}\sin(\phi)^2 + I_{zz}\cos(\phi)^2) \\
& (-K_\phi\phi - D_\phi\dot{\phi} + h(F_y\cos(\theta)\cos(\phi) + mg\sin(\phi)) \\
& \quad + \dot{\psi}I_{yz}(\dot{\psi}\sin(\phi)\cos(\phi)\cos(\theta) + \dot{\phi}\sin(\theta)\sin(\phi)\cos(\phi)) \\
& \quad + \dot{\psi}\dot{\theta}(\cos(\phi)^2 I_{yy} + \sin(\phi)^2 I_{zz})) \\
& \quad / (I_{xx}\cos(\theta)^2 + I_{yy}\sin(\theta)^2 \sin(\phi)^2 + I_{zz}\sin(\theta)^2 \cos(\phi)^2)]^T
\end{aligned}$$

Considering the full vehicle model with hypotheses exposed in the previous section, the physical domain defined for this system is:

$$\mathfrak{D} = x|0 < w_i \leq 150 \text{ rad/s}, 0 < v_x \leq 200 \text{ km/h}, 0 < |F_{rri}| \leq F_x \quad (119)$$

where $i = 1, 2, 3, 4$.

The collective objective with respect to the full vehicle model can be summarized in the following formulation of the problem. Let the relative mean rolling resistance coefficient error denoted by e_{Frr} and F_{rr}^{max} is upper bound of rolling resistance coefficient. The estimation technique of rolling resistance that ensures:

$$|e_{Frr}(t)| \leq 10\% \quad \forall t_f \geq t > 0 \text{ and } F_{rr} \leq F_{rr}^{max} \quad (120)$$

where t_f, t are end of simulation and time respectively.

In the next section, the development of the observer is presented based on the above defined system and problem formulation in equation (120).

4.2. Development of adaptive observers for nonlinear systems

This section is dedicated to the development of unknown input adaptive observer for nonlinear systems. The development is divided into two parts. First, the development of the observer for the regular system is presented and then the observer for the singular perturbed system is developed.

4.2.1. Unknown input adaptive high gain observer for regular systems

In this section, an observer is proposed to reconstruct the unknown state variables of the vehicle from the available measurements as shown in Figure 68. This is based on the use of adaptive high gain approach, knowing to be robust versus parametric uncertainties, modelling errors and disturbances as given in [120], [186], [187].

The aim of novel unknown input adaptive high gain observer is to estimate simultaneously the state (x) and the unknown input (\bar{u}) applied to a physical system using measured input (u), measured output (y) and a knowledge model (Σ) of the system. Firstly, the model is written under state space form and observability of the system is analysed thanks to numerical evaluation technique. The synthesis of the observer is presented in this section for the class of nonlinear systems with unknown input.

4.2.1.1. State space model

The initial model is written as:

$$\dot{x} = f(x, u) \quad (121)$$

Firstly, the model is written under the state space form. The unknown parameters here are assumed as unknown input. The state space variable is defined in equation (121). The measured input matrix is given by

$$u = (u_1, u_2, \dots, u_n)^T \quad (122)$$

The unknown parameters are considered as unknown input here, so the function defined as

$$\bar{u} = f(\bar{u}_1, \bar{u}_2, \dots, \bar{u}_p)^T \quad (123)$$

Finally, the measured output of this model is:

$$y = (y_1, y_2, \dots, y_m)^T \quad (124)$$

After substituting (122), (123), (124) in (121) the complete nonlinear state space model of the model is defined as:

$$\Sigma \begin{cases} \dot{x} = f(x, u) + G(u)\bar{u} \\ y = Cx \end{cases} \quad (125)$$

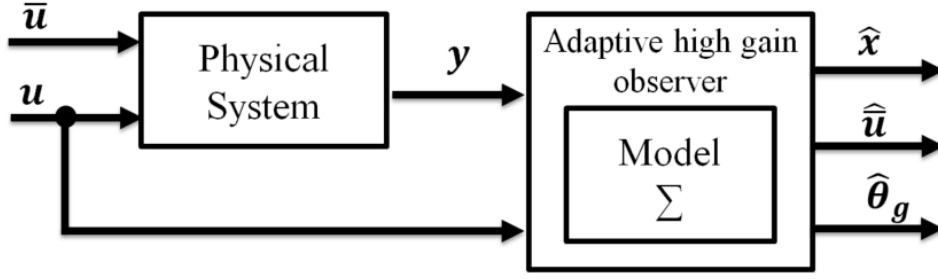


Figure 68 Unknown inputs adaptive high gain observer principle

4.2.1.2. Observer synthesis

The synthesis of the observer is presented in this section for the class of nonlinear systems with unknown inputs. Before presenting the proposed observer, let us introduce some definitions, notations and hypothesis. Let be a class of nonlinear systems whose measures are not affected by the unknown inputs. We assume that part of the state is directly measured. The nonlinear state space model of the model is given by

$$\Sigma \begin{cases} \dot{x} = f(x, u) + G(u)\bar{u} \\ y = Cx \end{cases} \quad (126)$$

$x = \begin{pmatrix} x^1 \\ X \end{pmatrix} \in \mathbb{R}^n$ is the state vector, so the part $x^1 \in \mathbb{R}^p$ is measured and $X \in \mathbb{R}^{n-p}$. $\bar{u} \in \mathbb{R}^m$ is unknown state vector of input and $u \in U$ is known input vector. U is the set of absolutely continuous functions with bounded derivatives of R^+ in U a compact set of R^u and $y \in R^p$ is the output vector.

In the unknown inputs observer theory, the state has to be separated into two parts $x = (x^1, X)^T$ where $x^1 = y$ are measured and X are unmeasured states. The breakdown of the state into measured and unmeasured parts leads to the breakdown of the state function

$$f(x, u) = \begin{pmatrix} f^1(x, u) \\ f_X(x, u) \end{pmatrix} \in R^n \quad (127)$$

where $f^1(x, u) \in \mathbb{R}^p$ and $f_X(x, u) \in \mathbb{R}^{n-p}$. In the same way, the function $G(u)$ is a matrix made up of two parts

$$G(u) = \begin{pmatrix} G^1(u) \\ G_X(u) \end{pmatrix} \in R^{n \times m} \quad (128)$$

where $G^1(u) \in \mathbb{R}^{p \times m}$ and $G_X(u) \in \mathbb{R}^{(n-p) \times m}$. Finally, the observation matrix is $C = (I_p \ 0_p \ \dots \ 0_p) \in \mathbb{R}^{p \times n}$.

$$\Sigma \begin{cases} \dot{x}^1 = f^1(x^1, X, u) + G^1(u)\bar{u} \\ \dot{X} = f_X(x^1, X, u) + G_X(u)\bar{u} \\ y = Cx^1 \end{cases} \quad (129)$$

For the synthesis of a nonlinear unknown input adaptive high gain observer to reconstruct the state and the unknown inputs of the above system, the following hypotheses must be satisfied:

(H4) The matrix $G(u)$ is of full rank in columns for all $t \geq 0$. This means that it can be divided according to

$$G(u) = \begin{pmatrix} G^1(u) \\ G_X(u) \end{pmatrix} \in R^{p \times m} \quad (130)$$

The first part $G^1(u) \in R^{m_0 \times m}$ is a full row matrix $m \leq m_0 \leq p$. That is, $\text{rank}(G^1(u)) = \text{rank}(G(u)) = \text{rank}(CG(u)) = m, \forall u \in U$ and $\forall t \geq 0$. The matrix $G^1(u) \in R^{m_0 \times m}$ is also such that there are two positive reals αG and βG and that for all $u \in U$ and all $t \geq 0$.

(H5) The derivative with respect to the time of the unknown input u is the unknown function and must be uniformly bounded, that is to say, $\forall t > 0, \sup \|\frac{\partial \bar{u}}{\partial t}\| \leq \rho \bar{u}$ where $\rho \bar{u} > 0$ is some unknown real number.

m_1 is the smallest number of rows in the matrix for which the matrix remains of full rank $m_1 \leq m_0 \leq p$ whatever the command applied. Thus, the decomposition of the matrix $G^1(u)$ of the equation gives us the following structures of the state and the state equation.

$$x = \begin{pmatrix} x^1 \\ X \end{pmatrix} \text{ where } x^1 \in \mathbb{R}^{m_1}, X \in \mathbb{R}^{p-m_1} \quad (131)$$

$$(x, u) = \begin{pmatrix} f^1(x, u) \\ f_X(x, u) \end{pmatrix} \quad (132)$$

$$\text{where } f^1(x, u) \in R^{m_1}, f_X(x, u) \in R^{p-m_1}$$

(H6) There exist a semi-positive definitive matrix $P(t) \in R^{(n-p) \times (n-p)}$ such that

- $\exists \alpha_1, \alpha_2; \forall t \geq 0: \alpha_1 I_{n-p} \leq P(t) \leq \alpha_2 I_{n-p}$
- $\exists \alpha_3 > 0; \exists u \in U; \forall x^1 \leq R^p; \forall \xi \in R^{n-p}:$

$$\dot{P}(t) + P(t) \left(\frac{\partial f_X}{\partial X} - Y_X^2(u) \frac{\partial f^1}{\partial X} \right) + \left(\frac{\partial f_X}{\partial X} - Y_X^2(u) \frac{\partial f^1}{\partial X} \right)^T P(t) \leq -\alpha_3 I_{n-p} \quad (133)$$

Notions and generalities for the candidate observer are given below:

- $\theta_1(t)$ be a real-valued function and let $\Delta_1(\theta_1)$ be the following diagonal matrix:

$$\Delta_1(\theta_1) = \text{diag} \left(\frac{1}{\theta_1}, \frac{1}{\theta_1^2}, \dots, \frac{1}{\theta_1^n} \right) \quad (134)$$

- Let S be the unique solution of the algebraic Lyapunov equation.

$$S + A^T S + S A = C^T C \quad (135)$$

where the unknown is the matrix S , the matrices A and C are defined in (40). It was shown in [26] that the equation (135) admits a unique solution S , which is symmetric positive definite and whose terms can be expressed as follows:

$$S(i, j) = (-1)^{(i+j)} C_{i+j-2}^{j-1} \text{ for } 1 \leq i, j \leq n \quad (136)$$

where $C_n^p = \frac{n!}{(n-p)!p!}$.

With the help state transformation presented in equation (56), the adaptive high gain observers are proposed next for a canonical form.

Under above-mentioned hypotheses and proposition, the observer based on the adaptive high gain with unknown input can be written as from [188]:

State:

$$\begin{cases} \dot{\hat{x}}^1 = f_1^1(\hat{x}^1, \hat{X}, u) + G^1(u)\hat{u} + \theta_1 \left[\frac{\partial \Psi}{\partial x} \right]^{-1} \\ \quad \cdot \Delta_1^{-1}(\theta_1) S_1^{-1} C_1^T (y - \hat{x}^1) \\ \dot{\hat{X}} = f_X(\hat{x}^1, \hat{X}, u) + Y_X(u)\hat{u} + 2\theta_1(y - \hat{x}^1) \end{cases} \quad (137)$$

Unknown estimation:

$$\hat{u} = \theta_1^2 (G^1(u))^+ (y - \hat{x}^1) \quad (138)$$

Adaptive gain:

$$\begin{cases} \dot{\theta}_1 = -\frac{\mu}{2} \theta_1(t) (a(\theta_1(t)) - 1) - g(t) \gamma(\|\tilde{y}(t)\|) \\ \quad \theta_1(0) \geq 1 \\ g(t) = \frac{M}{1 + \min(\rho, \frac{1}{T} \int_{\max(0, t-T)}^t \|\tilde{y}(\tau)\|^2 d\tau)} \end{cases} \quad (139)$$

Where $\hat{x} = [\hat{x}_1, \hat{x}_2, \dots, \hat{x}_n]^T \in \mathbb{R}^n$ where x and u is the state and input of the system; θ_1 is adaptive gain of the observer. $\mu = \frac{\lambda_{\min}(Q)}{\lambda_{\max}(S)}$ and $\gamma: \mathbb{R} \rightarrow \mathbb{R}^+$, $\tilde{y} = \gamma(\tilde{y})$ is a real-valued function satisfying the following properties:

- $\gamma(0) = 0$
- $\exists \gamma > 0; \forall \tilde{y} > 0, 0 < \gamma(\tilde{y}) \leq \gamma_{max}$
- Concerning the function γ , it was specified as follows in this application:

$$\gamma(\tilde{y}) = \frac{\|\tilde{y}\|^2}{1 + \|\tilde{y}\|^2} \quad (140)$$

From the equation of the system in (129) and (137) the observation error is $e = \tilde{x} = \hat{x} - x$.

4.2.2. Adaptive high gain observer for singularly perturbed systems

The observer design problem for linear two-time-scale systems has been widely studied since its first introduction by [119]. In this section, the unknown input adaptive high gain observer for the singular perturbed system is presented. The singular perturbed systems exhibit a fast and slow dynamic. The initial nonlinear system is given by:

$$\dot{x} = f(x, u) \quad (141)$$

Since the singular perturbed system is considered, the initial system is represented in the slow reduced system and fast reduced system.

$$\dot{x}_s = f_s(x_s, z, u) \quad (142)$$

$$\dot{x}_f = \varepsilon \dot{z} = f_f(x_s, z, u) \quad (143)$$

For the above representation we consider the nonlinear singularity perturbed systems in the following form:

$$\dot{x}_s = f_s(x_s, z, u) = a_1(x_s) + a_2(x_s)z + b_1(x_s)u \quad (144)$$

$$\varepsilon \dot{z} = f_f(x_s, z, u) = a_3(x_s) + a_4(x_s)z + b_2(x_s)u + \varepsilon s(z)u \quad (145)$$

where $x_s \in R^n$ is slow state variables, $z \in R^m$ are fast state variables of the system and the input is presented by $u \in R^r$, ε is a small parameter supposed to be known and constant. $a_i(\cdot)$, $b_i(\cdot)$ and $s(\cdot)$ are smooth vectors on their arguments.

Assumption 1: Let us assume that in the context the matrix $a_4(x)z$ is non-singular in the study domain.

It should be stressed that the system (144) and (145) represents a singularly perturbed system. An advantage of this representation is the possibility to decompose the real system into two subsystems of lower order and to assign state feedback for each lower-order subsystem.

In the first step, the manifold of the fast states is designed based on the reduced slow subsystem. The derivation is defined below.

4.2.2.1. The slow reduced systems

The slow manifold which is slow dynamics is defined by:

$$M_\varepsilon = \{Z \in R^m : z = h(x, u_s, \varepsilon \dot{u}_s, \dots, \varepsilon)\} \quad (146)$$

which is said to be an invariant manifold for (144) and (145) if the manifold condition given in [116], [118] is true, that is:

$$\begin{aligned} \varepsilon \frac{\partial h}{\partial x} [a_1(x) + a_2(x)z + b_1(x)u] + \varepsilon \frac{\partial h}{\partial (u_s^i)} u_s^{i+1} \\ = a_3(x) + a_4(x)z + b_2(x)u + \varepsilon s(z)u \end{aligned} \quad (147)$$

Equating this equation term by term in ε , we obtain a solution of the following form:

$$h(x, u_s, \varepsilon \dot{u}_s, \dots, \varepsilon) = h^0(x, u_s) + \varepsilon h^1(x, u_s, \dot{u}_s) + \varepsilon^2 h^2(x, u_s, \dot{u}_s, \ddot{u}_s) + \dots \quad (148)$$

The reduced slow dynamics is obtained by setting $\varepsilon = 0$ in equation (148) and solving with respect to z an algebraic-type vector equation, one obtains the so-called quasi-state solution z_0^s :

$$z_0^s = h^0(x, u_s) = -[a_4(x_s)]^{-1}[a_3(x_s) + b_2(x_s)u] \quad (149)$$

Substituting z_0^s to z into (148), we obtain the slow reduced dynamics at order 0 in ε as:

$$\dot{x}_s = f_s(x_s) + g_s(x_s)u_s \quad (150)$$

where

$$\begin{aligned} f_s &= a_1(x) - a_2(x)[a_4(x_s)]^{-1}a_3(x_s) \\ g_s &= b_1(x) - a_2(x)[a_4(x_s)]^{-1}b_2(x_s) \end{aligned}$$

Remark: To improve the approximation order in ε , we can substitute $h(x, u_s, \varepsilon \dot{u}_s, \dots, \varepsilon)$ at any prefix order of approximation to z in equation (144). This gives the slow dynamic on the basis of which a slow control can be designed up to any fixed order of approximation with respect to ε . An iterative approach can be used in (150).

4.2.2.2. The fast reduced system

The fast reduced system or boundary layer system is obtained by transforming the slow time scale t of the original system (144) and (150) to the fast time scale:

$$\tau = \frac{t - t_0}{\varepsilon} \quad (151)$$

Applying the usual change of state:

$$\eta = z - h^0(x, u_s) \quad (152)$$

We can express the original system in the fast time scale as:

$$\frac{dx}{d\tau} = \varepsilon[a_1(x) + a_2(x)z + b_1(x)u] \quad (153)$$

$$\frac{d\eta}{d\tau} = a_4(x)\eta + b_2(x)(u - u_0) + \varepsilon s(\eta)u - \left[\frac{\partial h^0}{\partial x} \frac{dx}{d\tau} + \frac{\partial h^0}{\partial u} \frac{du_s}{d\tau} \right] + O(\varepsilon) \quad (154)$$

where $(u - u_0) = u_f$ is the fast control. Assuming $\frac{du_s}{d\tau} = 0$ (slow control constant in the rapid time-scale) we obtain the fast reduced system, for $\varepsilon = 0$:

$$\frac{d\eta}{d\tau} = a_4(x_s)\eta + b_2(x_s)u_f \quad (155)$$

4.2.2.3. Observer synthesis

Our system is composed of two time scale slow and fast, so as the need to design two adaptive observers separately for the reconstruction of all the slow and fast dynamics. Therefore the adaptive observer is developed for slow reduced systems to estimate the state and unknown input observer is developed for the fast reduced systems.

As the state space model of the system is considered in equation (117):

$$\Sigma \begin{cases} \dot{x} = f(x, u) + G(u)\bar{u} \\ y = Cx \end{cases} \quad (156)$$

We divide the system into two-time scales as shown in (157)

$$\begin{aligned} \dot{x}_s &= f(x_s, z, u) + G(z, u) \\ \dot{x}_f &= \varepsilon \dot{z} = f(x_s, z, u) + G(z, u)\bar{u} \end{aligned} \quad (157)$$

Now applying adaptive high gain observer for the slow reduced systems given in [120],

$$\begin{aligned}
\dot{\hat{x}}_s &= f(\hat{x}_s, u) + G(u, \hat{x}_s) - \left[\frac{\partial \Psi \hat{x}_s}{\partial \hat{x}_s} \right]^{-1} \Lambda^{-1}(\theta_1) K C^T \tilde{x}(t) \\
\dot{\theta}_1 &= -\frac{\mu}{2} \theta_1(t) (a(\theta_1(t)) - 1) - g(t) \gamma(\|\tilde{y}(t)\|); \quad \theta_1(0) \geq 1 \\
g(t) &= \frac{M}{1 + \min(\rho, \frac{1}{T} \int_{\max(0, t-T)}^t \|\tilde{y}(\tau)\|^2 d\tau)}; \quad \theta_1(0) \geq 1
\end{aligned} \tag{158}$$

where x_s and u is the slow state and input of the system; Matrix K such that $A-KC$ is Hurwitz and θ_1 is the adaptive gain of the observer. $\mu = \frac{\lambda_{\min}(Q)}{\lambda_{\max}(S)}$ and $\gamma: R \rightarrow R^+$, $\tilde{y} = \gamma(\tilde{y})$ is a real-valued function satisfying the following properties:

- $\gamma(0) = 0$
- $\exists \gamma > 0; \forall \tilde{y} > 0, 0 < \gamma(\tilde{y}) \leq \gamma_{max}$
- Concerning the function γ , it was specified as follows in this application:

$$\gamma(\tilde{y}) = \frac{\|\tilde{y}\|^2}{1 + \|\tilde{y}\|^2} \tag{159}$$

Above defined unknown input adaptive high gain observer from equations (137-139) are applied for the fast reduced systems

$$\begin{aligned}
\varepsilon \begin{pmatrix} \dot{\hat{z}}^1 \\ \dot{\hat{f}} \end{pmatrix} &= \begin{pmatrix} l^1_1(\hat{x}_s, \varepsilon \hat{z}^1, \varepsilon \hat{z}^2, u) \\ 0 \end{pmatrix} + \begin{pmatrix} G^1(u) \\ 0 \end{pmatrix} \hat{f} + \theta_2 \Lambda_1^+(u) \Delta_1^{-1}(\theta_2) S_1^{-1} C_1^T (z^1 - \hat{z}^1) \\
\varepsilon \begin{pmatrix} \dot{\hat{z}}^2 \\ \vdots \\ \dot{\hat{z}}^q \end{pmatrix} &= \begin{pmatrix} l^2(\hat{x}_s, \varepsilon \hat{z}^1, \varepsilon \hat{z}^2, \varepsilon \hat{z}^3 u) \\ \vdots \\ l^q(\varepsilon \hat{z}, u) \end{pmatrix} + \begin{pmatrix} G^2(u) \\ \vdots \\ G^q(u) \end{pmatrix} \hat{f} + 2\theta_2 Y_X^2(u) (z^1 - \hat{z}^1) \\
\dot{\theta}_2 &= -\frac{\mu}{2} \theta_2(t) (a(\theta_2(t)) - 1) - g(t) \gamma(\|\tilde{y}(t)\|); \quad \theta_2(0) \geq 1 \\
g(t) &= \frac{M}{1 + \min(\rho, \frac{1}{T} \int_{\max(0, t-T)}^t \|\tilde{y}(\tau)\|^2 d\tau)}; \quad \theta_2(0) \geq 1
\end{aligned} \tag{160}$$

where z and u is the slow state and input of the system and θ_2 is the adaptive gain of the observer. $\mu = \frac{\lambda_{\min}(Q)}{\lambda_{\max}(S)}$. ε is a small parameter supposed to be known and constant. It is defined as

$$\varepsilon = \frac{\lambda_{\min}(f(x_s, z, u))}{\lambda_{\max}(f(x_s, z, u))} \tag{161}$$

where λ is eigenvalues of matrix $f(x_s, z, u)$.

In this section, the unknown input adaptive high gain observer is designed successfully for regular systems as well as singular perturbed systems. These different techniques for observing the state and unknown inputs will be applied in the following section to the problem related to the estimation of rolling resistance.

4.3. Application on the full vehicle for estimation of tyre rolling resistance

In this section, the application of above-developed observers on the full vehicle model for the estimation of tyre rolling resistance is presented. The numerical validation is also presented for each case.

4.3.1. Estimation of tyre rolling resistance for regular systems

The above-developed observer is applied to the full vehicle model defined in section 4.1. The system is said to be a regular system if thermal dynamics are not considered. This is supposed to have slow dynamics. A dedicated study is done in the next chapter to conclude on this. So in this section, the tyre temperature variation is not considered here. The model is written under state space form and observability of system is analysed.

4.3.1.1. State space model

In this section, the state-space model representation is presented for the above-developed vehicle model. The initial model is written as in equation (117):

$$\dot{x} = f(x, u) \quad (162)$$

The state variables of the model defined now with respect to the vehicle body reference frame are represented by vector x as follows:

$$x = [w_1, w_2, w_3, w_4, v_x, v_y, \dot{\psi}, \dot{\phi}, \dot{\theta}, \psi, \phi, \theta]^T \quad (163)$$

With the variables w_1, w_2, w_3, w_4 as angular speed, v_x, v_y are longitudinal and lateral speeds, $\dot{\psi}, \dot{\phi}, \dot{\theta}, \psi, \phi, \theta$ represents yaw pitch and roll rate and angle respectively.

Firstly, the model is written under the state space form. The rolling resistance is assumed here as unknown input. By assembling the chassis dynamics and the wheels dynamics with tyre/road force a complete state-space model of the vehicle is obtained. The state space variable is defined in equation (163), for the sake of simplicity forces are also assumed as measured input in first simulations. The measured input matrix is given by

$$u = (F_x, F_y, F_z, \delta, Tyw)^T \quad (164)$$

The rolling resistance force is considered as unknown input here, so the function defined as

$$\bar{u} = f(F_{rr1}, F_{rr2}, F_{rr3}, F_{rr4})^T \quad (165)$$

Finally, the measured output of this model is:

$$y = (w_1, w_2, w_3, w_4, v_x, v_y, \dot{\psi})^T \quad (166)$$

After substituting (164), (165), (166) in (162) the complete nonlinear state space model of the vehicle is defined as:

$$\Sigma \begin{cases} \dot{x} = f(x, u) + G(u)\bar{u} \\ y = Cx \end{cases} \quad (167)$$

4.3.1.2. Observer synthesis

The synthesis of the observer is presented in this section for the class of nonlinear systems with unknown input as described in the previous section. Before presenting the proposed observer, let us introduce some definitions, notations and hypothesis. Let be a class of nonlinear systems whose measures are not affected by the unknown inputs. We will assume that part of the state is directly measured. The nonlinear state space model of the vehicle is given by

$$\Sigma \begin{cases} \dot{x} = f(x, u) + G(u)\bar{u} \\ y = Cx \end{cases} \quad (168)$$

$x = \begin{pmatrix} x^1 \\ X \end{pmatrix} \in \mathbb{R}^n$ is the state vector, so the part $x^1 \in \mathbb{R}^p$ is measured and $X \in \mathbb{R}^{n-p}$. $\bar{u} \in \mathbb{R}^m$ is unknown state vector of input and $u \in U$ is known input vector. U is the set of absolutely continuous functions with bounded derivatives of R^+ in U a compact set of R^u and $y \in R^p$ is the output vector.

In the unknown inputs observer theory, the state has to be separated into two parts $x = (x_1, x_2)^T$ where $x^1 = y$ are the measured variables and $X = (\dot{\phi}, \dot{\theta}, \psi, \phi, \theta)^T$ the unmeasured variables. The breakdown of the state into measured and unmeasured parts leads to the breakdown of the state function

$$f(x, u) = \begin{pmatrix} f^1(x, u) \\ f_X(x, u) \end{pmatrix} \in R^n \quad (169)$$

where $f^1(x, u) \in \mathbb{R}^p$ and $f_X(x, u) \in \mathbb{R}^{n-p}$. In the same way, the function $G(u)$ is a matrix made up of two parts

$$G(u) = \begin{pmatrix} G^1(u) \\ G_X(u) \end{pmatrix} \in R^{n \times m} \quad (170)$$

where $G^1(u) \in \mathbb{R}^{p \times m}$ and $G_X(u) \in \mathbb{R}^{(n-p) \times m}$. Finally, the observation matrix is $C = \begin{pmatrix} I_p & 0_p & \dots & 0_p \end{pmatrix} \in \mathbb{R}^{p \times n}$.

$$\Sigma \begin{cases} \dot{x}^1 = f^1(x^1, X, u) + G^1(u)\bar{u} \\ \dot{X} = f_X(x^1, X, u) + G_X(u)\bar{u} \\ y = Cx^1 \end{cases} \quad (171)$$

Once the system is in this form, we can directly apply the unknown input adaptive high gain observer. Under the above mentioned hypotheses and proposition detailed in section 4.2.1.2, the observer based on the adaptive high gain with unknown input can be written as from equation (137-139):

State:

$$\begin{cases} \dot{\hat{x}}^1 = f_1^1(\hat{x}^1, \hat{X}, u) + G^1(u)\hat{u} + \theta_1 \left[\frac{\partial \Psi}{\partial X} \right]^{-1} \\ \quad \cdot \Delta_1^{-1}(\theta_1) S_1^{-1} C_1^T (y - \hat{x}^1) \\ \dot{\hat{X}} = f_X(\hat{x}^1, \hat{X}, u) + Y_X(u)\hat{u} + 2\theta_1 (y - \hat{x}^1) \end{cases} \quad (172)$$

Unknown estimation:

$$\dot{\hat{u}} = \theta_1^2 (G^1(u))^+ (y - \hat{x}^1) \quad (173)$$

Adaptive gain:

$$\begin{cases} \dot{\theta}_1 = -\frac{\mu}{2}\theta_1(t)(a(\theta_1(t)) - 1) - g(t)\gamma(\|\tilde{y}(t)\|) \\ \theta_1(0) \geq 1 \\ g(t) = \frac{M}{1 + \min(\rho, \frac{1}{T} \int_{\max(0, t-T)}^t \|\tilde{y}(t)\|^2 d\tau)} \end{cases} \quad (174)$$

where $\hat{x} = \begin{pmatrix} \hat{x}_1 \\ \hat{x}_2 \\ \vdots \\ \hat{x}_n \end{pmatrix} \in \mathbb{R}^n$ where x and u is the state and input of the system; θ_1 is adaptive gain of the observer. $\mu = \frac{\lambda_{\min}(Q)}{\lambda_{\max}(S)}$ and $\gamma: \mathbb{R} \rightarrow \mathbb{R}^+$, $\tilde{y} = \gamma(\tilde{y})$ is a real-valued function satisfying the following properties:

- $\gamma(0)=0$
- $\exists \gamma > 0; \forall \tilde{y} > 0, 0 < \gamma(\tilde{y}) \leq \gamma_{\max}$
- Concerning the function γ , it was specified as follows in this application:

$$\gamma(\tilde{y}) = \frac{\|\tilde{y}\|^2}{1 + \|\tilde{y}\|^2} \quad (175)$$

From the equation of the system (171) and (172) the observation error is $e = \hat{x} - x$.

Where:

$$G(u) = \left[(T_{yw1} - R_{l1}F_{xw1})/I_w + (R_{l1}F_{zw1})/I_w; (T_{yw2} - R_{l2}F_{xw2})/I_w + (R_{l2}F_{zw2})/I_w; (T_{yw3} - R_{l3}F_{xw3})/I_w + (R_{l3}F_{zw3})/I_w; (T_{yw4} - R_{l4}F_{xw4})/I_w + (R_{l4}F_{zw4})/I_w; \frac{(F_x - F_a)}{m}; \frac{(F_y)}{m}; M_z \right]$$

$$\begin{aligned} f_1^1(\hat{x}^1, \hat{X}, u) = & \left[0; 0; 0; 0; \hat{v}_y \dot{\hat{\psi}} \right. \\ & + h \left(\sin(\hat{\theta}) \left(\hat{\psi}^2 + \hat{\phi}^2 + \hat{\theta}^2 \right) - \sin(\hat{\phi}) \hat{\psi} - 2 \cos(\hat{\phi}) \hat{\phi} \hat{\psi} \right. \\ & \left. - \cos(\hat{\theta}) \cos(\hat{\phi}) \hat{\theta} + 2 \cos(\hat{\theta}) \sin(\hat{\phi}) \hat{\theta} \hat{\phi} + \sin(\hat{\theta}) \sin(\hat{\phi}) \hat{\phi} \right); \hat{v}_y \dot{\hat{\psi}} \\ & + h \left(\sin(\hat{\theta}) \left(\hat{\psi}^2 + \hat{\phi}^2 + \hat{\theta}^2 \right) - \sin(\hat{\phi}) \hat{\psi} - 2 \cos(\hat{\phi}) \hat{\phi} \hat{\psi} \right. \\ & \left. - \cos(\hat{\theta}) \cos(\hat{\phi}) \hat{\theta} + 2 \cos(\hat{\theta}) \sin(\hat{\phi}) \hat{\theta} \hat{\phi} + \sin(\hat{\theta}) \sin(\hat{\phi}) \hat{\phi} \right); \left(M_z \right. \\ & \left. - h(F_x \sin(\hat{\phi}) + F_y \sin(\hat{\theta}) \cos(\hat{\phi})) \right) \\ & \left. / \left(I_{yy} \sin(\hat{\theta})^2 + \cos(\hat{\theta})^2 \left(I_{yy} \sin(\hat{\phi})^2 + I_{zz} \cos(\hat{\phi})^2 \right) \right) \right] \end{aligned}$$

$$\begin{aligned}
f_x(\hat{x}^1, \hat{X}, u) = & \left[(-K_\theta \hat{\theta} - D_\theta \dot{\hat{\theta}} + h(mg \sin(\hat{\theta}) \cos(\hat{\phi}) - F_X \cos(\hat{\theta}) \cos(\hat{\phi})) \right. \\
& + \dot{\hat{\psi}} \left(\dot{\hat{\psi}} \sin(\hat{\theta}) \cos(\hat{\theta}) (I_{xy} + \cos(\hat{\phi})^2 I_{yz}) - \dot{\hat{\phi}} \cos(\hat{\theta})^2 I_{xx} + \sin(\hat{\phi})^2 \sin(\hat{\theta})^2 I_{yy} \right. \\
& + \sin(\hat{\theta})^2 \cos(\hat{\phi})^2 I_{zz} \\
& \left. \left. - \dot{\hat{\theta}} (\sin(\hat{\theta}) \sin(\hat{\phi}) \cos(\hat{\phi}) I_{yz}) \right) \right] \\
& / \left(I_{yy} \sin(\hat{\phi})^2 + I_{zz} \cos(\hat{\phi})^2 \right); \left(-K_\phi \hat{\phi} - D_\phi \dot{\hat{\phi}} \right. \\
& + h(F_Y \cos(\hat{\theta}) \cos(\hat{\phi}) + mg \sin(\hat{\phi})) \\
& + \dot{\hat{\psi}} I_{yz} \left(\dot{\hat{\psi}} \sin(\hat{\phi}) \cos(\hat{\phi}) \cos(\hat{\theta}) + \dot{\hat{\phi}} \sin(\hat{\theta}) \sin(\hat{\phi}) \cos(\hat{\phi}) \right) \\
& \left. + \dot{\hat{\psi}} \dot{\hat{\theta}} \left(\cos(\hat{\phi})^2 I_{yy} + \sin(\hat{\phi})^2 I_{zz} \right) \right) \\
& / \left(I_{xx} \cos(\hat{\theta})^2 + I_{yy} \sin(\hat{\theta})^2 \sin(\hat{\phi})^2 + I_{zz} \sin(\hat{\theta})^2 \cos(\hat{\phi})^2 \right); \dot{\hat{\psi}}; \dot{\hat{\theta}}; \dot{\hat{\phi}}
\end{aligned}$$

$$\dot{\hat{u}} = \begin{bmatrix} \theta_1^2 \left(\frac{I_w}{R_{l1}} F_{zw1} \right) (w_1 - \hat{w}_1) \\ \theta_1^2 \left(\frac{I_w}{R_{l2}} F_{zw2} \right) (w_2 - \hat{w}_2) \\ \theta_1^2 \left(\frac{I_w}{R_{l3}} F_{zw3} \right) (w_3 - \hat{w}_3) \\ \theta_1^2 \left(\frac{I_w}{R_{l4}} F_{zw4} \right) (w_4 - \hat{w}_4) \end{bmatrix}$$

Considering a nonlinear system in equation (168), for each input u , a matrix Ψ of output and its derivatives of state can be defined:

$$\Psi(x, u) = \begin{bmatrix} h_i \\ L_f h \\ \vdots \\ L_f^{n-1} h \end{bmatrix} \quad (176)$$

$$\Psi(x, u) = \begin{bmatrix} x_1 \\ (F_{x1} - \bar{u}_1 F_{z1}) R_l / I_w, \\ \vdots \\ x_4 \\ (F_{x4} - \bar{u}_4 F_{z4}) R_l / I_w, \end{bmatrix} \quad (177)$$

The system (28) satisfies local observability rank conditions at x_0 if:

$$\text{Rank} \left[\frac{\partial \Psi(x_0, u)}{\partial x} \right] = n = 4 \text{ or } \det \left[\frac{\partial \Psi}{\partial x} \right] \neq 0 \quad (178)$$

Invertibility of analytically establish matrix $\Psi(x)$ is difficult to compute. Thus, the invertibility of $\Psi(x)$ is numerically evaluated. If its jacobian never equals 0 on the operating trajectories, it yields that the transformation $\Psi(x)$ is invertible.

Hypothesis (H4) is verified because $\text{rank}(G^1(u)) = 4$. The unknown inputs are caused by a physical and mechanical phenomenon. In normal conditions of use, the unknown inputs have bounded time derivatives. Hypothesis (H5) is checked. The hypothesis is verified.

4.3.1.3. Numerical validation

As it has been shown in chapter 3, the vehicle model is correctly configured and validated. In this section validation of observer for estimation of rolling resistance is presented. The numerical validation done using vehicle simulator SCANer™ (Prosper) is presented.

The validation of observer is done numerically with the help of SCANer studio. Then, offline experimental validation is done on University Gustave Eiffel test tracks (see chapter 5). In this section, the estimation of each observer with the real value of F_{rr} for each case is compared. The precision of the observer is evaluated by calculating the relative mean estimation errors:

$$\bar{e}_{F_{rr_i}} = \frac{1}{N} \sum_{i=1}^N \left| \frac{F_{rr_i}(t_i) - \hat{F}_{rr_i}(t_i)}{F_{rr_i}(t_i)} \right| \leq 10\% \quad (179)$$

With t_i is counted from the instant when estimated values.

Different conditions are simulated on a passenger car in SCANer™ environment in order to get input torque measured velocities and forces for observers. Based on the above mentions hypotheses, two simulation scenarios were performed and then compared with the results of the observer. The different test scenarios are given in Table 8.

- Case 1: Car moving in a straight line at 50 km/h.

The comparisons of observer results with prosper for case 1 is shown in Figure 69, Figure 70 and Figure 71. The good reconstruction of state variables by the observer is done and also the estimation of rolling resistance. The errors (Figure 71) for the reconstruction is less than 1% for the state variables and between 1-7% relative mean errors in the estimation of rolling resistance for each wheel. It can be concluded that the unknown input adaptive high gain observer for the regular system is validated for straight-line simulations.

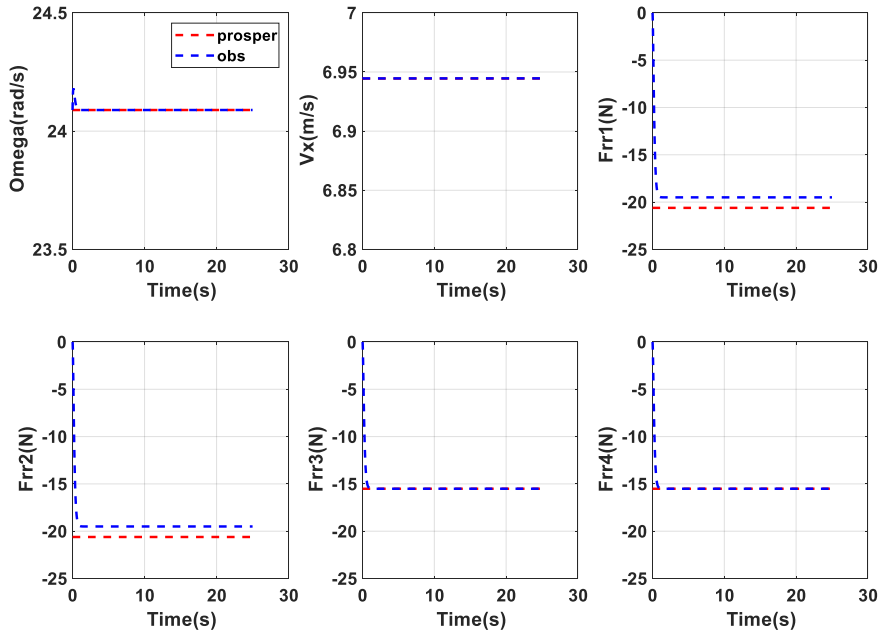


Figure 69 Comparison between Prosper results and observer estimation of rolling resistance (Case 1: straight line)

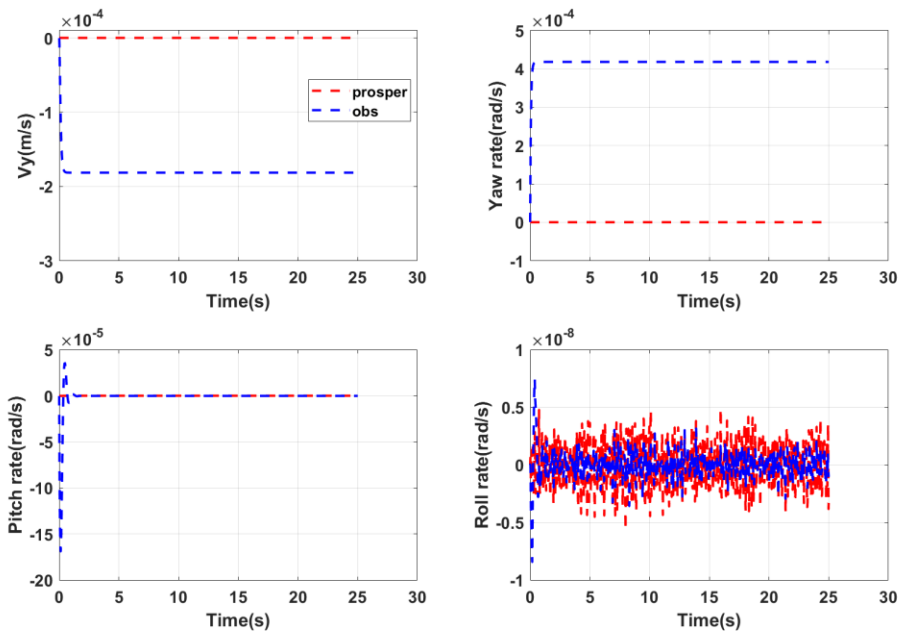


Figure 70 Comparison between Prosper results and observer estimation (Case 1: straight line)

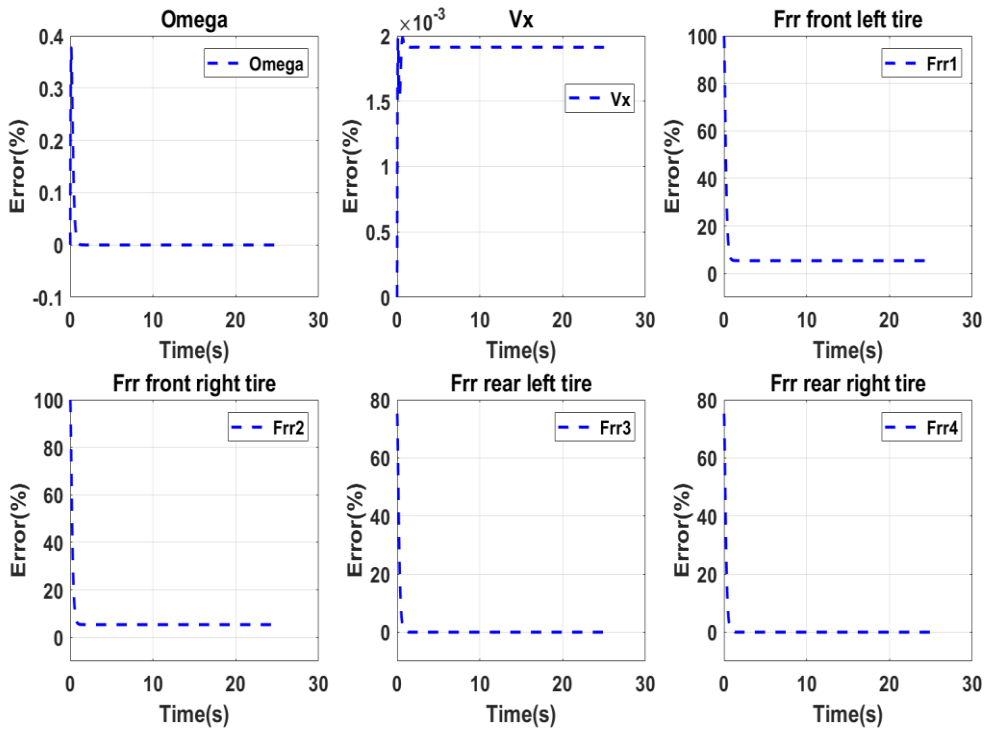


Figure 71 Estimation error results of the observer (Case 1: straight line)

- Case 2: Car moving at constant radius at 320m.

The comparisons of observer results with Prosper for case 2 are shown in Figure 72 and Figure 73. The good reconstruction of state variables by the observer is done and also the estimation of rolling resistance. The error (Figure 74) for the reconstruction is less than 1% for the state variables and errors in the estimation of rolling resistance for each wheel varies between 1-5% but the relative mean error is less than 5%. It can be concluded that the unknown input adaptive high gain as it gives $\bar{e}_{F_{rri}} < 10\%$.

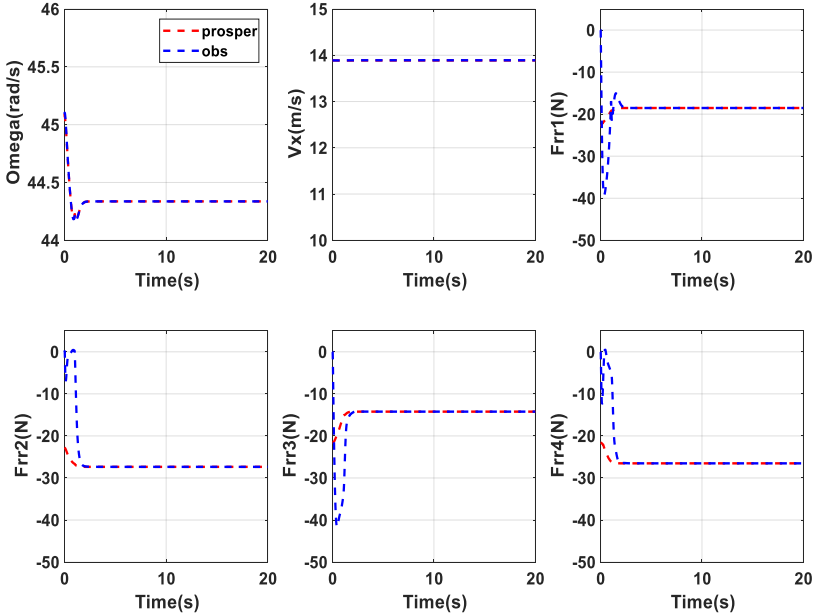


Figure 72 Comparison between Prosper results and observer estimation of rolling resistance (Case 2: Circle)

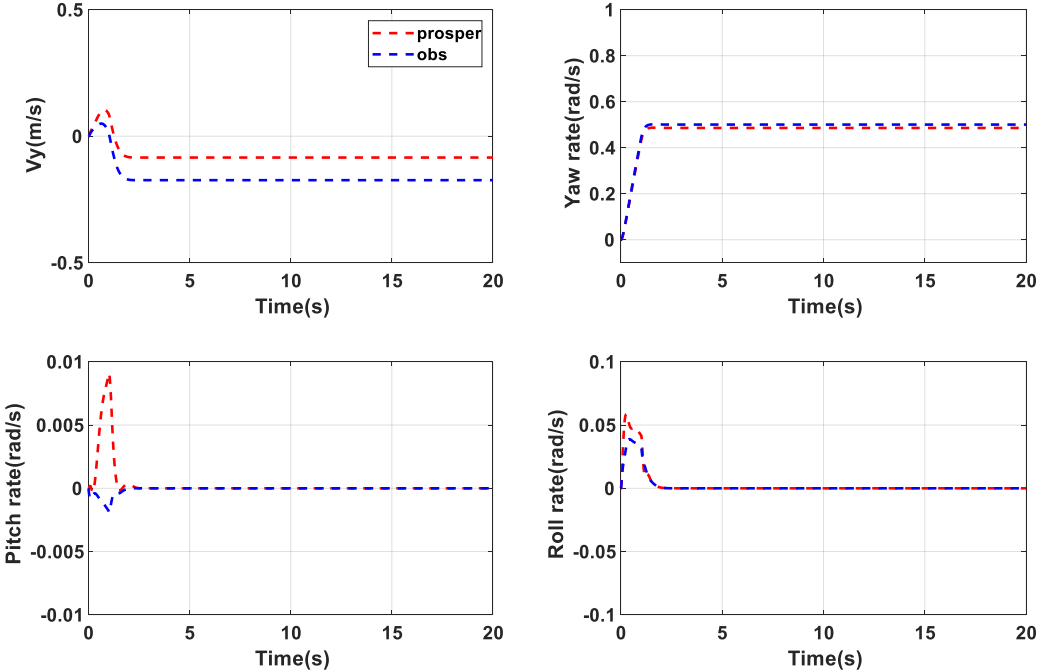


Figure 73 Comparison between Prosper results and observer estimation (Case 2: Circle)

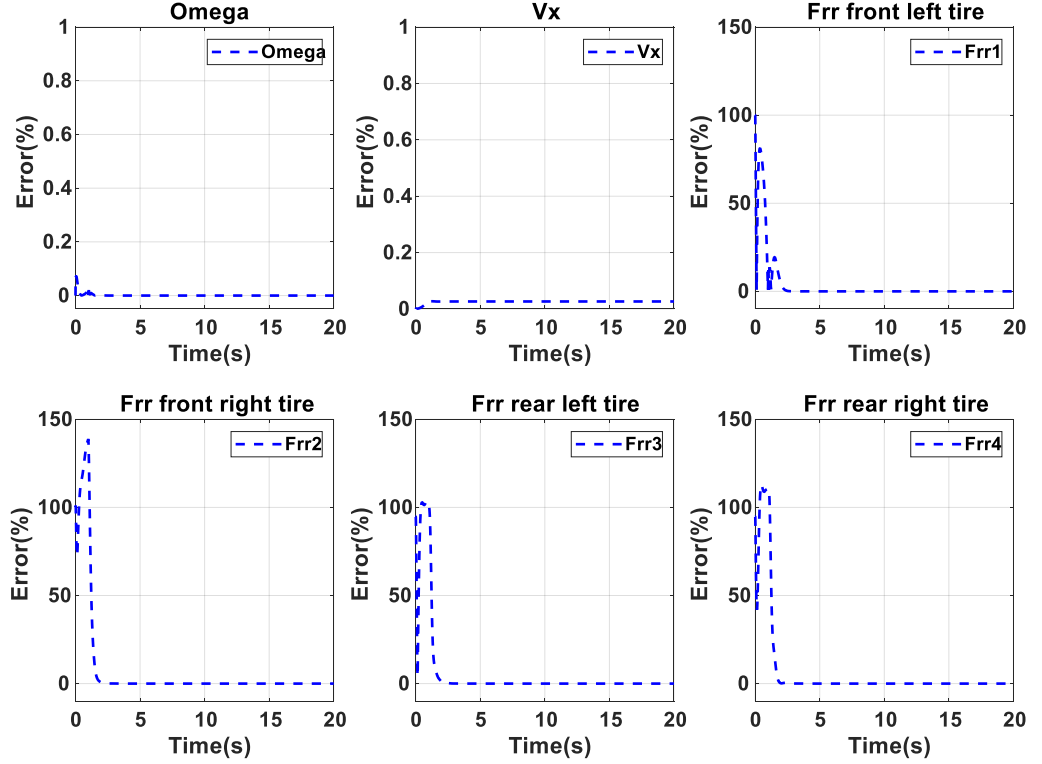


Figure 74 Estimation error results of the observer (Case 2: Circle)

4.3.2. Estimation of tyre rolling resistance for the singular perturbed system

In this section, the full vehicle model is considered as the singular perturbed system. This is mainly due to the consideration of tyre surface and carcass temperature; this is slow dynamics as confirmed from, the frequency analysis of experimental results in section 5.4.3.

4.3.2.1. State space model

The initial nonlinear system is given by:

$$\dot{x} = f(x, u) \quad (180)$$

Where x is the state vector and u is the input vector. f is the function of the matrices dependent of state vector i.e. (x) and input vector (u). The state vector is defined as

$$x = [T_{tread}, T_{carcass}, w_1, w_2, w_3, w_4, v_x, v_y, \psi, \dot{\phi}, \dot{\theta}, \psi, \phi, \theta]^T \quad (181)$$

With the variables $T_{tread}, T_{carcass}$ are tyre surface and carcass temperature respectively, w_1, w_2, w_3, w_4 as angular speed, v_x, v_y are longitudinal and lateral speeds, $\psi, \dot{\phi}, \dot{\theta}, \psi, \phi, \theta$ represents yaw pitch and roll rate and angle respectively.

Since the singular perturbed system is considered there is the possibility to decompose the real system into two subs systems of lower order described in the separate time scale, so the initial system will be represented in the slow reduced system and fast reduced system. So we can write the initial system x by dividing in two-time scale (x_s, z) as

$$\dot{x} = f(x_s, z, u) \quad (182)$$

The initial system is divided into $x_s = (T_{tread}, T_{carcass})$ for the slow dynamics system and $z = f(w_1, w_2, w_3, w_4, v_x, v_y, \dot{\psi}, \dot{\phi}, \dot{\theta}, \psi, \phi, \theta)$ for the fast dynamics systems. The singular perturbed system is considered so the initial system will be represented in the slow reduced system and fast reduced system.

$$\dot{x}_s = f_s(x_s, z, u) \quad (183)$$

$$\dot{x}_f = \varepsilon \dot{z} = f_f(x_s, z, u) \quad (184)$$

For the above representation we consider the nonlinear singularity perturbed systems in the following form:

$$\dot{x}_s = f_s(x_s, z, u) = a_1(x_s) + a_2(x_s)z + G_1(x)u \quad (185)$$

$$\varepsilon \dot{z} = f_f(x_s, z, u) = a_3(x_s) + a_4(x_s)z + G(x)u + \varepsilon s(z)u \quad (186)$$

The system can be represented in above mention singular perturbed system form, the matrices are defined below.

where

$$f_s(x_s, z, u) = ((Q_{SEL,t} + Q_{Friction\ forces} + Q_{conduction} + Q_{ambient,tread})/m_t c_t \\ (Q_{SEL,c} + k_c(T_{tread} - T_{carcass}) * s_t + Q_{ambient,carcass})/m_c c_v)$$

with

$$a_1(x_s) = ((Q_{conduction} + Q_{ambient,tread})/m_t c_t; (k_c(T_{tread} - T_{carcass}) * s_t \\ + Q_{ambient,carcass})/m_c c_v)$$

$$a_2(x_s)z = ((Q_{SEL,t} + Q_{Friction\ forces})/m_t c_t; Q_{SEL,c}/m_c c_v)$$

$$G_1(x_s)u = ((Q_{Friction\ forces})/m_t c_t; 0)$$

and $f_f(x_s, z, u)$ is defined in equation (186)

$$a_3(x_s) = (-R_{l1}F_{xw1})/I_w; (-R_{l2}F_{xw2})/I_w; (-R_{l3}F_{xw3})/I_w; (-R_{l4}F_{xw4})/I_w; \frac{(F_x - F_a)}{m}; \frac{(F_y)}{m}; M_z)$$

$$a_4(x_s)z = ((v_y \dot{\psi} + \dots; -v_x \dot{\psi} \dots, \dots (I_{xx} \cos(\theta)^2 + I_{yy} \sin(\theta)^2 \sin(\phi)^2 + I_{zz} \sin(\theta)^2 \cos(\phi)^2))$$

$$G(x_s)u = ((T_{yw1})/I_w + (R_{l1}F_{zw1})/I_w; (T_{yw2})/I_w + (R_{l2}F_{zw2})/I_w; (T_{yw3})/I_w \\ + (R_{l3}F_{zw3})/I_w; (T_{yw4})/I_w + (R_{l4}F_{zw4})/I_w; 0; 0; 0)$$

The state space form of the initial system can be written as

$$\Sigma \begin{cases} \dot{x} = f(x, u) + G(u)\bar{u} \\ y = Cx \end{cases} \quad (187)$$

where $u = (F_x, F_y, F_z, \delta, Tyw)^T$ and unknown input $\bar{u} = f(C_{rr1}, C_{rr2}, C_{rr3}, C_{rr4})^T$ the measured output $y = (w_1, w_2, w_3, w_4, v_x, v_y, \psi)^T$. Since the system is divided into two-time scales. So the state space of two-time scales can be written as

$$\dot{x}_s = f_s(x_s, z, u) + G(z, u) \quad (188)$$

$$\dot{x}_f = \varepsilon \dot{z} = f_f(x_s, z, u) + G(z, u)\bar{u} \quad (189)$$

4.3.2.2. Observer synthesis

The observer for slow and fast reduced systems are defined separately. The adaptive high gain observer is applied to slow reduced system as shown in equation (158).

$$\begin{aligned} \hat{x}_s &= \begin{bmatrix} \hat{T}_{tread} \\ \hat{T}_{carcass} \end{bmatrix} = f_s(\hat{x}_s, \hat{z}, u) - \left[\frac{\partial \Psi \hat{x}_s}{\partial \hat{x}_s} \right]^{-1} \Lambda^{-1}(\theta_1) S C^T \tilde{x}(t) \\ \dot{\theta}_1 &= -\frac{\mu}{2} \theta_1(t) (a(\theta_1(t)) - 1) - g(t) \gamma(\|\tilde{y}(t)\|); \quad \theta_1(0) \geq 1 \\ g(t) &= \frac{M}{1 + \min(\rho, \frac{1}{T} \int_{\max(0, t-T)}^t \|\tilde{y}(\tau)\|^2 d\tau)}; \quad \theta_1(0) \geq 1 \end{aligned} \quad (190)$$

Where

$$\frac{\partial \Psi \hat{x}_s}{\partial \hat{x}_s} = \begin{bmatrix} (Q_{SEL,t} + Q_{Friction\ forces} + h_c(T_{track}) * S_{cont} + h_{tread}(T_{ambient}) * S_{conv}) / m_t c_t \\ (Q_{SEL,c} + h_{carcass}(T_{ambient}) * S_{conv}) / m_c c_v \end{bmatrix}$$

$$S = \begin{bmatrix} 1 & -1 \\ -1 & 2 \end{bmatrix} \text{ and } \Lambda^{-1} = \begin{bmatrix} \theta_1 & 0 \\ 0 & \theta_1^2 \end{bmatrix}$$

The unknown input adaptive high gain observer developed in section 4.2 is applied for the fast reduced system.

$$\begin{aligned} \varepsilon \begin{pmatrix} \dot{z}^1 \\ \dot{f} \end{pmatrix} &= \begin{pmatrix} l^1(\hat{x}_s, \varepsilon \hat{z}^1, \varepsilon \hat{z}^2, u) \\ 0 \end{pmatrix} + \begin{pmatrix} G^1(u) \\ 0 \end{pmatrix} \hat{f} + \theta_2 \Lambda_1^+(u) \Delta_1^{-1}(\theta_2) S_1^{-1} C_1^T (z^1 - \hat{z}^1) \\ \varepsilon \begin{pmatrix} \dot{z}^2 \\ \vdots \\ \dot{z}^q \end{pmatrix} &= \begin{pmatrix} l^2(\hat{x}_s, \varepsilon \hat{z}^1, \varepsilon \hat{z}^2, \varepsilon \hat{z}^3 u) \\ \vdots \\ l^q(\varepsilon \hat{z}, u) \end{pmatrix} + \begin{pmatrix} G^2(u) \\ \vdots \\ G^q(u) \end{pmatrix} \hat{f} + 2\theta_2 Y_X^2(u) (z^1 - \hat{z}^1) \\ \dot{\theta}_2 &= -\frac{\mu}{2} \theta_2(t) (a(\theta_2(t)) - 1) - g(t) \gamma(\|\tilde{y}(t)\|); \quad \theta_2(0) \geq 1 \\ g(t) &= \frac{M}{1 + \min(\rho, \frac{1}{T} \int_{\max(0, t-T)}^t \|\tilde{y}(\tau)\|^2 d\tau)}; \quad \theta_2(0) \geq 1 \end{aligned} \quad (191)$$

where z and u is the fast state and input of the system and θ_2 is the adaptive gain of the observer.

$\mu = \frac{\lambda_{\min}(Q)}{\lambda_{\max}(S)}$. ε is a small parameter supposed to be known and constant. It is defined as

$$\varepsilon = \frac{\lambda_{\min}(f(x_s, z, u))}{\lambda_{\max}(f(x_s, z, u))} = 0.0005 \quad (192)$$

Where λ is Eigenvalues of matrix $f(x_s, z, u)$.

4.3.2.3. Numerical validation

In this section validation of observer for estimation of rolling resistance for the singular perturbed system is presented. As discussed previously the numerical validation of observer is done with the help of SCANeR studio (Prosper). Same conditions as previously are simulated on a passenger car in Prosper environment in order to get input torque, steering angle and measured velocities for observers.

- Case 1: Car moving in a straight line at 50 km/h.

The comparison of observer results with Prosper is shown in Figure 75, Figure 76, Figure 77 and Figure 78. In Figure 75 the results of the slow manifold are presented. The tyre surface temperature is estimated with the adaptive high gain observer. The error for tyre temperature is less than 3% for the tyre surface temperature and less than 4% for tyre carcass temperature. In Figure 76, Figure 77 and Figure 78 the results of the fast manifold is presented. The good reconstruction of state variables by the observer is done and also the estimation of rolling resistance. The errors (Figure 78) for the reconstruction is less than 1% for the state variables and 5% relative mean errors in the estimation of rolling resistance for each wheel as mentioned in the problem formulation. It can be concluded that the unknown input adaptive high gain observer for the singular perturbed system is validated.

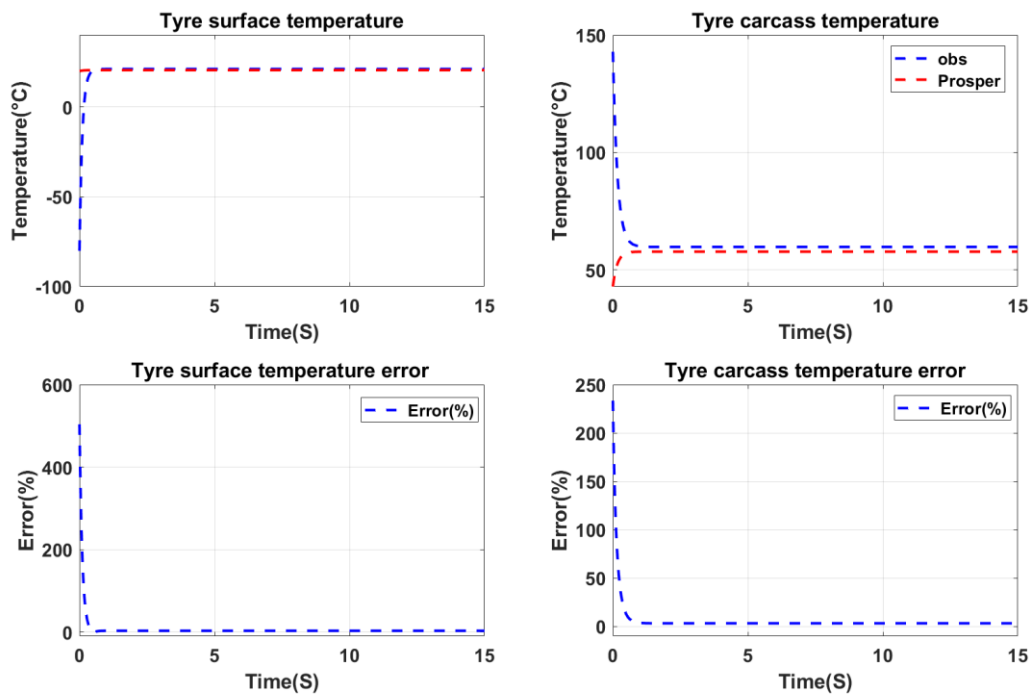


Figure 75 Tyre surface temperature state estimation comparison and percentage relative mean error (Case 1: straight line)

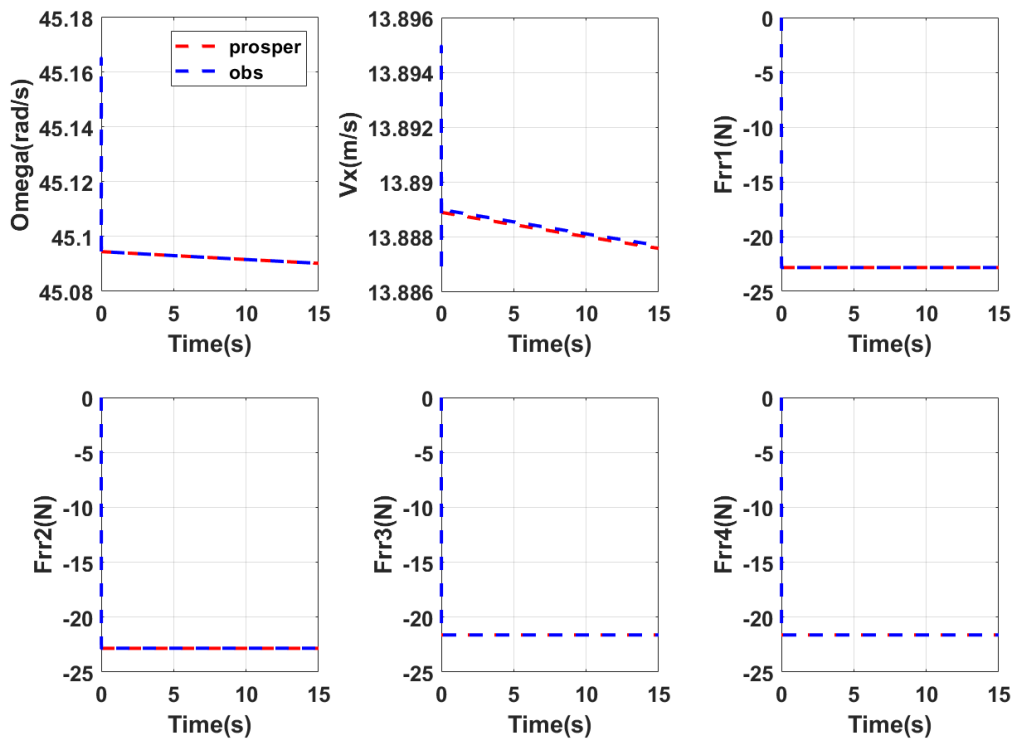


Figure 76 Comparison between Prosper results and observer estimation of rolling resistance (Case 1: straight line)

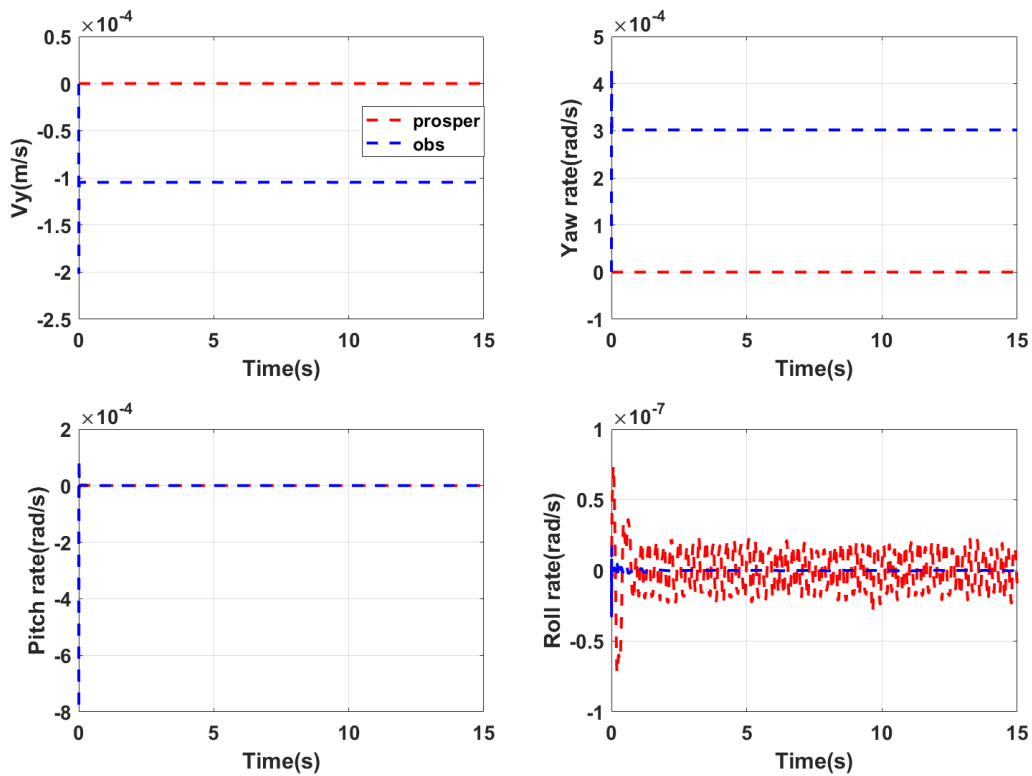


Figure 77 Comparison between Prosper results and observer estimation (Case 1: straight line)

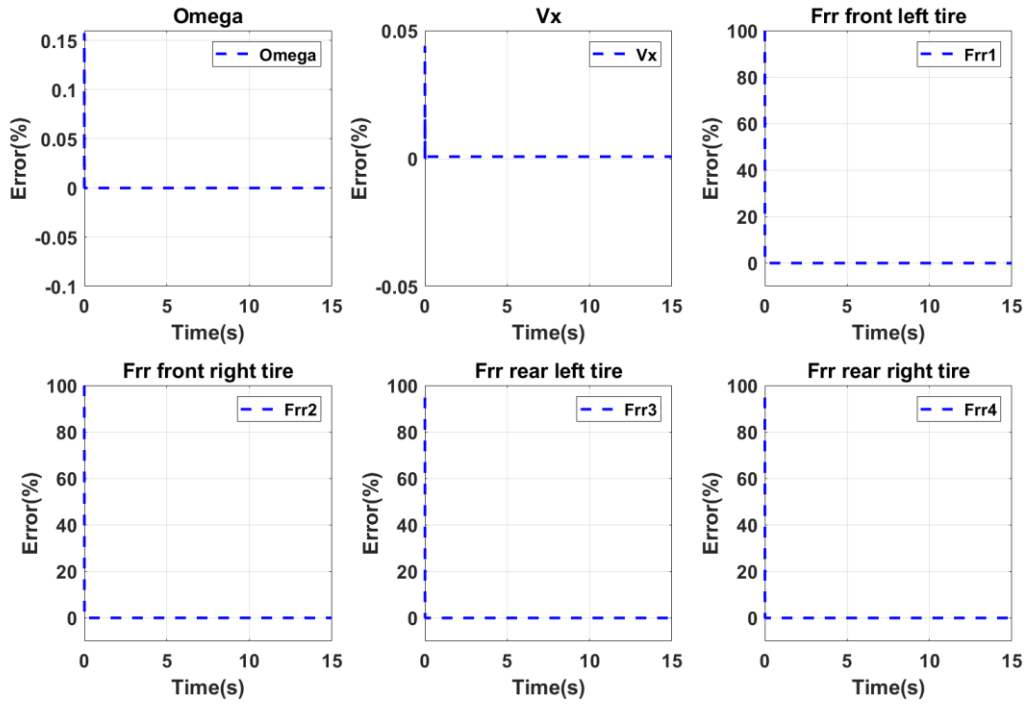


Figure 78 Estimation error results of the observer (Case 1: straight line)

- Case 2: Car moving in the curve at a constant radius at 320m.

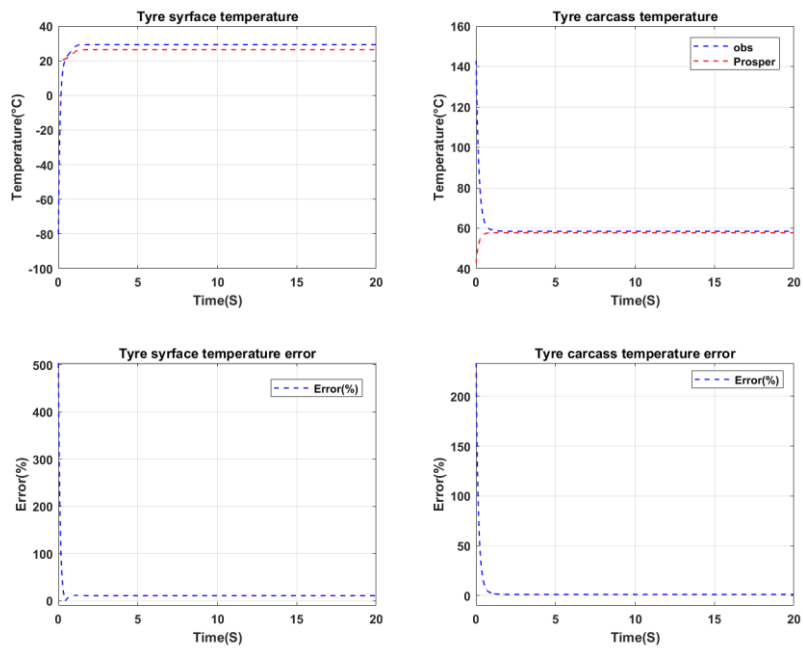


Figure 79 Tyre surface temperature state estimation comparison and percentage relative mean error (Case 2: Circle)

The comparison of observer results with Prosper for case 2 is shown in Figure 79, Figure 80, Figure 81 and Figure 82. In Figure 79 the results of slow dynamics are presented. The tyre surface temperature is estimated with the adaptive high gain observer. The error for tyre temperature is less than 12% for the tyre surface temperature and less than 5% for tyre carcass temperature. In Figure 80, Figure 81 and Figure 82 the results of the fast manifold are presented. The good reconstruction of state variables by the observer is done and also the estimation of rolling resistance. The errors Figure 82 for the reconstruction is less than 5% for the state variables and less than 8% relative mean errors in the estimation of rolling resistance for each wheel as mentioned in the problem formulation. It can be concluded from the results that the unknown input adaptive high gain observer for the singular perturbed system is validated.

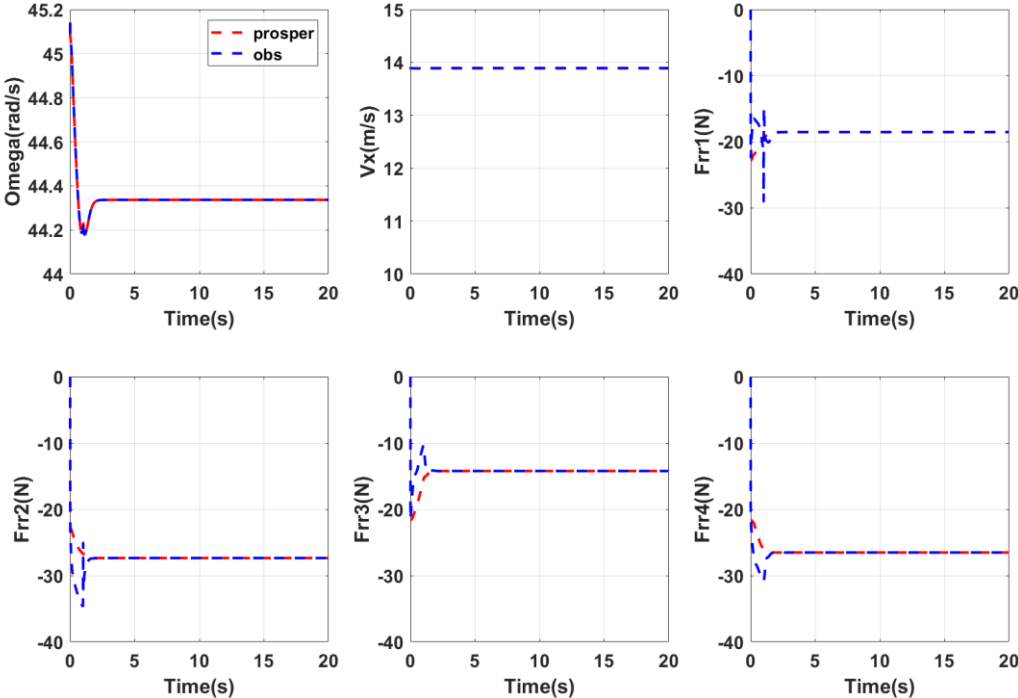


Figure 80 Comparison between Prosper results and observer estimation of rolling resistance (Case 2: Circle)

Unknown input adaptive high gain observer is successfully applied here. The precision of these observers is proved through simulation results. The observer reconstructed well the state variable with an error of less than 5% when compared to Prosper. The estimation errors for rolling resistance are less than 5% for straight line and 8% for the curve manoeuvres. It is not very significant as the magnitude of the rolling resistance force is not very high. The relative mean error is less than 10% allows us to validate the observer numerically.

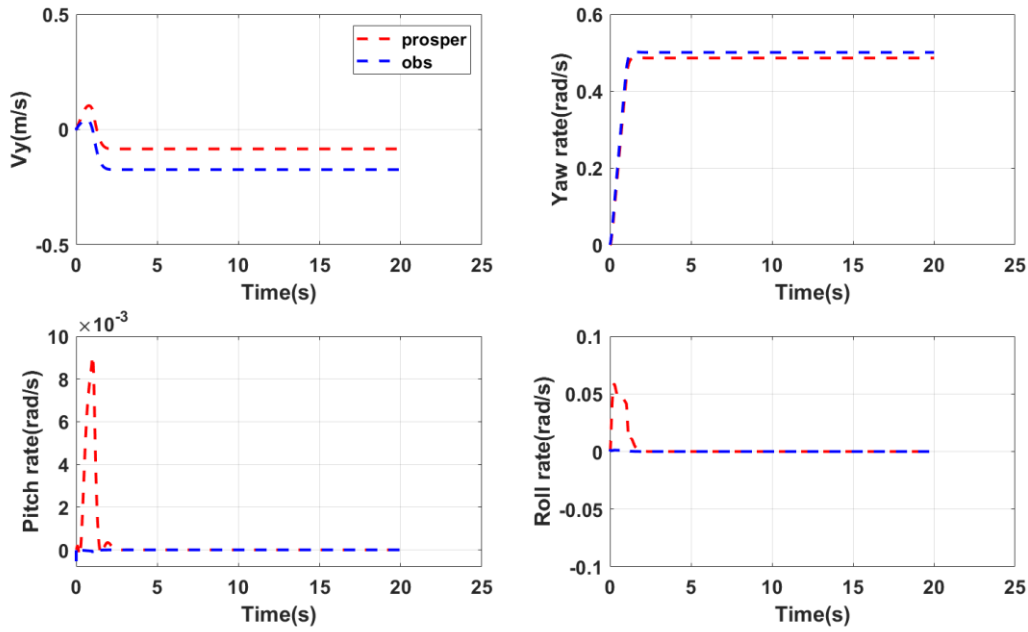


Figure 81 Comparison between Prosper results and observer estimation (Case 2: Circle)

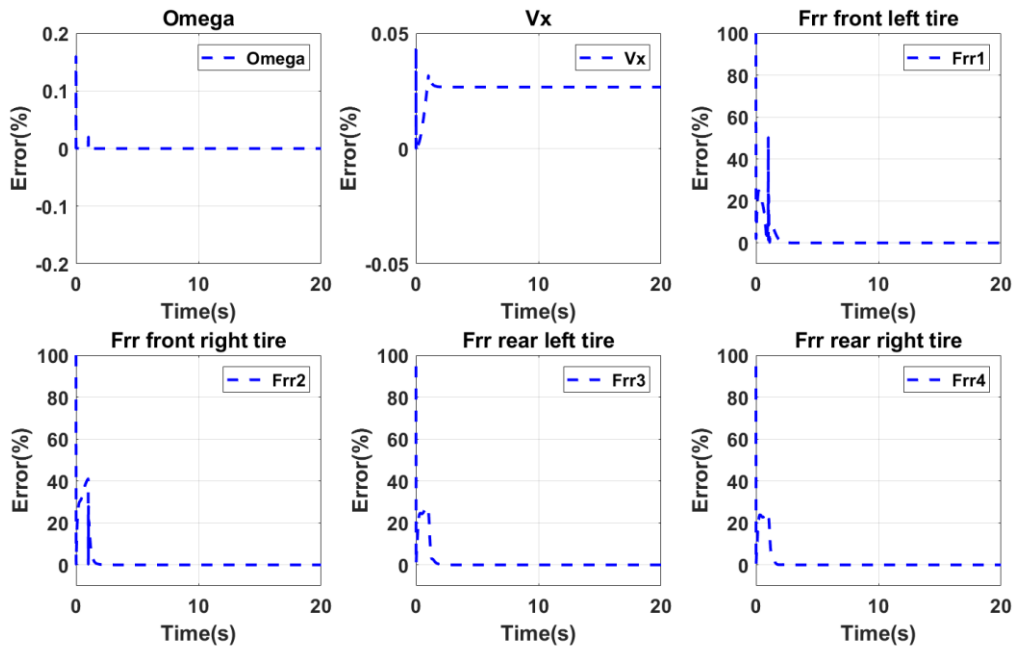


Figure 82 Comparison between Prosper results and observer estimation (Case 2: Circle)

4.4. Conclusion

The unknown input adaptive gain observer for the estimation of tyre rolling resistance force is developed for the regular system and singularly perturbed systems. This chapter presented the very first results of the estimation of rolling resistance using adaptive gain observers for full vehicle and validated numerically. This is a very promising solution to use in real driving conditions. The experimental validation of these developed observers is presented in Chapter 5.

Chapter 5
Instrumentation, Experimentation and
Validation

In this chapter instrumentation of test vehicle, design of experiments, post-processing of data and validation of above develop models are presented. The chapter starts with the description of the experimental site of University Gustave Eiffel in Nantes in section 5.1. The instrumentation of the test vehicle is also presented in section 5.1. The design of experiments (DoE) is discussed in section 5.2 and the realisation of experiments and their post-processing are discussed. The novel method for calculation of rolling resistance and its validation is done in section 5.3. The extensive study on the variation of tyre surface temperature is presented in section 5.4. The experimental validation of the developed model and observers are detailed in section 5.5. Section 5.6 summarized the main conclusions of this experimental work.

5.1. Instrumentation

In this section, the description of the test site and instrumentation of test vehicles are presented. Various sensors are mounted on the vehicle to respond to the needs to validate the models.

5.1.1. Experimental site description

Experiments were done on University Gustave Eiffel test track shown in Figure 83 for the top view and Figure 84 for the detailed view. It has been specially designed for the testing, calibration and certification of equipment for measuring surface characteristics (skid resistance, texture, rolling resistance, noise).

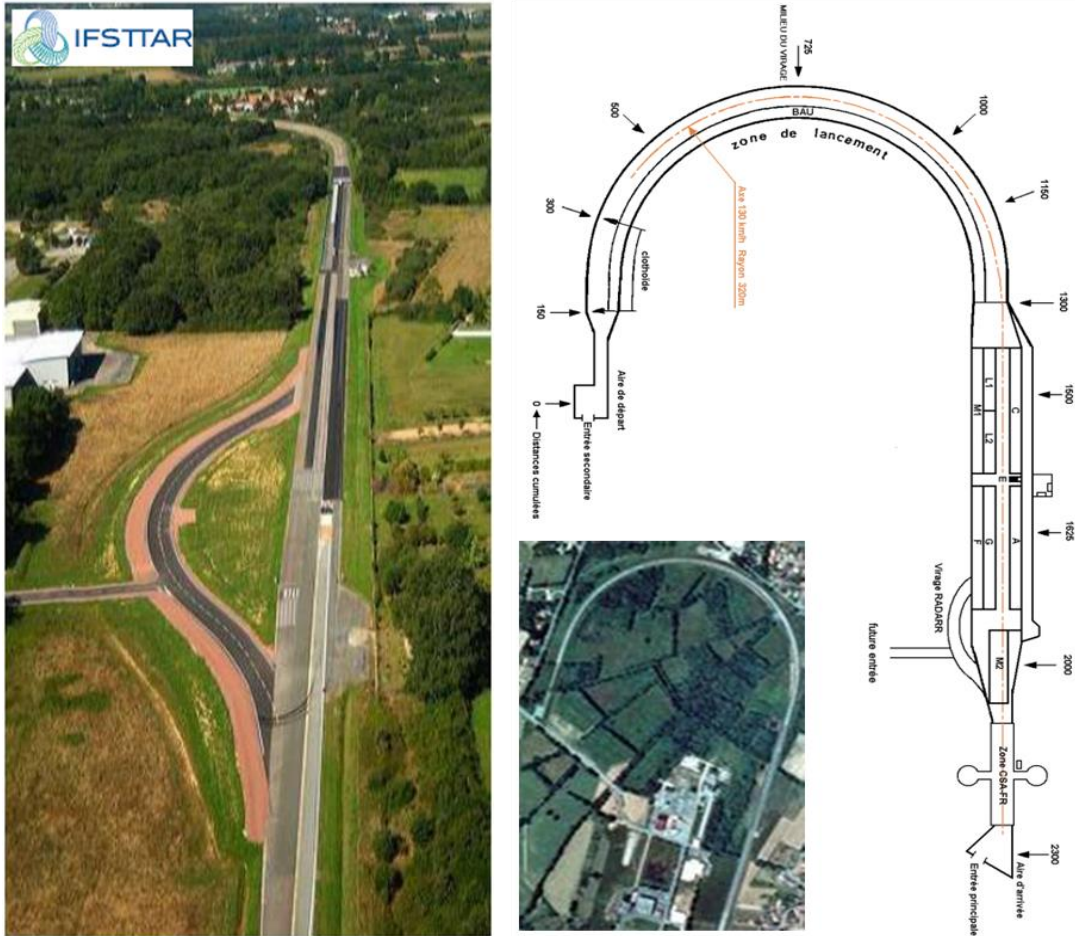


Figure 83 Photograph of test tracks at University Gustave Eiffel (top view)

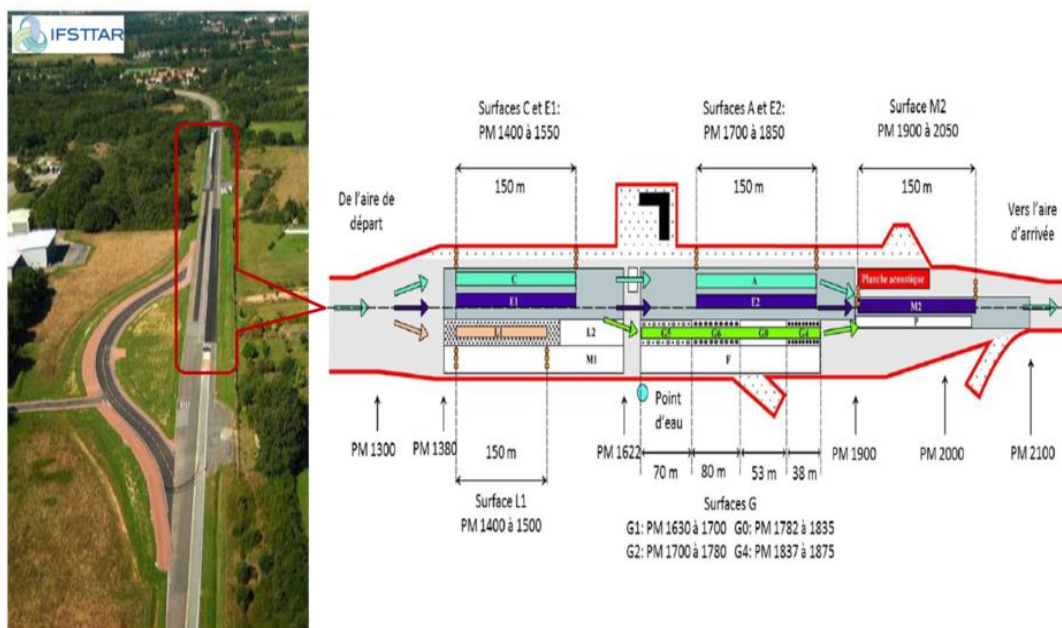
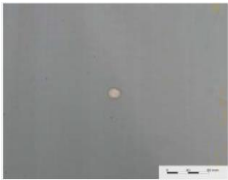





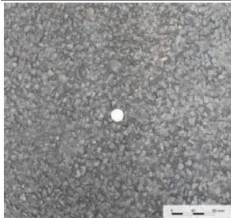
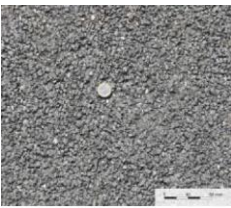




Figure 84 Detailed different test track at University Gustave Eiffel, Nantes [10]

The straight part forms the “test area” and contains 12 different pavement surfaces distributed in 4 parallel lines. The characterisation of test tracks used in the experimentation is given in Table 10. The below-mentioned test tracks were chosen for experiments because they cover a wide range of macrotexture (MPD) and a moderate range of road evenness (IRI) to focus on the effect of macrotexture on rolling resistance of tyres as defined in chapter 1.

Table 10 Characterization of test surfaces

Section	Mix type	Photo	MPD(mm)	IRI
L1	Epoxy Resin (smooth)		0.11	1.15
C1	Fine Surface Dressing 0.8/1.5 mm		0.33	1.83
L2	Sand Asphalt 0/4		0.71	1.68

E1	Dense Asphalt concrete 0/10 (new)		0.87	1.87
E2	Dense Asphalt concrete 0/10, (old)		1.12	1.59
E3	Stone mastic asphalt 0/10		1.13	1.60
M1	Very thin Asphalt concrete 0/10, class 1		1.42	1.59
M2	Very thin Asphalt concrete 0/6, class 2		1.30	1.69
F	High Skid Resistance Surface 1/3 «COLGRIP©»		1.42	1.41
A'	Coarse surface dressing 8/10		3.08	2.15

5.1.2. Test vehicle and sensors

The instrumented vehicle Clio 2 of University Gustave Eiffel is used for the experiments. It is mounted with Michelin energy saver 185/60 R15 tyres. Instrumented vehicles are equipped with different types of sensors that are controlled periodically in order to verify the reliability of the data provided by them. Calibrations and verifications are carried out internally or externally depending on the possibilities of implementing the various procedures. The sensors installed on the vehicle are:

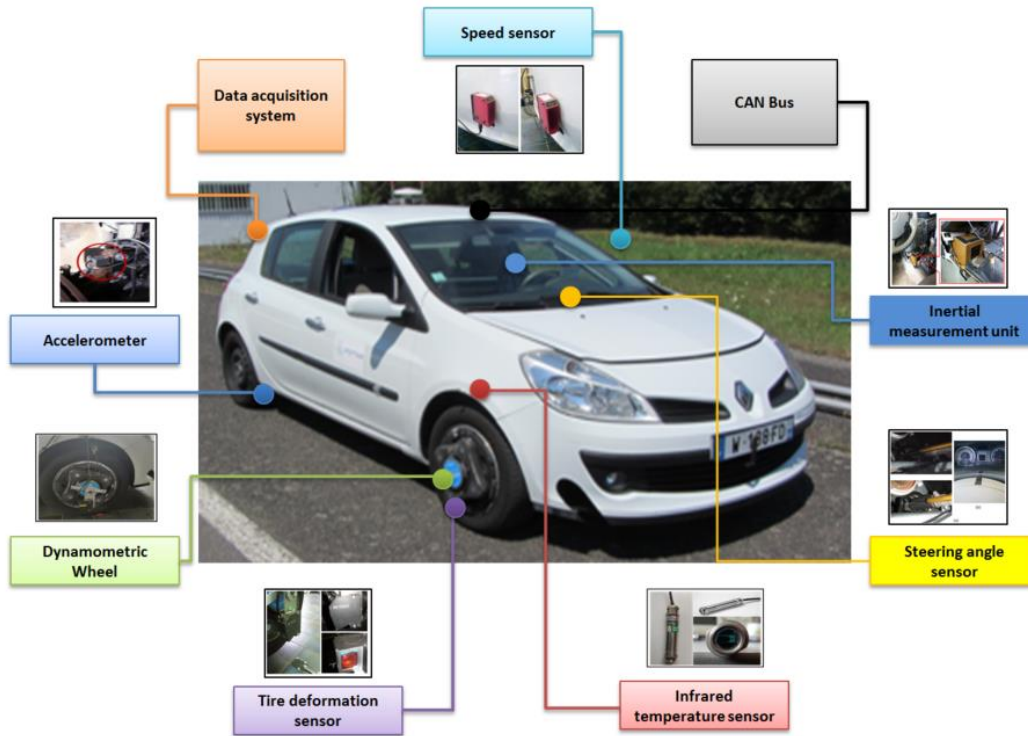


Figure 85 Univ. Gustave Eiffel instrumented vehicle with mounted sensors

- **Accelerometers**

The accelerometers that are mounted on a wheel of the Clio are Sensorex single-axis sensors (a single measurement axis). It measures in this configuration the vertical accelerations of the wheel flares and has a measuring range of +/- 10g (g being the acceleration of gravity equal to 9.81 m.s^{-2}). Their bandwidth is between 0 and 600 Hz.

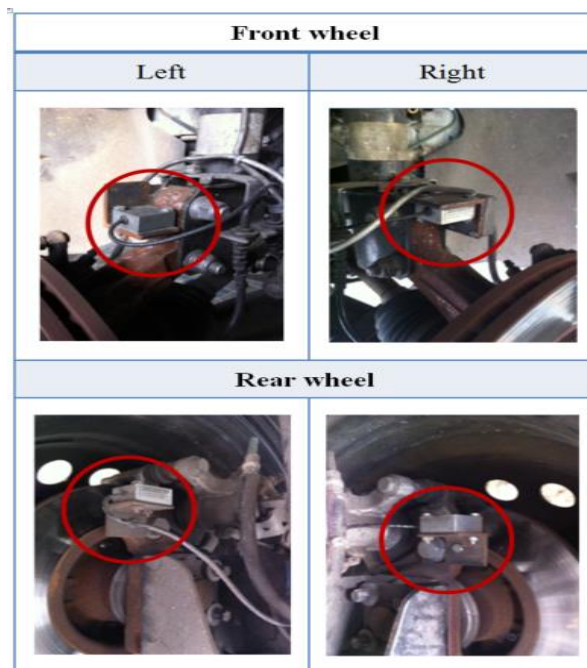


Figure 86 Accelerometer position

- **Inertial unit**

The inertial unit is a multi-axis measuring instrument (three axes of measurement) brand Crossbow model VG700AA-201. It is mounted inside the vehicle, under the dashboard and very close to the centre of gravity of the vehicle (see Figure 87).

Three accelerometers measure the acceleration of the vehicle along three orthogonal axes (X, Y and Z) which form a direct trihedral and with the earth as reference. These have a measurement range of +/- 2g (g being the acceleration of gravity equal to 9.81 m.s²).



Figure 87 Inertial unit position

- **Steering angle sensor**

The direction of the vehicle is equipped with a Vischay potentiometer which indicates a tension, this one is converted in degree by the software. (see Figure 88)

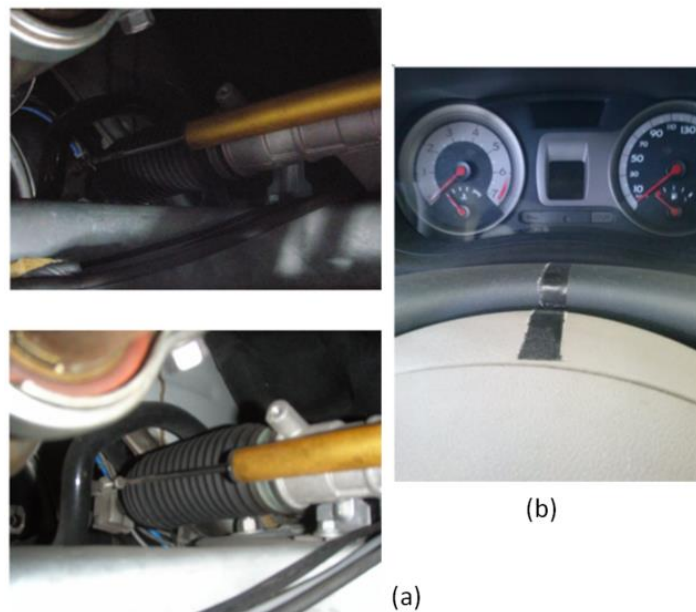


Figure 88 Mounted steering angle sensor (a) Sensor position (b) Initial position

- **Speed sensor**

The Clio 2 is equipped with a Corrsys Datron Sensor S-400 cortex. It is placed under the vehicle at the location of the spare wheel. The sensor s-400 is a non-contact optical speed sensor. It analyses the variations of the spatial frequency produced by the movement of the microstructure of the road. The signals are then conditioned to give velocities in the two directions (longitudinal and transverse).



Figure 89 Speed sensor

- **Data acquisition system**

The vehicle is instrumented with National Instrument cDAQ-9138 data acquisition system. It contains 8 Slot Compact DAQ Controller, Celeron 1.06 GHz controls the timing, synchronization, and data transfer between C Series I/O modules and an integrated computer. It incorporates a Celeron processor and 32 GB of non-volatile storage for data logging and on-board monitoring. The cDAQ-9138 offers a wide variety of expansion and standard connectivity options, including USB, Ethernet, RS-232 serial, RS-485 / RS-422 serial, and MXI-Express. The cDAQ-9138 combined with eight C Series I/O modules for CAN recording and measurement, analogue I/O, digital I/O and counters/timers.

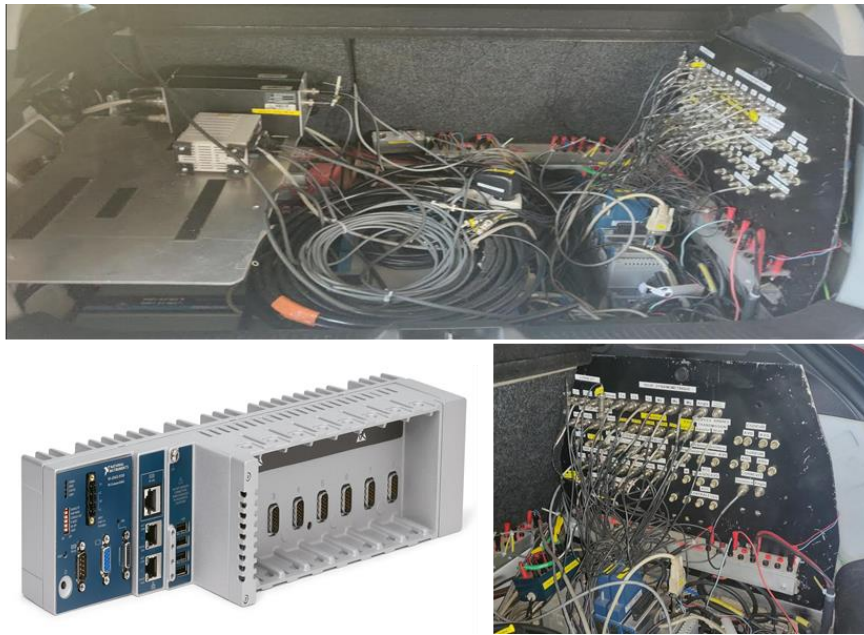


Figure 90 Data acquisition system

- **Tyres**

Initially, it was planned to use different rolling resistance tyres in experiments. But due to climatic and time constraints, all the experiments were done on a single type of tyres. In this DoE the tests are done with tyre Michelin energy saver 185/60 R15 mounted on both axle of the vehicle. These tyres are known for less rolling resistance due to its material composition. According to the tyre manufacturer, various technologies used to create the energy Saver tyre that is both efficient, with good grip and which provides the vehicle with low fuel consumption thanks to its latest generation silica contained in its rubber and to the deep ribs of its tread.

5.1.2.1. Focus on tyre instrumentation

Particular attention was given to the instrumentation of tyre. Since the validation of the multi-physical model required the temperature sensors installed on the tyres in addition to the dynamometric wheel. The special device was designed in-house by Technician Sebastien Buisson to mount MB Flex infrared sensor on the tyre. The tyre deformation sensor for the calculation of rolling resistance is also installed.

- **Dynamometric wheel**

The Clio 2 is equipped with 50 kN dynamometer sensor data type RoaDyn S625 from KISTLER [189]. This sensor gives forces and moments in three directions at the wheel centre as reference. It is mounted at the front right wheel. The RoaDyn S625 wheel force transducer (WFT) has a modular, versatile design for mounting on hubs and rim geometries. Four 3-component strain gage load cells are connected by adapter parts to a rim and the vehicle hub. The signals are amplified immediately in the load cells and fed via short cables to the wheel electronics. Here they are filtered, digitized and coded. The data stream is transmitted via a rotor/stator pair to the wheel inner side, transformed in the on-board electronic unit and output to a data acquisition device.



Figure 91 Dynamometric wheel mounted on the front right tyre

- **Temperature sensor**

The instrumented vehicle is mounted with infrared temperature sensors OPTCSLT10 at the opposite side of the contact patch. The infrared temperature sensor has a ± 1 °C of accuracy. The maximum temperature it can measure is 350°C. There are 5 sensors mounted on the vehicle. The four sensors are measuring the tyre temperature and one sensor (in blue) is measuring the pavement temperature.

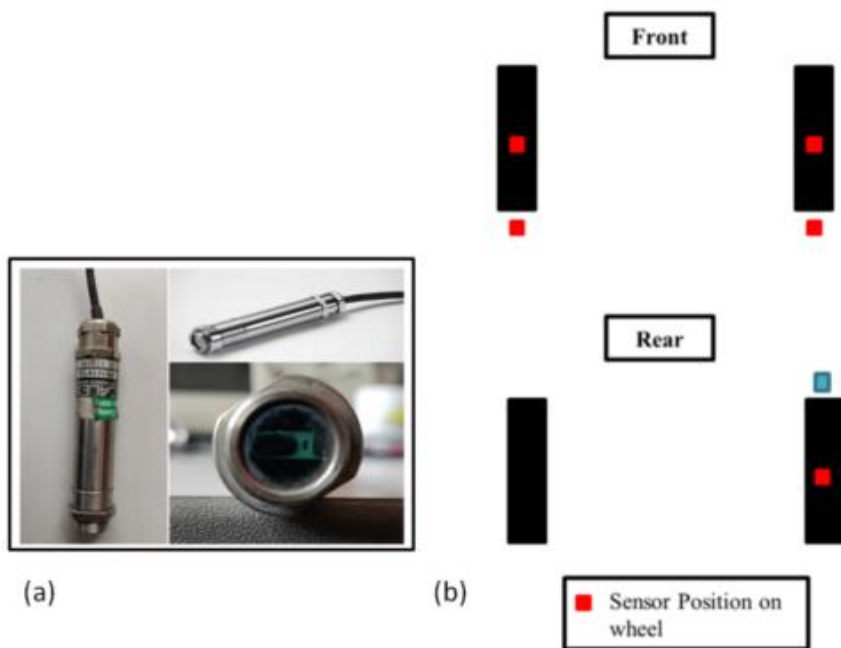


Figure 92 (a) Infrared temperature sensor (b) Mounted sensor position on the vehicle

Another kind of temperature sensors mounted on the vehicle is MB Flex infrared sensor for multi-beam flexible system by Texys. This sensor also has an accuracy of ± 1 °C and can measure from 20°C to 200°C. It has CAN type output.



Figure 93 MB Flex infrared sensor for multi-beam flexible system

- **Tyre deformation sensor**

It is necessary to use an external sensor to measure the tyre deformation. This is a LK-G157 laser sensor from Keyence Corporation (see Figure 94) Its measuring range is ± 40 mm and has an output of ± 10.8 volts.



Figure 94 Tyre deformation sensor

5.2. Design of experiments

In this section, the planning of experiments is presented. As discussed above the design of experiments have four objectives:

- Calibrate and tune the parameters of the MPT model as well as the FVM vehicle model.
- Validate the developed vehicle model experimentally.
- Validate the novel method to consider as reference for rolling resistance measurements
- Validate the approach of estimating the rolling resistance of the full vehicle.

To attain the above objectives two DoE were carried out. In the first DoE, the goal is to calibrate and tune the model and validate the developed vehicle model experimentally. The vehicle has a standard load (i.e. 1502 Kg) and pressure condition (i.e. 2 bars and 2.2 bars in front and rear tyres respectively). While planning the DoE to validate the vehicle model, the main idea is to cover different manoeuvres. Therefore 10 different test scenarios are constructed to validate our model. These scenarios cover different speeds and manoeuvres. The test scenarios are given in Table 11.

Table 11 Proposed 1st Test scenarios (DoE) to validate the vehicle model

Test no.	Trajectory	Speed (Km/h)	Comments	Repetition
1	Straight line	50	Constant speed	10
2	Straight line	80	Constant speed	10
3	Curve at 220m	40	Constant speed	5
4	Curve at 220m	60	Constant speed	5
5	Curve at 220m	80	Constant speed	5
6	Curve at 320m	40	Constant speed	5
7	Curve at 320m	60	Constant speed	5
8	Curve at 320m	80	Constant speed	5
9	Chicane	60	Constant speed	10
10	Straight line	Acceleration & Braking	Variable speed	10

In the second DoE, the goal is to validate the novel method to calculate the rolling resistance experimentally with determining the influence of different factors and also to validate our approach to estimate rolling resistance.

The rolling resistance is influenced by several factors such as speed, pressure, temperature, road roughness etc. The focus is given to these factors while designing the experiments. The five principal factors which have been identified based on the state of the art (in chapter 1), as being able to have a direct or indirect influence on the result, and which have also been selected for testing, are recalled below.

1. Tyre inflation pressure
2. Load
3. Speed
4. Surface roughness
5. Ambient air temperature

These factors influence rolling resistance with different magnitudes. These factors have been varied accordingly. The variation of parameters depends on the limitations of experimental conditions. Different manoeuvres are also added during the design of the experiment to understand the loss of energy because of the lateral deformation of the tyre tread.

Table 12 Influencing Factors with different scenarios on Michelin energy saver 185/60 R15

Factors	Scenarios
Speed	- Constant speed - Variable (brake and acceleration)

Road surface characteristics	- Smooth (L1, L2, C1, M3) - Intermediate(E1, E2, E3, M1,M2,F) - Rough (A')
Inflation pressure	- 2.2 bar - 1.5 bar - 3.3 bar
Load	- Standard (1290 Kg) - Loaded (1550 Kg)
Manoeuvres	- Straight Trajectory - Chicane Trajectory - Curve (220m and 320m)
Ambient air temperature	- ~20°C - ~40°C

A plan was developed by varying the factors selected (detailed above) and by voluntarily retaining, in order to limit the number of scenarios (while maintaining a sufficient level of robustness of the plan) and with 10 repetitions. A complete factorial design with 6 factors at average 3 levels and 10 tests per scenario required 410 tests with limitations of the experiment site. The DoE of 410 tests is proposed below for the realization:

Table 13 Proposed 2nd Test scenarios (DoE) for rolling resistance validation

Test scenarios	Description	Test track	Speed	Inflation pressure	Load	Ambient air Temp
1	- Straight line - Constant speed	L1, L2, C1, M3, E1, E2, E3, M1, M2, F, A'	50 Km/h	2.2b	Standard	~20°C
2	- Straight line - Constant speed	L1, L2, C1, M3, E1, E2, E3, M1, M2, F, A'	80 Km/h	2.2b	Standard	~20°C
3	- Straight line - Constant speed - High ambient air temperature	L1, E2, M1, A'	50 Km/h	2.2b	Standard	~40°C
4	- Straight line - Constant speed - High ambient air temperature	L1, E2, M1, A'	80 Km/h	2.2b	Standard	~40°C
5	- Straight line - Constant speed - Tyre pressure variation	E1, E3, M2	50 Km/h	1.3b, 2.2b,3.2b	Standard	~20°C
6	- Straight line - Accelerate 0 to 100 Km/h and Brake to 0 km/h	C1, E1, E3, M2, F,	Variable	2.2b	Standard	~20°C
7	- Straight line - Constant speed - Vehicle load variation	E2, M1,	50 Km/h	2.2b	Loaded	~20°C
8	- Chicane - Constant speed	E3,A,E2,M3	60 & 80 Km/h	2.2b	Standard	~20°C

5.2.1. Post-processing and analysis of experimental data

The analysis and post-processing of the data are done using MATLAB. The step-wise analysis of the data is provided below:

1. Raw data file

The output file is given in “.txt” format. This contains the measurements of all the sensors. It has 65 columns from different sensors.

2. Extracting an excel file

In this part, the file is extracted from the formatted file for the analysis. The start of the test track was identified with a position of the sensor, which is represented by the pick in the column named “Cellule” as shown in Figure 95. This is the actual length of the track and data is extracted only for this reason in the file.

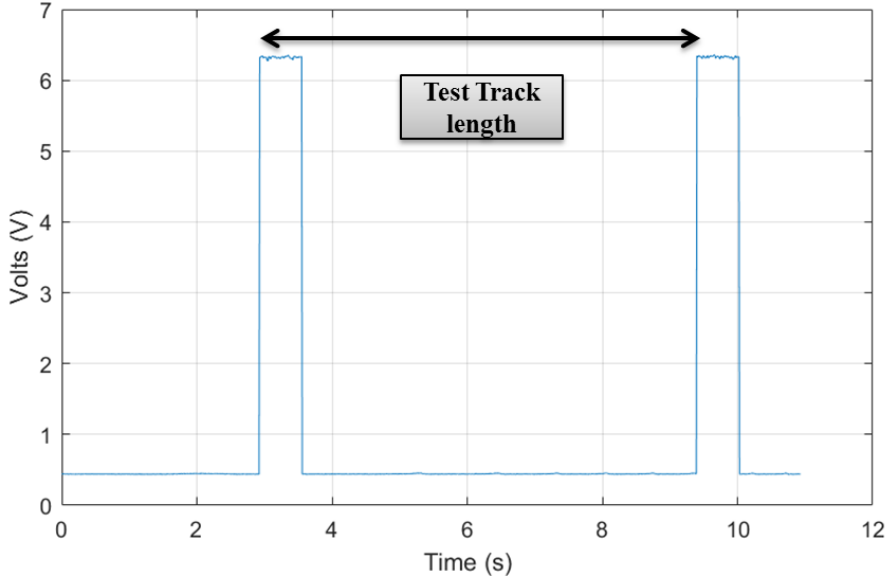


Figure 95 Cellule sensor for pointing out the start of the test track

3. Filtering

Filtering is one of the important aspects of data processing. During experiments, data are sampled at 100 Hz and contain a lot of noisy signals. It is very important to identify the cut off frequency. A comparison is done to identify the cut-off frequency as shown in Figure 96. After taking all this into account, a low pass Butterworth filter of order 2 with cut-off frequency 2 Hz is chosen to filter the experimental data. Finally, after all the above steps the data are ready for analysis.

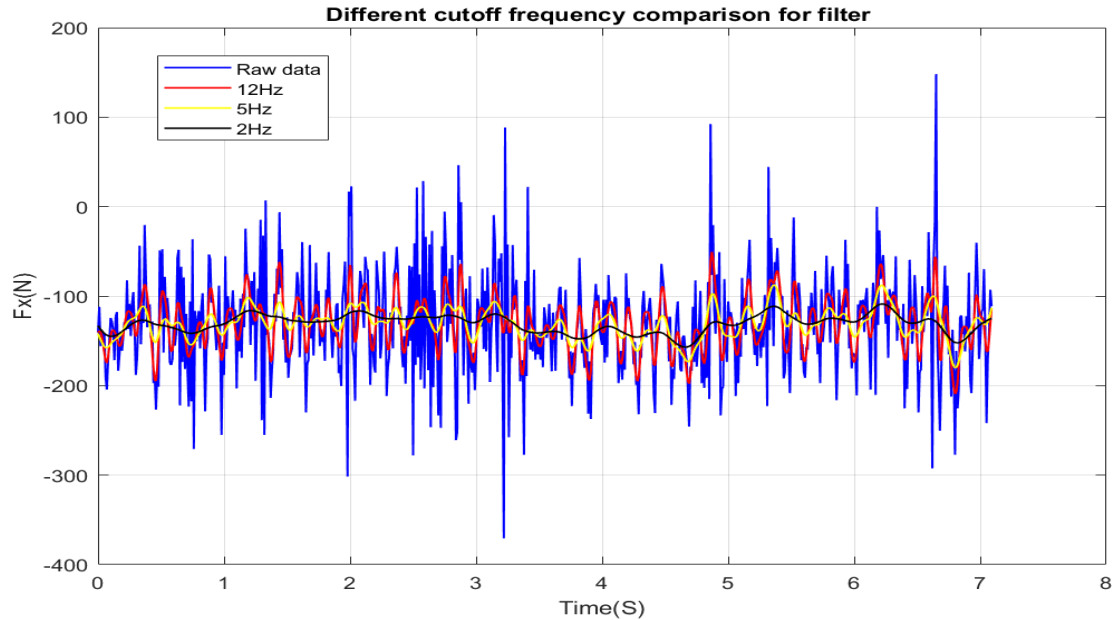


Figure 96 Different cut-off frequency comparison for low pass Butterworth filter

5.3. Reference tyre rolling resistance

It is known fact that the experimental validation of estimation of rolling resistance is difficult as it is impossible to get an absolute rolling resistance value for specific tyre and it requires a dedicated rolling resistance measuring equipment such as trailer [20]. Since the objective of the thesis is to estimate the rolling resistance on the real vehicle, the use of the trailer for validation is not recommended as it does not match the real vehicle conditions. In various studies [8], [21], [69] in literature the experimentation validation approach has never been used before. In this section, the method of calculating the rolling resistance force on the real vehicle with the help of the dynamometric wheel is discussed. The impact of influencing factors is also discussed to validate the method of calculation.

To measure the rolling resistance on the real vehicle, a method is developed and validated relatively with the help of results obtained in the Project ROSANNE [9], [29].

5.3.1. Reference rolling resistance method

The method which is proposed here calculates the rolling resistance force using rolling resistance moment. It can be indirectly called the longitudinal drag force.

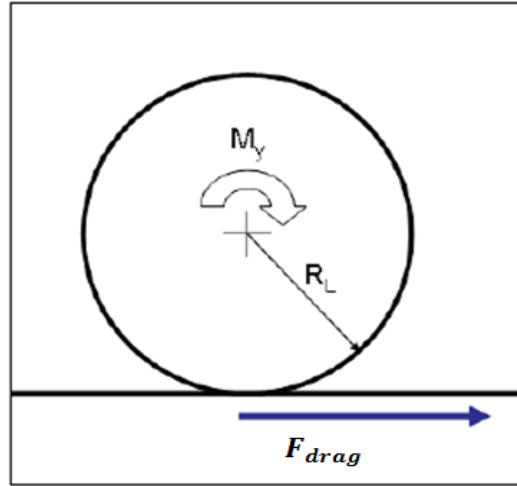


Figure 97 Relationship between M_y and F_{drag}

When a torque is applied to the rim in braking or traction the contact patch is deformed and the tyre reacts with a longitudinal force so that

$$M_y = F_{drag} R_L = \frac{\dot{E}_{diss}}{\omega} \quad (193)$$

F_x is longitudinal force, R_L is the effective loaded radius, ω is angular velocity and \dot{E}_{diss} dissipation rate. We can also write it again as

$$F_{drag} = F_{rr} = \frac{M_y}{R_L} \quad (194)$$

$$C_{rr} = \frac{F_{rr}}{F_z} \quad (195)$$

Since we calculate the loaded radius for with the help of tyre deformation sensor we can use equation (194) to calculate the longitudinal force F_{drag} which is nothing but rolling resistance force. We can also calculate the coefficient of rolling resistance using equation (195).

5.3.2. Loaded radius calculation

In these experiments, Michelin energy saver 185/60 R15 is used as mentioned. It has unloaded radius (R_F) of 300mm. The standard inflation pressure of 2.2 bars is used to inflate the tyre. The loaded effective radius (R_L) is calculated using equation (196) during the experiments.

$$R_L = R_{L\ static} \pm deformation_{dynamic} \quad (196)$$

Where $R_{L\ static}$ is static loaded radius and $deformation_{dynamic}$ is the change in tyre deformation during rolling and it is measured using tyre deformation sensor during experimentations. In Figure 98 the measurement of tyre deformation sensor is shown. The negative sign represents the decrease in the static loaded radius. The peaks in the figure are mainly due to change in the test track or if sensor encountered some hole. The static loaded radius ($R_{L\ static}$) is calculated as 290mm.

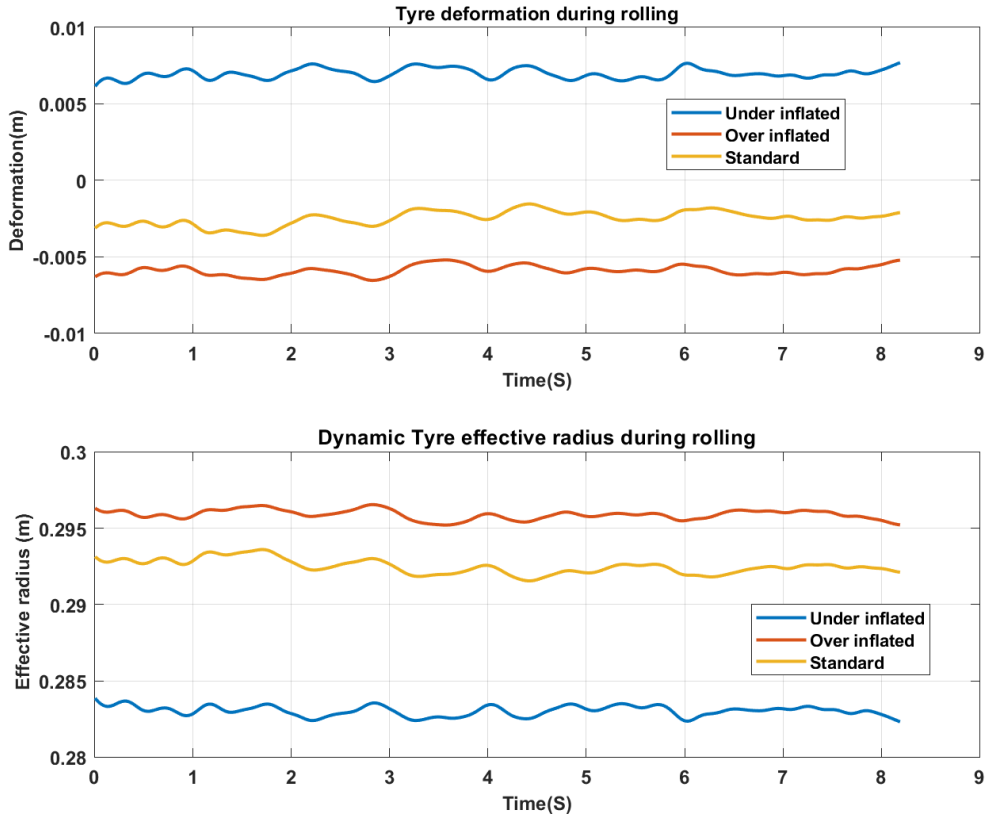


Figure 98 Tyre deformation and effective radius measured during experiments

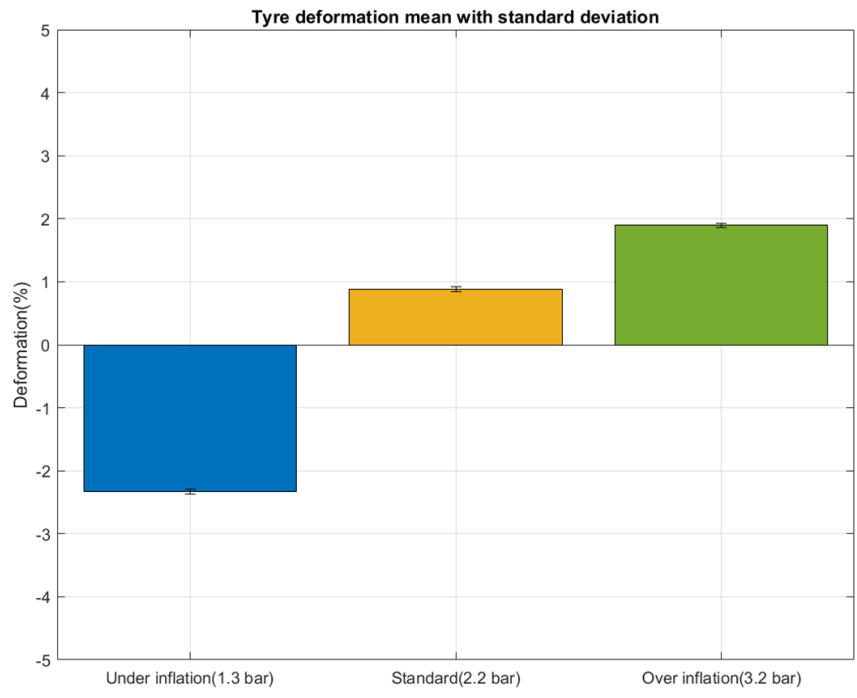


Figure 99 Tyre deformation mean in percentage for different conditions

In Figure 99 the percentage of deformation is given for different conditions of experiments. The error is the standard deviation (10 repetitions) of the measured values. In Table 14, the calculation of the loaded radius is shown. This is used for calculation in equation (194) of rolling resistance force.

Table 14 Loaded radius used in the calculation

Conditions	$R_{L\ static}$ (mm)	Mean Tyre def. (%)	R_L (mm)	$R_L = \text{Function of } R_F$ (300mm)
Standard	290	0.86	292.5	$\sim 0.975R_F$
Over inflation	290	2.03	296	$\sim 0.986R_F$
Under inflation	290	-2.40	283	$\sim 0.943R_F$

5.3.3. Rolling resistance influencing factors

In this section results using a novel method are presented. The results for different influencing parameters are presented separately. The main focus is on calculating the coefficient of rolling resistance and its coefficient of variation. The mean values with a standard deviation of each influencing parameter are presented here. In the end, the overall results are discussed.

5.3.3.1. Influence of ambient temperature on Crr

It is very difficult to vary the ambient temperature but it was a very hot summer afternoon. The tests for lower temperature were done early morning and for higher temperature in the afternoon with a significant temperature difference $\sim 20^\circ\text{C}$. The results are presented separately for different speeds and 4 different test tracks.

❖ Speed 50km/h

The results for 50 km/h are shown in Figure 100. The other parameters were kept constant for the test vehicle as shown in Table 13. It is concluded from Figure 100 that for higher ambient air temperature the Crr is lower as compared to lower ambient air temperature. The temperature of the tyre surface is observed with $\sim 20^\circ\text{C}$ more for higher ambient air temperature. It means that there is a direct effect of ambient air temperature for lower speed on rolling resistance. The 15°C increase in tyre surface temperature decreases the rolling resistance up to 5% for lower speed.

Table 15 Parameter table ambient air temperature

Parameters	Tyre inflation pressure	Load	Speed	Ambient air temperature	Test track
Varied				x	
Constant	x	x	x		x

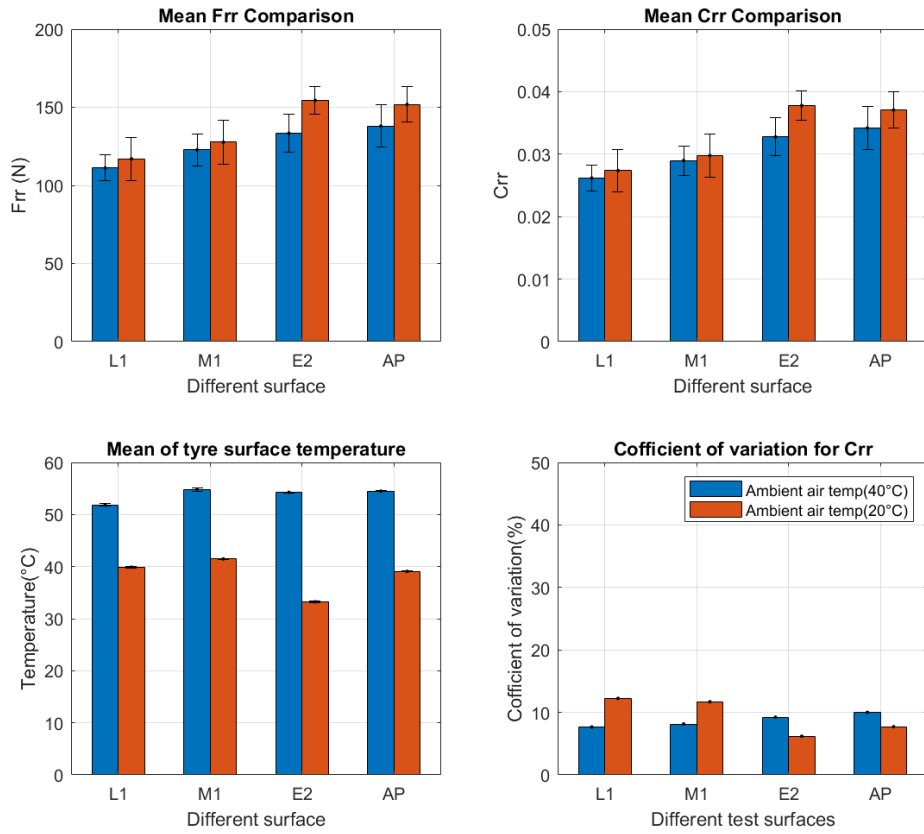


Figure 100 Bar plot of tyre rolling resistance force, coefficient and tyre temperature

❖ **Speed 80km/h**

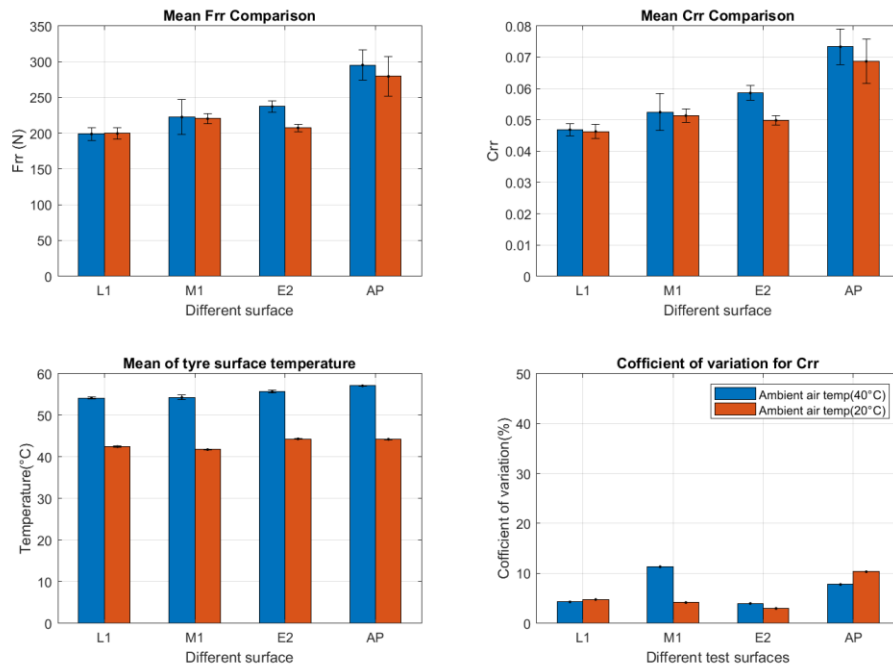


Figure 101 Bar plot of tyre rolling resistance force, coefficient and tyre temperature

The results for the different test track at 80 km/h are shown in Figure 101. It is concluded from Figure 101 that it is difficult to differentiate the impact of ambient air temperature for higher speeds. The temperature of the tyre surface is observed with $\sim 10^{\circ}\text{C}$ more for higher ambient air temperature. It means that for higher speed the effect of ambient air temperature is not significant on rolling resistance. It is mainly due to the lower gradient (the difference between tyre surface temperature and ambient air temperature) of tyre surface temperature which is due to the cooling of the tyre with air current at high speed.

The synthesis of the mean value of C_{rr} for different tracks at 50 km/h is given in Figure 102. The trend matches the literature results. At lower speed, the trend is fully representative of the literature whereas at the higher speed we cannot differentiate two ambient temperature conditions. It can be explained with the gradient between the tyre temperature during morning and afternoon at different speeds. It is observed that the gradient is $\sim 20^{\circ}\text{C}$ for 50 km/h and $\sim 10^{\circ}\text{C}$ for 80 km/h.

So it is important to include the impact of tyre surface temperature while estimating the rolling resistance of the tyre. The MPT model defined in Chapter 2 allowed us to take this effect into account.

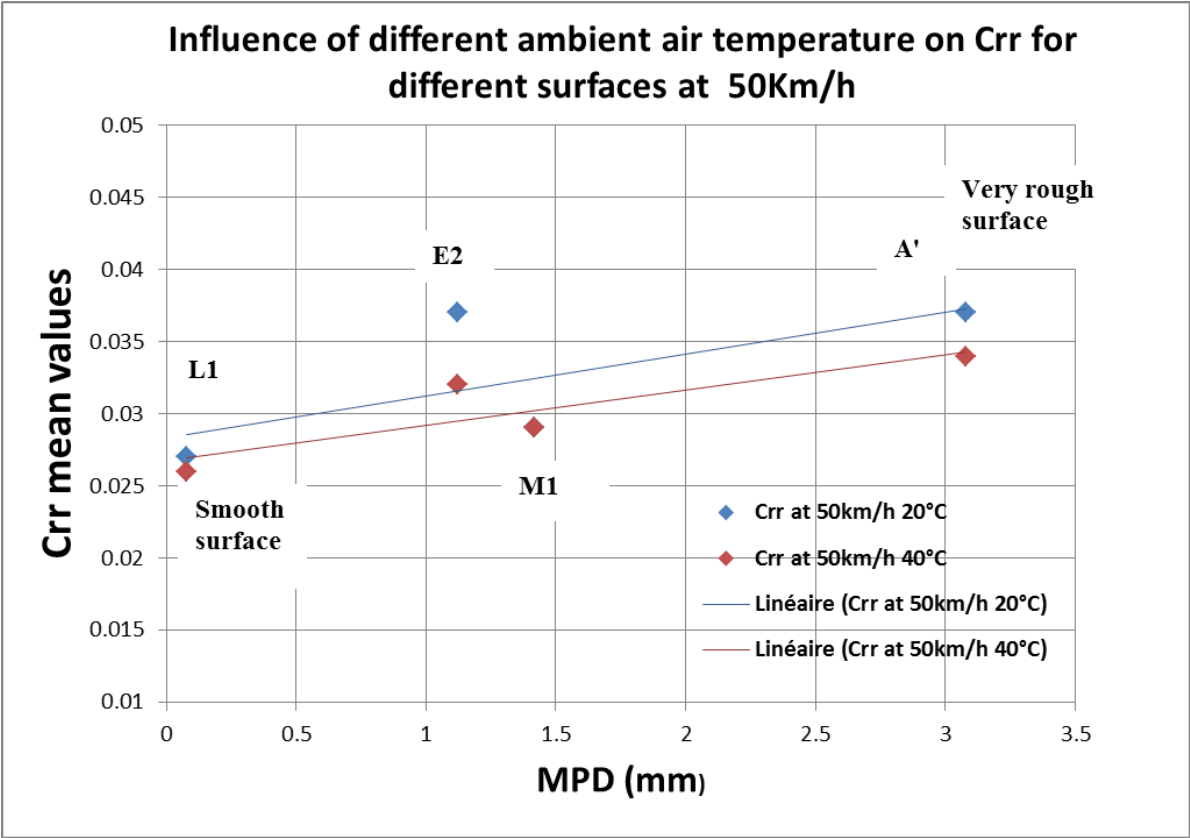


Figure 102 Crr trend for different surfaces at different ambient air temperature for 50 km/h

Since the ambient air temperature and tyre surface temperature influence directly the rolling resistance force and coefficient, therefore the correction of temperature is implemented for the rest of the analysis. The temperature correction is done according to ISO standards [20]. The rolling resistance force and the coefficient is calculated at 25°C using the equation (197). The values of constant K_t is taken from the [29] for the same tyre. The coefficient K_t is obtained by simple arithmetic calculations based on the slope and intercept values of the linear regression lines approximating the temperature influence on rolling resistance.

$$F_{r25} = F_{rr} [1 + K_t(t_{amb} - 25)], C_{r25} = \frac{F_{r25}}{F_z} \quad (197)$$

Where K_t is coefficient of temperature influence, $1/^\circ\text{C}$, F_{r25} is rolling resistance force at 25°C , and t_{amb} is the air temperature in $^\circ\text{C}$.

5.3.3.2. Influence of tyre inflation pressure on Crr

In this section, the inflation pressure of the tyre is varied as given in Table 16. The other parameters are tried to keep constant and inflation pressure is varied to two different values. The inflation pressure is measured before and after the test.

Table 16 Parameter table tyre inflation pressure

Parameters	Tyre inflation pressure	Load	Speed	Ambient air temperature	Test track
Varied	x				
Constant		x	X	x	x

The results are shown in Figure 103. The rolling resistance is calculated using the method as described above. It is concluded from Figure 103 that there is a direct impact of inflation pressure on the rolling resistance force. The underinflated tyre (1.3 bar) has high rolling resistance coefficient as compared to over-inflated tyre (3 bar). The tyre surface temperature for both inflation pressures is around 42°C but the corrected rolling resistance is calculated with the help of equation (197). The tests are done on 3 different test tracks and the influence of inflation pressure has been same for 3 test track as shown in Figure 104.

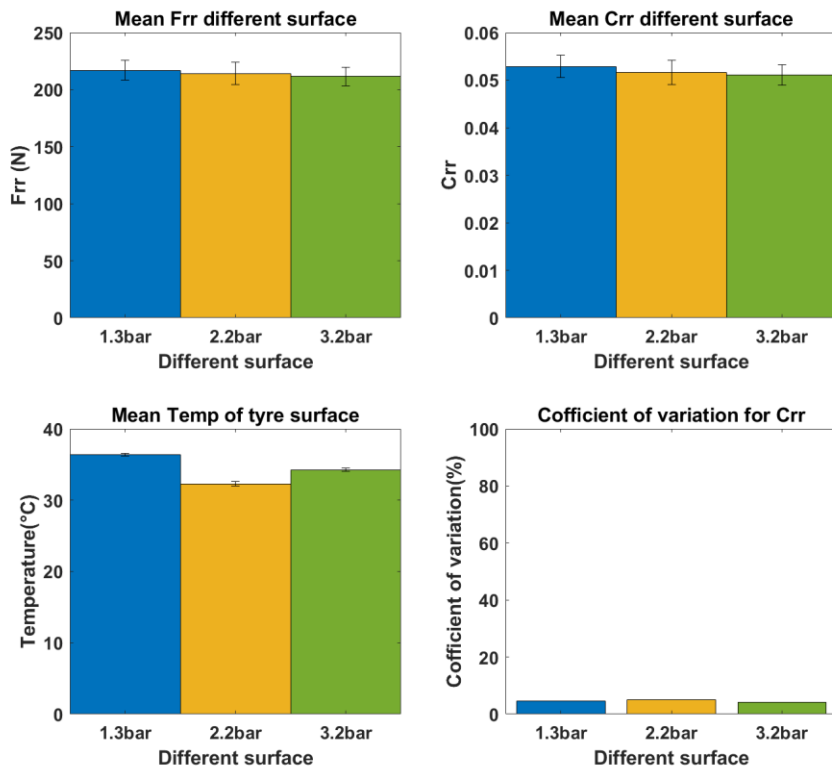


Figure 103 Bar plot of mean rolling resistance at 50 km/h on the E1 test track and coefficient of variation

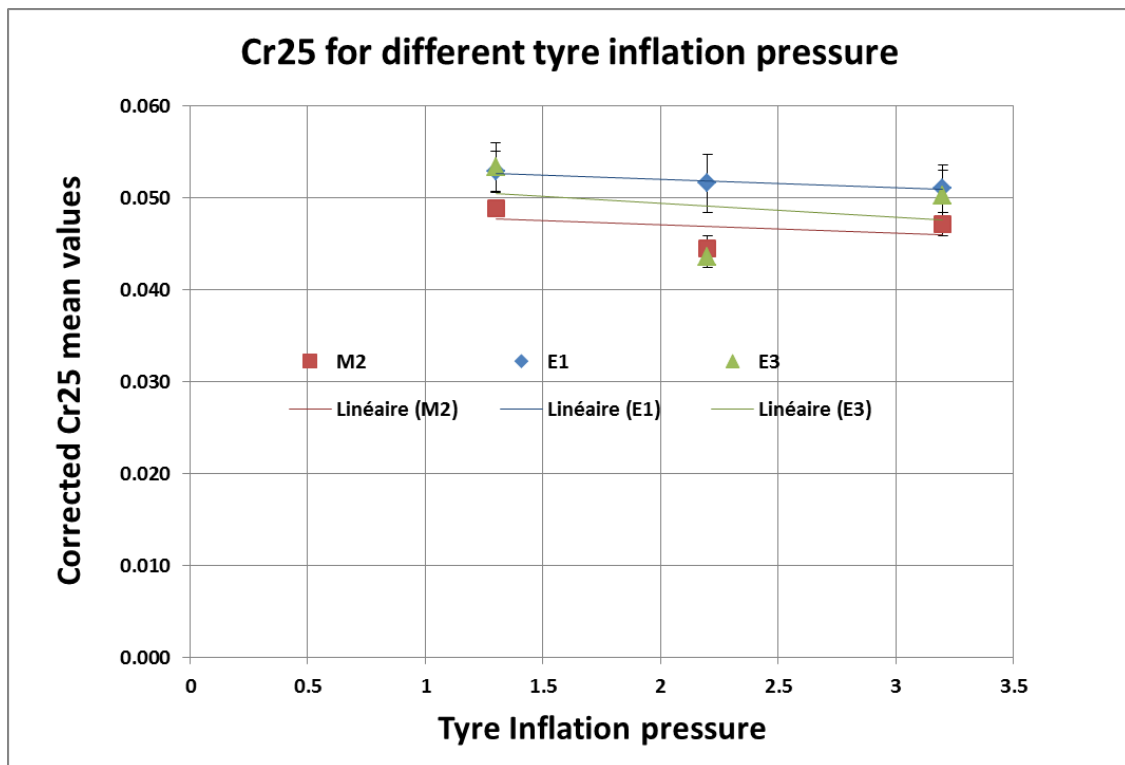


Figure 104 Corrected rolling resistance coefficient for different tyre inflation pressure on different test tracks

Mean value of Cr25 (coefficient of rolling resistance) is observed as 0.053 ± 0.003 for under-inflation and 0.051 ± 0.003 for over inflation. Since the difference in Cr25 is not significant therefore it is difficult to separate the rolling resistance coefficients for different inflation pressure. This is same for the different test tracks (see Figure 104). This may be due to the difference between pressure which isn't significant during rolling as tyre surface temperature is higher for the underinflated tyre and it can increase the tyre inflation pressure. Therefore it is important also to monitor the tyre pressure during the rolling which can play a significant role in tyre rolling resistance. In Figure 104 the Cr25 at 2.2 bars is slightly less than values at the 3.3 bars; this is mainly because the tests at 2.2bar were done at a different day, and it affects rolling resistance as the ambient temperature was lower on that day.

5.3.3.3. Influence of vehicle load on Crr

As shown in Table 17 load of the test vehicle is varied. Additional ~200 kg (as it was possible to add only two more passengers) is added to the test vehicle. The rolling resistance force and coefficient are calculated. The results are shown in Figure 105. It is shown in Figure 105 the Crr is lower for the loaded vehicle which is coherent with the literature results. The Mean value of Crr (coefficient of rolling resistance) for loaded is 0.039 ± 0.004 and 0.041 ± 0.003 for normal condition. Since the increased load is not significant on each tyre it is difficult to separate two cases.

Table 17 Parameter table tyre load

Parameters	Tyre inflation pressure	Load	Speed	Ambient air temperature	Test track
Varied		x			
Constant	x		x	x	x

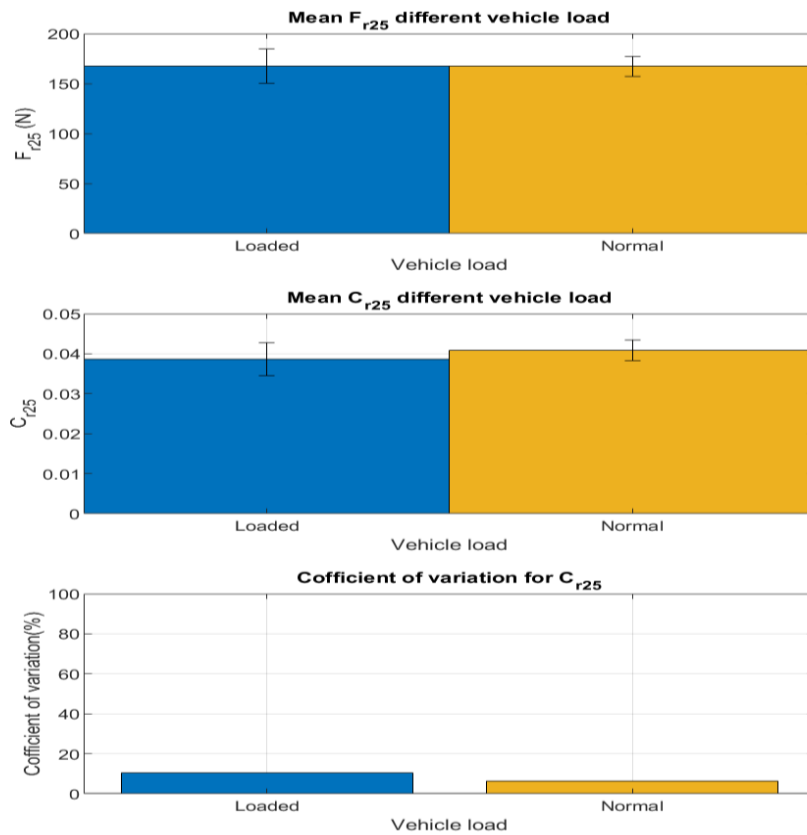


Figure 105 Bar plot of rolling resistance, tyre temperature and coefficient of variation

5.3.3.4. Influence of vehicle speed on C_{rr}

The test is done for two different speeds (50 km/h and 80 km/h) as shown in Table 13. These speeds are chosen as they are used in standard rolling resistance test. The results are shown in Figure 106 for different test tracks. It is concluded that speed has a direct impact on rolling resistance force. The mean value of corrected C_{r25} (coefficient of rolling resistance) is varied from 0.052 to 0.071 at 80 km/h and from 0.031 to 0.049 at 50 km/h. It is also remarked that the temperature of the tyre surface is also higher for the high-speed condition which is mainly due to an increase in energy dissipation and increase in the number of cycles of deformation. The higher magnitude of C_{r25} for 80 km/h is also influenced by the aerodynamic force of the tyre as it is directly impacting rolling resistance.

Table 18 Parameter table speed

Parameters	Tyre pressure	inflation	Load	Speed	Ambient air temperature	Test track
Varied				X		
Constant		X	X		X	X

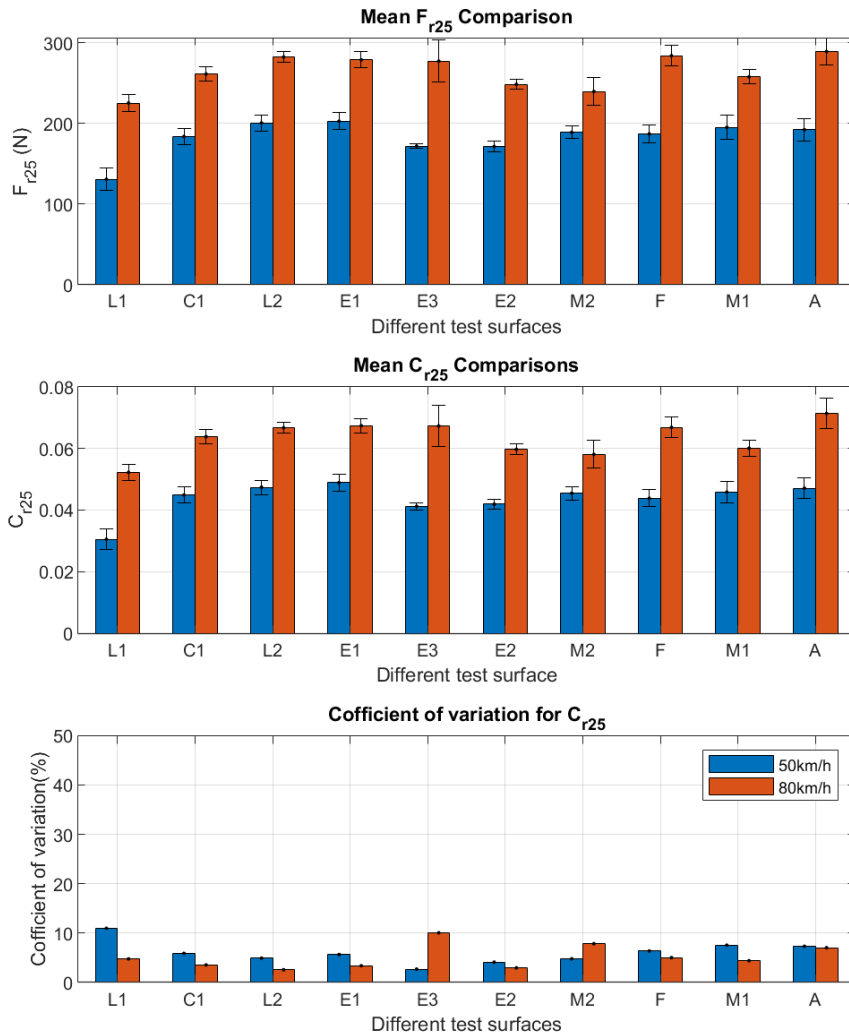


Figure 106 Bar plot of tyre rolling resistance force, coefficient and tyre temperature for different surfaces in increasing order of MPD

The rolling resistance force and coefficient are calculated for different speeds on different road surfaces. The characteristics of road surfaces are given in Table 10 in increasing order of MPD (i.e; macrotexture). It is seen from Figure 106 that C_{rr} has the same tendency as we change the surface. In Figure 107 the trend is shown for two different speeds and it is coherent with the results in the literature [36].

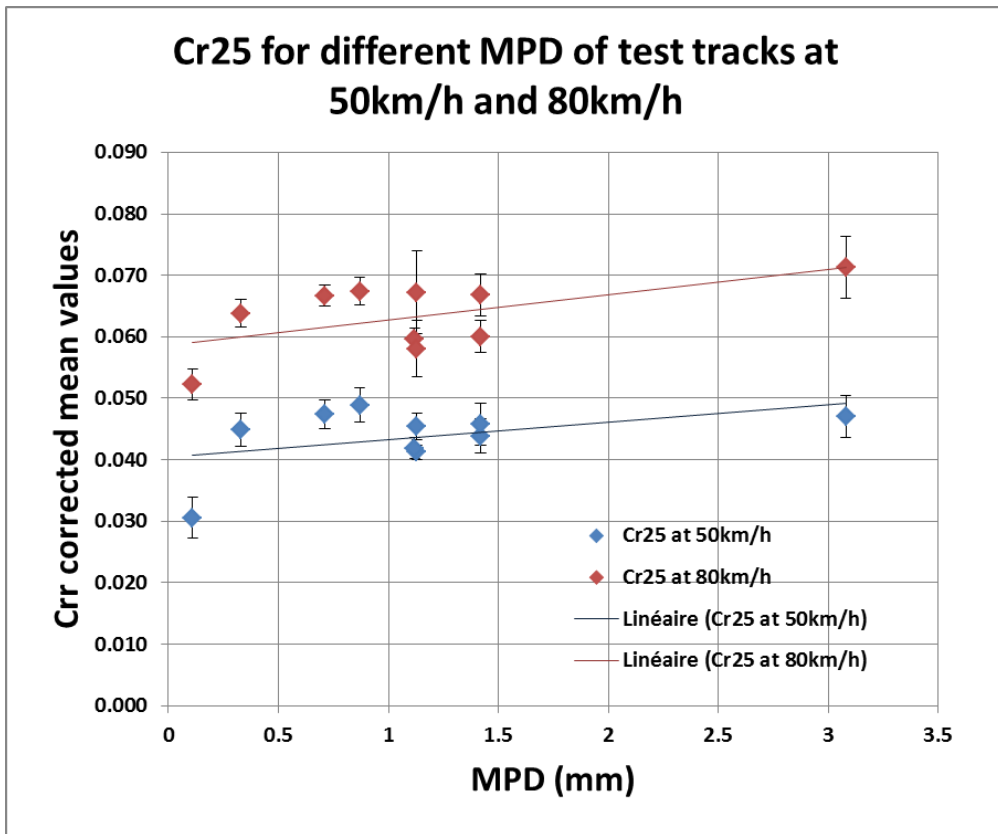


Figure 107 Corrected Crr trend for different surfaces at 50 km/h and 80 km/h

5.3.3.5. Influence of road surface roughness on Crr

The test is done for different macro roughness surfaces and international roughness index as given in Table 10. L1 is a smooth surface whereas AP is a very rough surface. In this section road surface impact on rolling resistance is discussed for different vehicle speeds at 25°C (corrected temperature). The other parameters were kept constant as shown in Table 19.

Table 19 Parameter table different roughness surface

Parameters	Tyre inflation pressure	Load	Speed	Ambient air temperature	Test track
Varied					x
Constant	x	x	x	x	

The results are presented separately for two different speeds and the corrected rolling resistance coefficient is calculated with the help of equation (197) at 25°C temperature.

❖ Speed at 50 km/h

The results for different test track at 50 km/h are shown in Figure 108. The rolling resistance coefficient (Crr) of L1 is lowest and A is highest in all the surfaces although there are some outliers such as surface E1 which is due to the age of the test track (more than 20 years). The coefficient of variation given in Figure 108 allows us to have confidence in the conclusion.

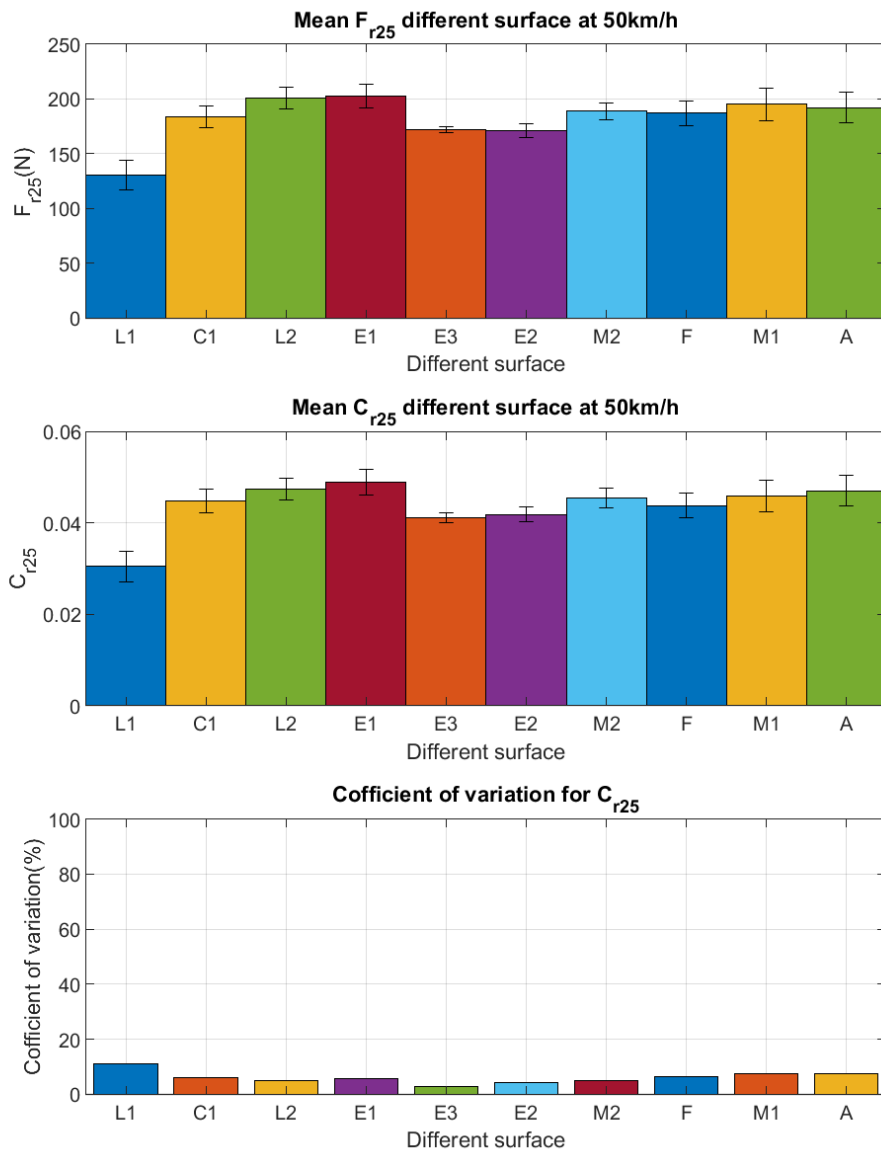


Figure 108 Bar plot of rolling resistance, tyre temperature and coefficient of variation

In Figure 109 and Figure 110 the trend with respect to different MPD and IRI is given. This trend is consistent with literature results [36].

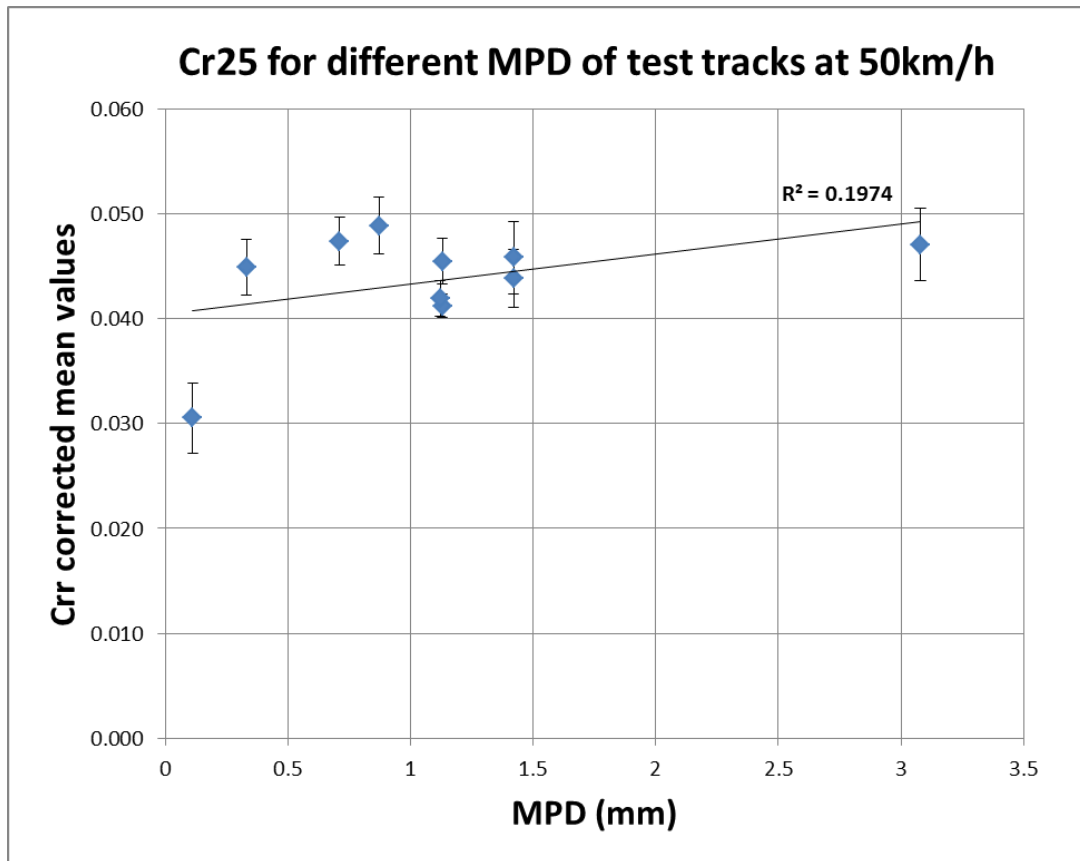


Figure 109 Crr trend for different surfaces at 50 km/h for different MPD values

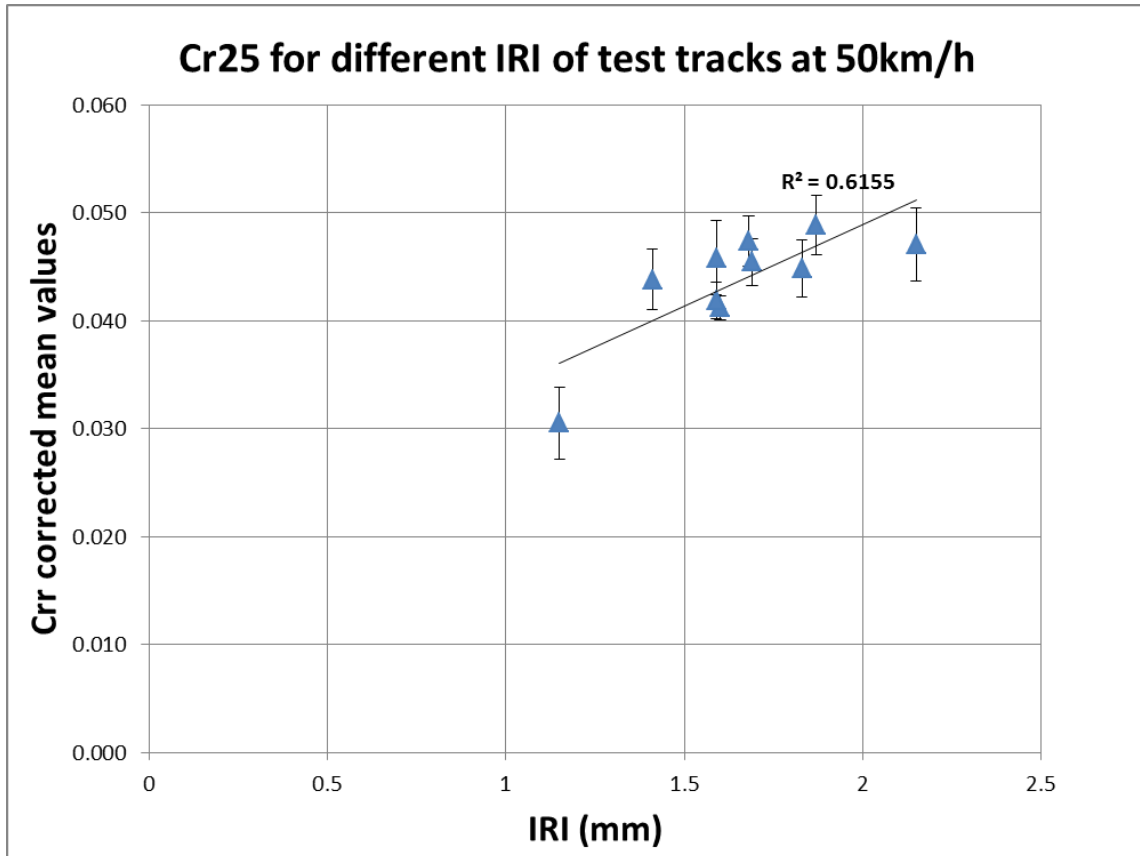


Figure 110 Crr trend for different surfaces at 50 km/h for different IRI values

❖ Speed at 80 km/h

The results for different test tracks at 80 km/h are shown in Figure 111. In Figure 112 and Figure 113 the trend with respect to different MPD and IRI is given. It has also shown the same trend as at 50 km/h. The weak linear regression MPD is observed at both speed (see Figure 109 and Figure 112) and similar weak linear regression is also seen in the literature [36]. This is due to the fact that there are other texture scales involved in the rolling resistance force generation. As the texture is composed of a range of scales each of which contributes differently to the generation of forces at the tyre-road interface shown in [190]. An approach of multi-scale analysis of road roughness can improve this regression.

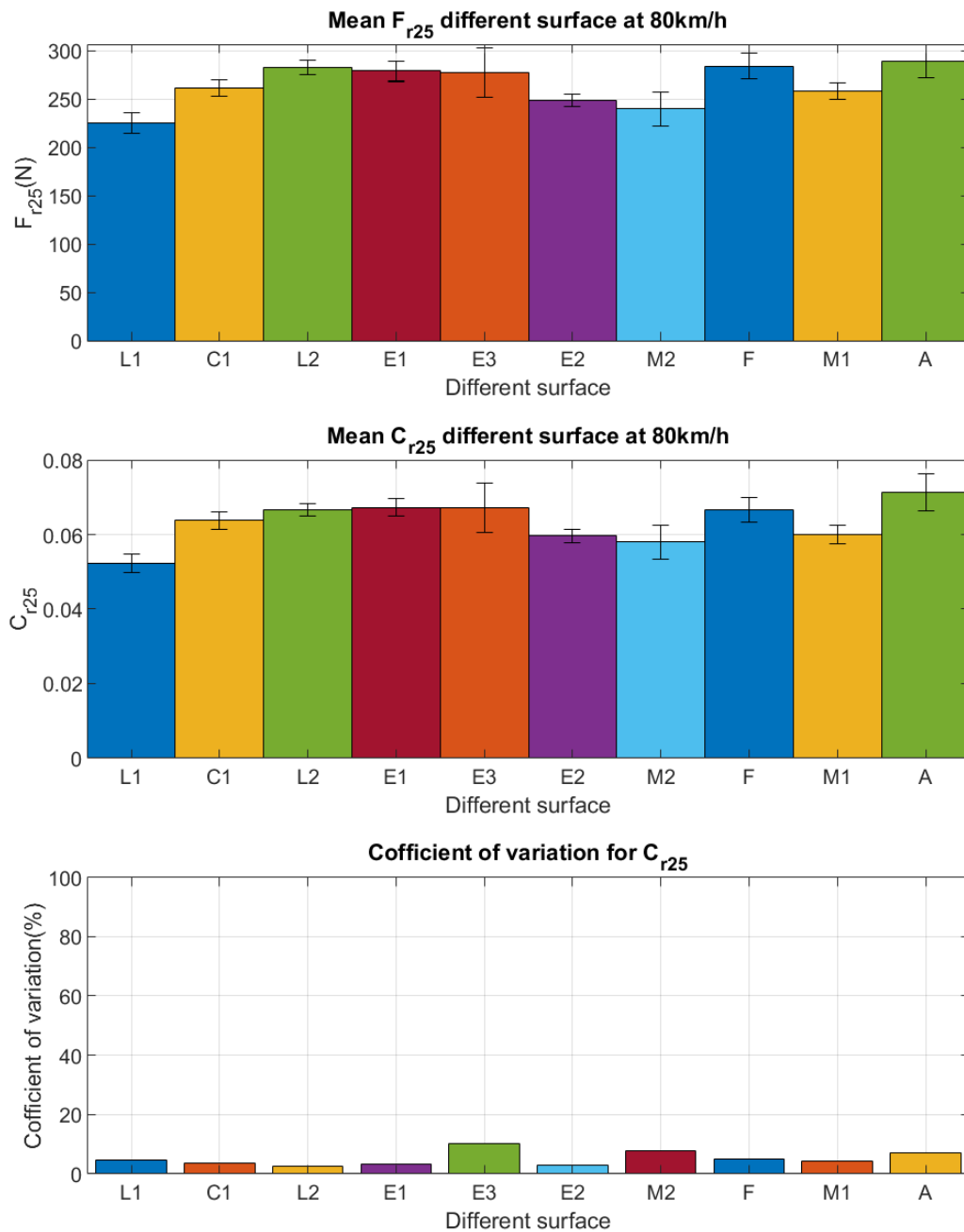


Figure 111 Bar plot of rolling resistance, tyre temperature and coefficient of variation

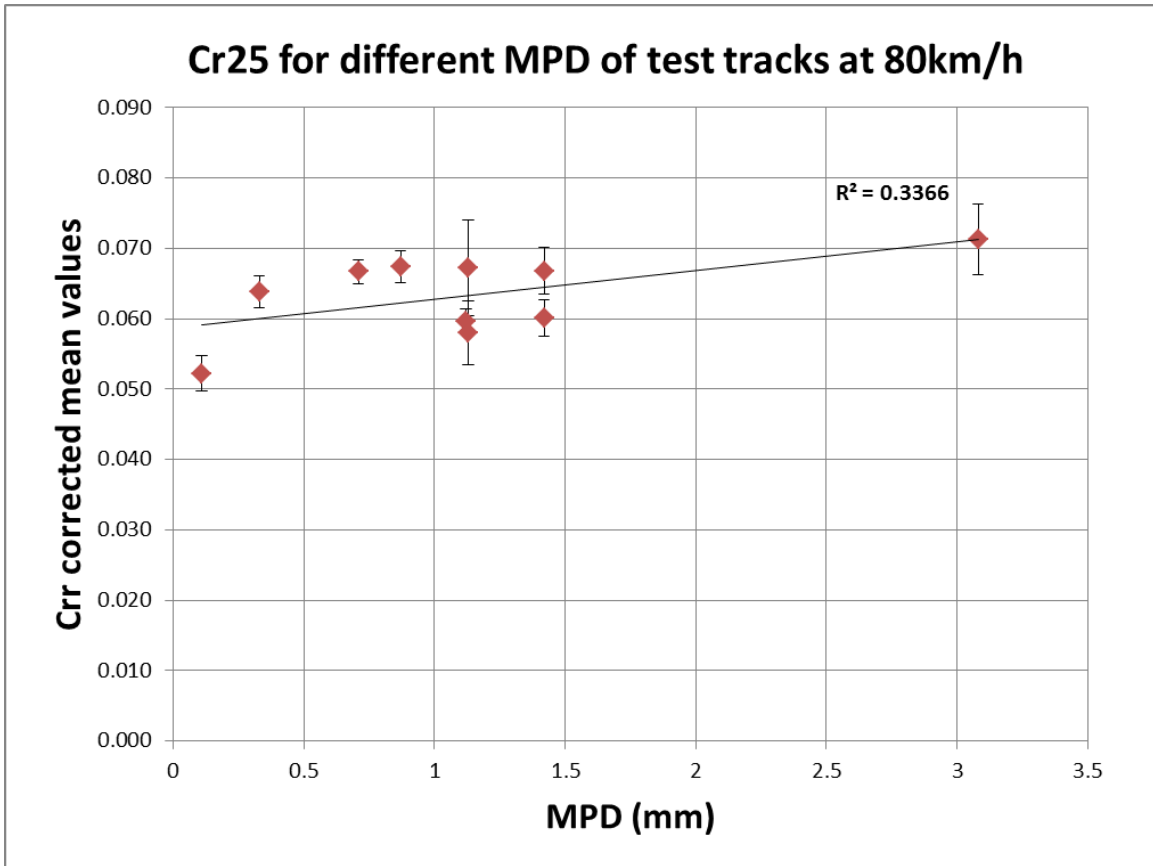


Figure 112 Crr trend for different surfaces at 80 km/h for different MPD values

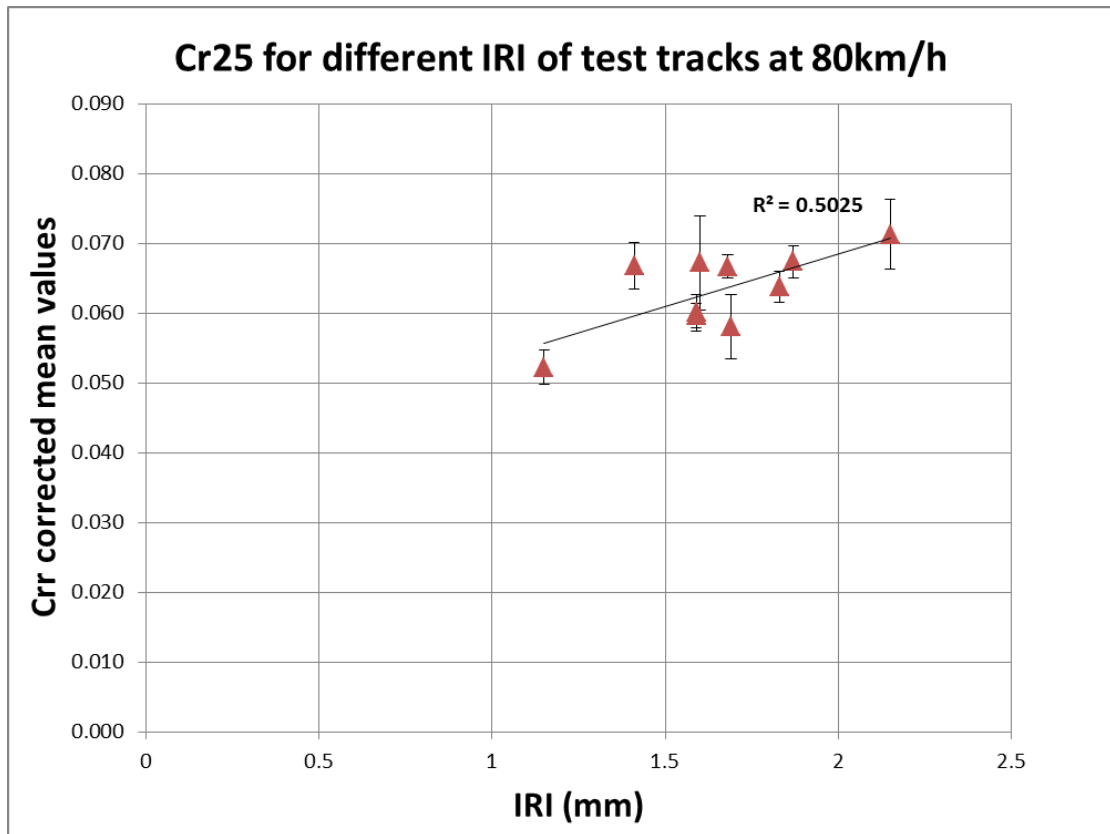


Figure 113 Crr trend for different surfaces at 80 km/h for different IRI values

5.3.4. Validation of reference rolling resistance

The calculation of rolling resistance and the study of the impact of influencing parameters was done in this section. The above results are consistent with the results of the literature [36] (Mainly ROSANE project) presented in chapter 1. The magnitudes of the values given above are the corrected mean values of rolling resistance with standard deviation. It is important to keep in mind that experimental data contain measurement noise and the small difference is not significant to separate the results and make a concrete conclusion. The influence of tyre inflation pressure and load is difficult to assess as it is difficult to separate the values. The influence of speed is visible although it is still necessary to consider the role played by aerodynamic force at wheel level. The ambient temperature results are also in accordance with literature [36]. The expected results are also obtained for higher speed where the change is not identified as significant. The trend related to the impact of road roughness is consistent with literature results except the values coming for the E1 test track. Initial inspection shows that ageing of test track put E1 as outliers but further analysis is needed to identify the exact reason for this outlier. This validates that the selected influencing parameters of rolling resistance. The magnitude of C_{rr} for different MPD is also compared with the C_{rr} in ROSANE project. The values obtained here are smaller than the values obtained in ROSANE project by the factor of 10. This is mainly because the values measured in ROSANE project are on different tyre, load, pressure and on the dedicated trailer which minimises parasitic losses.

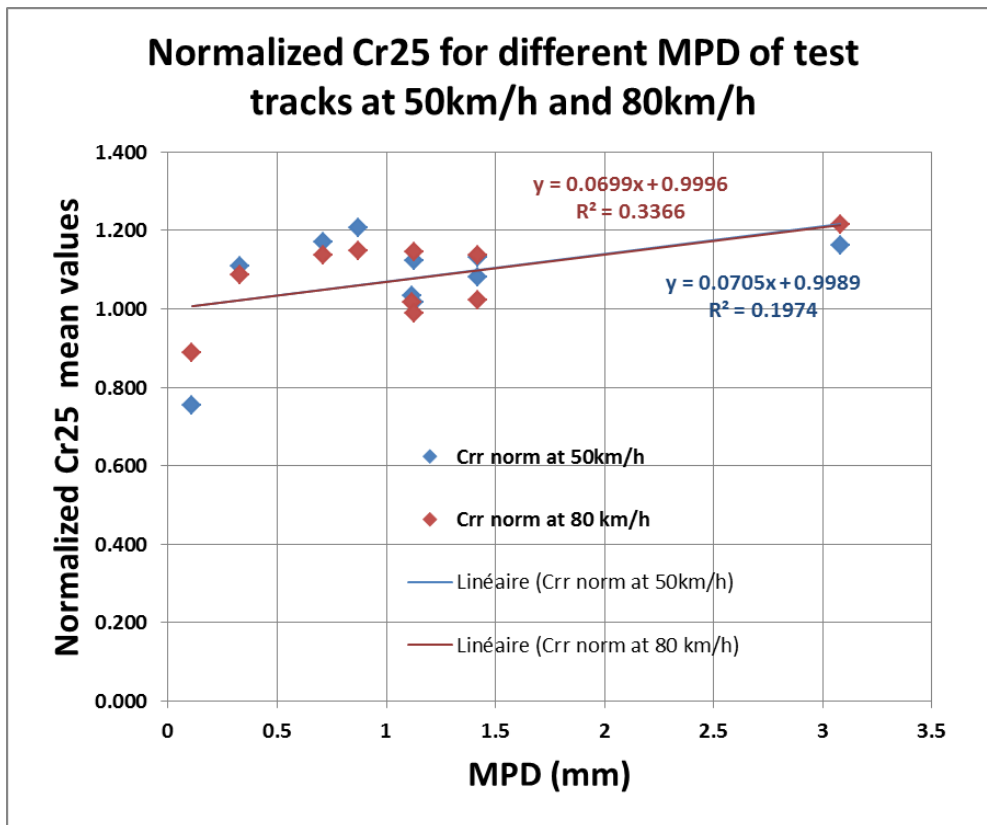


Figure 114 Normalized C_{rr} trend for different test surfaces

Therefore to avoid the influence of these factors the normalised values of C_{rr} is calculated to assess the effect of MPD on the trends with literature. The trends on different surfaces for different speeds are compared with the trends given by ROSANE project. In Figure 114 the normalized C_{rr} evolution is presented. The trend results from the literature are presented in Figure 115. These trends from

experiment results are coherent with the trends from literature [36]. It validates our assumption and method to calculate the rolling resistance.

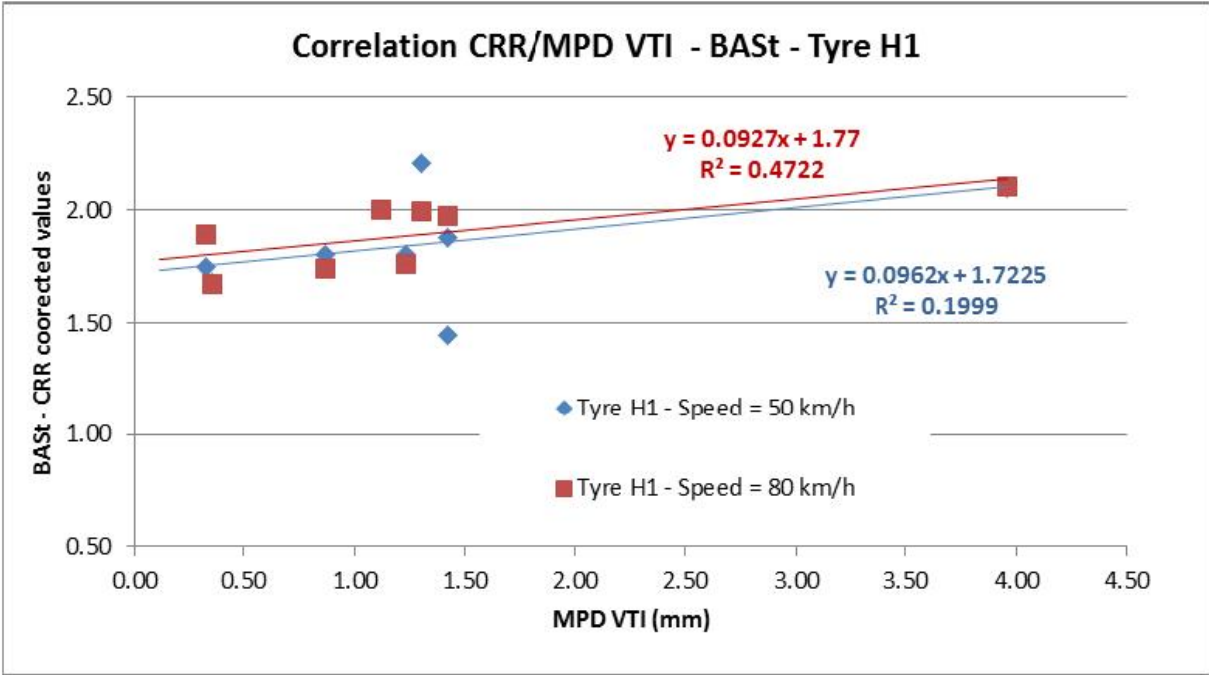


Figure 115 Rolling resistance coefficient as a function of MPD from [36]

5.3.5. Conclusion

In this section, the post-processing and analysis of DoE are done. The objectives of the experiments were to identify the method to calculate the rolling resistance coefficient, to study the influence of several parameters and compare the results with the trends seen in the literature. The calculated rolling resistance force will be used as the reference while comparing it with an estimated value in the next chapter. The syntheses of all the influencing parameters are presented below.

Parameters	Tyre Inflation pressure	Vehicle load	Vehicle speed	Ambient air temperature	Road surface characteristics
Change in parameters	↗	↗	↗	↗	↗
Crr trends in literature	↘	↗	↗	↘	↗
Crr trends in DoE results	→	→	↗	↘	↗

Figure 116 Syntheses of comparison of DoE results and literature results

The trend of the influencing parameters shows similar trends as studies are done in literature except for the tyre inflation pressure and load. This is due to the fact that the range of variation load and inflation pressure was too small to entail significant effect on rolling resistance in our experiments. The small tool for the extraction and filtering of data is also developed during this post-processing. The detailed study on tyre temperature variation will be done in the next section.

5.4. Experimental investigation of the variation of tyre surface temperature

In this section, the experimental investigation of the variation of tyre surface temperature is presented. There are two objectives to this study. The first objective is to evaluate tyre surface temperature variation with respect to the position of the sensor on the vehicle as well as on the tyre itself. This will conclude on circumferential and lateral direction variation of tyre surface temperature on the tyre. The second objective is to identify the relationship between vehicle speed and tyre surface temperature. This is important to identify the singularly perturbed nature of our systems. The tyre surface temperature variation with respect to vehicle manoeuvres and pavement temperature is also presented.

5.4.1. Tyre surface temperature variation in different conditions

In this section, the tyre surface temperature evolution is shown for various sensors installed on the vehicle (see Figure 117). The analysis is done for the DoE presented in Table 13.

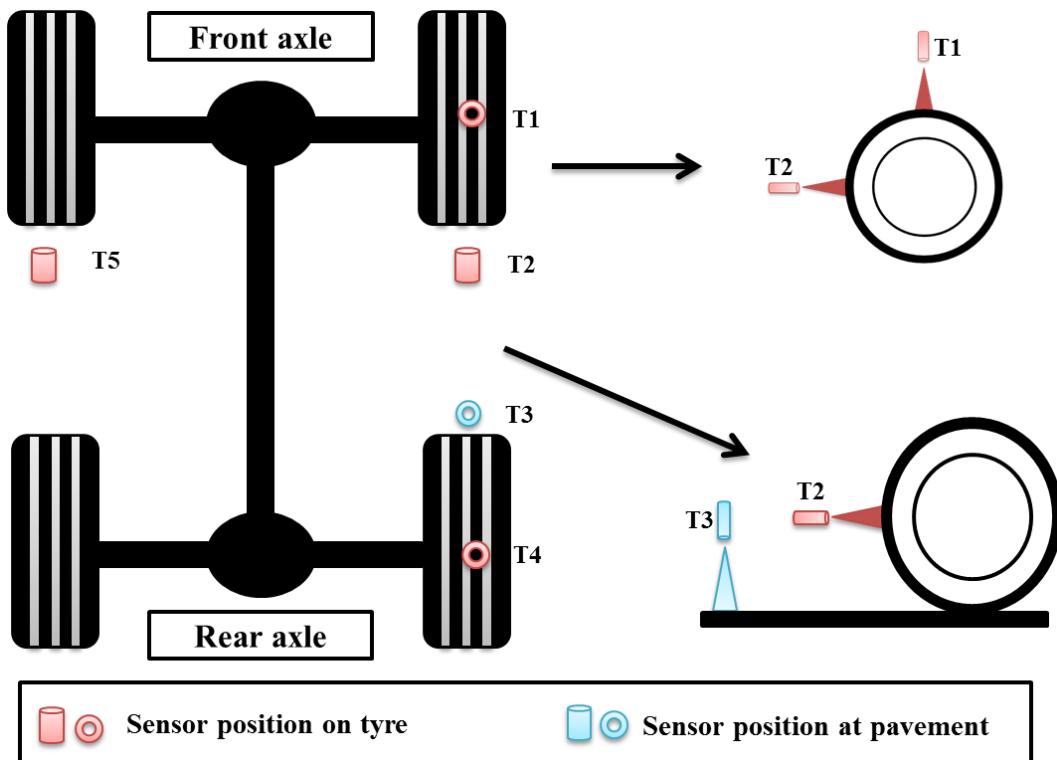


Figure 117 Tyre temperature infrared sensor installed position on the vehicle

In Figure 118 the main comparison scenarios between the sensors are shown. The temperature difference between T1 and T2 is circumferential variation. The temperature difference between T2 and T5 will permit to confirm the hypotheses that the temperature is the same on a given axle. The T2 and T3 difference will allow monitoring the temperature difference between pavement and tyre.

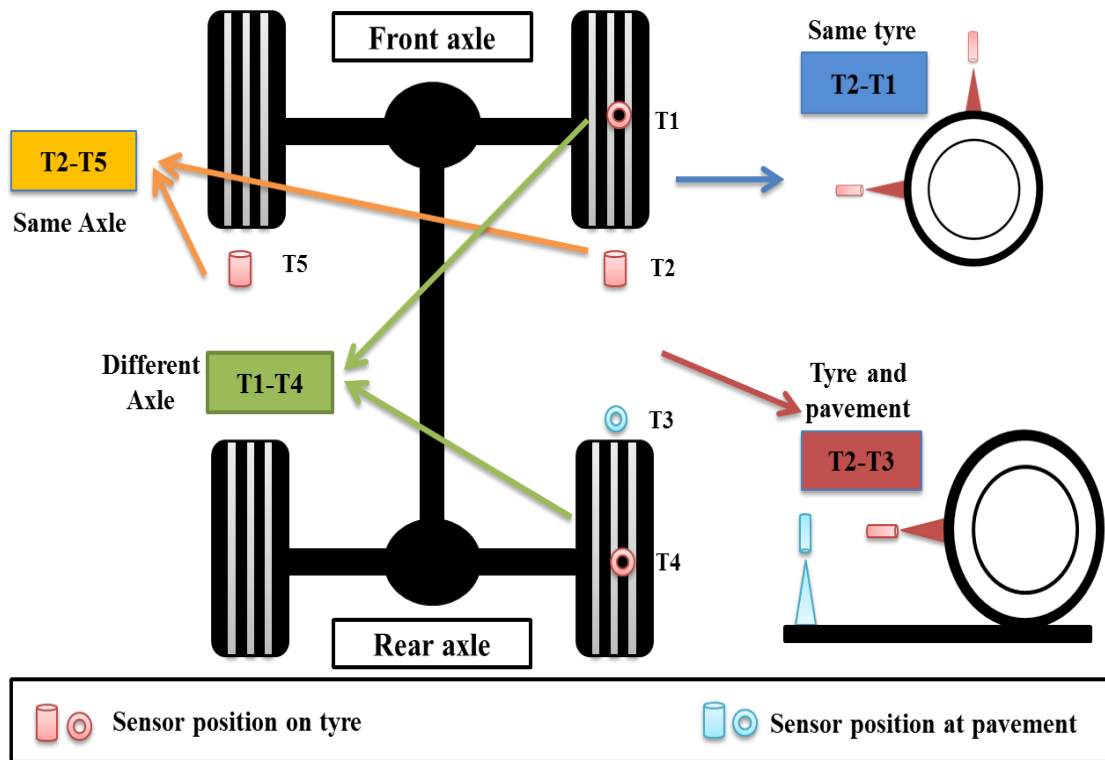


Figure 118 Description of sensor comparison between positions

5.4.1.1. Variation at a constant speed

In this test, the vehicle is moving in a straight line at a constant velocity. The distributions of tyre surface temperature for two different speeds during the test are presented in Figure 119 and Figure 120. The distribution is concentrated for 50 km/h whereas it is dispersed in two places for 80 km/h. This is mainly due to the ambient temperature. During the 80 km/h tests, the ambient temperature is appeared more dispersed between 16°C and 25°C whereas it was stable around 25°C for 50 km/h. Therefore the mean values are compared with the standard deviation to understand the evolution of temperature at two speeds (see Figure 121). The tyre surface temperature is higher for 80 km/h by 5°C which is mainly due to faster dissipation of energy from deformation. It is also seen that the temperature of the pavement is higher at 80 km/h. This shows that there is more transfer of heat to the pavement through convection for higher speeds.

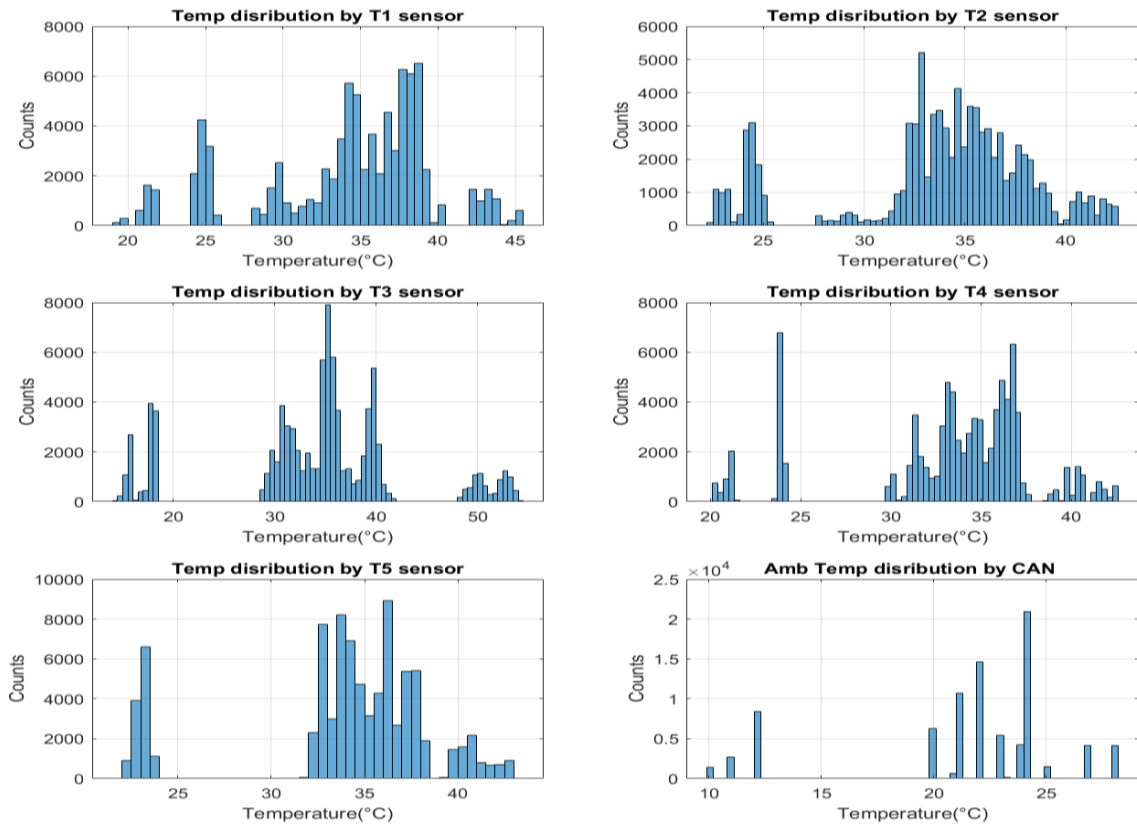


Figure 119 Distribution of tyre surface temperature at 50 km/h

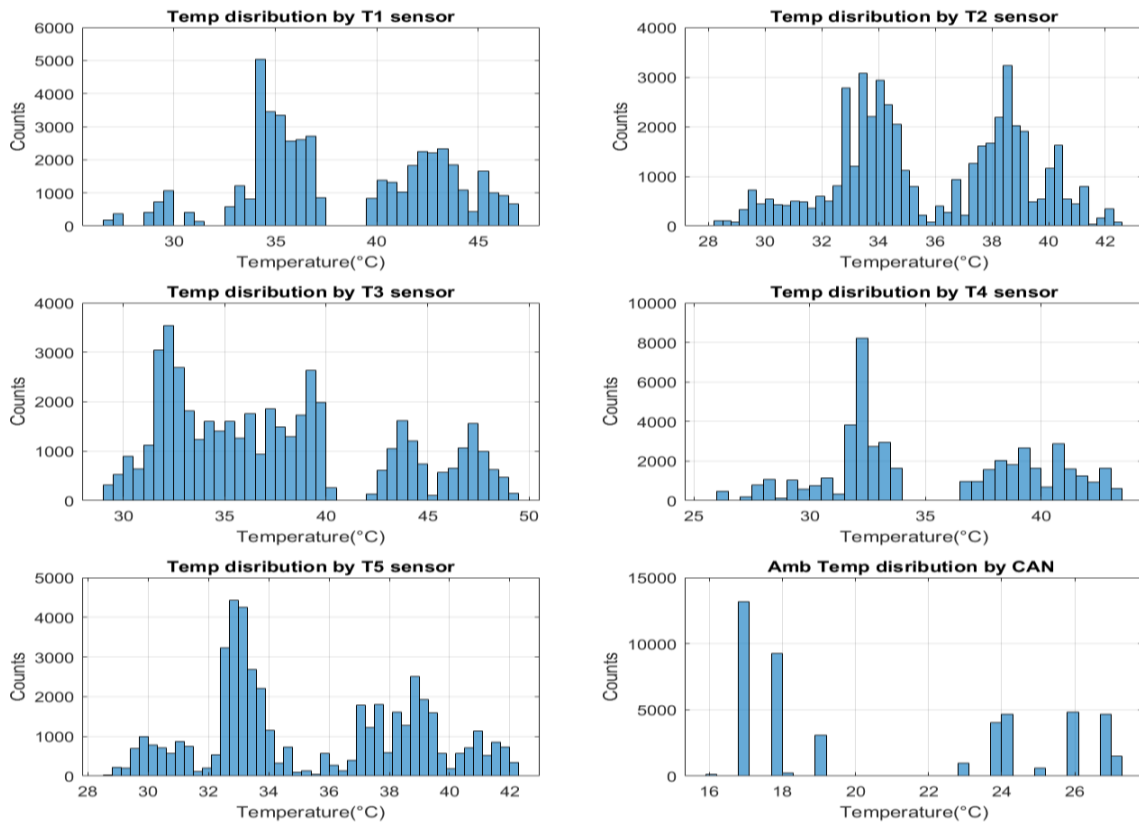


Figure 120 Distribution of tyre surface temperature at 80 km/h

The temperature difference between the sensors is given in Figure 122 and Figure 123. When the vehicle is travelling at 50 km/h in a straight line, the differences are constant and under the threshold of 1°C which is less than the accuracy of the sensor whereas for the vehicle travelling at 80km/h in a straight line, the temperature measured by T1 sensor shows higher temperature than T2. It is also concluded that the temperature of pavement was lower than the tyre surface by 2°C for higher speed.

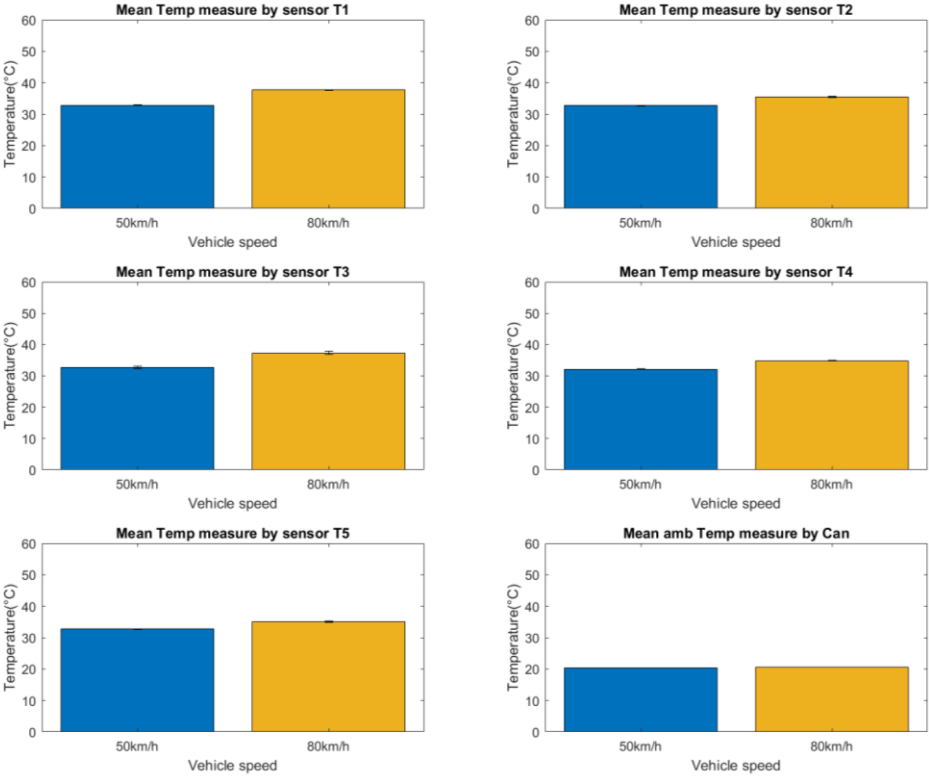


Figure 121 Mean tyre surface temperature for two different speeds

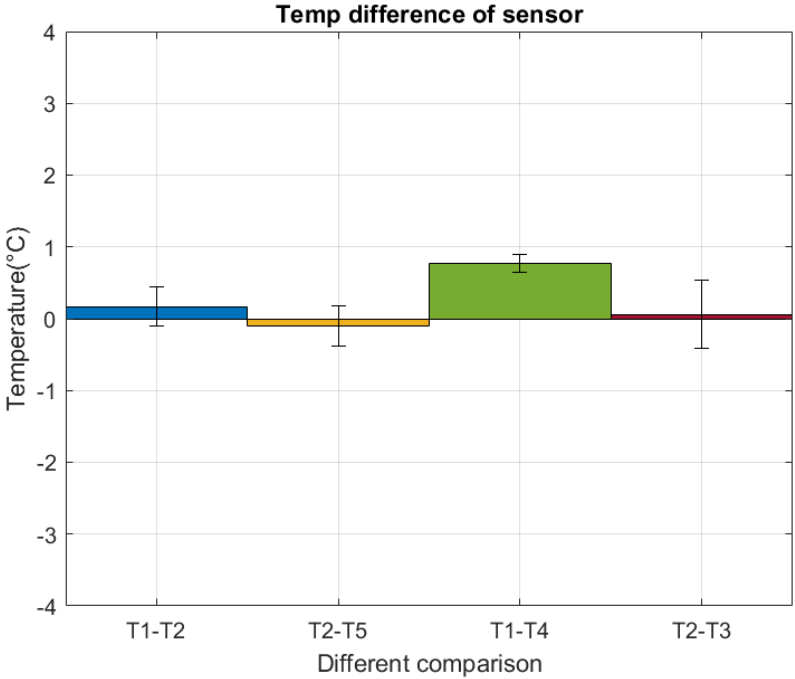


Figure 122 Mean temperature difference for different sensor positions at 50 km/h

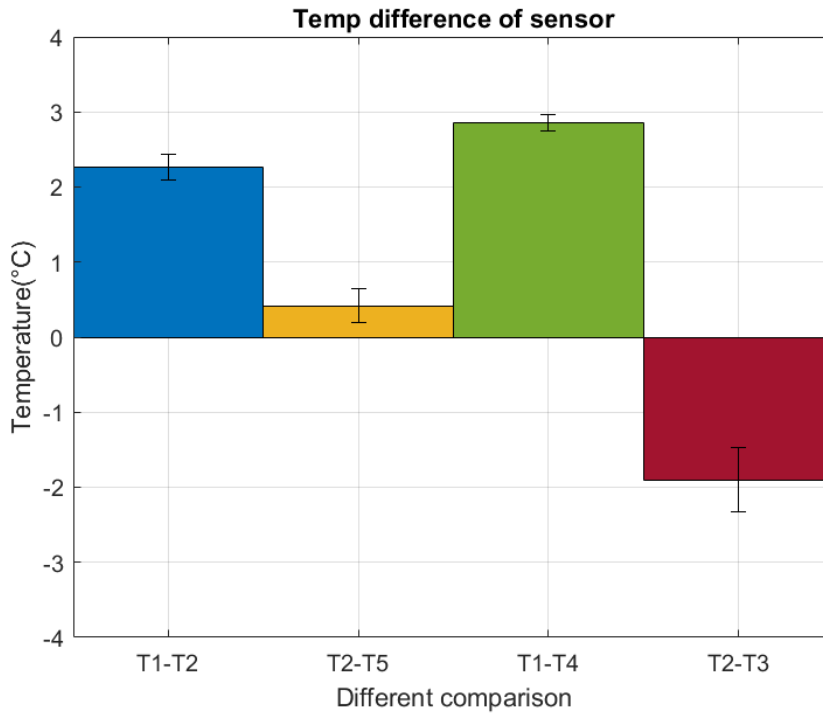


Figure 123 Mean temperature difference for different sensor positions at 80 km/h

5.4.1.2. Variation at different ambient temperature

The tests were done at two different ambient temperatures and the results are shown in Figure 124 and Figure 125.

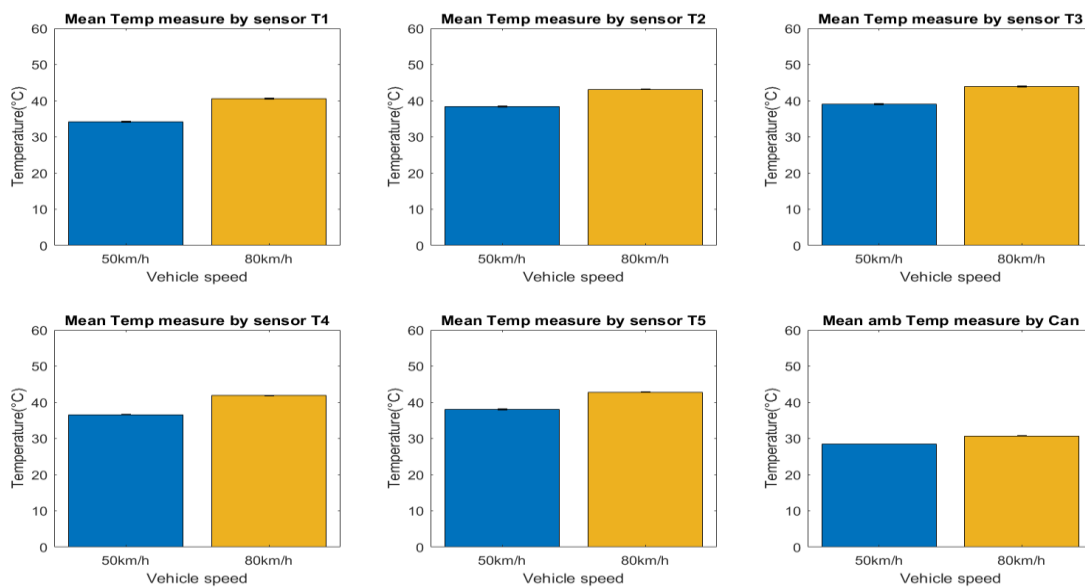


Figure 124 Impact of variation speed on tyre surface temperature at 20°C ambient air temperature

It can be concluded that at low ambient air temperature vehicle at 80 km/h exhibited higher tyre surface temperature when it is compared to vehicle moving at 50 km/h. A difference of 10°C is seen

between the two speeds, whereas at higher ambient air temperature (around 40°C), a significant increase is seen in tyre surface temperature when it is compared to low ambient air temperature. This is due to the less cooling of tyre surface temperature due to hot ambient air and pavement. On the contrary, there is no significant difference in tyre surface temperature for both speeds; it is due to the saturation of temperature achieved at a higher speed. During these experiments sensor T3 was faced toward the tyre sculpture so we couldn't measure the pavement temperature.

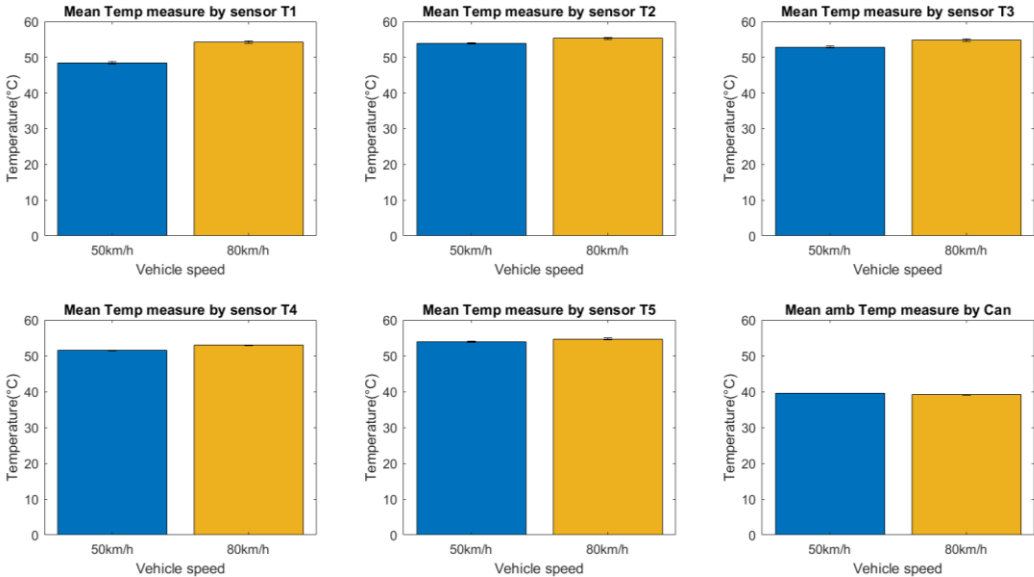


Figure 125 Impact of variation speed on tyre surface temperature at 40°C ambient air temperature

5.4.1.3. Variation on different test surfaces

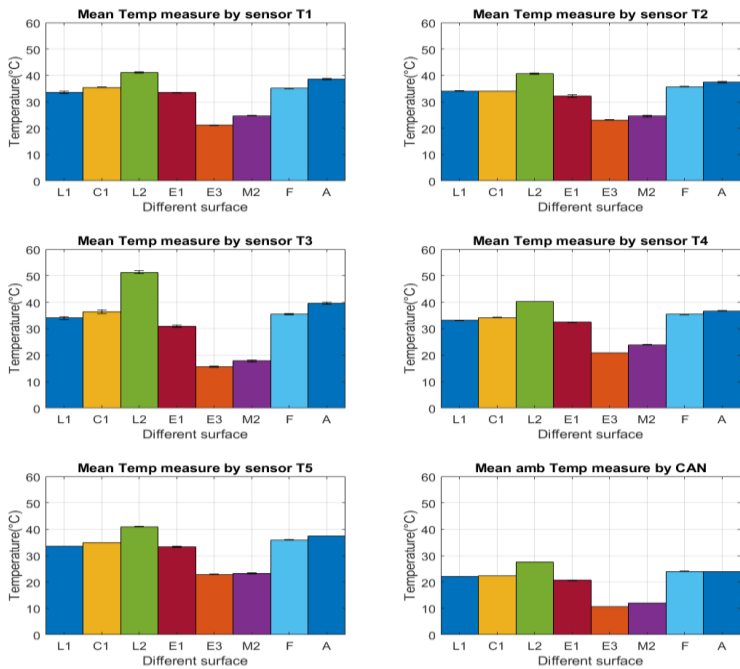


Figure 126 Mean tyre surface temperature for different surfaces as 50 km/h

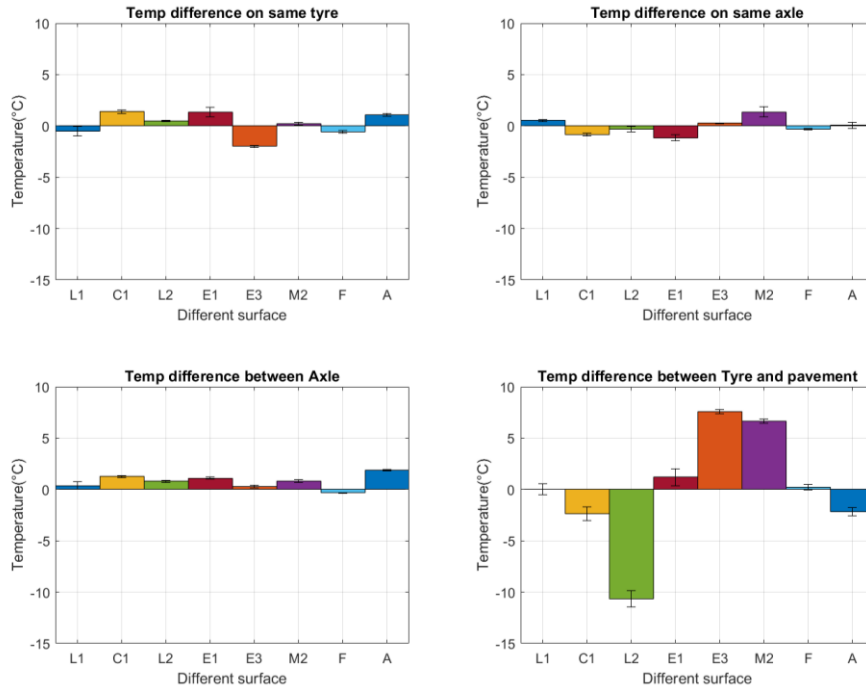


Figure 127 Temperature difference for different sensor positions for different test tracks at 50 km/h

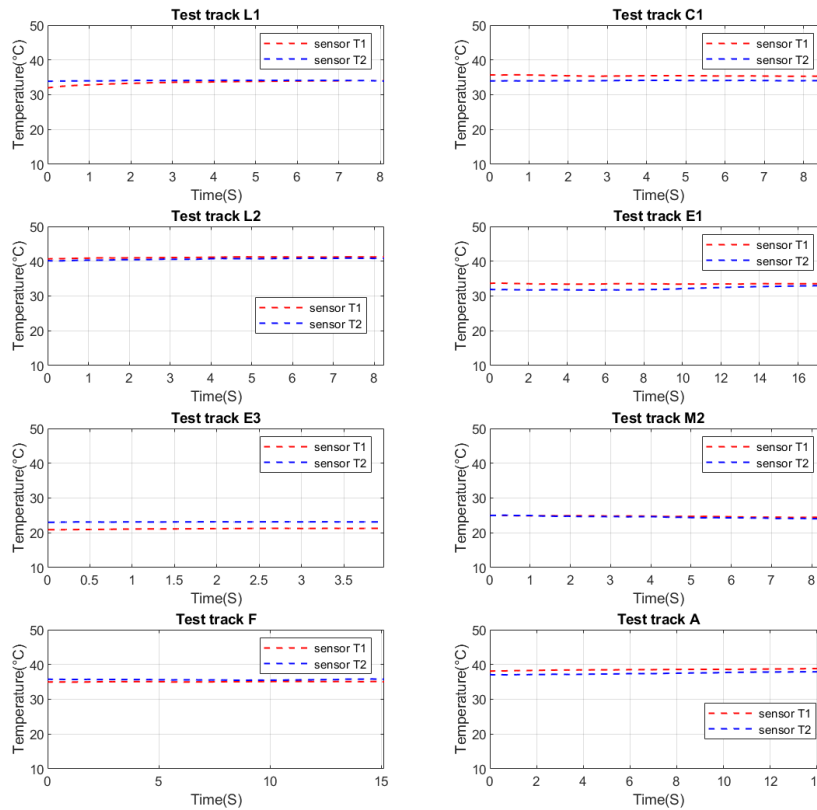


Figure 128 Circumferential tyre surface temperature variation for different test tracks at 50km/h

In this section, the tyre surface temperature variations on different test tracks are analysed (see Figure 126 and Figure 129). The results are presented for two different speeds. The tyre surface temperature for different test tracks is directly influenced by the ambient temperature. The ambient temperature is varying in the range of 10°C to 25°C. Therefore, the significant impact of different macro roughness is

difficult to assess. In case of the same ambient temperature of test track F and A, the tyre temperature increases slightly on high roughness surfaces. The pavement temperature is also influenced by the ambient temperature and its exposition directly to the sunlight; therefore some test surfaces temperature is higher than the tyre surface temperature.

The comparison between different sensor measurements at 50 km/h is also done and the results are given in Figure 127 and Figure 128. The temperature difference between pavement and tyre surface varies up to 11°C (test track L2). This is mainly due to the higher ambient temperature. The circumferential temperature variation of the tyre during the test is also analysed (see Figure 128). The temperature difference between T1 and T2 is less than 2°C. Therefore it is difficult to make any conclusion on circumferential variation at 50 km/h.

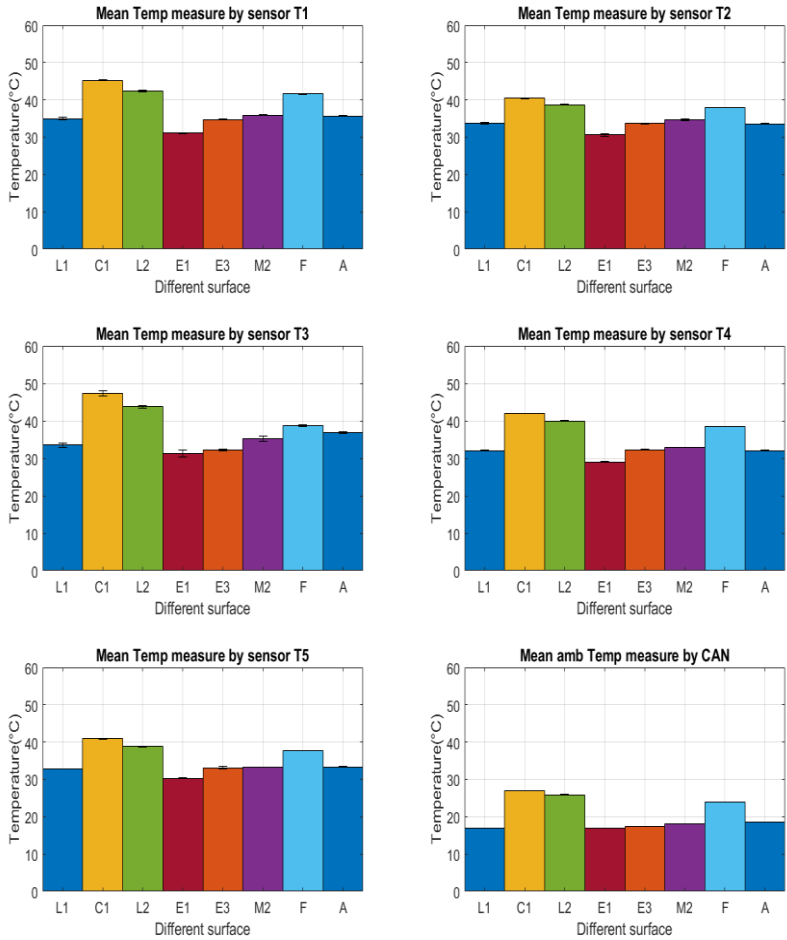


Figure 129 Mean tyre surface temperature for different surfaces as 80 km/h

The tyre surface temperature at 80 km/h is higher than the tyre surface temperature at 50 km/h of all the test surfaces (Figure 130). The tyre surface temperature at 80 km/h is also influenced by the ambient temperature and cooling due to air current. At the same ambient temperature for test track (E, E3, M2, A), the impact of road roughness is also seen on the tyre surface temperature, the tyre surface temperature increasing with the increase in the road roughness. The circumferential temperature variation is presented in Figure 131. The temperature measured by T1 is greater than T2 by 1°C to 5°C on different test tracks; it means tyre surface temperature is higher near the engine as compared to near contact area. This is contrary to literature but after investigation, it is found that the T2 is measuring

the temperature in tyre groove whereas T1 is measuring on the tyre surface. So it is difficult to conclude on the circumferential temperature variation.

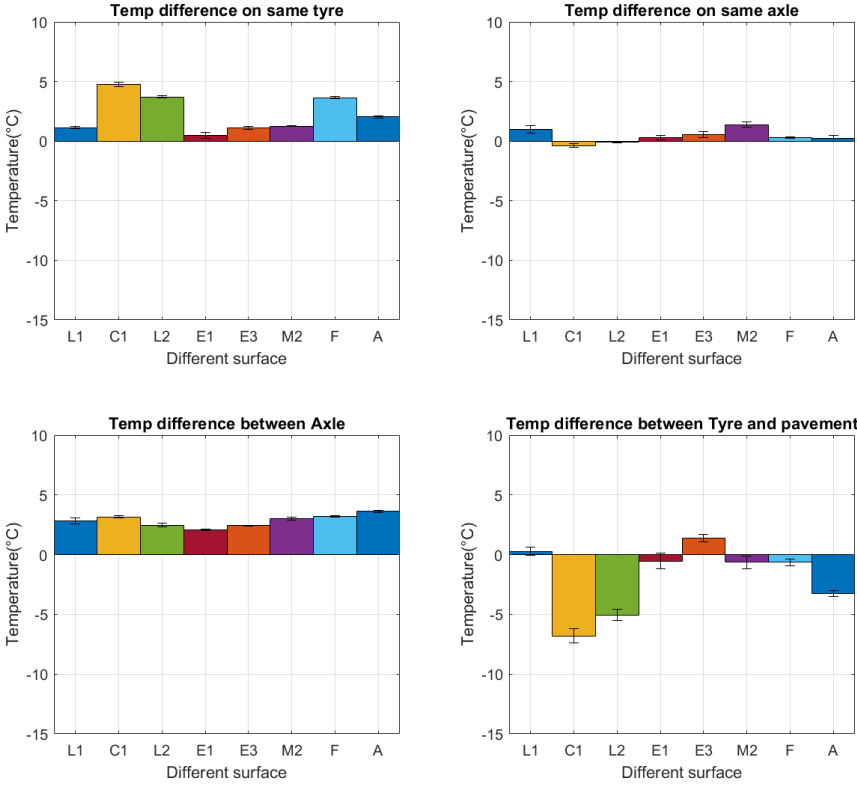


Figure 130 Temperature difference for different sensor positions for different test tracks at 80 km/h

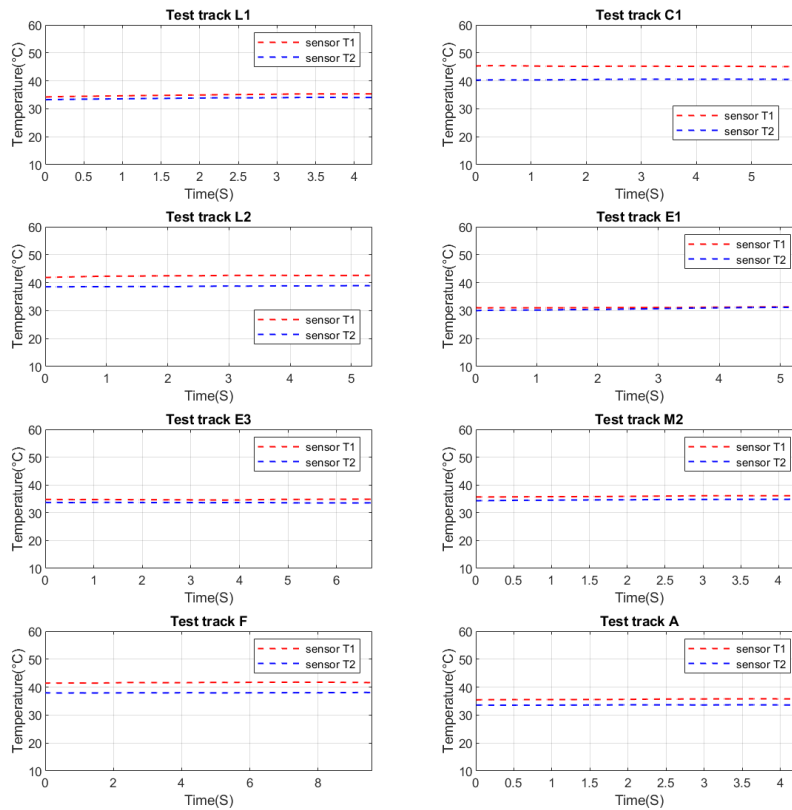


Figure 131 Circumferential tyre surface temperature variation for different test tracks at 80 km/h

5.4.1.4. Variation at different vehicle manoeuvres

The tyre surface temperature variations for three different manoeuvres (lane change according to ISO standard, turns, acceleration and braking) are analysed. During these manoeuvres either the heat is generated or tyre is exposed to cool down.

i. Lane change at 60 km/h

The variation of tyre surface temperature is shown in Figure 132. It can be seen an increase and decrease in the tyre temperature during the lane change manoeuvres. The tyre surface temperature varies between 39°C and 44°C. The pavement temperature is higher than the tyre surface, it is due to the higher ambient temperature or the fact that the test surface was exposed directly to the sunlight. The tyre surface temperature increases up to 5 °C during manoeuvres. The variations are shown in Figure 133 conclude that the circumferential variation goes up to 5°C, the temperature variation on the same axle is less than 1°C whereas on different axle goes up to 5°C. The temperature of pavement is greater than 10°C of tyre surface temperature. Therefore it is important to monitor the tyre surface temperature during manoeuvres.

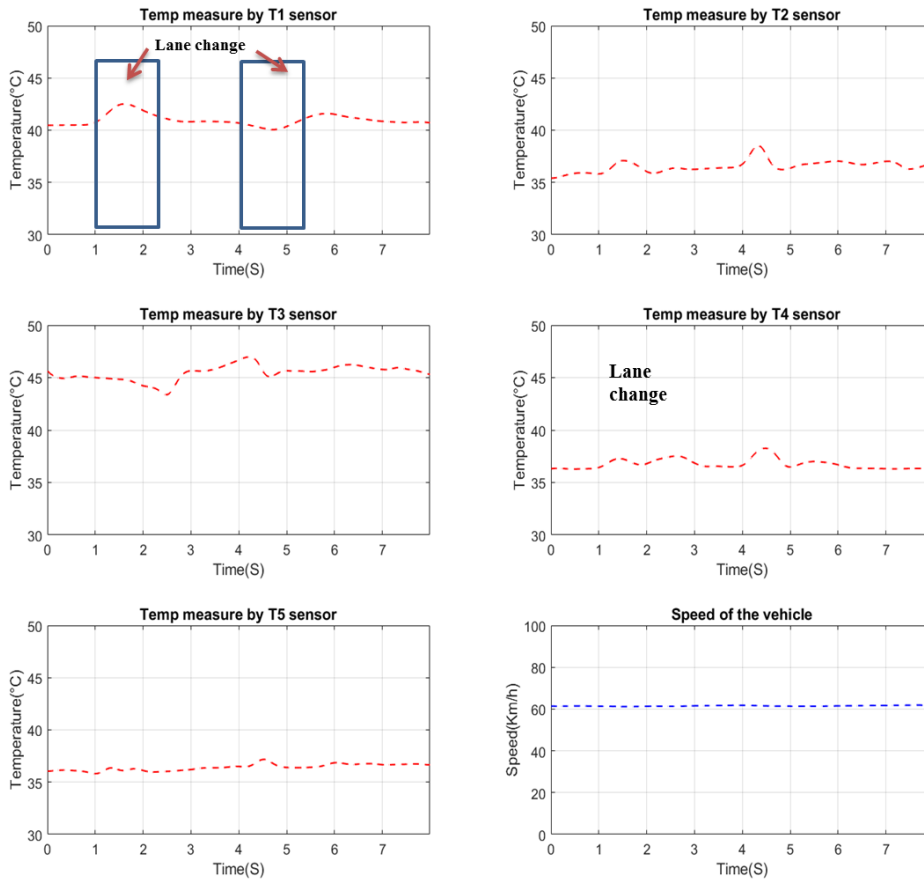


Figure 132 Variation of mean tyre surface temperature for lane change at 60km/h

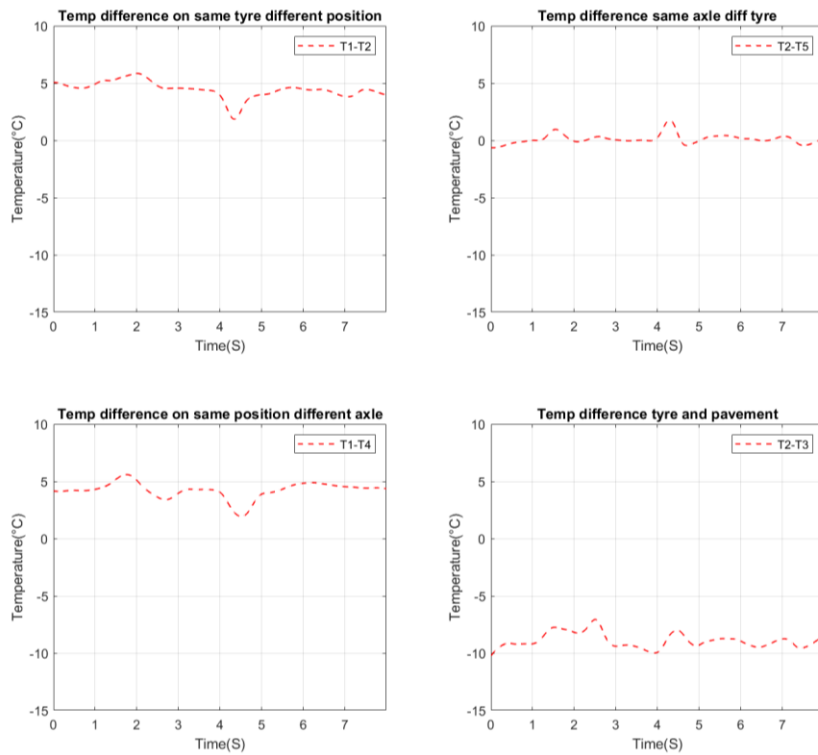


Figure 133 Temperature difference for different sensor positions for lane change at 60 km/h

ii. Acceleration and braking

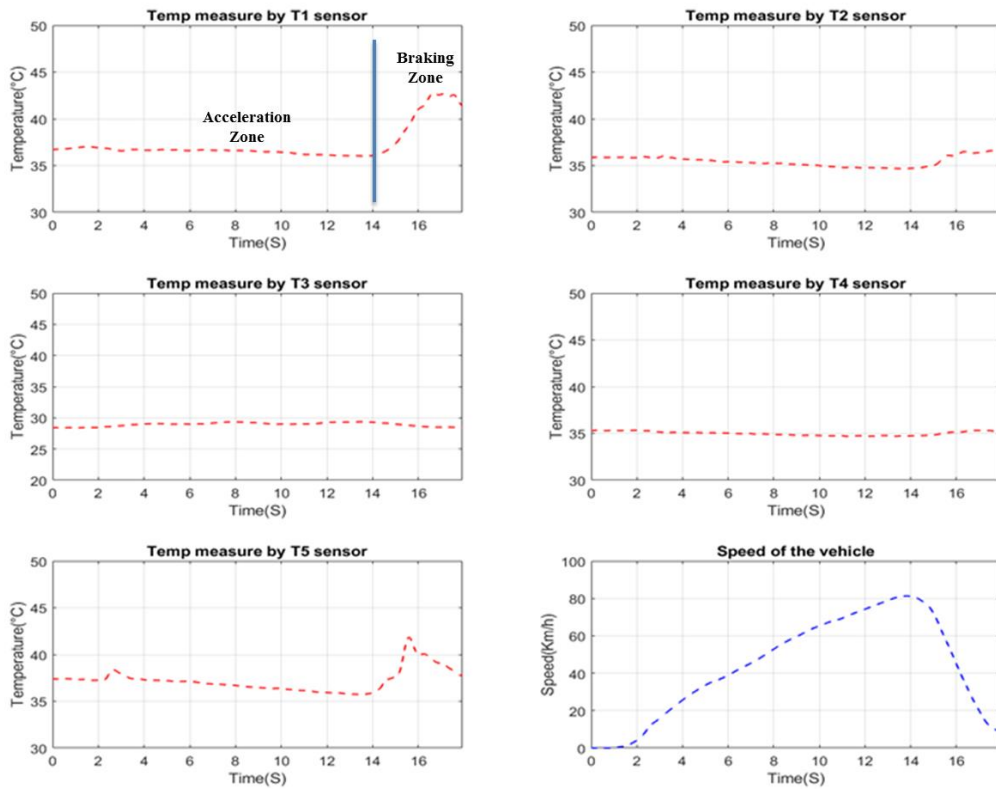


Figure 134 Variation of mean tyre surface temperature for acceleration and braking

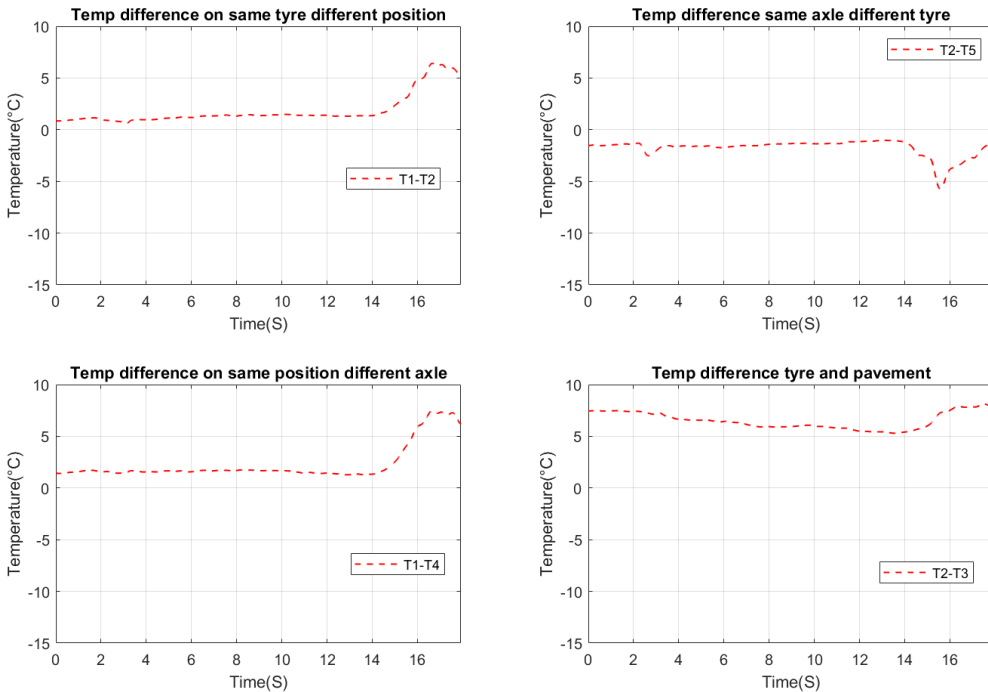


Figure 135 Temperature difference for different sensor positions for acceleration and braking

The variation of tyre surface temperature while accelerating (from 0 to 80 km/h) and braking are analysed, the results with speed variation are given in Figure 134. During acceleration, the tyre surface temperature is decreasing whereas it is increasing rapidly during the braking phase. It is decreasing

during acceleration due to the cooling from air current and increasing as a result of the heat generation due to friction between tyre–pavement interactions. The tyre surface temperature increases up to 10 °C during some manoeuvres. This test is done on the test track “F” (Table 13). The results on other test tracks can be found in the appendix F. The variations shown in Figure 135 led to conclude that the circumferential variation goes up to 6°C during braking; the temperature variation on the same axle is less than 1°C whereas on the different axle it goes up to 8°C. The temperature of the pavement is less than 10°C of tyre surface temperature. This manoeuvre will be used to evaluate tyre surface temperature and speed relationship.

iii. Curve with constant radius and speed

The tyre surface temperature for a cornering manoeuvre is also analysed as shown in Figure 136. When the vehicle is moving in the curve the tyre surface temperature varies up to 5°C. The variations are shown in Figure 137 and we can observe that the circumferential variation goes up to 8°C, the temperature variation on the same axle is less than 4°C due to the turning manoeuvre whereas on different axles it goes up to 10°C. The temperature of pavement is higher than the tyre surface temperature by 10°C. This is due to the fact that the test surface was exposed directly to the sunlight. This means that the tyre surface temperature increases during manoeuvres which can influence the rolling resistance of the tyre.

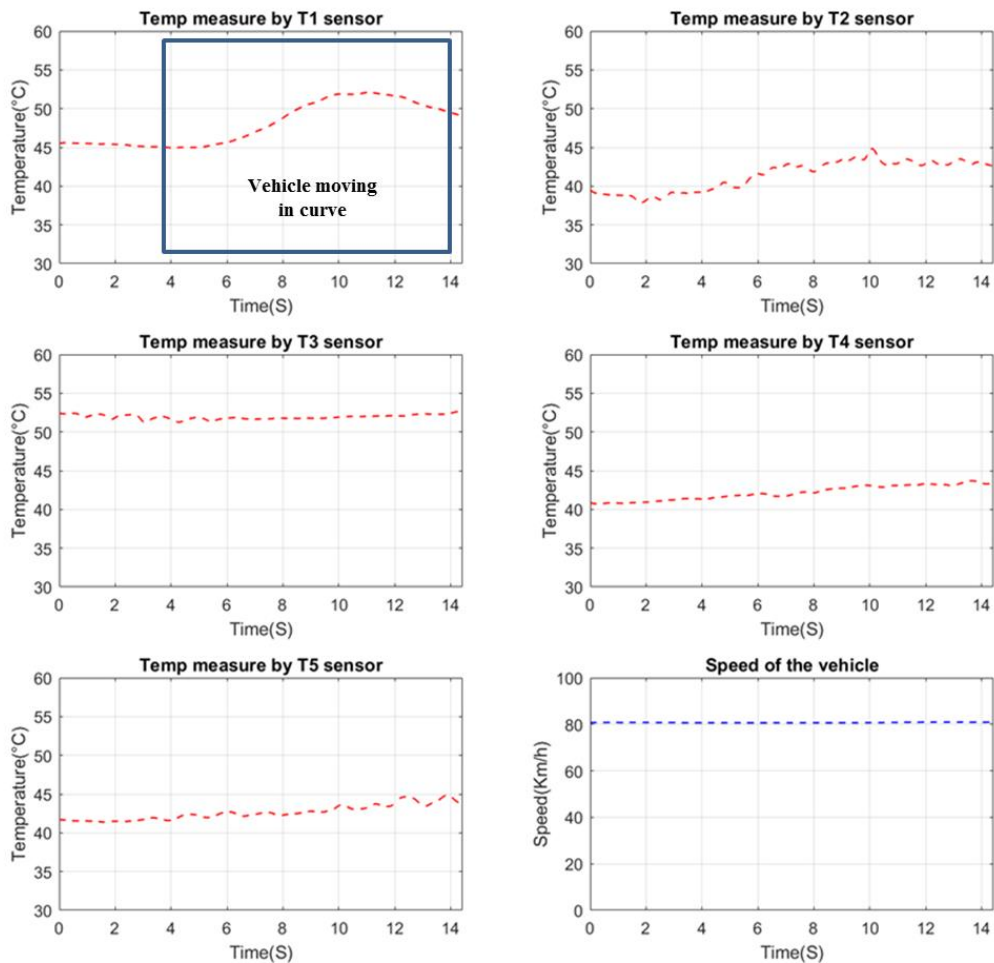


Figure 136 Variation of mean tyre surface temperature for vehicle moving in curve 220m at 80 km/h

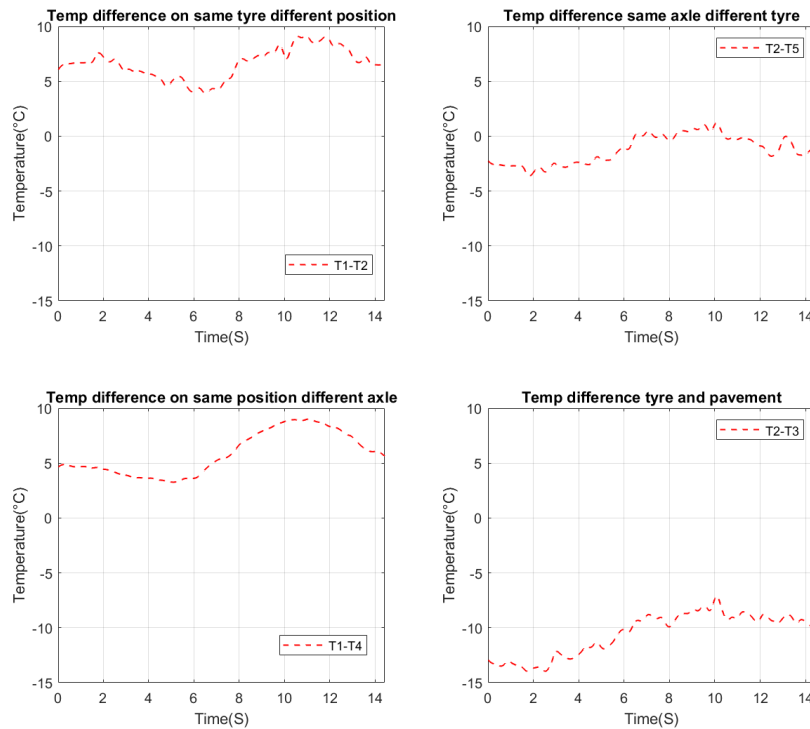


Figure 137 Temperature difference for different sensor positions in curve 220m at 80 km/h

5.4.2. Lateral Tyre surface temperature variation

In this section, the variation of tyre surface temperature in the lateral direction is presented. The installation of MB Flex temperature sensor is shown in Figure 138. This mounting instrument designed and copyright by Mr Sebastien Buisson was presented in chapter 5. The measurement point on the tyre surface is also given in Figure 138. These measurement points are considered along the width of the tyre. The results for DoE presented in Table 11 are discussed here.

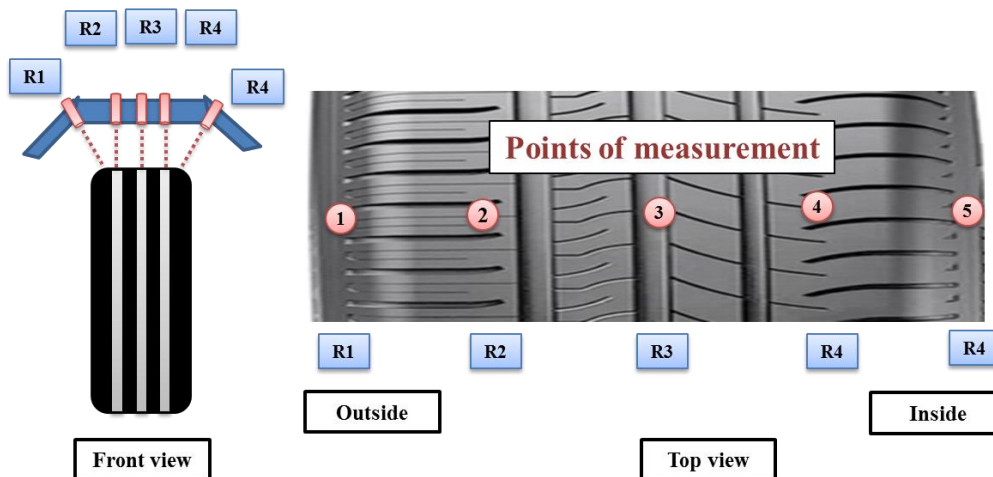


Figure 138 MB Flex sensor measurement points front and top view

5.4.2.1. Variation for various test track with different roughness

In this section, the result of tyre temperature variation in the lateral direction for a test track is discussed. The test is done on various test tracks at a constant velocity. Here, the results on the M3 test track at a constant speed of 80 km/h are presented (see Figure 139, Figure 140 and Figure 141). The

measurement points are shown in Figure 140. The temperature at the centre of the tyre contact area is 6°C higher than the temperature at the edges (see Figure 141). The point R3 has shown less temperature, it is due to the location of measurement point which is in the groove of the tyre (Figure 140). The polynomial fit of degree 2 which gives the best fit is calculated with regression for the variation of tyre surface temperature along with the tyre width as shown in Figure 140. This polynomial curve of tyre surface temperature could be explained by the parabolic load distribution therefore the heat generation due to hysteresis is higher at the centre of the contact patch and lower at shoulders. The impact of different road roughness on lateral tyre surface temperature variation is difficult to assess due to the varying ambient temperature.

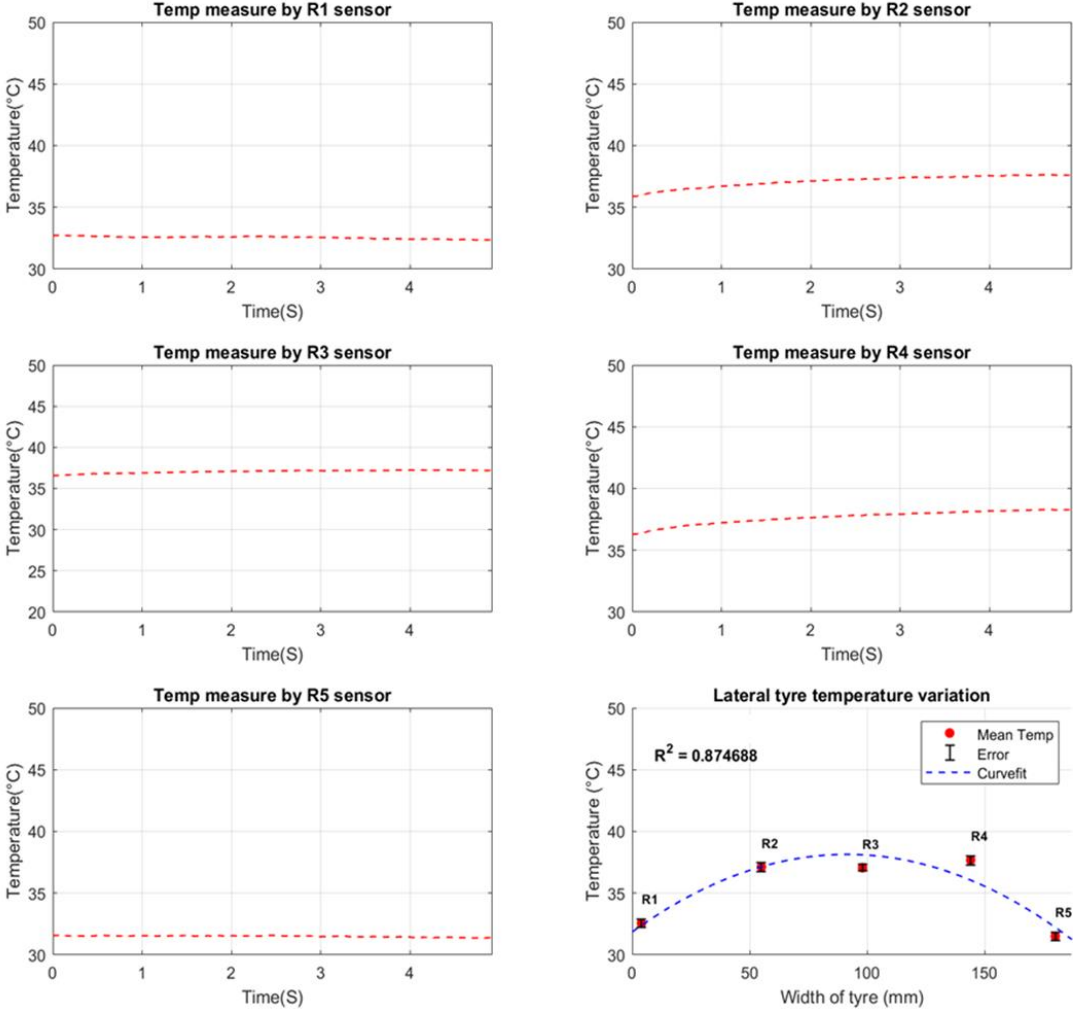


Figure 139 Variation of tyre surface temperature measurement points in the lateral direction for the M3 test track at 80 km/h

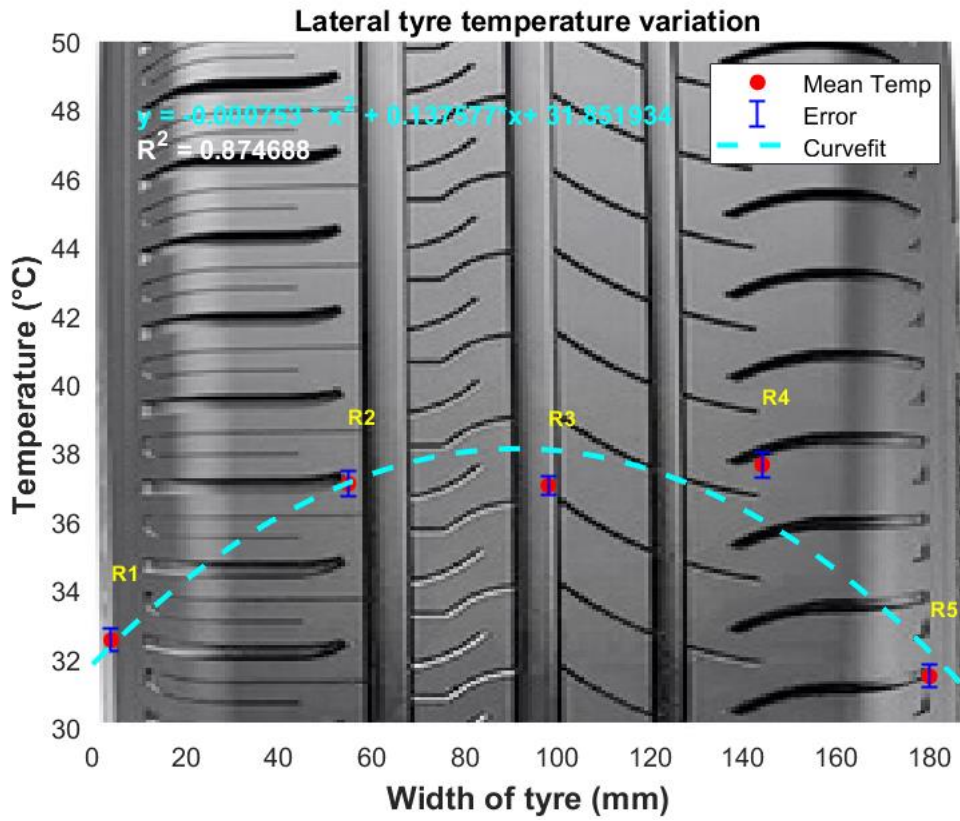


Figure 140 Curve fit of lateral mean tyre temperature variation and points on the tyre

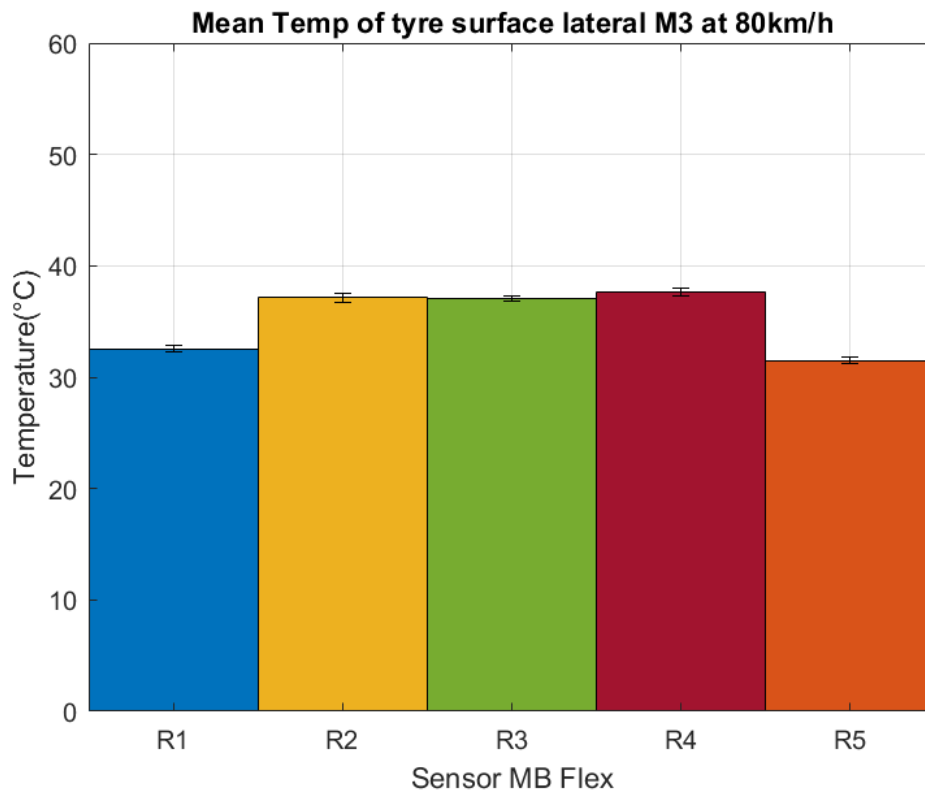


Figure 141 Mean tyre surface temperature with a standard deviation

5.4.2.2. Variation at a constant speed

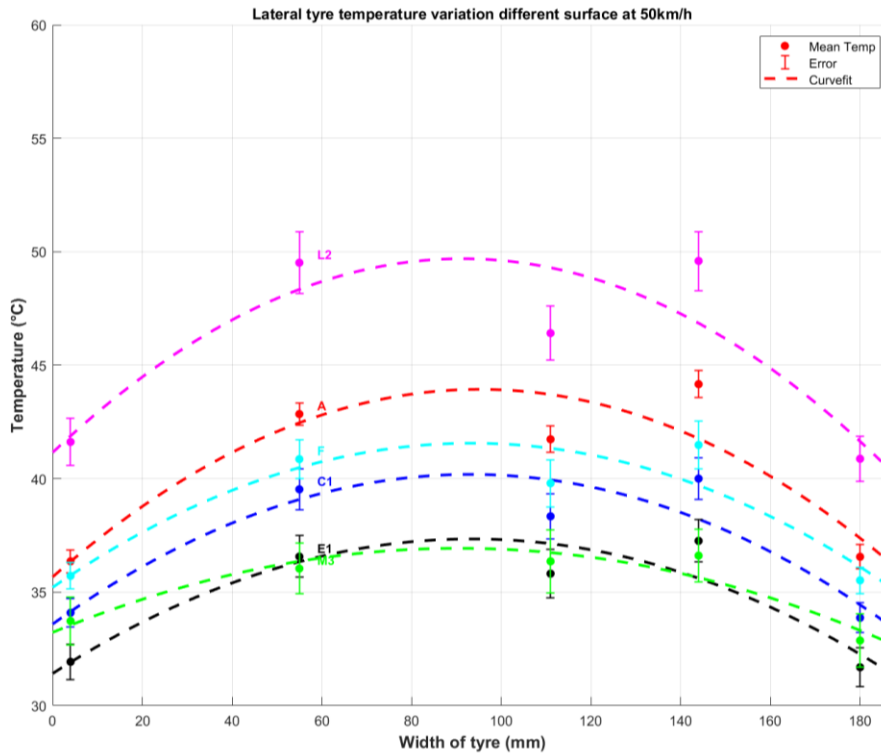


Figure 142 Tyre surface mean temperature curve fit for different test tracks at 50 km/h

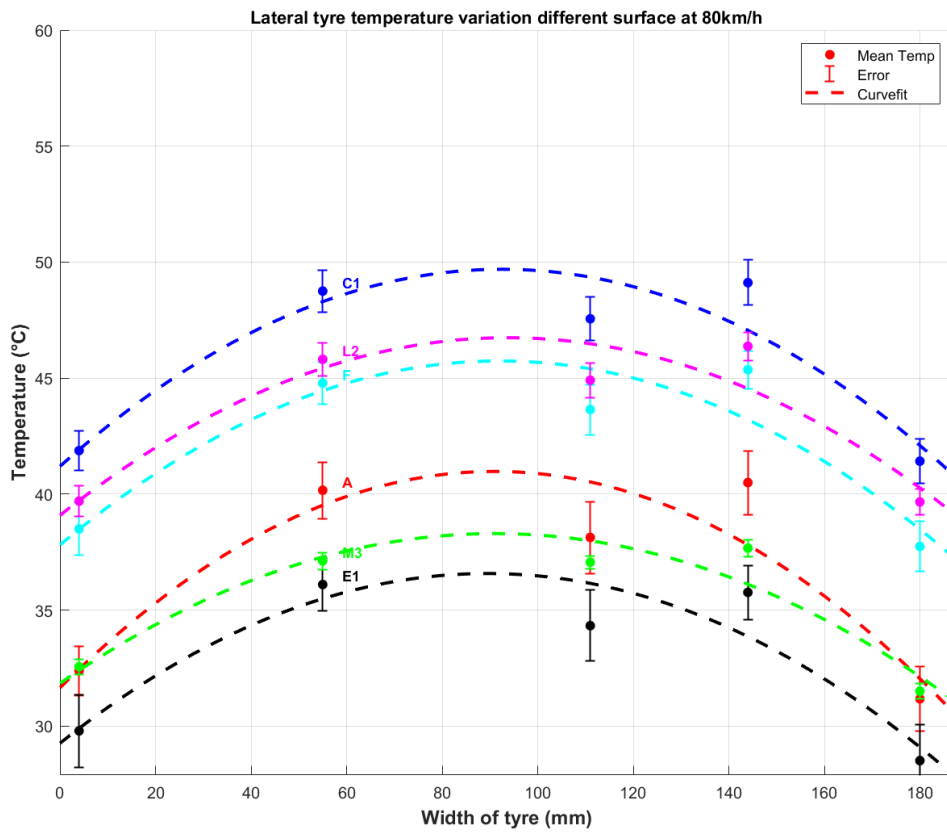


Figure 143 Tyre surface mean temperature curve fit for different test tracks at 80 km/h

The results of the lateral variation of the tyre surface temperature for the various test tracks at 50 km/h and 80 km/h are analysed and presented in Figure 142 and Figure 143. The variation follows the same trend as previously, the shoulders have less temperature as compared to the middle of the tyre. The temperature at the centre of the contact area is 6°C higher for all test tracks at 50 km/h as well as for 80 km/h. It means the heat generation is concentrated at the centre of the tyre contact area as more deformation is occurring.

5.4.2.3. Variation at different vehicle manoeuvres

In this section, the lateral tyre surface temperature variation for three different vehicle manoeuvres is presented. First, the results for lane change manoeuvres are analysed and presented in Figure 144 and Figure 145. During the manoeuvres, the temperature increases up to 4°C, this is higher than the accuracy of the measurement. The tyre surface temperature at the centre rib of the tyre is higher than the temperature at the tyre shoulder rib by 7°C. This seems constant throughout manoeuvres.

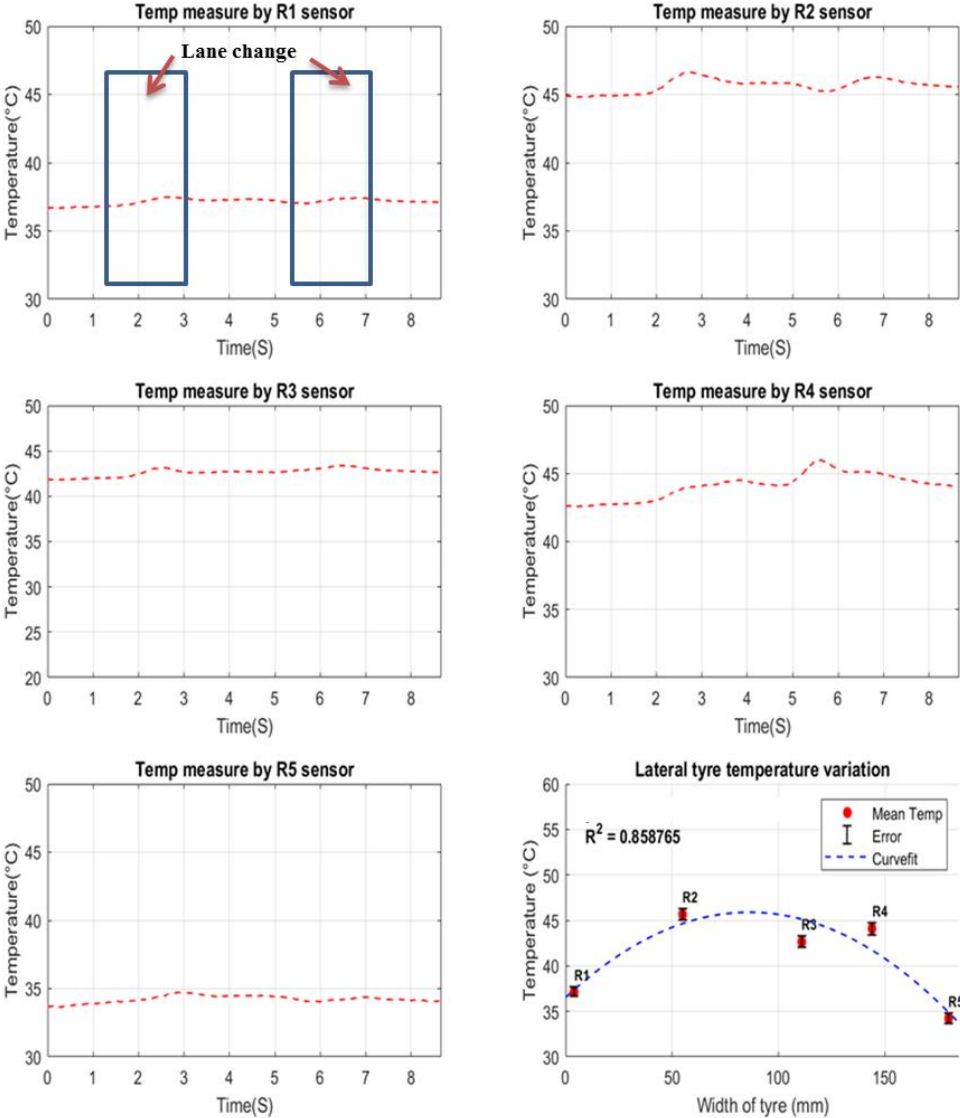


Figure 144 Variation of lateral mean tyre surface temperature for lane change at 60 km/h

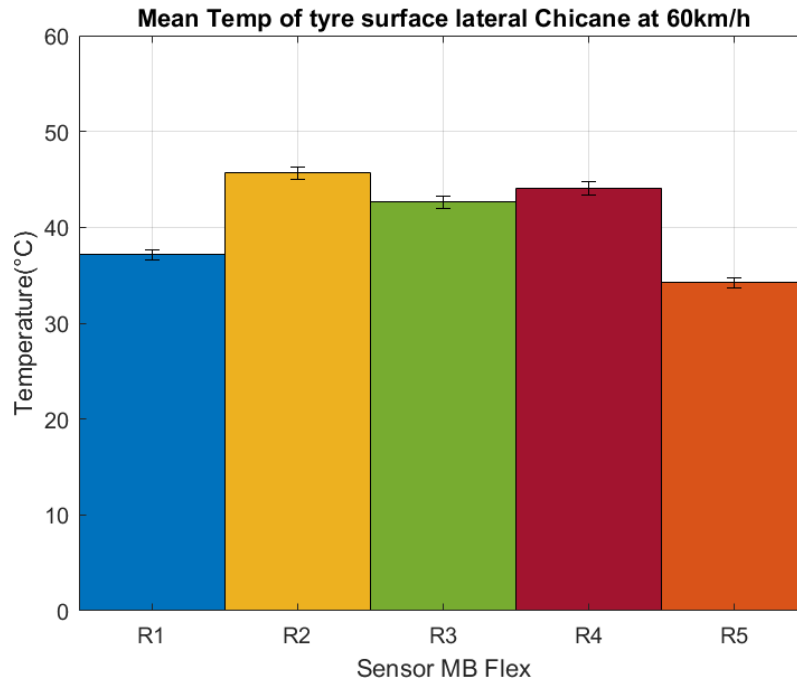


Figure 145 Mean Temp of tyre surface in the lateral direction for lane change at 60 km/h

In Figure 146 and Figure 147 the results for the acceleration and braking is presented. The cooling due to air current is seen during acceleration and generation of heat due to friction during braking. The tyre shoulder temperature cools down by 3°C and centre rib cools down by 1.5°C during acceleration. During braking tyre surface temperature increases by 2°C on tyre edges and 10°C at the centre rib. During acceleration, the tyre surface temperature at the centre of the tyre is just 4°C higher than tyre edges but during braking, the difference rises up to 12°C. The variation of tyre surface temperature is similar to the circumferential variation presented previously. This variation is in line with the hypotheses in the literature.

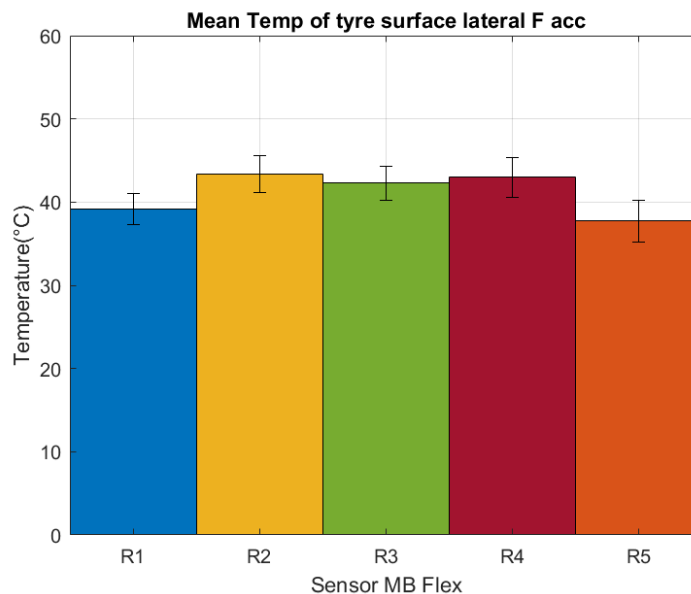


Figure 146 Variation of lateral mean tyre surface temperature for acceleration and braking

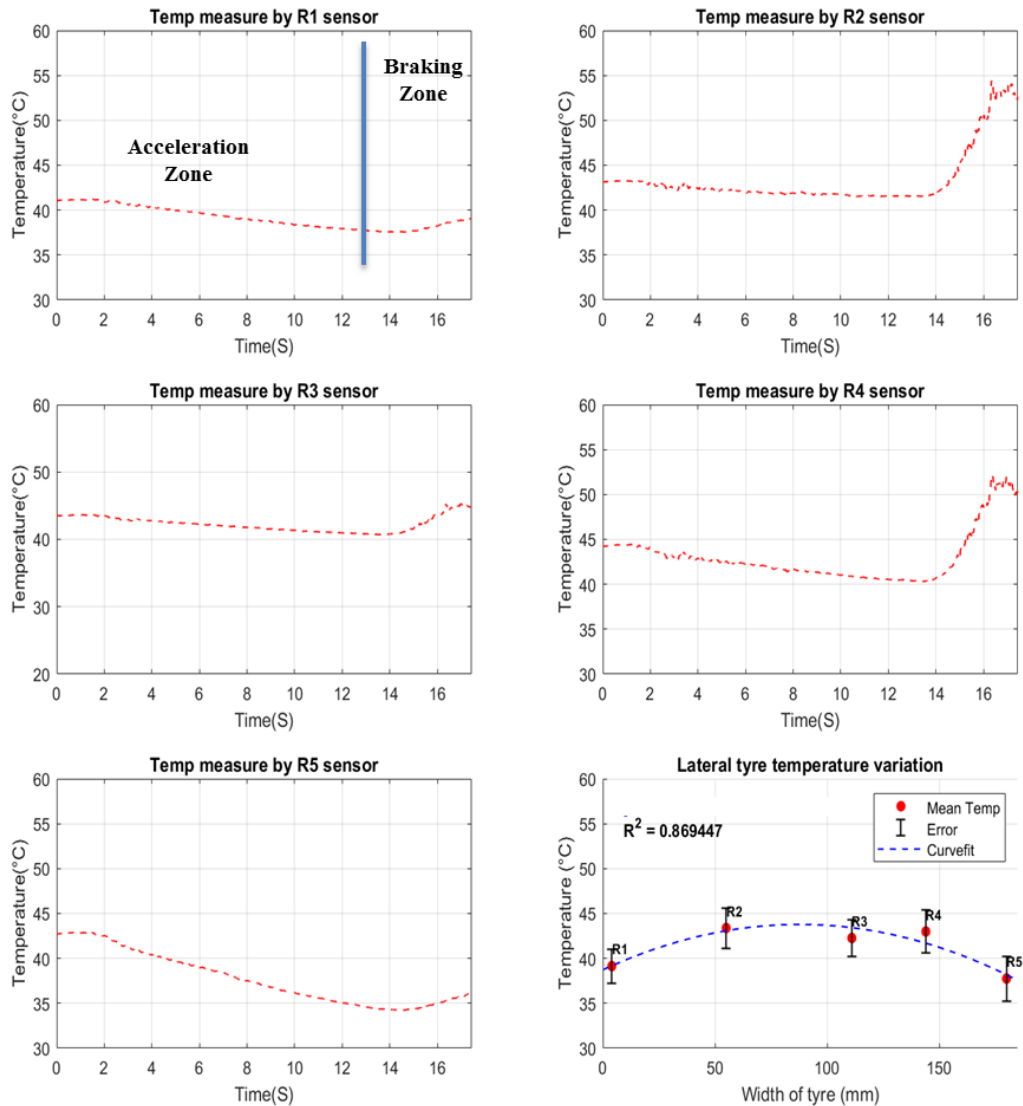


Figure 147 Variation of lateral mean tyre surface temperature for acceleration and braking

The results of the curve with 220m radius at 80 km/h manoeuvre are presented in Figure 148 and Figure 149. During the manoeuvres, the temperature increases up to 7°C. The tyre surface temperature at the centre rib is high than tyre edges by 10°C. This high temperature is seen due to the high ambient temperature on the day of the test.

In three different types of manoeuvres (discussed above), the tyre surface temperature is increasing during manoeuvres. It is mainly due to the heat generated either due to the friction or tyre deformation. The temperature increases up to 10°C. The lateral tyre surface temperature variation study allows us to understand the variation of temperature along the width of the tyre. It can be concluded that the tyre surface temperature is lower at shoulders rib by 6°C as compared to the centre rib of the tyre. It is due to heat generation from higher deformation at the centre rib. So our work needs to monitor the tyre surface temperature as it influences directly rolling resistance. In the experiment results of rolling resistance in section 5.3.3.1, it is shown that the decrease in rolling resistance up to 3% with 10°C increase of tyre surface temperature.

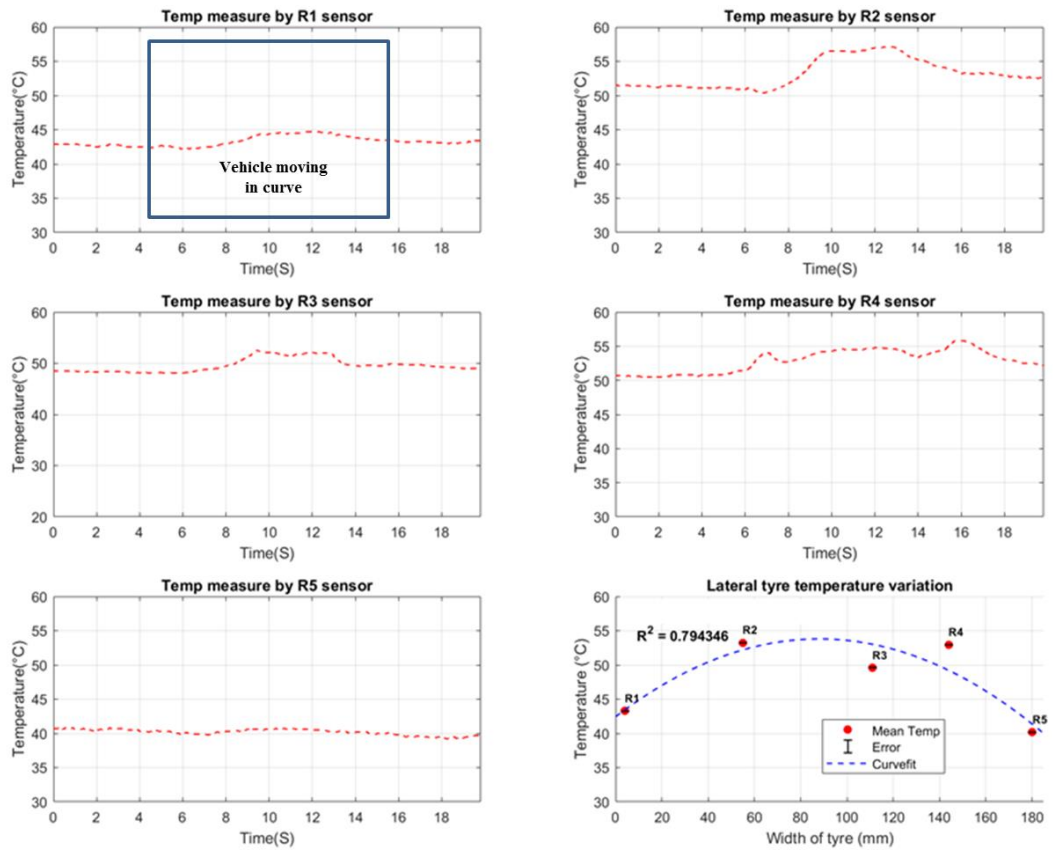


Figure 148 Variation of lateral mean tyre surface temperature in 220m curve at 80 km/h

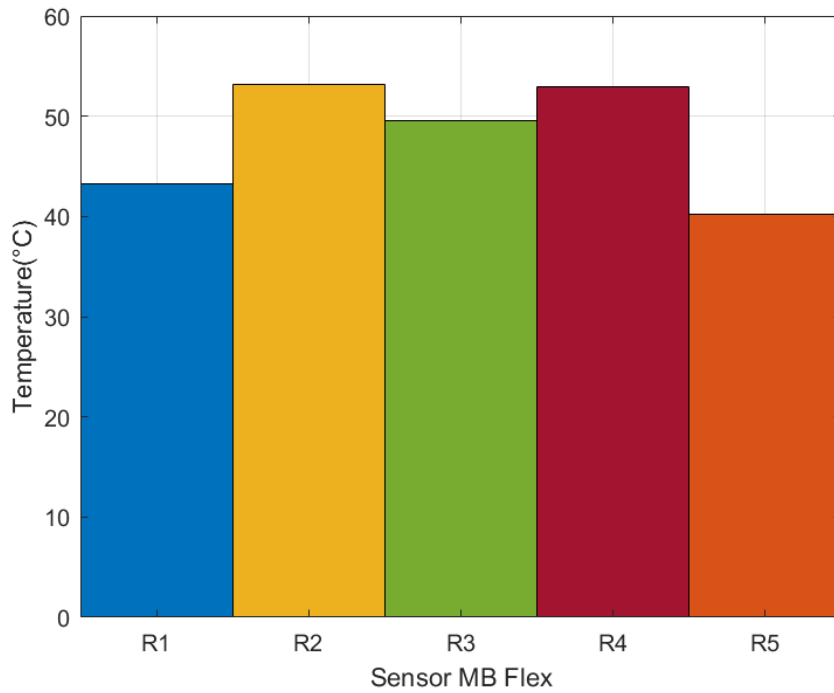


Figure 149 Mean tyre surface temperature in the lateral direction in the 220m curve at 80 km/h

5.4.3. The relation between tyre surface temperature and speed

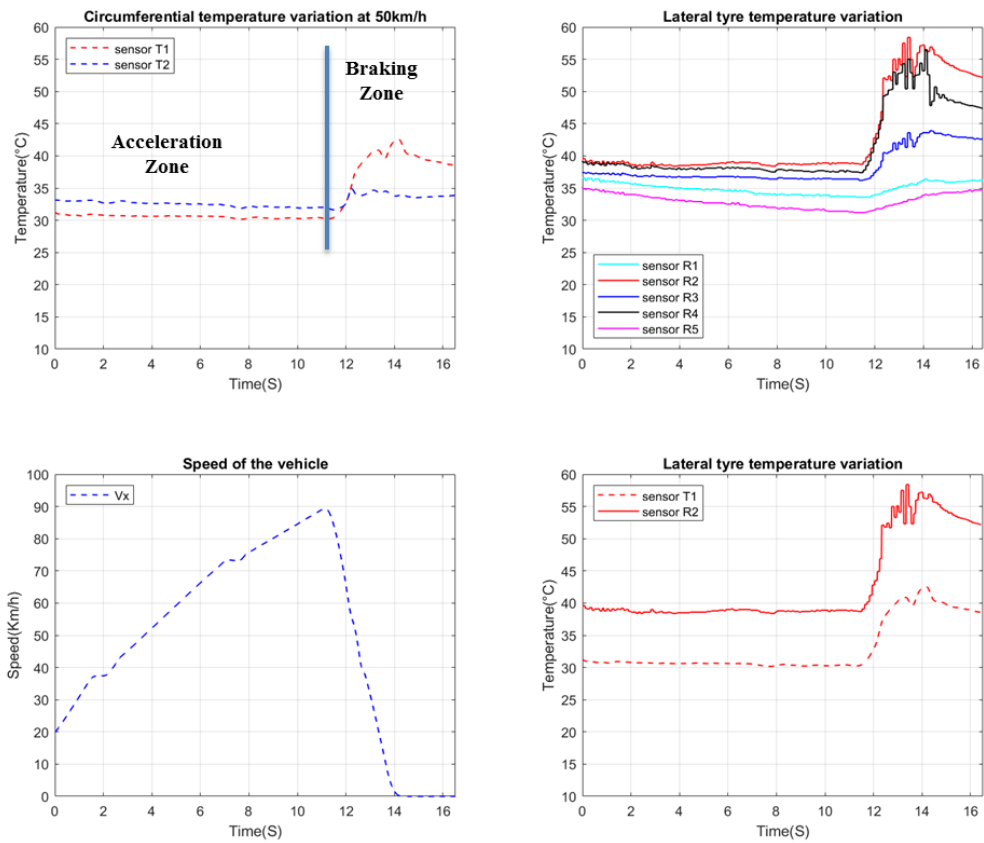


Figure 150 Comparison of circumferential and lateral variation of tyre surface temperature for varying speed

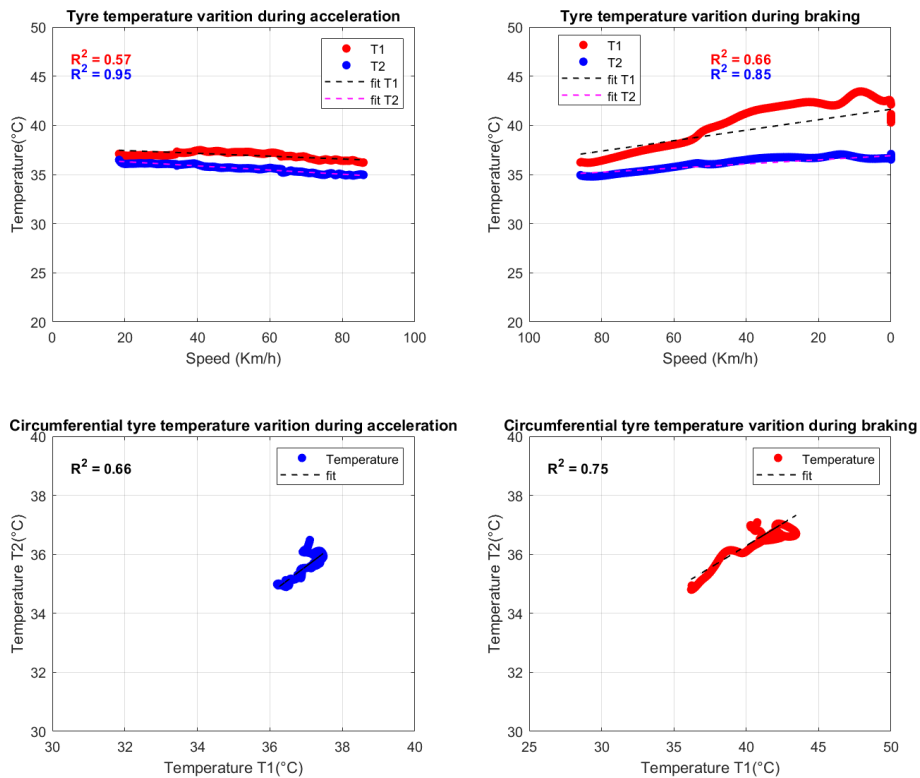


Figure 151 Vehicle speed and tyre surface temperature relationship with circumferential variation

In this section, the relationship between tyre surface temperature and vehicle speed is presented. The acceleration and braking manoeuvres are used to identify the relationship. The data acquisition system from instrumented vehicle and HBM are synchronised before the analysis with the help of z accelerometer. In Figure 150 the circumferential and lateral measurements are presented for accelerating and braking manoeuvres. When comparing both, the measurements of all the sensors show the same trends and dynamics. The sensor T1 and R2 are measuring the tyre surface temperature at the same rib on the tyre. On comparing these two it is found that the temperature measured by MB Flex is higher than tyre surface temperature. This is due to the sensor distance from the tyre rib. The MB Flex sensors are located closer as compared to T1 due to the installation constraints on the instrumented vehicle.

In Figure 151 the tyre surface temperature and vehicle speed relationship are analysed. During acceleration T1 and T2 varies with speed with linear regression of 0.95 and 0.57. It is found that the tyre surface temperature varies very slowly as compared to the speed of the vehicle. It means that thermal dynamics are slower than the mechanical one. Also during braking manoeuvres, the tyre surface temperature increases with decreasing speed with a negative slope. The variation for tyre surface temperature is slower than the speed variation. The variation of tyre surface temperature between T1 and T2 is linear for the lower temperature. This conclusion will be used in the next section for the validation of the tyre model in section 5.5.1.1.

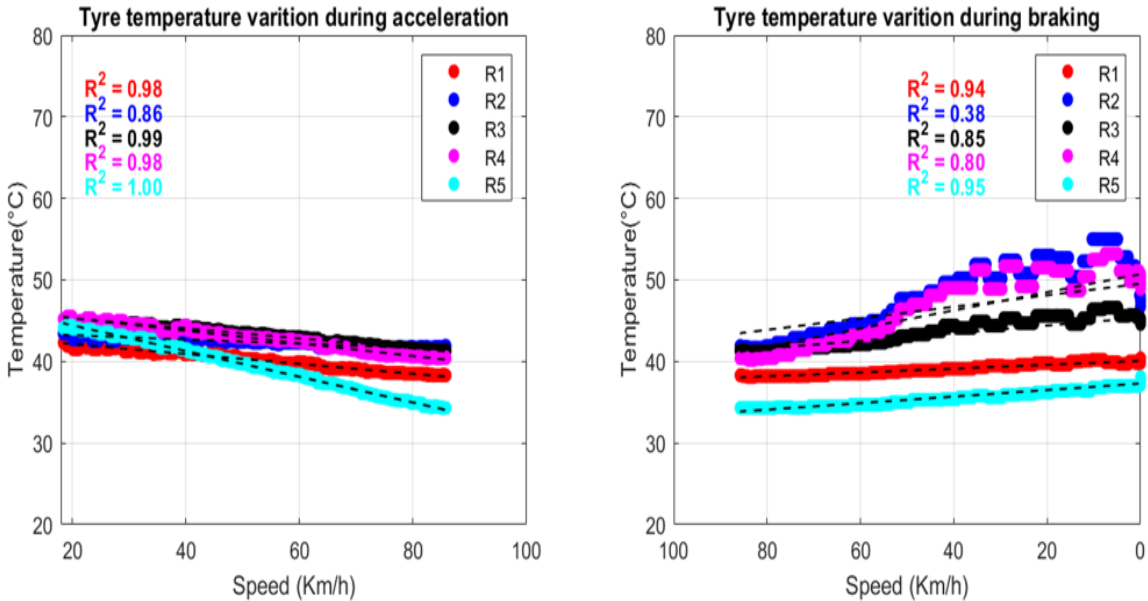


Figure 152 Vehicle speed and tyre surface temperature relationship with lateral variation

The variation of tyre surface temperature along with the width of the tyre (outside rib to inside rib) with speed is also studied. In Figure 152 the relationship between the tyre surface temperature for the different sensor on tyre width and vehicle speed are presented. During accelerations, the linear regression coefficients are ranging between 0.86 and 0.95. It can be concluded that the temperature varies very slowly as compared to the speed of the vehicle at any point along the width of the tyre. It also confirms the previous hypothesis that temperature has slow dynamics. Similar results are found during braking manoeuvres with a negative slope.

5.4.4. Conclusion

The evaluation of tyre surface temperature is done successfully in this section. The syntheses of the tyre surface temperature and different comparison results are given in Table 20.

Table 20 Synthesis of tyre surface temperature in different Scenarios

Scenarios	Tyre surface temperature variation	Temperature between Tyre and pavement	Tyre temperature on the different axle	Tyre temperature on the Same axle
Constant speed	<ul style="list-style-type: none"> -The tyre surface temperature is higher at 80km/h than 50km/h -The temperature difference is 5°C 	<ul style="list-style-type: none"> -At 50km/h the pavement and tyre temperature is the same, -At 80km/h, the pavement temperature is higher by 2°C due to high ambient temperature 	<ul style="list-style-type: none"> -At 50km/h no difference -At 80km/h, the front axle tyres is hotter by 3°C 	<ul style="list-style-type: none"> -The temperature is same on both tyre of the axle
Different test track	<ul style="list-style-type: none"> -The variation tyre temperature for different test tracks is similar to ambient temperature at 50km/h -So it is difficult to assess the influence of road roughness on tyre surface temperature -Whereas at 80km/h the tyre surface temperature is increasing with the increase in the road roughness on a few tracks, this is due to the higher pavement temperature 	<ul style="list-style-type: none"> -The temperature varies depending on ambient temperature -Some pavement are hotter than tyre surface temperature by 10°C -In some cases, the tyre surface is hotter by 5°C -This is due to the ambient temperature and direction of sunlight 	<ul style="list-style-type: none"> -No significant difference is seen 	<ul style="list-style-type: none"> -The difference is under the accuracy of the sensor
Vehicle manoeuvres	<ul style="list-style-type: none"> -During all the manoeuvres the tyre surface temperature in the range of 5 to 10°C -This increase in tyre surface temperature due to more deformation from lateral manoeuvres, or the heat generation due to the friction -It is also found that during acceleration the tyre tends to cool down due to the cool air current. 	<ul style="list-style-type: none"> -During lane change and curve manoeuvres the pavement was hotter than tyre surface temperature in the range of 7 to 10°C -This is due to the high ambient temperature and sunlight during summers -During acceleration and braking the pavement was cooler than tyre surface temperature by 7°C average. -This is because the test was done in the early morning. 	<ul style="list-style-type: none"> -The front axle always has high tyre surface temperature due to presence of engine heat, also the manoeuvres (steering angle, Fy) applied to front axle only 	<ul style="list-style-type: none"> -No significant difference is found for lane change manoeuvres -The difference up to 5°C seen for braking and curve manoeuvres -It is mainly due to the sensor measuring point changes due to steering angle

The tyre surface temperature increases up to 5°C for the high speed. The tyre surface variation due to different road roughness is difficult to assess since the ambient temperature varies significantly. The surface temperature increases up to 10°C for different vehicle manoeuvres. The temperature difference between pavement and tyre surface is also significant in some cases and influencing directly the tyre temperature. The tyre temperature on the front axle is always greater than the rear axle due to the engine heat contribution. The impact of heat is also seen in the circumferential temperature variation.

The syntheses of circumferential and lateral variation of tyre surface temperature with respect to speed, test tracks and vehicle manoeuvres are presented in Table 21. The lateral temperature variation study concludes that the temperature of the centre ribs of the tyre is always higher than tyre edges by 6 to 10°C. It is concluded from this study that tyre surface temperature is influenced by speed, pavement temperature, ambient temperature and vehicle manoeuvres.

Table 21 Synthesis of circumferential and lateral variation of tyre surface temperature

	Tyre surface temperature variation	
	Circumferential	Lateral
Speed	<ul style="list-style-type: none"> -Same magnitude of temperature for T1 and T2 at 50km/h -T1 > T2 by 2.2°C at 80km/h -At constant speed no significant circumferential variation is found in experiments. Also, T2 is measuring the temperature at the tyre grooves and T1 at the tyre surface. 	<ul style="list-style-type: none"> -At 50km/h and 80km/h, the same range of variation is seen along the width of the tyre. -The temperature as the centre ribs is higher than shoulder rib by 6°C. - The lateral temperature variation is found and coherent with the literature
Different test track	<ul style="list-style-type: none"> -The difference is under accuracy range at 50km/h -At 80km/h the difference rises to 5°C for some test tracks. -This is maybe higher engine temperature at high speed -The difference due to groove and surface should also be taken into account 	<ul style="list-style-type: none"> -The temperature is higher for high ambient temperature -Again the mean difference between temperature as the centre ribs are higher than shoulder rib by 6°C.
Vehicle manoeuvres	<ul style="list-style-type: none"> -During lane change manoeuvres the T1>T2 in the range of 5°C. -During braking this difference goes up to 7°C. -During curve it goes up to 10°C. - It is due to high ambient and pavement temperature. -T1>T2 conclude on the circumferential variation as temperature increasing at T1 due to engine heat 	<ul style="list-style-type: none"> -During lane change and curve manoeuvres temperature as the centre ribs are higher than shoulder rib by 7 and 6°C respectively. -During acceleration this difference is 4°C and in braking, it rises to 12°C. due to friction -The lateral variation is conclusive for the tyre surface -It edges are cooler than the centre of the contact area due to less deformation.

It is concluded that the tyre surface temperature is the same on the both tyre of the same axle. This conclusion on the same axle is useful for the experimental validation observer as the tyre surface temperature estimation is done for all four tyres and the sensors were installed only on three tyres. The linear regression confirms that the circumferential and lateral tyre surface temperature varies linearly. The relationship between tyre surface temperature and speed conclude that the temperature varies slowly as compared to speed. Therefore with thermal dynamics the system becomes singularly perturbed systems. Therefore, the systems must be divided into two timescale dynamics. Slow dynamics from the thermal model and fast dynamics for the rest of the systems.

5.5. Experimental validation

There are two main problems discussed in this section. Firstly, the experimental validation of the model developed in this thesis is exposed. Then, the validation of the observer technique to estimate experimentally rolling resistance is detailed.

The model developed in this thesis (Chapter 2 and 3) is made up of two modules, the Multi physical tyre model (MPT) and the vehicle model which need calibration and validation. The validation of the MPT model requires the tyre temperature measurements performed with infrared temperature sensors. The vehicle model requires a good knowledge of the dynamical behaviour through various sensors installed on the instrumented vehicle.

5.5.1. Model validation

In this section, the experimental validation of the full vehicle model is presented. Ten different test scenarios were constructed and described in Chapter 3 (see Table 10) to validate our model. These scenarios cover a wide range of speeds and manoeuvres. Experiments were performed for the above scenarios and compared with the developed model (Figure 60). Steer angle and torque was given as input to the model with the same input parameters and initial conditions as used for simulation as Prosper (SCANeR Studio).

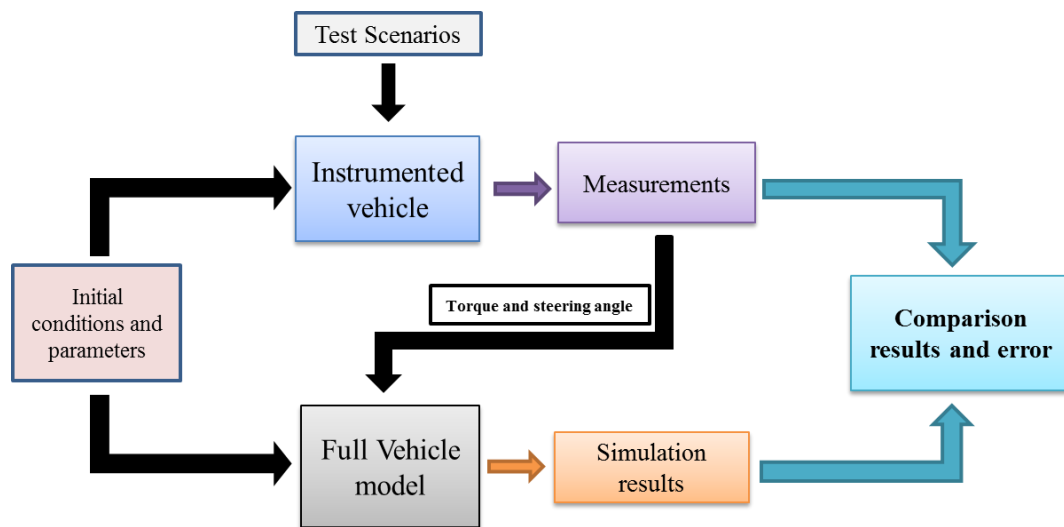


Figure 153 Methodology of model validation

The validation of the model is evaluated by calculating the relative mean errors of speed and position vectors:

$$ME = \frac{1}{N} \sum_{i=1}^N \left| \frac{ref(t_i) - model(t_i)}{ref(t_i)} \right| \quad (198)$$

With t_i is counted from the instant when model start converging to real ones (approx. 2sec) to end of simulation and N number of samples in this period.

The validation of the tyre model is done first.

5.5.1.1. Validation of the MPT model

In this section, the experimental validation of multi-physical tyre model is presented. The temperature sensors were calibrated before mounting on the vehicle. The longitudinal force is directly measured by the dynamometric wheel mounted on the front right tyre.

In reality, it is difficult to measure the tyre temperature in the contact zone experimentally because of measurement complexity and price. In Figure 154 the exact point of measurement by the infrared sensor (blue circle) during experiments is shown. The above-developed model can estimate the tyre temperature in the contact zone as shown in the red circle in Figure 154. To match the exact measurement point (blue) by developed model, an additional cooling effect is added to the model. To represent this cooling effect, simple cooling law (199) has been developed. This law takes into account the increase in the area of cooling due to tread structure, interior conduction of heat from carcass and tread surface and transfer of heat in the ambient environment. The cooling due to inside air is not considered here.

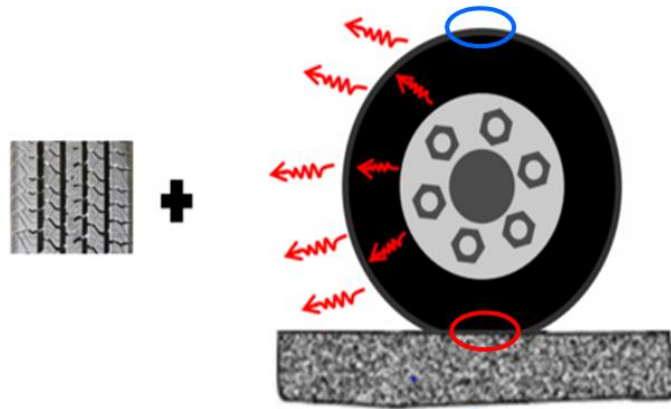


Figure 154 Cooling of a tyre contact (red) to measured point (blue)

To construct a law, two zones of cooling are assumed; one is linear which is at lower temperature difference and the other one is nonlinear at higher temperature difference represented in Figure 155. The linear variation is validated and confirmed from the results obtained in section 5.4.3. This cooling mainly depends on rubber properties, tyre void ratio and rubber material. It is very difficult to characterize the rubber parameters to consider the cooling in the nonlinear region as shown in Figure 155. So cooling law is developed which is based on the “Newton’s law of cooling” for the linear region which follows linearly the cooling of the tyre surface. The corrected temperature by cooling law is given by

$$T_{new} = T_{amb} + (T_{surf} - T_{amb})e^{-rt} - K(T_{surf} - T_{carcass}) \quad (199)$$

With T_{amb} is ambient temperature, T_{surf} tread surface temp at contact (red circle), $T_{carcass}$ is carcass temperature, r convection coefficient air and surface, t time and K internal convection coefficient. The temperature calculated after applying this law is shown in black colour in figures.

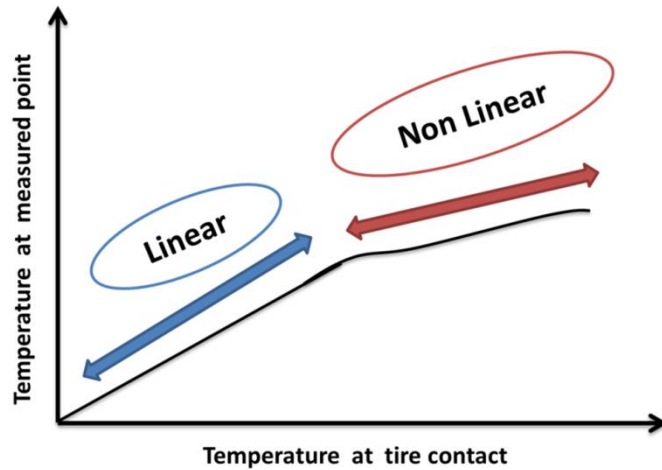


Figure 155 Cooling behaviour of contact temperature (hypotheses)

Therefore the results will be compared after applying the above developed cooling effect.

In order to validate the model, the longitudinal force and tyre surface temperature have been analysed. Vehicle speed and torque are used to calculate the tyre forces and tyre surface temperature. Here the simulation results for test scenarios 1 and 10 are presented.

- Car moving at 50 km/h in a straight line

In this experiment, the car was moving in a straight line and with constant velocity. Figure 156 exhibits the comparison between experimental (in blue) and simulated (in red) values of longitudinal forces. The standard mean error between longitudinal forces is less than 5%.

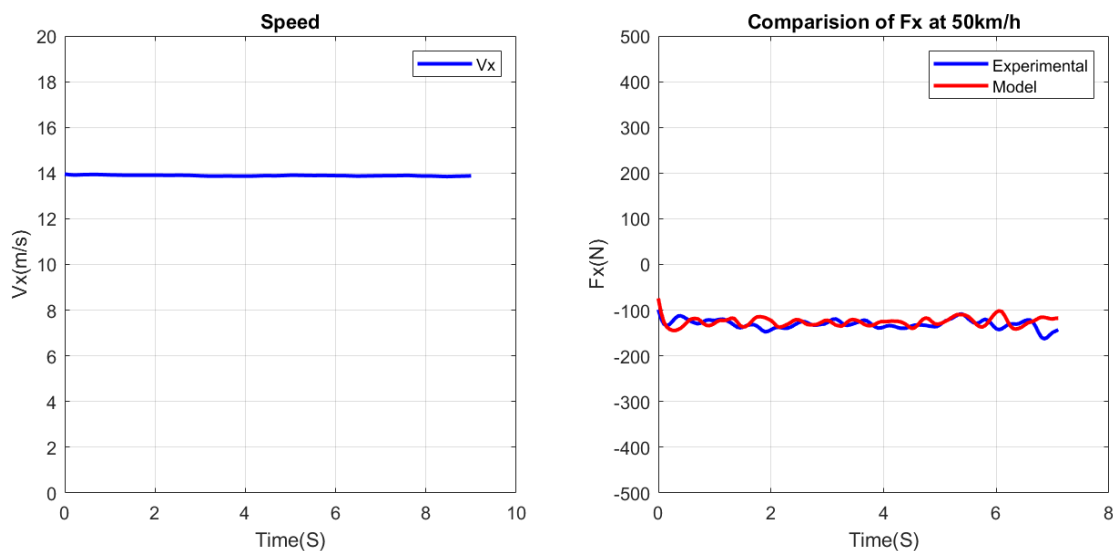


Figure 156 Comparison of tyre forces between model and experimental at 50 km/h

In Figure 157, the tyre surface temperature comparison between the developed model and measurements is shown. After considering the cooling effect as mentioned above, temperature calculated by model (in black) is compared with measured tyre surface temperature (in blue) by an infrared sensor which gives a standard deviation of 0.87°C . In Figure 157 the speed is given in orange colour which is constant. It is concluded from Figure 156 and Figure 157 that the model is giving the

same magnitude of longitudinal forces and tyre surface temperature with an error of less than 10%. Therefore, the model is validated for straight-line manoeuvres.

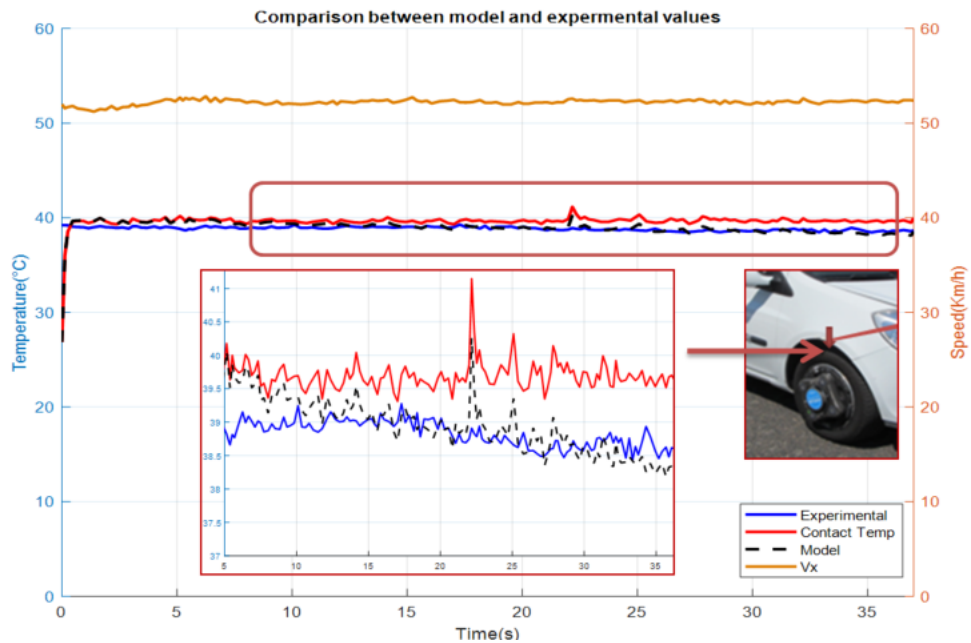


Figure 157 Comparison of tyre surface temp between model and experimental at 50 km/h

- Vehicle accelerating and braking in a straight line

In the second test condition, the test vehicle was accelerated from 0 to 115 km/h and then braked until stop (Figure 158). This test experiment is done to analyse the heat generation while accelerating and braking and also the cooling effect after braking. Figure 158 shows the comparison of tyre forces. The longitudinal force given by the tyre model presents the same behaviour as experimentally measured tyre forces with a standard deviation of 10%.

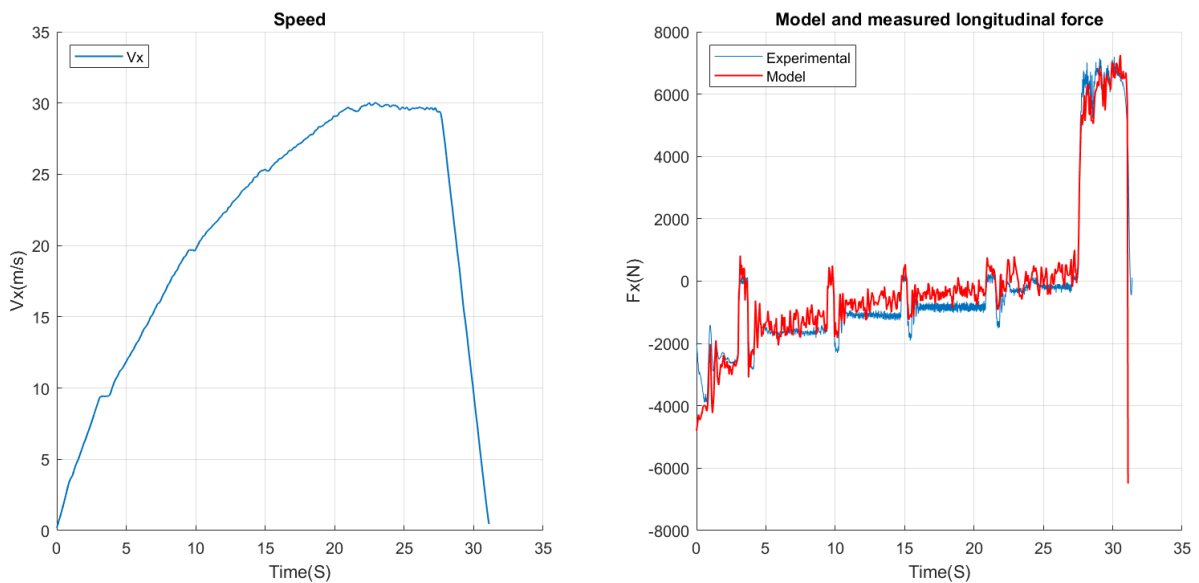


Figure 158 Comparison of tyre forces between model and experimental for accelerating and braking

The result of the tyre surface temperature comparison is presented in Figure 159. The measured tyre temperature (in blue) and tyre tread temperature calculated by the model (in red) show the same

dynamics. The tyre surface temperature calculated by model (in black) is compared with measured tyre surface temperature. The relative mean error of comparison is 2.8°C. The error is mainly in braking manoeuvres (see Figure 159). During braking, the heat is generated in the contact zone and dissipated when the tyre reaches the measured zone. Since the results of both test conditions are in the accuracy range of the infrared sensor and less than 10%. Therefore it can be concluded that the above developed multi-physical tyre model is validated experimentally.

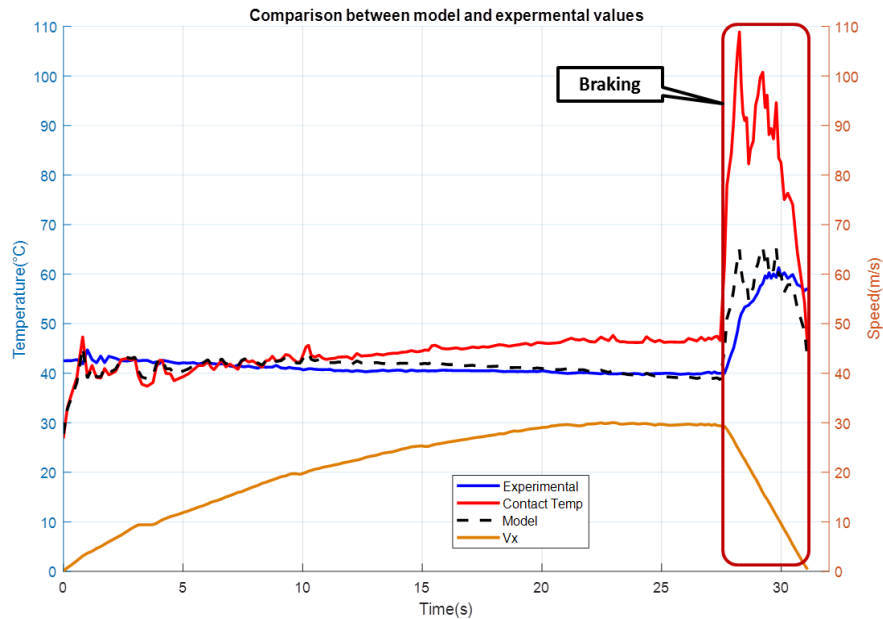


Figure 159 Comparison of tyre surface temperature between model and experiment for accelerating and braking

5.5.1.2. Validation of the full vehicle model

In this section, the experimental validation of the full vehicle model is presented. The comparison results for test scenarios 1, 7 and 10 are presented. The other tests can be found in appendix E. The validation is demonstrated by calculating relative mean error (<10%) when comparing longitudinal and lateral speed, the roll, pitch and yaw rate and trajectory of the model with experimental results.

- Car moving at 50 km/h in a straight line

In this experiment, the car was moving in a straight line and with constant velocity. We can conclude from Figure 160 that for a straight line our vehicle model is following the curves coming from experiments. The roll, pitch and yaw are very small with a negligible difference, it is mainly assumed to be due to the noise in the measurements. The comparison shows good trends with a relative mean error of less than 5% for parameters. This little variation in magnitude of the developed model can be explained by the assumptions done regarding dynamical behaviour. It can be concluded from above Figure 160 that our vehicle model is showing good behaviour and validated for straight-line manoeuvres.

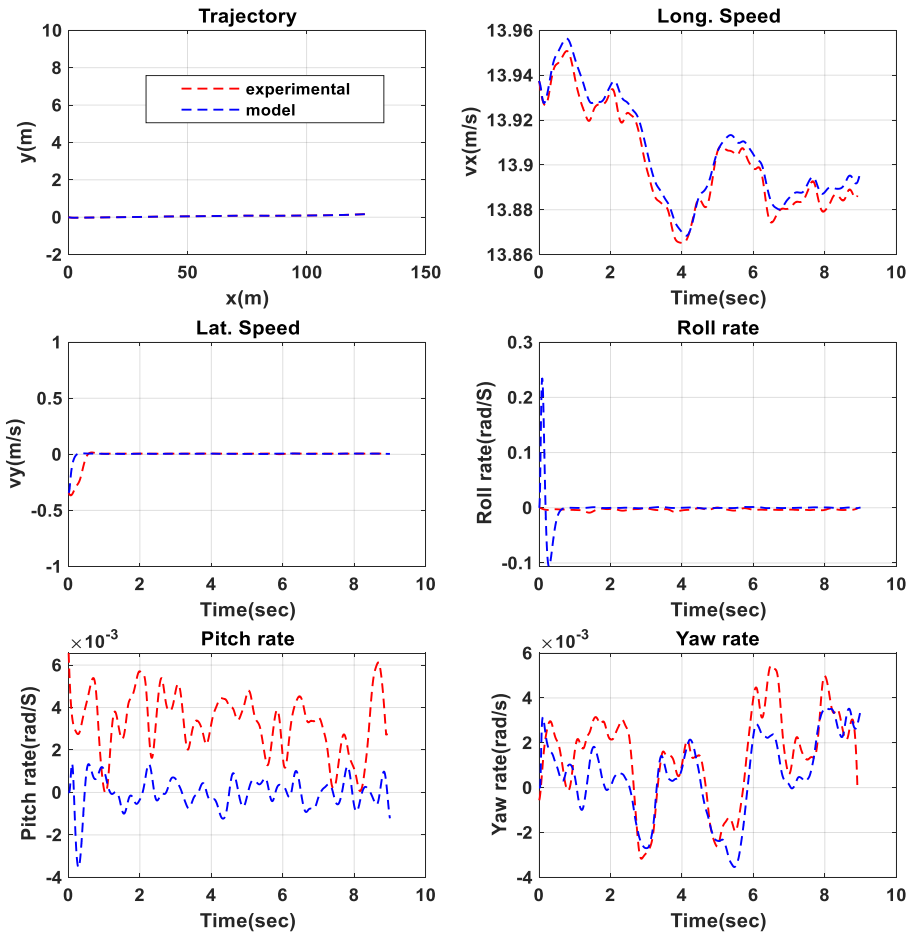


Figure 160 Results comparison between model and experimentation for straight line

- Vehicle moving in constant Radius of 320m

In this test, the car was moving on a curve with a constant radius of 320m. The results were compared and presented in Figure 161. It is observed from Figure 161 that model results are showing the same dynamics as the experimental results. The comparison shows good trends with a relative mean error of less than 5% for parameters. This variation in magnitude isn't very alarming as the developed model is more simplified as compared to the real vehicle. It can be concluded from below Figure 161 that our vehicle model is validated for cornering manoeuvres.

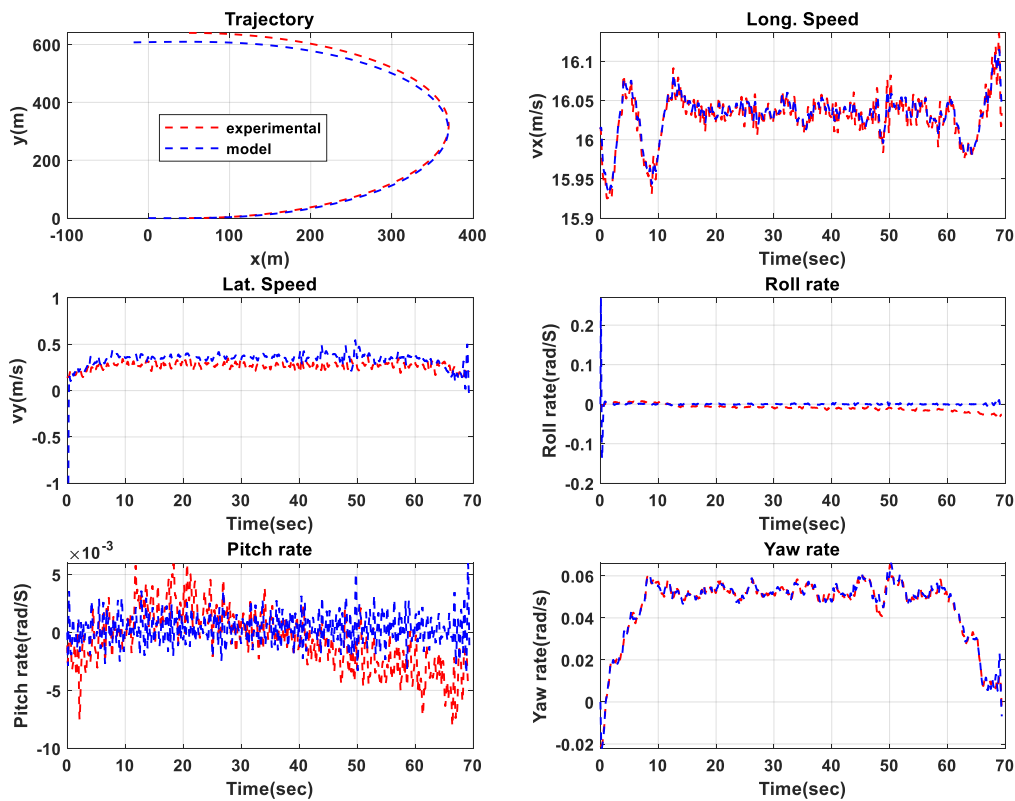


Figure 161 Results comparison between model and experimentation for a circle with radius 320m (Test 2)

- Vehicle accelerating and braking in a straight line

The comparison results of this test scenario are presented in Figure 162. The errors are less than 7% except for the braking manoeuvres where the error in the velocity is going up to 14%. The difference is mainly due to the noise in the experimental values and simplification of the model as compared to the real vehicle. The values for roll, pitch and yaw rate are also following the same trend but there is more noise in the measurements which can explain the gap. It can be concluded from the above Figure 162 that our vehicle model is showing good behaviour in manoeuvres and validated.

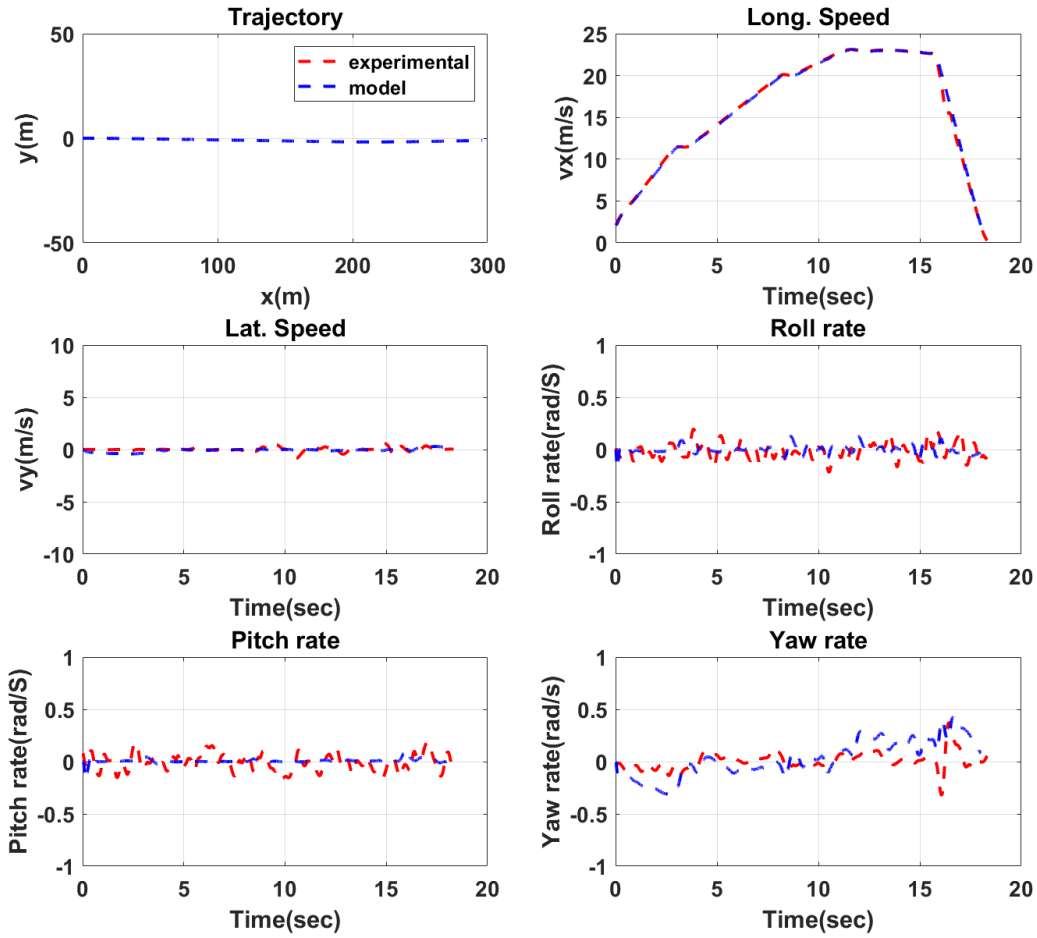


Figure 162 Comparison of speed variables between experiments and model for the vehicle is accelerating and braking

In this section, the experimental validation of FVM (full vehicle model) is presented. The MPT model is validated by presenting the comparison of forces and temperature. The full vehicle model is validated by comparing longitudinal and lateral speed, the roll, pitch and yaw rate and trajectory of the model with experimental results. The relative mean errors of all the parameters are less than 10% as shown in results. This is under the criteria defined for the thesis and in the acceptable range as the magnitude is very small for the absolute values. The difference is mainly due to a few simplifications of the developed model by comparison with a real vehicle with noise in measurements. So we can conclude that our model is exhibiting a comparable dynamic behaviour than the real car.

5.5.2. Experimental validation of rolling resistance estimation

In this section, the experimental validation of observers developed in chapter 4 is presented. In order to validate the observer, the rolling resistance force is compared with the experimental rolling resistance force presented in the previous chapter. The precision of the observer is evaluated by calculating the relative mean estimation errors:

$$\bar{e}_{F_{rri}} = \frac{1}{N} \sum_{i=1}^N \left| \frac{F_{rri}(t_i) - \hat{F}_{rri}(t_i)}{F_{rri}(t_i)} \right| \quad (200)$$

with t_i is counted from the instant when estimated values.

Due to the availability of the single dynamometric wheel on the instrumented vehicle, the reference rolling resistance force is available only for the front right tyre. Therefore validated FVM model is used to calculate rolling resistance forces for the rest of the tyres. The front right tyre force is compared with forces given by dynamometric wheel on various test tracks. The results are presented in Figure 163 and Figure 164. The relative mean error for this comparison is less than 10% for 50 km/h and 80 km/h. This also validates the forces for the rest of the tyres. Therefore it will be used for the calculation of reference rolling resistance for other tyres on the vehicle. The methodology of comparison and estimation is presented in Figure 165.

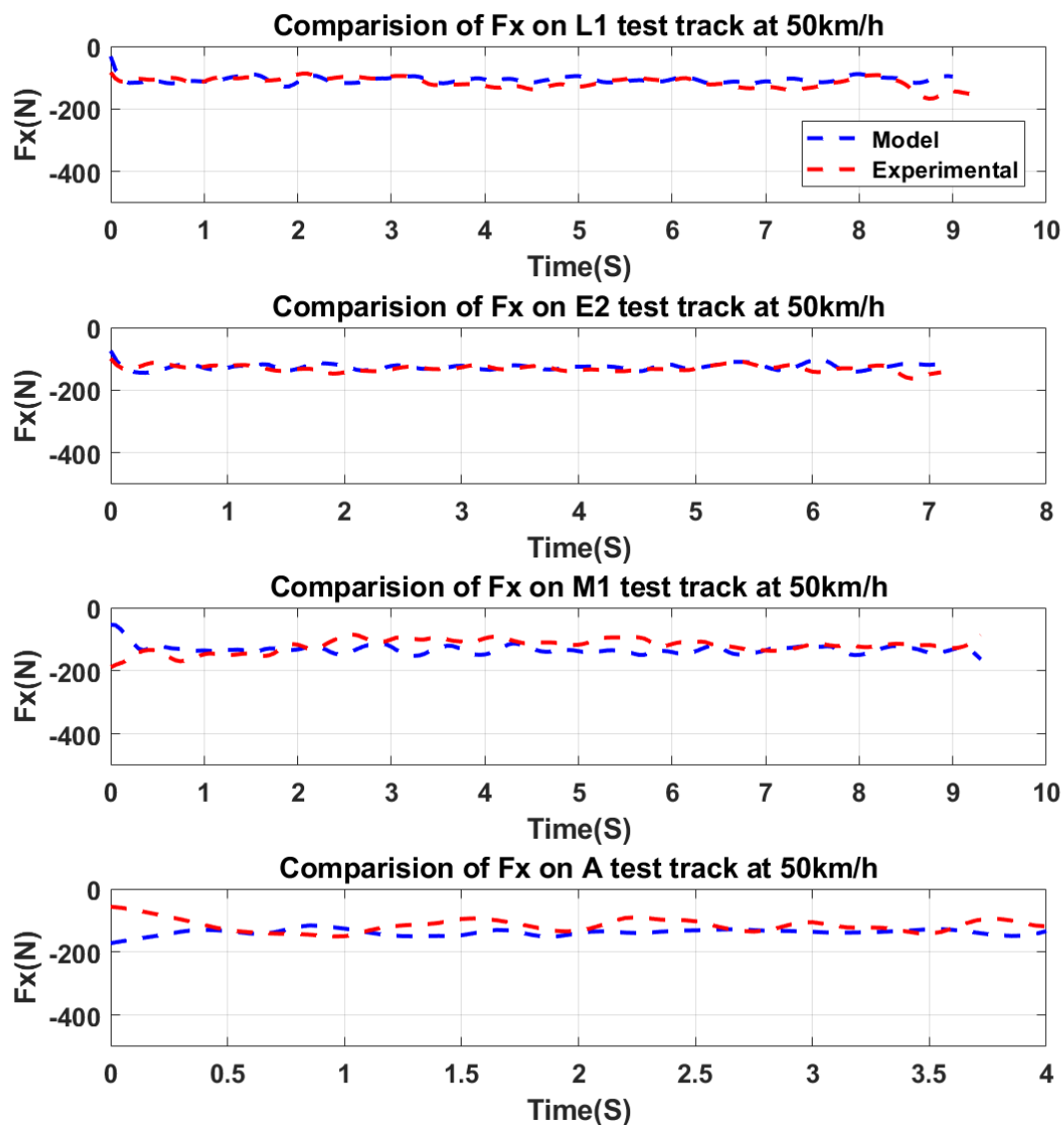


Figure 163 Comparison of longitudinal force between model and experiment for different test tracks at 50 km/h

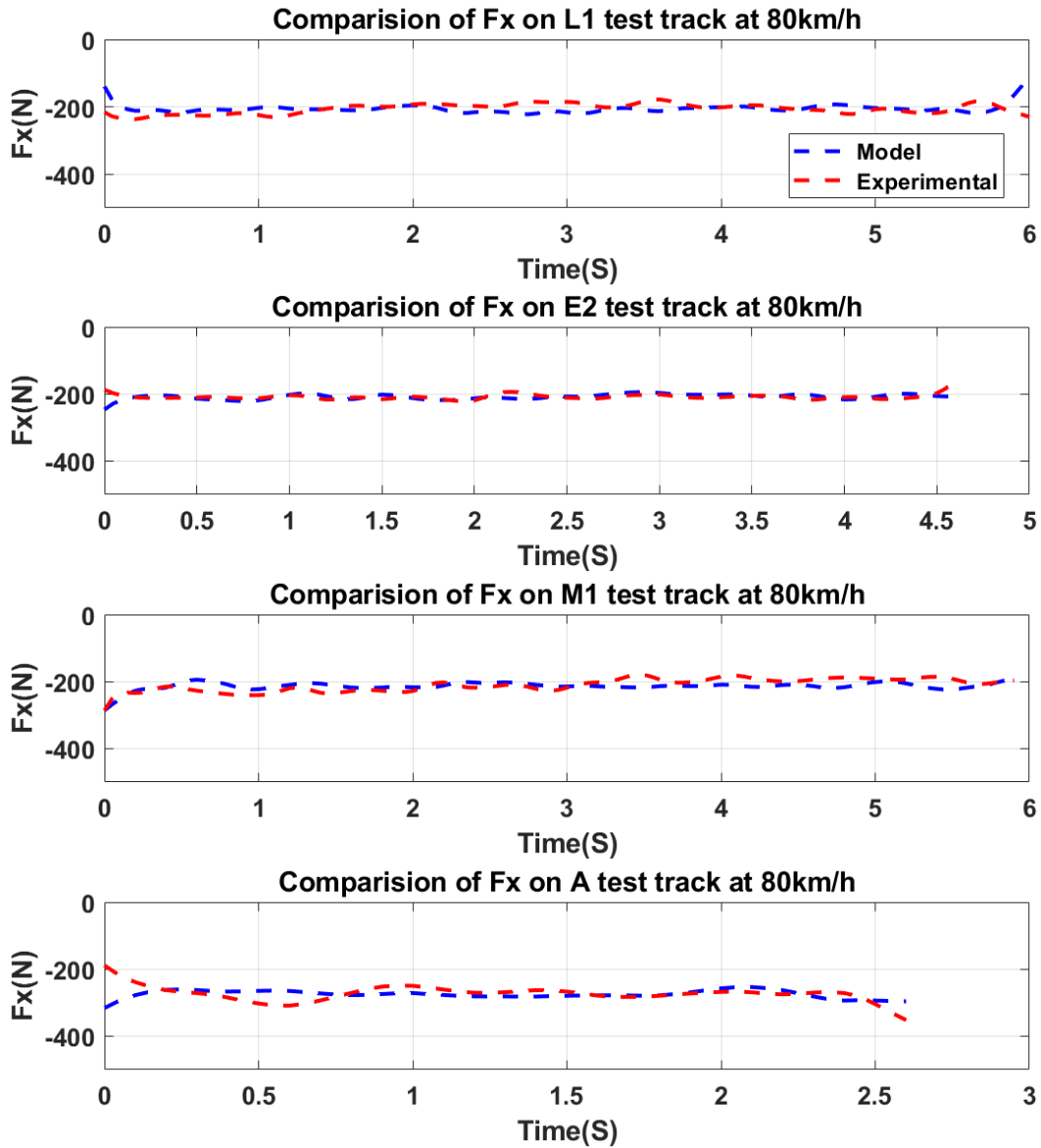


Figure 164 Comparison of longitudinal force between model and experiment for different test tracks at 80 km/h

In order to implement the previous observer on the vehicle, it is necessary to measure the torque applied to the wheel, the angular speed of the wheel and the vehicle speed. The signal is accessible on the data acquisition system. This is an offline validation for the real driving condition in which initial parameters, torque, steering angle and measured velocities are given as input for observers. The scenarios for validation are presented in Table 11. Only two estimations of each simulation scenarios are presented here. The observer is compared with the real value of F_{rr} for each case. The precision of the observer is evaluated by calculating the relative mean estimation errors as shown in equation (200). The other results can be found in appendix H.

During numerical validation, the tyre effective radius was available in data but in experiments, it is difficult to measure effective radius for all the tyres due to complex installation and no physical sensor is able to measure it directly. Therefore, in addition to the estimation of rolling resistance forces, the tyre effective radius is also estimated as unknown input.

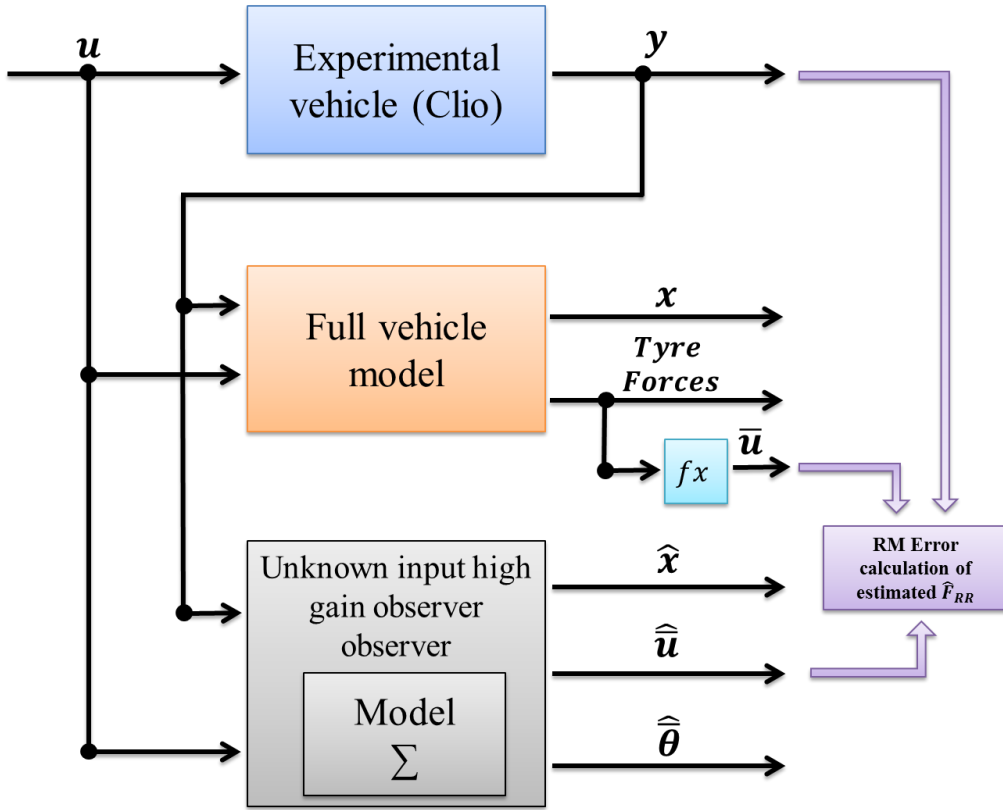


Figure 165 Methodology of estimation and comparison

5.5.2.1. Estimation of tyre rolling resistance for regular systems

The observer presented in section 4.2 is validated here. It is based on the complete vehicle model. The state variables of the observer are represented by a vector \hat{x} as follows:

$$\hat{x} = [\hat{w}_1, \hat{w}_2, \hat{w}_3, \hat{w}_4, \hat{v}_x, \hat{v}_y, \hat{\psi}, \hat{\phi}, \hat{\theta}, \hat{\psi}, \hat{\phi}, \hat{\theta}]^T \quad (201)$$

With the variables $\hat{w}_1, \hat{w}_2, \hat{w}_3, \hat{w}_4$ as reconstructed angular speed, \hat{v}_x, \hat{v}_y are reconstructed longitudinal and lateral speeds, $\hat{\psi}, \hat{\phi}, \hat{\theta}, \hat{\psi}, \hat{\phi}, \hat{\theta}$ represents yaw pitch and roll rate and angle respectively.

The rolling resistance and effective tyre radius are considered as unknown input here.

$$\hat{u} = \hat{f}(\hat{C}_{rr1}, \hat{C}_{rr2}, \hat{C}_{rr3}, \hat{C}_{rr4}, \hat{R}_{fl}, \hat{R}_{fr}, \hat{R}_{rl}, \hat{R}_{rr})^T \quad (202)$$

Also, the measured outputs are:

$$y = (w_1, w_2, w_3, w_4, v_x, v_y, \psi, \phi)^T \quad (203)$$

The observability condition is satisfied. The same initial conditions are used for both model and experiments. The initial conditions for the observer are:

$$\hat{x}(0) = \begin{bmatrix} \hat{w}_1(0), \hat{w}_2(0), \hat{w}_3(0), \hat{w}_4(0), \hat{v}_x(0), \hat{v}_y(0), \hat{\psi}(0), \hat{\phi}(0), \hat{\theta}(0), 0, 0, 0 \\ 0, 0, 0, 0, 10, 0.290, 0.290, 0.290, 0.290, 5 \end{bmatrix}^T \quad (204)$$

- Case 1: Car moving in a straight line at 50 km/h.

The comparisons of observer results with experimental results for instrumented vehicle moving in a straight line are analysed here. The good reconstruction of state variables is done by the developed observer with a relative mean error less than 1% as shown in Figure 166. The estimation of rolling resistance for each tyre is presented in Figure 167. The relative mean error of rolling resistance estimation for each wheel is less than 10% (see Figure 168). Some peaks in the relative mean error are seen which is due to the noise in the data. This validates the observer for the straight line conditions as it satisfied the criteria of validation in equation (120). The adaptive gain and zoom on its variation during simulation is also presented in Figure 169. The comparison of the estimated tyre radius with measured tyre radius is also presented in Figure 170. The relative mean estimation error for the tyre radius is less than 1%. It is concluded from the results that the developed observers are validated experimentally for the straight-line.

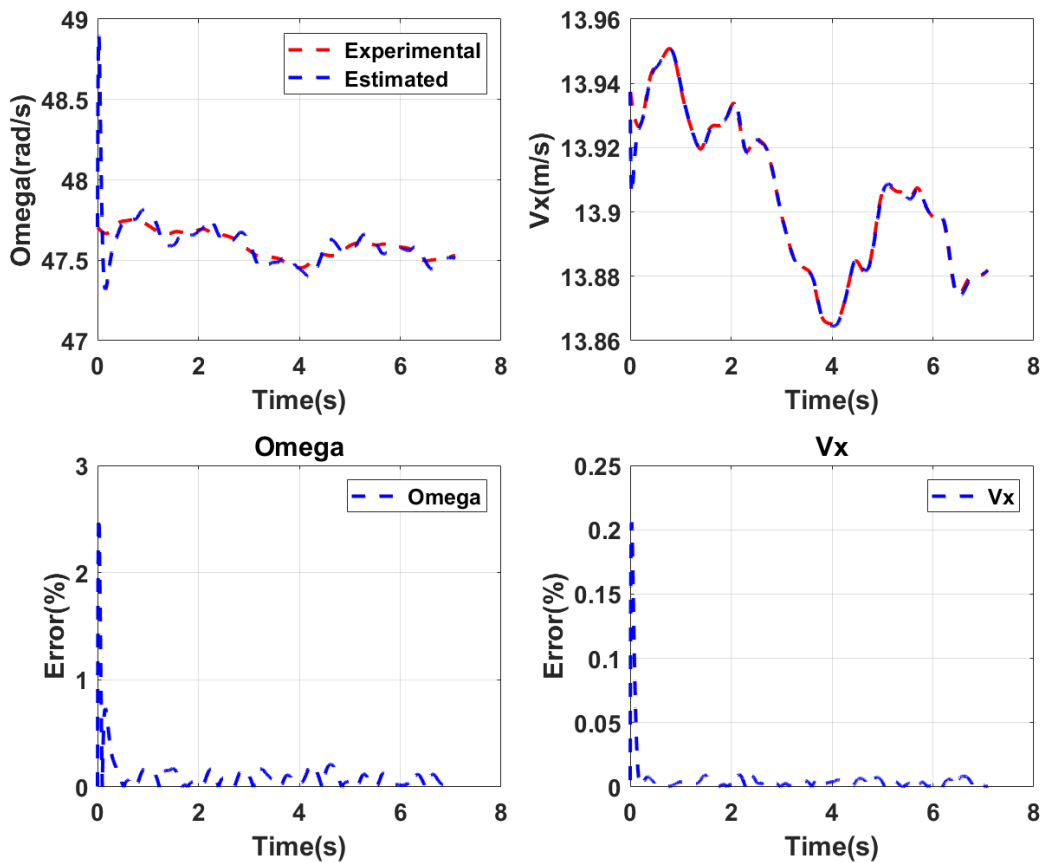


Figure 166 State variable comparison and error between experimental results and observer (straight line)

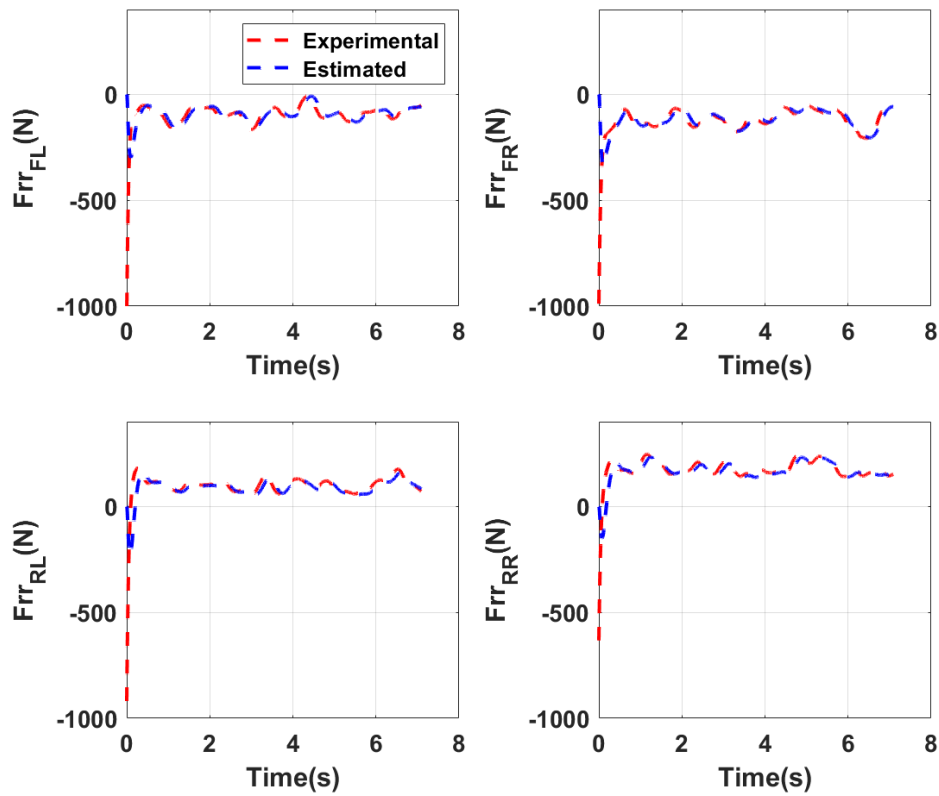


Figure 167 Comparison between experimental and estimated rolling resistance force (Straight line)

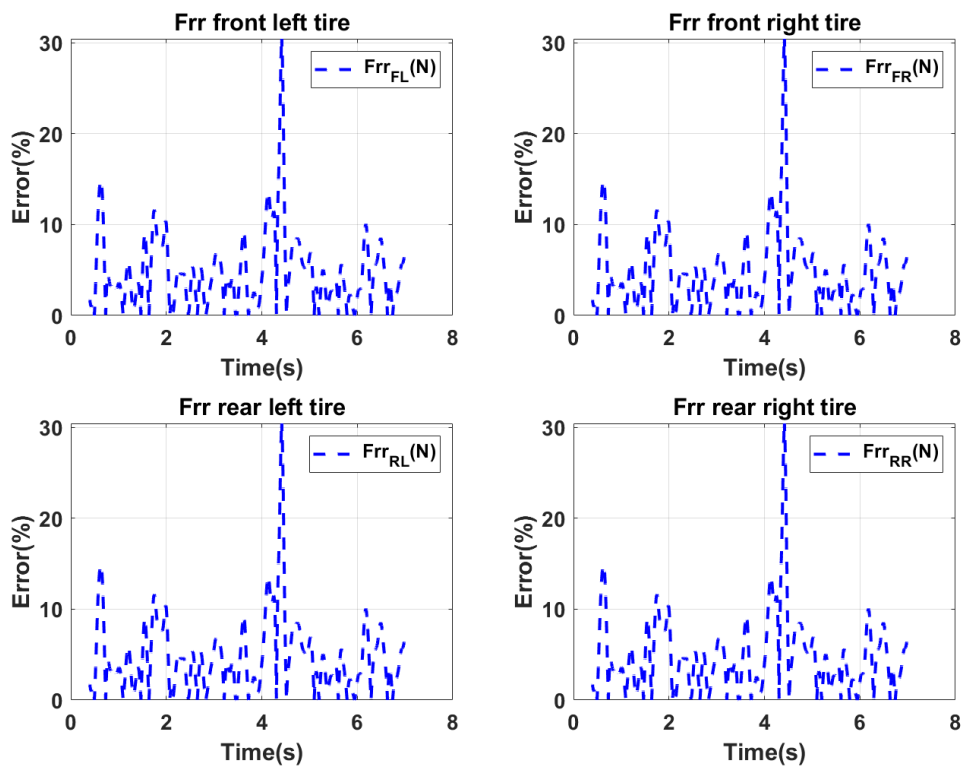


Figure 168 Estimation error results of observer estimation (Straight line)

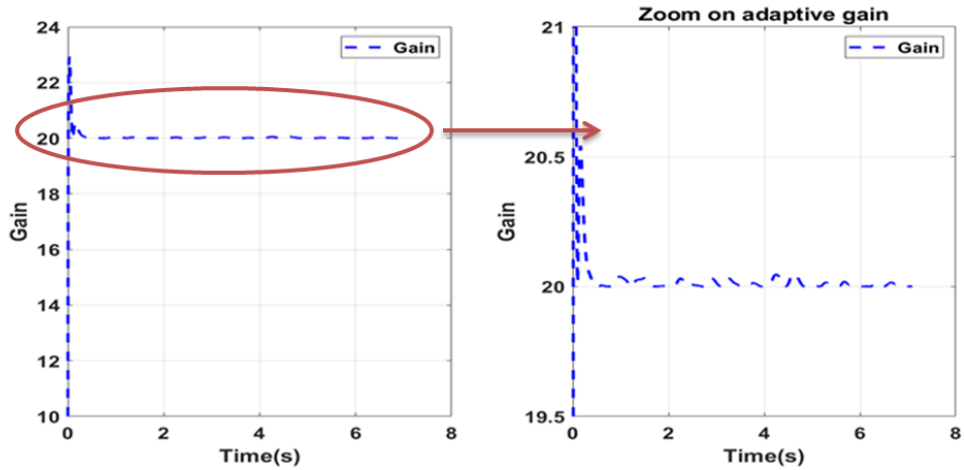


Figure 169 Adaptive gain and zoom on adaptive gain (straight line)

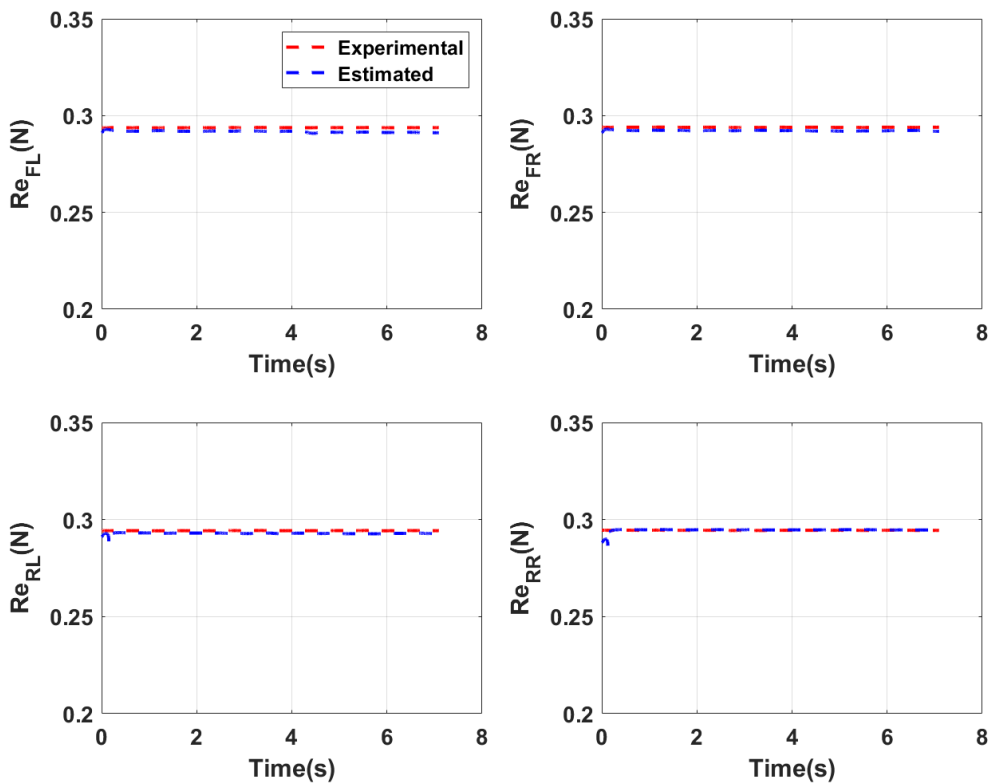


Figure 170 Comparison between experimental and estimated tyre effective radius (Straight line)

- Case 2: Car moving in constant radius at 320m at 80 km/h

The comparisons of observer results with experimental results for instrumented vehicle moving in a curve at constant speed are presented here. The good reconstruction of state variables is done by the developed observer with a relative mean error less than 2% as shown in Figure 171 and Figure 172. The comparison of estimation of rolling resistance with experimental values for each tyre is presented in Figure 173. The relative mean error of rolling resistance estimation for each wheel is less than 10% (see Figure 174). This validated the observer for curve manoeuvres at a constant speed as it satisfies the criteria of validation i.e. relative mean errors less than 10%. The adaptive gain and zoom on its

variation during simulation is also presented in Figure 175. The comparison of the estimated tyre radius with measured tyre radius is also presented in Figure 176, the relative mean estimation error less than 5%. It is concluded from the results that the developed observers are validated experimentally for the curve manoeuvres.

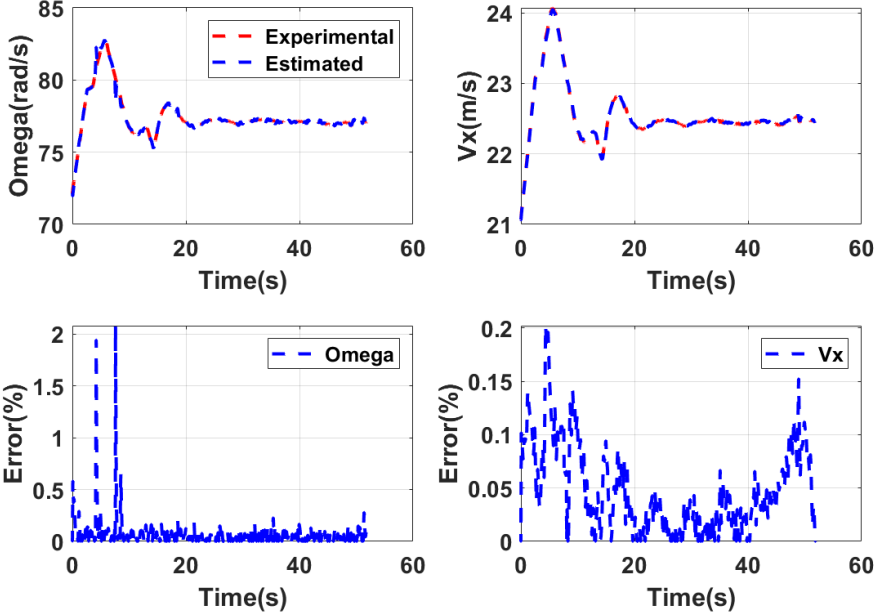


Figure 171 State variable comparison and error between experimental results and observer (curve with 320m radius at 80km/h)

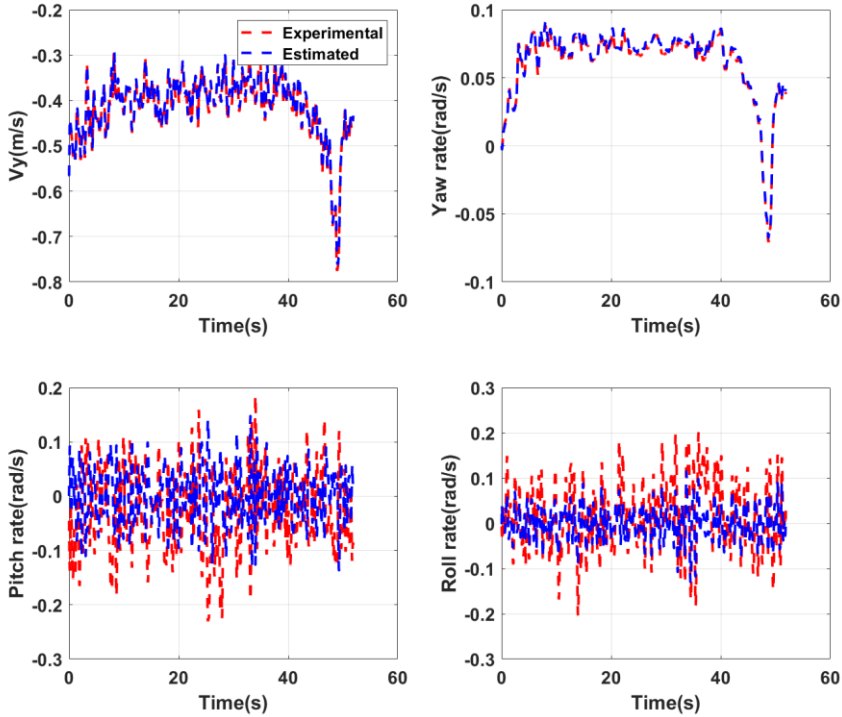


Figure 172 State variable comparison and error between experimental results and observer (curve with 320m radius at 80km/h)

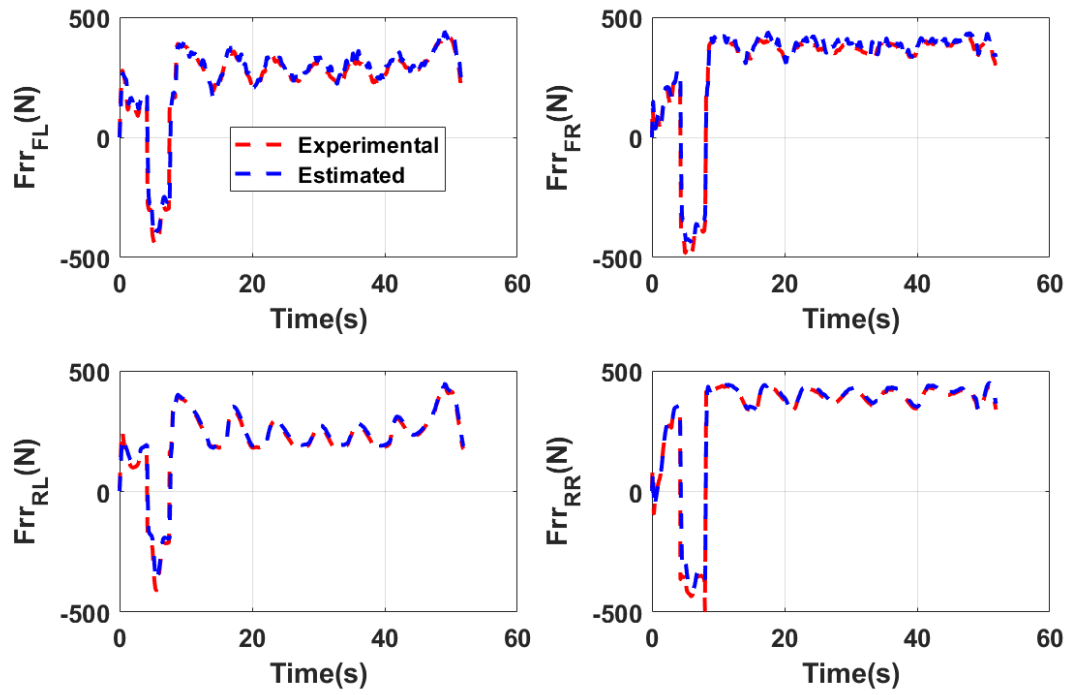


Figure 173 Comparison between experimental and estimated rolling resistance force observer (curve with 320m radius at 80 km/h)

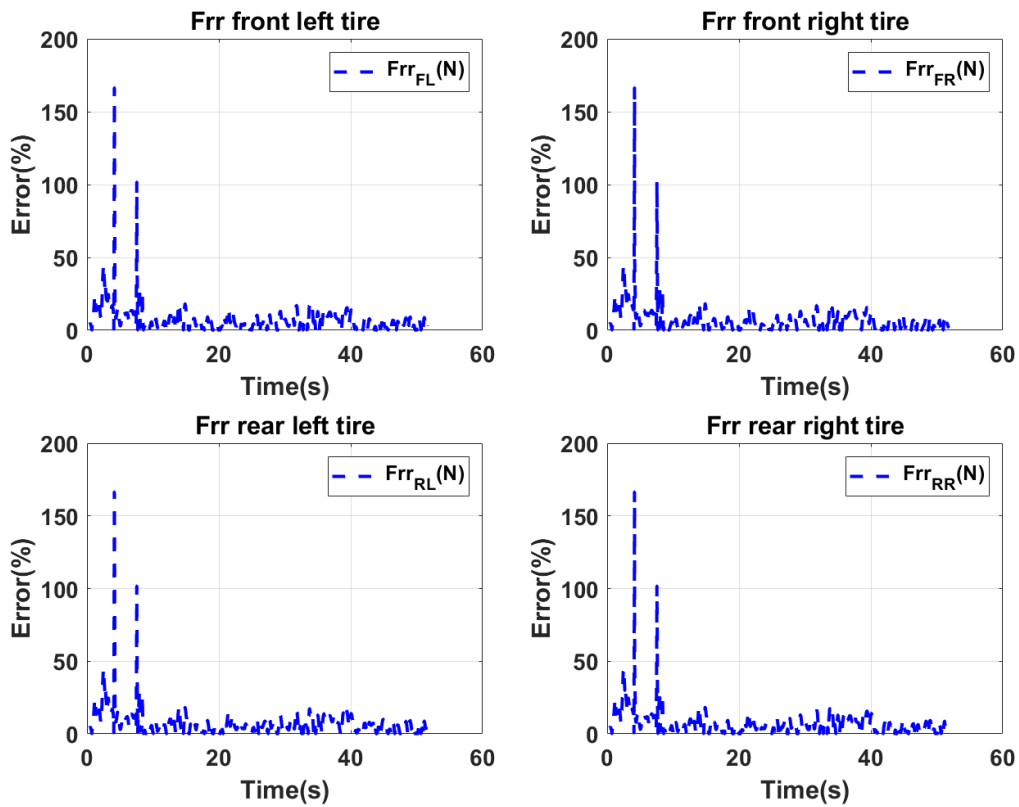


Figure 174 Estimation error results of observer estimation observer (curve with 320m radius at 80 km/h)

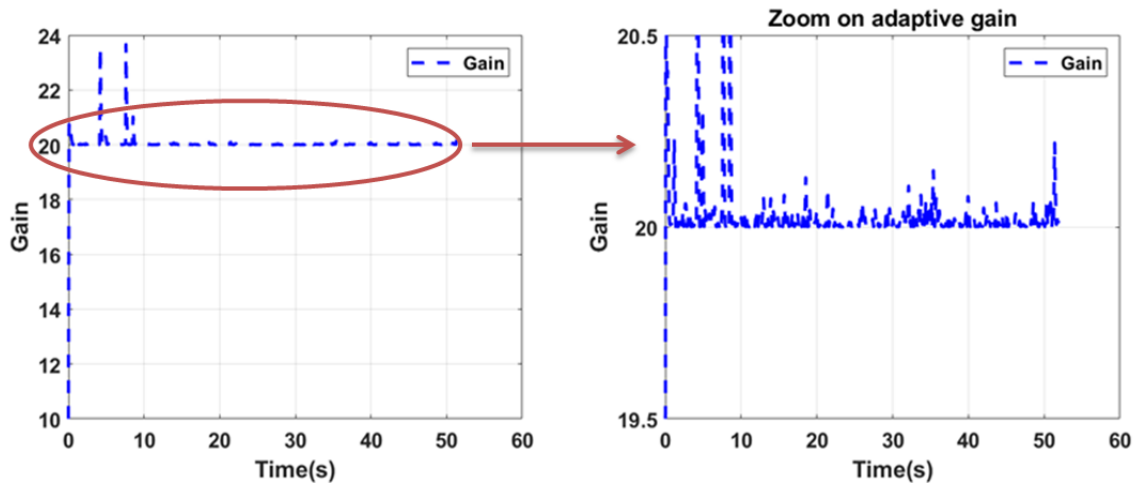


Figure 175 Adaptive gain and zoom on the adaptive gain observer (curve with 320m radius at 80 km/h)

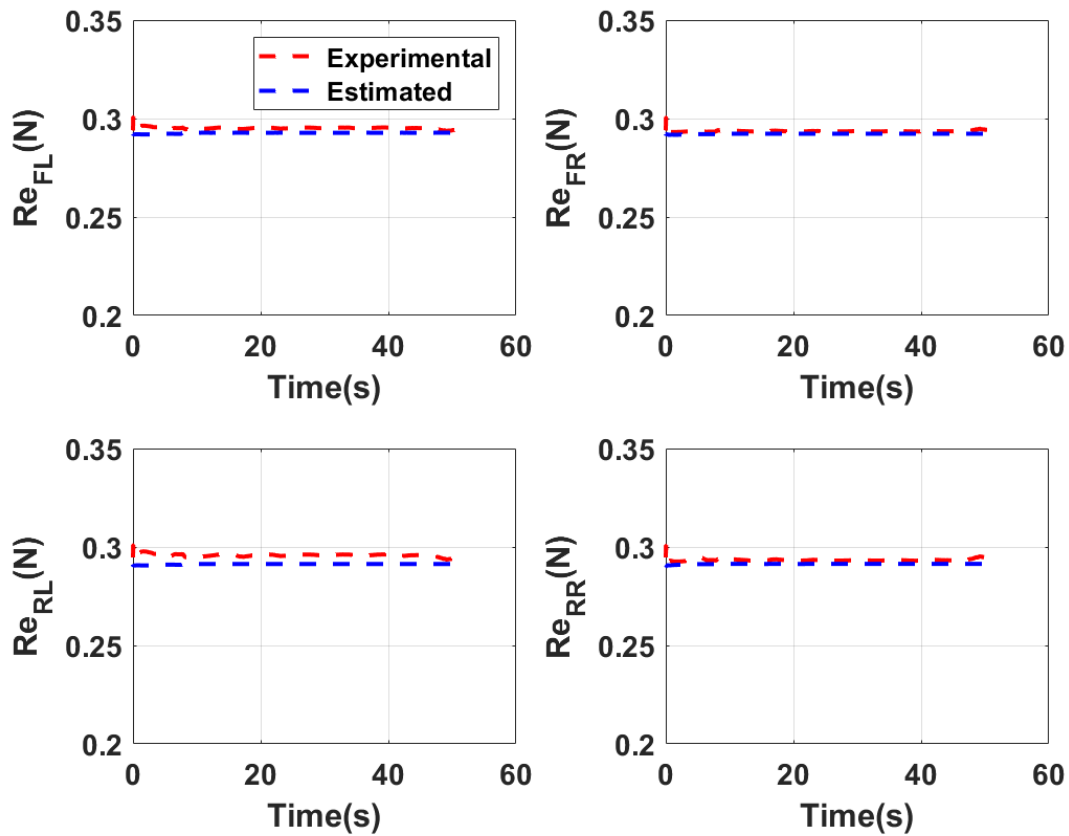


Figure 176 Comparison between experimental and estimated tyre effective radius (curve with 320m radius at 80 km/h)

5.5.2.2. Estimation of tyre rolling resistance for the singular perturbed system

In this section, the full vehicle model is considered as the singular perturbed system. This is mainly due to the consideration of tyre surface and carcass temperature; this has slow dynamics.

The state vector is defined as

$$\hat{x} = [\hat{T}_{tread}, \hat{T}_{carcass}, \hat{w}_1, \hat{w}_2, \hat{w}_3, \hat{w}_4, \hat{v}_x, \hat{v}_y, \hat{\psi}, \hat{\phi}, \hat{\theta}, \hat{\dot{\psi}}, \hat{\dot{\phi}}, \hat{\dot{\theta}}]^T \quad (205)$$

Where the variables $\hat{T}_{tread}, \hat{T}_{carcass}$ are state estimation of tyre surface and carcass temperature respectively, With the variables $\hat{w}_1, \hat{w}_2, \hat{w}_3, \hat{w}_4$ as reconstructed angular speed, \hat{v}_x, \hat{v}_y are reconstructed longitudinal and lateral speeds, $\hat{\psi}, \hat{\phi}, \hat{\theta}, \hat{\dot{\psi}}, \hat{\dot{\phi}}, \hat{\dot{\theta}}$ represents yaw pitch and roll rate and angle respectively.

The rolling resistance and effective tyre radius are considered as unknown input here.

$$\hat{u} = \hat{f}(\hat{C}_{rr1}, \hat{C}_{rr2}, \hat{C}_{rr3}, \hat{C}_{rr4}, \hat{R}_{fl}, \hat{R}_{fr}, \hat{R}_{rl}, \hat{R}_{rr})^T \quad (206)$$

Also, the measured outputs are:

$$y = (w_1, w_2, w_3, w_4, v_x, v_y, \psi, \phi)^T \quad (207)$$

The initial conditions for the observer are

$$\hat{x}(0) = \begin{bmatrix} \hat{w}_1(0), \hat{w}_2(0), \hat{w}_3(0), \hat{w}_4(0), \hat{v}_x(0), \hat{v}_y(0), \hat{\psi}(0), \hat{\phi}(0), \hat{\theta}(0), 0, 0, 0 \\ , 0, 0, 0, 0, 10, 0.290, 0.290, 0.290, 0.290, 5, \\ 273, 300, 1, 273, 300, 1, 273, 300, 1, 273, 300, 1 \end{bmatrix}^T \quad (208)$$

- Case 1: Car moving in a straight line at 50 km/h.

The comparisons of observer results with experimental values for case 1 are analysed here. In Figure 177 the results of slow dynamics are presented. The tyre surface temperature is estimated with the adaptive high gain observer. The relative mean error is less than 1% for the tyre surface temperature. In Figure 178 the results of fast dynamics are presented. There is a good reconstruction of state variables by the developed observer. It is confirmed with a relative mean error which is less than 1% as shown in Figure 178. The estimation of rolling resistance for each tyre is presented in Figure 179. The relative mean error of rolling resistance estimation for each wheel is less than 10% (see Figure 180). The adaptive gain and its variation during simulation are also presented in Figure 181. The comparison of the estimated tyre radius with measured tyre radius is also presented in Figure 182. The relative mean estimation error for the tyre radius is less than 1%. The comparison results in term of relative mean error are under the criteria of validation, therefore it is concluded from the results that the developed observers are validated experimentally for the straight-line.

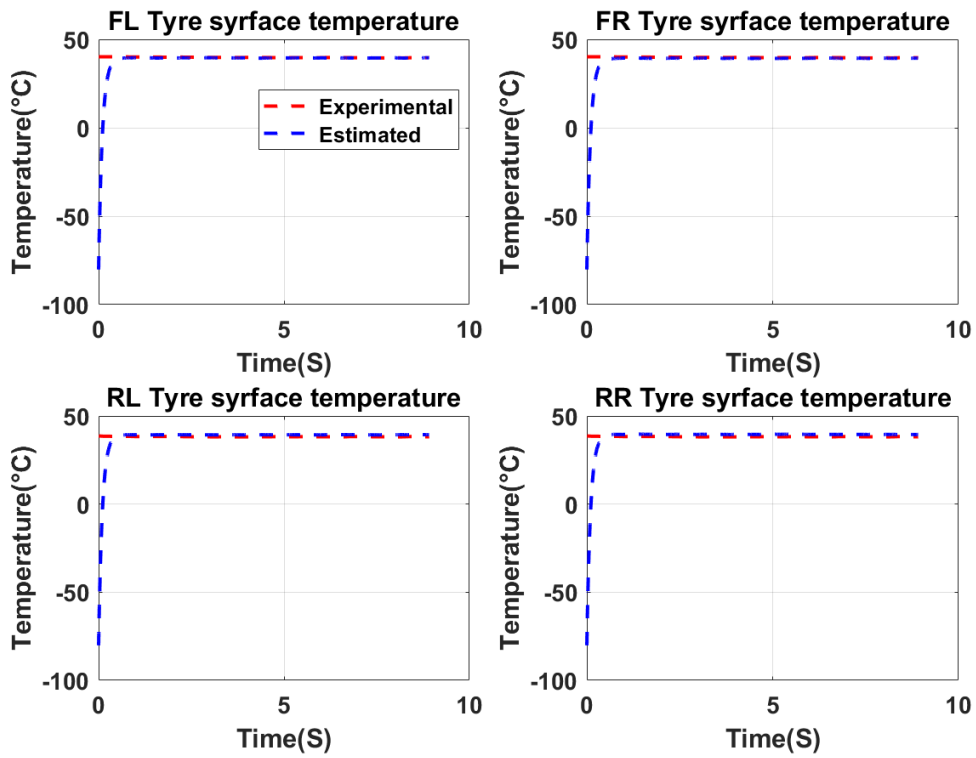


Figure 177 Tyre surface temperature state estimation comparison and percentage relative mean error (Case 1: straight line)

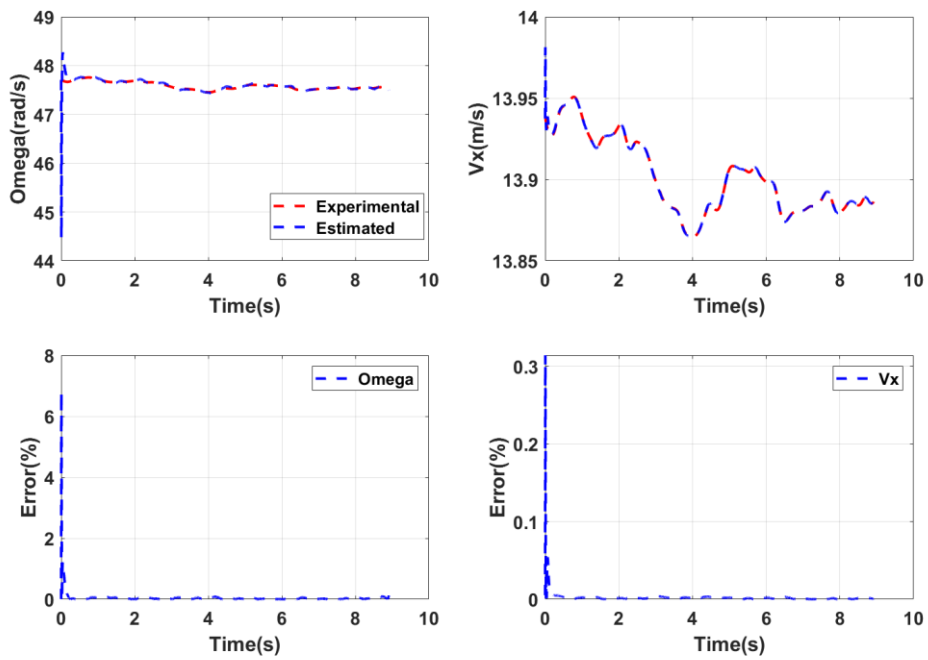


Figure 178 State variable comparison and error between experimental results and observer (straight line)

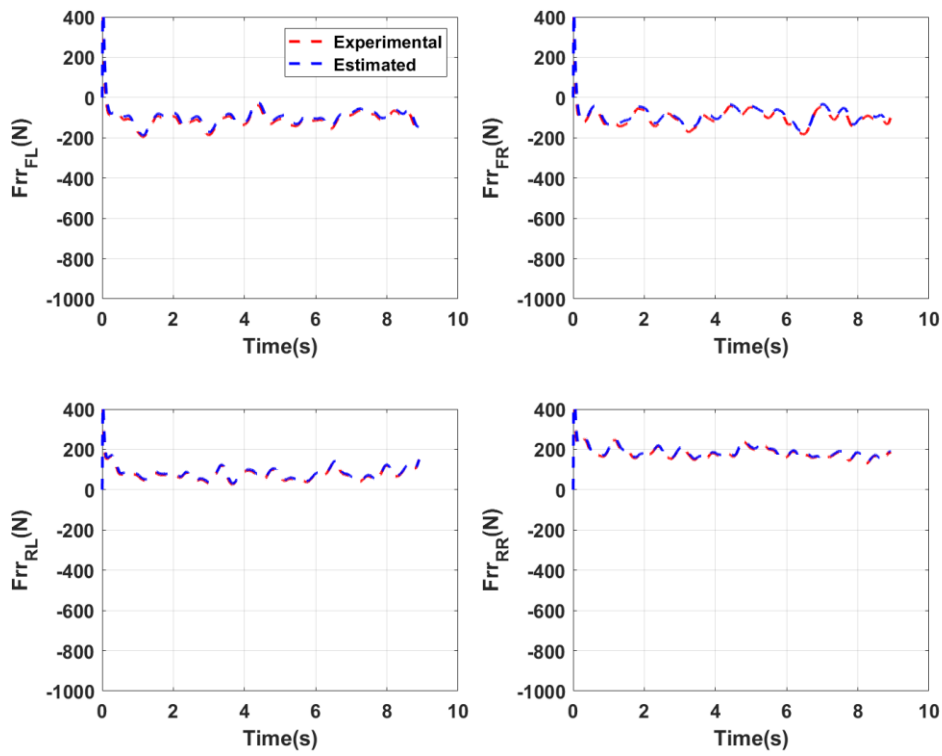


Figure 179 Comparison between experimental and estimated rolling resistance force (Straight line)

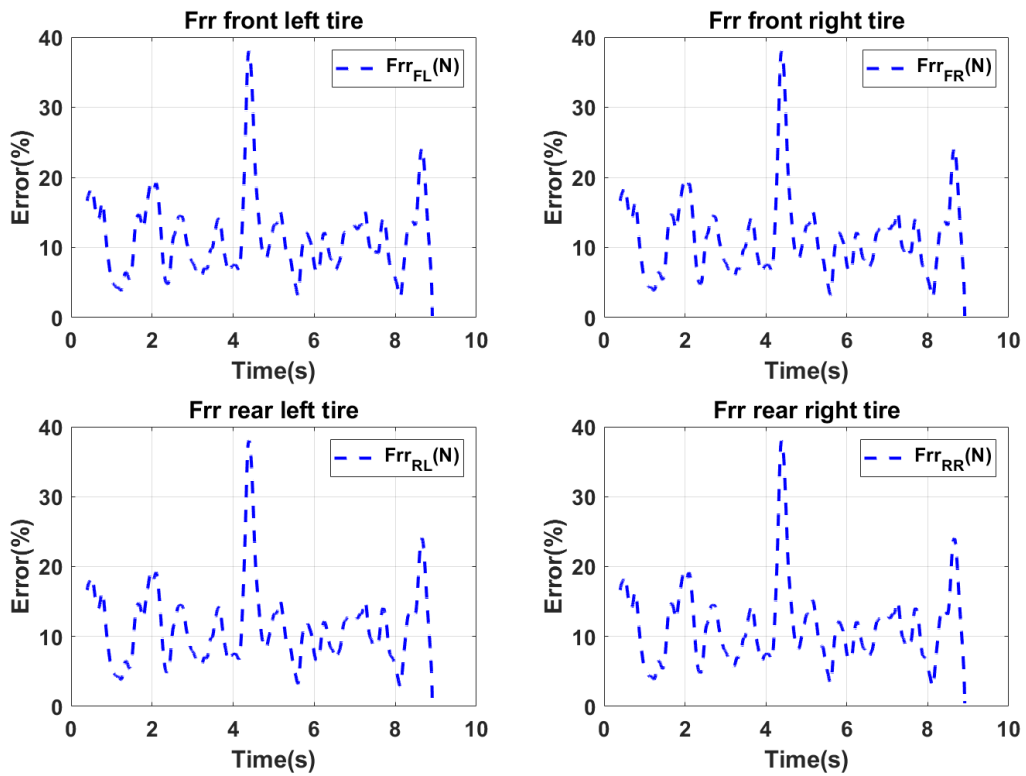


Figure 180 Estimation error results of observer estimation (Straight line)

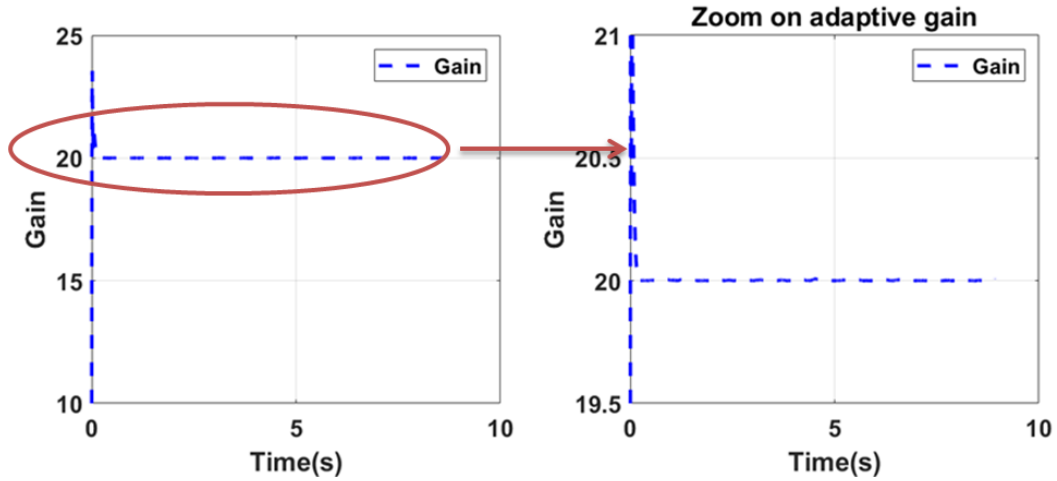


Figure 181 Adaptive gain and zoom on adaptive gain (straight line)

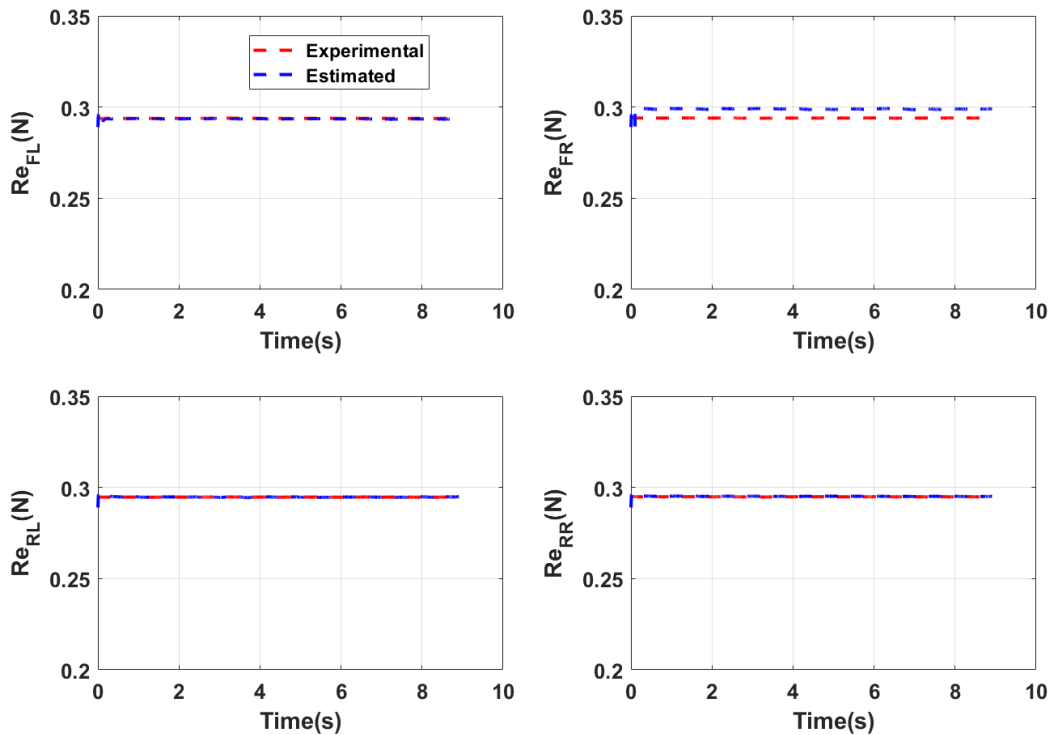


Figure 182 Comparison between experimental and estimated tyre effective radius (Straight line)

- Case 2: Car moving in constant radius at 320m at 80 km/h

The comparisons of observer results with experimental values for case 2 are analysed here. In Figure 183 the results of slow dynamics are presented. The tyre surface temperature is estimated with the adaptive high gain observer. The relative mean error is less than 1% for the tyre surface temperature. In Figure 184 the results of fast dynamics are presented. There is a good reconstruction of state variables by the developed observer. It is confirmed with a relative mean error which is less than 0.5% as shown in Figure 184 and Figure 185. The estimation of rolling resistance for each tyre is presented in Figure 186. The relative mean error of rolling resistance estimation for each wheel is less than 10% (see Figure 187). The adaptive gain and its variation during simulation are also presented in Figure

189. The comparison of the estimated tyre radius with measured tyre radius is also presented in Figure 188; the relative mean estimation error for the tyre radius is less than 1%. The comparison results in term of relative mean error are under the criteria of validation, therefore it is concluded from the results that the developed observers are validated experimentally for the cornering manoeuvres.

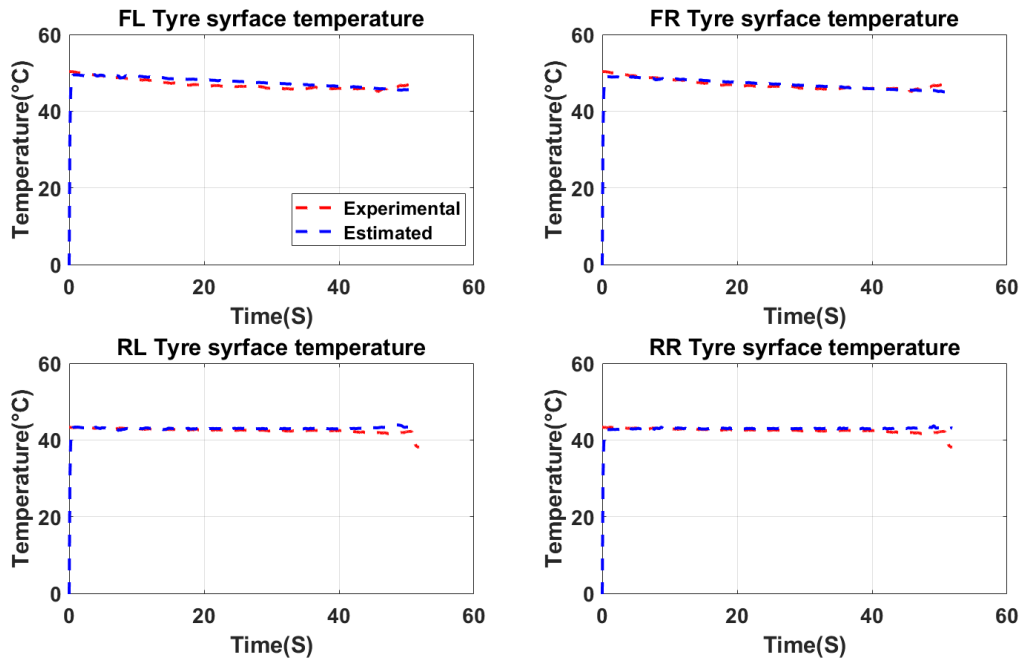


Figure 183 Tyre surface temperature state estimation comparison and percentage relative mean error (curve with 320m radius at 80 km/h)

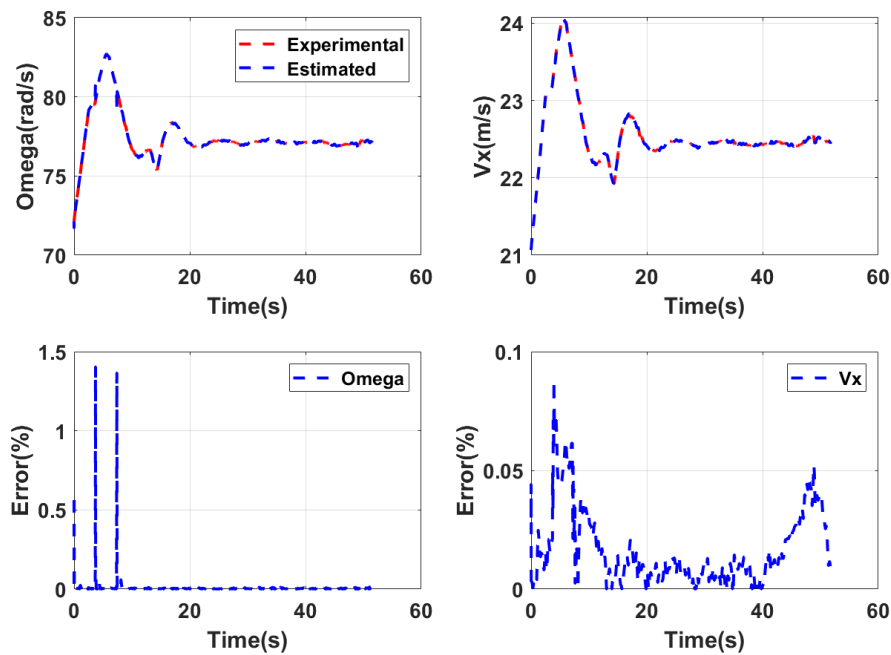


Figure 184 State variable comparison and error between experimental results and observer (curve with 320m radius at 80 km/h)

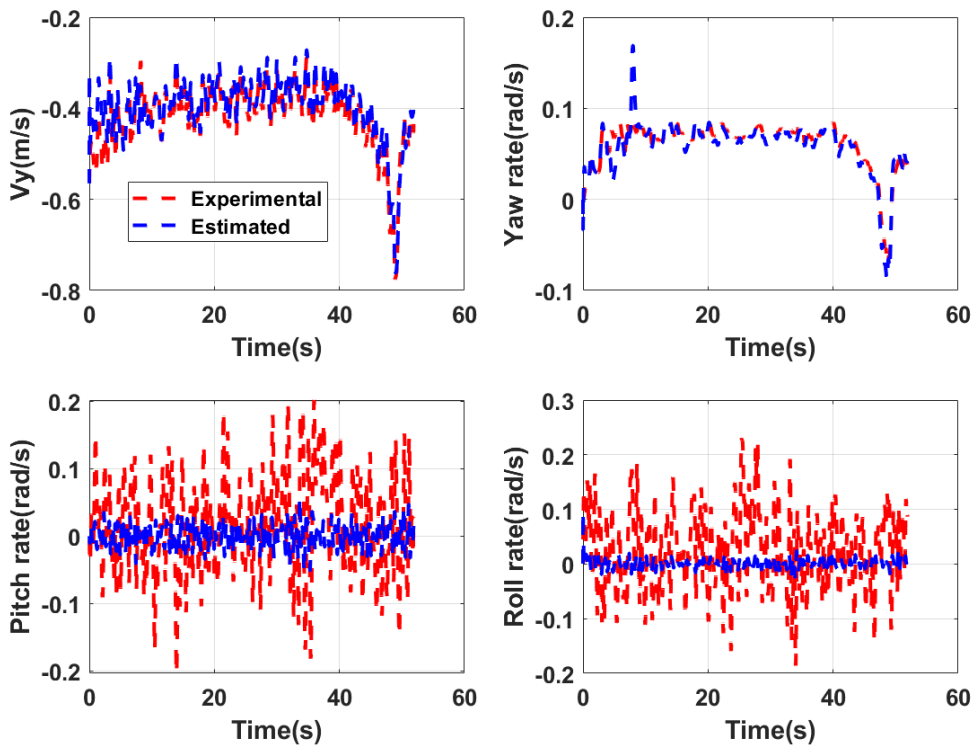


Figure 185 State variable comparison and error between experimental results and observer (curve with 320m radius at 80 km/h)

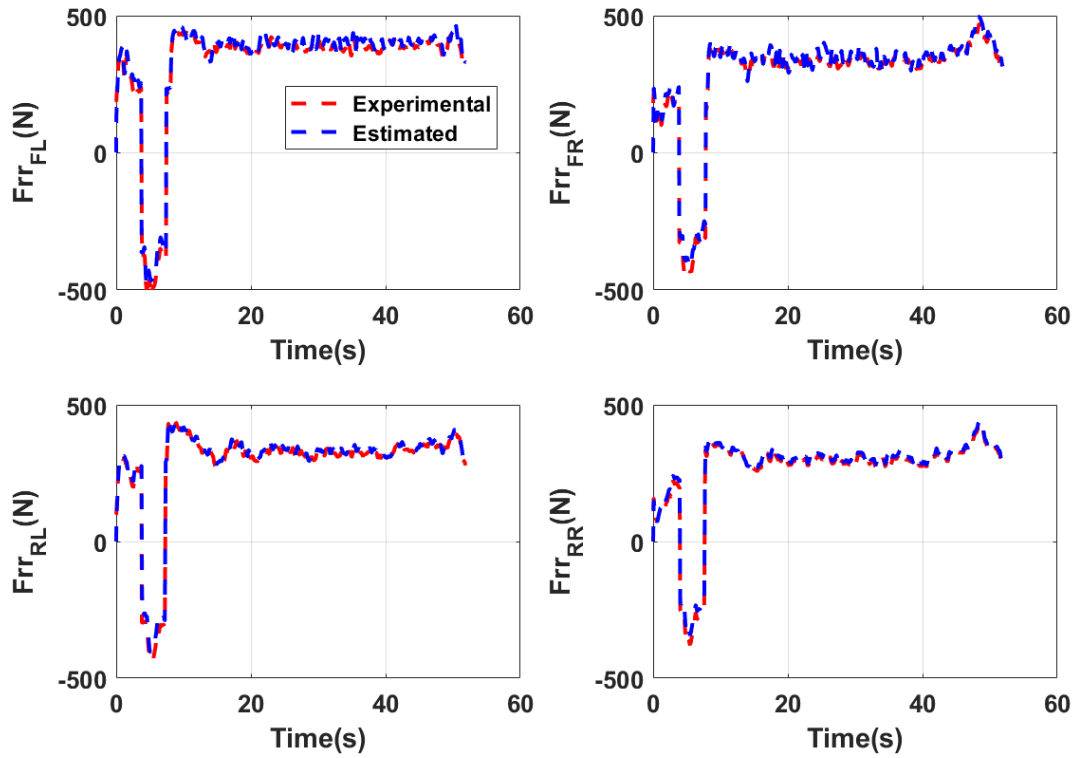


Figure 186 Comparison between experimental and estimated rolling resistance force observer (curve with 320m radius at 80 km/h)

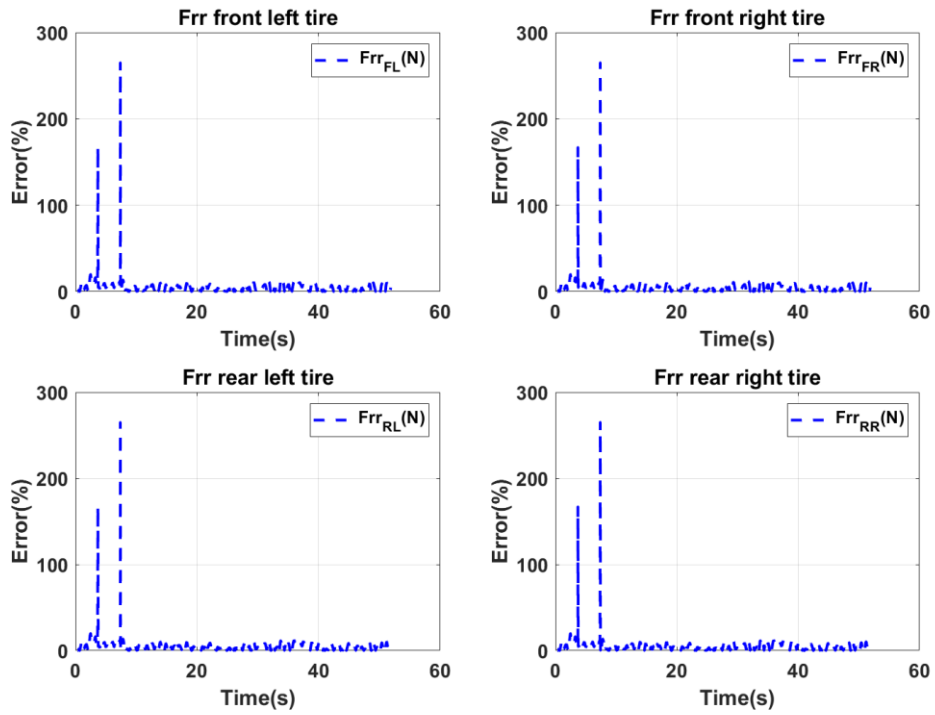


Figure 187 Estimation error results of observer estimation observer (curve with 320m radius at 80 km/h)

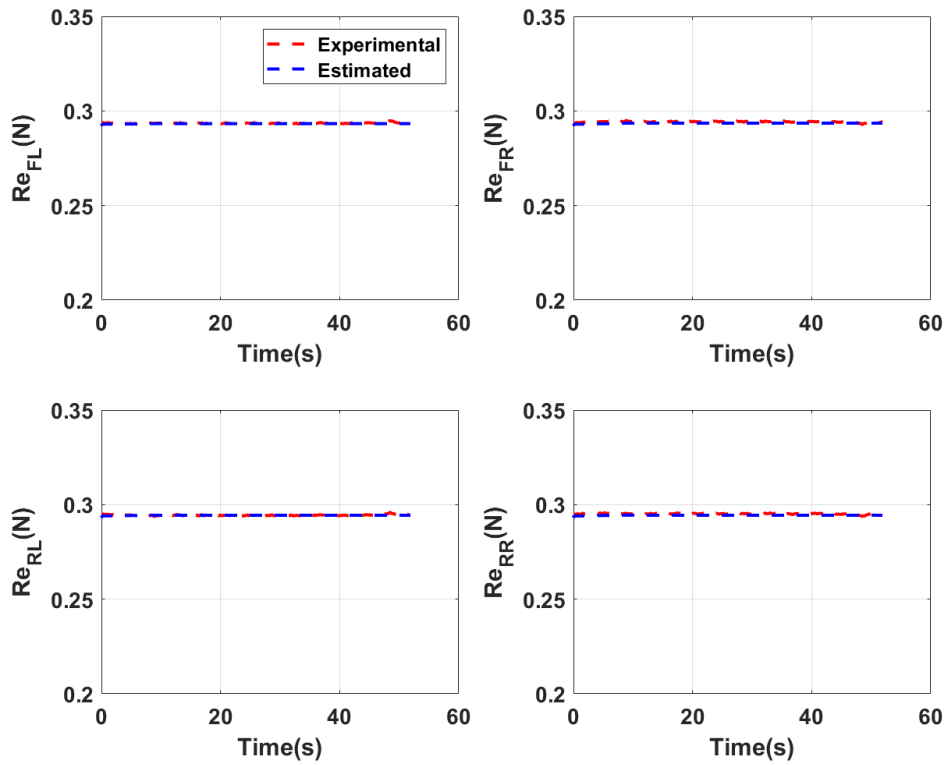


Figure 188 Comparison between experimental and estimated tyre effective radius (curve with 320m radius at 80 km/h)

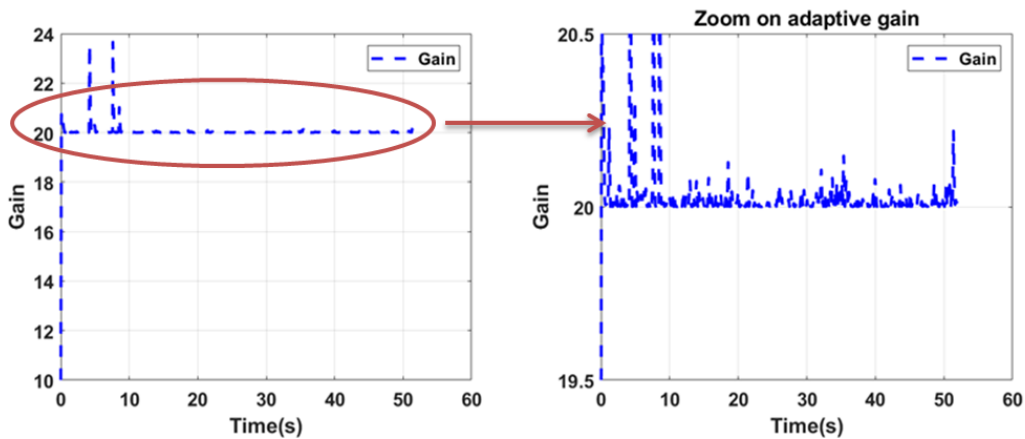


Figure 189 Adaptive gain and zoom on the adaptive gain of the observer (curve with 320m radius at 80 km/h)

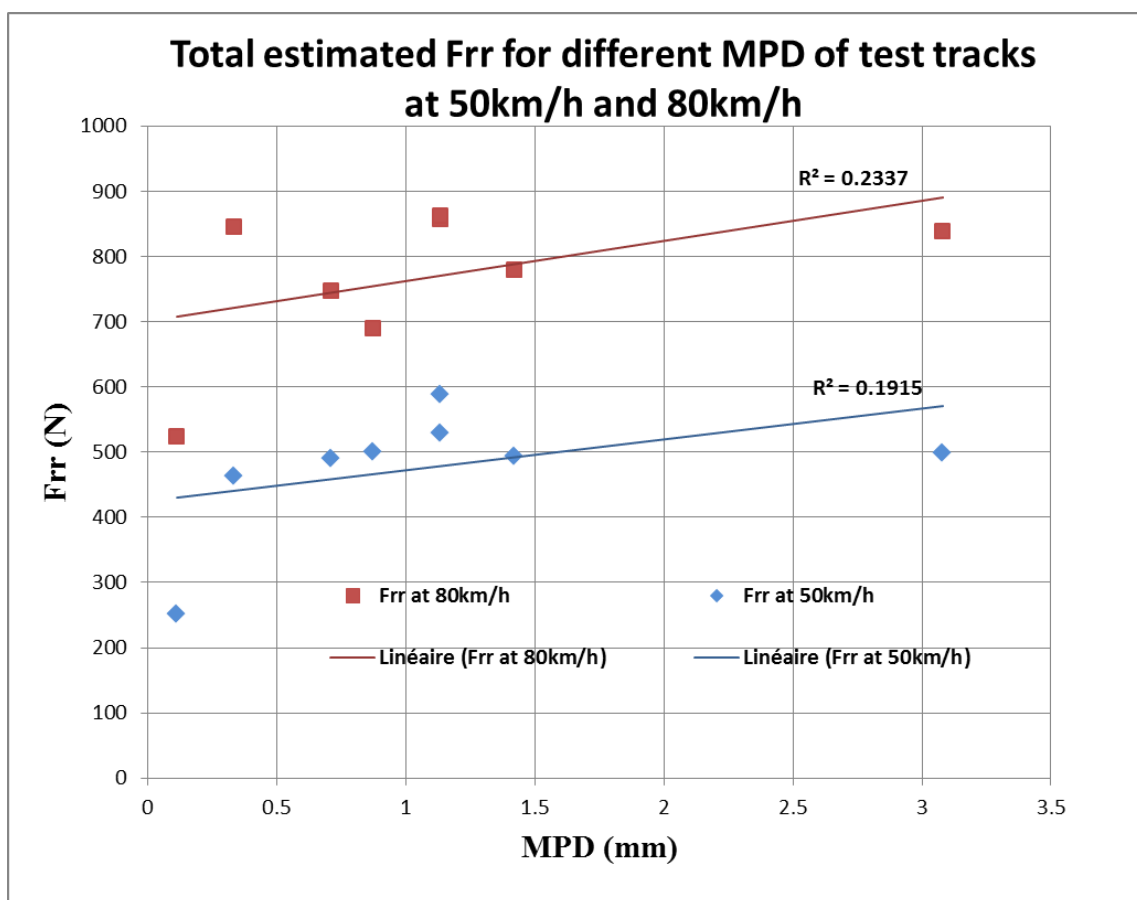


Figure 190 The total mean estimated rolling resistance for different test tracks at a different speed

The impact of road roughness was presented in section 6.3 and concluded on an increase of rolling resistance with an increase in road roughness. In order to validate the impact of road roughness on rolling resistance, the tyre rolling resistance is estimated for different test tracks with the help of developed observer. The different road profiles are also given as input with other parameters to estimate the rolling resistance. The estimated mean rolling resistance of complete vehicle is calculated for different test tracks and speed. It is presented in Figure 190. It validates the impact of speed on rolling resistance as it increases with increase in the speed. It also validates the impact of road roughness considered by the developed observer. The rolling resistance increases with an increase in road roughness. The regression coefficients are 0.19 (resp. 0.23) at 50 km/h (resp. 80 km/h) (see

Figure 190). The regression is indeed weak because there are many external factors on test tracks which can contribute to rolling resistance (such as degradation of test track due to old age, dust or temperature of test track etc.) but the general trend of the curve is increasing. The normalised estimated mean Crr (see Figure 191) is also compared with the trend obtained during experiments (see Figure 114 and Figure 115). Both curves seem to show a trend of increase in Crr with an increase in road roughness. Nevertheless, these results need to be confirmed by considering higher road roughness values.

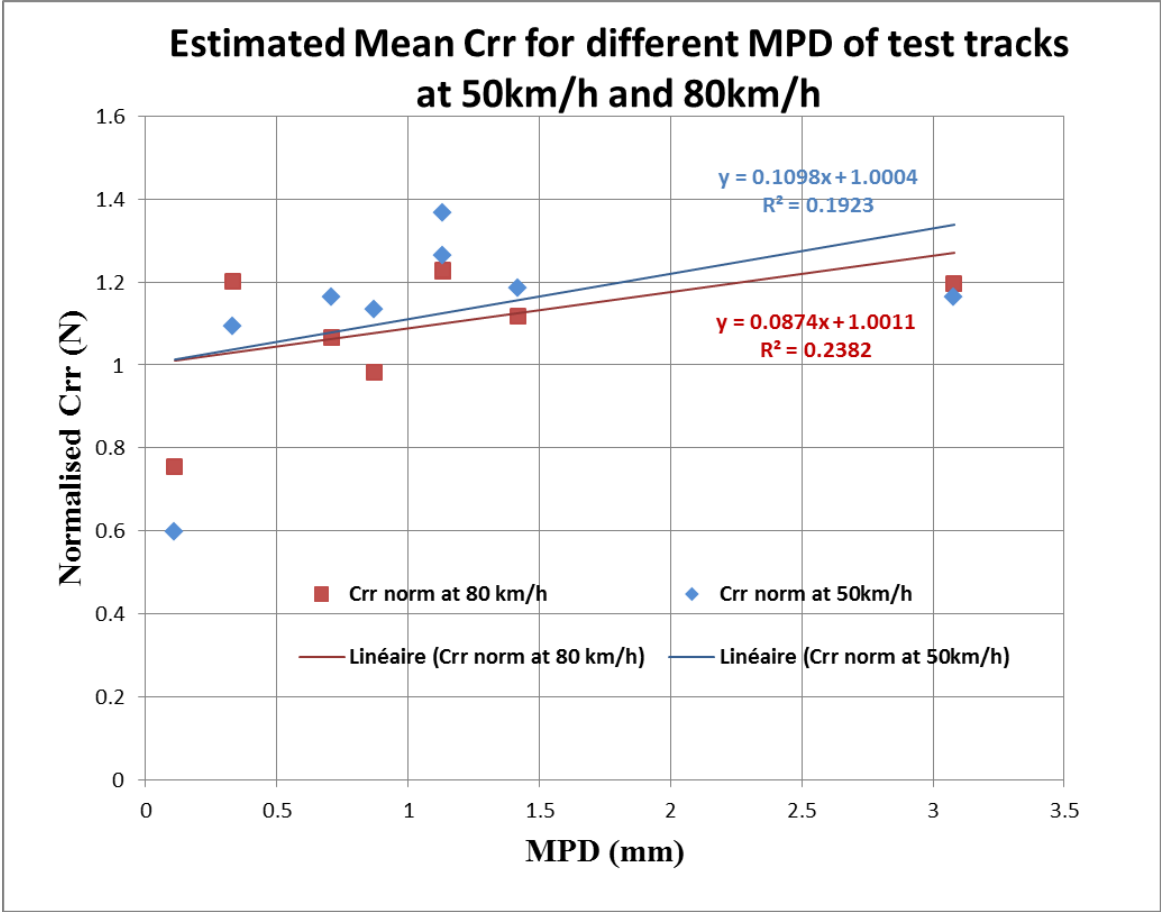


Figure 191 Normalised estimated mean Crr for different road roughness at a different speed (observer)

Estimation of rolling resistance for all the wheels of a vehicle independently was the main goal. The nonlinear observer is applied in order to get a robust and accurate estimation of rolling resistance forces. The unknown input adaptive high gain observer for regular systems and singularly perturbed systems is successfully applied here. The precision of these observers is proved through the simulation results presented above. Its robustness is used to detect the variation in the input. The observer reconstructed well the state variable with an error of 1% maximum in offline experimental validation. The accurate estimation of the rolling resistance force is done by the developed observer. The estimation error is less than 10% for both cases. This is a very promising solution to use in real driving conditions. These two observers are experimentally validated. The difference in the estimation of the two observers is very small and difficult to separate in the above cases. Table 22 summarises the overall performance of these observers. The developed observers take into account the impact of road roughness. The results presented in Figure 190 and Figure 191 validates it. Despite weak regression, the trend shows an increase in rolling resistance with an increase in road roughness.

Table 22 Global performance of developed observers

Observer	Regular system	Singularly perturbed system
Advantages	<ul style="list-style-type: none"> - A good estimation of Frr and R for all the tyres - Good reconstruction of all the state variables - Consider the mechanical influencing parameters (speed, road roughness etc.) - Easy to implement as compared to singularly perturbed systems 	<ul style="list-style-type: none"> - Tyre surface temperature is also estimated using state estimation - Consider more influencing factor of rolling resistance (Temperature, speed, road roughness) - A good estimation of Frr and R for all four wheels - Good reconstruction of all the state variables
Limitations	<ul style="list-style-type: none"> - Do not consider tyre temperature influence on rolling resistance; - Difficult to separate the temperature effect during experiments 	<ul style="list-style-type: none"> - Complex model as compare to regular systems - Two-time scale are more complicated to handle

5.6. Conclusion

The experimentation site is presented first with the characterization of test tracks. The detailed instrumentation of Clio 2 is also discussed with its various mounted sensors. The two different designs of experiments (DoE) and its realization is described. In the first DoE, the goal is to calibrate and tune the model and validate the developed vehicle model experimentally. The other objectives of the experiments were to identify the method to calculate the rolling resistance coefficient, to study the influence of several parameters and compare the results with the trends found in the literature. The calculated rolling resistance force was used as the reference while comparing it with an estimated rolling resistance force. The evaluation of tyre surface temperature is done successfully. The extensive study on variation of tyre surface temperature concluded that the tyre surface temperature varies linearly in the circumferential and lateral direction. The syntheses of the study were presented. It is also concluded that the variation of tyre surface temperature is slower than the variation in vehicle speed. Therefore the system with thermal model becomes a singularly perturbed system. This calculation of tyre surface temperature was also used in the experimental validation of the observer. The developed vehicle model and tyre model was experimentally validated successfully with the relative mean error is less than 10%. The unknown input adaptive high gain observer for regular systems and singularly perturbed systems is successfully applied and experimentally validated. The precision of these observers is proved through the simulation results presented above. Its robustness is used to detect the variation in the input. The observer reconstructed well the state variable and accurate estimation of the rolling resistance force is done by the developed observer. The relative mean estimation errors are less than 10% and less than the defined criteria. In Table 22 the overall performance of these observers are summarised. The develop observers also take into account the impact of road roughness. The comparison shows similar trends as in the literature. Therefore the developed observers are validated successfully while taken into account the impact of roughness and tyre temperature. This is a very promising solution to use in real driving conditions.

Chapter 6

Conclusion and perspectives

In this section, some conclusion and recommendation of future work are presented.

6.1. Conclusion

The primary objective of this thesis was to develop a system for the estimation of the tyre rolling resistance of a vehicle in real driving conditions. An indirect approach of nonlinear unknown input adaptive gain observers is used. These observers are based on the mathematical model of complete vehicle. Particular attention is paid to the inclusion of infrastructure characteristics (geometry, surface properties) and thermal properties in the model. The multi-physical dynamic nature of tyre road contact model let us considered the various influencing factor of rolling resistance such as road roughness, tyre temperature etc. This approach ensured us an accurate and robust estimation in time. It reduces the sensitivity to measurement noise and ensures convergence in finite time of the numerical model.

The state of art on the rolling resistance force is done in the first part of chapter 1. It is concluded that the rolling resistance is one of the most important parameters affecting the fuel consumptions and the performance of a vehicle. The definition and mechanism of rolling resistance are presented with the different influencing parameters. The main influencing parameters are speed, load, tyre inflation pressure, temperature and road roughness. If there is a change in any above mentioned parameters, they have a direct influence on rolling resistance.

The existing empirical models of rolling resistance coefficient are presented. These models are obtained with correlation methods for controlled conditions. This is specific to a few tracks with limitations. The comparison of different rolling resistance measurement method concluded that the experimental methods are inaccessible, uncertain, low reproducibility of the measurements and the high cost of physical sensors attached to vehicle tyres. Due to these limitations, the syntheses of different methods conclude that the virtual sensor method seems to be the best suited for the requirement. In the virtual sensor method, it is possible to take into account tyre-related as well as pavement design-related influencing factor while estimating the rolling resistance. It has a low cost of implementation as well as easy hand on experience. Therefore this method was developed in this thesis.

The state of art presented in the second part of chapter 1 outlined the advantages and disadvantages of existing observer techniques. The advantages of the adaptive gain observer are discussed and identified. This motivated us to develop adaptive gain observer for estimating tyre rolling resistance force. Two nonlinear observers adaptive high gain and adaptive sliding mode observer were applied and compared in order to get a robust and accurate estimation of rolling resistance force.

In the simulation, the adaptive high gain observer gave better results on cases presenting noise or variations than the adaptive sliding mode observer. The comparison allowed us to consider the adaptive high gain observer that shows high practical interest due to its robustness and finite-time convergence modelling error and parameter uncertainty. But it remained to validate this observation on a complete vehicle. The accurate estimation of rolling resistance also depends on considering its influencing parameters into the model; therefore in chapter 2 the development of multi-physical tyre model was done. The brief literature review on the existing tyre models presented at the starting of chapter concluded that semi-empirical model such as Pacejka's Magic Formula was the model that best describes steady-state tyre behaviour but it cannot be used in this thesis as its weakness of not describing dynamic tyre behaviour and requiring a lot of experiments to calibrate. The finite element based sophisticated thermo-mechanical models developed in literature predict accurate tyre temperature, but they require significant computational power, in addition to a large amount of

information related to the internal structure of the tyre. The physical model such as brush model is very comparable with results of magic formula. Nevertheless, this representation is more realistic, because of the more advanced vertical pressure distribution. It fits our requirement for estimating rolling resistance. But it lacks to include the thermal effect. Therefore brush model based multi-physical model is developed. The physical nature of the model allows us to minimize the number of parameters required to feed the model. The multi-physical tyre model presented in this chapter is an indispensable tool to have accurate results since the tyre tread's and carcass's temperature. So this chapter concluded that the developed physical model takes into account the influencing parameters of rolling resistance. In chapter 2 a full model is developed which can simulate all vehicle manoeuvres and consider the effect of pavement. The tyre model developed in chapter 2 is also coupled with this model. The numerical validation of FVM (full vehicle model) is done with the help of SCANeR Studio (Prosper). The overall relative mean errors of all the scenarios are less than 8% as shown in Table 7. The difference is mainly due to the simplification of the developed model by comparison with the complex simulator model. So we can conclude that the comparison results are following the simulator results with good dynamic behaviour. This developed model will be considered as a system for the development of unknown input adaptive high gain observer to estimate tyre rolling resistance.

The development of multi-physical tyre model is one of the major contributions of our work. On the other hand, the synthesis of non-linear observers is another major contribution of our work. This work has aimed to synthesize observers who estimate the non-measurable quantities (effective radius, rolling resistance force) using exclusively measured quantities (angular velocities, vehicle speed and motor torque).

The development of unknown input adaptive gain observer for the estimation of tyre rolling resistance force is done in chapter 4. The adaptive gain approach is a novel approach for the unknown input observers in the automotive domain. This chapter presented the very first results of the estimation of rolling resistance using adaptive gain observers for full vehicle and validated numerically. The choice of unknown input adaptive gain observer technique was made for its well-known characteristics of robustness, precision and the convergence. The results show a satisfactory estimation of the effective radius and/or rolling resistance force. In each case, we have carried out a study of the observability of the identified different observation models.

In the first part of chapter 5, the design of experiments (DoE) is done. It also focused on the instrumentation of the vehicle with the mounted sensors. The objective of DoE was to calculate the reference rolling resistance coefficient, to study the influence of parameters, to compare the results with the trends in the literature and to validate the developed models. The calculated rolling resistance force was used as the reference while comparing it with an estimated rolling resistance force. The extensive study on variation of tyre surface temperature concluded that the tyre surface temperature varies linearly in the circumferential and lateral direction. It also concluded that the variation of tyre surface temperature is slower than the variation in vehicle speed. Therefore the multi-physical nature of the model is considered as a singularly perturbed system. The developed vehicle model and multi-physical tyre model was experimentally validated successfully with the relative mean error of less than 10%. The unknown input adaptive high gain observer for regular systems and singularly perturbed systems is successfully applied and experimentally validated. The precision of these observers is proved through the simulation results presented above. Its robustness is used to detect the variation in the input. The observer reconstructed well the state variable and accurate estimation of the rolling resistance force is done by the developed observer. The developed observers also take into account the impact of road roughness. The comparison shows similar trends as in the literature. Therefore the

developed observers are validated successfully while taken into account the impact of roughness and tyre temperature.

6.2. Perspectives

The work done in this thesis is original since a little work has been done on the estimation and experimental validation of rolling resistance for a vehicle in real driving conditions. Despite the significant amount of work done in this thesis, there is still an area of improvements and additional research work. In light of the results obtained in the course of our work, a certain number of perspectives can be drawn.

6.2.1. Modelling

Additional work can be proposed on short term dealing with the multi-physical model. The model can be improved by implementing a flexible carcass along the vertical and longitudinal direction. In the thermal model, the cooling from the air inside the tyre isn't considered in this work and it might be interesting to explore and include this effect in the thermal model. This could improve the accuracy of the model for the estimation of tyre temperature. It is also possible to include a model to estimate the length of the contact area. It is considered as constant in this work because in dry road conditions the variation can be neglected but for the wet condition is it important to integrate a physical model of contact length as it varies with the thickness of water on the road as demonstrated by [159]. There exist the empirical models of contact length is also proposed in the literature [191] can be investigated initially.

The multi-physical model developed in this thesis is valid only in the dry condition. In literature, the authors in [36] have shown that water film on the pavement increases passenger car tyre rolling resistance considerably. The authors believe that slightly wet road surfaces increase the cooling effect on the tyre thus decreasing its temperature and increasing rolling resistance. A change of tyre temperature by just 4°C may lead to certain tyres to a 6% increase of tyre rolling resistance. When there is more water on the road the cooling effect is even stronger and on top of this, certain energy must be supplied by the tyre to pump-away water from the tyre/road interface region leading to further increase of rolling resistance[36]. Therefore it is indispensable to improve the developed model to work in wet condition. It is recommended to integrate the hydrodynamics model into the model. The hydrodynamic model previously developed by [159] at University Gustave Eiffel can be investigated for the integration. One of the main hypothesis in the thesis is that the vehicle is running on a levelled road. In reality, the environment may include difficult features such as undulating terrain and deformable surfaces. Therefore, the improvement of the vehicle model can also be done by including the load transfer phenomenon. There are two main types of load transfer exist; lateral load transfer and longitudinal load transfer. Lateral load transfer occurs during cornering and is the shift of mass across the wheels due to the centrifugal force and the lateral acceleration. The longitudinal load transfer occurs when a car is accelerating or braking. It is necessary for the stability of the vehicle.

6.2.2. Experimentation

This thesis is enriched with more than 420 experiments and in literature, this kind of vast measurements campaign for the validation of rolling resistance estimation is rather rare. During the thesis, particular attention was given on the instrumentation of the vehicle for the validation of the multi-physical model and vehicle model. In our experimentation, we used external temperature sensors to measure the temperature at the tyre surface. It is mainly due to the complexity of experimentation

which is not complex to install and cheaper. Therefore the tyre surface temperature in the contact zone is still difficult to measure. Validation of the multi-physical model using temperature sensor embedded in tyre temperature is the future prospect of this work. This is possible by instrumenting the tyre with thermocouples, accelerometers and “rotating collector **SR20AW**” which allows the transmission of measurement signals from a rotating element to an acquisition system. This will measure the temperature of the tyre carcass, air inside tyre and inflation pressure. It will help make more concrete conclusion of variation of rolling resistance with tyre temperature and inflation pressure.

In this thesis, experiments are done only one kind of tyre i.e. Energy saver which has low rolling resistance tyre. The literature has highlighted the effect of the rheological characteristics of the rubber of tyres on the rolling resistance [7]. Therefore the experiments with different tyres (high rolling resistance) could be interesting for comparison in future.

6.2.3. Estimation technique

The developed model still depends on more number of parameters than classical brush model, like dynamic friction between tread and road, rheological characteristics (tyre stiffness) of the rubber. These parameters are not easily available and need tyre manufacturer to communicate. Therefore the parameters estimators and identification technique should be explored to reduce the number of input parameters.

We have worked with singular perturbed system in this thesis and applied the existing technique in the automotive application. This approach should be explored further. For example, the estimation approach for the singular perturbed system is developed for continuous systems; it is possible to explore the application for discrete systems. In this work, the 100Hz sampling frequency of data acquisition is used for all the sensors, but in reality, the acquisition frequency of slow dynamics systems is far less than the fast dynamic systems. Variable sampling frequency can affect the accuracy of the rolling resistance estimation using the singular perturbed technique but while working in a discrete domain it can avoid the influence of sampling rate. Further research should focus on the real-time implementation of the observer in order to verify the influence of sampling rate, measurement noise, simplifying modelling assumptions and saturations.

6.2.4. Real-time estimation

Despite the whole work done during this thesis, only the offline validation of rolling resistance estimation was performed. Even though the offline validation gives promising results it is impossible to be very conclusive on the real-time estimation because we didn't go until the end of the validation procedure due to time constraint. Therefore, the next step of validation will be the real-time estimation of rolling resistance. But the above-recommended improvements will increase the complexity of the model which will impact on the real-time estimation of rolling resistance therefore a balance is needed to be found between the model and real-time estimation. Further integration of the proposed approaches on-board a vehicle for online validation and accompanied by a robustness analysis. This can be extended to the application on trucks and an autonomous vehicle in future. The collaboration between University Gustave Eiffel and Cerema can continue to work together on this aspect in future.

In the end, the optimization algorithm should be proposed to reduce the rolling resistance in real driving conditions. It can be implemented for driving assistance systems (ADAS) for Eco driving.

References

- [1] U. Shahzad, “Global Warming: Causes, Effects and Solutions,” *Durreesamin J. Aust.*, vol. August, no. 4, pp. 1–7, 2015.
- [2] “IPCC — Intergovernmental Panel on Climate Change.” [Online]. Available: <https://www.ipcc.ch/>. [Accessed: 14-Apr-2020].
- [3] “Transport: increasing oil consumption and greenhouse gas emissions hamper EU progress towards environment and climate objectives — European Environment Agency.” [Online]. Available: <https://www.eea.europa.eu/themes/transport/term/increasing-oil-consumption-and-ghg>. [Accessed: 05-Mar-2020].
- [4] “CO₂ and Greenhouse Gas Emissions - Our World in Data,” 2020. [Online]. Available: <https://ourworldindata.org/co2-and-other-greenhouse-gas-emissions>. [Accessed: 06-Mar-2020].
- [5] “Greenhouse gas emissions from transport in Europe — European Environment Agency,” 2016. [Online]. Available: <https://www.eea.europa.eu/data-and-maps/indicators/transport-emissions-of-greenhouse-gases/transport-emissions-of-greenhouse-gases-12>. [Accessed: 05-Mar-2020].
- [6] K. Holmberg, P. Andersson, and A. Erdemir, “Global energy consumption due to friction in passenger cars,” *Tribol. Int.*, vol. 47, pp. 221–234, 2012.
- [7] Michelin, *The tyre rolling resistance and fuel savings*. Clermont Ferrand, France: Société de Technologie Michelin, 2003.
- [8] S. Das and B. Redrouthu, “Tyre modelling for rolling resistance,” Chalmers University of Technology, Goteborg, Sweden, 2014.
- [9] U. Sandberg, U. Hammarström, R. Karlsson, J. A. Ejsmont, and A. Bergiers, “Rolling resistance-Basic information and State-of-the-Art on measurement methods(MIRIAM),” 2011.
- [10] U. Sandberg, A. Bergiers, J. A. Ejsmont, L. Goubert, and M. Zoller, “Rolling Resistance – Measurement Methods for Studies of Road Surface Effects (MIRIAM),” 2012.
- [11] U. Hammarström, R. Karlsson, and H. Sorensen, “Road surface effects on rolling resistance – coastdown measurements with uncertainty analysis in focus (ECRPD),” 2008.
- [12] M. D. Meyer, L. S. Watson, and R. E. Skinner, “Tires and passenger vehicle fuel economy, Transportation Research Board,” 2006.
- [13] J. Y. Wong, *Theory of ground vehicles*, 4th ed. John Wiley, 2001.
- [14] A. Miege, “Tyre model for truck ride simulations,” University of Cambridge, 2004.
- [15] S. K. Clark and R. N. Dodge, *A Hand book for rolling resistance of pneumatic tires*. 1979.
- [16] J. Ejsmont, S. Taryma, and G. Ronowski, “Parameters influencing rolling resistance and possible correction procedures (ROSSANE),” 2013.
- [17] U. Hammarstrom, J. C. Eriksson, R. Karlsson, and M. Yahya, “Rolling resistance model, fuel consumption model and traffic energy saving potential from changed road surface conditions,” Linköping Sweden, 2012.
- [18] Y. Nakajima, “Rolling Resistance of Tires,” in *Advanced Tire Mechanics*, no. i, Springer Nature Singapore Pte Ltd. 2019, 2019, pp. 931–1017.

- [19] S. Boere, "Prediction of road texture influence on rolling resistance," Eindhoven University of Technology, 2009.
- [20] A. Bergiers, J. A. Ejsmont, L. Goubert, R. Karlsson, and U. Sandberg, "Comparison of Rolling Resistance Measuring Equipment - Pilot Study (MIRIAM)," 2011.
- [21] C. El Tannoury, S. Moussaoui, F. Plestan, N. Romani, and G. Pita-Gil, "Synthesis and application of nonlinear observers for the estimation of tire effective radius and rolling resistance of an automotive vehicle," *IEEE Trans. Control Syst. Technol.*, vol. 21, no. 6, pp. 2408–2416, 2013.
- [22] M. Bouteldja, M. Djemai, and L. Fridman, "Dynamics observation and parameters identification of heavy vehicle via second order sliding mode," in *2010 11th International Workshop on Variable Structure Systems (VSS)*, 2010, pp. 463–468.
- [23] D. Beach and J. Schroeder, *The Pneumatic Tire*, no. February. National highway traffic safety administration, 2006.
- [24] D. J. Schuring, "Rolling resistance of tires measured under transient and equilibrium conditions on Calspan's tire research facility," 1976.
- [25] R. Karlsson, U. Hammarström, H. Sörensen, and O. Eriksson, "Road surface influence on rolling resistance Coastdown measurements for a car and an HGV," 2011.
- [26] L. Nielsen and T. Sandberg, "A New Model for Rolling Resistance of Pneumatic Tires," *SAE Transactions*, vol. 111. SAE International, pp. 1572–1579, 2002.
- [27] Y. Sebsadji, "Numerisation et Reconstruction 3D de la Geometrie de la Route par Observateurs et Stereovision," 2009.
- [28] Setra, "SETRA, Recommandations techniques pour la conception générale et la géométrie de la route. Aménagement des routes principales (sauf les autoroutes et routes express à deux chaussées), guide technique, Réf B9413, 1994." p. 145, 1994.
- [29] U. Sandberg *et al.*, "Road surface influence on tyre/road rolling resistance," 2011.
- [30] S. Boere, I. L. Arteaga, A. Kuijpers, and H. Nijmeijer, "Tyre/road interaction model for the prediction of road texture influence on rolling resistance," *Int. J. Veh. Des.*, vol. 65, no. 2/3, p. 202, 2014.
- [31] K. Chatti, "Effect of Pavement Conditions on Rolling Resistance and Fuel Consumption," *Pavement Life Cycle Assessment Workshop*. 2010.
- [32] V. Cerezo, M. T. Do, D. Prevost, and M. Bouteldja, "Friction/water depth relationship - In situ observations and its integration in tire/road friction models," *Proc. Inst. Mech. Eng. Part J J. Eng. Tribol.*, vol. 228, no. 11, pp. 1285–1297, Nov. 2014.
- [33] ISO 13473-1, "ISO Characterization of pavement texture by use of surface profiles — Part 1: Determination of mean profile depth. ISO Standard 13473-1," 1997.
- [34] A. A. Popov, D. J. Cole, D. Cebon, and C. B. Winkler, "Energy Loss in Truck Tyres and Suspensions," *Veh. Syst. Dyn.*, vol. 33, no. sup1, pp. 516–527, Jan. 1999.
- [35] D. J. Schuring, "The Rolling Loss of Pneumatic Tires," *Rubber Chem. Technol.*, vol. 53, no. 3, pp. 600–727, Jul. 1980.
- [36] U. Sandberg, A. Bergiers, J. A. Ejsmont, L. Goubert, and R. Karlsson, "Road surface influence on tyre/road rolling resistance (MIRIAM)," 2011.

- [37] J. Bryce, J. Santos, G. Flintsch, S. Katicha, K. McGhee, and A. Ferreira, “Analysis of rolling resistance models to analyse vehicle fuel consumption as a function of pavement properties,” *Asph. Pavements*, pp. 263–273, 2014.
- [38] A. Bergiers, U. Sandberg, J. A. Ejsmont, R. Karlsson, and L. Goubert, “MIRIAM: an international round robin test to compare rolling resistance measurement methods,” 2011.
- [39] F. Anfosso-lédée, V. Cerezo, and R. Karlsson, “Experimental validation of the rolling resistance measurement method,” 2013.
- [40] L. G. Andersen, J. K. Larsen, E. S. Fraser, B. Schmidt, and J. C. Dyre, “Rolling Resistance Measurement and Model Development,” *J. Transp. Eng.*, vol. 141, no. 2, p. 04014075, 2014.
- [41] T. Sandberg, “Heavy Truck Modeling for Fuel Consumption Simulations and Measurements,” 2001.
- [42] C. E. Tannoury, F. Plestan, S. Moussaoui, and N. Romani, “Tyre effective radius and vehicle velocity estimation: A variable structure observer solution,” in *Eighth International Multi-Conference on Systems, Signals & Devices*, 2011, pp. 1–6.
- [43] H. B. Pacejka, *Tyre and Vehicle Dynamics*. Elsevier, 2006.
- [44] J. Svendenius, “Construction of Novel Semi-Empirical Tire Models for Combined Braking and Cornering,” no. April, pp. 2–67, 2003.
- [45] J. Svendenius, “Tire Modeling and Friction Estimation,” *Department of Automatic Control Lund University*. pp. 1–194, 2007.
- [46] A. Sorniotti and M. Velardocchia, “Enhanced Tire Brush Model for Vehicle Dynamics Simulation,” in *SAE Technical Paper Series*, 2008, vol. 2008, no. 724, pp. 776–790.
- [47] U. K. and L. Nielsen, *Automotive control*, vol. 59, no. 9. 2006.
- [48] P. E. R. Sahlholm, “Distributed Road Grade Estimation for Heavy Duty Vehicles, PhD Thesis,” KTH School of Electrical Engineering, 2011.
- [49] L. Segel and L. Xiaopei, “Vehicular resistance to motion as influenced by road roughness and highway alignment,” *Aust. Road Res.*, 1982.
- [50] R. Merzouki, B. Ould-Bouamama, M. A. Djeziri, and M. Bouteldja, “Modelling and estimation of tire–road longitudinal impact efforts using bond graph approach,” *Mechatronics*, vol. 17, no. 2–3, pp. 93–108, Mar. 2007.
- [51] “J1269: Rolling Resistance Measurement Procedure for Passenger Car, Light Truck, and Highway Truck and Bus Tires - SAE International.” [Online]. Available: https://www.sae.org/standards/content/j1269_200609/. [Accessed: 03-Dec-2019].
- [52] “J2452: Stepwise Coastdown Methodology for Measuring Tire Rolling Resistance - SAE International.” [Online]. Available: https://www.sae.org/standards/content/j2452_199906/. [Accessed: 03-Dec-2019].
- [53] “ISO - ISO 18164:2005 - Passenger car, truck, bus and motorcycle tyres — Methods of measuring rolling resistance.” [Online]. Available: <https://www.iso.org/standard/33328.html>. [Accessed: 03-Dec-2019].
- [54] “ISO - ISO 28580:2018 - Passenger car, truck and bus tyre rolling resistance measurement method — Single point test and correlation of measurement results.” [Online]. Available: <https://www.iso.org/standard/67531.html>. [Accessed: 03-Dec-2019].

- [55] “Regulation No 117 of the Economic Commission for Europe of the United Nations (UNECE) — Uniform provisions concerning the approval of tyres with regard to rolling sound emissions and/or to adhesion on wet surfaces and/or to rolling resistance [2016/1350] - Publications Office of the EU.” [Online]. Available: <https://op.europa.eu/en/publication-detail/-/publication/48d3ed27-604f-11e6-9b08-01aa75ed71a1/language-en>. [Accessed: 03-Dec-2019].
- [56] P. Andersson, C. Hoever, J. Winroth, and W. Kropp, “Numerical Modelling of Tyre/Road Interaction,” in *Exploratory Workshop: Modern Methods of Vibro-Acoustic Studies With Automotive Applications*, University of Pitesti, Romania, 2011, p. 10.
- [57] L. G. Andersen, “Rolling Resistance Modelling Asset Management System, PhD Thesis,” Roskilde University, 2015.
- [58] P. Cenek, “Rolling Resistance Characteristics of New Zealand Road Surfaces,” in *Vehicle-Road Interaction*, 100 Barr Harbor Drive, PO Box C700, West Conshohocken, PA 19428-2959: ASTM International, 1994, pp. 248-248–15.
- [59] R. Rajamani, “LATERAL VEHICLE DYNAMICS,” in *Vehicle Dynamics and Control*, vol. 37, no. 12, 2001, pp. 2077–2078.
- [60] K. B. Singh and S. Taheri, “Estimation of tire–road friction coefficient and its application in chassis control systems,” *Syst. Sci. Control Eng.*, vol. 3, no. 1, pp. 39–61, 2015.
- [61] C. Canudas-de-Wit and R. Horowitz, “Observers for Tire/road Contact Friction using only wheel angular velocity information,” in *Proceedings of the 38th IEEE Conference on Decision and Control*, 1999, pp. 3932–3937.
- [62] M. Doumiati, A. Victorino, A. Charara, and D. Lechner, “Lateral load transfer and normal forces estimation for vehicle safety: experimental test,” *Veh. Syst. Dyn.*, vol. 47, no. 12, pp. 1511–1533, Dec. 2009.
- [63] J. Ryu, “State and parameters estimation for vehicle dynamics control using gps, PhD Thesis,” Stanford university, 2004.
- [64] N. K. M’Sirdi, A. Rabhi, and A. Naamane, “Vehicle Models and Estimation of Contact Forces and Tire Road Friction,” 2011, pp. 351–358.
- [65] J. J. Rath, K. C. Veluvolu, D. Zhang, Q. Zhang, and M. Defoort, “Estimation of Road Adhesion Coefficient Using Higher-Order Sliding Mode Observer for Torsional Tyre Model,” in *Lecture Notes in Computer Science (including subseries Lecture Notes in Artificial Intelligence and Lecture Notes in Bioinformatics)*, vol. 8103 LNAI, no. PART 2, 2013, pp. 202–213.
- [66] J. P. Gauthier, H. Hammouri, and S. Othman, “A Simple Observer for Nonlinear Systems Applications to Bioreactors,” *IEEE Trans. Automat. Contr.*, vol. 37, no. 6, pp. 875–880, 1992.
- [67] A. Levant, “Higher-order sliding modes, differentiation and output-feedback control,” *Int. J. Control*, vol. 76, no. 9/10, pp. 924–941, 2003.
- [68] Y. Shtessel, C. Edwards, L. Fridman, and A. Levant, *Sliding Mode Control and Observation*, no. June. New York, NY: Springer New York, 2014.
- [69] R. Andersson, “Online Estimation of Rolling Resistance and Air Drag for Heavy Duty Vehicles,” KTH Institute of engineering and technology, 2012.
- [70] K. B. Singh, M. A. Arat, and S. Taheri, “Literature review and fundamental approaches for vehicle and tire state estimation,” *Veh. Syst. Dyn.*, pp. 1–23, Nov. 2018.

- [71] S. Johansson, "Tire/Road Friction Estimation for Front Wheel Driven Vehicle," Lund University, 2015.
- [72] R. Rajamani, "Observers for Lipschitz nonlinear systems," *IEEE Trans. Automat. Contr.*, vol. 43, no. 3, pp. 397–401, 1998.
- [73] H. K. Khalil, *Nonlinear Systems*, 3rd ed. Prentice Hall, 1999.
- [74] R. Rajamani, *Vehicle Dynamics and Control*. Springer-Verlag, 2012.
- [75] R. Rajamani, H. S. Tan, B. K. Law, and W. Bin Zhang, "Demonstration of integrated longitudinal and lateral control for the operation of automated vehicles in platoons," *IEEE Trans. Control Syst. Technol.*, vol. 8, no. 4, pp. 695–708, Jul. 2000.
- [76] R. Hermann and A. J. Krener, "Nonlinear Controllability and Observability," *IEEE Trans. Automat. Contr.*, vol. 22, no. 5, pp. 728–740, 1977.
- [77] J. K. Hedrick, "Analysis and control of nonlinear systems," *J. Dyn. Syst. Meas. Control. Trans. ASME*, vol. 115, no. 2B, pp. 351–361, Jun. 1993.
- [78] M. Farza, M. M'Saad, and M. Sekher, "A set of observers for a class of nonlinear systems," in *IFAC Proceedings Volumes (IFAC-PapersOnline)*, 2005, vol. 38, no. 1, pp. 765–770.
- [79] H. Hammouri and M. Farza, "Nonlinear observers for locally uniformly observable systems," *ESAIM Control. Optim. Calc. Var.*, vol. 9, pp. 353–370, Mar. 2003.
- [80] F. Liu, "Syntheses of observers with unknown inputs for non-linear systems, PhD Thesis," University of Caen, 2007.
- [81] L. L. Scharf and S. Sigurdsson, "Fixed Point Implementation of Fast Kalman Predictors," *IEEE Trans. Automat. Contr.*, vol. 29, no. 9, pp. 850–852, 1984.
- [82] G. Chen, *Approximate Kalman Filtering*, 2nd ed. World Scientific, 1993.
- [83] R. E. Kalman and R. S. Bucy, "New results in linear filtering and prediction theory," *Trans. ASME. Ser. D, J. basic Eng.*, p. 109, 1961.
- [84] A. J. Krener and A. Isidori, "Linearization by output injection and nonlinear observers," *Syst. Control Lett.*, vol. 3, no. 1, pp. 47–52, Jun. 1983.
- [85] M. Zeitz, "The extended Luenberger observer for nonlinear systems," *Syst. Control Lett.*, vol. 9, no. 2, pp. 149–156, Aug. 1987.
- [86] C. Kravaris, J. Hahn, and Y. Chu, "Advances and selected recent developments in state and parameter estimation," *Comput. Chem. Eng.*, vol. 51, pp. 111–123, Apr. 2013.
- [87] J. Tsinias, "Further results on the observer design problem," *Syst. Control Lett.*, vol. 14, no. 5, pp. 411–418, Jun. 1990.
- [88] G. Ciccarella, M. Dalla Mora, and A. Germani, "A Luenberger-like observer for nonlinear systems," *Int. J. Control*, vol. 57, no. 3, pp. 537–556, 1993.
- [89] M. Arcak, "A global separation theorem for a new class of nonlinear observers," in *Proceedings of the IEEE Conference on Decision and Control*, 2002, vol. 1, pp. 676–681.
- [90] M. Arcak and P. Kokotovic, "Nonlinear observers: a circle criterion design," in *Proceedings of the IEEE Conference on Decision and Control*, 1999, vol. 5, pp. 4872–4876.
- [91] W. Respondek, A. Pogromsky, and H. Nijmeijer, "Time scaling for observer design with

- linearizable error dynamics,” *Automatica*, vol. 40, no. 2, pp. 277–285, Feb. 2004.
- [92] F. E. Thau, “Observing the state of non-linear dynamic systems,” *Int. J. Control*, vol. 17, no. 3, pp. 471–479, 1973.
- [93] H. Hammouri, F. S. Ahmed, and S. Othman, “Observer design based on immersion technics and canonical form,” *Syst. Control Lett.*, vol. 114, pp. 19–26, Apr. 2018.
- [94] V. I. Utkin, *Sliding Modes in Control and Optimization*. Springer Berlin Heidelberg, 1992.
- [95] S. Drakunov and V. Utkin, “Sliding mode observers. Tutorial,” in *Proceedings of the IEEE Conference on Decision and Control*, 1995, vol. 4, pp. 3376–3378.
- [96] J. Slotine, J. Hedrick, and E. Misawa, “Nonlinear state estimation using sliding observers,” in *1986 25th IEEE Conference on Decision and Control*, 1986, pp. 332–339.
- [97] V. I. Utkin, “Survey Paper: Variable Structure Systems with Sliding Modes,” *IEEE Trans. Automat. Contr.*, vol. 22, no. 2, pp. 212–222, 1977.
- [98] A. Kojić, A. M. Annaswamy, A. P. Loh, and R. Lozano, “Adaptive control of a class of nonlinear systems with convex/concave parameterization,” *Syst. Control Lett.*, vol. 37, no. 5, pp. 267–274, Aug. 1999.
- [99] A. P. Loh, A. M. Annaswamy, and F. P. Skantze, “Adaptation in the presence of a general nonlinear parameterization: An error model approach,” *IEEE Trans. Automat. Contr.*, vol. 44, no. 9, pp. 1634–1652, 1999.
- [100] K. Busawon, M. Farza, and H. Hammouri, “Observer design for a special class of nonlinear systems,” *Int. J. Control*, vol. 71, no. 3, pp. 405–418, Jan. 1998.
- [101] R. Marino and P. Tomei, *Global adaptive observers and output-feedback stabilization for a class of nonlinear systems*, vol. 160. Publ by Springer-Verlag Berlin, 1991.
- [102] R. Marino and P. Tomei, “Global Adaptive Observers for Nonlinear Systems via Filtered Transformations,” *IEEE Trans. Automat. Contr.*, vol. 37, no. 8, pp. 1239–1245, 1992.
- [103] M. Oueder, M. Farza, R. Ben Abdennour, and M. M’Saad, “A dynamic high gain observer for a class of MIMO non triangular systems,” in *IFAC Proceedings Volumes (IFAC-PapersOnline)*, 2011, vol. 44, no. 1 PART 1, pp. 686–691.
- [104] T. Menard, A. Maouche, B. Targui, I. Bouraoui, M. Farza, and M. M’Saad, “Adaptive high gain observer for uniformly observable systems with nonlinear parametrization,” in *2014 European Control Conference (ECC)*, 2014, pp. 1735–1740.
- [105] G. Kreisselmeier, “Adaptive Observers with Exponential Rate of Convergence,” *IEEE Trans. Automat. Contr.*, vol. 22, no. 1, pp. 2–8, 1977.
- [106] G. Lüders and K. S. Narendra, “An Adaptive Observer and Identifier for a Linear System,” *IEEE Trans. Automat. Contr.*, vol. 18, no. 5, pp. 496–499, 1973.
- [107] A. Koji and A. M. Annaswamy, “Adaptive control of nonlinearly parameterized systems with a triangular structure,” *Automatica*, vol. 38, no. 1, pp. 115–123, Jan. 2002.
- [108] N. Kazantzis, N. Huynh, and R. A. Wright, “Nonlinear observer design for the slow states of a singularly perturbed system,” *Comput. Chem. Eng.*, no. March, pp. 797–806, 2005.
- [109] M. Djemai and J. P. Barbot, “Singularly Perturbed Method for the Control Design of a Synchronous Motor with its PWM Inverter.”

- [110] P. D. Christofides, “Robust output feedback control of nonlinear singularly perturbed systems,” *Automatica*, vol. 36, no. 1, pp. 45–52, Jan. 2000.
- [111] A. Kumar, P. D. Christofides, and P. Daoutidis, “Singular perturbation modeling of nonlinear processes with nonexplicit time-scale multiplicity,” *Chem. Eng. Sci.*, vol. 53, no. 8, pp. 1491–1504, Apr. 1998.
- [112] M. Djemai, J. A. Hernandez, and J. P. Barbot, “Nonlinear control with flux observer for a singularly perturbed induction motor,” in *Conference on Decision and Control*, USA, 1993, pp. 1–6.
- [113] T. Braun, J. Reuter, and J. Rudolph, “A singular perturbation approach to nonlinear observer design with an application to electromagnetic actuators,” *Int. J. Control*, pp. 1–14.
- [114] P. Krishnamurthy and F. Khorrami, “A singular perturbation based approach for systems with nonlinear input uncertainties,” *2011 Chinese Control Decis. Conf.*, no. 1, pp. 1477–1482, 2011.
- [115] P. Krishnamurthy and F. Khorrami, “A singular perturbation based global dynamic high gain scaling control design for systems with nonlinear input uncertainties,” *IEEE Trans. Automat. Contr.*, no. 1, pp. 1–6, 2013.
- [116] P. Kokotovic, H. K. Khalil, and J. O’Reilly, *Singular Perturbation Methods in Control Analysis and Design*. 1999.
- [117] R. Castro-Linares, J. Alvarez-Gallegos, and V. Vasquez-Lopez, “Sliding Mode Control and State Estimation for a Class of Nonlinear Singularly Perturbed Systems,” *Dyn. Control*, pp. 25–46, 2001.
- [118] M. Djemai, J. P. Barbot, and H. K. Khalil, “Digital multirate control for a class of non-linear singularly perturbed systems,” *Int. J. Control*, vol. 72, no. 10, pp. 851–865, Jan. 1999.
- [119] B. Porter, “Singular perturbation methods in the design of full-order observers for multivariable linear systems,” *Int. J. Control*, vol. 26, no. 4, pp. 589–594, 1977.
- [120] A. K. Sharma, M. Bouteldja, and V. Cerezo, “High gain and sliding mode adaptive observers comparison: estimation of tire rolling resistance,” in *2018 6th International Conference on Control Engineering & Information Technology (CEIT)*, 2018, pp. 1–7.
- [121] J. Liu, S. Laghrouche, M. Harmouche, and M. Wack, “Adaptive-gain second-order sliding mode observer design for switching power converters,” *Control Eng. Pract.*, vol. 30, pp. 124–131, Sep. 2014.
- [122] M. Oueder, “Synthese des observateurs pour les systems non-linear, PhD Thesis,” University of Caen and Basse Normandie, 2014.
- [123] J. Liu, S. Laghrouche, M. Harmouche, and M. Wack, “Adaptive-gain second-order sliding mode observer design for switching power converters,” *Control Eng. Pract.*, vol. 30, pp. 124–131, Sep. 2014.
- [124] J. A. Moreno and M. Osorio, “A Lyapunov approach to second-order sliding mode controllers and observers,” in *2008 47th IEEE Conference on Decision and Control*, 2008, no. June 2014, pp. 2856–2861.
- [125] “SCANer Studio - AVSimulation.” [Online]. Available: <https://www.avsimulation.fr/solutions/>. [Accessed: 13-Jun-2019].
- [126] C. Canudas-de-Wit, P. Tsiotras, and E. Velenis, “Dynamic friction models for longitudinal road/tire interaction,” *Veh. Syst. Dyn.*, 2003.

- [127] R. Merzouki, M. Bouteldja, H. Imine, and J. C. Cadiou, "Friction force estimation and adaptive control for tire-road contact," in *2004 IEEE/RSJ International Conference on Intelligent Robots and Systems (IROS) (IEEE Cat. No.04CH37566)*, vol. 3, pp. 2434–2439.
- [128] H. Dugoff, P. S. Fancher, and L. Segel, "Tire performance characteristics affecting vehicle response to steering and braking control inputs: final report," 1969.
- [129] G. Mavros, H. Rahnejat, and P. D. King, "Transient analysis of tyre friction generation using a brush model with interconnected viscoelastic bristles," *Proc. Inst. Mech. Eng. Part K J. Multi-body Dyn.*, vol. 219, no. 3, pp. 275–283, 2005.
- [130] J. Svendenius, "Tire Models for Use in Braking Applications," Department of Automatic Control, Lund Institute of Technology (LTH), 2003.
- [131] J. Holtschulze, H. Goertz, and T. Hüsemann, "A simplified tyre model for intelligent tyres," *Veh. Syst. Dyn.*, vol. 43, no. SUPPL., pp. 305–316, 2005.
- [132] J. Svendenius, "Tire Modeling and Friction Estimation," *Dep. Autom. Control Lund Univ.*, p. 194, 2007.
- [133] S. K. Srirangam, K. Anupam, C. Kasbergen, and A. Scarpas, "Development of a thermomechanical tyre–pavement interaction model," *Int. J. Pavement Eng.*, vol. 16, no. 8, pp. 721–729, Sep. 2014.
- [134] R. B. Kogbara, E. A. Masad, E. Kassem, A. (Tom) Scarpas, and K. Anupam, "A state-of-the-art review of parameters influencing measurement and modeling of skid resistance of asphalt pavements," *Constr. Build. Mater.*, vol. 114, pp. 602–617, Jul. 2016.
- [135] S. K. Srirangam, K. Anupam, C. Kasbergen, A. Scarpas, and V. Cerezo, "Study of Influence of Operating Parameters on Braking Friction and Rolling Resistance," *Transp. Res. Rec. J. Transp. Res. Board*, vol. 2525, no. 1, pp. 79–90, Jan. 2015.
- [136] K. Falk, A. Nazarinezhad, and M. Kaliske, "Tire Simulations Using a Slip Velocity , Pressure and Temperature Dependent Friction Law," no. December, 2015, pp. 1–10.
- [137] T. Tang, K. Anupam, C. Kasbergen, and A. Scarpas, "Study of Influence of Operating Parameters on Braking Distance," *Transp. Res. Rec. J. Transp. Res. Board*, vol. 2641, no. 1, pp. 139–148, Jan. 2017.
- [138] M. M. Davari, "A Multi - Line Brush Based Tyre Model to Study the Rolling Resistance and Energy Loss," in *4th International Tyre Colloquium: Tyre Models for Vehicle Dynamics Analysis*, 2015, no. January, pp. 1–9.
- [139] G. Rill, "TMeasy–A Handling Tire Model based on a three-dimensional slip approach," in *Conference: Proceedings of the XXIII International Symposium on Dynamic of Vehicles on Roads and on Tracks*, 2013, no. October, pp. 1–10.
- [140] J. Svendenius, "Tire Models for Use in Braking Applications," Lund Institute of Technology, 2003.
- [141] N. Xu, K. Guo, X. Zhang, and H. R. Karimi, "An Analytical Tire Model with Flexible Carcass for Combined Slips," *Math. Probl. Eng.*, vol. 2014, pp. 1–9, 2014.
- [142] E. Velenis *et al.*, "Dynamic Tire Friction Models for Combined Longitudinal and Lateral Vehicle Motion," *Veh. Syst. Dyn.*, vol. 43, no. 1, pp. 3–29, 2005.
- [143] P. Lugner, H. Pacejka, and M. Plöchl, "Recent advances in tyre models and testing procedures," *Veh. Syst. Dyn.*, vol. 43, no. 6–7, pp. 413–426, Jun. 2005.

- [144] Y. J. Lin and S. J. Hwang, "Temperature prediction of rolling tires by computer simulation," *Math. Comput. Simul.*, vol. 67, no. 3, pp. 235–249, 2004.
- [145] C. Hoever, "The influence of modelling parameters on the simulation of car tyre rolling losses and rolling noise," Chalmers university of technology, 2012.
- [146] T. Tang, K. Anupam, C. Kasbergen, R. Kogbara, A. Scarpas, and E. Masad, "Finite Element Studies of Skid Resistance under Hot Weather Condition," *Transp. Res. Rec. J. Transp. Res. Board*, vol. 2672, no. 40, pp. 382–394, Dec. 2018.
- [147] T. Tang, K. Anupam, C. Kasbergen, A. Scarpas, and S. Erkens, "A finite element study of rain intensity on skid resistance for permeable asphalt concrete mixes," *Constr. Build. Mater.*, vol. 220, pp. 464–475, Sep. 2019.
- [148] S. Chae, "Nonlinear finite element modeling and analysis of a truck tire, PhD Thesis," Penn State University, 2006.
- [149] K. Anupam, S. K. Srirangam, A. Scarpas, and C. Kasbergen, "Influence of temperature on tire-pavement friction analyses," *Transp. Res. Rec.*, vol. 2369, pp. 114–124, 2013.
- [150] A. Sornioti, "Tire Thermal Model for Enhanced Vehicle Dynamics Simulation," in *SAE Technical Paper Series*, 2009, vol. 1.
- [151] F. Farroni, D. Giordano, M. Russo, and F. Timpone, "TRT: Thermo racing tyre a physical model to predict the tyre temperature distribution," *Meccanica*, vol. 49, no. 3, pp. 707–723, 2014.
- [152] P. Février and G. Fandard, "Thermal and mechanical tyre modelling for handling simulation," *ATZ Worldw.*, vol. 110, no. 5, pp. 26–31, May 2008.
- [153] F. Farroni, A. Sakhnevych, and F. Timpone, "Physical modelling of tire wear for the analysis of the influence of thermal and frictional effects on vehicle performance," *Proc. Inst. Mech. Eng. Part L J. Mater. Des. Appl.*, vol. 231, no. 1–2, pp. 151–161, 2017.
- [154] O. Ozerem and D. Morrey, "A brush-based thermo-physical tyre model and its effectiveness in handling simulation of a Formula SAE vehicle," *J. Automob. Eng.*, vol. 233, no. 1, pp. 107–120, 2019.
- [155] D. P. Kelly and R. S. Sharp, "Time-optimal control of the race car: Influence of a thermodynamic tyre model," *Veh. Syst. Dyn.*, vol. 50, no. 4, pp. 641–662, 2012.
- [156] J. Deur, J. Asgari, and D. Hrovat, "A 3D brush-type dynamic tire friction model," *Veh. Syst. Dyn.*, vol. 42, no. 3, pp. 133–173, 2004.
- [157] M. Gafvert and J. Svendenius, "Construction of Novel Semi-Empirical Tire Models for Combined Braking and Cornering," no. April, pp. 2–67, 2003.
- [158] M. M. Davari, J. Jerrelind, A. S. Trigell, and L. Drugge, "Extended brush tyre model to study rolling loss in vehicle dynamics simulations," *Int. J. Veh. Des.*, vol. 73, no. 4, p. 255, 2017.
- [159] J. Gerthoffert, V. Cerezo, M. Thiery, M. Bouteldja, and M. T. Do, "A Brush-based approach for modelling runway friction assessment device," *International Journal of Pavement Engineering*, Taylor and Francis Ltd., 2019.
- [160] F. Conte, "Expanding the brush tire model for energy studies," KTH university of technology, 2014.
- [161] Corrolaro A, "Essentially of Temperature Management while Modeling and Analysing Tires

- Contact Forces, PhD Thesis,” Universita’ Degli Studi Di Napoli Federico II, Napoli, 2014.
- [162] K. A. Grosch, “The Relation between the Friction and Viscoelastic Properties of Rubber,” in *Proc. Royal Society London A*, 2011, vol. 37, no. 2, pp. 386–403.
- [163] A. J. Niskanen and A. J. Tuononen, “Accelerometer tyre to estimate the aquaplaning state of the tyre-road contact,” in *IEEE Intelligent Vehicles Symposium, Proceedings*, 2015, vol. 2015-Augus, no. June 2015, pp. 343–348.
- [164] H. Diwakar, “Full Vehicle Model of a formula student car,” Delft university of technology, 2018.
- [165] L. Dugard, O. Sename, S. Aubouet, and B. Talon, “Full vertical car observer design methodology for suspension control applications,” *Control Eng. Pract.*, vol. 20, no. 9, pp. 832–845, 2012.
- [166] M. Ouahi, J. Stéphant, and D. Meizel, “Evaluation of torque observer in automotive context,” *IFAC Proc. Vol.*, vol. 44, no. 1 PART 1, pp. 5076–5081, 2011.
- [167] S. T. Hirtle, “Eight degree of freedom vehicle model with pitch, yaw, tire control and sensor inputs,” California Polytechnic State University, 2015.
- [168] S. Do Na, J. S. Jang, K. S. Kim, and W. S. Yoo, “Dynamic vehicle model for handling performance using experimental data,” *Adv. Mech. Eng.*, vol. 7, no. 11, pp. 1–12, 2015.
- [169] S. Yang, Y. Lu, and S. Li, “An overview on vehicle dynamics,” *Int. J. Dyn. Control*, vol. 1, no. 4, pp. 385–395, Dec. 2013.
- [170] R. N. Jazar, *Vehicle Dynamics: Theory and application*, 2nd ed. Springer, 2008.
- [171] C. Canudas de Wit, R. Horowitz, and P. Tsiotras, “Model-based observers for tire/road contact friction prediction,” in *New Directions in nonlinear observer design*, no. October, 2007, pp. 23–42.
- [172] K. Min, Y.-S. Byun, and Y. C. Kim, *International journal of vehicle systems modelling and testing.*, vol. 10, no. 4. Inderscience Enterprises Ltd, 2015.
- [173] J. D. Setiawan, M. Safarudin, and A. Singh, “Modeling, simulation and validation of 14 DOF full vehicle model,” in *International Conference on Instrumentation, Communication, Information Technology, and Biomedical Engineering 2009*, 2009, pp. 1–6.
- [174] A. Pazoiki, S. Rakheja, and D. Cao, “Modeling and validation of off-road vehicle ride dynamics,” *Mech. Syst. Signal Process.*, vol. 28, pp. 679–695, Apr. 2012.
- [175] H. Haiyan and H. Qiang, “Three dimensional modeling and dynamic analysis of four-wheel-steering vehicles,” *Acta Mech. Sin.*, vol. 19, no. 1, pp. 79–88, Feb. 2003.
- [176] “CarSim Overview.” [Online]. Available: <https://www.carsim.com/products/carsim/index.php>. [Accessed: 13-Jun-2019].
- [177] “Adams - The Multibody Dynamics Simulation Solution.” [Online]. Available: <https://www.mscsoftware.com/product/adams>. [Accessed: 13-Jun-2019].
- [178] J. Wang, D. A. Wilson, W. Xu, and D. A. Crolla, “Active suspension control to improve vehicle ride and steady-state handling,” in *Proceedings of the 44th IEEE Conference on Decision and Control, and the European Control Conference, CDC-ECC ’05*, 2005.
- [179] P. Sathishkumar, J. Jancirani, D. John, and S. Manikandan, “Mathematical modelling and simulation quarter car vehicle suspension,” *IOSR J. Mech. Civ. Eng.*, vol. 3, no. 1, pp. 1280–

1283, 2014.

- [180] R. Krtolica and D. Hrovat, “Optimal active suspension control based on a half-car model: An analytical solution,” *IEEE Trans. Automat. Contr.*, 1992.
- [181] W. Gao, N. Zhang, and H. P. Du, “A half-car model for dynamic analysis of vehicles with random parameters,” in *5 th Australasian Congress on Applied Mechanics, ACAM,10-12 December 2007, Brisbane, Australia*, 2007, p. 6.
- [182] A. F. Jahromi, R. B. Bhat, and W. F. Xie, “Integrated ride and handling vehicle model using Lagrangian quasi-coordinates,” *Int. J. Automot. Technol.*, vol. 16, no. 2, pp. 239–251, Apr. 2015.
- [183] K. Min, Y.-S. Byun, and Y. C. Kim, “Modelling and validation of 16 DOF full vehicle model for guidance control,” *Int. J. Veh. Syst. Model. Test.*, vol. 10, no. 4, pp. 392–416, 2015.
- [184] K. Berntorp, “Derivation of a Six Degrees-of-Freedom Ground-Vehicle Model for Automotive Applications,” 2013.
- [185] A. K. Sharma, M. Bouteldja, and V. Cerezo, “Multi-physical model for tyre-road contact – the effect of surface texture,” *Int. J. Pavement Eng.*, pp. 1–18, 2020.
- [186] C. S. Liu and P. He, “Unknown input estimation for a class of nonlinear systems and its application to automotive engine controls,” in *Proceedings of the American Control Conference*, 2009, pp. 1195–1200.
- [187] M. Ouahi, J. Stéphant, and D. Meizel, “Simultaneous observation of inputs and state of wheeled vehicle model,” *IFAC Proc. Vol.*, vol. 7, no. PART 1, pp. 533–538, 2010.
- [188] M. Oueder, M. Farza, R. Ben Abdennour, and M. M’Saad, “A high gain observer with updated gain for a class of MIMO non-triangular systems,” *Syst. Control Lett.*, vol. 61, no. 2, pp. 298–308, 2012.
- [189] Kistler, “Measurement Systems and Sensors | Kistler.” [Online]. Available: <https://www.kistler.com/en/>. [Accessed: 14-Jan-2020].
- [190] M. Kane and V. Edmondson, “Skid resistance: understanding the role of road texture scales using a signal decomposition technique and a friction model,” *Int. J. Pavement Eng.*, 2020.
- [191] L. Jones, “Modélisation des forces de contact entre le pneu d’un avion et la piste,” 2012.
- [192] A. Tornambe, “Use of asymptotic observers having-high-gains in the state and parameter estimation,” in *Proceedings of the IEEE Conference on Decision and Control*, 1989, vol. 2, pp. 1791–1794.
- [193] J. P. Gauthier and I. A. K. Kupka, “Observability and observers for nonlinear systems,” *SIAM J. Control Optim.*, vol. 32, no. 4, pp. 975–994, Aug. 1994.
- [194] S. Nicosia and A. Tornambe, “High-gain observers in the state and parameter estimation of robots having elastic joints,” *Syst. Control Lett.* 13, vol. 13, pp. 331–337, 1989.
- [195] L. Menini and A. Tornambè, “High-gain observers for nonlinear systems with trajectories close to unobservability,” *Eur. J. Control*, vol. 20, no. 3, pp. 118–131, 2014.
- [196] J. Slotine and W. Li, *Applied Nonlinear Control Slotine*, 20th ed. Prentice Hall, 1991.
- [197] V. S. Emelyanov, K. S. Korovin, and V. L. Levantovskiy, “A drift algorithm in control of uncertain processes,” *Probl. Control Inf. Theory*, vol. 15, no. 6, pp. 425–438, 1986.

- [198] Q. Zhang, “Adaptive observer for multiple-input-multiple-output (MIMO) linear time-varying systems,” *IEEE Trans. Automat. Contr.*, vol. 47, no. 3, pp. 525–529, Mar. 2002.
- [199] Q. Zhang and A. Clavel, “Adaptive observer with exponential forgetting factor for linear time varying systems,” in *Proceedings of the IEEE Conference on Decision and Control*, 2001, vol. 4, pp. 3886–3891.
- [200] M. Farza, M. M’Saad, T. Maatoug, and M. Kamoun, “Adaptive observers for nonlinearly parameterized class of nonlinear systems,” *Automatica*, vol. 45, no. 10, pp. 2292–2299, Oct. 2009.
- [201] Michelin, *The Tire Grip*. Société de Technologie Michelin, 2001.
- [202] L. Seddiki, A. Rabhi, N. Kouider M’sirdi, and Y. Delanne, “Comparative Analysis of Tire Pavement Contact Models,” 2017.
- [203] W. Liang, J. Medanic, and R. Ruhl, “Analytical dynamic tire model,” *Veh. Syst. Dyn.*, vol. 46, no. 3, pp. 197–227, Mar. 2008.
- [204] C. Canudas de Wit and P. Tsiotras, “Dynamic tire friction models for vehicle traction control,” in *Proceedings of the 38th IEEE Conference on Decision and Control*, 1999, vol. 4, pp. 3746–3751.
- [205] E. Velenis, P. Tsiotras, C. C. De Wit, and M. Sorine, “Dynamic Tire Friction Models for Combined Longitudinal and Lateral Vehicle Motion,” *Veh. Syst. Dyn.*, 2005.
- [206] J.-J. Martinez, J.-C. Avila, and C. Canudas de Wit, “A New Bicycle Vehicle Model with Dynamic Contact Friction,” *IFAC Proc. Vol.*, vol. 37, no. 22, pp. 625–630, Apr. 2004.
- [207] J. N. Van Ginkel, “Estimating the Tire-Road Friction Coefficient Based on Tire Force Measurements,” 2014.
- [208] G. Gim and P. E. Nikraves, “Analytical model of pneumatic tyres for vehicle dynamic simulations. Part 1. Pure slips,” *Int. J. Veh. Des.*, vol. 11, no. 6, pp. 589–618, Dec. 1990.
- [209] E. Esmailzadeh, A. Goodarzi, and G. R. Vossoughi, “Optimal yaw moment control law for improved vehicle handling,” *Mechatronics*, vol. 13, no. 7, pp. 659–675, Sep. 2003.
- [210] H.-J. Kim and Y.-P. Park, “Investigation of robust roll motion control considering varying speed and actuator dynamics,” *Mechatronics*, vol. 14, no. 1, pp. 35–54, Feb. 2004.

List of figures

Figure 1 Distribution of emission of greenhouse gases.....	8
Figure 2 Global distribution of CO ₂ emission sector-wise [4]	9
Figure 3 Distribution of CO ₂ emission sector wise for France [4]	9
Figure 4 Distribution of CO ₂ emission by fuel type for France[4].....	10
Figure 5 Distribution of CO ₂ in the EU in the transport sector [5].....	11
Figure 6 Breakdown of passenger car energy consumption, as approximated for a speed of 60km/h [6]	11
Figure 7 Percentage loss of vehicle energy with respect to different usage [1]	12
Figure 8 Thesis follow-up steps	14
Figure 9 Methodology of tyre rolling resistance force estimation	14
Figure 10 Resistive forces acting on a vehicle [1].....	18
Figure 11 Graphical representation of rolling resistance force [20].....	20
Figure 12 Mechanism of rolling resistance force [1]	21
Figure 13 Effect of tyre pressure on the different road surface on the rolling resistance coefficient [14]	22
Figure 14 Inflation pressure influence on rolling resistance for speed 50 and 80 km/h Load 400 kg [17]	23
Figure 15 Load influence on rolling resistance for speed 50 and 80 Km/h, inflation pressure 2.1 bar.	23
Figure 16 Effect of speed on the rolling resistance coefficient [1].....	24
Figure 17 Illustration of the various scale of road roughness[30]	25
Figure 18 Road surface texture surface [33]	26
Figure 19 Definition of road surface mean profile depth [34]	26
Figure 20 Effect of texture on numerous phenomena as a function of wavelength range [20].....	26
Figure 21 Rolling resistance coefficient as a function of MPD [30], [40]	27
Figure 22 Effect of ambient temperature on rolling resistance [1].....	28
Figure 23 Influence of air temperature on rolling resistance for different tyres and different speeds [5]	28
Figure 24 Effect of tyre diameter on different road surface [27]	29
Figure 25 Effect of tyre diameter on rolling resistance[13]	30
Figure 26 Rolling resistance phenomenon [35].....	32
Figure 27 FEM Tyre model [20]	34
Figure 28 Drum test to measure rolling resistance [8]	35
Figure 29 Rolling resistance measuring trailers from different laboratories (a) BRRC (b) TUG (c) BASt (d) FKFS.....	36
Figure 30 Stability in the sense of Lyapunov [99]	44
Figure 31 Longitudinal dynamics of a wheel [7]	51
Figure 32 Determinant of Jacobien matrix	55
Figure 33 Gain for adaptive high gain and SOSM observer	56
Figure 34 Estimation results of rolling resistance for case 3.....	57
Figure 35 Estimation errors for case 3	58
Figure 36 Tyre-model categories main characteristics[44]	61
Figure 37 Spider chart for different Tyre-model categories.....	62
Figure 38 Comparison of different tyre models (longitudinal forces).....	64
Figure 39 Comparison of different tyre models (lateral forces).....	64
Figure 40 Multi physical tyre model	66
Figure 41 The brush tyre model[170].....	67

Figure 42 Schematic of (a) Multi-bristles brush model with 3 parameters Maxwell model [172] (b) Wheel reference coordinate system.....	68
Figure 43 Dynamic friction model example values taken from [172].....	69
Figure 44 Heat exchange model between tyre and road.....	70
Figure 45 Quarter car model with integrated Multi-physical tyre model.....	73
Figure 46 Sensitivity study for the mechanical block of the multi-physical tyre model.....	74
Figure 47 Sensitivity study on slip variation for the thermal block of the multi-physical tyre model ..	75
Figure 48 Sensitivity study on load variation for the thermal block of the multi-physical tyre model.	76
Figure 49 Tyre tread surface and Carcass temperature for variation of speed from 60 to 80 Km/h	77
Figure 50 Thermal model simulation results for variable speed	77
Figure 51 Contact patch deflection at different road roughness.....	78
Figure 52 Evolution of contact area with speed, Contact area at road surface roughness 0mm considered as reference and 1 means all (100%) the bristle in contact.	79
Figure 53 Block diagram of the 3D vehicle model	84
Figure 54 Vehicle Axis System ISO 8855-2011	85
Figure 55 A three-dimensional dynamic model of full vehicle.....	86
Figure 56 A dynamic model of the full vehicle. The wheels are numbered from the front left wheel to the rear right wheel [197]	86
Figure 57 Independent suspensions.....	88
Figure 58 (a) Tyre slip and steer angles on the wheel-fixed frame[196] (b) Wheel reference coordinate system.....	89
Figure 59 Interface of SCANeR™ Studio (Prosper)	91
Figure 60 Methodology of model validation.....	92
Figure 61 Comparison of position variables between Prosper and model for vehicle moving in a straight line at 50 km/h.....	93
Figure 62 Comparison of speed variables between Prosper and model for vehicle moving in a straight line at 50 km/h.....	93
Figure 63 Comparison of position variables between Prosper and model for vehicle moving in a curve of 320m at 60 km/h	94
Figure 64 Comparison of speed variables between Prosper and model for vehicle moving in a curve of 320m at 60 km/h.....	95
Figure 65 Comparison of position variables between Prosper and model for the vehicle is accelerating and braking	96
Figure 66 Comparison of speed variables between Prosper and model for the vehicle is accelerating and braking	96
Figure 67 Block diagram of the complete vehicle model.....	100
Figure 68 Unknown inputs adaptive high gain observer principle.....	103
Figure 69 Comparison between Prosper results and observer estimation of rolling resistance (Case 1: straight line).....	114
Figure 70 Comparison between Prosper results and observer estimation (Case 1: straight line).....	114
Figure 71 Estimation error results of the observer (Case 1: straight line).....	114
Figure 72 Comparison between Prosper results and observer estimation of rolling resistance (Case 2: Circle).....	115
Figure 73 Comparison between Prosper results and observer estimation (Case 2: Circle).....	115
Figure 74 Estimation error results of the observer (Case 2: Circle).....	116
Figure 75 Tyre surface temperature state estimation comparison and percentage relative mean error (Case 1: straight line)	119

Figure 76 Comparison between Prosper results and observer estimation of rolling resistance (Case 1: straight line).....	120
Figure 77 Comparison between Prosper results and observer estimation (Case 1: straight line).....	120
Figure 78 Estimation error results of the observer (Case 1: straight line).....	121
Figure 79 Tyre surface temperature state estimation comparison and percentage relative mean error (Case 2: Circle).....	121
Figure 80 Comparison between Prosper results and observer estimation of rolling resistance (Case 2: Circle).....	122
Figure 81 Comparison between Prosper results and observer estimation (Case 2: Circle).....	123
Figure 82 Comparison between Prosper results and observer estimation (Case 2: Circle).....	123
Figure 83 Photograph of test tracks at University Gustave Eiffel (top view)	125
Figure 84 Detailed different test track at University Gustave Eiffel, Nantes [10]	126
Figure 85 Univ. Gustave Eiffel instrumented vehicle with mounted sensors	128
Figure 86 Accelerometer position	128
Figure 87 Inertial unit position.....	129
Figure 88 Mounted steering angle sensor (a) Sensor position (b) Initial position.....	129
Figure 89 Speed sensor.....	130
Figure 90 Data acquisition system	131
Figure 91 Dynamometric wheel mounted on the front right tyre	132
Figure 92 (a) Infrared temperature sensor (b) Mounted sensor position on the vehicle.....	132
Figure 93 MB Flex infrared sensor for multi-beam flexible system	133
Figure 94 Tyre deformation sensor	133
Figure 95 Cellule sensor for pointing out the start of the test track	136
Figure 96 Different cut-off frequency comparison for low pass Butterworth filter	137
Figure 97 Relationship between M_y and F_{drag}	138
Figure 98 Tyre deformation and effective radius measured during experiments.....	139
Figure 99 Tyre deformation mean in percentage for different conditions.....	139
Figure 100 Bar plot of tyre rolling resistance force, coefficient and tyre temperature.....	141
Figure 101 Bar plot of tyre rolling resistance force, coefficient and tyre temperature.....	141
Figure 102 Crr trend for different surfaces at different ambient air temperature for 50 km/h	142
Figure 103 Bar plot of mean rolling resistance at 50 km/h on the E1 test track and coefficient of variation.....	143
Figure 104 Corrected rolling resistance coefficient for different tyre inflation pressure on different test tracks	144
Figure 105 Bar plot of rolling resistance, tyre temperature and coefficient of variation	145
Figure 106 Bar plot of tyre rolling resistance force, coefficient and tyre temperature for different surfaces in increasing order of MPD.....	146
Figure 107 Corrected Crr trend for different surfaces at 50 km/h and 80 km/h.....	147
Figure 108 Bar plot of rolling resistance, tyre temperature and coefficient of variation	148
Figure 109 Crr trend for different surfaces at 50 km/h for different MPD values	149
Figure 110 Crr trend for different surfaces at 50 km/h for different IRI values.....	149
Figure 111 Bar plot of rolling resistance, tyre temperature and coefficient of variation	150
Figure 112 Crr trend for different surfaces at 80 km/h for different MPD values	151
Figure 113 Crr trend for different surfaces at 80 km/h for different IRI values.....	151
Figure 114 Normalized Crr trend for different test surfaces	152
Figure 115 Rolling resistance coefficient as a function of MPD from [30]	153
Figure 116 Syntheses of comparison of DoE results and literature results	153
Figure 117 Tyre temperature infrared sensor installed position on the vehicle	154

Figure 118 Description of sensor comparison between positions	155
Figure 119 Distribution of tyre surface temperature at 50 km/h	156
Figure 120 Distribution of tyre surface temperature at 80 km/h	156
Figure 121 Mean tyre surface temperature for two different speeds.....	157
Figure 122 Mean temperature difference for different sensor positions at 50 km/h	158
Figure 123 Mean temperature difference for different sensor positions at 80 km/h	158
Figure 124 Impact of variation speed on tyre surface temperature at 20°C ambient air temperature .	158
Figure 125 Impact of variation speed on tyre surface temperature at 40°C ambient air temperature .	159
Figure 126 Mean tyre surface temperature for different surfaces as 50 km/h.....	159
Figure 127 Temperature difference for different sensor positions for different test tracks at 50 km/h	160
Figure 128 Circumferential tyre surface temperature variation for different test tracks at 50km/h	160
Figure 129 Mean tyre surface temperature for different surfaces as 80 km/h.....	161
Figure 130 Temperature difference for different sensor positions for different test tracks at 80 km/h	162
Figure 131 Circumferential tyre surface temperature variation for different test tracks at 80 km/h ...	163
Figure 132 Variation of mean tyre surface temperature for lane change at 60km/h	164
Figure 133 Temperature difference for different sensor positions for lane change at 60 km/h	164
Figure 134 Variation of mean tyre surface temperature for acceleration and braking	165
Figure 135 Temperature difference for different sensor positions for acceleration and braking	165
Figure 136 Variation of mean tyre surface temperature for vehicle moving in curve 220m at 80 km/h	166
Figure 137 Temperature difference for different sensor positions in curve 220m at 80 km/h.....	167
Figure 138 MB Flex sensor measurement points front and top view.....	167
Figure 139 Variation of tyre surface temperature measurement points in the lateral direction for the M3 test track at 80 km/h.....	168
Figure 140 Curve fit of lateral mean tyre temperature variation and points on the tyre	169
Figure 141 Mean tyre surface temperature with a standard deviation.....	169
Figure 142 Tyre surface mean temperature curve fit for different test tracks at 50 km/h	170
Figure 143 Tyre surface mean temperature curve fit for different test tracks at 80 km/h	170
Figure 144 Variation of lateral mean tyre surface temperature for lane change at 60 km/h	171
Figure 145 Mean Temp of tyre surface in the lateral direction for lane change at 60 km/h	172
Figure 146 Variation of lateral mean tyre surface temperature for acceleration and braking	172
Figure 147 Variation of lateral mean tyre surface temperature for acceleration and braking	173
Figure 148 Variation of lateral mean tyre surface temperature in 220m curve at 80 km/h.....	174
Figure 149 Mean tyre surface temperature in the lateral direction in the 220m curve at 80 km/h.....	174
Figure 150 Comparison of circumferential and lateral variation of tyre surface temperature for varying speed.....	175
Figure 151 Vehicle speed and tyre surface temperature relationship with circumferential variation .	175
Figure 152 Vehicle speed and tyre surface temperature relationship with lateral variation.....	176
Figure 153 Methodology of model validation.....	179
Figure 154 Cooling of a tyre contact (red) to measured point (blue).....	180
Figure 155 Cooling behaviour of contact temperature (hypotheses).....	181
Figure 156 Comparison of tyre forces between model and experimental at 50 km/h	181
Figure 157 Comparison of tyre surface temp between model and experimental at 50 km/h	182
Figure 158 Comparison of tyre forces between model and experimental for accelerating and braking	182
Figure 159 Comparison of tyre surface temperature between model and experiment for accelerating and braking	183
Figure 160 Results comparison between model and experimentation for straight line.....	184

Figure 161 Results comparison between model and experimentation for a circle with radius 320m (Test 2)	185
Figure 162 Comparison of speed variables between experiments and model for the vehicle is accelerating and braking.....	186
Figure 163 Comparison of longitudinal force between model and experiment for different test tracks at 50 km/h.....	187
Figure 164 Comparison of longitudinal force between model and experiment for different test tracks at 80 km/h.....	188
Figure 165 Methodology of estimation and comparison.....	189
Figure 166 State variable comparison and error between experimental results and observer (straight line).....	190
Figure 167 Comparison between experimental and estimated rolling resistance force (Straight line).....	191
Figure 168 Estimation error results of observer estimation (Straight line)	191
Figure 169 Adaptive gain and zoom on adaptive gain (straight line).....	192
Figure 170 Comparison between experimental and estimated tyre effective radius (Straight line)....	192
Figure 171 State variable comparison and error between experimental results and observer (curve with 320m radius at 80km/h).....	193
Figure 172 State variable comparison and error between experimental results and observer (curve with 320m radius at 80km/h).....	193
Figure 173 Comparison between experimental and estimated rolling resistance force observer (curve with 320m radius at 80 km/h).....	194
Figure 174 Estimation error results of observer estimation observer (curve with 320m radius at 80 km/h)	194
Figure 175 Adaptive gain and zoom on the adaptive gain observer (curve with 320m radius at 80 km/h)	195
Figure 176 Comparison between experimental and estimated tyre effective radius (curve with 320m radius at 80 km/h).....	195
Figure 177 Tyre surface temperature state estimation comparison and percentage relative mean error (Case 1: straight line)	197
Figure 178 State variable comparison and error between experimental results and observer (straight line).....	197
Figure 179 Comparison between experimental and estimated rolling resistance force (Straight line).....	198
Figure 180 Estimation error results of observer estimation (Straight line)	198
Figure 181 Adaptive gain and zoom on adaptive gain (straight line).....	199
Figure 182 Comparison between experimental and estimated tyre effective radius (Straight line)....	199
Figure 183 Tyre surface temperature state estimation comparison and percentage relative mean error (curve with 320m radius at 80 km/h)	200
Figure 184 State variable comparison and error between experimental results and observer (curve with 320m radius at 80 km/h).....	200
Figure 185 State variable comparison and error between experimental results and observer (curve with 320m radius at 80 km/h).....	201
Figure 186 Comparison between experimental and estimated rolling resistance force observer (curve with 320m radius at 80 km/h).....	201
Figure 187 Estimation error results of observer estimation observer (curve with 320m radius at 80 km/h)	202
Figure 188 Comparison between experimental and estimated tyre effective radius (curve with 320m radius at 80 km/h).....	202

Figure 189 Adaptive gain and zoom on the adaptive gain of the observer (curve with 320m radius at 80 km/h)	203
Figure 190 The total mean estimated rolling resistance for different test tracks at a different speed .	203
Figure 191 Normalised estimated mean Crr for different road roughness at a different speed.....	204
Figure 192 Lumped form of LuGre tyre model with punctual contact [133].....	236
Figure 193 Brush tyre model, deformation of the tyre rubber (Top: a side view and bottom: top view)	239
Figure 194 Schematic of Quarter Car model.....	243
Figure 195 Schematic of Half Car model.....	244
Figure 196 Schematic two DoF of bicycle model	244
Figure 197 Schematic of three DoF bicycle model	244
Figure 198 Schematic of Full Car model	245
Figure 199 Schematic of eight DoFs full car model.....	245
Figure 200 Comparison of position variables between prosper and model for vehicle moving in straight line at 80km/h.....	246
Figure 201 Comparison of speed variables between prosper and model for vehicle moving in straight line at 80km/h.....	247
Figure 202 Comparison of position variables between prosper and model for vehicle moving in curve of 220m at 40km/h	247
Figure 203 Comparison of position speed between prosper and model for vehicle moving in curve of 220m at 40km/h.....	248
Figure 204 Comparison of position variables between prosper and model for vehicle moving in curve of 220m at 80km/h	248
Figure 205 Comparison of speed variables between prosper and model for vehicle moving in curve of 220m at 80km/h.....	249
Figure 206 Comparison of position variables between prosper and model for vehicle moving in curve of 320m at 40km/h	249
Figure 207 Comparison of speed variables between prosper and model for vehicle moving in curve of 320m at 40km/h.....	250
Figure 208 Comparison of position variables between prosper and model for vehicle moving in curve of 320m at 60km/h	250
Figure 209 Comparison of speed variables between prosper and model for vehicle moving in curve of 320m at 60km/h.....	251
Figure 210 Comparison of position variables between prosper and model for vehicle moving in curve of 320m at 80km/h	251
Figure 211 Comparison of speed variables between prosper and model for vehicle moving in curve of 320m at 80km/h.....	252
Figure 212 Comparison of position variables between prosper and model for vehicle is changing lane at 60km/h.....	252
Figure 213 Comparison of speed variables between prosper and model for vehicle is changing lane at 60km/h.....	253
Figure 214 Comparison of speed variables between experimental data and model.....	254
Figure 215 Comparison of speed variables between experimental data and model.....	254
Figure 216 Comparison of speed variables between experimental data and model.....	255
Figure 217 Comparison of speed variables between experimental data and model.....	255
Figure 218 Comparison of speed variables between experimental data and model.....	256
Figure 219 Comparison of speed variables between experimental data and model.....	256
Figure 220 Comparison of speed variables between experimental data and model.....	257

Figure 221 Variation of tyre surface temperature for lane change at 80km/h.....	258
Figure 222 Variation of tyre surface temperature between sensors for lane change at 80km/h.....	258
Figure 223 Variation of tyre surface temperature for braking manoeuvres on E3.....	259
Figure 224 Gradient of tyre surface temperature for braking manoeuvres on E3.....	259
Figure 225 Variation of tyre surface temperature for acceleration manoeuvres on E3.....	260
Figure 226 Gradient of tyre surface temperature for acceleration manoeuvres on E3.....	260
Figure 227 Variation of tyre surface temperature for braking manoeuvres on M2.....	261
Figure 228 Gradient of tyre surface temperature for braking manoeuvres on M2.....	261
Figure 229 Variation of tyre surface temperature for acceleration manoeuvres on M2.....	262
Figure 230 Gradient of tyre surface temperature for acceleration manoeuvres on M2.....	262
Figure 231 Variation of tyre surface temperature for braking manoeuvres on C1.....	263
Figure 232 Gradient of tyre surface temperature for braking manoeuvres on C1.....	263
Figure 233 Variation of tyre surface temperature measurement points in the lateral direction for the M3 test track at 50km/h.....	264
Figure 234 Variation of tyre surface temperature measurement points in the lateral direction for the M2 test track at 80km/h.....	264
Figure 235 Adaptive gain for both observers.....	265
Figure 236 Determinant of jacobien matrix for the different observation techniques.....	265
Figure 237 Estimation of rolling resistance force.....	266
Figure 238 The error comparison for the estimation and observation.....	266
Figure 239 State variable comparison and error between experimental results and observer (straight line).....	267
Figure 240 Comparison between experimental and estimated rolling resistance force (Straight line).....	267
Figure 241 Estimation error results of observer estimation (Straight line).....	268
Figure 242 Adaptive gain and zoom on adaptive gain (straight line).....	268
Figure 243 Comparison between experimental and estimated tyre effective radius (Straight line)....	269
Figure 244 Tyre surface temperature state estimation comparison and percentage relative mean error (curve radius 220m at 40km/h).....	269
Figure 245 State variable comparison and error between experimental results and observer (curve radius 220m at 40km/h).....	270
Figure 246 State variable comparison and error between experimental results and observer (curve radius 220m at 40km/h).....	270
Figure 247 Comparison between experimental and estimated rolling resistance force observer (curve radius 220m at 40km/h).....	271
Figure 248 Estimation error results of observer estimation observer (curve radius 220m at 40km/h).....	271
Figure 249 Adaptive gain and zoom on adaptive gain observer (lane change).....	272
Figure 250 Comparison between experimental and estimated tyre effective radius (curve radius 220m at 40km/h).....	272
Figure 251 Tyre surface temperature state estimation comparison and percentage relative mean error (curve radius 220m at 40km/h).....	273
Figure 252 State variable comparison and error between experimental results and observer (curve radius 220m at 40km/h).....	273
Figure 253 State variable comparison and error between experimental results and observer (curve radius 220m at 40km/h).....	274
Figure 254 Comparison between experimental and estimated rolling resistance force observer (curve radius 220m at 40km/h).....	274
Figure 255 Estimation error results of observer estimation observer (curve radius 220m at 40km/h).....	275
Figure 256 Adaptive gain and zoom on adaptive gain observer (lane change).....	275

Figure 257 Comparison between experimental and estimated tyre effective radius (curve radius 220m at 40km/h)	276
Figure 258 Tyre surface temperature state estimation comparison and percentage relative mean error (lane change)	276
Figure 259 State variable comparison and error between experimental results and observer (lane change)	277
Figure 260 State variable comparison and error between experimental results and observer (lane change)	277
Figure 261 Comparison between experimental and estimated rolling resistance force observer (lane change)	278
Figure 262 Estimation error results of observer estimation observer (lane change)	278
Figure 263 Adaptive gain and zoom on adaptive gain observer (lane change)	279
Figure 264 Comparison between experimental and estimated tyre effective radius (lane change)	279

List of tables

Table 1 Comparison of rolling resistance measurement methods	38
Table 2 Synthesis of different observation techniques	48
Table 3 Simulation test plan	56
Table 4 Simulated errors of estimated values for two observers.....	58
Table 5 Simulated errors of estimated values for two observers.....	58
Table 6 Synthesis of different tyre models.....	63
Table 7 Synthesis of different vehicle model in the literature.....	83
Table 8 Test conditions	91
Table 9 Summary of results in a relative mean error (RME) for test scenarios	97
Table 10 Characterization of test surfaces.....	126
Table 11 Proposed 1 st Test scenarios (DoE) to validate the vehicle model.....	134
Table 12 Influencing Factors with different scenarios on Michelin energy saver 185/60 R15.....	134
Table 13 Proposed 2 nd Test scenarios (DoE) for rolling resistance validation.....	135
Table 14 Loaded radius used in the calculation	140
Table 15 Parameter table ambient air temperature.....	140
Table 16 Parameter table tyre inflation pressure	143
Table 17 Parameter table tyre load.....	144
Table 18 Parameter table speed.....	145
Table 19 Parameter table different roughness surface.....	147
Table 20 Synthesis of tyre surface temperature in different Scenarios	177
Table 21 Synthesis of circumferential and lateral variation of tyre surface temperature	178
Table 22 Global performance of developed observers.....	204
Table 23 Parameter and factor values used in the calculation.....	235
Table 24 Test conditions	246

Appendix

A. Different Observers for nonlinear systems

In most applications, the process must be controlled or monitored in real-time and this requires being able to access the variations as a function of time of the state variables. This access is not always possible either due to the lack of suitable sensors or the high cost of some of these sensors. To overcome this problem, a state observer (an estimator) is generally used to reconstruct unmeasured state variables. The observer is an algorithm which provides an estimate $\hat{x}(t)$ of the state $x(t)$ of the system, from the measurements of the output $y(t)$ and the input $u(t)$.

The field of state and parameter estimation of non-linear systems is still largely open. We will see that there is no universal method for the synthesis of such observers, the possible approaches are:

i. Kalman filter

The first one which has met a great success in the past is based on the Kalman filter which is used as a nonlinear observer [81]–[83]. The attractiveness of the Kalman filter is mainly due to its implementation simplicity independently of the system complexity. Nevertheless, a major drawback of this method is the lack of guaranteed stability.

ii. Nonlinear transformation methods

This technique is based on a change of coordinates which makes it possible to transform a nonlinear system into a linear system. Once the transformation has been carried out, the use of a linear observer (Luenberger or Kalman filter) will suffice to estimate the state of the transformed system, therefore the state of the original system using the reverse coordinate change. A Luenberger-type observer is designed and sufficient conditions for the asymptotic stability of the error can be derived. Thus, the resulting class of systems constitutes a subclass of triangular systems with the particularity that nonlinearities only depend on the measured inputs and outputs.

iii. Extended nonlinear observers

Above method has been extended by [81], [82]. Later [78], [83] considered the method of linearization by a nonlinear change of coordinates, so a Luenberger-type observer can be developed for such systems. [79] has also developed an observer for non-linear systems in this sense. This is the case of the extended Kalman filter and the extended Luenberger observer, the gain of the observer is calculated using the linearized system around the estimated trajectory. It is further developed as generalized Luenberger observers [88], [89]. In this case, the design of this type of observer consists of adding a second gain to the Luenberger observer inside the non-linear part of the system.

iv. High gain observers

This observer is based on the observable canonical form. The pioneer contribution has been made in [66] where the authors gave a necessary and sufficient condition giving rise to the well-known single output triangular canonical form. This canonical form is composed of a fixed linear dynamics component and a nonlinear triangular controlled one. Using this canonical form, the authors have designed a high gain observer under some global Lipchitz assumption on the controlled part. The gain of the proposed observer is issued from an algebraic Lyapunov equation that can be explicitly solved. The main characteristic of the high gain observer proposed in [66] lies in the easiness of its implementation since the observer is a copy of the model with a gain whose expression is explicitly

given. Moreover, the tuning of the observer is achieved through the choice of a single scalar design parameter. A different non-linear observer called high-gain observer based on the approximate annulation of non-linearity was presented by [192] and was then improved by [66], [193].

The effectiveness of such an observer has been highlighted through many successful industrial applications [66], [188], [194], [195]. There is however the main drawback of this observer that is worth to be noticed, namely the specification of the design parameter is generally carried out through a try and error procedure to get a satisfactory compromise between the accuracy of the observer and its sensitivity to noise measurements.

v. Sliding mode observers

Sliding mode technique has been the focus of growing literature since the work done by [97]. Sliding surfaces have been first used for the development of feedback controllers [94], [196]. Next researchers have tried to exploit their excellent robustness and performance properties to design linear and nonlinear sliding observers [67], [68], [94]–[96]. The fundamental difference between a sliding mode observer and other observer approaches is that in other approaches the observer reconstructs the original state vector asymptotically, however, in sliding mode approach a suitable discontinuous output injection is used to guarantee finite-time convergence by a deliberate induction of an attractive hyperplane. Robustness, insensitivity properties and simplicity of design make sliding observers a powerful approach. Analysis and comparison of several types of observers can be found in [78] [87] showing that a sliding mode observer is a good approach from the point of view of robustness, ease of design and overall evaluation. The concept of higher order sliding mode has been introduced by [197], the principle of action has, through corrective discontinuous terms, the higher order derivatives of the measurement error y . The main advantages are conservation benefits of the sliding mode observer is its robustness and convergence in finite time, reduction of the effects of chattering and the improvement of the performance of the observer.

vi. Adaptive observers

Another kind of observer for joint estimation of missing states and constant parameters in linear and nonlinear state-space systems has motivated a lot of work, for adaptive control, or recently fault detection and isolation in dynamic systems. Some early works on adaptive observers for linear systems can be found in [101]–[106] while more recent results are reported in [103], [104], [198], [199]. These authors consider systems that can be transformed into a certain canonical form. The adaptive observers help to estimate simultaneously the system states and the unknown parameters. These methods do not require the considered nonlinear systems to be linearizable, instead, they assume the existence of some Lyapunov functions satisfying particular conditions. A very few results are available in the literature that addresses state and parameter estimation in the presence of nonlinear parameterizations [98], [99], [107]. Nonlinear parameterizations are inevitable in many realistic dynamic models, even in the case where only a few state variables are considered. When considered, the nonlinear parameterization assumes, as the linear one, that the unknown parameters appear in the model through functions that are known, i.e. these functions do not involve non-measured states. [103], [200] propose an approach which allows the design of adaptive observers for a class of uniformly observable nonlinear MIMO systems with general nonlinear parameterizations. Two main features of the proposed approach are worth to be mentioned. Firstly, the convergence of the proposed observer is guaranteed under a well-defined persistent excitation condition. Secondly, the structure of the proposed observer is simple and it can be used with different observers among which adaptive high gain like observers [66], [93], [100] and adaptive sliding mode like observers [94]. This is achieved

through the specification of a design function in the observer gain which is calibrated through the choice of a single design parameter.

vii. Observers for singularly perturbed systems

A great number of today's problems are brought about by present-day technology are highly complex and large in dimension by nature. A major difficulty in control system design is to reconcile the large-scale and fuzzy real problems with the simple, well-defined problems that control theory can handle. The usefulness of the singular perturbation approach to overcome these difficulties is evident from the results surveyed in [116]. The suggested observer approach is based on a two times scale separation of the observer error dynamics, where the subsystem in the fast time scale is caused by a high-gain injection, and the error dynamics in the slow time scale is designed such that, together with interconnection conditions, the complete system is asymptotically stable. Hence, the considered approach can also be regarded as a high gain observer design. However, here it is not assumed that a linear system dominates the nonlinearities. On the contrary, the equivalent expression of the high-gain injection term, (i.e. the slow manifold) which can be obtained from the collapsed fast subsystem, is exploited to construct nonlinear observer injections for the slow subsystem. In that manner, additional information about the unmeasured states might be obtained and employed for the observer design.

In the literature, singular perturbation techniques related to observer design can be found where observers are designed for classes of nonlinear singularly perturbed systems [108], [109], [112]–[115], or in controller-observer schemes for nonlinear singularly perturbed systems [117], [118]. Approaches, where the singular perturbation method is used to establish the observers are rarely considered. An early approach for linear systems can be found in [119]. However, all the above approaches presuppose the availability of a dynamic process model that does not exhibit time-scale multiplicity (a process dynamic response characteristic that naturally arises in a multitude of applications), and most importantly, the sensor dynamics is not integrated into their respective observer design frameworks, and thus its impact on the viability and performance of the proposed observer remains inevitably unaddressed. The state estimation problem becomes not only theoretically challenging due to the multiple timescales but practically an intriguing and important one. Indeed, one could in principle realize the design of the nonlinear observer through the restriction of the process dynamics on the slow manifold (the reduced-order process dynamic model), and thus capitalizing on all the computational and analytical advantages that the lower-dimensionality of the problem of interest brings, followed by a detailed, rigorous and insightful analysis on the impact of the ignored fast dynamics (otherwise known as “parasitic”) on the convergence properties of the reduced-order observer [116]. It should be emphasized, that the design of nonlinear observers based on the reduced-order process dynamic model on the slow manifold is motivated by the fact that model-based estimation problems for systems/processes exhibiting time-scale multiplicity, and thus stiff dynamics, may lead to ill-conditioned observer gains and potentially undermine the convergence properties of an observer designed for the full-order singularly perturbed system [110], [111].

B. Different tyre models

The safety of ground vehicles relies deeply on tyre-road interaction. Improving durability, safety and controllability have been the main concerns for tyres in recent years. Several academic and industrial researchers are working on attaining an accurate prediction of tyre friction characteristics. Therefore, developing a tyre model that can simulate forces and moments as a function of tyre excitations is of primary importance. However, currently used models have shown a certain lack of accuracy in some specific cases. This lack of accuracy is believed to be partly due to tyre temperature variation. Actually, tyre temperature is not constant on normal operating conditions and this latter induces some changes in tyre performance [135], [201].

i. Semi empirical model

Two famous empirical models to describe the input output formulas for a tyre are presented in this section.

a. Magic formula

This model is developed by Pacejka, and described in [43]. This model describes pre-sliding and sliding in just one equation. This means that the model is differentiable, which is an advantage. Furthermore, the magic formula model is a very accurate representation of actual tyre dynamics. But this comes at a cost since the model depends on a lot of parameters which might be difficult to obtain. [202] has also mentioned the Pacejka model with similar advantages. This model of Pacejka called "magic formula" makes it possible to calculate the longitudinal F_x and lateral F_y interactions (in N) as a function of the longitudinal slip, drift α (in degrees), the camber angle and the normal force F_z . Longitudinal and lateral forces are given by:

$$F_x = D_x \sin[C_x \arctan\{B_x \kappa_x - E_x (B_x \kappa_x - \arctan(B_x \kappa_x))\}] + S_{vx} \quad (209)$$

$$F_y = D_y \sin[C_y \arctan\{B_y \kappa_t - E_y (B_y \kappa_t - \arctan(B_y \kappa_t))\}] + S_{vy} \quad (210)$$

with:

κ_x : Longitudinal slip ratio, κ_t : Lateral slip ratio, B: coefficient of stiffness, C: form factor, D: maximum value of curve, E: Curve

The mathematical formula of Pacejka's model has been computed using MATLAB to calculate the steady-state force and moment response to sideslip and longitudinal slip. The magic formula will be used as a reference for comparing other models. Values from below Table 23 are used in the calculation taken from [43].

Table 23 Parameter and factor values used in the calculation

Parameter	Value	Parameter	Value
C_x	1.5	C_y	1.3
E_x	-1	E_y	-3
μ_x	1.26	μ_y	1

b. LuGre Model

The LuGre friction model comes as a result of adding the Stribeck effect to the Dahl model [126]. It can be formulated as a lumped model or as a distributed model depending on the shape of the friction contact between surfaces [126]. This dynamic friction model predicts the transient behaviour of the tyre-road forces under varying velocity circumstances. The LuGre dynamic model presents a concise form that is very appropriate in control analyses. It has been advantageously utilized in vehicle state estimation problems and tyre slips control design. The LuGre model captures crucial aspects of friction, such as striction, the Stribeck effect, stick-slip, zero slip displacement and hysteresis. One of the most important advantages of the LuGre tyre model is its ability to reflect the surface conditions, the effects of tyre vertical force and the effects of the vehicle speed on the friction force [203].

In this section three forms of LuGre tyre model are going to be presented: the lumped form, the average lumped form and the distributed form. Finally, MATLAB/Simulink is used to implement the static equations for the distributed model and the dynamic equations for the lumped model.

All the equations that are going to be introduced are valid for both lateral and longitudinal motion; the only thing that changes is the values of the fitting parameters, which are different due to the anisotropy of the friction characteristics.

Punctual tyre-road friction contact is assumed in lumped friction models. The deflections of the bristles are modelled by the following formulas, and the representation of the wheel with lumped friction is depicted in Figure 192.

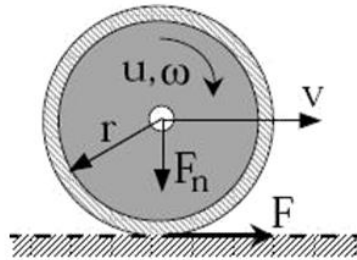


Figure 192 Lumped form of LuGre tyre model with punctual contact [204]

$$\begin{aligned} \dot{z} &= v_{sx} - \frac{\sigma_0 |v_{sx}|}{g(v_{sx})} z \\ F_x &= (\sigma_0 z + \sigma_1 \dot{z} + \sigma_2 v_{sx}) F_z \\ g(v_{sx}) &= \mu_c + (\mu_s - \mu_c) e^{-\sqrt{|v_{sx}/v_{st}|}} \end{aligned} \quad (211)$$

where z is the internal friction state of bristle elastic deflection, μ_c is the normalized Coulomb friction, μ_s is the normalized static friction, v_{sx} is the relative velocity between sliding bodies, v_{st} is the Stribeck relative velocity, F_z is the normal force, σ_0 is the rubber longitudinal lumped stiffness, σ_1 is the rubber longitudinal lumped damping and σ_2 is the viscous relative damping [204].

The average lumped form of the LuGre tyre model includes the average bristle deflection for simplicity of tyre-dynamics analysis and computational efficiency. The presence of a contact area

between the tyre and the road is assumed in the distributed form of the LuGre tyre model. The lumped form of the LuGre tyre model is an ordinary differential equation that can be resolved by time integration. Nevertheless, the distributed form assumes normal pressure distribution and is formulated using a partial differential equation which should be resolved in both time and space [126], [205]. The steady-state distributed model is used in the vehicle-dynamics analysis for parameters-fitting purposes, while the lumped model is used for the development of control strategy [171], [204], [206]. As demonstrated in [126], the lumped LuGre model is a good approximation of the distributed LuGre model, as they have similar steady-state and dynamic behaviour. The LuGre model is well known for describing special cases of friction situations. It has been introduced in the tyre modelling by [126] to describe the dynamic process when applying a brake torque on the tyre. It also deals with the velocity dependence on friction. The lumped form has to be used for control and estimation purposes but to be able to match the s parameters in the equations to experimental data the steady-state version of the distributed approach must be used.

Two semi empirical models for describing the force-slip relation have been described above. Many more models are described in the literature, but after the introduction of the Magic Formula, it has become the most popular tyre model. The LuGre model is interesting while it tries to deal with the dynamics in the friction surface.

ii. Physical model

Models in this category tend to be simpler and have equations and expressions with a logical physical background. The brush tyre model is a common type of physical tyre model. It approximates the tyre as fitted on a rigid rim, with the tread modelled as springs, or bristles, which can deform in the longitudinal, lateral and vertical direction. Physical tyre models have decent accuracy and do not require many input variables, as most equations and expressions are determined during the computational process. Most physical models are quite simple and thereby the computational effort required is not large. The models are also adaptable to change and modifications to include effects and parameters not already present. Doing so will however add complexity and computational effort.

a. Dugoff model

This analytical model is presented in [128]. In this simplified model the effects of camber and turn slip are neglected. Furthermore, a uniform vertical pressure distribution is assumed in the tyre. It is a model that gives an analytical relationship of the longitudinal and lateral force as a function of drift angle α , slip rate k and load F_z with a fixed coefficient of friction.

Longitudinal and lateral forces given by Dugoff model is given by:

$$\begin{aligned}
 F_x &= K_x \frac{\kappa}{1 - \kappa} \tau \\
 F_y &= K_y \frac{\tan \alpha}{1 - \kappa} \tau \\
 \tau &= \begin{cases} \sigma < 1: (2 - \sigma)\sigma \\ : 1 \end{cases} \\
 \sigma &= \frac{(1 - \kappa)\mu F_z}{2 \sqrt{K_x^2 \kappa^2 + K_y^2 \tan^2 \alpha}}
 \end{aligned} \tag{212}$$

where: Longitudinal slip ratio, K_x : Longitudinal stiffness K_y : Lateral stiffness τ : Coupling between the efforts.

The advantage of this model is that it does not require a large number of parameters. And since it is an analytical model, these parameters can be derived intuitively. The drawback of this method is that the gradient cannot be computed directly, since there are different equations for sliding and pre-sliding. Furthermore, the model is a very simplified representation. Therefore, the shape of the tyre curve is limited, such that a peak in the tyre curve cannot be modelled [207].

b. Gim model

[208] proposes a method of analytical calculation of the different forces acting on the wheel from the internal pressures in the inner tube and the different flexibilities and stiffness of the tyre. Author [208] consider:

- The contact area as a rectangle,
- The tyre model is based on determining the pressure along the contact surface. Which is at the origin of the normal force,
- The normal force is deduced from the integration of the pressure along with the contact.

The longitudinal and lateral forces are a function of the vertical load F_z , longitudinal and lateral sliding, l_n length of the contact surface, K_x longitudinal and K_y lateral stiffness and μ_x, μ_y the coefficient of friction. Tyre forces are given by:

$$\begin{aligned} F_x &= C_s \kappa l_n^2 + \mu_x F_z (1 - l_n^2 + 2l_n^3) \\ F_y &= C_\alpha \kappa l_n^2 + \mu_y F_z (1 - 3l_n^2 + 2l_n^3) \end{aligned} \quad (213)$$

with:

$$C_s = K_x W/2, C_\alpha = K_y W/2 \text{ and } l_n = 2l_r \left(1 - \frac{2Wl_r^2}{3\mu F_z} \left((K_x \kappa)^2 + (K_y \kappa_t)^2 \right)^{1/2} \right)$$

c. Kiencke model

Sds The author in [47] uses two techniques, the first is the calculation of the coefficient of friction by the extended Burckhardt model, this coefficient is a function of the slip resultant S , and the forces acting on the tyre, based on the transformation of the speed of the centre of gravity. The second is the calculation of the speeds of the different points of contact between the wheels and the ground. From the forces acting on the tyre, they evaluate the displacement of the centre of the resultants (point of detachment) with respect to the vertical projection of the centre of the wheel [47].

The coefficient of friction is:

$$\begin{aligned} \mu &= (c_1(1 - \exp(-c_2 S)) - c_3 S \exp(-c_4 S V_G))(1 - c_5 F_z^2) \\ S &= (\kappa^2 + \kappa_t^2)^{1/2} \end{aligned} \quad (214)$$

where c_1, c_2, c_3 : parameters in function of ground, c_4 : is the function of maximum driving speed, c_5 : is the function of the maximum load of the wheel, S : Total slip, V_G : The speed at the centre of gravity of the vehicle, F_z : vertical load.

The slip ratio is defined as:

For braking

$$\kappa = \frac{V_r - V_m}{V_m} \quad (215)$$

$$\kappa_t = \tan(\alpha)$$

For Driving

$$\kappa = \frac{V_r - V_m}{V_r} \quad (216)$$

$$\kappa_t = (1 - \kappa_t)\tan(\alpha)$$

where $V_r = r_{eff}\omega$, ω : angular speed, r_{eff} : effective radius of wheel and V_m : the longitudinal speed at the centre of the wheel.

The forces can be defined as

$$F_x = \mu \frac{F_z}{S} (\kappa \cos(\alpha) - c_{\mu t} \kappa_t \sin(\alpha)) \quad (217)$$

$$F_y = \mu \frac{F_z}{S} (c_{\mu t} \kappa_t \cos(\alpha) + \kappa \sin(\alpha))$$

with μ : Friction coefficient and $c_{\mu t}$: coefficient of ponderation (varies between 0.9 to 0.95).

d. Brush model

The Brush Tyre model is a very simplified way to model the creation of forces and torques between tyre and road. A great number of works describes this approach, [43], [129]–[131] and it was quite popular in the 1960s and 1970s before empirical approaches became the most used. In this section, its basis is discussed.

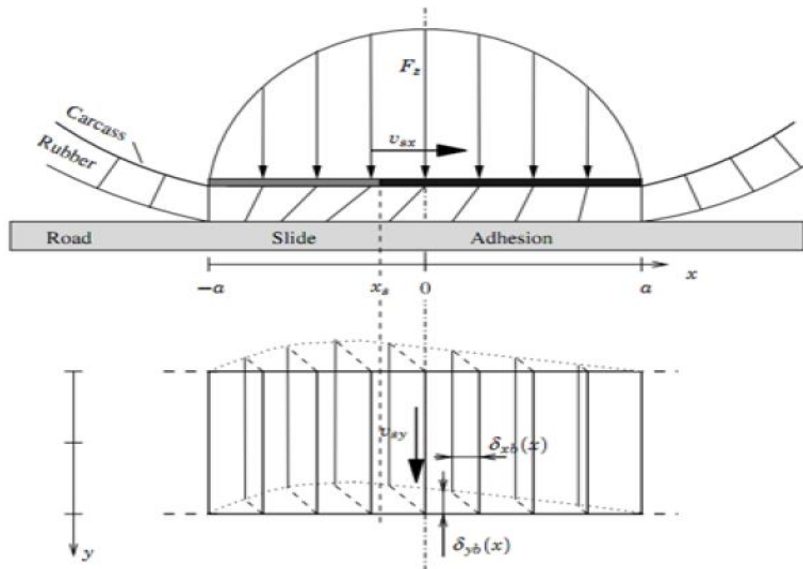


Figure 193 Brush tyre model, deformation of the tyre rubber (Top: a side view and bottom: top view)

The Brush Tyre model describes the generation of forces in the contact patch considering the contact region formed by small volumes of rubber, acting as springs. Considering a system of the coordinate axis is set in such a way that the origin is in the middle of the contact patch. Thus the x-axis is pointing forward, along the longitudinal direction of the wheel, and the y-axis is pointing laterally. The contact patch is $2a$ long. On the top of the bristles, a vertical pressure distribution is applied, and they are stretched longitudinally and laterally because of the slip velocity v_s . This model is based on these assumptions:

- the friction between the bristles and the ground is described by the simple Coulomb model
- the normal load has a parabolic distribution along with the contact patch, assuming zero value at the edges;

$$F_{x,y} = \mu F_z \text{ if } F_{x,y} > \mu F_z \text{ (Sliding condition)} \quad (218)$$

where μ is the friction coefficient between bristles and road, F_x and F_y are the longitudinal and lateral force respectively generated by the stretching of the bristle and F_z is the vertical load applied on that bristle. In this way it is possible to divide the contact patch into the adhesive and the sliding region;

- the carcass is considered as infinitely stiff;
- each bristle is assumed to deform independently in the longitudinal and lateral directions;

In the adhesive region, the bristles adhere to the road surface and the deformation is allowed by the static friction. In the sliding region, instead, the forces produced are a function of the sliding friction through equation (92) and (96), thus the resulting force is independent of bristle deformation [132], [157][30]. From Figure 193 it is possible to depict the deformation of the bristle δ_{xb} along with the x-axis as well the deformation δ_{yb} along the y-axis. Considering a slip angle α , in the adhesion region the bristle is forced to follow a straight line with slope equal to $\tan \alpha$, from the leading edge $(a, 0)$ as long as no sliding occurs. Thus the lateral deformation δ_{yb} is the function of the longitudinal coordinate x :

$$\delta_{yb} = (a - x) \tan \alpha \quad (219)$$

Consequently, assuming the lateral stiffness of the bristle equal to c_{py} , the lateral force per unit of length in the adhesion region for each bristle is:

$$F_{yb,a} = c_{py} \delta_{yb} \quad (220)$$

The sliding region occurs when the relation in equation 18 is true, in this case, when:

$$F_{yb,a} > \mu F_{zb} \quad (221)$$

where F_{zb} is the normal load applied on top of the bristle at the x coordinate.

If equation (90) is valid, then the lateral force is equal to:

$$F_{yb,s} = \mu F_{zb} \quad (222)$$

The total lateral force is equal to the sum of the forces generated by each bristle along with the whole contact patch as well the aligning torque M_z is the algebraic sum of the aligning torques of each bristle around z-axis:

$$F_y = \int_{-x_t}^a F_{yb,a} dx + \int_{-a}^{-x_t} F_{yb,s} dx \quad (223)$$

$$M_z = \int_{-x_t}^a x F_{yb,a} dx + \int_{-a}^{-x_t} x F_{yb,s} dx$$

where x_t is the longitudinal coordinate where sliding occurs. The bristles have similar behaviour in the longitudinal direction. For pure longitudinal slip, if v_x is the longitudinal wheel centre speed, the coordinate for a bristle tip at the contact area front edge is after time Δt :

$$x_l = a - v_x \Delta t \quad (224)$$

On the other hand, the upper tip of the bristle, which moves with a velocity $R_e \omega$, has the coordinate:

$$x_u = a - R_e \omega \Delta t \quad (225)$$

Consequently, the longitudinal bristle deformation is:

$$\delta_{xb} = x_l - x_u = \kappa_x (v_x \Delta t) = \kappa_x (a - x) = -\kappa_x (x - a) \quad (226)$$

Introducing the longitudinal bristle stiffness c_{px} and dividing the region in adhesion and sliding part, as done before, it is possible to obtain the same result for the total longitudinal force:

$$F_x = \int_{-x_t}^a F_{xb,a} dx + \int_{-a}^{-x_t} F_{xb,s} dx \quad (227)$$

where $F_{xb,a} = c_{px} \delta_{xb}$ (adhesion region) and $F_{xb,s} = \mu F_{zb}$ (sliding region).

The following equations use a parabolic vertical pressure distribution. This has an advantage since modelling based on a uniform pressure distribution results in an asymptotic behaviour in which full slip is not reached [140], [157] author solve equations (92) and (96) to get

$$F_x = \begin{cases} \mu F_z (1 - \lambda_x^3) \text{sgn} \sigma_x & \text{if } |\sigma_x| \leq \frac{1}{\theta_x} \\ \mu F_z \text{sgn} \sigma_x & \text{if } |\sigma_x| > \frac{1}{\theta_x} \end{cases} \quad (228)$$

$$F_y = \begin{cases} \mu F_z (1 - \lambda_y^3) \text{sgn} \alpha & \text{if } |\tan \alpha| \leq \frac{1}{\theta_y} \\ \mu F_z \text{sgn} \alpha & \text{if } |\tan \alpha| > \frac{1}{\theta_y} \end{cases} \quad (229)$$

where

$$\lambda_x = 1 - \theta_x |\sigma_x|, \lambda_y = 1 - \theta_y |\tan \alpha|, \quad \theta_x = \frac{2c_{px} l^2}{3\mu F_z} \text{ and } \theta_y = \frac{2c_{py} l^2}{3\mu F_z}$$

In these equations l is the half-length of the contact patch, and c_{px} and c_{py} the longitudinal and lateral stiffness per length unit respectively. $1/\theta_x$ and $1/\theta_y$ represent the tyre slip at which complete sliding is reached. From this point, the force is simply put equal to the force limit F_z .

In this section, the brush model is presented, as proposed in [43]. The brush model is an analytical tyre model, meaning that it only depends on the physical parameters of the tyre. In the brush model, the tyre is described as a series of elastic elements, which can deflect in contact with the road. In this demonstration, the friction coefficient μ is assumed to be equal for both lateral and longitudinal

direction, and not a function of the velocity of the wheel centre v_x . These assumptions make the problem much easier compared to reality. In the same way, the assumption on the symmetric normal load is not true, because the point of the normal load is not the origin in reality but it is a point shifted forward. Moreover, using just one line of bristles, it doesn't allow to have a 3D picture of all the forces acting in the contact patch, and this is a big drawback if the effects of camber angle have to be studied. However, even with these assumptions, the brush tyre model reaches to explain the nature of the forces in the contact patch with a strong physical background. Meanwhile, it requires a smaller number of model parameters for describing the steady-state characteristic. In fact, this model is very comparable to the Dugoff model presented earlier and has the same advantages and disadvantages. Nevertheless, this representation is more realistic, because of the more advanced vertical pressure distribution [30].

C. Different Vehicle models

A considerable number of the literature in this area has been devoted to various vehicle models. The literature review shows that vehicle modelling can be classified into three categories: Quarter Car, bicycle or Half Car and Full Car models.

i. Quarter car

The Quarter Car model is the simplest model to simulate the response of the vehicle to road disturbance which is shown in Figure 194. The main assumption of the Quarter Car model is that all wheels can be moved independently; therefore, the suspension system is modelled using two DOFs: one for the body motion and the other for the tyre. The dynamics of the Quarter Car model can be described as linear or nonlinear equations based on the elements of the model. The linear model consists of a linear spring that corresponds to the tyre stiffness and car spring, and viscous damping to account for the tyre damping and car damper [178], [179].

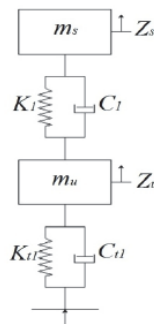


Figure 194 Schematic of Quarter Car model

ii. Bicycle model

The bicycle model is also known as a half-car model. In this type of model, the vehicle is cut along the main axes of symmetry (longitudinal and lateral). Thus, thanks to this model, we can study the suspensions side by side or axle by axle. In the first case, we neglect the rolling motion and in the second case, the effect of the pitch.

In side by side suspension model, the dependency of wheels located in the front and rear axles or the left and right of the body which is shown in Figure 195. The Half Car model has four DoF to present bounce and pitch of the body and wheels, motion in the perpendicular axis of vehicle planar motion [180], [181]. In axle by axle suspension system, the coupling dynamics between the wheels located in the front and rear axles would improve the accuracy of the simulation of the suspension travel. However, in the Half Car model, the effect of the coupling between the wheels located on the same axle (roll motion), which is a significant DoF of the body in dynamic simulation of a vehicle rollover, is not considered.

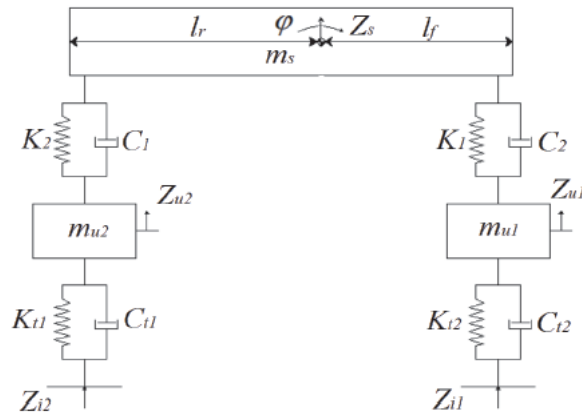


Figure 195 Schematic of Half Car model

For the studies of the longitudinal dynamics, which is utilized as a model for lane keeping and yaw rate control, has two DoFs including yaw rate and lateral motion of the vehicle [59], [209]. The schematic bicycle model is shown in Figure 196. In the 2-DoF model, it is assumed that the vehicle has a constant speed.

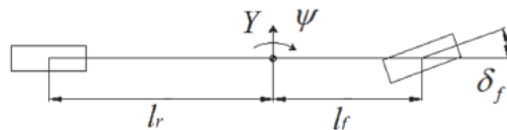


Figure 196 Schematic two DoF of bicycle model

In the 3-DoF model, the lateral motion, yaw rate and roll motion are considered as the DoFs of the handling system which is presented in Figure 197. The roll motion has a significant effect on vehicle dynamics, especially in cornering. The roll motion is studied in the control system using an anti-roll bar as the actuation system [43], [210]. In the study of vehicle motion, one needs to consider the effect of traction and braking, because in actual manoeuvring the speed is not constant.

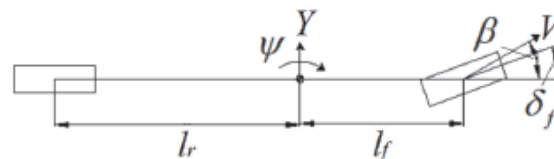


Figure 197 Schematic of three DoF bicycle model

iii. Full car model

The Full Car model studies the dynamics of the suspension system considering the dependency of all wheels on road disturbance which is shown in Figure 198. There are seven DoFs in the Full Car model: bounce, roll and pitch are the three DoF of the body, and the motions of the four wheels are defined by four DoFs. The dynamic equations of the full Car model can be either linear or nonlinear [182] depending on the properties of suspension system elements, such as nonlinear car spring. The full Car model has the best precision to simulate the dynamics of the suspension system if the vehicle

has a constant speed with no steering angle. However, these assumptions are not valid in most cases of vehicle manoeuvring.

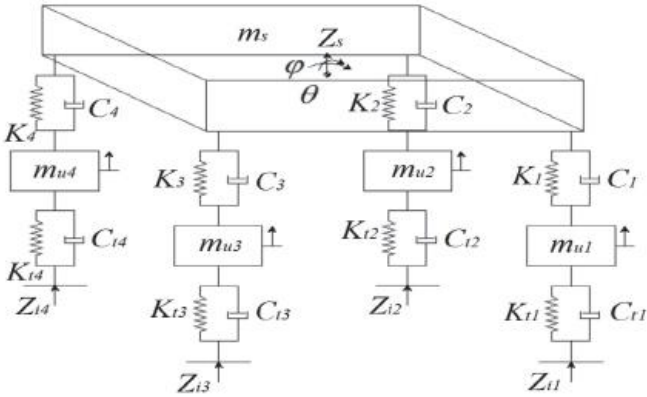


Figure 198 Schematic of Full Car model

The coupled longitudinal and lateral dynamic model with eight DoF consists of lateral, longitudinal, roll and yaw motions, and four DoFs for wheel motions as shown in Figure 199. This model with 8-DoF is an accurate nonlinear model which is used to study the differential braking system. However, in this model, the effect of the coupling between the ride and handling systems is neglected.

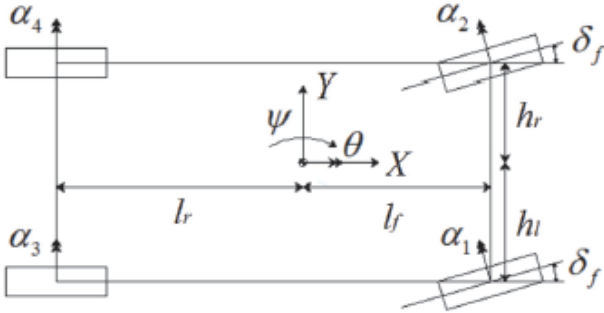


Figure 199 Schematic of eight DoFs full car model

D. Numerical validation of vehicle

In this annex the figure s of the below table test are given.

Table 24 Test conditions

Test no.	Trajectory	Speed (Km/h)	Comments
1	Straight line	50	Constant speed
2	Straight line	80	Constant speed
3	Curve at 220m	40	Constant speed
4	Curve at 220m	60	Constant speed
5	Curve at 220m	80	Constant speed
6	Curve at 320m	40	Constant speed
7	Curve at 320m	60	Constant speed
8	Curve at 320m	80	Constant speed
9	Chicane	60	Constant speed
10	Straight line	Acceleration & Braking	Variable speed

- Test 2

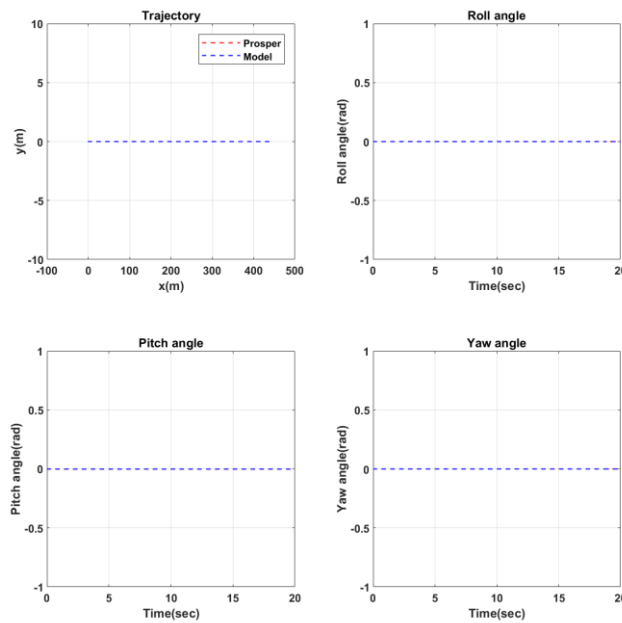


Figure 200 Comparison of position variables between prosper and model for vehicle moving in straight line at 80km/h

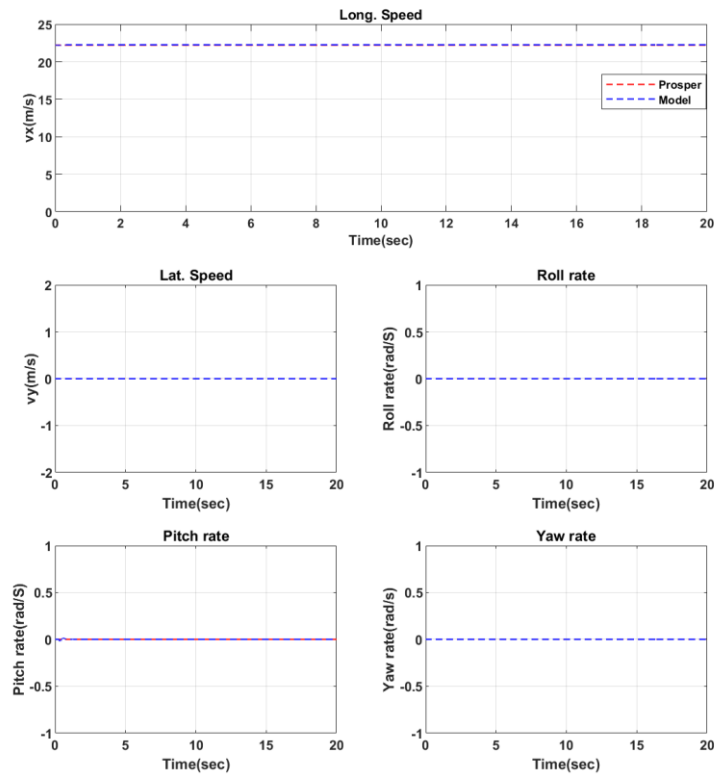


Figure 201 Comparison of speed variables between prosper and model for vehicle moving in straight line at 80km/h

- Test 3

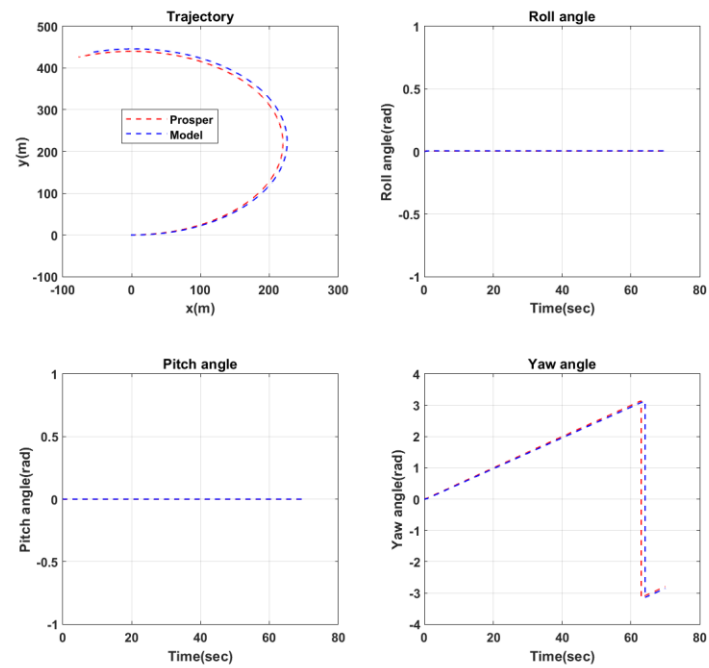


Figure 202 Comparison of position variables between prosper and model for vehicle moving in curve of 220m at 40km/h

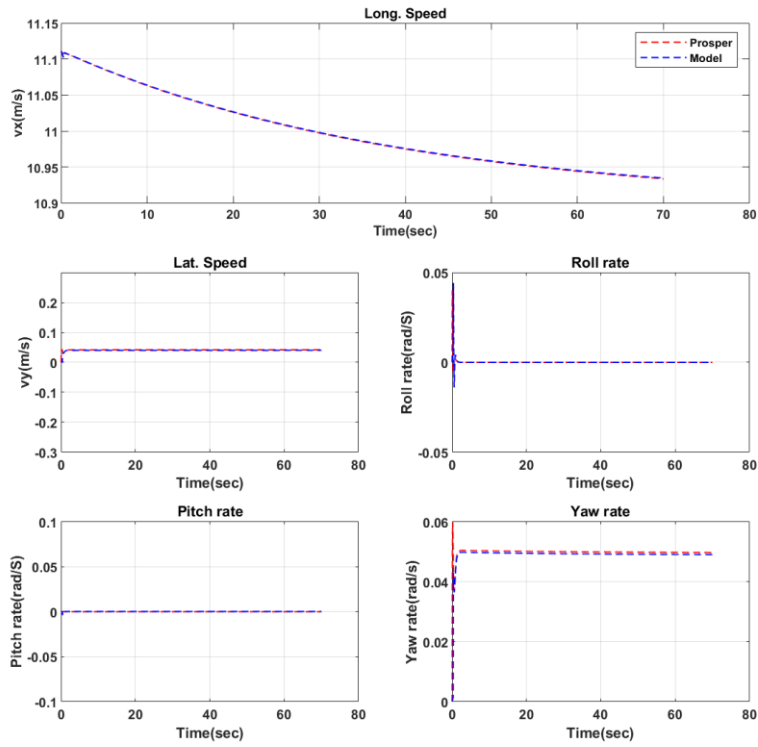


Figure 203 Comparison of position speed between prosper and model for vehicle moving in curve of 220m at 40km/h

- Test 5

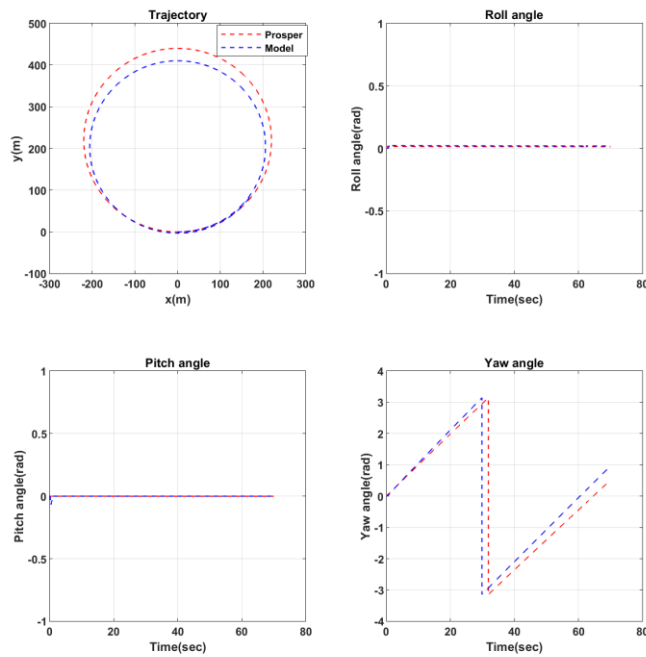


Figure 204 Comparison of position variables between prosper and model for vehicle moving in curve of 220m at 80km/h

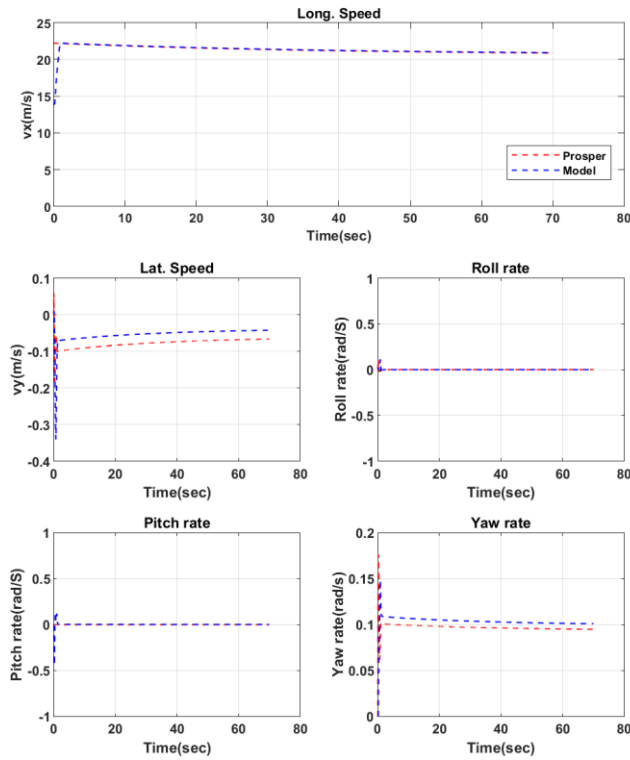


Figure 205 Comparison of speed variables between prosper and model for vehicle moving in curve of 220m at 80km/h

- Test 6

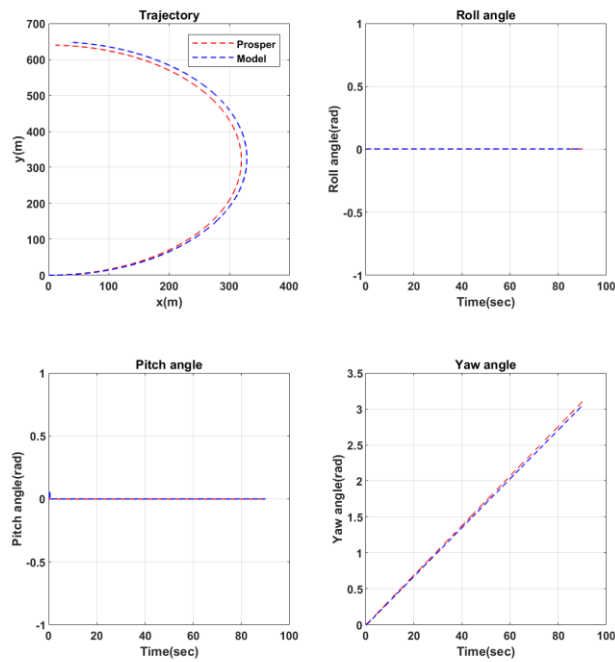


Figure 206 Comparison of position variables between prosper and model for vehicle moving in curve of 320m at 40km/h

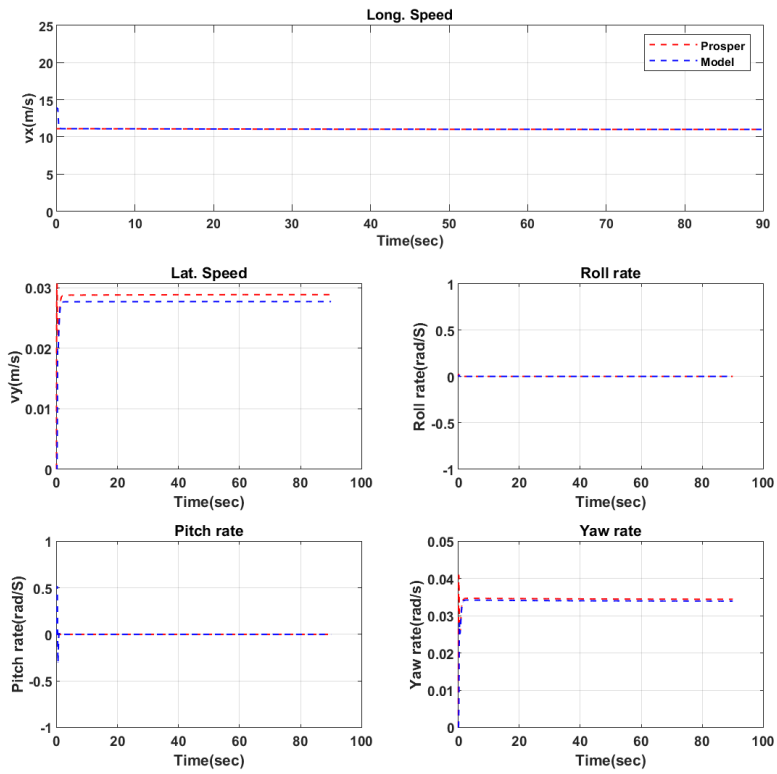


Figure 207 Comparison of speed variables between prosper and model for vehicle moving in curve of 320m at 40km/h

- Test 7

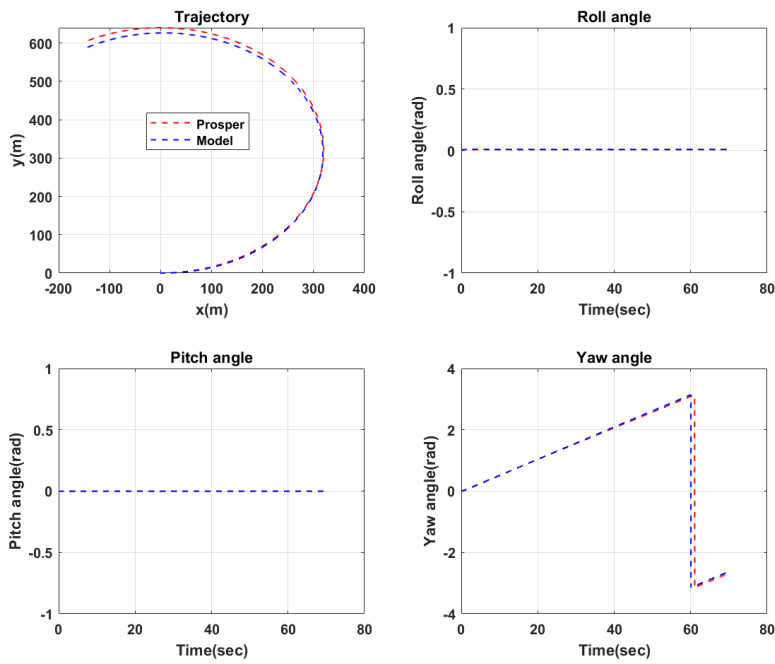


Figure 208 Comparison of position variables between prosper and model for vehicle moving in curve of 320m at 60km/h

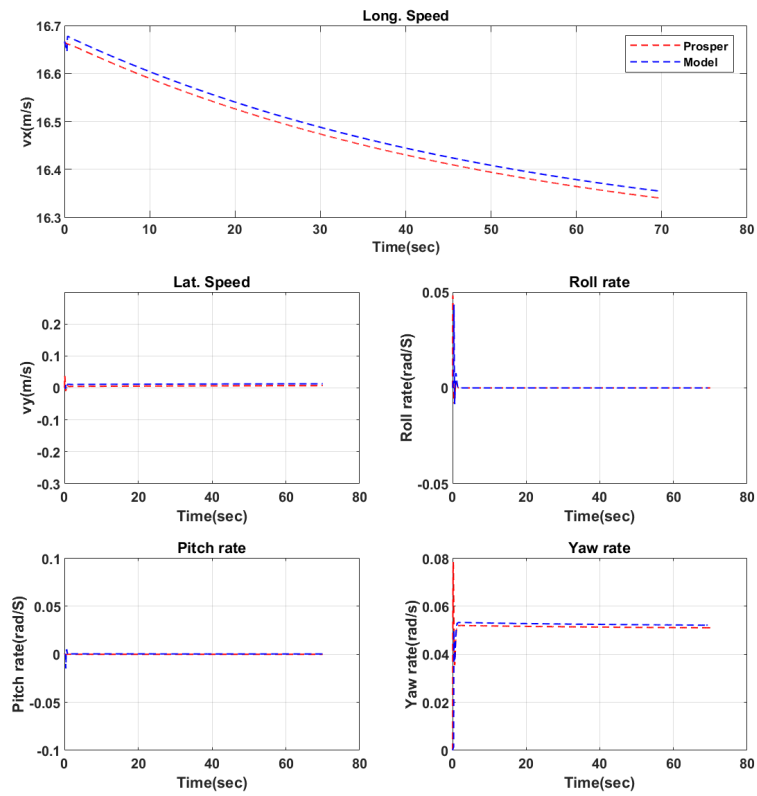


Figure 209 Comparison of speed variables between prosper and model for vehicle moving in curve of 320m at 60km/h

- Test 8

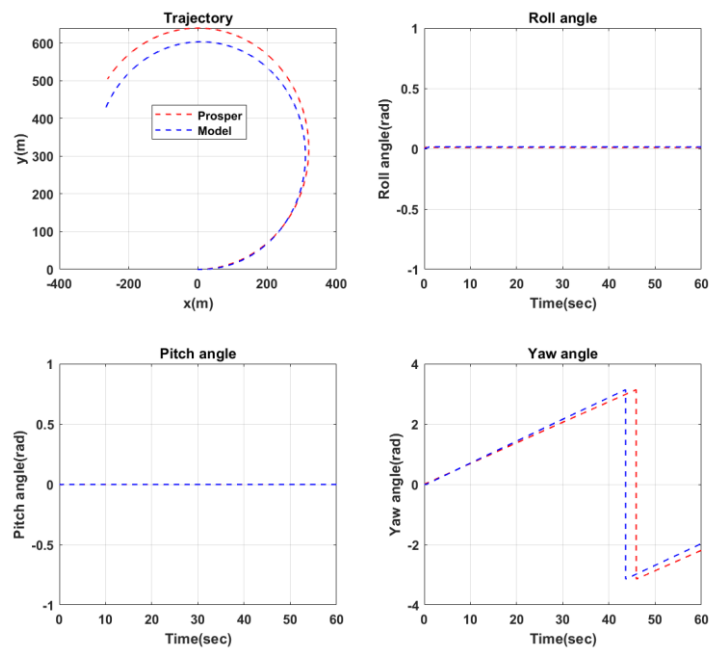


Figure 210 Comparison of position variables between prosper and model for vehicle moving in curve of 320m at 80km/h

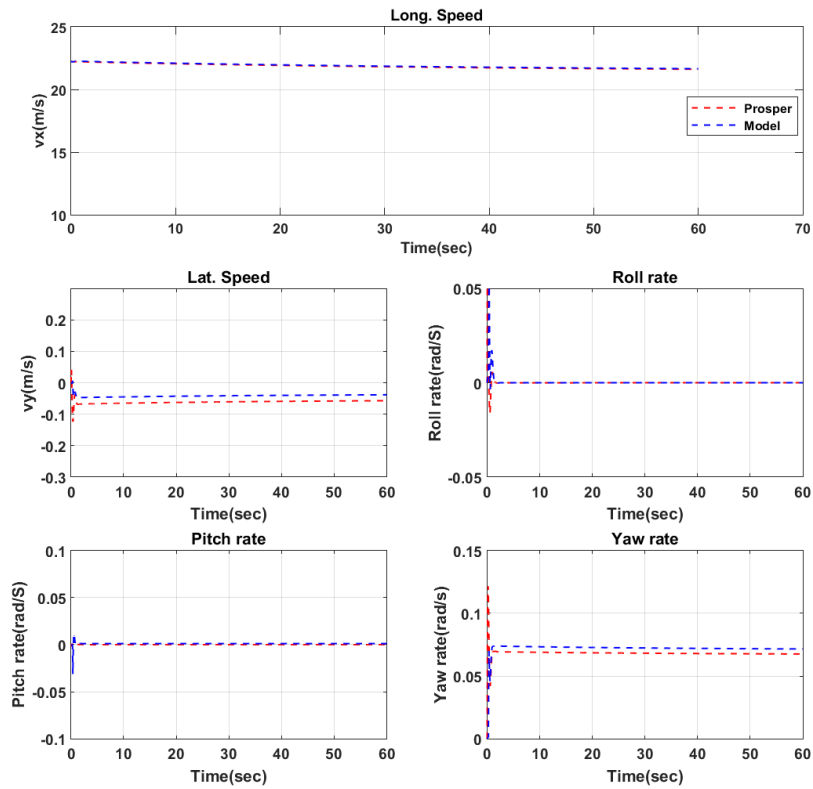


Figure 211 Comparison of speed variables between prosper and model for vehicle moving in curve of 320m at 80km/h

- Test 9

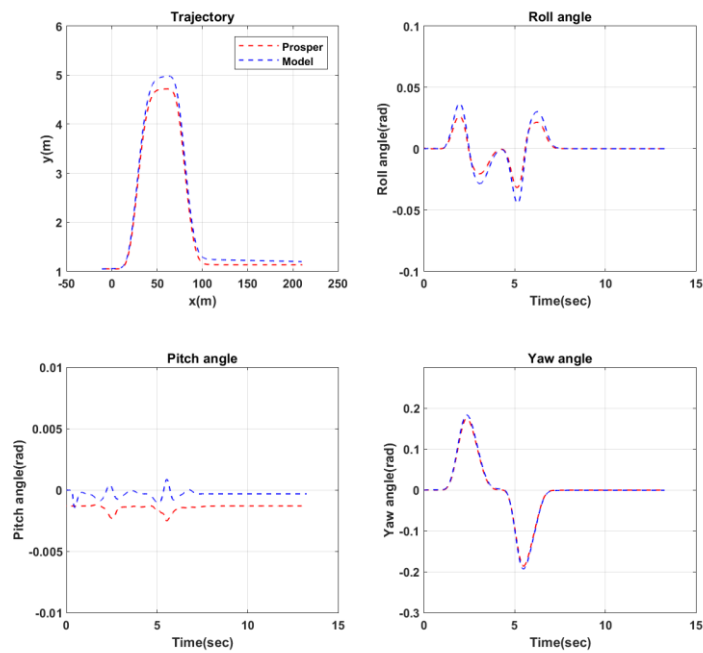


Figure 212 Comparison of position variables between prosper and model for vehicle is changing lane at 60km/h

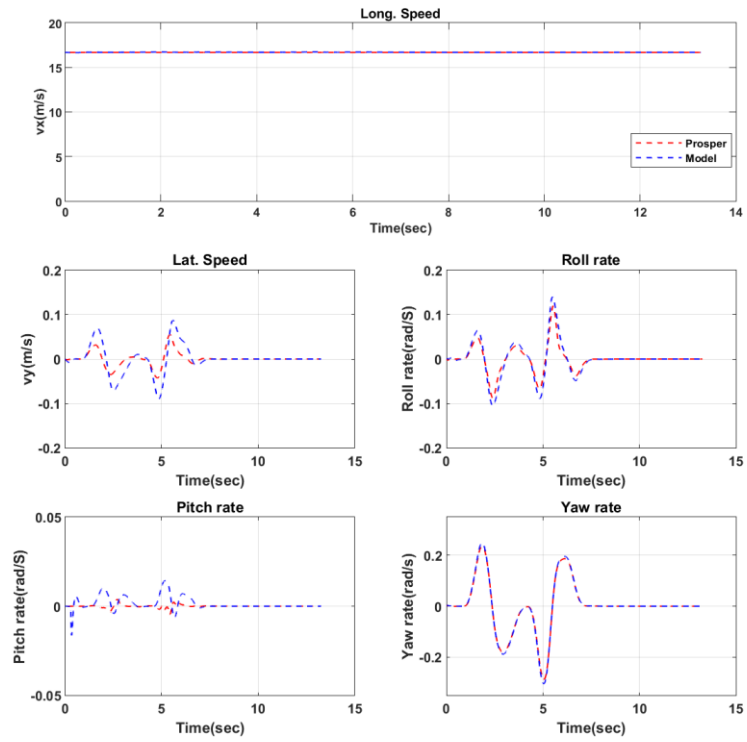


Figure 213 Comparison of speed variables between prosper and model for vehicle is changing lane at 60km/h

E. Experimental validation of vehicle

- Test 2

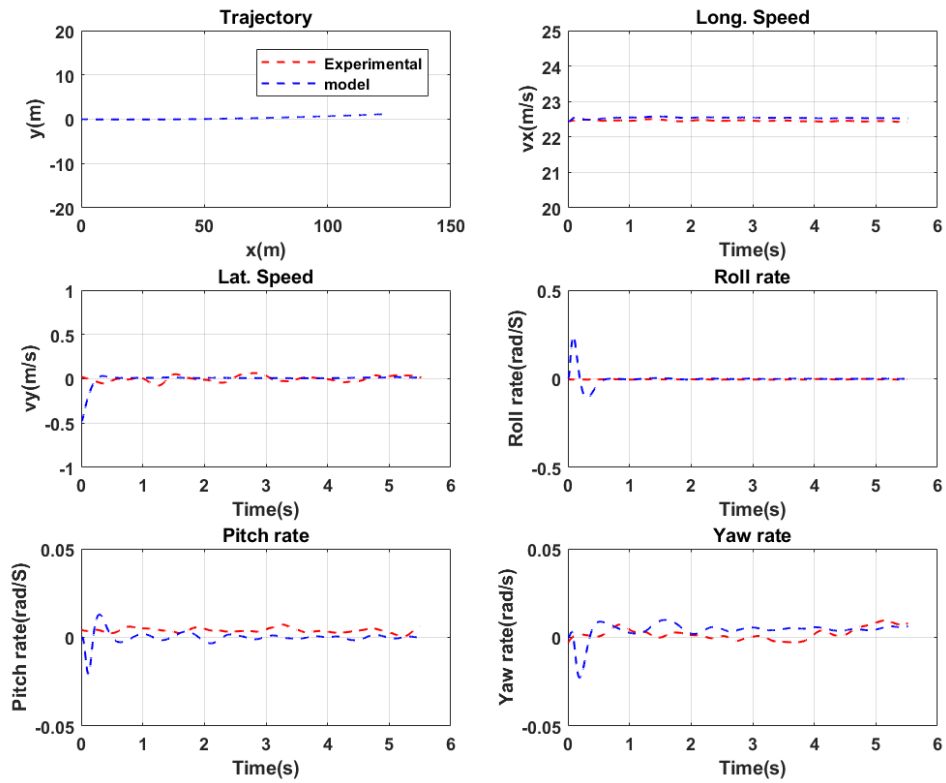


Figure 214 Comparison of speed variables between experimental data and model

- Test 3

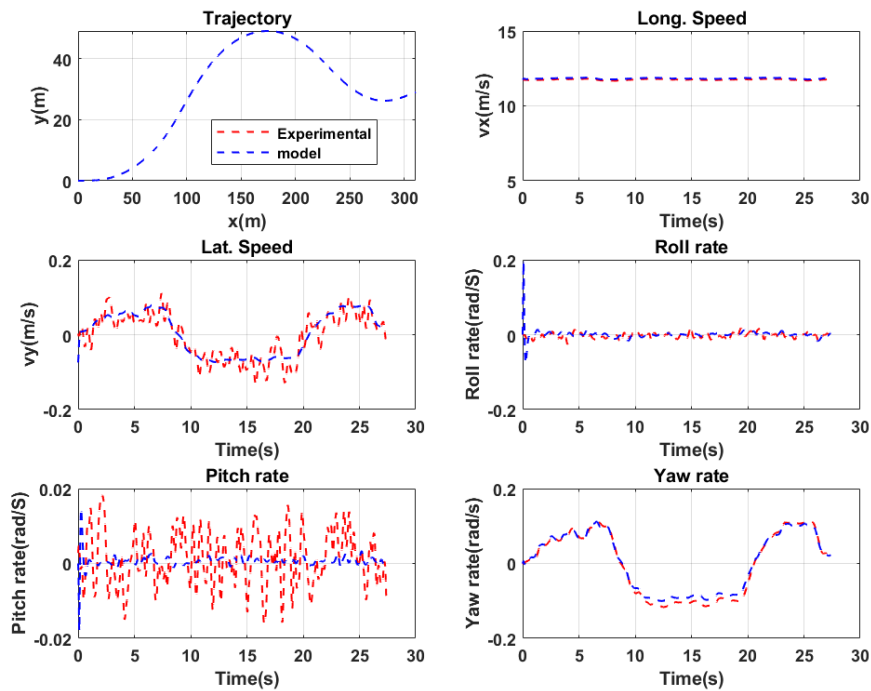


Figure 215 Comparison of speed variables between experimental data and model

- Test 5

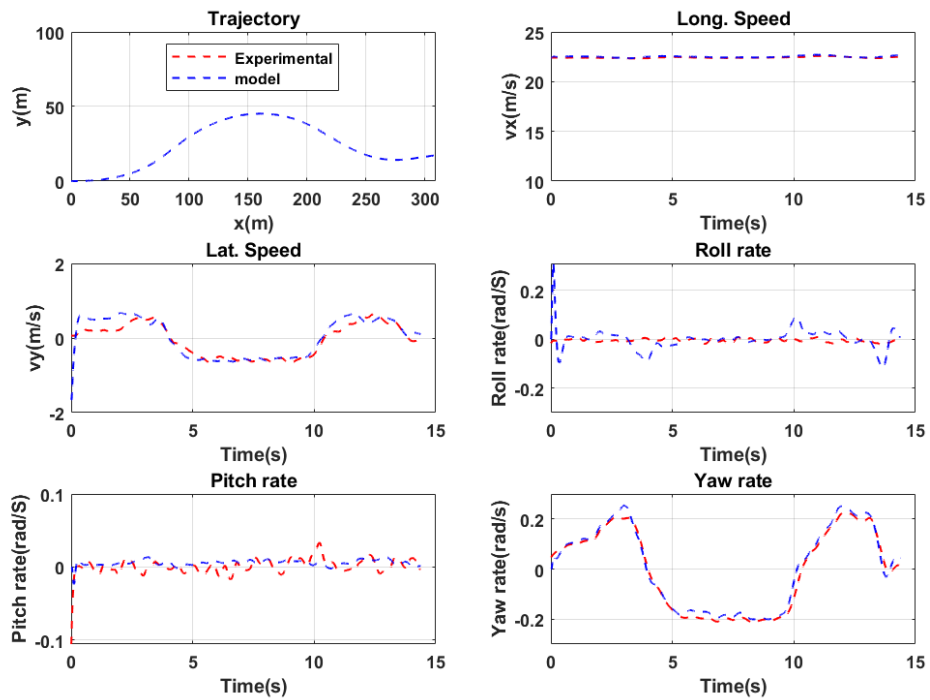


Figure 216 Comparison of speed variables between experimental data and model

- Test 6

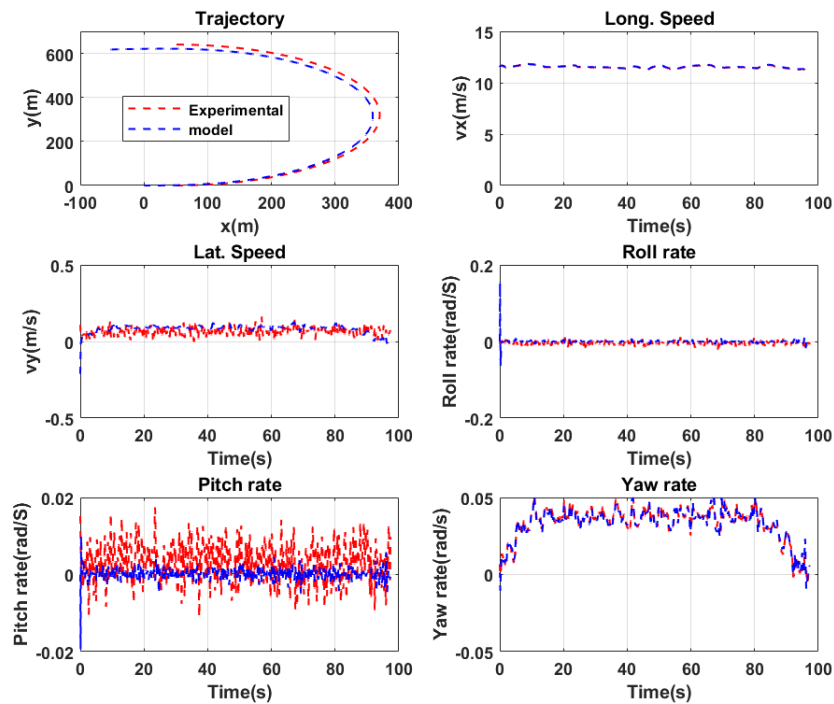


Figure 217 Comparison of speed variables between experimental data and model

- Test 7

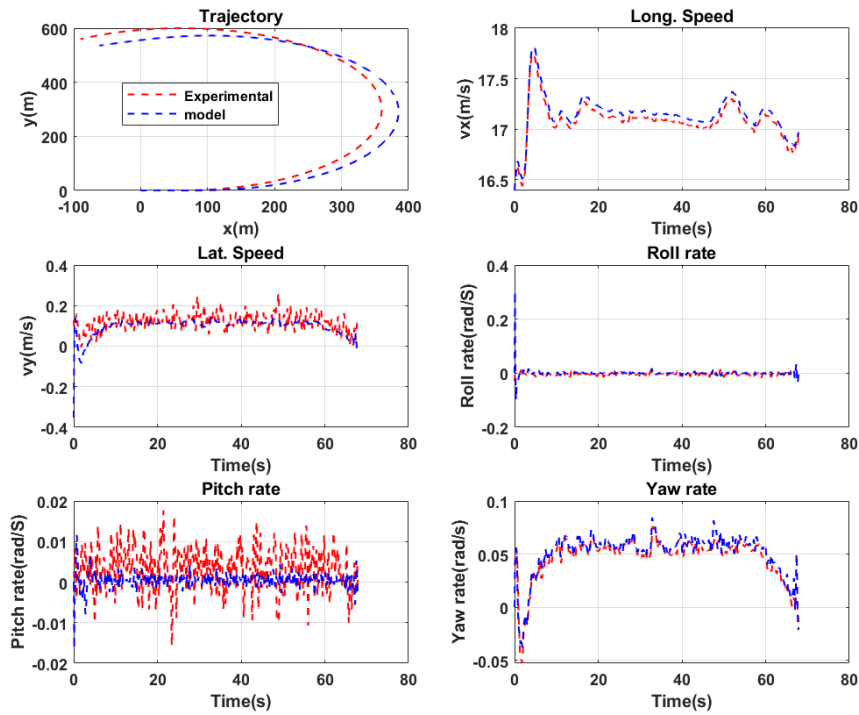


Figure 218 Comparison of speed variables between experimental data and model

- Test 8

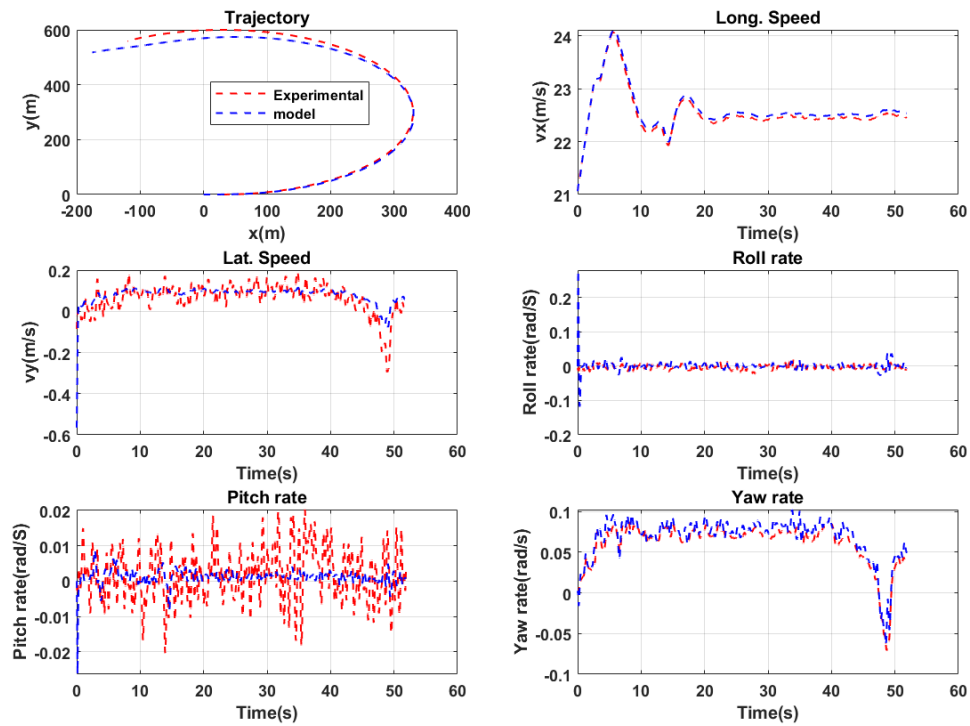


Figure 219 Comparison of speed variables between experimental data and model

- Test 9

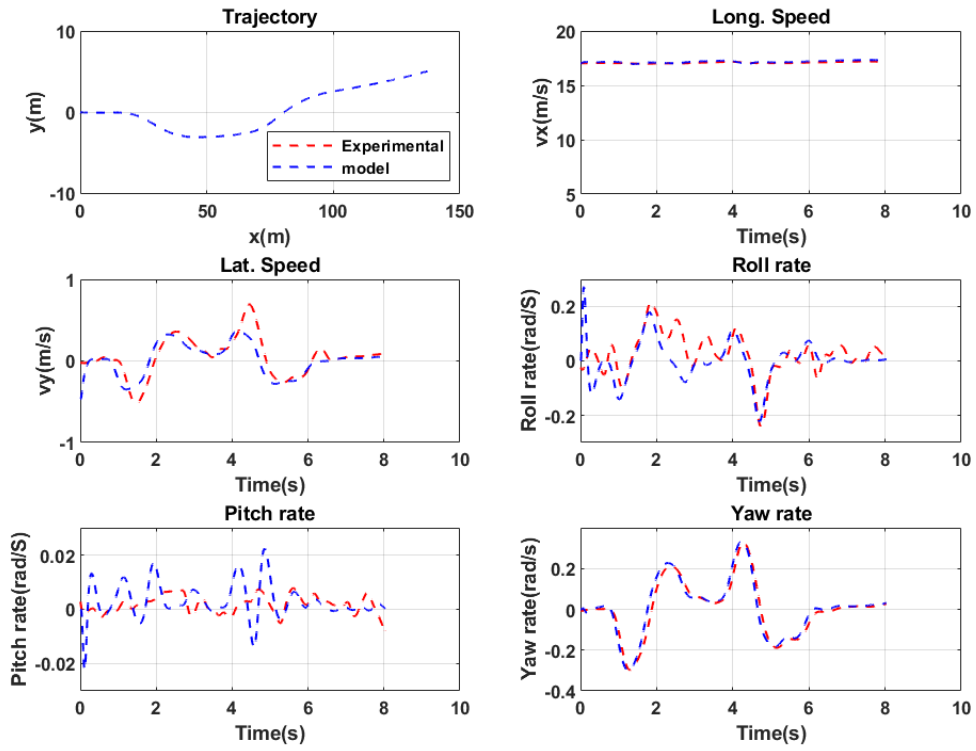


Figure 220 Comparison of speed variables between experimental data and model

F. Evaluation of tyre surface temperature

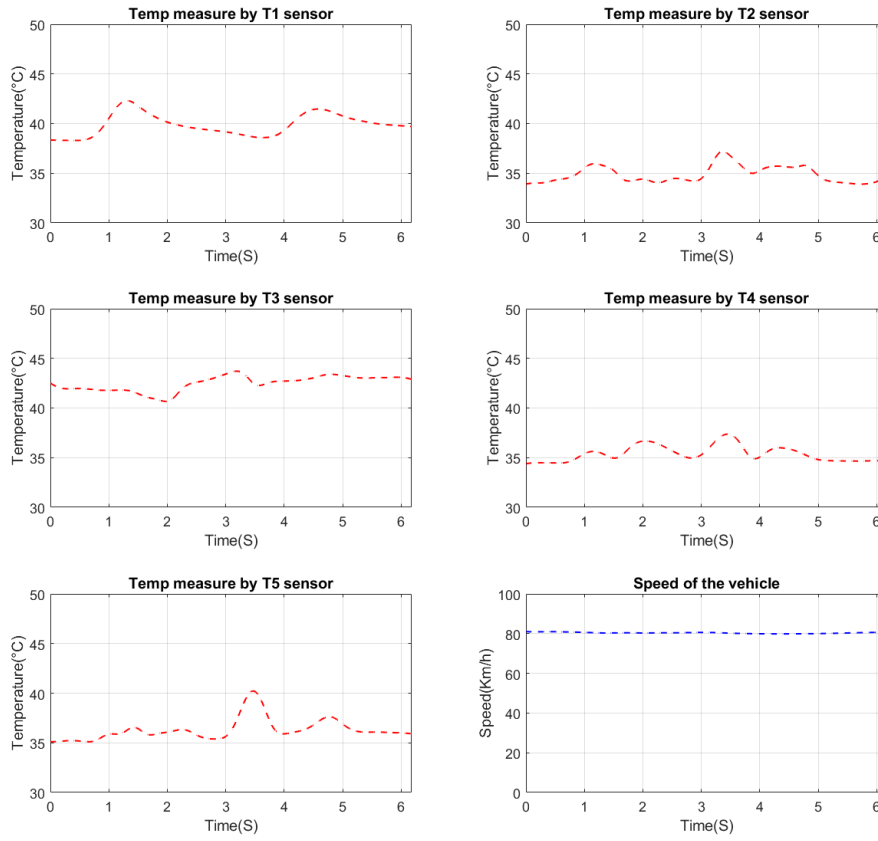


Figure 221 Variation of tyre surface temperature for lane change at 80km/h

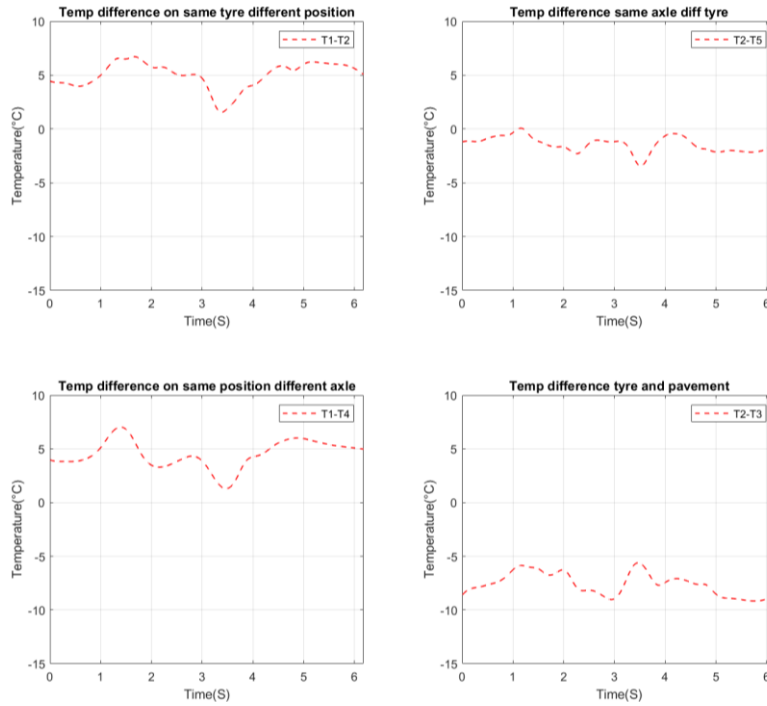


Figure 222 Variation of tyre surface temperature between sensors for lane change at 80km/h

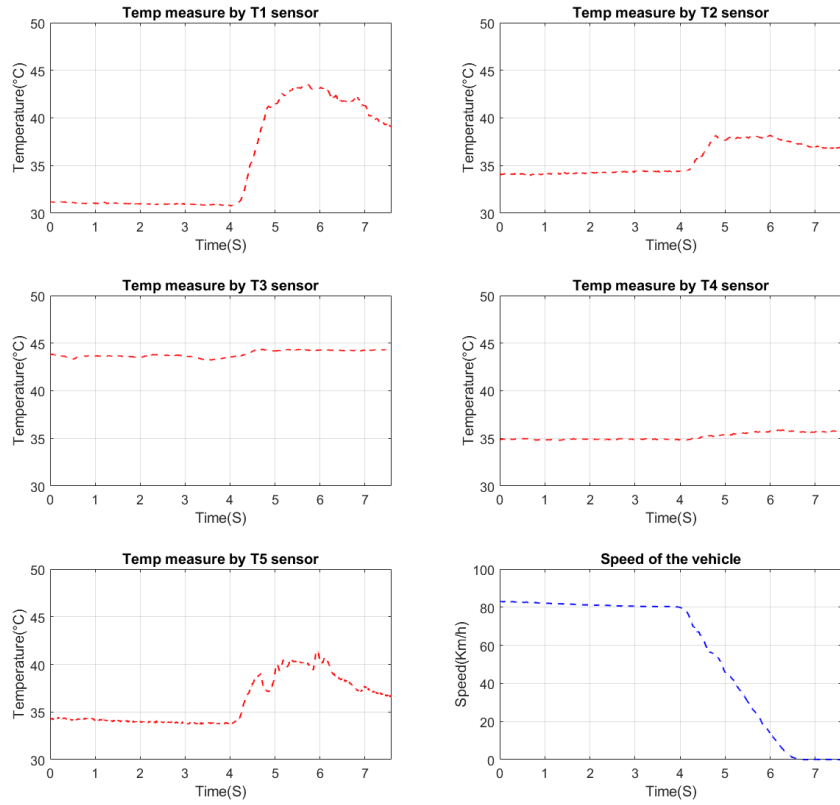


Figure 223 Variation of tyre surface temperature for braking manoeuvres on E3

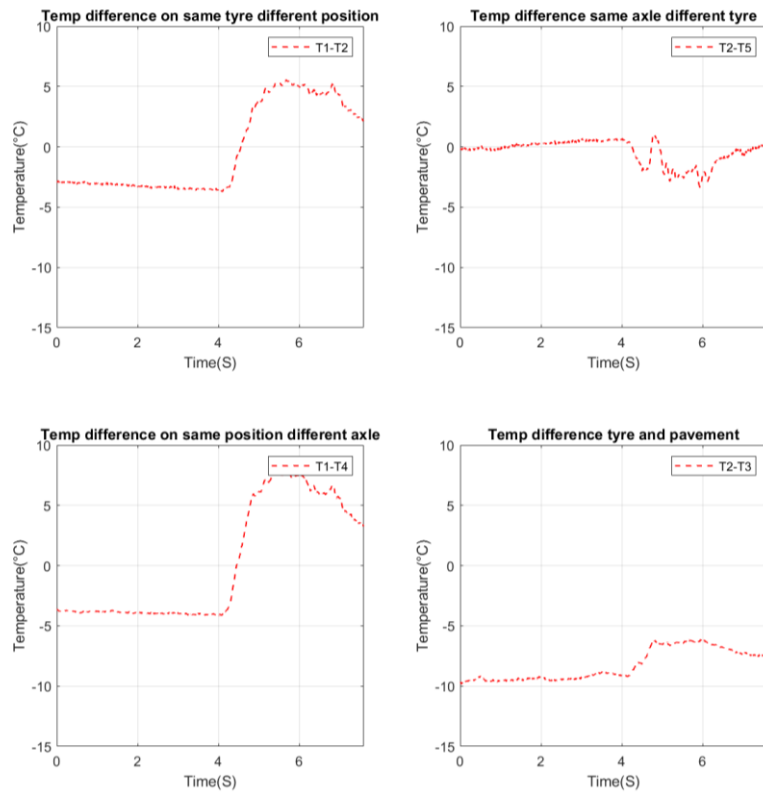


Figure 224 Gradient of tyre surface temperature for braking manoeuvres on E3

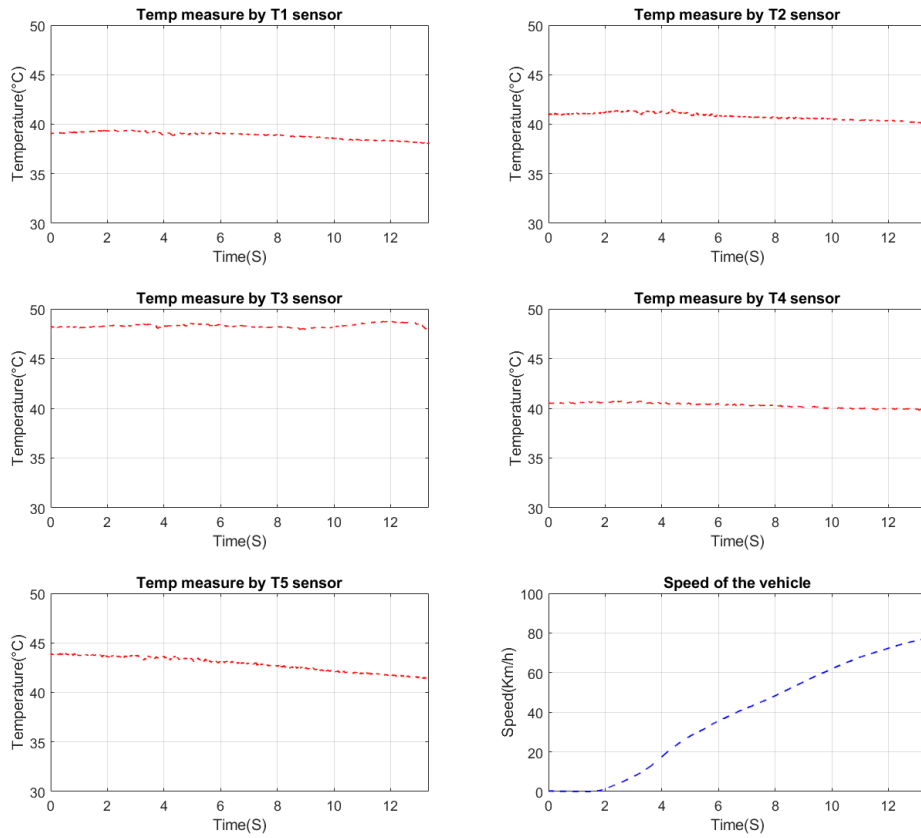


Figure 225 Variation of tyre surface temperature for acceleration manoeuvres on E3

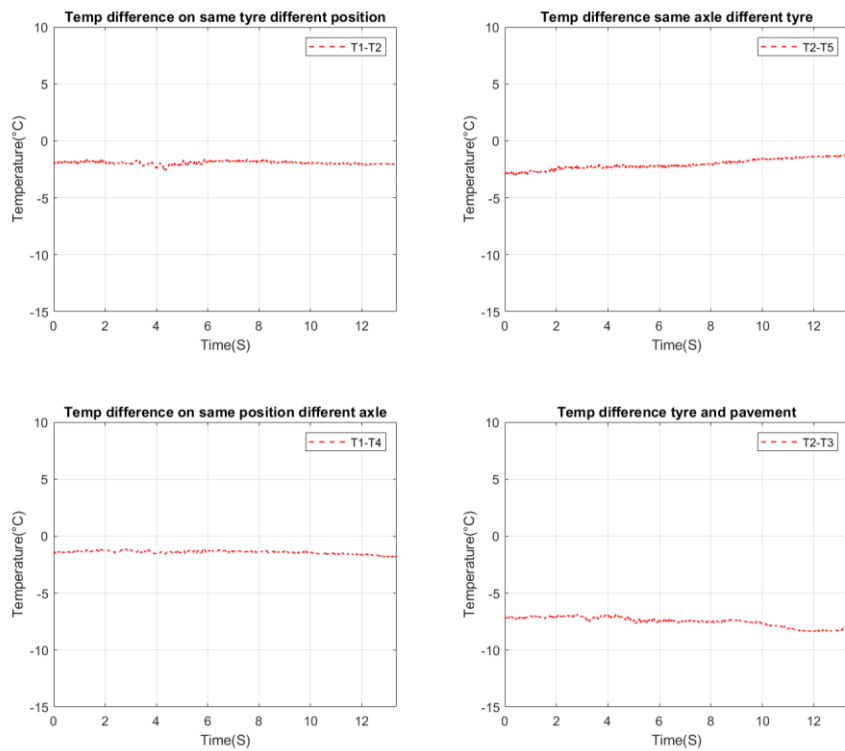


Figure 226 Gradient of tyre surface temperature for acceleration manoeuvres on E3

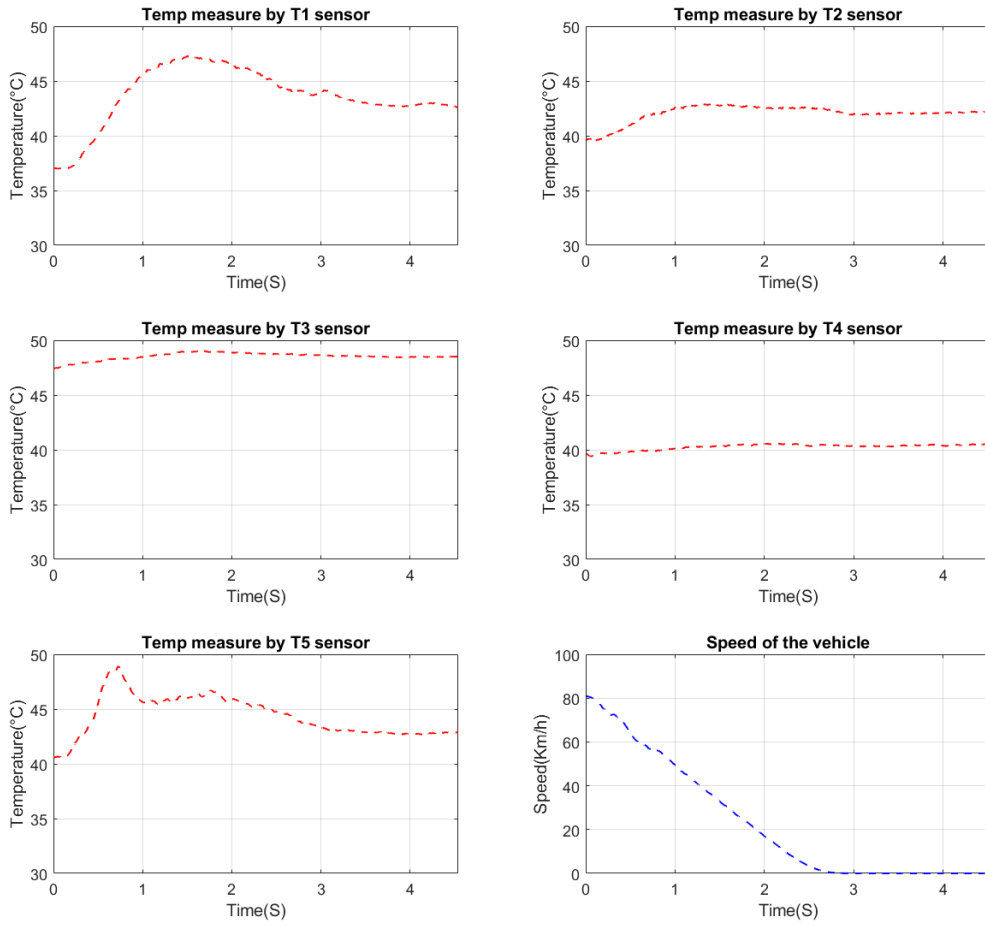


Figure 227 Variation of tyre surface temperature for braking manoeuvres on M2

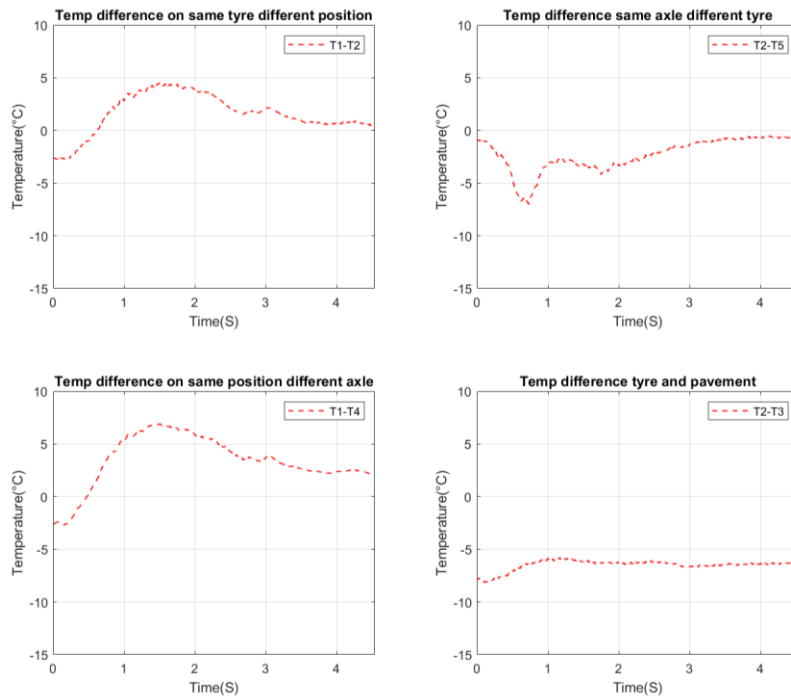


Figure 228 Gradient of tyre surface temperature for braking manoeuvres on M2

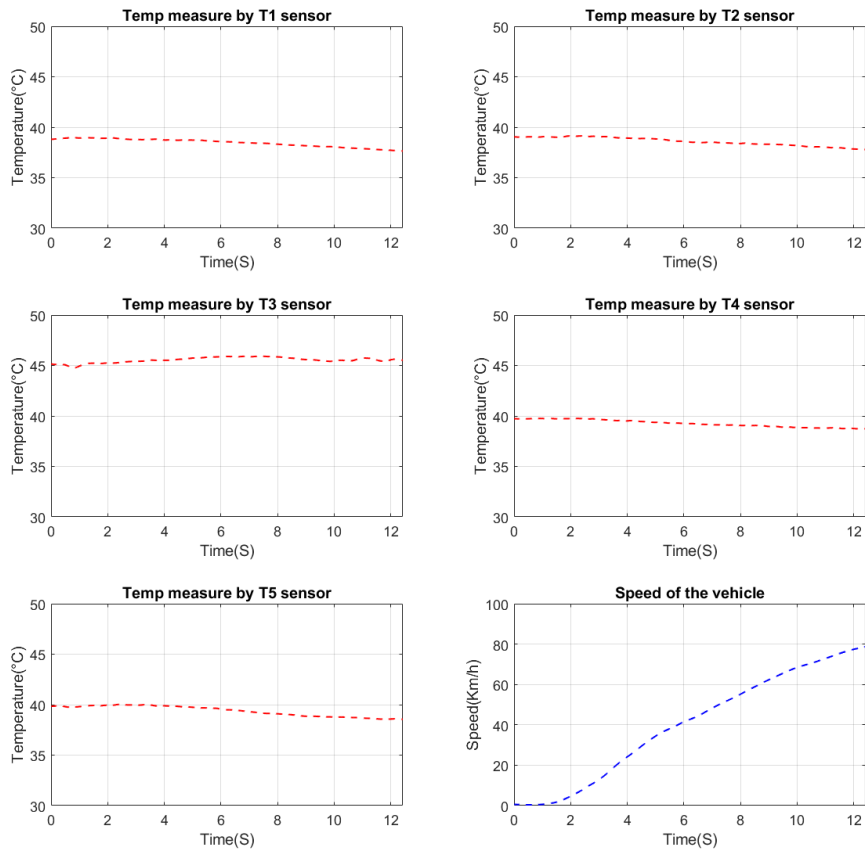


Figure 229 Variation of tyre surface temperature for acceleration manoeuvres on M2

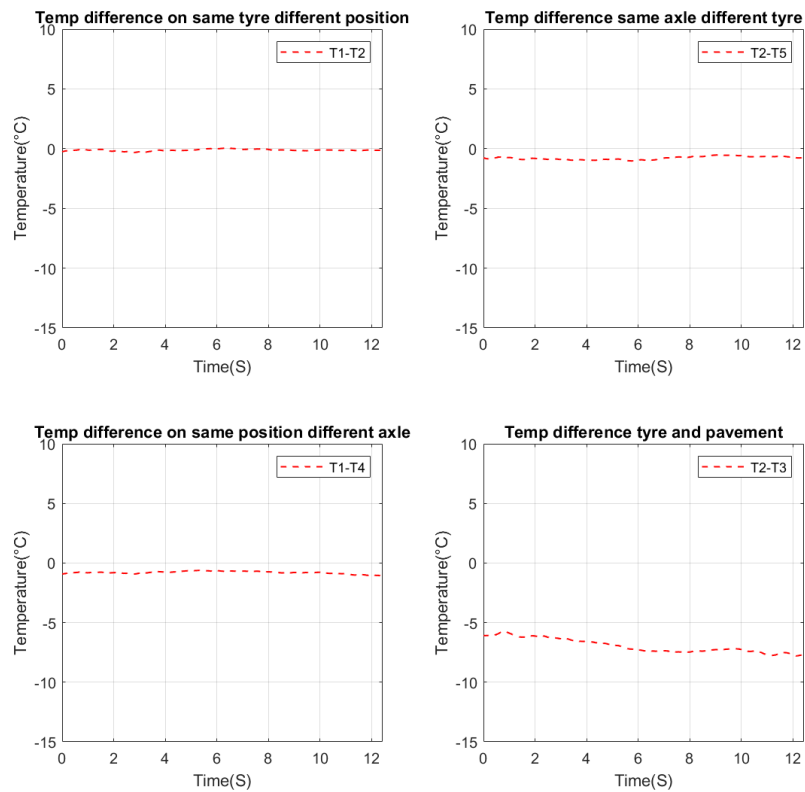


Figure 230 Gradient of tyre surface temperature for acceleration manoeuvres on M2

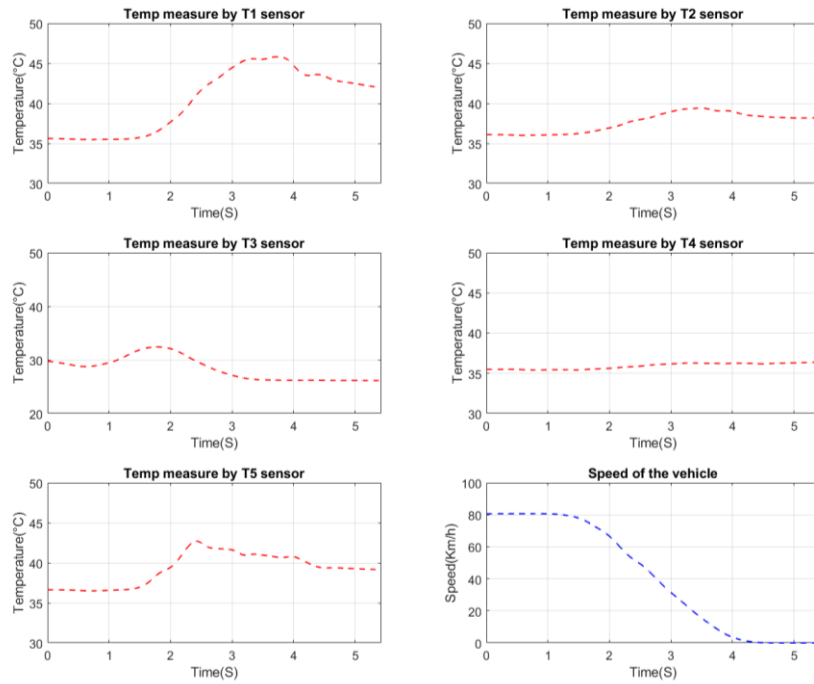


Figure 231 Variation of tyre surface temperature for braking manoeuvres on C1

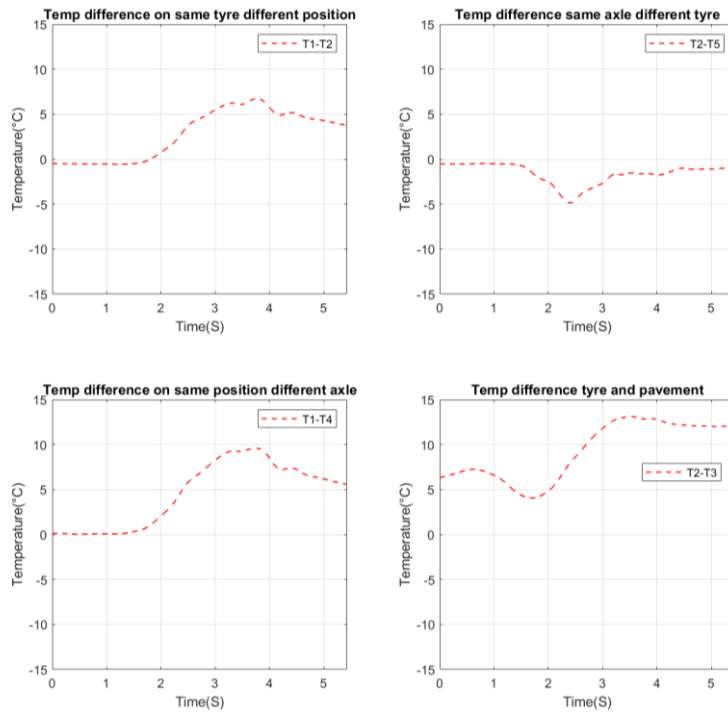


Figure 232 Gradient of tyre surface temperature for braking manoeuvres on C1

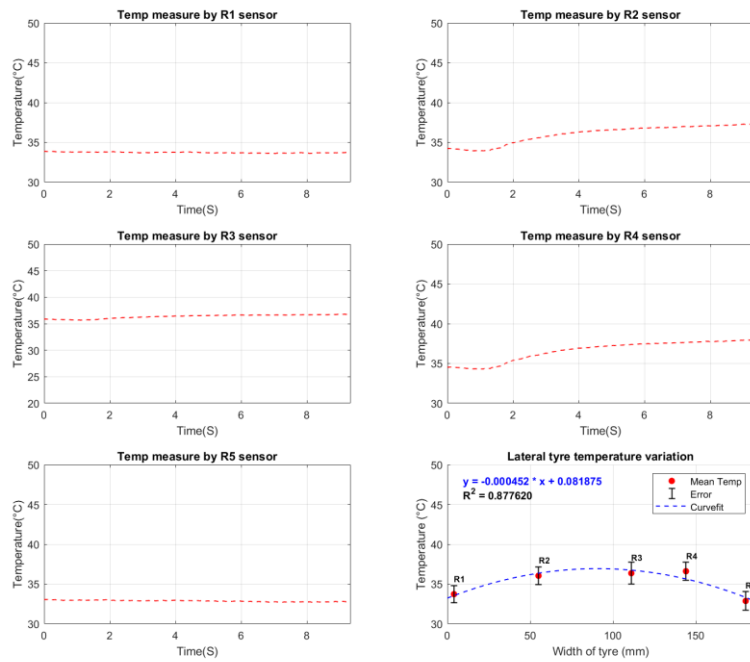


Figure 233 Variation of tyre surface temperature measurement points in the lateral direction for the M3 test track at 50km/h

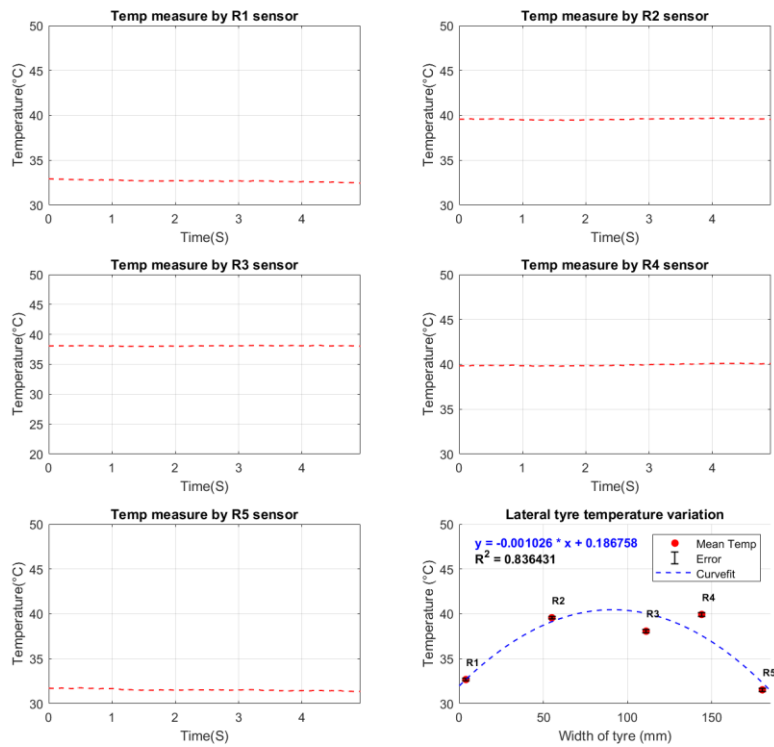


Figure 234 Variation of tyre surface temperature measurement points in the lateral direction for the M2 test track at 80km/h

G. Observer comparison results:

Case 4 simulation results of vehicle moving from 50 to 80 km/h on smooth surface in chapter 1 (comparison between different observer technique for the estimation of rolling resistance).

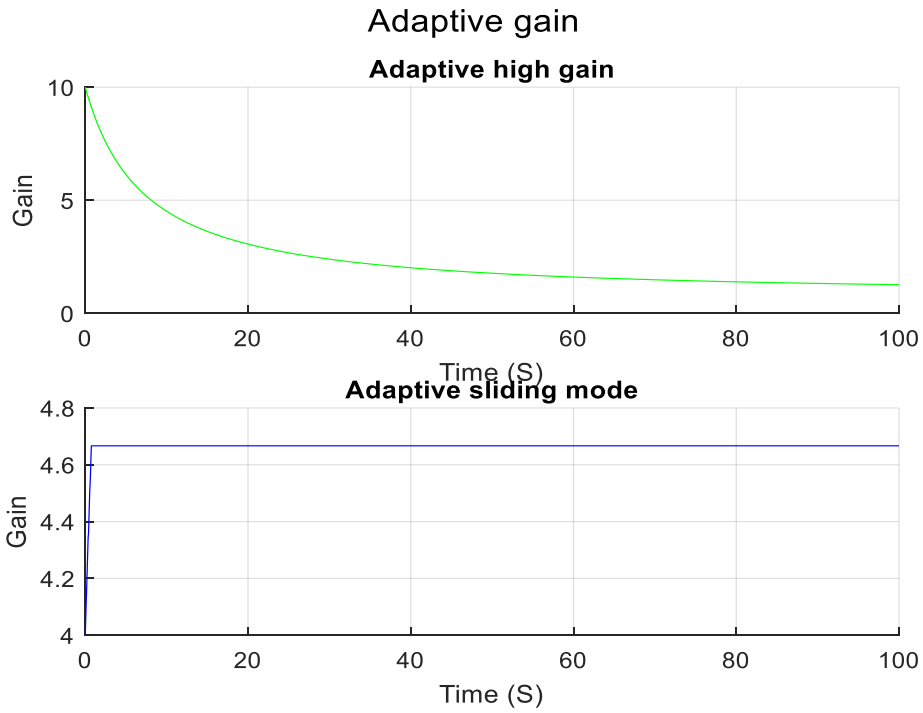


Figure 235 Adaptive gain for both observers

Determinant Jacobian

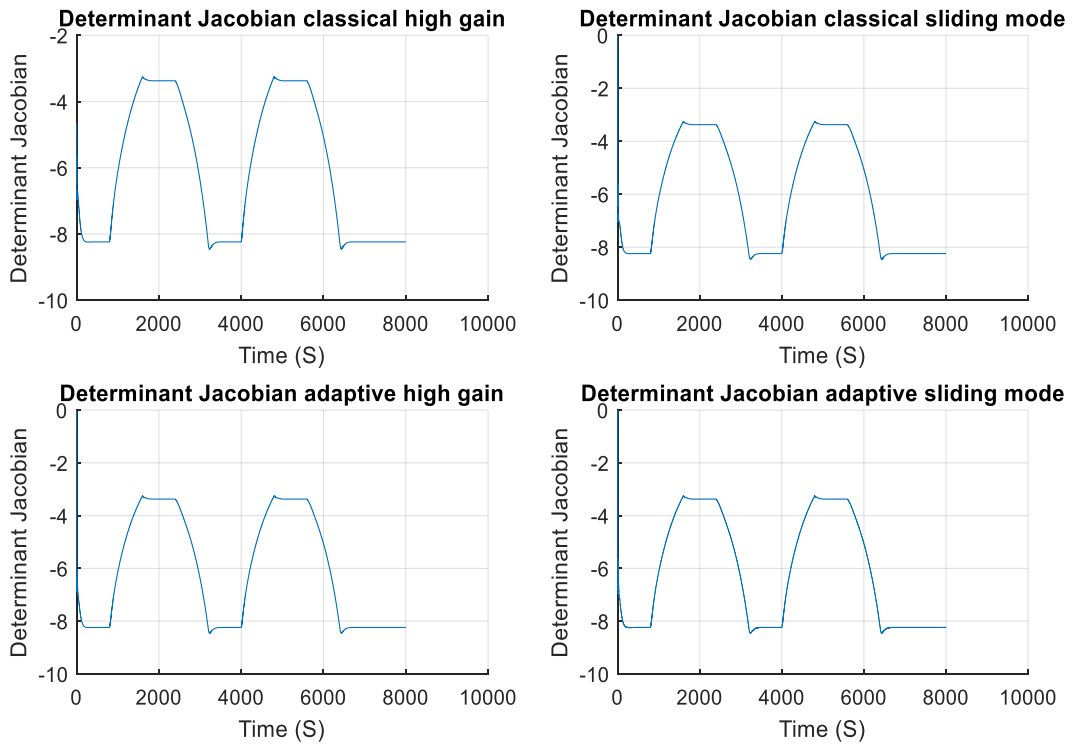


Figure 236 Determinant of jacobien matrix for the different observation techniques

Fr estimation different techniques

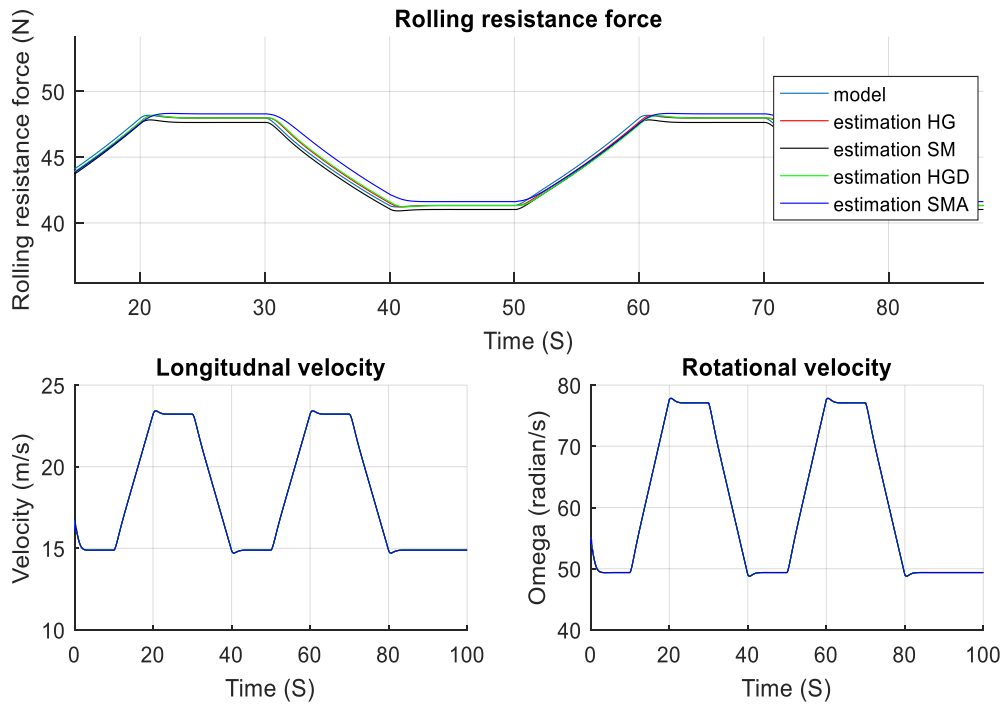


Figure 237 Estimation of rolling resistance force

Errors(%)

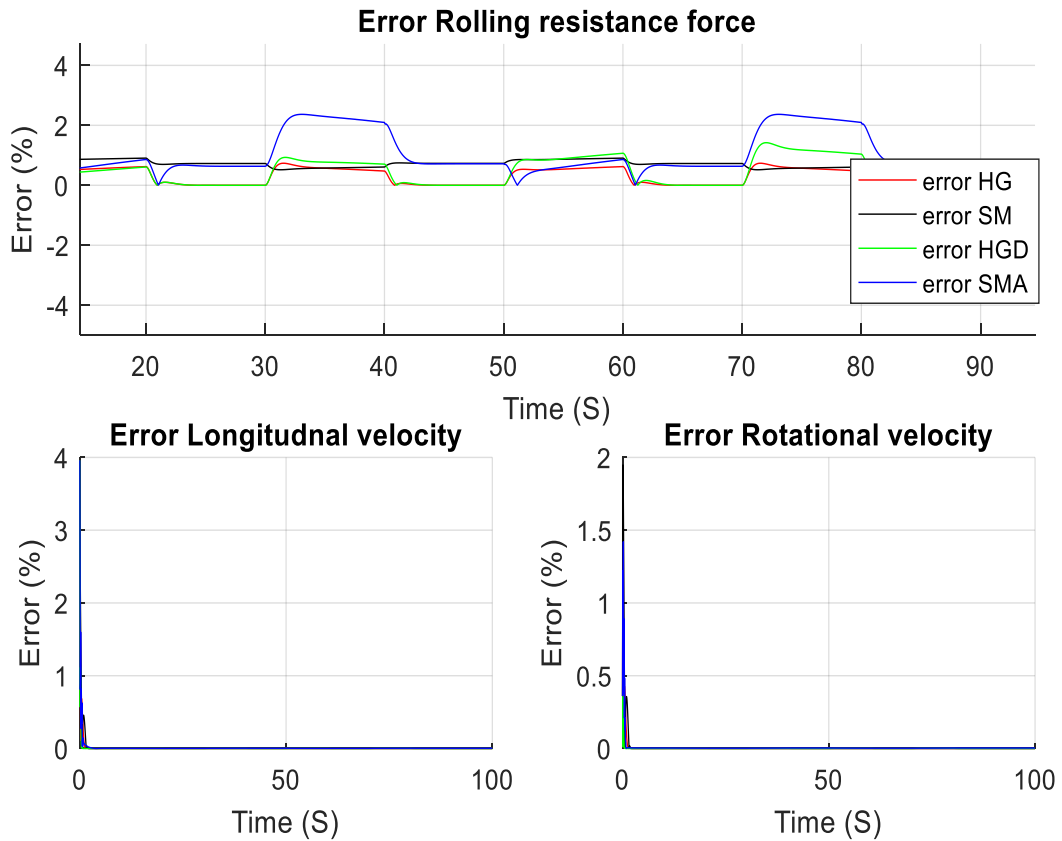


Figure 238 The error comparison for the estimation and observation

H. Experimental validation of singular perturbed observer

- Test 2

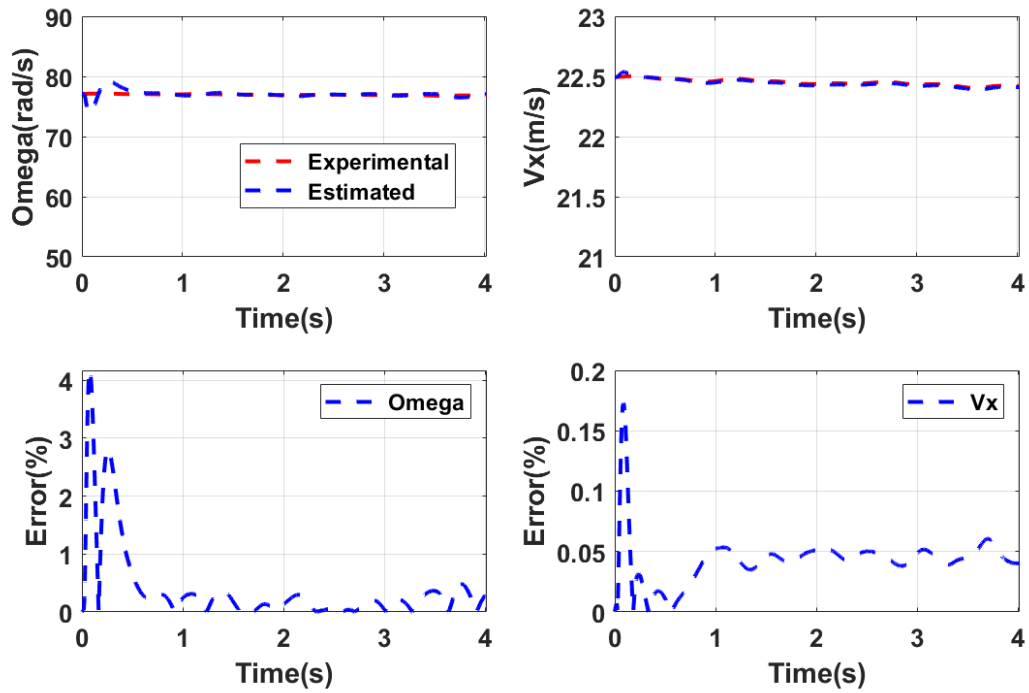


Figure 239 State variable comparison and error between experimental results and observer (straight line)

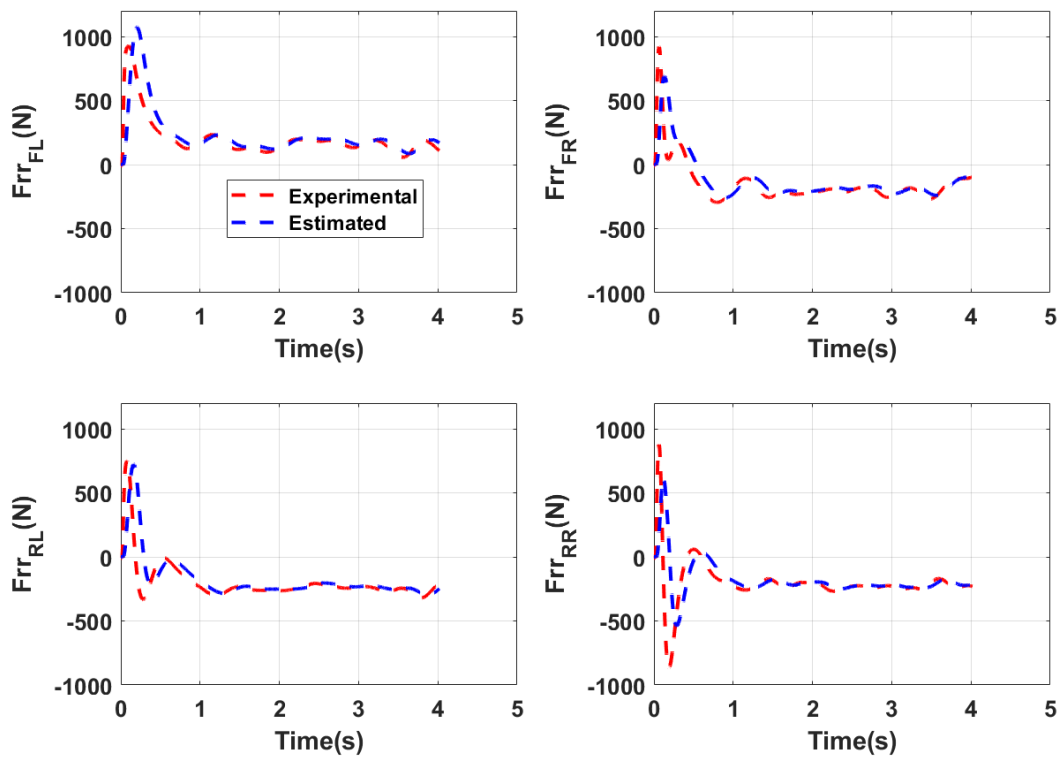


Figure 240 Comparison between experimental and estimated rolling resistance force (Straight line)

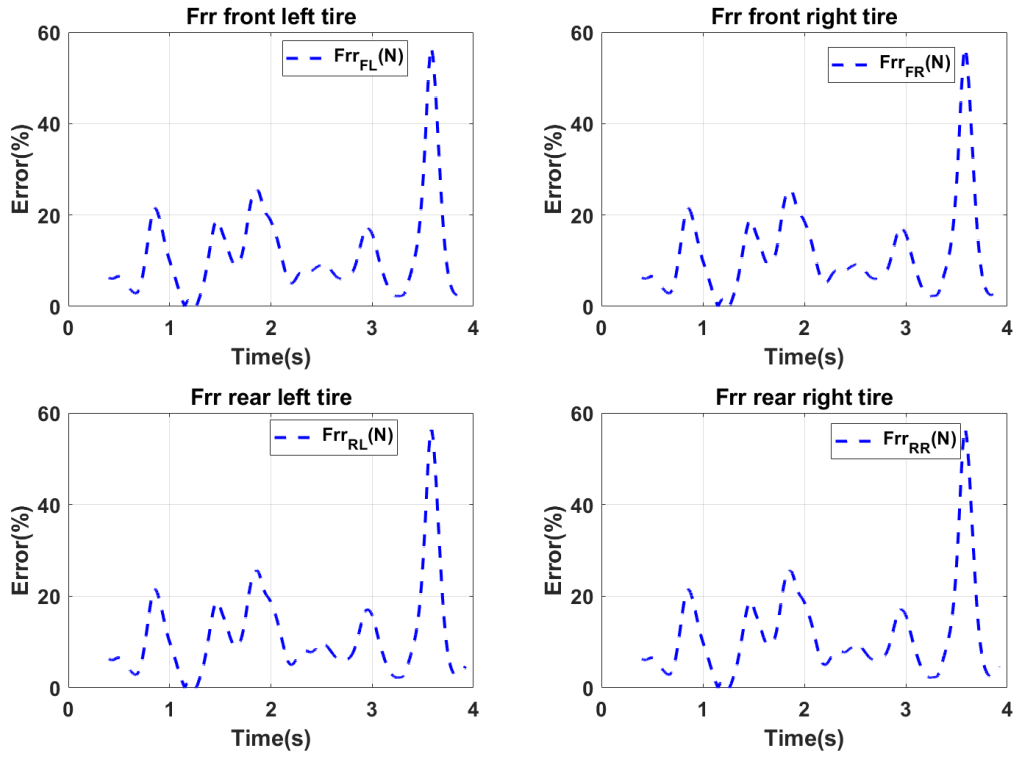


Figure 241 Estimation error results of observer estimation (Straight line)

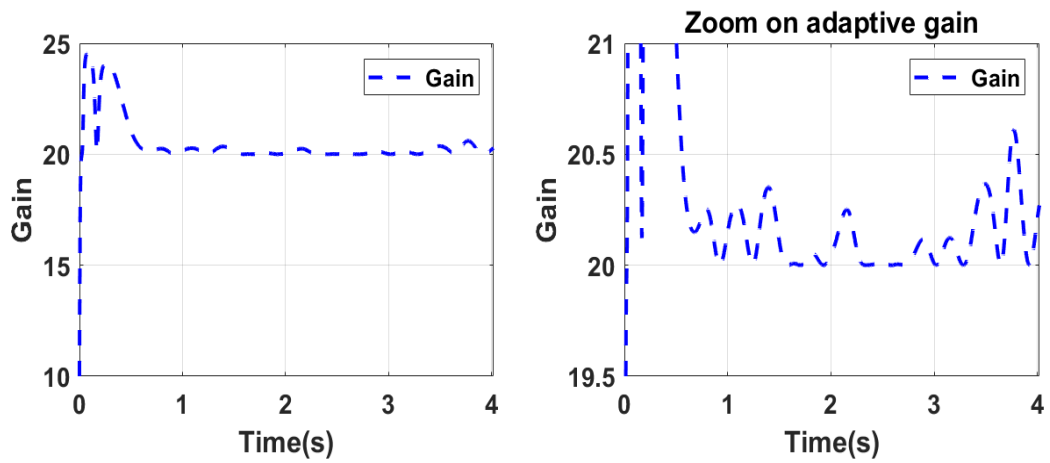


Figure 242 Adaptive gain and zoom on adaptive gain (straight line)

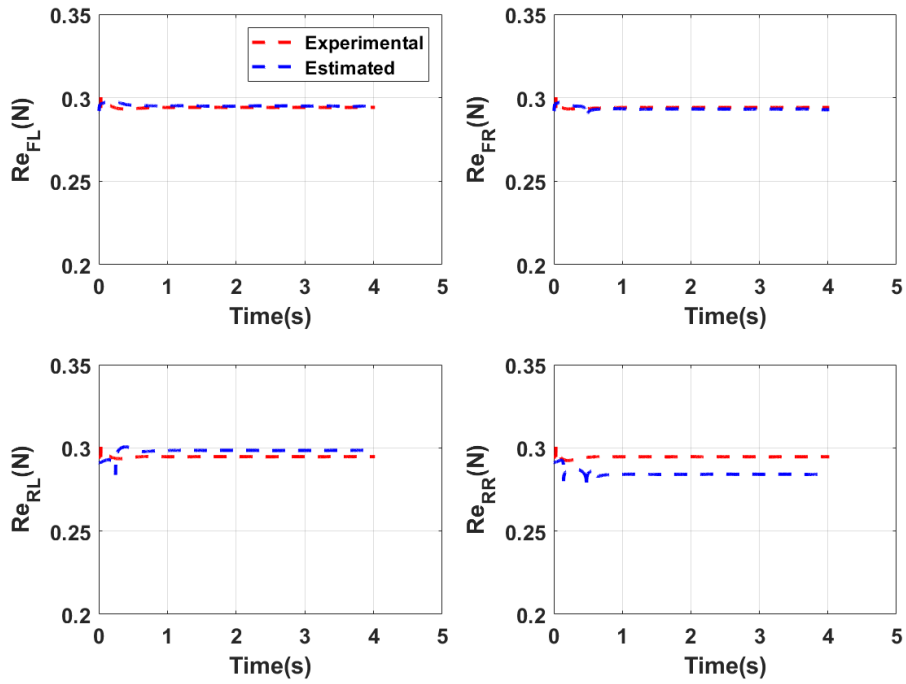


Figure 243 Comparison between experimental and estimated tyre effective radius (Straight line)

- Test 3

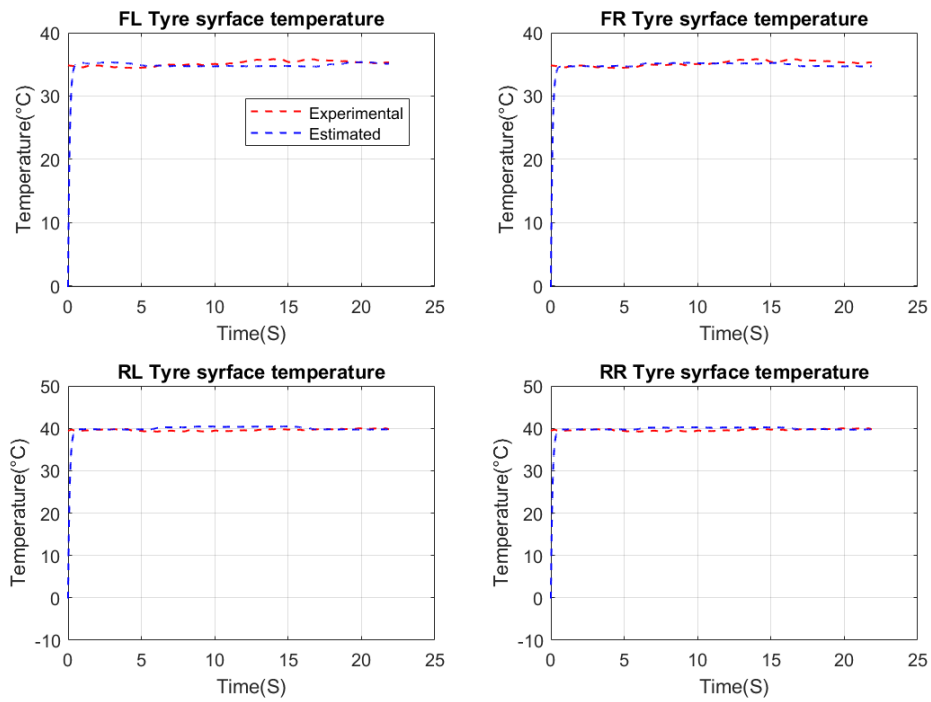


Figure 244 Tyre surface temperature state estimation comparison and percentage relative mean error (curve radius 220m at 40km/h)

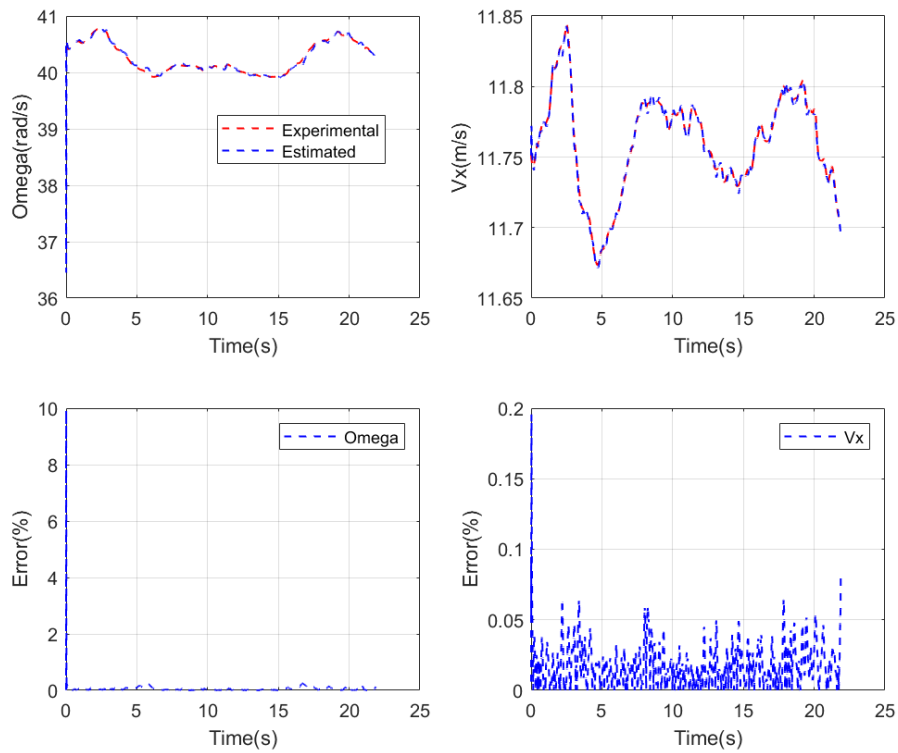


Figure 245 State variable comparison and error between experimental results and observer (curve radius 220m at 40km/h)

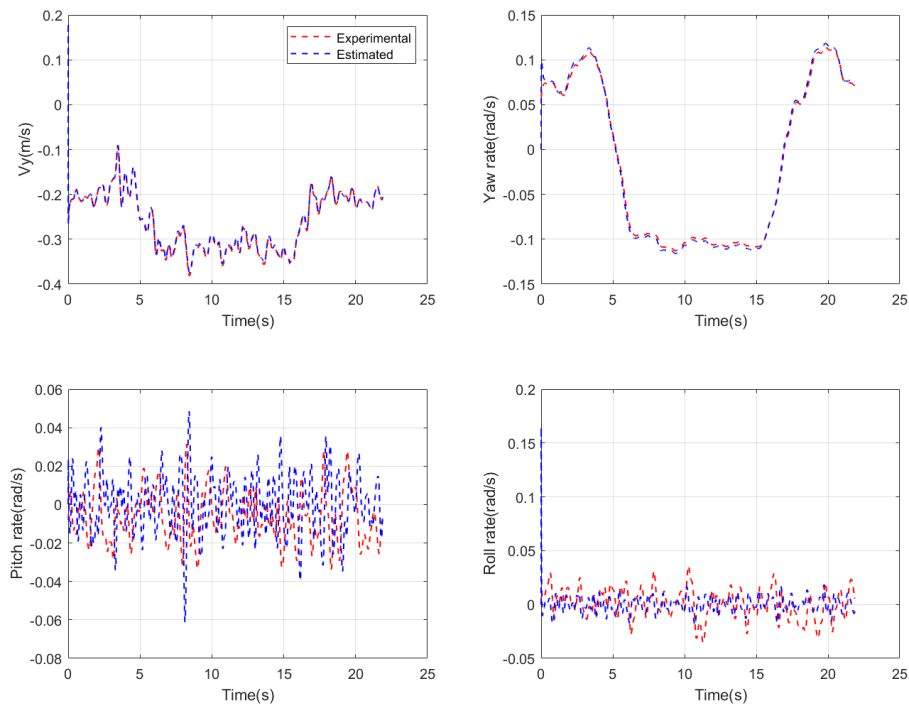


Figure 246 State variable comparison and error between experimental results and observer (curve radius 220m at 40km/h)

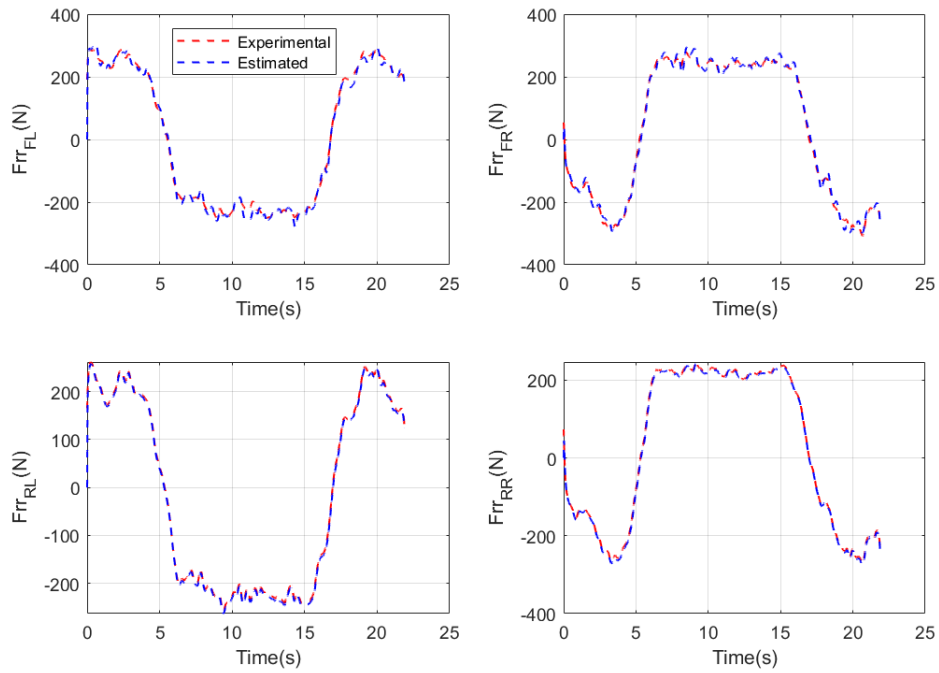


Figure 247 Comparison between experimental and estimated rolling resistance force observer (curve radius 220m at 40km/h)

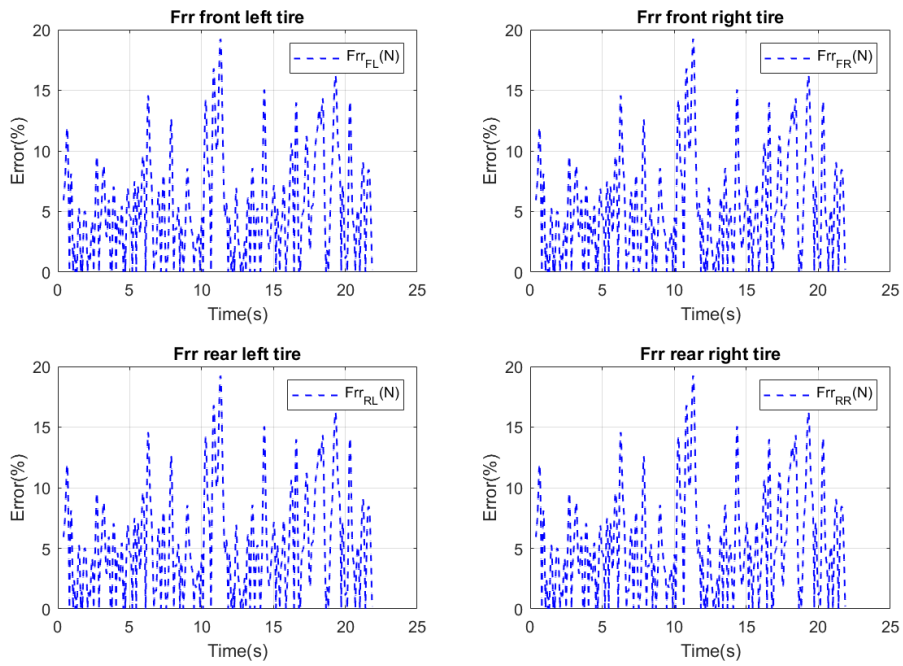


Figure 248 Estimation error results of observer estimation observer (curve radius 220m at 40km/h)

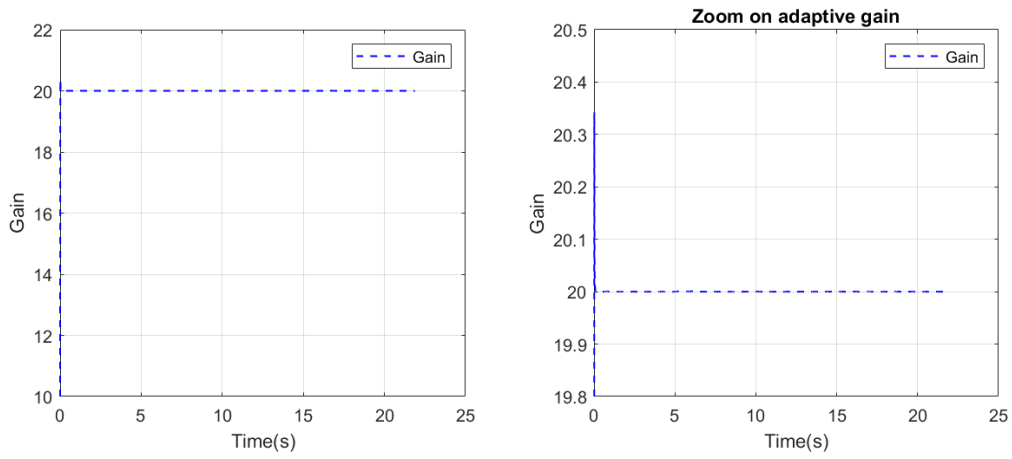


Figure 249 Adaptive gain and zoom on adaptive gain observer (lane change)

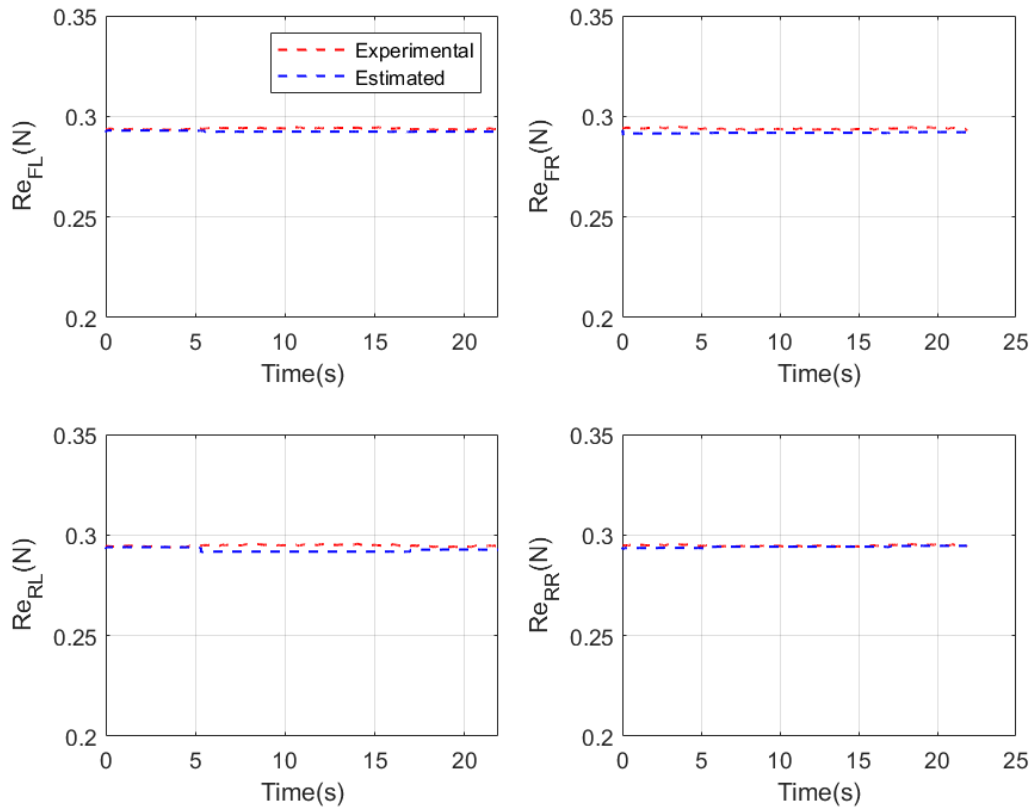


Figure 250 Comparison between experimental and estimated tyre effective radius (curve radius 220m at 40km/h)

- Test 4

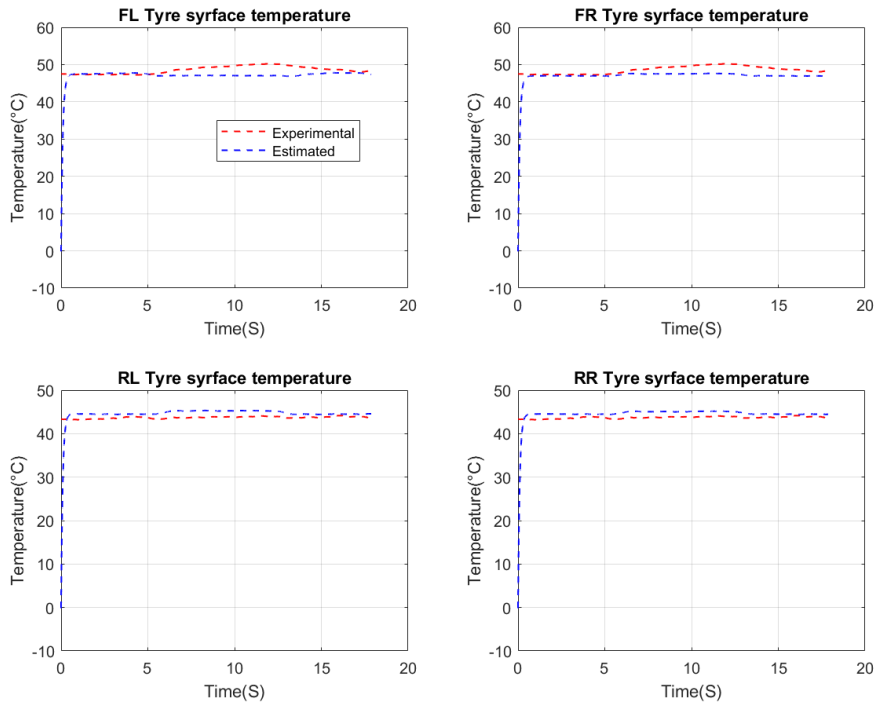


Figure 251 Tyre surface temperature state estimation comparison and percentage relative mean error (curve radius 220m at 40km/h)

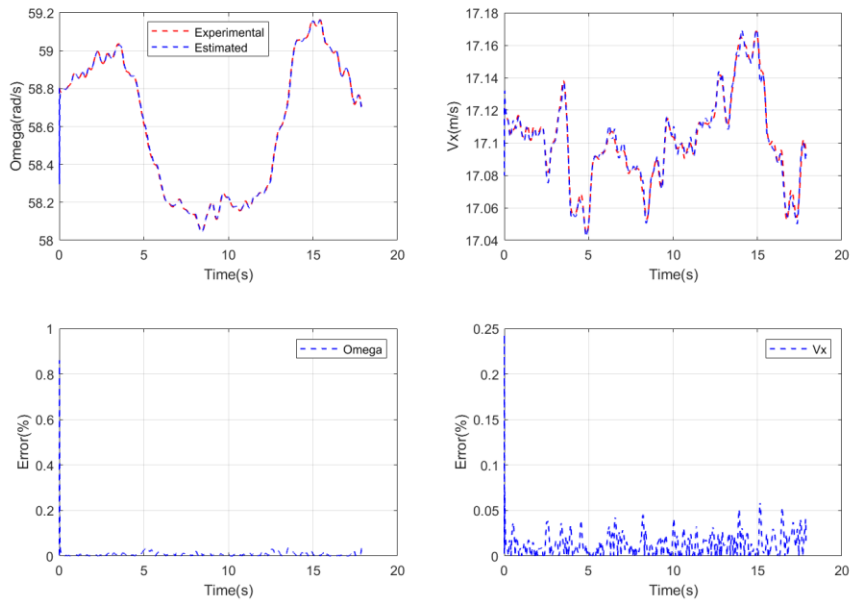


Figure 252 State variable comparison and error between experimental results and observer (curve radius 220m at 40km/h)

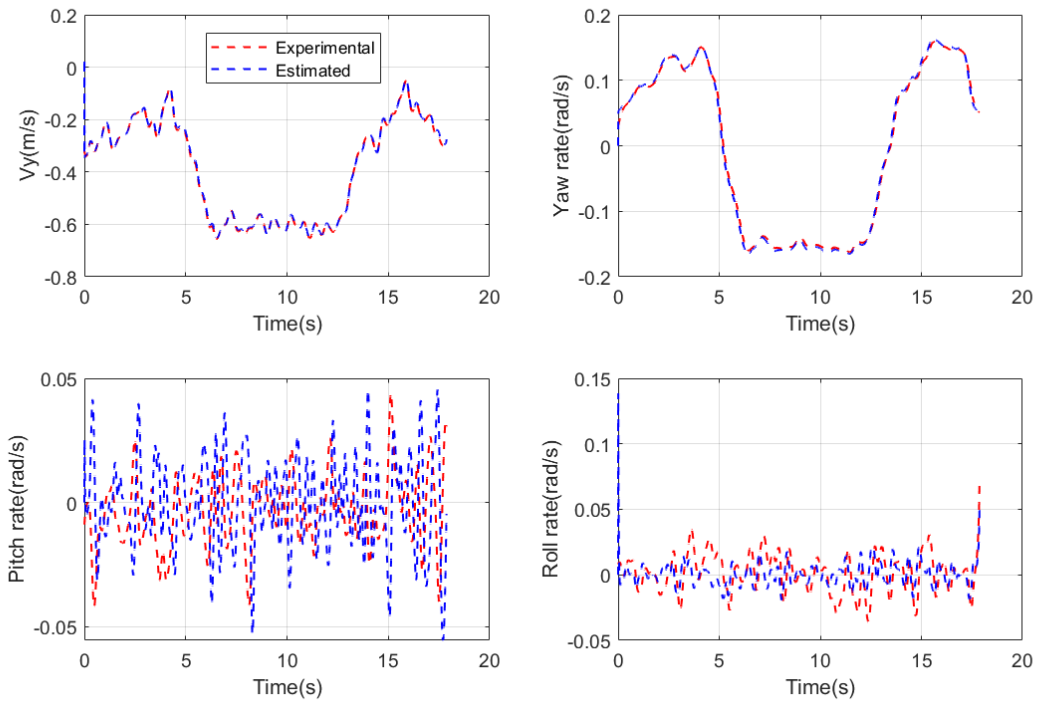


Figure 253 State variable comparison and error between experimental results and observer (curve radius 220m at 40km/h)

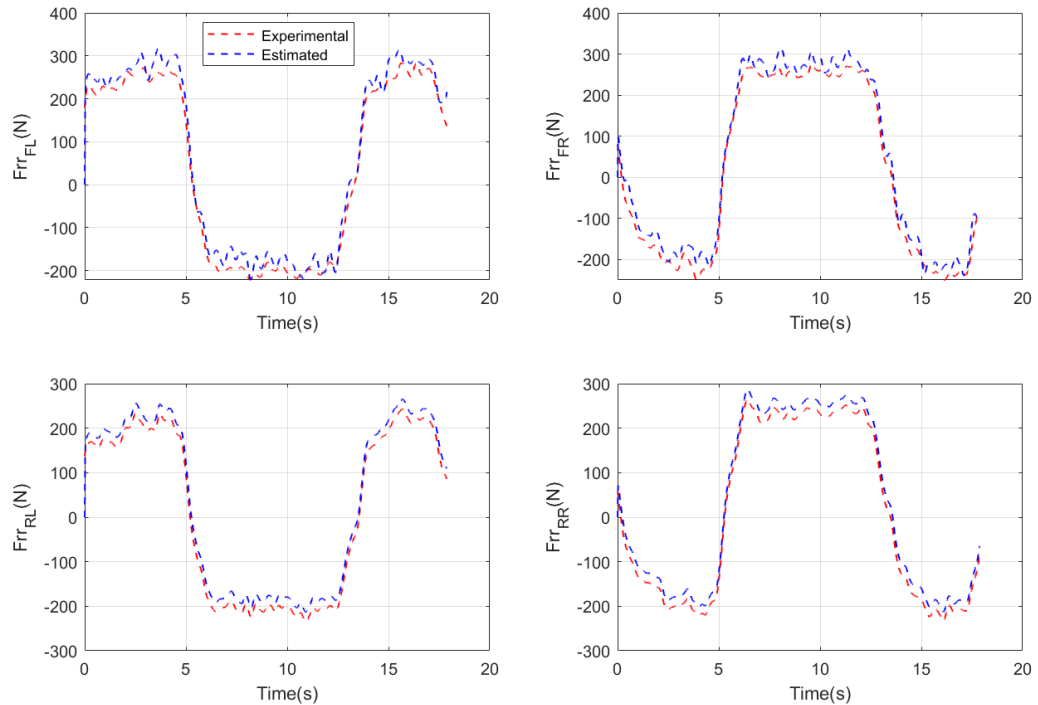


Figure 254 Comparison between experimental and estimated rolling resistance force observer (curve radius 220m at 40km/h)

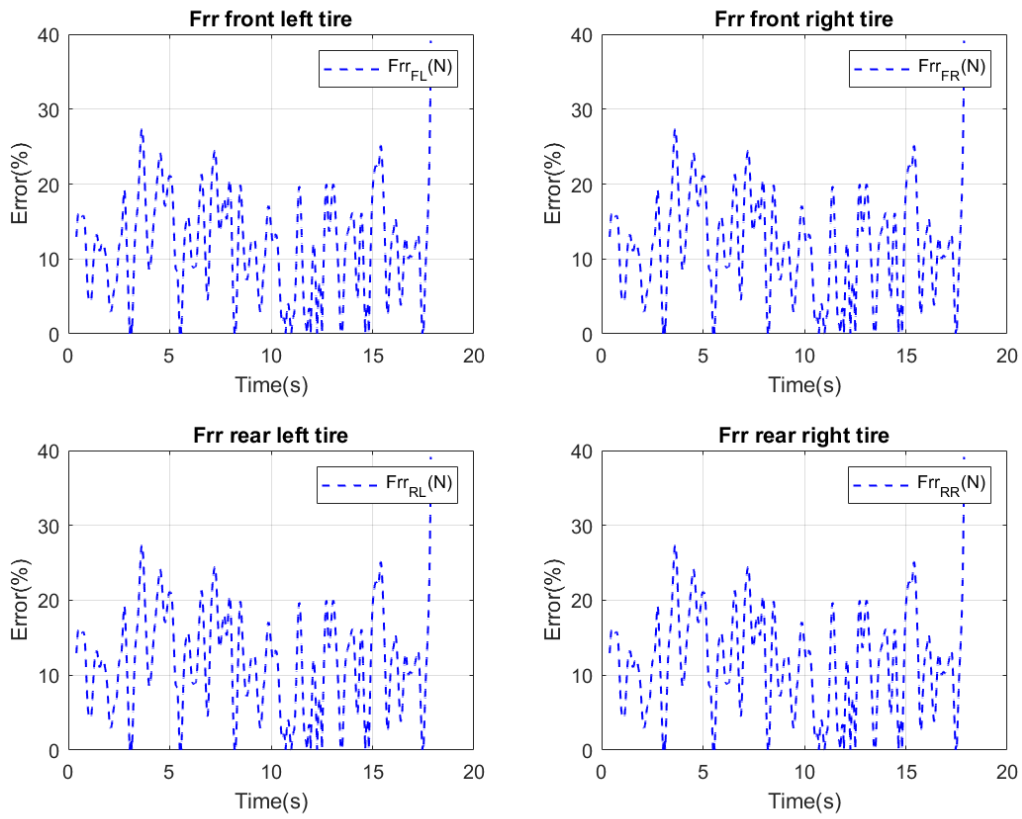


Figure 255 Estimation error results of observer estimation observer (curve radius 220m at 40km/h)

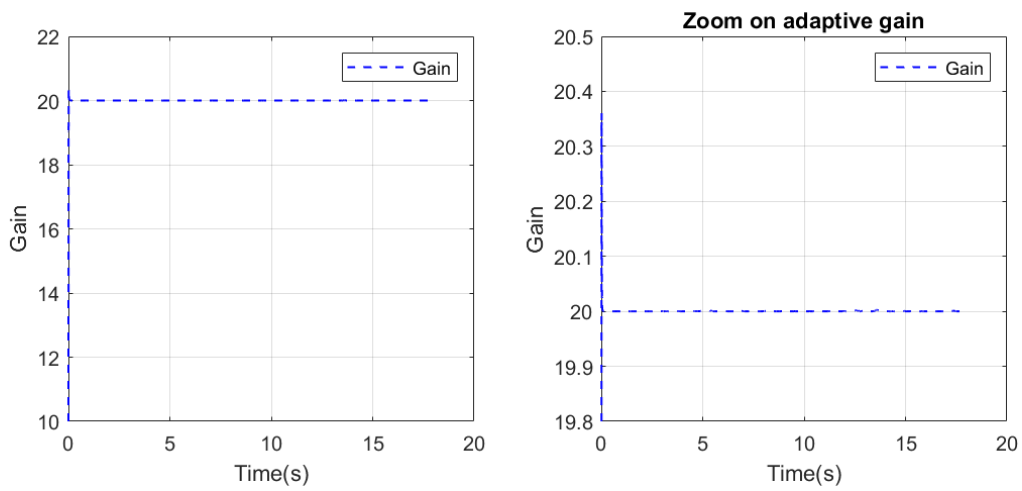


Figure 256 Adaptive gain and zoom on adaptive gain observer (lane change)

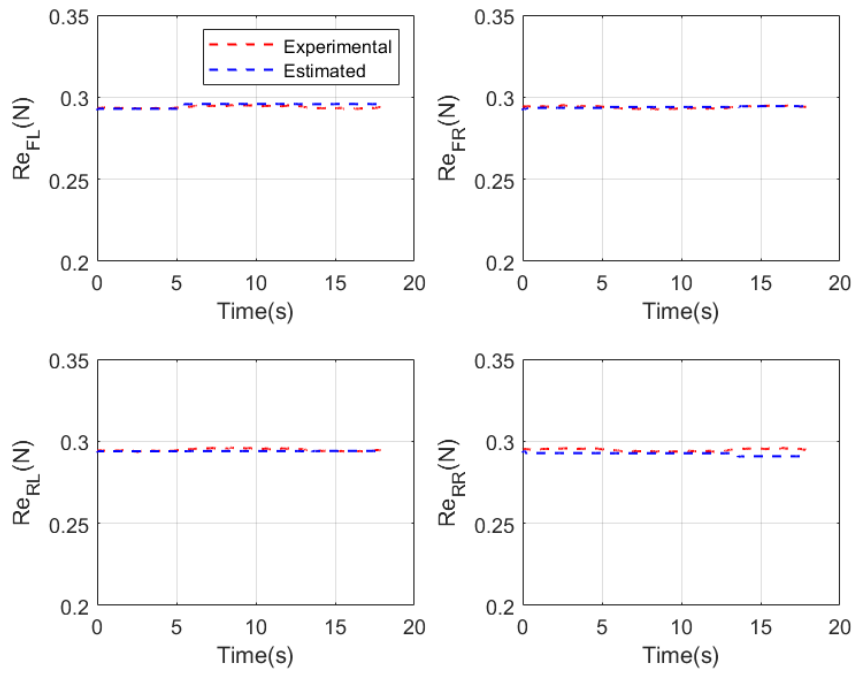


Figure 257 Comparison between experimental and estimated tyre effective radius (curve radius 220m at 40km/h)

- Test 9

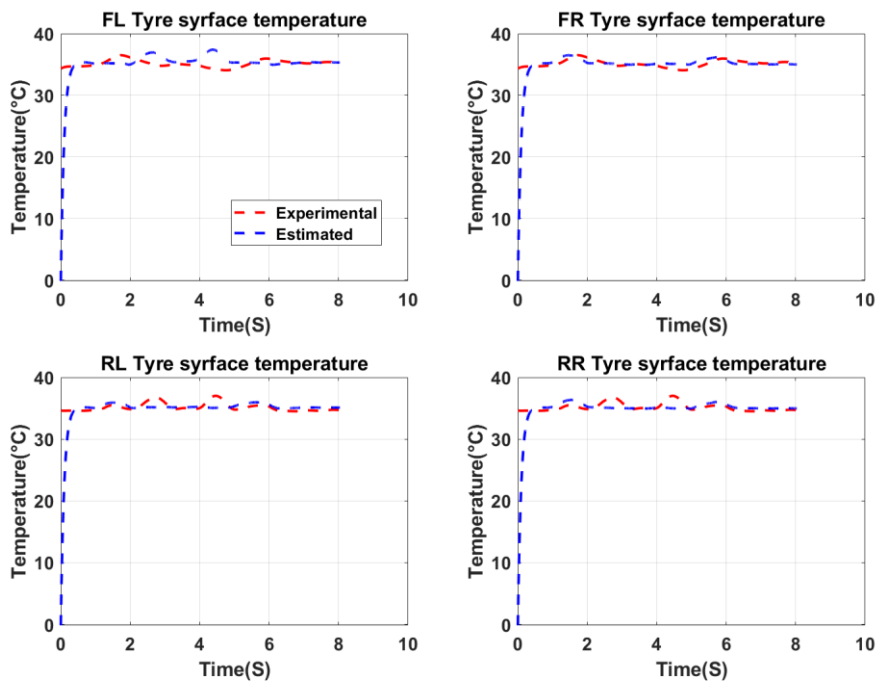


Figure 258 Tyre surface temperature state estimation comparison and percentage relative mean error (lane change)

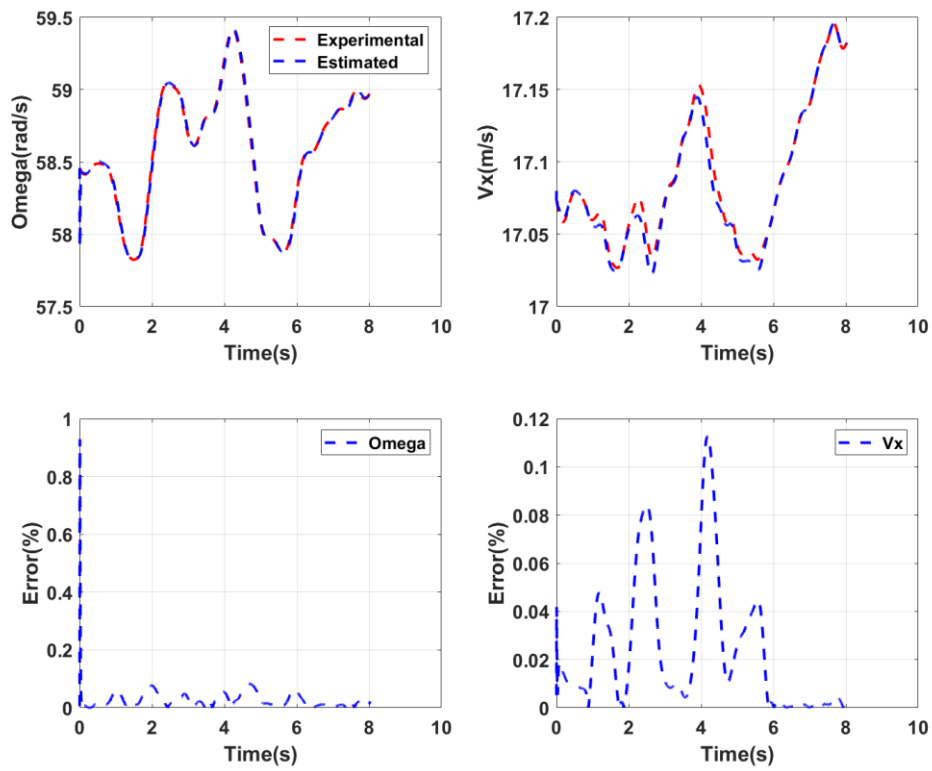


Figure 259 State variable comparison and error between experimental results and observer (lane change)

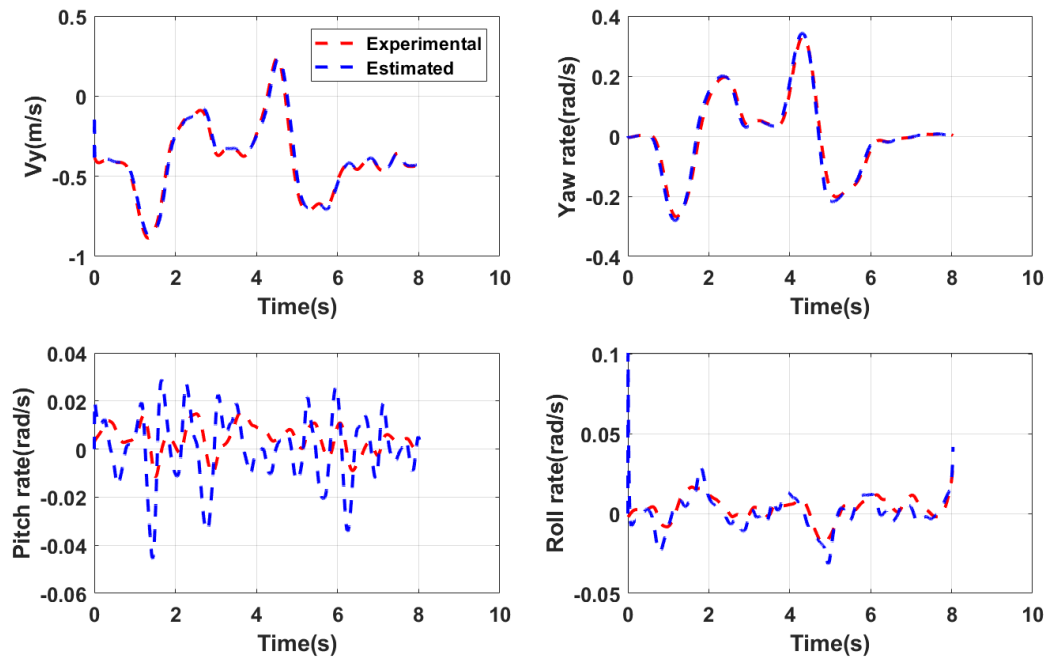


Figure 260 State variable comparison and error between experimental results and observer (lane change)

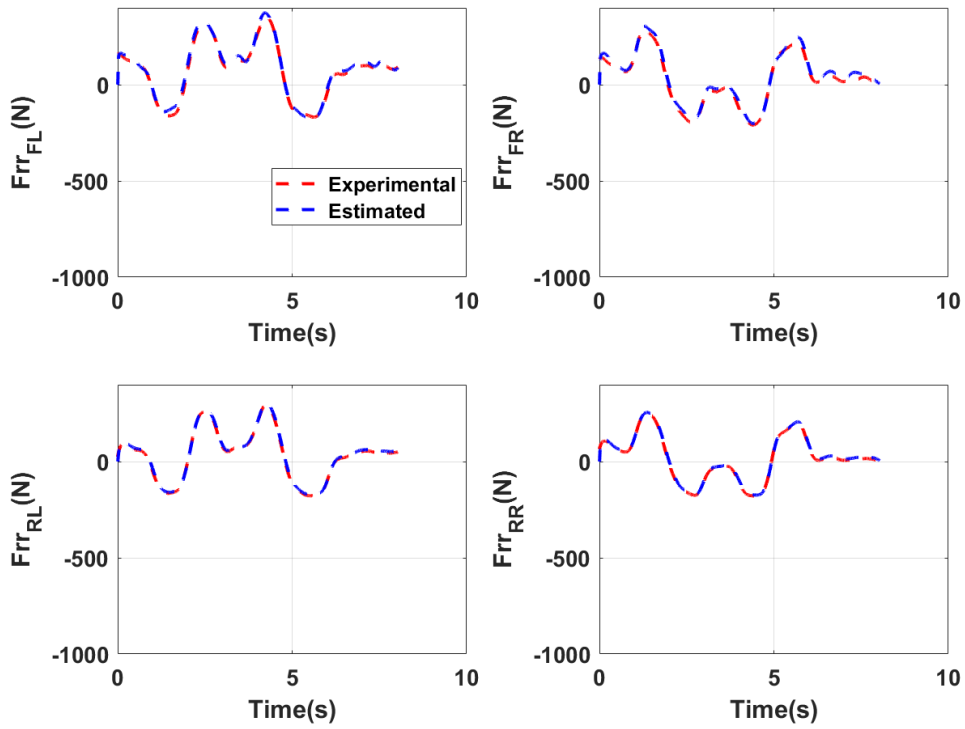


Figure 261 Comparison between experimental and estimated rolling resistance force observer (lane change)

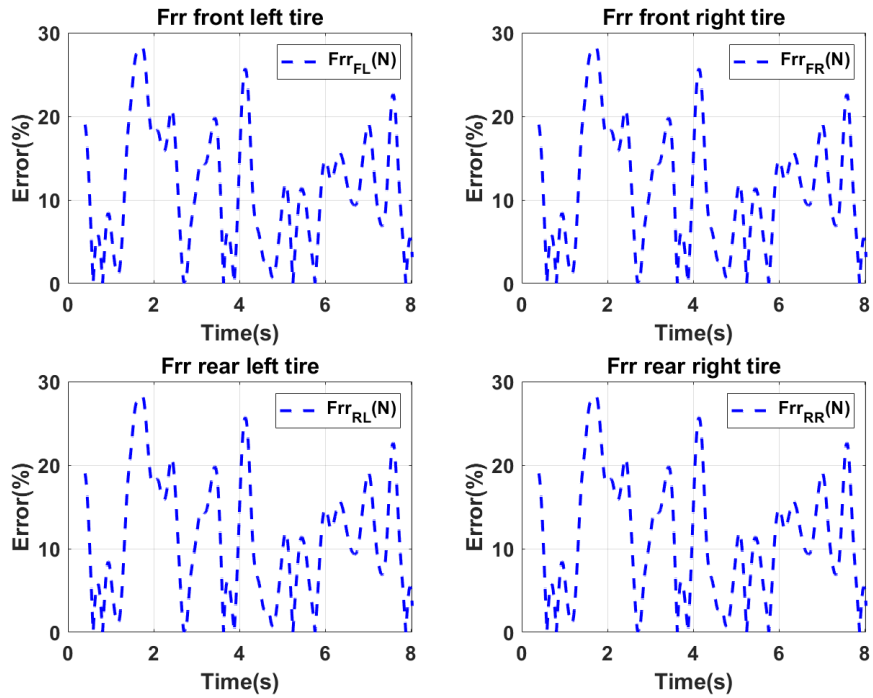


Figure 262 Estimation error results of observer estimation observer (lane change)

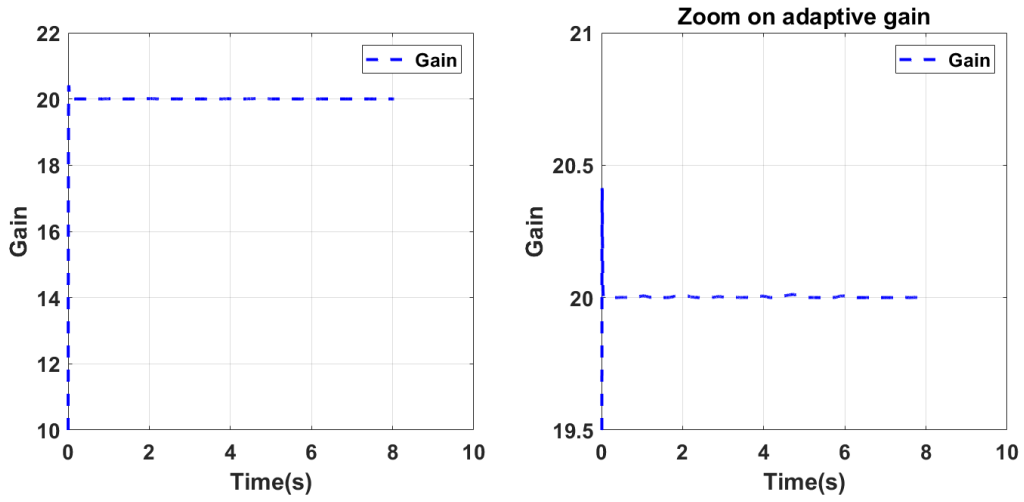


Figure 263 Adaptive gain and zoom on adaptive gain observer (lane change)

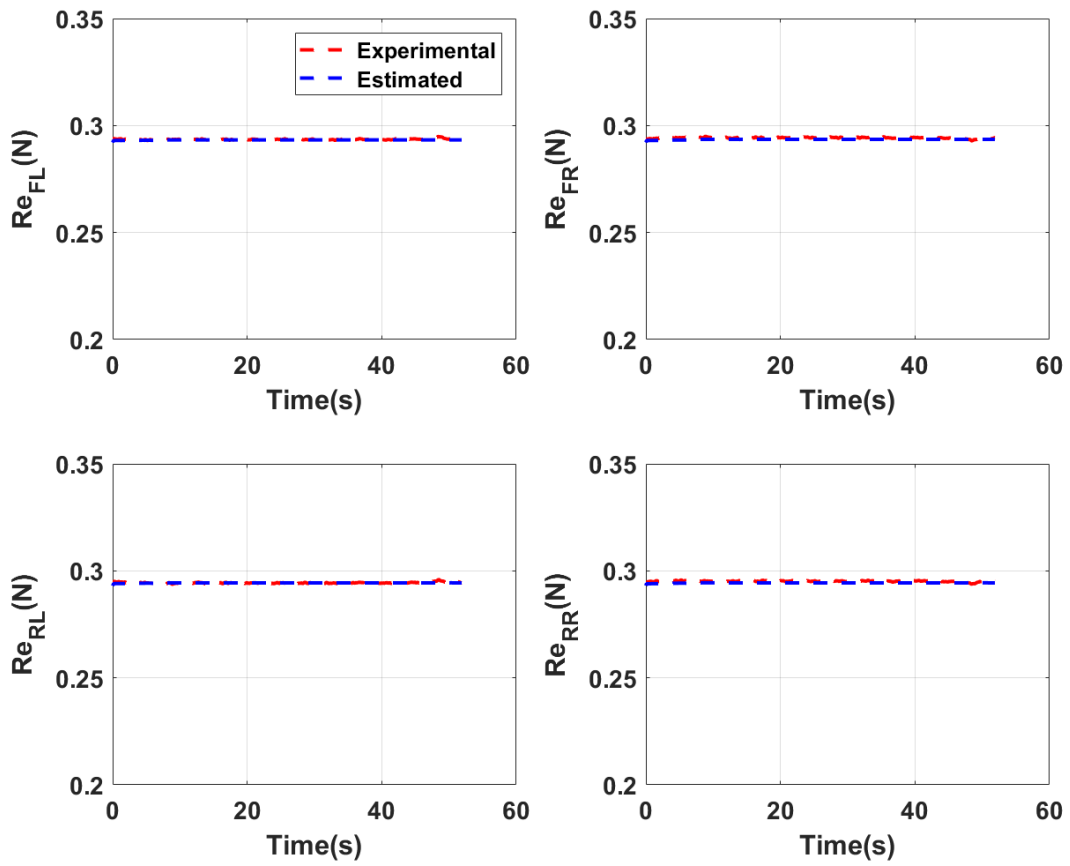


Figure 264 Comparison between experimental and estimated tyre effective radius (lane change)

Titre : Contribution à la synthèse d'observateur à gain variable pour les systèmes non linéaires: application à l'estimation de la résistance au roulement

Mots clés : Résistance au roulement, Modèle multi-physique, Observateurs de gain adaptatifs

Résumé: Les émissions de CO₂ provenant du transport routier représentent une part importante des émissions globales et contribuent au changement climatique en cours. En effet, la consommation de carburant est affectée entre autre par une source importante de perte d'énergie, représentée par la résistance au roulement liée au contact pneumatique/chaussée. Les études montrent que les pertes d'énergie liées à la résistance au roulement représentent environ 20% pour un véhicule léger. Elle est due essentiellement à la déformation répétitive du pneu et dépend fortement des paramètres du pneu tels que la pression de gonflage, la température, mais également de la dynamique du véhicule et de l'infrastructure. Elle est non mesurable directement à l'aide d'un capteur.

L'objectif principal de cette thèse est d'estimer

précisément et de manière fiable la résistance au roulement d'un véhicule en conditions réelles de conduite et en prenant en compte les caractéristiques de l'infrastructure. Pour atteindre cet objectif, une approche dite « indirecte », consiste à utiliser des capteurs logiciels, type observateur. Un modèle multi-physique du contact pneumatique /chaussée a été développé et intégré dans le modèle complet du véhicule. Un observateur à gain adaptatif est développé pour assurer une estimation précise et robuste. Cette approche d'observation a été choisie pour sa robustesse vis-à-vis des erreurs de modélisation, les incertitudes paramétriques et pour sa convergence rapide en temps fini. Une validation expérimentale sera mise en place sur les pistes de Université Gustave Eiffel, afin de valider l'approche d'estimation avec un véhicule instrumenté.

Title: Contribution to the variable gain observer synthesis for nonlinear systems: application on the estimation of tyre rolling resistance

Keywords: Rolling resistance, Multi-physical model, Adaptive gain observers

Abstract: CO₂ emissions from road transport account for a significant share of global greenhouse gas emissions and therefore contribute to on-going climate change. In fact, fuel consumption is influenced by one of major source of energy loss among others, represented by the rolling resistance linked to tyre/road contact. Studies show that energy losses due to rolling resistance represent approximately 20% for a light vehicle. It is mainly due to the repetitive deformation of the tyre. It is highly dependent on tyre parameters such as inflation pressure, load, speed and temperature, but also on vehicle dynamics and characteristics of the infrastructure. It is not directly measurable with a physical sensor. The main objective of this thesis is to develop a system for the estimation of the tyre rolling resistance of a vehicle in real driving conditions.

In order to achieve this objective, an indirect approach of estimation by using software sensor such observer. A multi-physical model of the tyre/road contact has been developed to integrate the various influencing parameters of rolling resistance and coupled with the full vehicle model. Indeed, the complexity of the model and the driving situations make this estimation difficult. Therefore, a variable gain (adaptive) unknown input observer is developed to ensure an accurate and robust estimation. This observation approach has been chosen for its robustness against modeling errors, parametric uncertainties and for its rapid convergence in finite time. An offline experimental validation is done on the test tracks of University Gustave Eiffel, Nantes in order to validate the estimation approach with an instrumented vehicle.